

# **Gas atomized precursor alloy powder for oxide dispersion strengthened ferritic stainless steel**

by

**Joel Rodney Rieken**

A dissertation submitted to the graduate faculty  
in partial fulfillment of the requirements for the degree of  
DOCTOR OF PHILISOPHY

Major: Materials Science and Engineering

Program of Study Committee:

Iver Anderson, Major Professor

Matthew Kramer

Scott Chumbley

Xiaoli Tan

Frank Peters

Iowa State University

Ames, Iowa

2011

Copyright © Joel Rodney Rieken, 2011. All rights reserved.

Dedicated to Lisa,  
my wife and best friend

## Table of Contents

<b>LIST OF FIGURES .....</b>	<b>IX</b>
<b>LIST OF TABLES.....</b>	<b>XXIII</b>
<b>ABSTRACT.....</b>	<b>XXVI</b>
<b>CHAPTER 1. INTRODUCTION .....</b>	<b>1</b>
1.1 THESIS ORGANIZATION.....	1
1.2 PURPOSE OF STUDY.....	2
<b>CHAPTER 2. STRUCTURAL MATERIALS FOR FUTURE GENERATION</b>	
<b>POWER PLANTS .....</b>	<b>5</b>
2.1 WORLD ENERGY CONCERNS.....	5
2.2 FUTURE GENERATION POWER REACTORS.....	6
2.2.1 <i>Ultra Supercritical Coal-Fired Power Reactors</i> .....	6
2.2.2 <i>Future Generation Nuclear Reactors</i> .....	8
2.3 MATERIAL SELECTION.....	14
2.3.1 <i>Ultra Supercritical Coal-Fired Reactors</i> .....	14
2.3.2 <i>Generation IV Nuclear Fission Reactors and First Generation Fusion Reactors</i> .....	16
<b>CHAPTER 3. OXIDE DISPERSION STRENGTHENING .....</b>	<b>38</b>
3.1 OXIDE DISPERSION STRENGTHENING MECHANISMS .....	38
3.1.1 <i>Strengthening Mechanisms</i> .....	38
3.2 ODS CREEP RESISTANCE.....	49
3.2.1 <i>Creep in Oxide Dispersion Strengthened Materials</i> .....	53
3.3 OXIDE PARTICLE FORMATION AND GROWTH .....	57
3.3.1 <i>Precipitation</i> .....	57
3.3.2 <i>Precipitate Growth</i> .....	59
3.3.3 <i>Precipitate Coarsening</i> .....	59
3.3.4 <i>Summary</i> .....	62
3.4 MECHANICAL ALLOYING.....	62
3.4.1 <i>Mechanical Alloying Process</i> .....	63
3.4.2 <i>Problems with Mechanical Alloying</i> .....	64
3.5 FE-BASED OXIDE DISPERSION STRENGTHENED ALLOYS.....	66

3.5.1	<i>Mechanical Alloying Process and Consolidation .....</i>	66
3.5.2	<i>Macrostructure and Microstructure .....</i>	67
3.5.3	<i>Recrystallization of Deformed ODS Microstructures.....</i>	69
3.5.4	<i>Mechanical Properties .....</i>	70
3.5.5	<i>Precipitate Thermal Stability.....</i>	73
3.6	<b>ADVANCED NANOSTRUCTURED FERRITIC ALLOYS (NFAs).....</b>	75
3.6.1	<i>Mechanical Alloying Process and Particulate Consolidation.....</i>	75
3.6.2	<i>NFA Microstructure .....</i>	77
3.6.3	<i>Mechanical Properties .....</i>	81
3.6.4	<i>Thermal Stability and Coarsening of Nanoclusters.....</i>	85
3.6.5	<i>Irradiation Resistance.....</i>	88
3.6.6	<i>Summary .....</i>	90
<b>CHAPTER 4. GAS ATOMIZATION REACTION SYNTHESIS (GARS)</b>		
<b>PROCESSING.....</b>		<b>91</b>
4.1	<b>CHEMICAL RESERVOIR (CR) ALLOYS .....</b>	93
4.1.1	<i>GARS Processing Parameters .....</i>	98
4.1.2	<i>Resulting Oxygen Content.....</i>	106
4.2	<b>THEORETICAL PARTICLE COOLING CURVES.....</b>	111
4.2.1	<i>Droplet Model.....</i>	112
4.2.2	<i>Cooling Curves.....</i>	120
4.2.3	<i>Solidification Curves .....</i>	124
4.3	<b>GARS OXIDATION MODEL .....</b>	126
4.4	<b>SUMMARY .....</b>	130
4.5	<b>ACKNOWLEDGMENTS.....</b>	131
4.6	<b>VARIABLE IDENTIFICATION.....</b>	132
<b>CHAPTER 5. HEAT TREATMENT.....</b>		<b>136</b>
5.1	<b>INTERNAL OXIDATION PROCEDURE .....</b>	136
5.1.1	<i>Internal Oxidation Model.....</i>	140
5.1.2	<i>Reaction Kinetics .....</i>	145
5.2	<b>SUMMARY .....</b>	149
5.3	<b>ACKNOWLEDGEMENTS.....</b>	149



## CHAPTER 6. ATOMIZED PRECURSOR ALLOY POWDER FOR OXIDE

### DISPERSION STRENGTHENED FERRITIC STAINLESS STEEL ..... 150

6.1	ABSTRACT .....	150
6.2	INTRODUCTION.....	151
6.3	BACKGROUND .....	152
6.3.1	<i>Mechanical alloying (MA)</i> .....	152
6.3.2	<i>Innovative molten ODS processing</i> .....	153
6.4	EXPERIMENTAL METHODS .....	155
6.4.1	<i>Gas Atomization and Powder Consolidation</i> .....	155
6.4.2	<i>Mechanical Testing</i> .....	156
6.4.3	<i>Electron Microscopy and Synchrotron Analysis</i> .....	157
6.5	RESULTS .....	158
6.5.1	<i>As-consolidated Microstructure</i> .....	160
6.5.2	<i>Initial Dispersoid Analysis</i> .....	161
6.5.3	<i>Preliminary Mechanical Properties</i> .....	163
6.6	DISCUSSION .....	165
6.6.1	<i>As-Atomized Powders</i> .....	165
6.6.2	<i>Dispersoid Formation</i> .....	166
6.6.3	<i>Initial Mechanical Properties (Tensile Strength)</i> .....	168
6.7	SUMMARY .....	168
6.8	ACKNOWLEDGEMENTS.....	169

## CHAPTER 7. MICROSTRUCTURE EVOLUTION OF GAS-ATOMIZED FE-

### BASED ODS ALLOYS..... 170

7.1	ABSTRACT .....	170
7.2	INTRODUCTION.....	171
7.3	BACKGROUND .....	172
7.4	EXPERIMENTAL METHODS .....	172
7.4.1	<i>Gas Atomization Reaction Synthesis</i> .....	172
7.4.2	<i>Consolidation</i> .....	173
7.4.3	<i>Electron Microscopy</i> .....	174
7.4.4	<i>Synchrotron Phase Analysis</i> .....	174
7.5	EXPERIMENTAL RESULTS.....	175
7.5.1	<i>Chemical Reservoir Alloy Composition</i> .....	175

7.5.2	<i>Alloy CR-112 Microstructure .....</i>	<i>175</i>
7.5.3	<i>Alloy CR-118 Microstructure .....</i>	<i>178</i>
7.5.4	<i>Alloy CR-126 Microstructure .....</i>	<i>181</i>
7.5.5	<i>Synchrotron Phase Analysis.....</i>	<i>184</i>
7.6	DISCUSSION .....	187
7.6.1	<i>As-atomized Surface Oxide .....</i>	<i>188</i>
7.6.2	<i>CR-Alloy Microstructure Evolution .....</i>	<i>190</i>
7.7	FUTURE PLANS AND TECHNOLOGY OUTLOOK .....	191
7.8	SUMMARY .....	194
7.9	ACKNOWLEDGEMENTS.....	195
 <b>CHAPTER 8. GAS ATOMIZED CHEMICAL RESERVOIR ODS FERRITIC STAINLESS STEELS .....</b>		<b>196</b>
8.1	ABSTRACT .....	196
8.2	INTRODUCTION.....	197
8.3	PROCEDURE .....	198
8.3.1	<i>Gas Atomization Reaction Synthesis (GARS) .....</i>	<i>198</i>
8.3.2	<i>Consolidation.....</i>	<i>200</i>
8.3.3	<i>Heat Treatment.....</i>	<i>200</i>
8.3.4	<i>Electron Microscopy.....</i>	<i>201</i>
8.3.5	<i>X-ray Diffraction .....</i>	<i>201</i>
8.4	EXPERIMENTAL RESULTS.....	202
8.4.1	<i>Reactive Gas Atomization Processing .....</i>	<i>202</i>
8.4.2	<i>As-Atomized Microstructure Analysis .....</i>	<i>203</i>
8.4.3	<i>As-Consolidated Microstructure Analysis.....</i>	<i>205</i>
8.4.4	<i>As-Reacted Microstructure Analysis .....</i>	<i>207</i>
8.4.5	<i>X-ray Diffraction Analysis.....</i>	<i>212</i>
8.5	DISCUSSION .....	214
8.5.1	<i>Gas Atomization Reaction Synthesis .....</i>	<i>214</i>
8.5.2	<i>Microstructure Analysis .....</i>	<i>215</i>
8.5.3	<i>Dispersoid Stability .....</i>	<i>219</i>
8.6	SUMMARY .....	221
8.7	ACKNOWLEDGEMENTS.....	221

## CHAPTER 9. INNOVATIVE POWDER PROCESSING OF OXIDE DISPERSION

### STRENGTHENED (ODS) FERRITIC STAINLESS STEELS ..... 222

9.1	ABSTRACT .....	222
9.2	INTRODUCTION.....	223
9.3	PROCEDURE .....	224
9.3.1	<i>Gas Atomization Reaction Synthesis</i> .....	224
9.3.2	<i>Hot Consolidation and Thermal Treatment</i> .....	225
9.3.3	<i>Microstructure Characterization</i> .....	226
9.4	RESULTS .....	228
9.4.1	<i>Gas Atomization Reaction Synthesis</i> .....	228
9.4.2	<i>Dispersoid Formation</i> .....	231
9.4.3	<i>Dispersoid Thermal Stability</i> .....	234
9.4.4	<i>Phase Identification</i> .....	236
9.4.5	<i>Microhardness Evaluation</i> .....	239
9.5	DISCUSSION .....	241
9.5.1	<i>Gas Atomization Reaction Synthesis</i> .....	241
9.5.2	<i>Dispersoid Formation</i> .....	243
9.5.3	<i>Thermal Stability</i> .....	245
9.6	SUMMARY .....	248
9.7	ACKNOWLEDGEMENTS.....	249

## CHAPTER 10. REACTIVE GAS ATOMIZATION PROCESSING FOR FE-BASED

### ODS ALLOYS ..... 250

10.1	ABSTRACT .....	250
10.2	INTRODUCTION.....	251
10.3	EXPERIMENTAL .....	252
10.4	RESULTS .....	257
10.4.1	<i>As-atomized microstructure</i> .....	257
10.4.2	<i>As-HIPed microstructure</i> .....	261
10.4.3	<i>As-reacted microstructure</i> .....	264
10.4.4	<i>Microhardness evaluation</i> .....	266
10.5	FURTHER EVALUATION, ANALYSIS AND DISCUSSION .....	269
10.5.1	<i>GARS process control</i> .....	269
10.5.2	<i>Microstructural evolution</i> .....	270

10.5.3	<i>Dislocation substructure</i> .....	276
10.6	SUMMARY .....	278
10.7	ACKNOWLEDGEMENTS.....	279
<b>CHAPTER 11. A NOVEL FE-BASED ODS FABRICATION PROCESS .....</b>		<b>280</b>
11.1	ABSTRACT .....	280
11.2	INTRODUCTION.....	281
11.3	EXPERIMENTAL .....	282
11.4	RESULTS .....	287
11.4.1	<i>As-Atomized Powders</i> .....	287
11.4.2	<i>Oxide Dispersoid Formation</i> .....	291
11.4.3	<i>Thermal-Mechanical Treatment (TMT)</i> .....	295
11.4.4	<i>Initial Mechanical Properties</i> .....	298
11.5	DISCUSSION .....	301
11.5.1	<i>Precursor Powder Formation</i> .....	301
11.5.2	<i>Microstructure Evolution</i> .....	303
11.5.3	<i>Thermal Mechanical Treatment (TMT)</i> .....	303
11.5.4	<i>Mechanical Properties</i> .....	305
11.6	SUMMARY .....	306
11.7	ACKNOWLEDGEMENTS.....	307
<b>CHAPTER 12. GENERAL CONCLUSIONS .....</b>		<b>309</b>
<b>FINAL ACKNOWLEDGMENTS .....</b>		<b>313</b>
<b>REFERENCES.....</b>		<b>314</b>

## List of Figures

Figure 2.1. Schematic illustrating the working of a heat engine [18].....	6
Figure 2.2. H <sub>2</sub> O temperature and pressure phase diagram [19].....	7
Figure 2.3. Ultra supercritical coal-fired power plant schematic [23] .....	8
Figure 2.4. Evolution of USA fission reactors [16] .....	10
Figure 2.5. Schematic of generation IV supercritical-water-cooled fission reactor [16].....	11
Figure 2.6 ITER demonstration device for the use of fusion power [28].....	12
Figure 2.7. Deuterium-Tritium fusion reaction [29].....	13
Figure 2.8 Basic design of a theoretical fusion power plant [29].....	14
Figure 2.9. Yield strength (a) and rupture life stress tests (b) for possible structural materials [31] .....	15
Figure 2.10. Yield strength (a) and ultimate tensile strength (b) as a function of temperature for Fe-based ODS commercial alloys (MA956 and PM2000) and advanced nanostructured ferritic alloys (MA957 and 12YWT) [1] .....	16
Figure 2.11 Radiation damage phenomena normalized to material melting temperature [35].....	18
Figure 2.12. Power density capability of proposed structural materials [42].....	22
Figure 2.13. A relative comparison of tensile strength (orange), thermal conductivity (blue), elastic modulus (green), and thermal expansion (red) for potential nuclear reactor structural materials [43-48].....	24
Figure 2.14. Relative power density comparison for potential structural component materials, based on material properties found in the literature [1, 43-48].....	25
Figure 2.15. Larson-Miller plot for a select group of radiation resistant materials [36].....	26
Figure 2.16. Larson-Miller plot for Fe-based ODS ferritic alloys [1] .....	26
Figure 2.17. Parabolic scaling constants for different oxides [51] .....	28
Figure 2.18. Radiation induced swelling for different structural materials as a function of displacement dose [57].....	29

Figure 2.19. Neutron induced $\alpha$ -particle production cross-sections in pure Fe (a) and pure Ni (b) [64] .....	31
Figure 2.20. Operating temperature window for reactor structural materials [65] .....	32
Figure 2.21. Calculated radioactivity as a function of time after reactor shutdown [67] .....	35
Figure 3.1. A random arrangement of obstacles in a dislocation slip plane, highlighting the obstacle spacing (L) and critical bend angle $\Phi_c$ [3] .....	39
Figure 3.2. Illustrating the Orowan process, when dislocations bend between particles (a), bypassing the particles leaving a dislocation loop (b), highlighting dislocation screw (c), and edge (d) type [70] .....	41
Figure 3.3. Orowan theoretical model predictions compared with experimental results: (A) single crystal copper containing $Al_2O_3$ or BeO oxide dispersoids and (B) polycrystalline Co-Ni-Cr superalloy with $Ni_3Ti$ precipitates (verification of Orowan looping was performed using transmission electron microscopy) [74, 75] .....	43
Figure 3.4. The work hardening rate for precipitate strengthened Cu-Be with shearable particles (a), oxide dispersion hardened Cu-BeO with non-shearable particles (b), and pure copper (c) [76] .....	44
Figure 3.5. Flow-stress of TD-Ni and pure Ni as a function of temperature [78] .....	45
Figure 3.6. Typical creep deformation curve with a constant applied load, adapted from [85] .....	50
Figure 3.7. Creep deformation mechanism map for pure polycrystalline materials [85] .....	52
Figure 3.8. Weak beam TEM micrograph identifying a dislocation attached to a dispersoid particle in dispersion strengthened MA6000 [90] .....	54
Figure 3.9. The normalized creep rate as a function of stress for fine grained dispersion strengthened Al-2.16C-0.80O (wt.%) [91] .....	56
Figure 3.10. Change in Gibbs free energy as a function of nucleus size (A) and thermodynamic nucleation barrier comparison for homogeneous and heterogeneous nucleation (B) [92] .....	58
Figure 3.11. Mechanical milling followed by hot deformation processing for the formation of an ODS microstructure [12] .....	63

Figure 3.12. Microstructural evolution during mechanical milling of both ductile and brittle powders (typical of ODS alloys) [101] .....	64
Figure 3.13. Relative processing rate comparison between MA processing and RSP (i.e., gas atomization) [103, 104] .....	65
Figure 3.14. Mechanically alloyed Fe-based ODS processing method [108] .....	67
Figure 3.15. As-received MA956 rod macrostructure: (a) transverse section and (b) longitudinal section highlighting the long columnar grains [4] .....	68
Figure 3.16. ODS microstructure of as-received (a) PM2000 and (b) MA956 [4, 110] .....	68
Figure 3.17. Nucleation of grain recrystallization in as-consolidated MA ODS materials, illustrating that grain boundary junctions act as barriers to grain boundary bulge formation [112] .....	69
Figure 3.18. Bright field TEM image of the dislocation substructure found in MA 956 after 47% cross-section reduction with a recovery anneal at 800°C for 1 hour [5] .....	70
Figure 3.19. Elevated temperature yield (dashed) and tensile (solid) strength (A) and total elongation (B) comparison of Fe-based ODS MA956 (red) and PM2000 (blue) [106, 107] .....	72
Figure 3.20. Creep resistance of Fe-based ODS alloys MA956 and PM2000 compared to Ni-based superalloys IN 100 (precipitate strengthened) and IN 617 (solid solution strengthened) [105] .....	73
Figure 3.21. Coarsening rate of Y-Al mixed oxide precipitates at 1350°C found in Fe-based ODS MA956 and PM2000 [109] .....	74
Figure 3.22. Bright field TEM images used to characterize precipitate stability and coarsening rate at 1350°C for Fe-based ODS PM2000 (blue a=1hr, b=6hr, and c=607hr) and MA956 (red d=1hr, f=6hr, and e=607hr) [109] .....	74
Figure 3.23. Schematic of the mechanical alloying, consolidation, and subsequent working and heat treatment process for the formation of a NFA [9] .....	76
Figure 3.24. NFA microstructural evaluation of cluster radius (r), volume fraction (f), number density (N), and Vickers hardness (DPH) [119] .....	77
Figure 3.25. Microstructure of as-consolidated NFA MA957 highlighting the dislocation substructure (A) and dispersoid distribution (B) [121] .....	79

Figure 3.26. Grain structure of as-consolidated MA957 (A) and as-recrystallized (1400°C) MA957 (B) [111] .....	80
Figure 3.27. Vickers hardness values for various Fe-based and NFAs consolidated at different temperatures (red = 850°C and blue = 1150°C) [13, 68, 119] .....	82
Figure 3.28. Tensile strength (A) and total elongation (B) values as a function of temperature for NFAs MA957 and 12YWT compared to Fe-based ODS alloys 12Y1, MA956, and PM2000 [1] .....	83
Figure 3.29. Yield strength values as a function of temperature for NFA MA957 in the cold-worked (CW), as-extruded, and recrystallized condition (A) and creep resistance properties found in fine-grained and recrystallized MA957 compared to austenitic stainless steel (15/15Ti) and ferritic/martensitic stainless steel (EM12) (B) [123].....	84
Figure 3.30. Atom probe tomography (APT) elemental maps of MA957 comparing the coarsening of nano-cluster particles in the as-consolidated condition (A) and annealed at 1300°C for 24hrs condition (B) [117].....	86
Figure 3.31. Nano-cluster stability analysis of alloy 14YWT at 1000°C as a function of time (A) and nano-cluster coarsening rate predictions for alloy 14YWT as a function of time and temperature (B) [124] .....	87
Figure 3.32. Neutron induced hardening as a function of dose (dpa) at 325°C displayed as an increase in yield strength for alloys MA957, MANET 2, and F82H (A), and decrease in ductility as a function of dose (dpa) at 325°C for MA957, MANET 2, and F82H (B) [123] .....	89
Figure 3.33. As-irradiated microstructural comparison of MA957 (a and c) and martensitic stainless steel F82H (b and d) highlighting He bubble formation throughout the microstructure [125] .....	90
Figure 4.1. High pressure gas atomizer with highlighted reaction zone a) and b) and actual image of atomization spray illustrating ligament formation during shearing of the metal (blue arrow) and droplet formation (green arrow) c).....	91
Figure 4.2. The ODS microstructure evolution during hot consolidation (or heat treatment) of GARS precursor powder: a) initial low temperature consolidation showing intact PPBs, b) dissociation of the PPBs (simulating heat treatment) and O diffusion into the $\alpha$ -(Fe,Cr) matrix, and c) formation of Y-enriched oxide dispersoids throughout the microstructure.....	92



Figure 4.3. Thermodynamic stability of oxides comparing the free energy of formation between $\text{Cr}_2\text{O}_3$ and $\text{Y}_2\text{O}_3$ (see purple arrows) at the atomization temperature (1700°C) used for these GARS trials [128] .....	94
Figure 4.4. Fe-Cr binary phase diagram [130].....	96
Figure 4.5. A schematic showing the gas flow features for a close-coupled atomization nozzle: a) closed wake and b) open wake configuration [140].....	100
Figure 4.6. High speed video (8,000 fps) stills (in time sequence) showing the atomization stream being pinched and lifted due to the gas recirculation zone, and subsequently sheared by the high velocity gas along the periphery of the pour tube, adapted from [143].....	102
Figure 4.7. Typical pour tube geometry, a) trumpet and b) straight, with c) gas nozzle schematic .....	104
Figure 4.8. a) Ames Lab - USDOE high pressure gas atomization (HPGA) nozzle (45°) and b) HPGA nozzle with attached über halo.....	104
Figure 4.9. Resulting O content as a function of particle size and reactive atomization gas composition .....	105
Figure 4.10. Chemical granular plot for each CR-alloy .....	107
Figure 4.11. As-atomized powder morphology with accompanying AES depth profiles (note vertical dashed red line indicating oxide layer thickness): a) and d) dia. 20-53 $\mu\text{m}$ , b) and e) dia. 5-15 $\mu\text{m}$ and c) and f) dia. < 5 $\mu\text{m}$ .....	108
Figure 4.12. As-atomized surface oxide analysis of an as-atomized powder with dia. ~58 $\mu\text{m}$ : a) and b) SEM images showing the original as-atomized particle and extracted TEM specimen following FIB milling preparation.....	108
Figure 4.13. TEM analysis of the surface oxide (see yellow arrow, outlined by dashed red lines) as a function of powder size (note the layer of Au (green arrow) used to protect the surface oxide layer during FIB milling and matrix (red arrow)): a) dia. ~2 $\mu\text{m}$ and b) dia. ~58 $\mu\text{m}$ .....	109
Figure 4.14. a) bright field (BF) TEM analysis with b) accompanying EDS linescan of the surface oxide phase (see yellow arrow, outlined by dashed red lines), indicating a Cr-enriched surface oxide phase .....	110

Figure 4.15. Theoretical particle cooling curves for CR-156 (T vs. t): note that the alloy solidus temperature ( $T_s$ ) is marked by the horizontal dashed red line and liquidus temperature ( $T_L$ ) is marked by the horizontal dashed blue line .....	122
Figure 4.16. Theoretical particle cooling curves for CR-156 (T vs. D): note that the alloy solidus temperature ( $T_s$ ) is marked by the horizontal dashed red line and liquidus temperature ( $T_L$ ) is marked by the horizontal dashed blue line .....	122
Figure 4.17. Theoretical particle cooling curves for CR-156 (D vs. t) .....	123
Figure 4.18. As-atomized powder morphology as a function of particle size: a) dia. < 20 $\mu$ m and b) dia. 45-75 $\mu$ m (note the satellite particles (red arrow) and surface dimples (yellow arrow)).....	123
Figure 4.19. Initial solidification velocity a) and resulting dendrite tip radius b) as a function of particle undercooling: note the green arrow indicating a particle dia. of 15 $\mu$ m .....	125
Figure 4.20. Solidification velocity (CR-156) as a function of solid fraction (%) for varying droplet diameters.....	126
Figure 4.21. Predicted oxide layer thickness (CR-156) as a function of droplet diameters: note the red arrow highlighting the inflection point that indicates droplet solidification .....	128
Figure 4.22. Comparison of predicted oxide layer thickness with experimentally determined values (see Table 4.5).....	129
Figure 4.23. The range of Cr <sub>2</sub> O <sub>3</sub> parabolic rate constants (see red lines) used for the GARS oxidation model compared to literature values [167-174] .....	130
Figure 5.1. Internal oxidation (Rhines pack) experimental setup .....	137
Figure 5.2. Schematic of the diffusionless internal oxidation within these Rhines packs, adapted from Gesmundo et al. [182].....	138
Figure 5.3. SEM analysis of cross-sectioned stainless steel (Fe-16.0Cr-1.25Y at.%) cubes after Rhines pack heat treatment at 1100°C for 4hrs (A), 12hrs (B), and 24hrs (C) revealing the internal oxidation of Fe <sub>17</sub> Y <sub>2</sub> IMC precipitates, and (D) the subsequent formation of mixed (Y,Cr) <sub>2</sub> O <sub>3</sub> dispersoids .....	139
Figure 5.4. Comparison of the experimentally determined O diffusivity coefficient and literature values for O, Cr, and Fe diffusion in $\alpha$ -Fe.....	144

Figure 5.5. Cross-sectioned as-atomized CR-156 powders, showing the solidification structure of the Y-enriched IMC precipitates (see yellow arrow): a) dia. ~50 $\mu$ m, b) dia. ~20 $\mu$ m, and c) dia. ~5 $\mu$ m (note regions of apparent solute trapped Y in sample c) .....	146
Figure 5.6. Heat treatment predictions for CR-118 as a function of particle size for heat treatment temperatures ranging from 1000-1300°C.....	148
Figure 5.7. Predicted heat treatment procedure for each CR-alloy as a function of particle size for a temperature of 1200°C. ....	148
Figure 6.1. Basic MA processing method for the formation of an ODS microstructure, adapted from [12] .....	153
Figure 6.2. ODS microstructure evolution during consolidation of GARS precursor powders: A) low temperature consolidation showing no dissociation of the PPBs, B) initial dissociation of the PPBs during high temperature consolidation and O diffusion into the ferritic matrix, and C) formation of Y-enriched oxide dispersoids throughout the microstructure .....	154
Figure 6.3. The GARS chemical reservoir ODS consolidation process [194] .....	155
Figure 6.4. As-atomized precursor ODS ferritic stainless steel powder (dia. 20-53 $\mu$ m): A) Surface analysis and B) Cross-sectional analysis .....	155
Figure 6.5. A) FEA analysis of the tensile bar geometry, B) tensile bar test specimen, C) room temperature plastically deformed tensile bar .....	157
Figure 6.6. AES compositional depth profiles: A) CR-96, B) CR-112, and C) CR-118 .....	159
Figure 6.7. Low temperature HIPed (850°C) microstructures for CR-96 (purple), CR-112 (green), and CR-118 (blue).....	160
Figure 6.8. 1300°C as-HIP microstructures for alloy CR-96 (purple), CR-112 (green), and CR-118 (blue).....	161
Figure 6.9. As-consolidated (1300°C HIP) HE-XRD patterns A) CR-112 and B) CR-118.....	162
Figure 6.10. STEM images with corresponding EDS results for CR-96 (purple), CR-112 (green), and CR-118 (blue).....	163
Figure 6.11. Elevated temperature tensile strength comparison of Fe-based ODS alloys .....	164
Figure 6.12. Surface and cross-sectional failure analysis of fractured tensile bar specimens CR-96 (purple), CR-112 (green), and CR-118 (blue).....	165

Figure 6.13. Oxide free energy of formation as a function of temperature [201] .....	167
Figure 7.1. AES depth profile (A) and SEM cross-sectional analysis with EDS chemical linescan (B) for as-atomized CR-112 powders .....	176
Figure 7.2. Microstructure comparison of 850°C as-HIPped CR-112 (outlined in green: SEM images A and B) and 1300°C as-HIPped CR-112 (outlined in blue: SEM images C and D) .....	177
Figure 7.3. Microstructure comparison of 850°C as-HIPped CR-112 (outlined in green: TEM BFI images A and B) and 1300°C as-HIPped CR-112 (outlined in blue: TEM BFI images C and D) .....	178
Figure 7.4. AES depth profile (A) and SEM cross-sectional analysis with EDS linescan (B) for as-atomized CR-118 powders .....	179
Figure 7.5. Microstructure comparison of 850°C as-HIPped CR-118 (outlined in green: SEM images A and B) and 1300°C as-HIPped CR-118 (outlined in blue: SEM images C and D) .....	180
Figure 7.6. Microstructure comparison of 850°C as-HIPped CR-118 (outlined in green: TEM BFI images A and B) and 1300°C as-HIPped CR-118 (outlined in blue: TEM BFI images C and D) .....	181
Figure 7.7. AES depth profile (A) and SEM cross-sectional analysis with EDS linescans (B) for as-atomized CR-126 powders .....	182
Figure 7.8. Microstructure comparison of 850°C as-HIPped CR-126 (outlined in green: SEM images A and B) and 1300°C as-HIPped CR-126 (outlined in blue: SEM images C and D) .....	183
Figure 7.9. Microstructure comparison of 850°C as-HIPped CR-126 (outlined in green: TEM BFI images A and B) and 1300°C as-HIPped CR-126 (outlined in blue: TEM BFI images C and D) .....	184
Figure 7.10. HE-XRD phase analysis for as-atomized powders (red), 850°C HIP microstructure (green), and 1300°C HIP microstructure (blue): (A) CR-112, (B) CR-118, and (C) CR-126 .....	186
Figure 7.11. Comparison of the thermodynamic stability for potential oxides that could form within these CR-alloy microstructures during powder consolidation [213] .....	191
Figure 7.12. Resulting oxygen content relative to as-atomized powder particle size for different reactive gas concentrations .....	192

Figure 7.13. EPMA elemental composition map of as-atomized CR-118 powders showing: (A) as-solidified microstructure, (B) titanium microsegregation, and (C) yttrium microsegregation .....	193
Figure 7.14. Comparison of approximate mechanical alloying and gas atomization processing rates [101, 104] .....	194
Figure 8.1. A) Gas atomization reaction synthesis processing and oxygen exchange reaction: B) initial configuration of low temperature consolidated powders, C) partially dissociated prior particle boundary oxide, and D) dispersoid formation .....	198
Figure 8.2. Reactive gas injection position: A) schematic of the high pressure gas atomizer (HPGA), B) close-coupled HPGA nozzle, and C) near-field über halo .....	199
Figure 8.3. A) 316L stainless steel HIP can and B) as-consolidated (700°C) HIP bar (CR-156Y-Hf) .....	200
Figure 8.4. Resulting oxygen content measured from as-atomized powder particles relative to reaction gas content and injection point .....	203
Figure 8.5. Auger depth profiles and as-atomized SEM surface images: A1-A2) CR-118Ti-Y, B1-B2) CR-144Hf-Y, and C1-C2) CR-156Y-Hf .....	204
Figure 8.6. As-atomized SEM cross-sectional analysis of CR-alloy powders blended and CIPped (400MPa) in 75 vol.% Cu powder: A1-A2) CR-118Ti-Y, B1-B2) CR-144Hf-Y, and C1-C2) CR-156Y- Hf.....	205
Figure 8.7. As-consolidated SEM cross-sectional analysis of HIPped (700°C-300Mpa-4hr) CR-alloy powders: A1-A2) CR-118Ti-Y, B1-B2) CR-144Hf-Y, and C1-C2) CR-156Y-Hf .....	206
Figure 8.8. As-consolidated TEM-BFI analysis of HIPped (700°C-300Mpa-4hr) CR-alloys: A1-A2) CR-118Ti-Y, B1-B2) CR-144Hf-Y, and C1-C2) CR-156Y-Hf.....	207
Figure 8.9. As-reacted SEM analysis of heat treated (1300°C-1hr) CR-alloys: A1-A2) CR-118Ti-Y, B1-B2) CR-144Hf-Y, and C1-C2) CR-156Y-Hf .....	208
Figure 8.10. As-reacted TEM-BFI analysis of heat treated (1300°C-1hr) CR-alloys: A1-A2) CR- 118Ti-Y, B1-B2) CR-144Hf-Y, and C1-C2) CR-156Y-Hf.....	209
Figure 8.11. As-reacted (H.T. 1200°C-2.5hr) CR-118Ti-Y EFTEM chemical mapping of nano-metric oxide dispersoids .....	210
Figure 8.12. As-reacted (H.T. 1200°C-2.5hr) CR-144Hf-Y EFTEM chemical mapping of nano-metric oxide dispersoids .....	211

Figure 8.13. As-reacted (H.T. 1200°C-2.5hr) CR-156Y-Hf EFTEM chemical mapping of nano-metric oxide dispersoids .....	211
Figure 8.14. X-ray diffraction phase analysis of as-atomized, as-consolidated, and as-reacted CR-118Ti-Y (blue), CR-144Hf-Y (red), and CR-156Y-Hf (green) .....	213
Figure 8.15. Crystallite size analysis of resulting nano-metric oxide dispersoids formed during heat treatment of CR-118Ti-Y (blue), CR-144Hf-Y (red), and CR-156Y-Hf (green) .....	213
Figure 8.16. Free energy of formation for potential CR-alloy oxides [128] .....	217
Figure 9.1. 316L stainless steel HIP can geometry and resulting as-consolidated HIP bars .....	226
Figure 9.2. As-atomized powder (dia. < 20µm) morphology: A) CR-164HfY and B) CR-166TiY .....	228
Figure 9.3. AES depth profile chemical surface analysis of as-atomized powders (~20µm in dia.): A) CR-164HfY and B) CR-166TiY .....	229
Figure 9.4. TEM/STEM analysis of a CR-164HfY (dia. ~2µm) powder particle: A) and B) bright field images (BFIs) identifying the surface oxide layer and C) high angle annular dark field (HAADF) image with EDS linescan across the surface oxide layer .....	230
Figure 9.5. Cross-sectional SEM-EPMA analysis of the CR-alloy powders with corresponding Y-concentration map: A) and C) CR-164HfY and B) and D) CR-166TiY .....	231
Figure 9.6. SEM (BEC) analysis of the as-HIPed and heat treated microstructure: A) and C) CR-164HfY (outlined in red) and B) and D) CR-166TiY (outlined in blue) .....	232
Figure 9.7. TEM (BFI) analysis of the as-HIPped and heat treated microstructure: A) and C) CR-164HfY (outlined in red) and B) and D) CR-166TiY (outlined in blue) .....	234
Figure 9.8. SEM (BEC) analysis of CR-164HfY (outlined in red) and CR-166TiY (outlined in blue) following heat treatment at 1200°C: A) and D) 2.5hrs, B) and E) 100hrs, and C) and F) 1,000hrs .....	235
Figure 9.9. TEM-BFI analysis of CR-164HfY (outlined in red) and CR-166TiY (outlined in blue) following heat treatment at 1200°C: A) and D) 2.5hrs, B) and E) 100hrs, and C) and F) 1,000hrs .....	236
Figure 9.10. Accompanying TEM-BFI with STEM-EDS linescan chemical analysis of the nano-metric oxide dispersoids: A) and B) CR-164HfY and C) and D) CR-166TiY .....	237

Figure 9.11. XRD results revealing dispersoid phase formation and phase stability for CR-164HfY (red lines) and CR-166TiY (blue lines).....	238
Figure 9.12. A) microhardness evaluation as a function of heat treatment time for CR-164HfY (red line) and CR-166TiY (blue line) and B) grain growth analysis as a function of heat treatment time compared to predicted values for CR-164HfY (red line) and CR-166TiY (blue line) .....	240
Figure 9.13. Resulting powder O content as a function of reactive atomization gas concentration: CR-164HfY (red circle) and CR-166TiY (blue circle).....	241
Figure 9.14. Pour tube exit geometry and atomization spray characteristics: A) and B) CR-164HfY and C) and D) CR-166TiY.....	242
Figure 9.15. Resulting dispersoid size and distribution: A) CR-164HfY (outlined in red) and B) CR-166TiY (outlined in blue).....	244
Figure 9.16. A) average dispersoid radius ( $r^3$ ) as a function of heat treatment time at 1200°C, and B) relative $\alpha$ -Fe atomic diffusion coefficient for each alloying addition [181, 227, 228, 234, 235].....	245
Figure 10.1. (a) 316L stainless steel HIP can and cap and (b) as-HIPed rod made from CR-A.....	254
Figure 10.2. Sample bars prior to cold rolling (a and c) and cross-sectioned bars following 20-80% RA (b and d), where samples in a) and b) were made from powders with dia. of 20-53 $\mu$ m (CR-A) and c) and d) were made from powders with dia. of 5-20 $\mu$ m (CR-B).....	255
Figure 10.3. As-atomized powder morphology with accompanying AES depth profile: a) and d) were made from 20-53 $\mu$ m (CR-A), b) and e) were made from 5-20 $\mu$ m (CR-B), and c) and f) were made from dia. < 5 $\mu$ m (CR-C).....	259
Figure 10.4. Cross-section SEM analysis of as-CIPed powders: a) 20-53 $\mu$ m (CR-A), b) 5-20 $\mu$ m (CR-B), and c) dia. < 5 $\mu$ m (CR-C) .....	260
Figure 10.5. An example of the EPMA chemical maps used to identify Y and Hf microsegregation in as-atomized powders from CR-B: a) backscattered electron (BSE) image, b) Fe, c) Cr, d) Hf, e) Y, and f) O .....	261
Figure 10.6. Resulting as-HIPed microstructures following low temperature consolidation (700°C - 200MPa - 4hrs) of the size classified powders: a) with dia. of 20-53 $\mu$ m (CR-A), b) with dia. of 5-20 $\mu$ m (CR-B), and c) with dia. < 5 $\mu$ m (CR-C) .....	261

Figure 10.7. TEM micrographs following low temperature HIP consolidation (700°C - 200MPa - 4hrs) of the size classified powders: a) and d) with dia. of 20-53µm (CR-A), b) and e) with a dia. of 5-20µm (CR-B), and c) and f) with a dia. < 5µm (CR-C).....	263
Figure 10.8. Resulting heat treated microstructures (1200°C - 2.5hrs - Vac.) of as-HIPed samples made from: a) 20-53µm (CR-A), b) 5-20µm (CR-B), and c) dia. < 5µm (CR-C). ....	265
Figure 10.9. TEM micrographs of the heat treated (1200°C - 2.5hrs - Vac.) as-HIPed samples made from powders with: a) and d) dia. of 20-53µm (CR-A), b) and e) dia. of 5-20µm (CR-B), and c) and f) dia. < 5µm (CR-C).....	266
Figure 10.10. Resulting alloy microhardness following dispersoid formation and subsequent cold rolling and annealing trials on samples made from size classified powders identified as CR-A (green), CR-B (blue), and CR-C (red) .....	268
Figure 10.11. Resulting O content as a function of reactive atomization gas concentration for several (labeled) close size fractions .....	270
Figure 10.12. XRD data revealing dispersoid formation following elevated temperature heat treatment of CR-A (green trace and peak marker), CR-B (blue trace and peak marker), and CR-C (red trace and peak marker) with reference peak positions (adjacent black dashed lines) for Y <sub>2</sub> O <sub>3</sub> , Y <sub>2</sub> Hf <sub>2</sub> O <sub>7</sub> , and HfO <sub>2</sub> [232, 242, 243] .....	273
Figure 10.13. Kinetic phase diagram for an ideal A-B binary alloy adapted from Glicksman [244] (created from data produced by Aziz et al. [247]) .....	274
Figure 10.14. Description of mote isolation as a function of volume, where x indicates the fraction of mote free volume [248] .....	275
Figure 10.15. APT atom maps of the as-atomized powders: a) ~15µm dia. powder (CR-B) and b) ~5µm dia. powder (CR-C).....	276
Figure 10.16. Dislocation substructure after HIP and annealing, followed by ~80% RA and a 1hr anneal at 500°C in air in samples made from size classified powders of: a) 20-53µm (CR-A) and b) 5-20µm (CR-B) .....	278
Figure 11.1. (a) CR-B sample bar prior to cold rolling and (b) resulting cold rolled sheet following 85% RA .....	284
Figure 11.2. (a) SS-3 tensile specimen geometry before and after testing at room temperature .....	285



Figure 11.3. As-atomized powder morphology and cross-sectioned CIPed powders with EPMA WDS compositional maps of Y: a), b), and c) represent powders with a dia. < 20 $\mu$ m (CR-A) and d), e), and f) represent powders with a dia. between 45-75 $\mu$ m (CR-B) .....	288
Figure 11.4. An example of a pore found in cross-sectioned CIPed powders with a diameter between 45-75 $\mu$ m (CR-B) .....	289
Figure 11.5. AES depth profiles for as-atomized powders: a) with ~10 $\mu$ m dia. (CR-A) and b) with ~58 $\mu$ m dia. (CR-B) .....	290
Figure 11.6. As-atomized surface oxide analysis of a powder with ~58 $\mu$ m dia. (CR-B): a) and b) SEM images showing the original as-atomized particle and extracted TEM specimen following FIB milling, c) and d) bright field TEM images indentifying the surface oxide layer, and e) high angle annular dark field (HAADF) image with EDS linescan across the surface oxide layer .....	291
Figure 11.7. As-consolidated CR-alloy microstructure (a and c) and resulting microstructure following heat treatment at 1200°C (b and d): a) and b) for powders with a dia. < 20 $\mu$ m (CR-A) and c) and d) for powders with a dia. 45-75 $\mu$ m (CR-B) .....	292
Figure 11.8. TEM micrographs of the heat treated (1200°C) CR-alloy microstructure made from powders with: a), b), and c) dia. < 20 $\mu$ m and d), e) and f) dia. of 45-75 $\mu$ m .....	294
Figure 11.9. XRD results revealing dispersoid phase formation in CR-A (red lines) and CR-B (blue lines) .....	295
Figure 11.10. CR-alloy microhardness following dispersoid formation (horizontal dashed lines) compared to subsequent cold rolled (open box and open triangle) and annealed (closed box and closed triangle) microhardness: CR-A (red lines and boxes) and CR-B (blue lines and triangles) .....	296
Figure 11.11. Bright field (BF) STEM images showing the CR-alloy grain structure and dispersoid distribution following dispersoid formation (a and d) and after being cold rolled to 85% RA and then annealed at 500°C (b and e) or 500°C+800°C (c and f) for powders with: a), b), and c) a dia. < 20 $\mu$ m and d), e), and f) a dia. 45-75 $\mu$ m .....	297
Figure 11.12. A comparison of the a) tensile strength (UTS) and yield strength (YS) and b) total elongation as a function of temperature for CR-A (red line), CR-B (blue lines), and MA-956 (black lines) .....	299

Figure 11.13. Fracture analysis of the cross-section (a and c) and surface (b and d) of a ruptured room temperature tensile specimen made from powders with: a) and b) a dia. < 20 $\mu$ m and c) and d) a dia. 45-75 $\mu$ m .....	300
---	-----

Figure 11.14. Resulting O content in the as-atomized powders as a function of O content in the reactive atomization gas.....	302
--	-----

## List of Tables

Table 2.1. Possible generation IV type fission reactors .....	10
Table 2.2. Generation IV fission reactor operational conditions [16] .....	20
Table 2.3. Fusion operational performance goals for ITER, demonstration, and first generation reactors [36, 39-41] .....	21
Table 2.4. Radiation induced defect production in steels [33] .....	21
Table 2.5. Nuclear fission cross-section ( $n, \alpha$ ) reactions [58] .....	30
Table 2.6. Nuclear fusion cross-section ( $n, \alpha$ ) reactions [59-63] .....	30
Table 2.7. Cost summary for power plants starting in 2015 [66] .....	33
Table 2.8. Bulk quantity structural material cost [49, 65] .....	34
Table 2.9. Induced activity of elements, adapted from [68, 69] .....	35
Table 2.10. Description of generation IV fission reactor system in and out of core material considerations (note highlighted ODS material sections), adapted from [16] .....	36
Table 2.11. Proposed structural materials for fusion reactors, adapted from [33] .....	37
Table 3.1. Strengthening mechanisms in metals, adapted from [68] based on [70] .....	39
Table 3.2. Relationship between stress exponent ( $n$ ) and deformation mechanism during dislocation dominated creep [85] .....	51
Table 3.3. Coarsening rate limiting step identification exponent [94-97] .....	61
Table 3.4. Alloy composition for commercial Fe-based ODS MA956 and PM2000 [1, 106, 107] .....	66
Table 3.5. Alloy composition for NFAs MA957, 12YWT, and 14YWT [1, 2] .....	75
Table 3.6. Summary of the NCs composition from APT [6, 116-119] .....	78
Table 4.1. Individual alloying components, purpose, and ideal concentration for these CR-alloys .....	95
Table 4.2. Resulting as-atomized CR-alloy composition and resulting surface oxide phase .....	98
Table 4.3. GARS processing parameters for each CR-alloy .....	99
Table 4.4. Resulting O content as a function of as-atomized powder size .....	106

Table 4.5. Calculated surface oxide thickness, assuming $\text{Cr}_2\text{O}_3$ phase formation, based on the resulting bulk $\text{O}_2$ content in the as-atomized powders .....	111
Table 4.6. Variable identification .....	132
Table 4.7. Thermophysical properties used for experimental model .....	135
Table 5.1. Rhines pack heat treatment procedure .....	137
Table 5.2. Equilibrium constants for $\text{FeO}$ and $\text{Cr}_2\text{O}_3$ oxide formation per mole of compound [188] .....	141
Table 5.3. Equilibrium dissociation $P_{\text{O}_2}$ for $\text{FeO}$ and $\text{Cr}_2\text{O}_3$ .....	142
Table 5.4. Predicted equilibrium O solubility at the surface of the Rhines pack cubes and $G(\gamma)$ for the alloy system .....	143
Table 5.5. Values for the kinetic parameter $\gamma$ over the experimental temperature range.....	143
Table 5.6. Activation energy ( $Q$ ) and frequency factor ( $A$ ) values for the experimentally determined $D_{\text{O}}$ in $\alpha$ -(Fe,Cr) compared to literature values for the diffusion of O, Cr, and Fe in $\alpha$ -Fe.....	144
Table 5.7. Parabolic rate constant predictions for the internal oxidation of CR-118 as a function of $\gamma$ and $D_{\text{O}}$ .....	147
Table 6.1. Nominal alloy composition (wt. %) and atomization processing parameters .....	156
Table 6.2. As-atomized CR-alloy chemical composition .....	159
Table 7.1. Resulting as-atomized chemical composition and reactive atomization gas composition used in forming precursor oxide dispersion forming powders CR-112, CR-118, and CR-126 .....	173
Table 7.2. Rietveld refinement figures of merit ( $\chi^2$ , $R_p$ , and $wR_p$ ), $\alpha$ -Fe matrix lattice parameter measurements, and dispersoid vol. percent measurements for CR-112, CR-118, and CR-126 .....	185
Table 8.1. Reaction gas composition and inlet position .....	199
Table 8.2. Resulting as-atomized CR-alloy powder chemical composition .....	199
Table 8.3. CR-alloy heat treatment schedule .....	201
Table 8.4. Diffusion data for dispersoid forming elements .....	220

Table 9.1. Resulting chemical reservoir (CR) alloy composition with respect to powder particle size for CR-164HfY (dia. < 20 $\mu$ m) and CR-166TiY (dia. < 20 $\mu$ m).....	224
Table 9.2. Dispersoid number density as a function of heat treatment time at 1200°C .....	236
Table 9.3. Crystal structure parameters for each possible dispersoid phase [197, 232, 233] .....	238
Table 9.4. Calculated dispersoid radius as a function of heat treatment time at 1200°C .....	239
Table 9.5. Coarsening rate constant and initial dispersoid radius at 1200°C .....	246
Table 10.1. Resulting CR-156 alloy composition with respect to powder particle size: CR-A) 20-53 $\mu$ m, CR-B) 5-20 $\mu$ m, and CR-C) dia. < 5 $\mu$ m.....	253
Table 11.1 Resulting CR-166TiY alloy composition with respect to powder particle size: CR-A) dia. < 20 $\mu$ m and CR-B) 45-75 $\mu$ m .....	283

## Abstract

Gas atomization reaction synthesis (GARS) was employed as a simplified method for producing precursor powders for oxide dispersion strengthened (ODS) ferritic stainless steels (e.g., Fe-Cr-Y-(Ti,Hf)-O), departing from the conventional mechanical alloying (MA) process. During GARS processing a reactive atomization gas (i.e., Ar-O<sub>2</sub>) was used to oxidize the powder surfaces during primary break-up and rapid solidification of the molten alloy. This resulted in envelopment of the powders by an ultra-thin ( $t < 150$  nm) metastable Cr-enriched oxide layer that was used as a vehicle for solid-state transport of O into the consolidated microstructure. In an attempt to better understand the kinetics of this GARS reaction, theoretical cooling curves for the atomized droplets were calculated and used to establish an oxidation model for this process. Subsequent elevated temperature heat treatments, which were derived from Rhines pack measurements using an internal oxidation model, were used to promote thermodynamically driven O exchange reactions between trapped films of the initial Cr-enriched surface oxide and internal Y-enriched intermetallic precipitates. This novel microstructural evolution process resulted in the successful formation of nano-metric Y-enriched dispersoids, as confirmed using high energy X-ray diffraction and transmission electron microscopy (TEM), equivalent to conventional ODS alloys from MA powders. The thermal stability of these Y-enriched dispersoids was evaluated using high temperature (1200°C) annealing treatments ranging from 2.5 to 1,000 hrs of exposure. In a further departure from current ODS practice, replacing Ti with additions of Hf appeared to improve the Y-enriched dispersoid thermal stability by means of crystal structure modification. Additionally, the spatial distribution of the dispersoids was found to depend strongly on the original rapidly solidified microstructure. To exploit this, ODS microstructures were engineered from different powder particle size ranges,

illustrating microstructural control as a function of particle solidification rate. The consolidation of ultra-fine powders (dia.  $\leq 5\mu\text{m}$ ) resulted in a significant reduction in dispersoid size and spacing, consistent with initial scanning electron microscopy studies on as-atomized cross-sectioned particles that suggested that these powders solidified above the threshold velocity to effectively solute trap  $\gamma$  within the  $\alpha$ -(Fe,Cr) matrix. Interestingly, when the solidification velocity as a function of particle size was extracted from the aforementioned theoretical particle cooling curves, it could be offered as supporting evidence for these microstructure observations. Thermal-mechanical treatments also were used to create and evaluate the stability of a dislocation substructure within these alloys, using microhardness and TEM analysis of the alloy sub-grain and grain structure. Moreover, elevated temperature tensile tests up to  $800^{\circ}\text{C}$  were used to assess the initial mechanical strength of the ODS microstructure.

## **Chapter 1. Introduction**

### **1.1 Thesis Organization**

This thesis begins with a general description of the purpose and goals of this study (Chapter 1). The literature review will discuss considerations for selecting structural materials for future generation power plants, and will compare several material candidates for such applications (Chapter 2). Furthermore, oxide dispersion strengthened (ODS) ferritic stainless steels will be reviewed, using a focused discussion centered around the strengthening mechanism, creep resistance, growth and formation, thermal stability, and processing of these alloys (Chapter 3). Additionally, specific examples of previously available commercial ODS ferritic stainless steels (MA956 and PM2000) will be evaluated and compared to a new superior type of ODS material termed nano-structured ferritic alloys (NFAs).

The novel gas atomization reaction synthesis (GARS) process used to create precursor chemical reservoir (CR) powders for the simplified production of ODS ferritic stainless steel alloys will be discussed in Chapter 4. This chapter was formulated near the end of this study, but will be used as prelude to explain the CR-alloy composition and microstructure using a compilation of experimental results combined with theoretical droplet cooling curves and calculated particle solidification velocities. Next, an internal oxidation model will be shown as a method for determining the consolidation or heat treatment procedure required for dispersoid formation in these CR-alloys (Chapter 5). The subsequent six chapters are comprised of individual papers that depict different aspects of this ODS study. Chapters 6 and 7 are used to demonstrate the microstructure evolution in these CR-alloys, highlighting the O exchange reaction between the initial Cr-enriched surface oxide phase and Y-enriched intermetallic precipitates, while demonstrating the need



to achieve an ideal balance between the initial concentrations of Y and O in these CR-alloys. Chapters 8 and 9 focus on the thermal stability of mixed Y-(Ti or Hf)-O dispersoids, which provided insight into the coarsening kinetics associated with these dispersoids, indicating increased thermal stability through the addition of Hf. Chapter 10 marks one of the more important discoveries of this study, which indicated that the atomized solidification structure predefines the spatial distribution of the Y-enriched dispersoids, signifying the need to utilize ultra-fine (e.g., dia.  $\leq 5\mu\text{m}$ ) precursor powders to reduce the ensuing dispersoid size and spacing. Lastly, Chapter 11 illustrates initial thermal mechanical treatments and grain structure stability in these CR-alloys. Additionally, this chapter will discuss the preliminary assessment of the elevated temperature mechanical properties associated with the CR-alloy microstructure.

General conclusions highlighting the main results of this study are provided in Chapter 12. In addition, an overall acknowledgement section and all references can be found at the end of this thesis.

## **1.2 Purpose of Study**

Oxide dispersion strengthening (ODS) has been shown to be an effective method for improving the high temperature strength and creep resistance of ferritic stainless steels [1, 2]. These ODS alloys contain a large number density of nano-metric oxide particles that impede dislocation movement and stabilize the alloy grain structure [3-6]. For this reason, ODS ferritic stainless steels are considered a viable choice for structural components within future generation fossil-fueled power plants (e.g., heat exchanger tubing) [7, 8]. Additionally, the enhanced microstructural stability associated with these ODS alloys has been shown to establish a strong resistance to neutron induced void swelling, promoting these steels as candidate materials for fuel cladding within future generation nuclear reactors [9, 10].

Traditionally, ODS ferritic alloys are fabricated from a precursor particulate that is made by a lengthy mechanical alloying (MA) process, by means of high-energy ball milling [11, 12]. This process has been proven as an effective method for creating nano-metric oxides throughout the consolidated ferritic stainless steel microstructure [13]. Although effective, this conventional procedure faces several processing challenges that has limited the widespread use of commercial ODS alloys (e.g., MA956 and PM2000), including the high cost of MA particulate, controlling alloy homogeneity and impurities, batch-to-batch variability, and anisotropic microstructure formation [9]. These processing challenges eventually lead to the recent termination of commercial availability of MA956 and PM2000 and provided motivation for the development of a fundamentally new and improved ODS fabrication process, which inspired the study presented in this thesis.

This thesis will be used to demonstrate the feasibility and control of gas atomization reaction synthesis (GARS) [14] as a novel processing method for the streamlined production of precursor stainless steel powder that, when consolidated, will undergo phase transformations resulting in the formation of an ODS microstructure [15]. This GARS process utilizes a reactive atomization gas that contains small additions of oxygen, in order to strategically surface oxidize atomized droplets *in situ* during rapid solidification. These atomized droplets were designed to solidify with two inherent chemical reservoirs for the eventual formation of an ODS microstructure from the resulting precursor powders. First, the formation of a kinetically favored metastable chromium (Cr) enriched surface oxide phase, which is trapped along prior particle boundaries (PPBs) during consolidation, was intended to function as a source (i.e., reservoir) of O for the formation of more thermodynamically stable oxide dispersoids. Second, specific alloying additions of yttrium (Y) were anticipated to function as dispersoid forming agents, which initially persist as intermetallic compound (IMC) precipitates throughout the rapidly solidified microstructure, and are intended to be subsequently converted into nano-

metric Y-enriched oxide dispersoids, though O exchange reactions with the Cr-enriched PPB oxide.

In an attempt to better understand the kinetics of this GARS reaction, theoretical cooling curves for the atomized droplets will be discussed as means for predicting the extent of surface oxidation (i.e., O addition) that occurs during this process. An internal oxidation model will then be evaluated as a processing tool to predict the required heat treatment time necessary for stable dispersoid formation in these CR-alloys. Additionally, the microstructure evolution that occurs during dispersoid formation will be examined. Next, the thermal stability of these Y-enriched dispersoids will be evaluated on the basis of CR-alloy composition. Furthermore, initial solidification structure as a function of precursor powder size will be discussed as a viable technique for controlling the ensuing ODS microstructure. Finally, preliminary thermal mechanical treatments will be shown as a method for modifying the CR-alloy sub-grain and grain structure, and elevated temperature tensile testing will be used to assess the initial mechanical properties of the CR-alloys.

## Chapter 2. Structural Materials for Future Generation Power Plants

### 2.1 World Energy Concerns

Energy concerns have become an increasingly important topic over the past several years. The rapid consumption of the world's fossil fuel supply, in conjunction with projected world population growth (i.e., 6 to 10 billion by 2050) and an ever existing strive to improve quality of life has prompted a large push towards efficient, clean, safe, and long lasting energy supplies [16, 17]. It has been estimated that the world's energy needs will more than double over the next four decades moving from 14TW to 25-60TW by 2050 [17]. This projected massive increase in energy demand has generated a great driving force towards improving the efficiency of current large energy producing technologies (e.g., coal-fired power plants and nuclear fission reactors) and exploring new alternative energy sources (e.g., fusion reactors).

To improve the efficiency of coal and fission power plants, as well as other heat engines, the operational temperature will need to be increased. This assumption is based on the Carnot cycle, which is the basis for the second law of thermodynamics [18]. This cycle can be used to interpret the efficiency of a heat engine as function of input temperature ( $t_2$ ) and output temperature ( $t_1$ ) (Figure 2.1). The efficiency of a heat engine is a direct function of  $\Delta t$  (i.e.,  $t_2 - t_1$ ), and assuming that the heat reservoir at low temperature ( $t_1$ ) is held at constant temperature, then efficiency will improve when the heat reservoir at high temperature ( $t_2$ ) is increased (Equation 1).

Increasing the operational temperature of a power reactor presents several challenges. The most important of these challenges is proper material selection. The materials in use will now be subjected to higher temperatures and pressures, which can often lead to shorter material life cycles. The design life of many structural components in future power reactors is approximately 60 yrs ( $\sim 10^5$  hours) [16]. Understanding reactor operational conditions is a critical step in selecting structural

material alloys. This chapter will highlight the proposed operational conditions for future reactors and projected structural materials. Many different materials and material systems are being considered as structural components for future reactors, but advanced oxide dispersion strengthened ferritic stainless steels are proving to be a prominent material choice. Advanced ferritic stainless steels (e.g., nanostructured ferritic alloys (NFAs) Section 3.6) have improved elevated temperature mechanical properties, in conjunction with good inherent oxidation, corrosion, and neutron radiation resistance over that of traditional ferritic stainless steels.

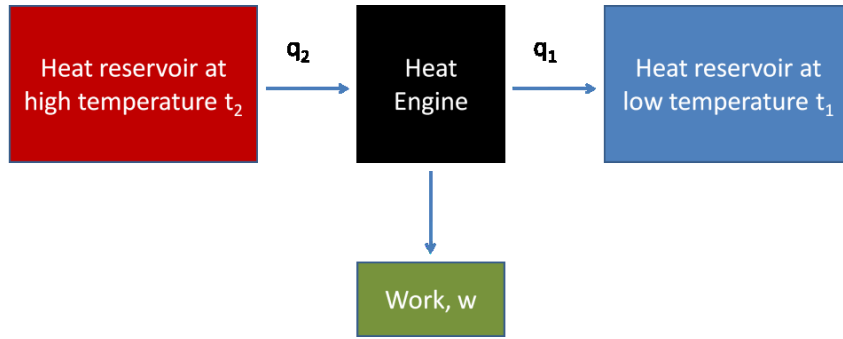


Figure 2.1. Schematic illustrating the working of a heat engine [18]

Equation 1

$$Efficiency = \frac{\text{work obtained}}{\text{heat input}} = \frac{w}{q_2} = \frac{q_2 - q_1}{q_2} = \frac{t_2 - t_1}{t_2}$$

## 2.2 Future Generation Power Reactors

### 2.2.1 Ultra Supercritical Coal-Fired Power Reactors

Ultra supercritical (USC) coal-fired power reactors operate in the supercritical water regime (Figure 2.2). A supercritical regime is derived from the thermodynamic term meaning, there is no clear distinction between a liquid and gaseous phase (i.e., a homogenous fluid) [19].

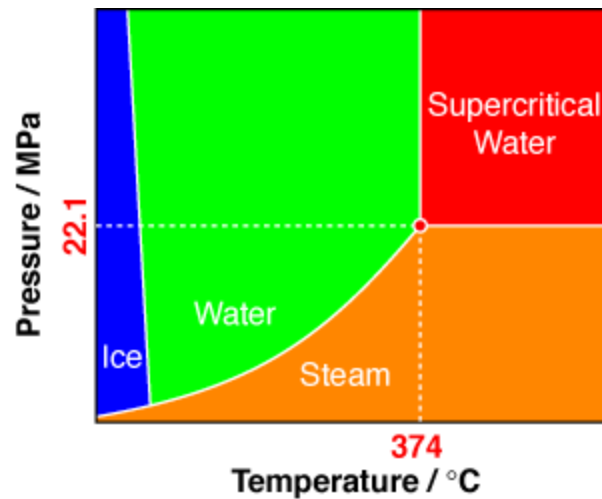


Figure 2.2. H<sub>2</sub>O temperature and pressure phase diagram [19]

Coal is one of the most abundant fossil fuel sources found in the world. The United States Department of Energy (USDOE) has estimated that the world contains a 350 year supply of coal (given current energy consumptions) [20]. USC coal-fired power reactors are currently being developed in the USA, and are part of the USDOE Fossil Energy FutureGen project [20]. The goal of FutureGen is to create revolutionary new, clean coal burning technology, while reducing green house emissions [21].

USC coal-fired reactors burn coal mixed with forced air to extremely high boiler temperature ( $T \sim 800^\circ\text{C}$ ). The thermal energy produced inside the boiler is extracted using a heat exchanger and is converted into mechanical energy. Inside the heat exchanger, water is converted into supercritical steam, and in return the steam powers a turbine engine. These reactors are planned to operate with  $760^\circ\text{C}/35\text{MPa}$  steam [22]. Early stage conventional pulverized coal (PC) power plants operate using  $565^\circ\text{C}/24\text{MPa}$  steam [7]. This dramatic increase in operating temperature and pressure will result in increased efficiencies of 37-47%, with an expected fuel cost savings of \$248M over the first 20 yrs of the plants life, and will result in a reduction of CO<sub>2</sub> and other related gas emissions by 22% [22]. A fundamental schematic of an USC coal-fired reactor is shown below (Figure 2.3).

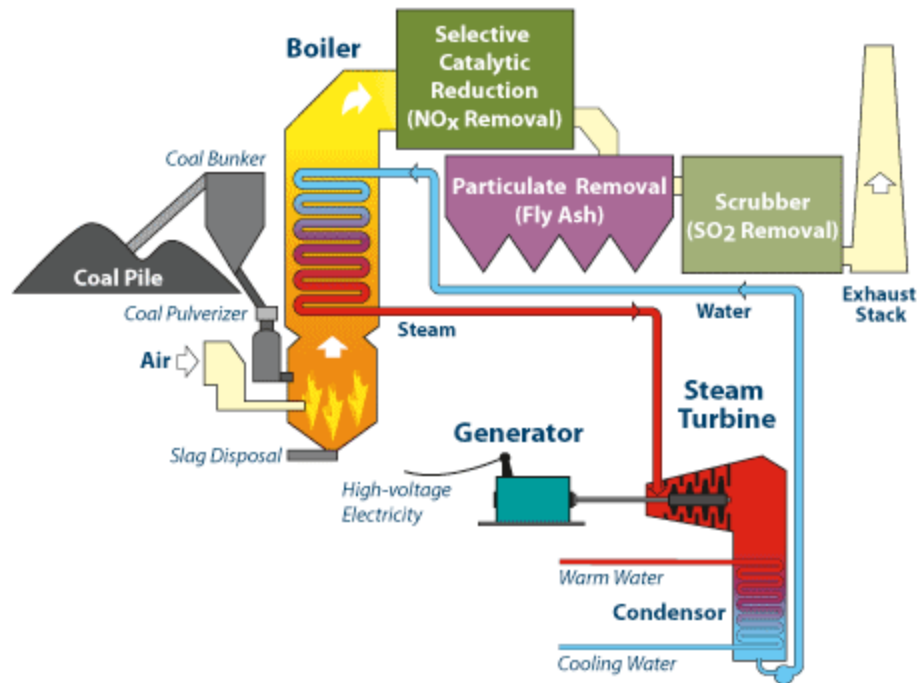


Figure 2.3. Ultra supercritical coal-fired power plant schematic [23]

### 2.2.2 Future Generation Nuclear Reactors

#### *Generation IV Fission Reactors*

Nuclear power is a prominent choice for clean, sustainable, and affordable energy. Currently, nuclear power plants are the largest non-greenhouse gas emitting source of energy and produce 16% of the world's electricity [16]. In comparison to fossil fuel power reactors, nuclear reactors release a significant more amount of energy per unit mass of fuel. The complete fission of one pound of  $^{235}\text{U}$  generates approximately the same amount of energy as 6,000 barrels of oil or 1,000 tons of coal [24]. Fission power reactors were first constructed in the USA in the early 1940's, and the first power plant went online producing electricity in 1951 [25]. Since then, the fission process has become a well established source of energy. Generation type IV fission reactors could operate at efficiencies between 44-50% (depending on reactor type) [16].

During the fission process a radioactive fuel material (i.e.,  $^{233}\text{U}$ ,  $^{235}\text{U}$ ,  $^{239}\text{Pu}$ , or  $^{241}\text{Pu}$ ) is bombarded with neutrons ( $^{238}\text{U}$  and  $^{232}\text{Th}$  are only fissionable in the presence of fast neutrons), and when the nucleus captures a neutron the internal force balance between protons and neutrons becomes highly unstable [25]. Due to this instability, the nucleus will split into two lighter nuclei and emit several neutrons. The mass of the resulting nuclei is less than the previous nucleus plus the neutrons, and this mass difference results in an energy product [26]. From Einstein's famous energy equation (i.e.,  $E = mc^2$ ) the amount of energy resulting from a single fission reaction can be determined. The energy from a fission reaction is converted into heat following several collisions among fission fragments, neutrons, structural materials, and fuel cladding [26]. The attractive, yet dangerous aspect of a fission reaction is the cascade effect or chain reaction that occurs. Where, the neutrons that are given off during the first fission reaction initiate successive fission reactions at an exponential rate. For this reason, control rods (e.g., B, Hf, or Cd) are used to absorb neutrons, reducing the concentration of neutrons to an optimum level [25].

During the fission process the ejected neutrons are moving at such a high velocity that interacting with another fissionable atom (e.g.,  $^{235}\text{U}$ ) is unlikely. In a thermal reactor the fission process is induced by neutrons that are in thermal equilibrium with the reactor core material [24]. A thermal reactor uses a moderator (e.g., water) to slow down the fast moving neutrons to equilibrium thermal energies. In a fast reactor no moderator is used, and the fast moving neutrons are used to convert large quantities of fertile  $^{238}\text{U}$  and  $^{232}\text{Th}$  to fissionable  $^{239}\text{Pu}$  and  $^{233}\text{U}$ , respectively [24]. Reactors that convert less fertile material to fissionable material than consumed (e.g., a thermal reactor) are called burner reactors, and reactors that convert more fertile material to fissionable material than consumed (e.g., a fast reactor) are called breeder reactors [25].



The evolution of nuclear fission reactors has led to the improvement of reactor efficiencies largely due to the increased neutron fluence, which results in higher in-core operating temperatures. A timeline illustrating the evolution of nuclear fission reactors in the USA is shown in Figure 2.4.

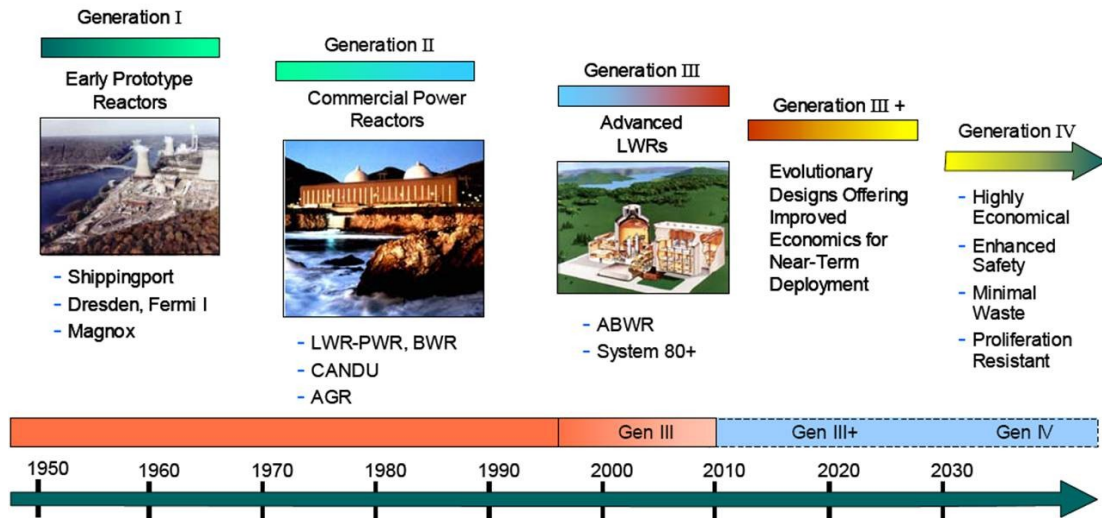


Figure 2.4. Evolution of USA fission reactors [16]

Several different generation IV fission reactors are being developed. A list of acronyms for generation type IV reactors is displayed in Table 2.1, and a schematic of a supercritical-water-cooled reactor system is shown in Figure 2.5.

Table 2.1. Possible generation IV type fission reactors

Generation IV System	Acronym
Gas-Cooled Fast Reactor System	GFR
Lead-Cooled Fast Reactor System	LFR
Molten Salt Reactor System	MSR
Sodium-Cooled Fast Reactor System	SFR
Supercritical-Water-Cooled Reactor System	SCWR
Very-High-Temperature Reactor System	VHTR

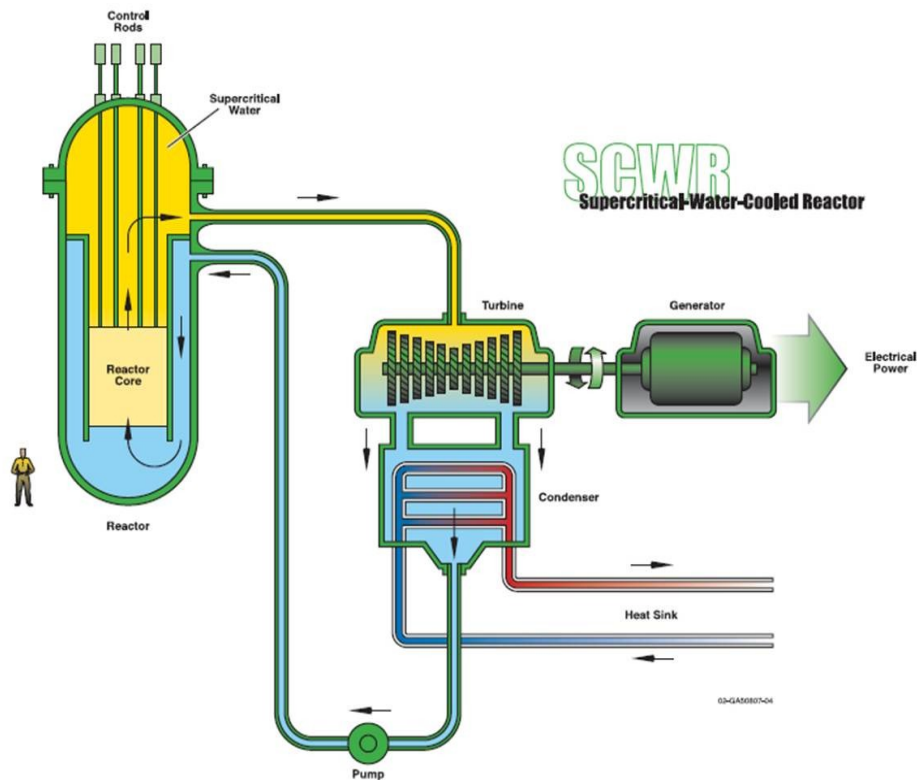


Figure 2.5. Schematic of generation IV supercritical-water-cooled fission reactor [16]

### *First Generation Fusion Reactors*

Nuclear fusion reactors are still in the early development stages, but considerable progress has been made towards harnessing the same power produced by the stars. Nuclear fusion, if sustained, could be a tremendous source of clean, abundant, renewable, and inexpensive energy. An international thermonuclear experimental reactor (ITER) is being built as a joint international project that focuses on research and development of fusion power. Many countries are part of the ITER project team including, the European Union, Japan, the People's Republic of China, India, the Republic of Korea, the Russia Federation, and the USA. A schematic showing the proposed ITER reactor is shown in Figure 2.6. Recently, A detailed plan highlighting the development of a fusion demonstration power plant within the next

35 yrs has been published [27]. This plan gives insight to the critical components required for a fusion power reactor, and gives a detailed description on the steps required to move forward into an era of fusion power.

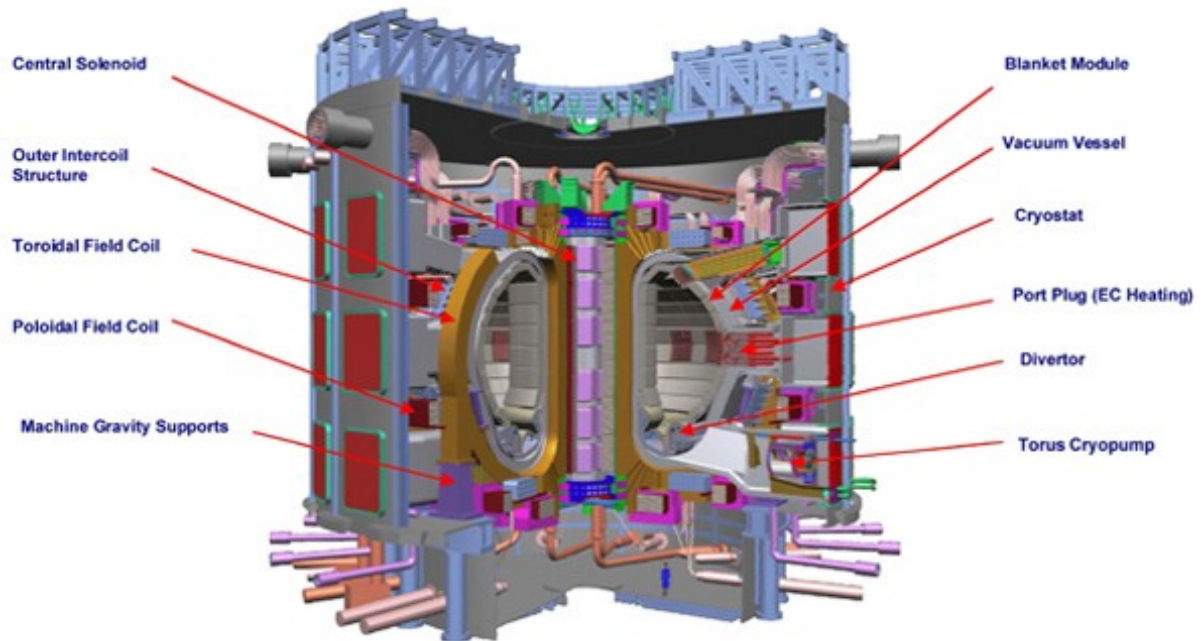


Figure 2.6 ITER demonstration device for the use of fusion power [28]

A fusion reaction occurs when two lighter nuclei are combined (i.e., fused together), resulting in the formation of a heavier nuclei and the ejection of a neutron(s). The mass difference between the two initial nuclei and the resultant nuclei can be used to calculate the reaction energy using Einstein's energy equation (i.e.,  $E=mc^2$ ), just as in a fission reaction. The two easiest nuclei that can be fused together are tritium (T) and deuterium (D), both isotopes of hydrogen. Tritium has a short half-life (i.e., ~12yrs), and is not readily found on Earth, but tritium can be bred from  $^6\text{Li}$  and  $^7\text{Li}$  transmutation reactions, while deuterium is readily available and can be extracted from seawater [25]. When accelerated to very high velocities, in order to overcome

repulsion forces, the hydrogen nuclei (D, T) will combine, resulting in the formation of a He nuclei and the ejection of a high energy neutron (Figure 2.7).

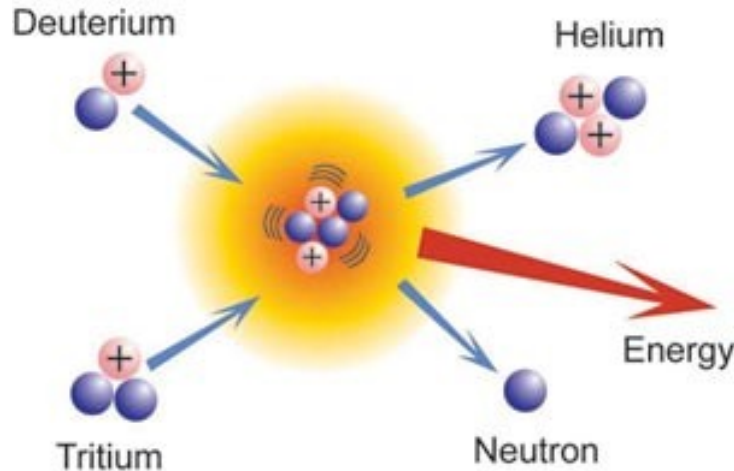


Figure 2.7. Deuterium-Tritium fusion reaction [29]

Extremely high temperatures are required to reach critical fusion velocities. These critical velocities can be achieved by ionization of the hydrogen fuel, during ionization the nucleus of the hydrogen atoms (D-T) is separated from its electrons and the gas changes to a state of plasma. Plasma can reach temperatures upwards of  $10^6$  °C and must be carefully controlled during the fusion reaction [27]. A strong magnetic field (i.e.,  $10^5$  times stronger than Earth's magnetic field) is used to control the plasma field inside a toroidal shaped core, in order to keep it away from the core wall [25]. During the fusion reaction the ejected neutron, with an energy of 14MeV, escapes the plasma field and strikes the first wall of the blanket material in the core of the reactor [30]. The large amount of heat generated during these collisions is converted to mechanical energy using a series of heat exchangers and a turbine generator. A schematic illustrating a theoretical design of a fusion power plant is shown in Figure 2.8.

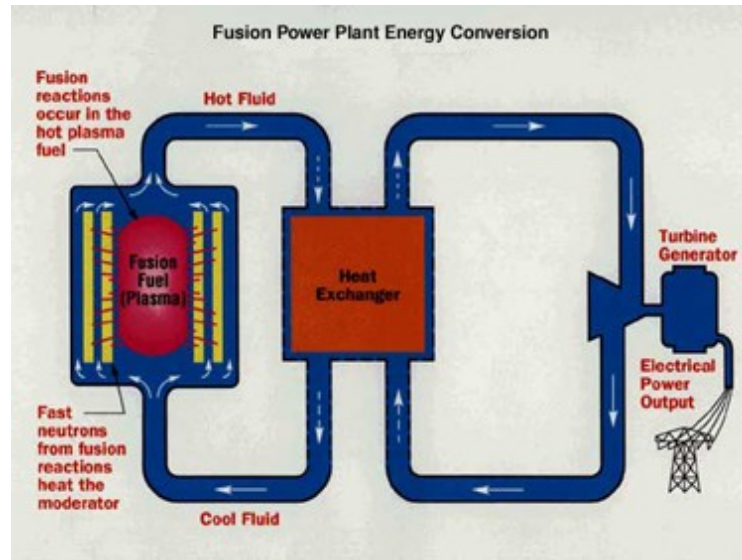


Figure 2.8 Basic design of a theoretical fusion power plant [29]

## 2.3 Material Selection

### 2.3.1 Ultra Supercritical Coal-Fired Reactors

Ferritic stainless steels, austenitic stainless steel, and Ni-based superalloys are being considered as the main structural components (i.e., boiler material and heat exchanger tubing) within ultra supercritical (USC) coal-fired reactors. USC boilers operate at a temperature  $\sim 800^{\circ}\text{C}$  and the heat exchanger tubing transports steam at a temperature of  $760^{\circ}\text{C}$  and a pressure of 35MPa [22]. The inherent strength and corrosion resistance of conventional ferritic stainless steels (e.g., HT91: Fe-12Cr-1.0Mo wt.%) is limited to a temperature of  $620^{\circ}\text{C}$  [7]. This limits the use of conventional ferritic stainless steels in new USC coal-fired reactors. Austenitic stainless steels and Ni-based superalloys offer improved strength and corrosion resistance at higher temperatures, but can be considerably more expensive than ferritic stainless steels (Table 2.8). A comparison of high temperature strengths for the considered alloys can be seen in Figure 2.9.

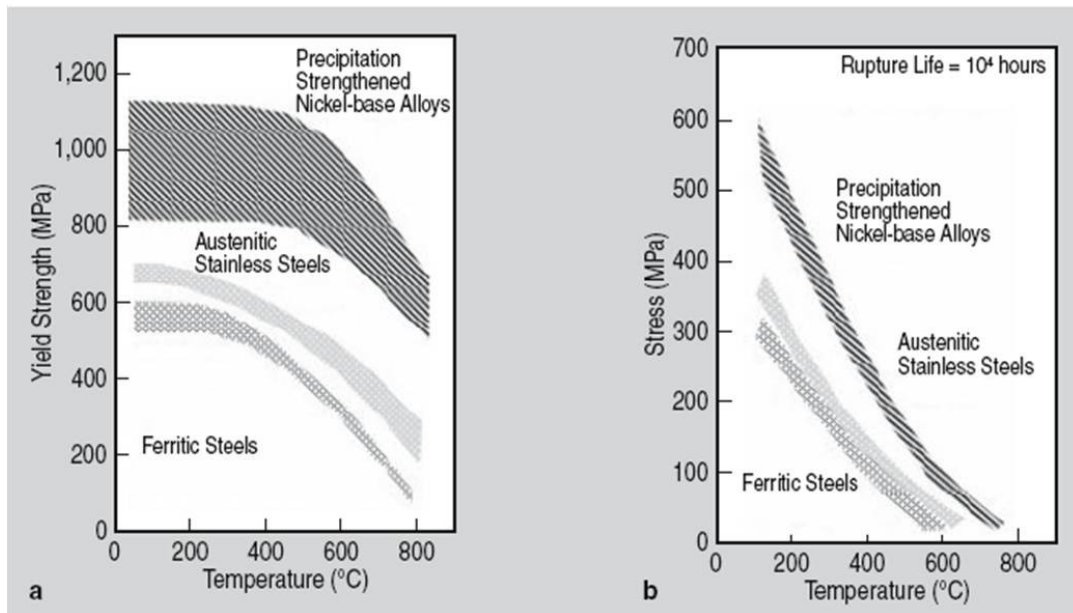


Figure 2.9. Yield strength (a) and rupture life stress tests (b) for possible structural materials [31]

Advanced oxide dispersion strengthened ferritic stainless steels known as nanostructured ferritic alloys (e.g., MA957) have demonstrated a vast improvement in high temperature strength over conventional ferritic stainless steels, with strengths comparable to Ni-based superalloys (Figure 2.10). Typically these advanced ODS alloys are chromia (i.e.,  $\text{Cr}_2\text{O}_3$ ) formers, which will not provide long term corrosion resistance to ultra supercritical steam, for this reason these alloys would require an alumina ( $\text{Al}_2\text{O}_3$ ) forming corrosion resistant bond coat.

The limiting factor, which prevents the use of advanced ODS ferritic stainless steel alloys in USC reactors, is the high cost of these alloys. This high cost stems from the expensive manufacturing process required to achieve an ideal ODS microstructure. This expensive processing route (Section 3.4: Mechanical Alloying) results in alloy costs similar to or greater than Ni-based superalloys (Table 2.8). If the manufacturing process could be simplified, and the cost for producing advanced ODS ferritic stainless steels was significantly reduced, the cost savings could

promote the use of such alloys over Ni-based superalloys for bulk structural components within USC coal-fired reactors.

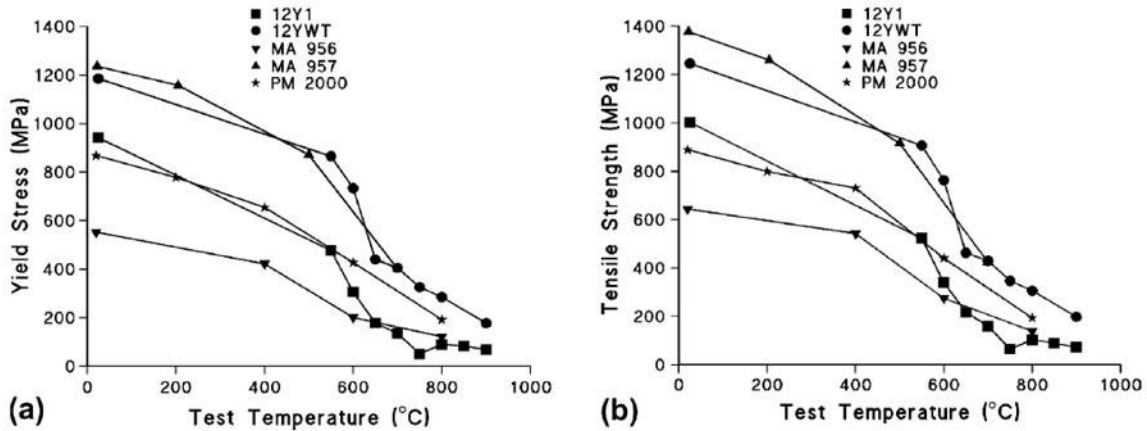


Figure 2.10. Yield strength (a) and ultimate tensile strength (b) as a function of temperature for Fe-based ODS commercial alloys (MA956 and PM2000) and advanced nanostructured ferritic alloys (MA957 and 12YWT) [1]

### 2.3.2 Generation IV Nuclear Fission Reactors and First Generation Fusion Reactors

Structural materials (regardless of reactor type) proposed for use in future generation nuclear reactors will need to meet rigorous material requirements. Material selection will be based on material properties, economic constraints, and environmental restrictions. The material properties of interest include, thermal (i.e., elevated temperature strength, creep resistance, and corrosion-oxidation resistance), nuclear (i.e., resistance to radiation induced: hardening, embrittlement, swelling, phase instabilities, creep, and helium embrittlement), and processing (i.e., fabrication, machining, and joining) [32]. The economics of producing a nuclear reactor are directly influenced by the inherent raw material, fabrication, and processing costs of its structural components. Improved materials and simplified processing routes offer an opportunity to reduce reactor capital costs. Also, the disposal of radioactive structural materials has become a growing environmental



concern. To address this concern, new structural materials are limited to the use of low or reduced activity elements (i.e., elements with a short-to-moderate radioactive life span).

### *Irradiation Damage*

The microstructure of neutron irradiated materials is constantly evolving. Irradiation damage in structural materials results from atomic displacements and nuclear transmutation reactions. The net effect of neutron irradiation is dependent on the balance between irradiation damage and thermal annealing, as well as the composition and microstructure of the alloy.

Atomic displacements occur during elastic collisions between nuclear reaction particles and atoms of a target material (e.g., in-core nuclear structural components). During these collisions an atom of the structural material can be moved from its lattice position forming a vacancy-interstitial pair (i.e., Frenkel pair) [33]. If the energy of the collision is sufficiently large, an atomic displacement cascade can occur, resulting in a large concentration of point defects throughout the lattice. Recombination of defect pairs can occur, but under continued elevated temperature irradiation conditions, defects will diffuse away from the heavily damaged area, due to a large defect concentration gradient. During the diffusion process the defects can be annihilated at defect sinks (e.g., dislocations, grain boundaries, and interfaces). Defects that do not recombine, or are not annihilated can lead to lattice swelling, and overall geometrical changes in the structural component [33].

Nuclear transmutation of atoms also can occur during interactions between nuclear particles and structural materials. The products of such reactions are generally unstable and decay via particle emission (e.g., helium and hydrogen). An important transmutation reaction within nuclear materials is neutron induced alpha-particle ( $^4\text{He}$ ) decay ( $n, \alpha$ ). During this reaction, unstable atomic nuclei will decay via  $\alpha$ -particle emissions. The emitted  $\alpha$ -particle can then diffuse and precipitate as a



defect impurity (e.g., helium gas bubble) within the structural material lattice, along grain boundaries, or interfaces, which can lead to swelling or embrittlement [34]. This reaction is directly influenced by neutron bombardment energies and the inherent nuclear cross-section of elements within the structural material. Elements with larger nuclear cross-sections are more likely to undergo nuclear transmutation reactions leading to increased defect impurity levels.

Radiation induced damage can result in the overall degradation of structural material properties. The different damaging phenomena include hardening, embrittlement, creep, and void swelling. The specific phenomena are directly influenced by the irradiation temperature, as displayed in Figure 2.11.

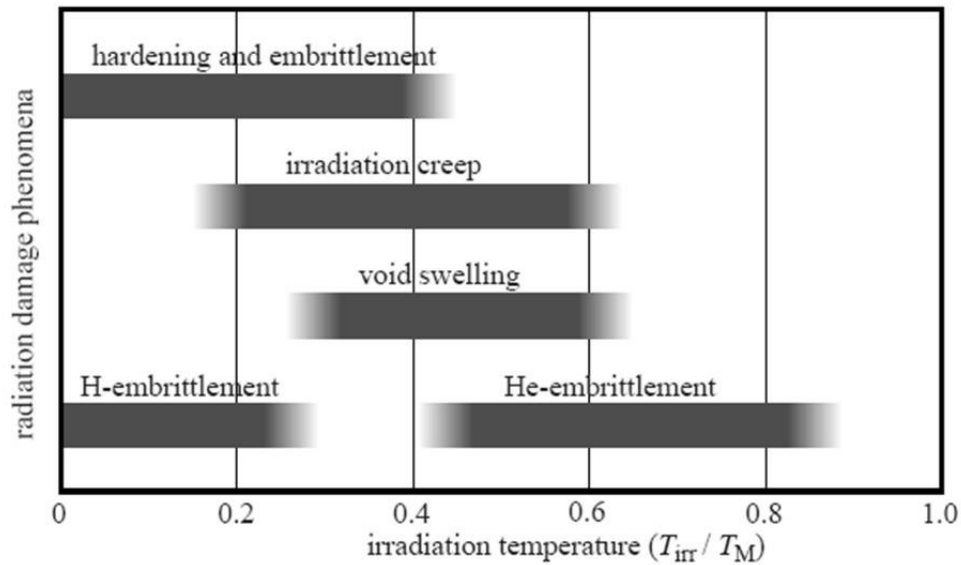


Figure 2.11 Radiation damage phenomena normalized to material melting temperature [35]

Irradiation at lower temperatures results in hardening and embrittlement at dose rates  $>0.1$  dpa, due to a loss in work-hardenability and ductility within a material [36]. During this stage, there is a severe loss in material fracture toughness, which can result in an increase of the ductile-to-brittle transition temperature (DBTT) for body-centered cubic (BCC) lattice structured materials. For this reason, reactors that

utilize BCC structural materials have a lower operating temperature constraint, which should hopefully prevent brittle fracture and catastrophic failure of structural components. Irradiation at intermediate temperatures can cause irradiation creep and void swelling within structural components. This stage is promoted by the formation of defect clusters typically at a dose rate  $>10$  dpa [37]. High temperature embrittlement can occur from the formation of transmutation helium that precipitates as bubbles along grain boundaries, leading to intergranular fracture at low stresses and dose rates  $>10$  dpa [37].

#### *Reactor Operation Conditions*

Structural materials in first generation fission reactors were subjected to a maximum dose rate of  $\sim 1$  dpa and maximum temperatures of  $300^{\circ}\text{C}$  [37]. Second generation thermal reactor structural materials were exposed to a maximum dose of  $\sim 30$  dpa and a maximum temperature of  $350^{\circ}\text{C}$ , while second generation fast reactors had a maximum dose rate of  $\sim 100$  dpa with maximum temperatures of  $600^{\circ}\text{C}$  [37]. The structural materials in fourth generation reactors will face an increasingly severe environment. Materials located in the reaction core of thermal and fast reactors will be subjected to neutrons with energies ranging from several MeV down to  $\sim 0.025$  eV and  $\sim 10$  KeV, respectively [38]. The pressures inside the reaction vessel will range with reactor type from  $\sim 0.1$ - $25$  MPa [16]. The maximum dose rate in fourth generation thermal reactors is 30 dpa with a maximum temperature of  $1000^{\circ}\text{C}$ , while fast reactors have a maximum dose rate of 150 dpa and a maximum temperature of  $850^{\circ}\text{C}$  [16]. A summary of fourth generation fission reactor conditions is listed in Table 2.2.

**Table 2.2. Generation IV fission reactor operational conditions [16]**

Reactor Type	Coolant Inlet Temp (°C)	Coolant Outlet Temp (°C)	Pressure (MPa)	Coolant
SCWR	290	500	25	Water
VHTR	600	1000	7	Helium
SFR	370	550	0.1	Sodium
LFR	600	800	0.1	Lead
GFR	450	850	7	Helium
MSR	700	1000	0.1	Molten Salt

Structural materials in fusion reactors will be subjected to high energy 14 MeV neutrons. A list of operational performance goals for the ITER, a large scale demonstration reactor, and a first generation fusion reactor are shown in Table 2.3. First generation fusion reactors will have a maximum proposed structural dose rate of 50-150 dpa and at a maximum proposed temperature of 550-1000°C [37].

Fusion reactor structural materials will also be subjected to high amounts of transmutation H and He, produced as a result of the energetic D-T fusion process. Impurity concentrations of ~1500 appm He are expected in fusion reactors compared to <10 appm He in fission reactors [37]. A comparison of radiation induced defect production in steels is show in Table 2.4.

**Table 2.3. Fusion operational performance goals for ITER, demonstration, and first generation reactors [36, 39-41]**

	ITER	DEMO	Reactor
Fusion power	0.5-1 GW	2-4 GW	3-4 GW
Neutron wall loading (first wall)	0.5-1 MW m <sup>-2</sup>	2-3 MW m <sup>-2</sup>	2-3 MW m <sup>-2</sup>
Integrated wall load (first wall)	0.3-1 MWy m <sup>-2</sup> 3-10 dpa	3-8 MWy m <sup>-2</sup> 30-80 dpa	10-15 MWy m <sup>-2</sup> 100-150 dpa
Operational mode	Pulsed (1000 s) < 5 × 10 <sup>4</sup> cycles	Quasi-continuous	Quasi-continuous
Plant lifetime			~30 FPy
Net plant efficiency			~30%

**Table 2.4. Radiation induced defect production in steels [33]**

Defect production (in steels)	Fusion neutrons (3-4 GW reactor, first wall conditions)	Fission neutrons (BOR 60 reactor)
Damage rate (dpa year <sup>-1</sup> )	20-30	~20
Helium (appm dpa <sup>-1</sup> )	10-15	≤1
Hydrogen (appm dpa <sup>-1</sup> )	40-50	≤10

### *Structural Material Alloy Selection*

Prominent alloy choices for both in and out-of-core structural components for nuclear reactors include, stainless steels (austenitic, ferritic, and ferritic/martensitic (F/M)), nickel (Ni)-based superalloys, vanadium (V)-based alloys, and silicon carbide/silicon carbide ( $\text{SiC}_f/\text{SiC}_m$ ) reinforced composites. Alloy systems are evaluated based on thermal and mechanical properties, resistance to radiation induced damage, economical constraints and radioactive decay behavior.

### Thermal and Mechanical Properties

The power density capability for structural materials is used to identify the maximum allowable heat load, as a function of neutron wall loading and thickness ( $\text{MWm}^{-2}$ ) for 1.0 mm thick first wall material [42]. A comparison of the select alloys shows that vanadium based alloys and ferritic-martensitic steels offer the greatest power potential, while austenitic stainless steels,  $\text{SiC}_f/\text{SiC}_m$  composites, and Ni-based superalloys (not shown) offer the worst power potential (Figure 2.12). Power density is a function of ultimate tensile strength, thermal conductivity, thermal expansion, and elastic modules (Equation 2) [42].

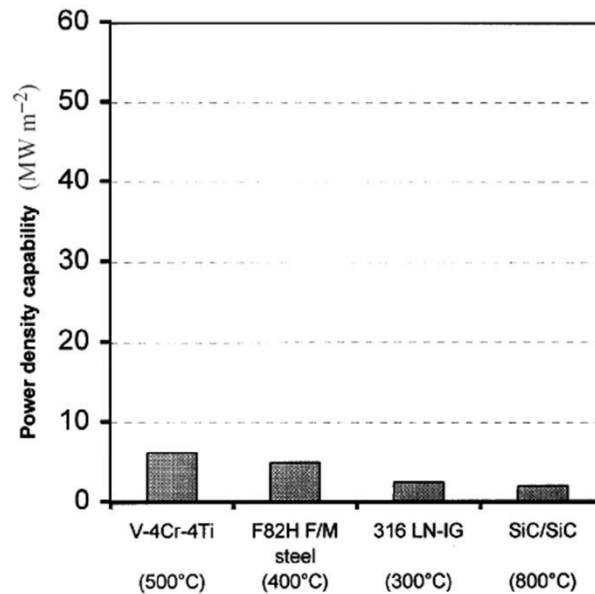


Figure 2.12. Power density capability of proposed structural materials [42]

$$\dot{Q} = \frac{R_M \lambda (1 - \nu)}{\alpha E}$$

Equation 2

$\dot{Q}$  = Power Density (MW m<sup>-2</sup>)

$R_M$  = Tensile Strength (MPa)

$\lambda$  = Thermal Conductivity (Wm<sup>-1</sup>K<sup>-1</sup>)

$\nu$  = Poisson Ratio

$\alpha$  = Thermal Expansion Coefficient (μm m<sup>-1</sup>K<sup>-1</sup>)

$E$  = Elastic Modules (GPa)

The power density of a structural material can be increased by improving alloy tensile strength and thermal conductivity, or by reducing its elastic modules and thermal expansion. Evaluation of these inherent material properties can help to identify specific shortfalls within an alloy. A relative comparison highlighting the material properties of interest can be seen in Figure 2.13.

This comparison shows what material properties are lacking, and thus should be modified for a particular alloy to gain in power density. As seen in Figure 2.12, martensitic stainless steels and V-based alloys contain near-ideal material properties for the greatest power potential. Austenitic stainless steels (e.g., 316L) are limited in power density due to poor thermal conductivity and large thermal expansions. Ni-based alloys offer ideal tensile strengths, but poor thermal conductivity and large thermal expansions, leading to a low power density. SiC<sub>f</sub>/SiC<sub>m</sub> composites have low tensile strengths, poor thermal conductivity, and a large elastic modules, all of which contributes to a low power density. Although ferritic stainless steels contain many ideal properties, its power density (e.g., 430SS) is severely limited by its tensile strength. Improving the tensile strength of a ferritic stainless steel alloy, through the addition of nano-metric oxide dispersoids, results in a vast increase in power density (Figure 2.14).

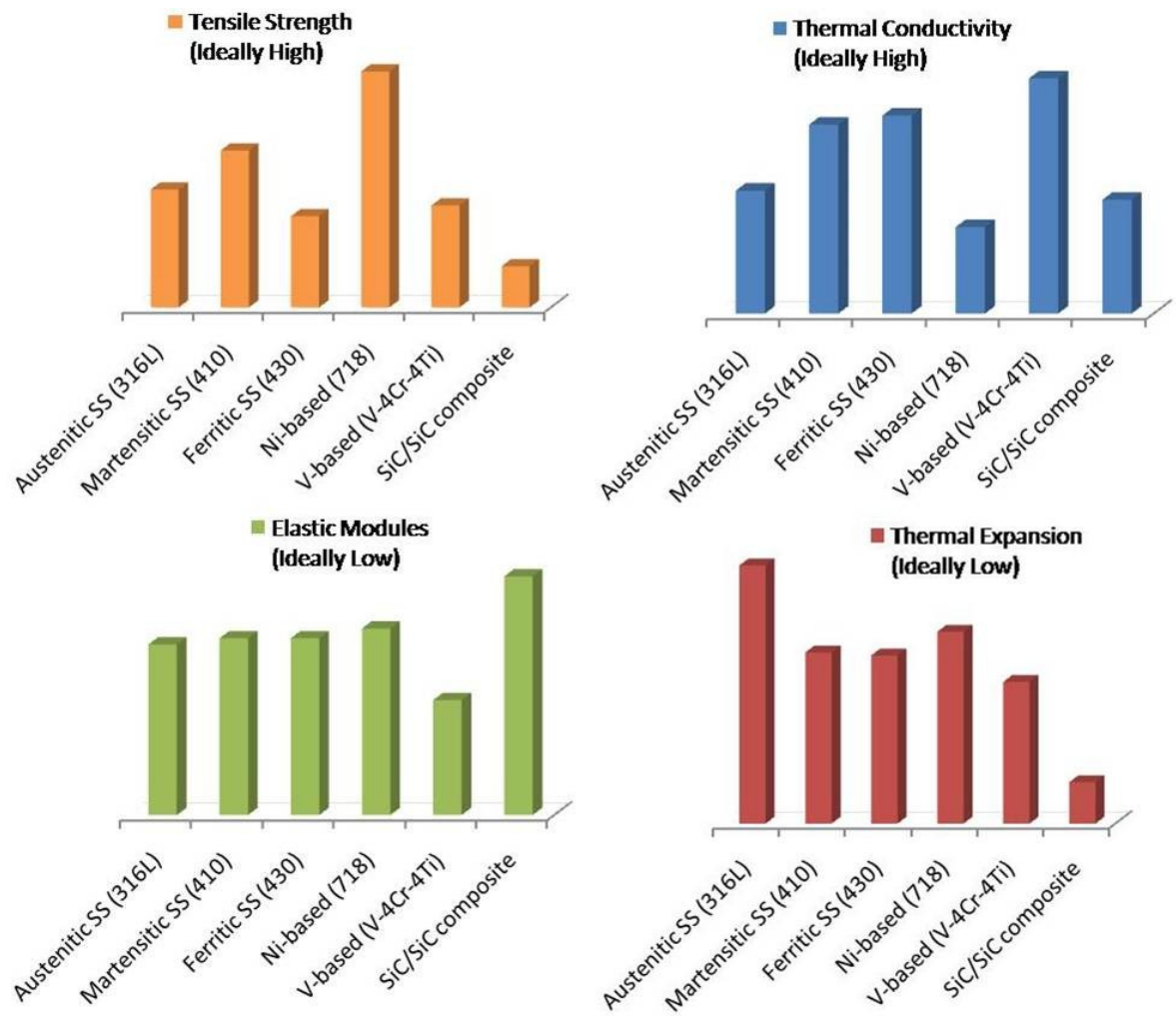
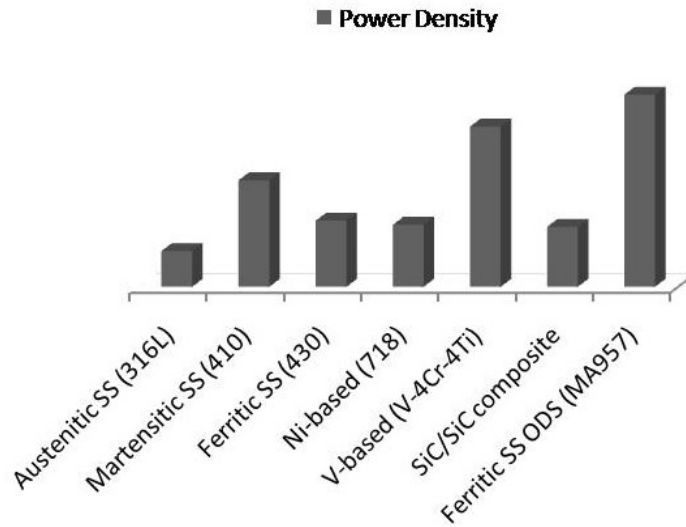


Figure 2.13. A relative comparison of tensile strength (orange), thermal conductivity (blue), elastic modulus (green), and thermal expansion (red) for potential nuclear reactor structural materials [43-48]



**Figure 2.14. Relative power density comparison for potential structural component materials, based on material properties found in the literature [1, 43-48]**

The creep rupture strength of potential nuclear structural materials is displayed in Figure 2.15. This Larson-Miller plot compares austenitic stainless steel (316 LN), a conventional 9-12%Cr ferritic-martensitic stainless steel (MANET), and vanadium based alloys (V-Cr-Ti). This figure shows that V-based alloys offer the greatest high temperature creep resistance.

The high temperature creep strength in ferritic stainless steels can be drastically improved through the addition of nano-metric oxide dispersoids. The creep rupture strength, as predicted using a Larson-Miller plot, for conventional Fe-based ODS ferritic stainless steels (e.g., MA-956) and advanced Fe-based nanostructured ferritic alloys (e.g., 12YWT) is shown in Figure 2.16. It can be seen that the high temperature creep strength of the advanced NFAs is comparable to V-based alloys (Figure 2.15).



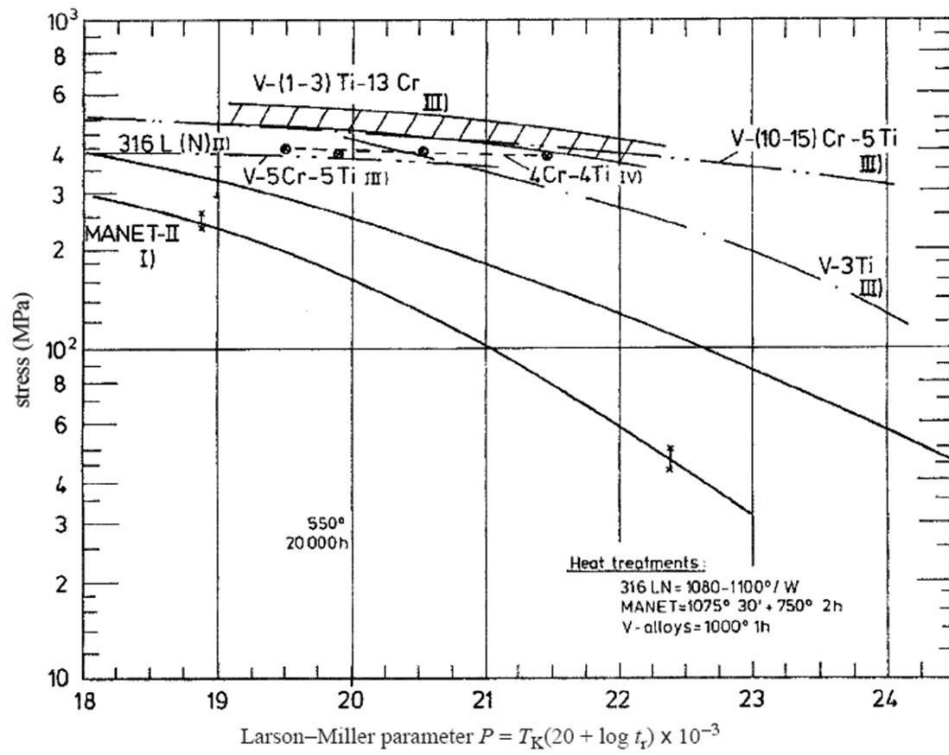


Figure 2.15. Larson-Miller plot for a select group of radiation resistant materials [36]

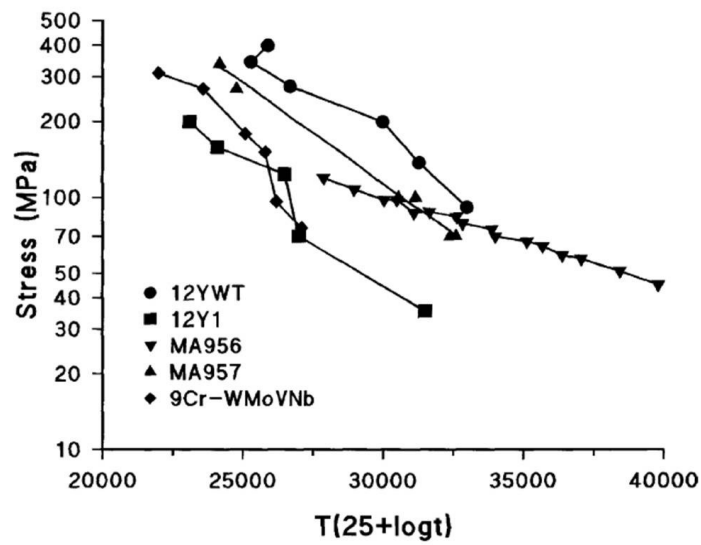


Figure 2.16. Larson-Miller plot for Fe-based ODS ferritic alloys [1]

### Oxidation and Corrosion Properties

Elevated temperature oxidation and corrosion resistance is highly dependent on alloy type. In many cases, structural materials will form a thin oxide layer which protects the alloy from further corrosion attack. The effectiveness of the oxide layer is dependent on environmental conditions and operating temperatures. During oxidizing conditions, most stainless steels and some Ni-based superalloys will form a protective chromium enriched surface oxide layer, typically chromia (i.e.,  $\text{Cr}_2\text{O}_3$ ) [49]. Generally, corrosion resistance in chromia forming alloys is increased with increasing chromium content. For this reason, ferritic stainless steels offer increased corrosion resistance in comparison to ferritic/martensitic steels. Chromia is protective up to  $\sim 900\text{-}1100^\circ\text{C}$  (alloy dependant), above which it can react with oxygen and form chromium trioxide (i.e.,  $\text{CrO}_3$ ) [49]. Chromium trioxide is highly volatile and can vaporize, leading to chromium metal loss and severe alloy degradation [50]. Also, chromia is not protective in chloride containing atmospheres, due to the formation of a volatile corrosion product [50].

Through the addition of aluminum, stainless steels and Ni-based superalloys can form a protective alumina (i.e.,  $\text{Al}_2\text{O}_3$ ) surface oxide layer. Alumina can offer better oxidation resistance and slower scaling kinetics than chromia, and does not suffer from oxidative evaporation [50]. Also, alumina is considered one of the best options for protection against sulfidation [50]. The parabolic scaling constants for several surface oxides are shown in Figure 2.17.

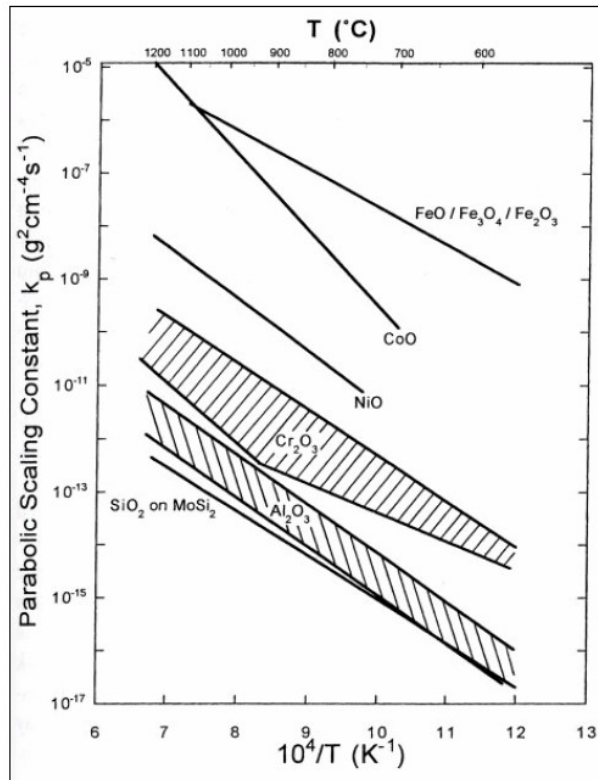


Figure 2.17. Parabolic scaling constants for different oxides [51]

Vanadium based alloys (e.g., V-4Cr-4Ti) have a large affinity for interstitial elements (e.g., O, N, H, and C), which can lead to embrittlement of the alloy [36]. The oxygen solubility in vanadium can range between 1-3 wt.% from RT-800°C, and the formation of a protective surface oxide layer is not effective at preventing oxygen uptake at temperatures where these alloys are proposed to operate [52]. For this reason, V-based alloys should be limited to environments with very low oxygen partial pressures (i.e.,  $<10^{-8}$  Pa), or restricted to reducing environments (e.g., molten Li cooled reactors) [53].

The oxidation behavior of  $\text{SiC}_f/\text{SiC}_m$  composites is quite complex and differs significantly from that of monolithic SiC. At high partial pressures of oxygen and high temperatures, SiC based composites will form a surface protective layer of

silica (i.e.,  $\text{SiO}_2$ ), but reaction rates and growth kinetics are highly dependent on processing methods and resultant porosity [54, 55]. Under intermediate partial pressures of oxygen  $\text{SiO}_2$  transforms to  $\text{SiO}$ , which is volatile and can lead to oxidative vaporization and corrosive attack of  $\text{SiC}$  [54]. Furthermore, the carbon layer located at the interface between the  $\text{SiC}$  matrix and fibers is highly susceptible to oxidation, resulting in interface separation and reduced mechanical strength [56].

### Radiation Induced Damage

Radiation induced swelling can lead to unacceptable dimensional instability within reactor structural components. The volume change is a direct function of displacement dose. Several structural alloys have been compared, and it can be deduced that BCC structured materials (e.g., commercial ferritic steels) offer the greatest resistance to neutron induced swelling (Figure 2.18).

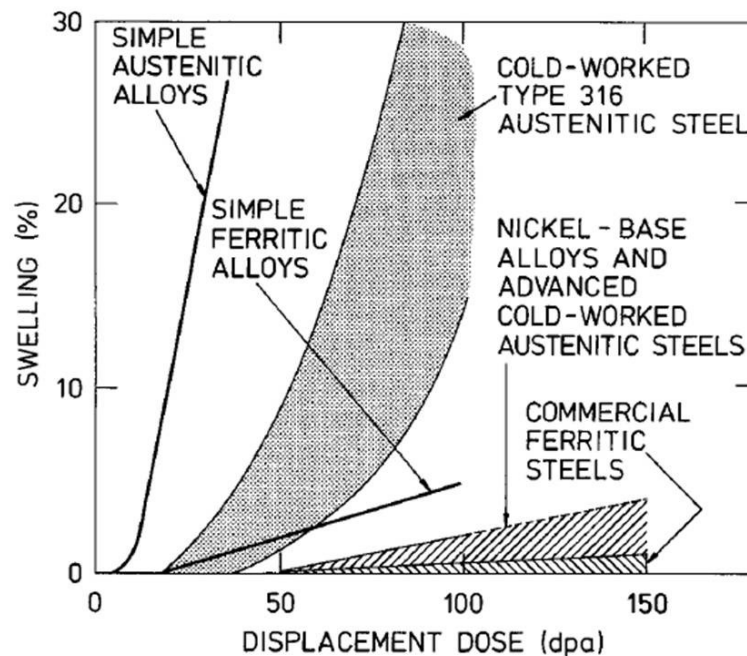


Figure 2.18. Radiation induced swelling for different structural materials as a function of displacement dose [57]

Transmutation reactions can also lead to swelling and embrittlement in structural materials. Neutron induced  $\alpha$ -particle decay transmutation reactions are directly related to a materials nuclear cross-section for reaction type (n,  $\alpha$ ). The  $\alpha$ -particle cross-section ( $\sigma$ ) for several structural material alloys under fission and fusion reactor conditions is shown in Table 2.5 and Table 2.6, respectively.

**Table 2.5. Nuclear fission cross-section (n,  $\alpha$ ) reactions [58]**

Reaction	Average Fission Cross-Sections	
Type-(n, $\alpha$ )	$E_{\text{eff}}$ (MeV)	$\sigma$ (mb)
$^{28}\text{Si}, ^{30}\text{Si}$	8.7, 10.2	0.56, 0.07
$^{51}\text{V}$	11.2	0.024
$^{56}\text{Fe}, ^{58}\text{Fe}$	9.6, 11.4	0.25, 0.019
$^{58}\text{Ni}$	7.6	4.4

**Table 2.6. Nuclear fusion cross-section (n,  $\alpha$ ) reactions [59-63]**

Reaction	Avg. Fusion Cross-Sections (mb)		
	14.1 MeV	14.5 MeV	14.9 MeV
$^{30}\text{Si} (n,\alpha) ^{27}\text{Mg}$	-	-	$70 \pm 10$
$^{51}\text{V}(n,\alpha) ^{48}\text{Sc}$	$15 \pm 2$	$17 \pm 3$	$19 \pm 4$
$^{58}\text{Fe} (n,\alpha) ^{55}\text{Cr}$	-	-	$21 \pm 2$
$^{58}\text{Ni} (n,\alpha) ^{55}\text{Fe}$	$125 \pm 16$	-	-

Further analysis of neutron induced  $\alpha$ -particle decay reactions in pure Fe (i.e., predominantly  $^{56}\text{Fe}$ ), and pure Ni (i.e., predominantly  $^{58}\text{Ni}$ ) can be seen in Figure 2.19. This comparison shows that the nuclear cross-section in Ni is approximately twice that of Fe at neutron energies near fusion conditions.

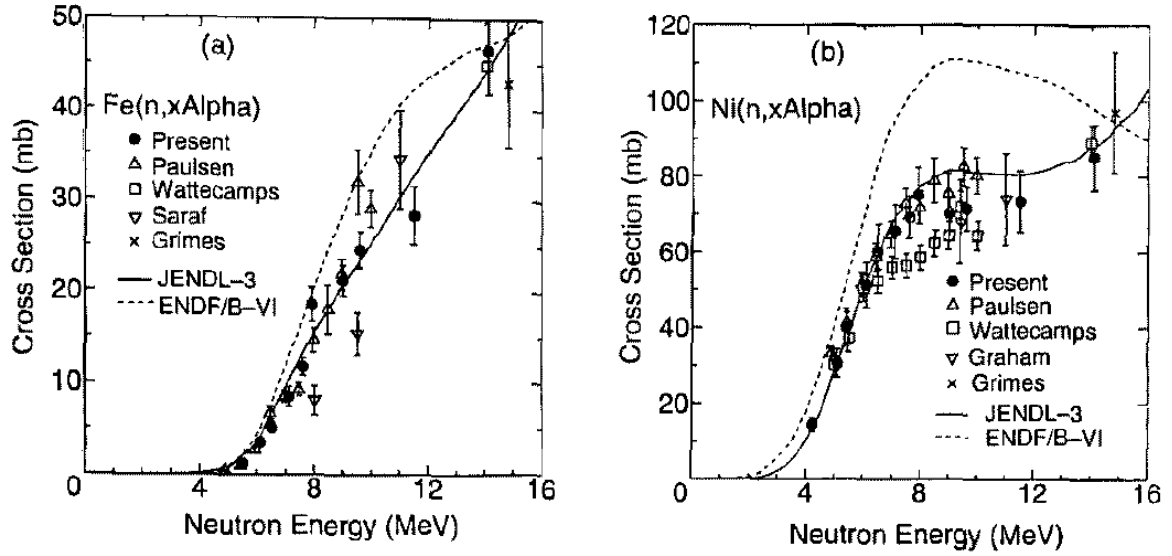


Figure 2.19. Neutron induced  $\alpha$ -particle production cross-sections in pure Fe (a) and pure Ni (b) [64]

Larger neutron induced  $\alpha$ -particle cross-sections will result in increased  $\alpha$ -particle decay reactions, which ultimately lead to the nucleation of He bubbles along grain boundaries and interfaces inside structural components [34]. Ni-based and Si-based structural components are the most susceptible to He induced swelling and embrittlement, due to larger nuclear ( $n, \alpha$ ) cross-sections. V-based and Fe-based alloys offer the lowest ( $n, \alpha$ ) cross-sections, which should help to minimize He nucleation within structural components.

Reactor operational temperature windows will be limited to the high temperature physical, mechanical, radiation resistance properties of its structural materials. The proposed operational temperature window for several reactor structural materials is

shown in Figure 2.20. The largest operational temperature range can be achieved using ODS ferritic steels, and the highest operational temperatures can be reached using SiC<sub>m</sub>/SiC<sub>f</sub> composites.

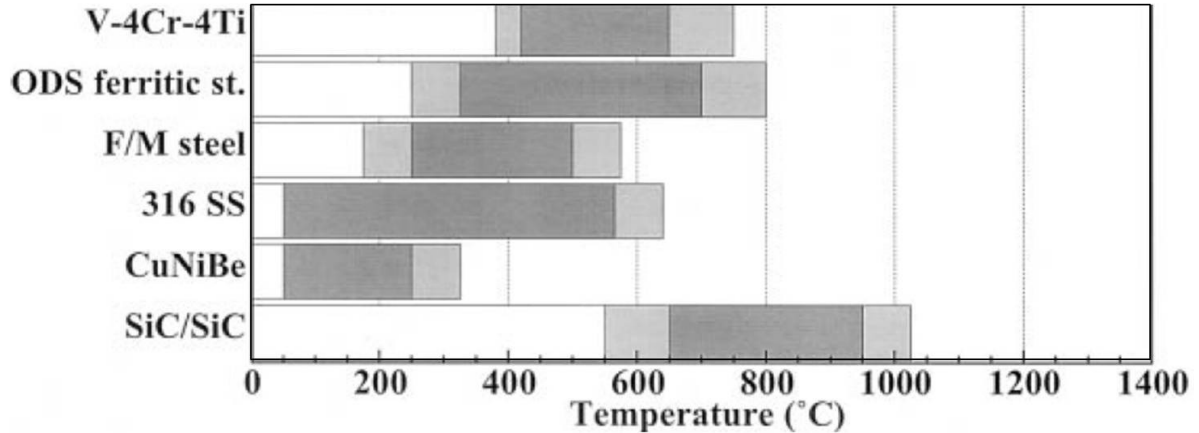


Figure 2.20. Operating temperature window for reactor structural materials [65]

### Nuclear Reactor Economics

The investment cost of nuclear reactors is dependent on several cost components, including operational, maintenance, and capital costs. Capital costs, which are directly influenced by structural material costs, make up a significant percentage of the reactor investment. A cost summary for power plants being built in the year 2015 is displayed in Table 2.7. This summary compares important parameters that are considered when building future nuclear, combined-cycle gas turbines (CCGT), coal fired, integrated coal gasification combined cycle (IGCC), and wind generated power plants.

Table 2.7. Cost summary for power plants starting in 2015 [66]

Parameter	Unit	Nuclear	CCGT	Coal Steam	IGCC	Wind (onshore)
Thermal efficiency	%	33	58	44	46	-
Investment cost	\$/KW	2000-2500	650	1400	1600	900
Construction period	Months	60	36	48	54	18
Plant Life	Years	40	25	40	40	20
Decommissioning	\$ Million	350	0	0	0	0
Unit Cost of fuel	\$ per MBtu or Ton	0.5/MBtu	6.00/MBtu	55/ton	55/ton	-

By reducing structural material costs it should be possible to improve the economics of building a nuclear reactor. A comparison of bulk quantity structural material costs are highlighted in Table 2.8. It can be seen that standard ferritic and austenitic stainless steels are the most inexpensive alloy choices, while V-4Cr-4Ti, SiC/SiC composites, and Fe-based ODS steels are the most expensive alloy choices. The high cost for improved elevated temperature material properties is rather apparent in these alloys. It is thought, that Fe-based ODS steels offer the greatest potential for significant alloy cost reduction, due to an inherent low raw material cost.



**Table 2.8. Bulk quantity structural material cost [49, 65]**

Material	Cost/kg (USD)	Notes
Austenitic Stainless Steel	~\$3-7	316L Plate form
Ferritic Stainless Steel	~\$2-5	446 Plate form
F/M Fe-9Cr steels	≤\$5.50	Plate form
V-4Cr-4Ti	~\$200	Plate form (Average between 1994 and 1996 US fusion program large heats)
SiC <sub>f</sub> /SiC <sub>m</sub> composites	~\$1000 ~\$200	Chemical vapor infiltration, and Chemical vapor reaction
Ni-based	~\$35	Inconel 718 Sheet (Special Metals)
Fe- based ODS	~\$165	MA956 Sheet (Special Metals)

### Environmental Constraints

The radioactivity, as a function of time after reactor shutdown, for select group of chemical elements is shown in Figure 2.21. It can be seen that of the proposed structural material alloys, the base materials Si and V offer the lowest induced activity, followed by Fe with a moderate activity, and Ni with a large activity. Classification of induced activity of elements is listed in Table 2.9. From this table it can be seen that radioactive Ni-based alloys would require an excessive amount of time to decay, and should be restricted to out-of-core applications.

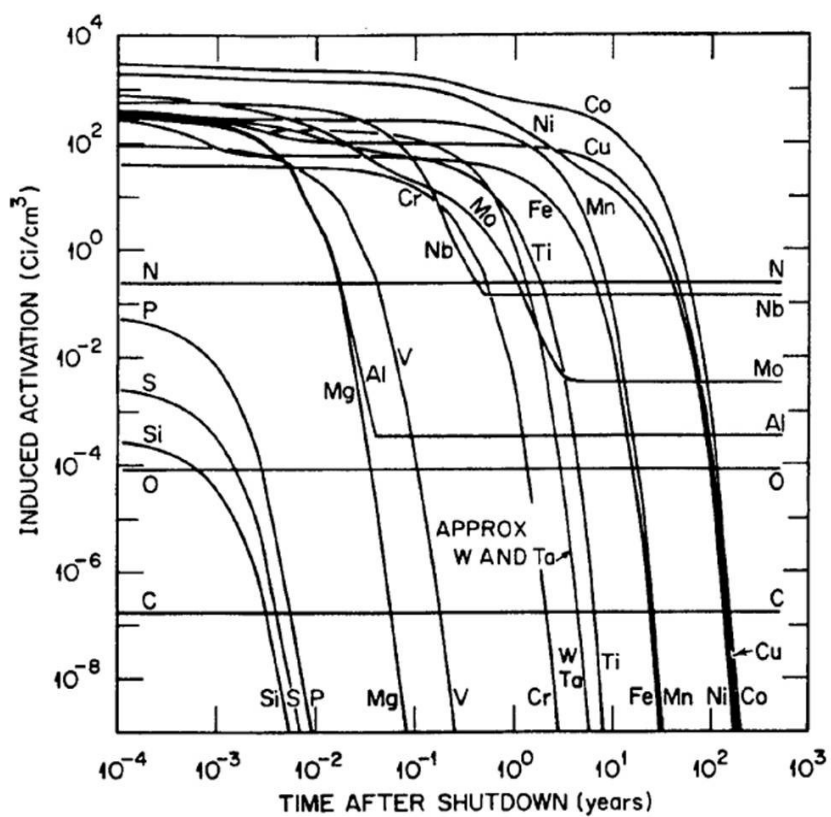


Figure 2.21. Calculated radioactivity as a function of time after reactor shutdown [67]

Table 2.9. Induced activity of elements, adapted from [68, 69]

Element Activity	Elements
Very low activation (decays within 2 weeks)	Li, Be, B, C, O, Mg, Si, P, S
Low activation (decays in 1 month – 5 years)	Ti, V, Cr, Zr, W, Pb, Y
Moderate activation (decays in 10-30 years)	Mn, Fe, Zn, Hf
High activation (does not decay in 100 years)	Al, Ni, Cu, Nb, Mo, Sn

### Alloy Placement

Several alloy systems have been selected as possible material choices for structural materials in future generation nuclear reactors. Alloy systems were selected on the premise of the aforementioned material properties. A group of proposed structural materials for future generation fission and fusion reactors are listed in Table 2.10 and Table 2.11, respectively.

**Table 2.10. Description of generation IV fission reactor system in and out of core material considerations (note highlighted ODS material sections), adapted from [16]**

			Structural Materials	
System	Spectrum, $T_{\text{outlet}}$	Cladding	In-Core	Out-of-Core
GFR	Fast, 850°C	Ceramic	Refractory metals and alloys, Ceramics, ODS Vessel F-M	Primary circuit: Ni-based superalloys, conventional F-M alloys with TBC or ODS
LFR	Fast, 550°C and Fast, 800°C	High Si F-M, Ceramics, or refractory alloys	-	High-Si austenitics, ceramics, or refractory alloys
MSR	Thermal, 700-800°C	Not Applicable	Ceramics, refractory metals, High-Mo, Ni-based alloys, Graphite	High-Mo Ni-based alloys
SFR	Fast, 520°C	F-M (HT9 or ODS)	F-M ducts, 316SS grid plate	Ferritics, austenitics
SCWR	Fast, Thermal, 550°C	F-M alloys, Incoloy 800, Inconel 690, 625, and 718, ODS	Same as cladding options	F-M
VHTR	Thermal, 1000°C	ZrC and surrounding graphite	Graphites, PyC, SiC, ZrC Vessel: F-M	Primary circuit: Ni-based superalloys, conventional F-M alloys with TBC or ODS
Abbreviations:				
F-M: Ferritic-martensitic stainless steels (typically 9 to 12 wt.% Cr)				
ODS: Oxide dispersion-strengthened steels (typically ferritic-martensitic)				
TBC: Thermal Barrier Coating				

**Table 2.11. Proposed structural materials for fusion reactors, adapted from [33]**

Function	First Wall	Breeding Blanket	Divertor
Structural Material	RAFM steel, ODS steel, V-base alloy, SiC/SiC <sub>f</sub>	RAFM steel, ODS steel, V-base alloy, SiC/SiC <sub>f</sub>	ODS steel, W-base alloy
Coolant	None	Water, helium, eutectic Pb-Li, Li	Water, helium

## Chapter 3. Oxide Dispersion Strengthening

Oxide dispersion strengthening (ODS) has become a well established method for increasing the high temperature strength of an alloy. Increased mechanical properties are highly dependent on the final microstructure of the alloy, following processing and heat treatment. Basic strengthening mechanisms related to ODS alloys, and traditional processing routes used to obtain an ODS microstructure will be discussed in this chapter. Several commercial Fe-based ODS alloys and advanced nanostructured ferritic alloys (NFAs) will be used to demonstrate potential microstructures, thermal mechanical properties, and preliminary thermal nuclear properties.

### 3.1 Oxide Dispersion Strengthening Mechanisms

#### 3.1.1 Strengthening Mechanisms

Several methods can be used to increase the strength of a metal alloy. Common strengthening methods include grain size refinement, work hardening, solid solution strengthening, precipitate strengthening, and dispersoid strengthening. Although effective at room temperature, several of these methods lose their effectiveness at elevated temperatures. For example, smaller grains can coarsen and large dislocation densities established from work hardening can be annealed away at elevated temperatures. For this reason, structural materials that are in service at elevated temperatures ( $T > 0.4T_m$ ) are most effectively strengthened with precipitates or dispersoids. Approximate service temperature limitations for specific strengthening methods are shown in Table 3.1.

Table 3.1. Strengthening mechanisms in metals, adapted from [68] based on [70]

Strengthening Mechanism	Effective Temperature
Work Hardening	$\sim 0.3 T_m$
Grain Size	$\sim 0.3 T_m$
Solid Solution Strengthening	$\sim 0.4 T_m$
Precipitation Strengthening	$\sim 0.6 T_m$
Oxide Dispersion Strengthening	$\sim 0.9 T_m$

Oxide dispersion strengthened materials contain an array of nano-metric oxide dispersoids which impede dislocation movement and stabilize dislocation substructures. Strength gains in these alloys are derived from the size, spacing, distribution, and volume fraction of the dispersed phase. Dispersoid strengthening can be fundamentally different than precipitate strengthening, with the two methods being separated based on particle-dislocation interactions. When a gliding dislocation meets an array of obstacles, it will first try to bend between them [71]. At a certain critical bend angle ( $\Phi_c$ ), the dislocation will bypass the obstacle and proceed along the slip plane until meeting another obstacle (Figure 3.1) [3].

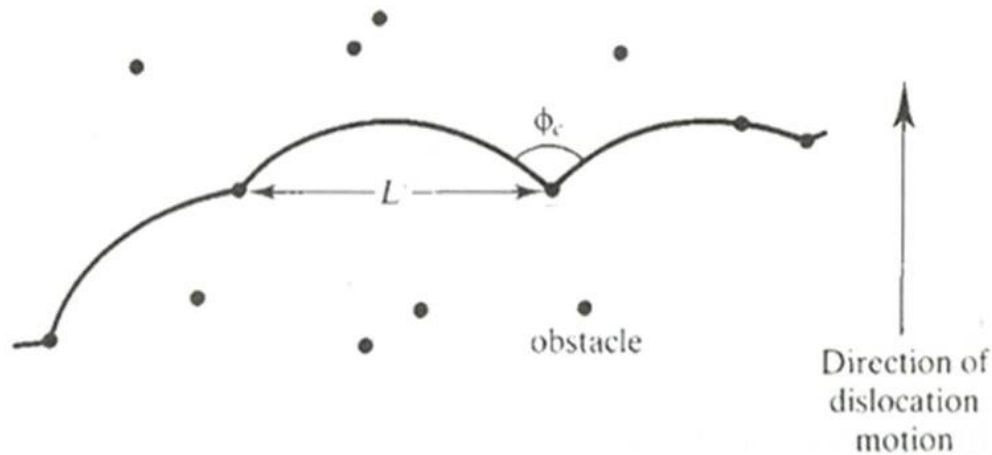


Figure 3.1. A random arrangement of obstacles in a dislocation slip plane, highlighting the obstacle spacing ( $L$ ) and critical bend angle  $\Phi_c$  [3]

The overall strength of the obstacle will determine dislocation flow. If the obstacle is strong and impenetrable to moving dislocations then  $\Phi_c$  will approach zero. In contrast,  $\Phi_c$  will approach  $180^\circ$  for obstacles that are weak and penetrable. The required shear stress for sustained dislocation motion is a function of the dislocation line tension and obstacle spacing (see Equation 3 and Equation 4) [71].

$$\tau(\text{strong obstacles}) \cong \frac{Gb}{L} \cos \frac{\Phi_c}{2} \quad \text{Equation 3}$$

$$\tau(\text{weak obstacles}) \cong \frac{Gb}{L} (\cos \frac{\Phi_c}{2})^{\frac{1}{2}} \quad \text{Equation 4}$$

$G$  = shear modules

$b$  = burgers vector

$L$  = obstacle spacing

$\Phi_c$  = critical bend angle

### *Strong Obstacles*

Strong obstacles are commonly referred to as Orowan particles, owing this to the specific dislocation bypassing mechanism. During this process a dislocation will migrate through an obstacle field by forming a dislocation loop around each particle, this is known as the Orowan process (Figure 3.2) [70].

An advanced examination of the strengthening effects by strong obstacles can be obtained by evaluating the average particle spacing, dislocation dipole effect, and dislocation line tension value [70]. Assuming the average particle spacing on a given slip plane is much greater than the size of the particles (i.e.,  $\lambda \gg r$ ), then the average particle spacing can be defined by Equation 5 [72]. From this equation, it

can be inferred that the flow stress for dislocation movement will be reduced by a factor of  $1/1.25$  (i.e., 0.8) [70].

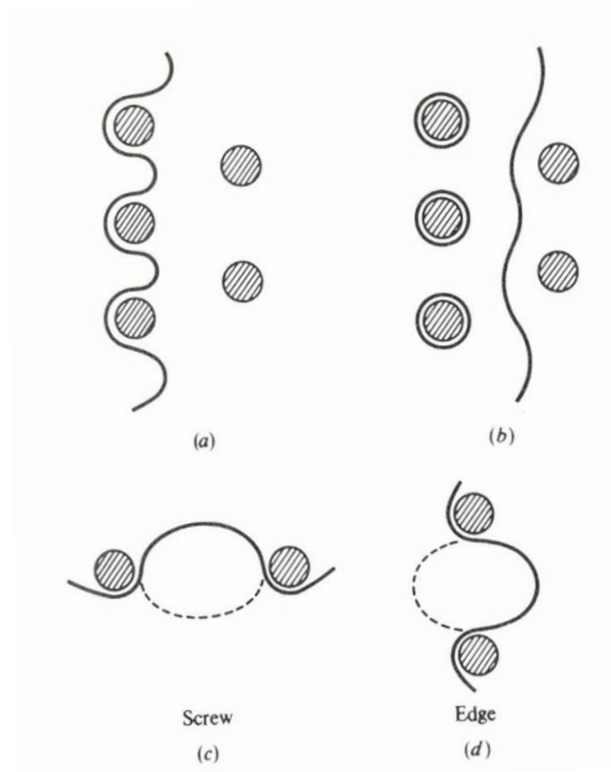


Figure 3.2. Illustrating the Orowan process, when dislocations bend between particles (a), bypassing the particles leaving a dislocation loop (b), highlighting dislocation screw (c), and edge (d) type [70]

$$\lambda_{avg} \cong 1.25r \left(\frac{2\pi}{3f}\right)^{\frac{1}{2}}$$

Equation 5

$\lambda$  = particle spacing

$r$  = particle radius

$f$  = volume fraction of particle phase

Dislocation dipole effects arise from the interaction between bending dislocation arms on opposite sides of neighboring particles. The dislocation arms have opposite



signs and are attracted towards each other, forming a dipole which reduces the bypass stress. The dislocation dipole will have a width equal to the diameter of the particles (i.e.,  $2r$ ), and the stress reduction can be written in a logarithmic term (i.e.,  $\ln(2r/r_0)$ , where,  $r_0$  is the dislocation core radius), which can be used to scale the dislocation line tension [70].

The line tension value of a screw dislocation is less than that of an edge dislocation by a factor of  $(1-\nu)^{-1}$ , where  $\nu$  is Poisson's ratio for the alloy. During the formation of an Orowan loop, the curvature for a screw dislocation is less than that for an edge dislocation, resulting in an increase in average obstacle spacing for screw dislocations compared to edge dislocations, which balances out the difference in line tension values. During shear stress calculations, the line tension value should represent the geometrical mean value for both edge and screw dislocations [70].

Combination of these factors results in a more precise estimate of the strengthening effects gained using strong particles (Equation 6) [70].

$$\tau(\text{Orowan particles}) \cong \frac{0.8 Gb}{2\pi(1-\nu)^{\frac{1}{2}}} \frac{\ln\left(\frac{2r}{r_0}\right)}{(\lambda - 2r)} \quad \text{Equation 6}$$

This theoretical model can be used to predict the resolved shear stress in both single crystal and polycrystalline metal alloys (Figure 3.3). The yield stress in polycrystalline materials is related to the resolved shear stress using the Taylor factor. The Taylor factor takes into account the average orientation of polycrystalline grains. For both face centered cubic and body centered cubic metals the most consistent value for the Taylor factor has been found to be 3.06 [73].

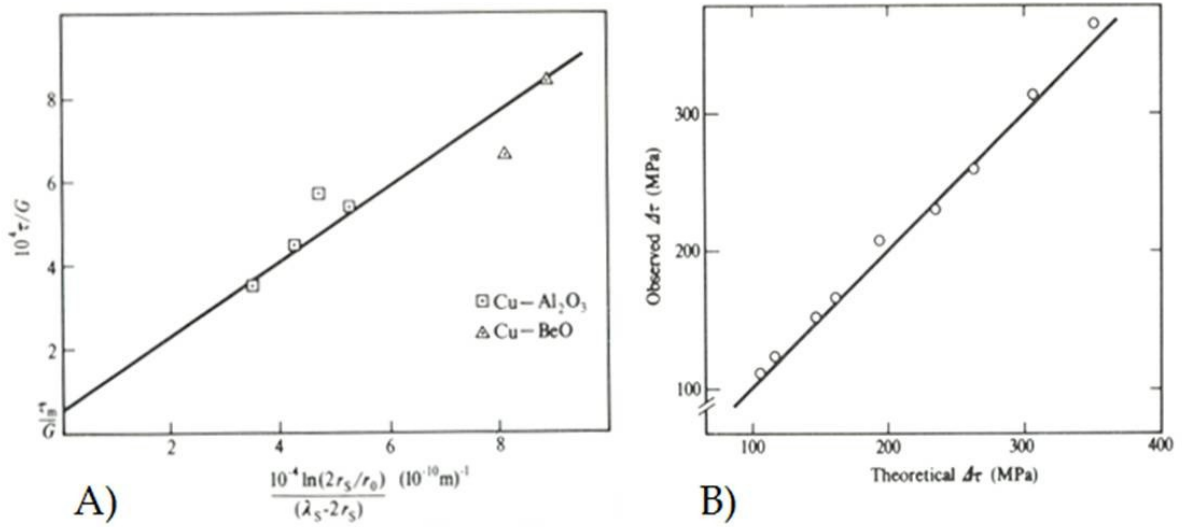


Figure 3.3. Orowan theoretical model predictions compared with experimental results: (A) single crystal copper containing Al<sub>2</sub>O<sub>3</sub> or BeO oxide dispersoids and (B) polycrystalline Co-Ni-Cr superalloy with Ni<sub>3</sub>Ti precipitates (verification of Orowan looping was performed using transmission electron microscopy) [74, 75]

The effectiveness of strong particle strengthening is highly dependent on the spacing of the particles. It can prove to be extremely difficult to obtain particle spacing that can significantly increase the strength of the alloy, but due to the substantial work hardening rate found in alloys containing strong particles (e.g., oxide dispersoids), specific processing routes can be used to introduce a large degree of stored energy into the material (Figure 3.4) [76]. This warrants the use of thermal-mechanical treatments (TMT) for alloys containing strong particles, in order to obtain a sizeable increase in alloy strength.

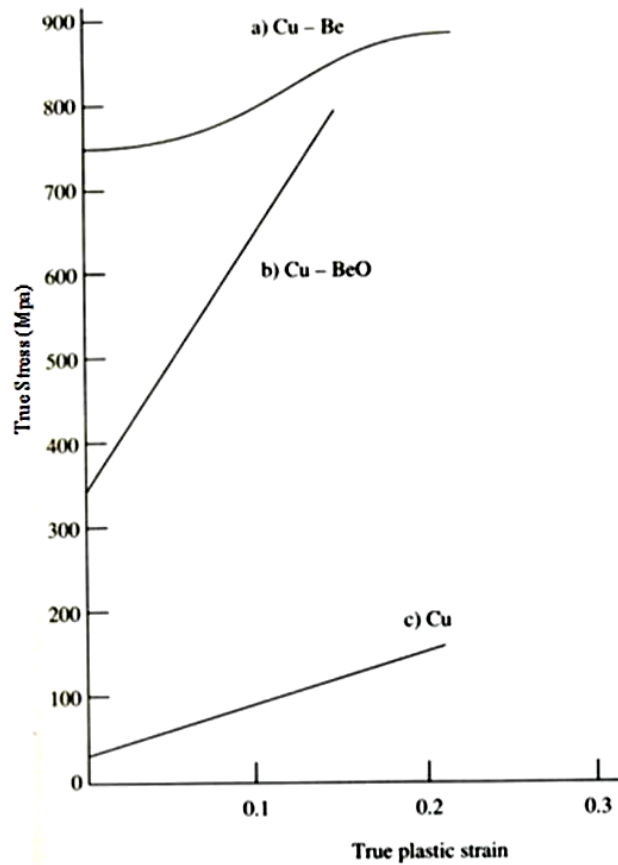


Figure 3.4. The work hardening rate for precipitate strengthened Cu-Be with shearable particles (a), oxide dispersion hardened Cu-BeO with non-shearable particles (b), and pure copper (c) [76]

The fundamental principal of using fine stable oxide dispersoids to inhibit recovery and recrystallization has been demonstrated using thoria dispersed nickel (TD-Ni) [77]. The microstructure of this alloy contains a low volume fraction ( $\sim 2.0$  vol.%) of thoria oxide particles with an average radius of 30nm. This material was processed using a series of thermal-mechanical treatments, leading to the formation of a cellular dislocation sub-grain structure with diameters ranging from 1-10 $\mu$ m. In order to identify the strength gains due to the nano-metric oxide dispersoids and the sub-grain structure, the material was tested in the as-received and fully recrystallized condition (Figure 3.5) [78].

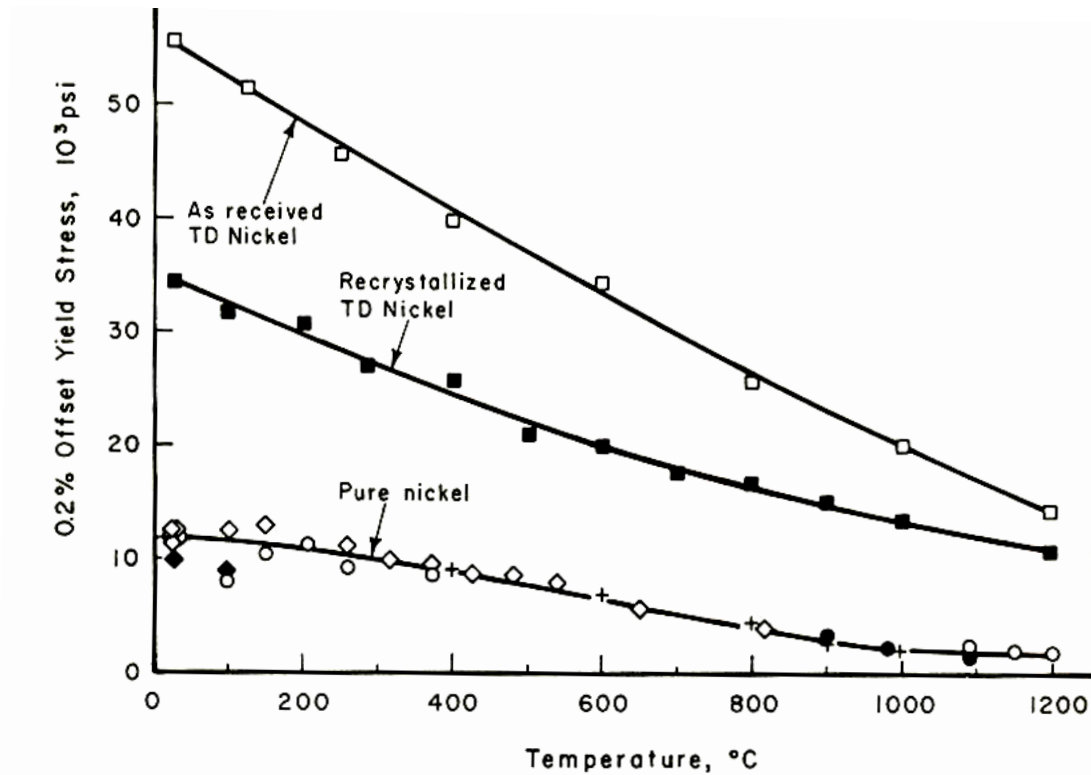


Figure 3.5. Flow-stress of TD-Ni and pure Ni as a function of temperature [78]

This comparison shows that the sub-grain structure plays a significant role in strengthening the material. The increase in strength due to the presence of oxide dispersoids can be predicted using the aforementioned hard particle resolved shear stress Orowan model (Equation 6), while the increase in strength due to the sub-grain structure can be best estimated using a Hall-Petch relationship for Ni [3]. The sub-grain structure was observed to be stable up to 1200°C, where the sub-grain boundaries showed no tendency to migrate in the presence of the thorium particles. This promotes the idea that the significant strength gains witnessed in ODS materials are of direct consequence to the large amounts of stored energy within the material [79].

ODS materials can utilize evenly distributed nano-metric oxide particles to initiate and stabilize sub-grain dislocation structures. The sub-grain structure achieved by thermal-mechanical processing results in a much finer grain structure compared to heavily deforming pure materials [80]. It has been shown that extensive plastic deformation of metal alloys containing strong particles leads to the formation of cells within the microstructure with dimensions approximately equal to the interparticle spacing of the dispersoids [3]. The stability of this sub-grain structure appears to be dependent on the size and spacing of the hard particles. It has been found that fine oxide dispersions can either accelerate or decelerate the recrystallization process depending on particle size and spacing [81]. Generally, a particle spacing greater than  $0.8\mu\text{m}$  will accelerate recrystallization, while those with smaller spacing will slow the process.

#### *Weak Obstacles*

Weak obstacles are sheared by moving dislocations. The strength increase provided by weak obstacles is a function of the force ( $F$ ) required to overcome the shear strength of such particles. Several sources can contribute to the overall value of the shearing force. These sources include coherency hardening, surface or chemical hardening, order hardening, and modulus hardening [70].

Coherency hardening results from the elastic stresses surrounding the particle in the alloy matrix. The stress field will attract or repel dislocations, resulting in an increase in yield strength [71]. This strengthening phenomenon is analogous to solid solution strengthening, except the particles can be orders of magnitude larger than a single solute atom, leading to a larger strain field and stronger interaction forces. The increase in resolved shear stress from coherency hardening can be approximated by Equation 7 and Equation 8 [71].

$$\tau_{coh} \cong 7|\epsilon_{coh}|^{\frac{3}{2}}G\left(\frac{rf}{b}\right)^{\frac{1}{2}} \quad \text{Equation 7}$$

$$\epsilon_{coh} = \frac{\alpha_p - \alpha_m}{\alpha_m} \quad \text{Equation 8}$$

$G = \text{shear modulus}$

$r = \text{particle radius}$

$f = \text{volume fraction}$

$b = \text{Burger's vector}$

$a = \text{lattice parameter}$

Surface or chemical hardening occurs as a result of the formation of new particle-matrix interface during the shearing process. Additional interfacial area is created when a dislocation enters and exits the particle. The increase in the surface energy associated with an increase in interfacial area requires work to be done to complete the process [70]. This hardening effect is thought to have a minimal impact on the overall strength of the alloy, except when the particles are extremely fine and contain a large surface area to volume ratio. The increase in resolved shear stress from chemical hardening can be approximated using Equation 9 and Equation 10 [71].

$$\tau_{chem} \cong 2G(\epsilon_{chem})^{\frac{3}{2}}\left(\frac{fr}{b}\right)^{\frac{1}{2}} \quad \text{Equation 9}$$

$$\epsilon_{chem} = \left(\frac{\gamma_s}{Gr}\right) \quad \text{Equation 10}$$

$\gamma_s = \text{particle-matrix interphase surface energy}$

Order hardening can arise when a particle contains an ordered crystal structure. Within this ordered crystal structure, it can be assumed that the bond energy

between atoms is in a low energy state. When a dislocation shears the particle, creating new interfacial surface area, the low energy bonds are broken and the ordered structure is disrupted. This can result in the formation of a high energy bond structure. The energy increase is commonly referred to as antiphase boundary energy (APBE) [71]. The difference between ordered hardening and chemical hardening is that the rise in APBE increases as the dislocation moves through the particle, instead of solely when the dislocation enters and exits the particle [71]. The increase in resolved shear stress from an ordered particle can be approximated using Equation 11-Equation 13 [71].

$$\tau_{ord} \cong 0.7G(\epsilon_{ord})^{\frac{3}{2}}\left(\frac{fr}{b}\right)^{\frac{1}{2}} \quad (\text{low } \epsilon_{ord}) \quad \text{Equation 11}$$

$$\tau_{ord} \cong 0.7G \left[ \epsilon_{ord}^{\frac{1}{2}} \left(\frac{fr}{b}\right)^{\frac{1}{2}} - 0.7\epsilon_{ord}f \right] \quad (\text{high } \epsilon_{ord}) \quad \text{Equation 12}$$

$$\epsilon_{ord} = \left( \frac{APBE}{Gb} \right) \quad \text{Equation 13}$$

Modulus hardening occurs when a dislocation enters a particle having a shear modulus different than that of the matrix, which results in alteration of the dislocation line tension (i.e.,  $Gb^2/2$ ) [70]. Knowing that the energy associated with a dislocation is a function of the shear modulus of the lattice, when a dislocation meets a particle with a different elastic modulus a change in energy is required to shear the particle and continue on the same slip plane [71]. The increase in resolved shear stress as a result in modulus hardening can be approximated by Equation 14 and Equation 15 [71].

$$\tau_{Gp} \cong 0.01G\epsilon_{Gp}^{\frac{3}{2}}\left(\frac{fr}{b}\right)^{\frac{1}{2}} \quad \text{Equation 14}$$

$$\epsilon_{Gp} = (G_p - G_m) / G_m \quad \text{Equation 15}$$

The total strength provided by weak particles results from a combination of all the aforementioned sources (see Equation 16). The effectiveness of the particles will be a function of particle size, volume fraction, distribution, and bond type.

$$\tau_{weak} = \tau_{coh} + \tau_{chem} + \tau_{ord} + \tau_{Gp} \quad \text{Equation 16}$$

### *Strengthening Summary*

The mechanism for strong and weak particle strengthening is inherently different. Classifying the particles within each alloy system can be important in forming an ideal microstructure. For the most part, dislocation interactions with oxide dispersoids (in a metal matrix) are thought to follow the Orowan bypassing process and are considered to be non-shearable (i.e., strong obstacles) [82]. Precipitate strengthening can be classified as strong or weak obstacle strengthening, but many precipitates are designed to be sheared by moving dislocations (e.g., Ni<sub>3</sub>Al- $\gamma'$  precipitates in Ni-based superalloys) [83]. A relative comparison can be made between the strength of the particles and the yield strength of the matrix material, but theoretical classification of strengthening particles can be misleading and should be verified using experimental analysis. The effective strengthening size of the particles is highly dependent on particle type. The size effectiveness of strong particles is known to scale indirectly with particle size (assuming a constant spacing), while the size effectiveness of weak particles has shown to be highly dependent on alloy system and particle chemistry, requiring a series of experimental testing to determine an ideal particle size (e.g., age hardening).

## **3.2 ODS Creep Resistance**

Creep is defined as the plastic deformation that takes place during a constant applied load and temperature in time [84]. This phenomenon generally occurs in metals at high temperature (i.e.,  $T > 0.4T_m$ ) and low stress levels (i.e.,  $\sigma \ll \sigma_y$ ). Creep behavior



can be separated into three stages, including primary, secondary, and tertiary creep as a function of time and strain (Figure 3.6). During primary creep (transient creep) the creep rate decreases with time and strain, during this stage dislocation densities are increased (analogous to work hardening), consequently decreasing the creep rate. Secondary creep is commonly referred to as steady-state creep, when work hardening effects are matched by annealing or recovery effects. Tertiary creep occurs when the creep rate increases continuously with time and strain. Typically, material failures are expected to take place during the tertiary creep stage [71].

Dislocation and diffusion creep are the primary deformation mechanisms that effect metals at high temperatures. The creep rate found at temperatures above  $0.5T_m$ , where dislocation creep (i.e., power-law creep) is the dominating mechanism, can be approximated using Equation 17 [85].

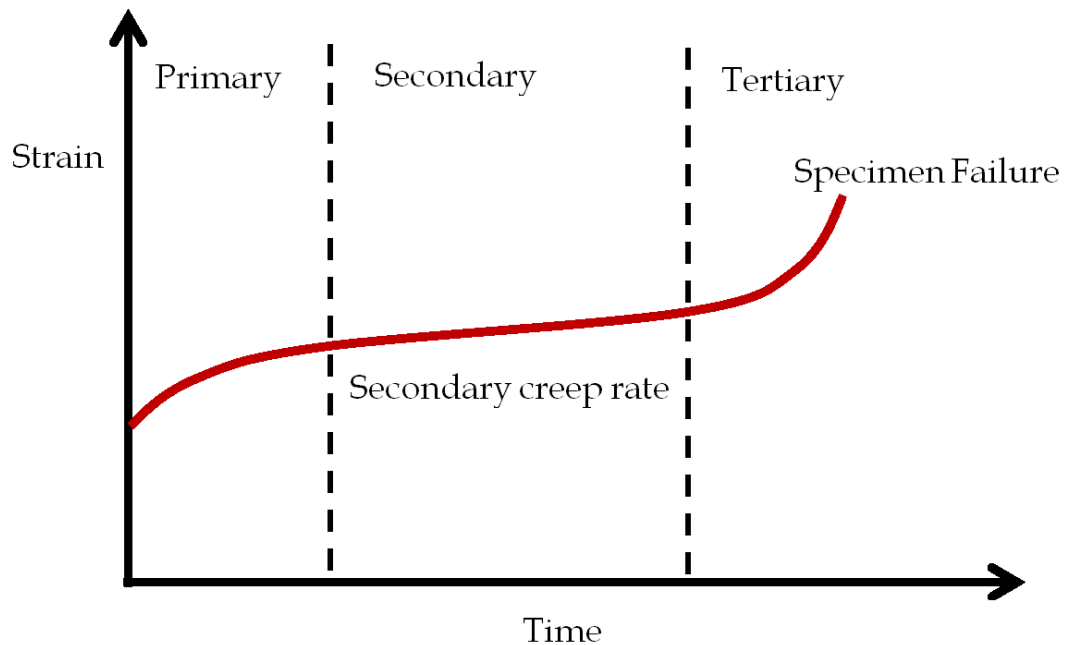


Figure 3.6. Typical creep deformation curve with a constant applied load, adapted from [85]

$$\dot{\epsilon} = A \frac{D_{eff} G b}{kT} \left(\frac{\sigma}{G}\right)^n$$

Equation 17

- $\dot{\epsilon}$  = strain rate

$D_{eff}$  = effective diffusion coefficient

$b$  = Burgers vector

$T$  = absolute temperature
- $A$  = dimensionless material constant

$G$  = shear modulus

$k$  = Boltzmann constant

$\sigma$  = applied stress

The stress exponent, n, typically has a value ranging from 3-8, which indicates the primary deformation mechanism (Table 3.2).

**Table 3.2. Relationship between stress exponent (n) and deformation mechanism during dislocation dominated creep [85]**

Stress Exponent (n)	Deformation Mechanism
~ 3	Dislocation glide
~ 5	Dislocation glide plus climb or lattice diffusion at high temperatures
~ 7	Dislocation core diffusion at low temperatures
~ 8	Lattice diffusion through a constant dislocation substructure

Diffusion dominated creep is dependent on the atomic diffusion path. At slightly elevated temperatures atomic diffusion will occur primarily along grain-boundaries (Coble creep), while at high temperatures atomic diffusion will predominantly occur throughout the lattice of the material (Nabarro-Herring creep). The creep rate due

to Coble and Nabarro-Herring diffusion creep deformation can be approximated using Equation 18 and Equation 19, respectively [85].

$$\dot{\epsilon}_{Co} = \frac{A_{Co} D_{GB} G b}{kT} \left(\frac{b}{d}\right)^3 \frac{\sigma}{G} \quad \text{Equation 18}$$

$$\dot{\epsilon}_{NH} = \frac{A_{NH} D_L G b}{kT} \left(\frac{b}{d}\right)^2 \frac{\sigma}{G} \quad \text{Equation 19}$$

$D_{GB}$  = grain boundary diffusion

$D_L$  = lattice diffusion

$d$  = grain diameter

Creep deformation maps are used to identify the primary creep mechanism at a given temperature and stress for a particular material system (Figure 3.7). The use of such maps can be critical to microstructure design and material life predictions.

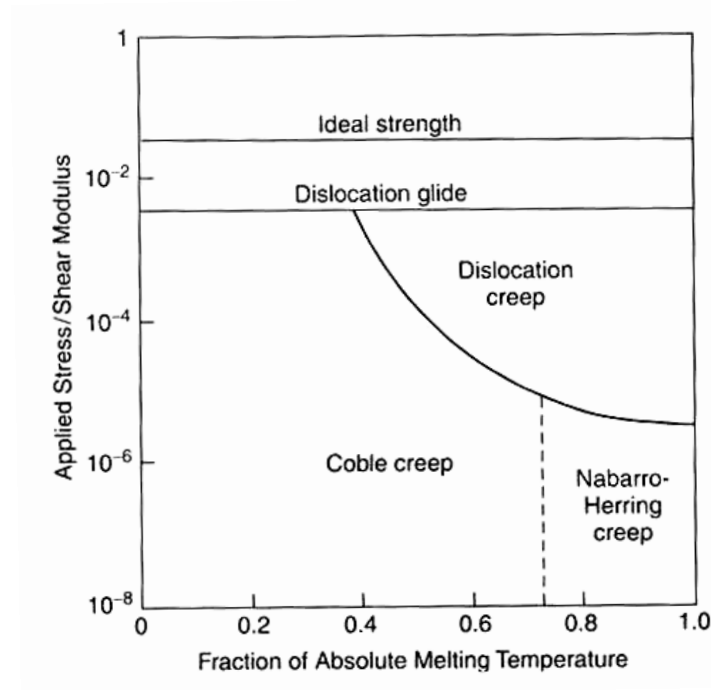


Figure 3.7. Creep deformation mechanism map for pure polycrystalline materials [85]

### 3.2.1 Creep in Oxide Dispersion Strengthened Materials

Creep resistance in ODS alloys is related to the strengthening mechanism (e.g., Orowan process), in which the dispersoids invoke a strong resistance to dislocation creep. The stress exponent ( $n$ ), defined by dislocation creep (Equation 17), is usually less than 10 for dispersoid free alloys, but has been found to be extremely high ( $n \gg 20$ ) in dispersion strengthened materials, in conjunction with unusually large activation energies required for creep deformation (i.e., activation energies for bulk lattice diffusion) [86]. This unusual creep behavior is thought to be linked to the threshold stress required for dislocations to climb dispersoids, and the detachment stress required to overcome the attractive interaction force between the dislocations and dispersoids [87].

Creep deformation in ODS materials can occur well below the Orowan stress (Equation 6) at elevated temperatures, due to dislocations climbing over localized dispersoids. The dislocation climb process requires an increase in the dislocation line length, resulting in an increase in energy. Thus, a threshold stress must be exceeded before the climbing process can occur. The addition of a threshold stress ( $\sigma_{th}$ ) variable to the conventional power law creep equation is not straight forward, because  $\sigma_{th}$  is a poor material constant which can vary greatly with temperature and stress [88]. Also, it has been shown that dislocation climb does not lead to unusually high stress exponents, suggesting that dislocation climb alone does not explain the creep behavior in ODS materials [89].

The concept of a detachment stress threshold arises from the attractive interaction between a dislocation and dispersoid particle. This attraction results when the stress field surrounding the dislocation is relaxed at the incoherent or strained dispersoid/matrix interface by slipping and rapid diffusion [88]. A dislocation located at the detachment edge of a dispersoid particle after slow creep deformation is shown in Figure 3.8. Further research has shown that detachment stress required

to overcome this attractive force is far greater than stress predictions for dislocation climb [87].

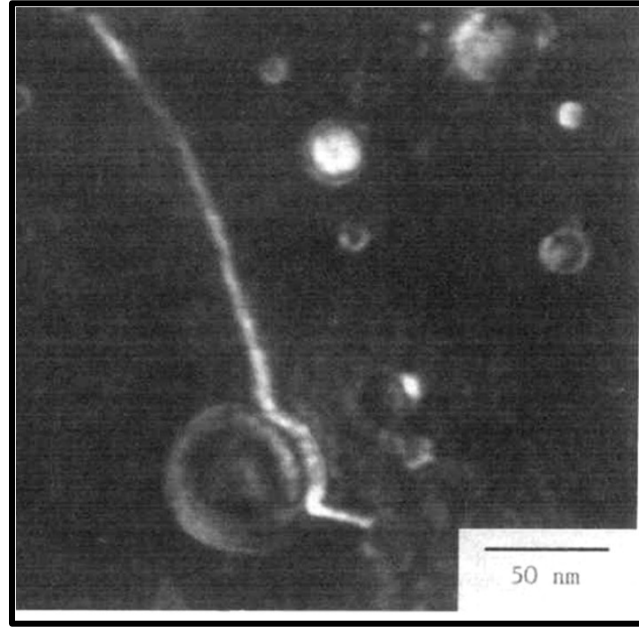


**Figure 3.8. Weak beam TEM micrograph identifying a dislocation attached to a dispersoid particle in dispersion strengthened MA6000 [90]**

An Arrhenius type model for predicting dislocation creep in ODS materials has been developed and has demonstrated moderate success in predicting dislocation creep in ODS alloys (Equation 20) [88]. This model considers the activation energy required for dislocation detachment from attractive dispersoid interfaces.

$$\dot{\epsilon} = \dot{\epsilon}_0 * \exp\left(-\frac{E_d}{k_B T}\right) \quad \text{Equation 20}$$

$$\dot{\epsilon}_0 = \frac{D_v \lambda \rho}{b} \quad \text{Equation 21}$$

$D_v$  = volume diffusivity

$\lambda$  = particle spacing

$\rho$  = density of mobile dislocations

$b$  = Burgers vector

$k_B$  = Boltzmann's constant

$T$  = absolute temperature

$E_d$  = activation energy required for dislocation detachment

The activation energy required for dislocation detachment is a function of the dislocation line tension, relaxation parameter, and applied stress (see Equation 22) [88].

$$E_d = Gb^2r \left[ (1 - k) \left( 1 - \frac{\sigma}{\sigma_d} \right) \right]^{\frac{3}{2}} \quad \text{Equation 22}$$

$G$  = shear modules

$b$  = Burgers vector

$r$  = dispersoid radius

$k$  = relaxation parameter

$\sigma$  = applied tensile stress     $\sigma_d$  = detachment stress

For a relaxation parameter equal to unity (i.e.,  $k=1$ ), no attraction between the dispersion particles and the dislocation exists, but for a relaxation parameter less than unity (i.e.,  $k<1$ ), an attractive interaction is present and increases as  $k$  approaches zero. The relaxation parameter has shown to be dependent on particle spacing, size, and volume fraction, and can be determined experimentally using Equation 23, where the resolved shear stress required for dislocation detachment in polycrystalline materials is related to  $\sigma_d$  by the Taylor factor [88].

$$\tau_d = \tau_o \sqrt{1 - k^2} \quad \text{Equation 23}$$

$\tau_d$  = detachment resolved shear stress

$\tau_o$  = Orowan resolved shear stress

The experimental creep behavior in dispersion strengthened Al-2.16C-0.80O (wt.%) was used to test the validity of this creep model (Figure 3.9). This alloy contains  $\text{Al}_2\text{O}_3$  and  $\text{Al}_4\text{C}_3$  dispersion strengthening particles, and displays characteristic ODS

creep behavior at intermediate strain rates with an extremely high stress exponent value (i.e.,  $n \approx 200$ ) [91]. The creep mechanism during intermediate strain rates was found to be controlled by interactions between single dislocations and dispersion particles using *in situ* TEM analysis. At higher strain rates ( $\dot{\epsilon}/D_v > 10^{12} \text{ m}^{-2}$ ) the effectiveness of the dispersion particles is negated, due to the formation of a large dislocation networks which also can be found in dispersoid-free materials. At low strain rates and high temperatures the degradation in creep strength is thought to be related to the materials fine grain size, and the creep mechanism is most likely controlled by the onset of grain boundary sliding [91].

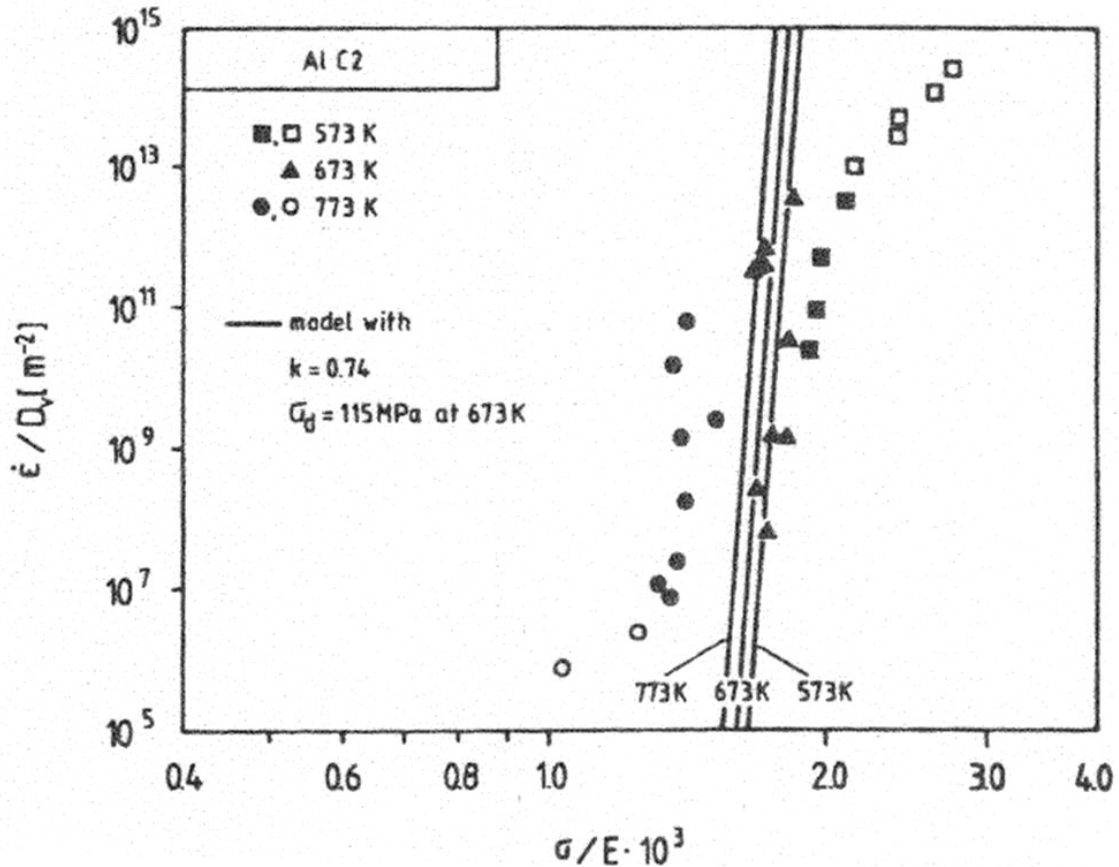


Figure 3.9. The normalized creep rate as a function of stress for fine grained dispersion strengthened Al-2.16C-0.80O (wt.%) [91]

This model seems to be well suited for predicting creep behavior in ODS materials when dislocation creep is the primary deformation mechanism at intermediate strain rates. In order to better understand the creep properties of ODS materials a detailed creep analysis is required on a per alloy basis, due to the strong dependence between creep behavior and microstructural features in ODS alloys. Furthermore, the development of creep mechanism maps for specific ODS alloys will be necessary for predicting creep behavior during elevated temperature operation of these materials.

### 3.3 Oxide Particle Formation and Growth

The effectiveness of oxide dispersion strengthening (ODS) is highly dependent on alloy microstructure (see Strengthening Mechanisms 3.1). The ideal ODS microstructure should contain an array of evenly distributed, finely spaced, nano-scale oxide particles. The distribution and size of such particles will depend on thermodynamic and kinetic mechanisms. The formation of second phase particles, within a solid-solution parent phase matrix, has been shown to result from precipitation [80]. Precipitation is a thermally activated process, in which a critical nucleation energy barrier must be overcome to progress forward with nucleation and growth.

#### 3.3.1 Precipitation

During homogeneous nucleation, precipitation of a second phase occurs by means of nucleation and growth without the benefit of preexisting defects or impurities. The thermodynamics of nucleation are governed by the relationship between the change in volumetric Gibbs free energy ( $\Delta G_v$ ), interfacial energy ( $\sigma$ ), and strain energy ( $\epsilon$ ) in solids (Equation 24) [80].

$$\Delta G = \Delta G_v + \sigma + \epsilon$$

Equation 24



It can be seen in Figure 3.10A, that a critical thermodynamic nucleation barrier ( $\Delta G^*$ ) must be overcome before nuclei growth becomes energetically favorable. This barrier can be very large and is unlikely to be overcome during homogeneous nucleation (see Figure 3.10B).

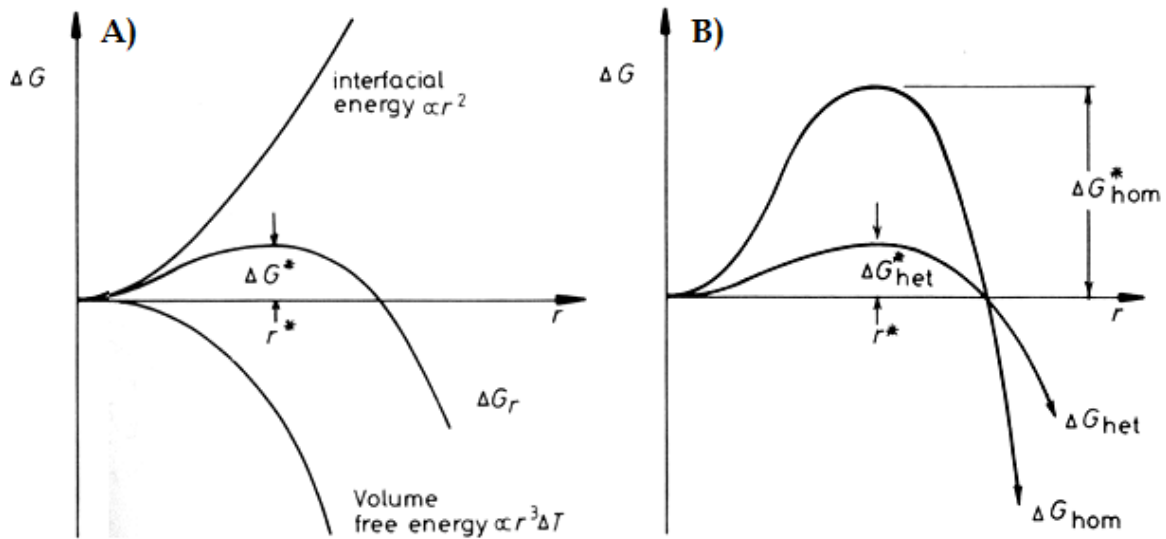


Figure 3.10. Change in Gibbs free energy as a function of nucleus size (A) and thermodynamic nucleation barrier comparison for homogeneous and heterogeneous nucleation (B) [92]

Heterogeneous nucleation occurs at regions with higher than average free energy, such as dislocations or grain boundaries. During precipitation the nucleus replaces part of the high energy dislocation line or grain boundary and uses the favorable change in Gibbs free energy to drive the reaction [92]. For this reason, heterogeneous nucleation requires less energy and has a smaller nucleation barrier than homogeneous nucleation (see Figure 3.10B). Several common defects that promote heterogeneous nucleation include grain boundaries, grain edges, grain corners, dislocations, surfaces, and impurity particles [80]. Furthermore, the precipitation formation rate can also be impacted by the presence of such defects, when considering the increased concentrations of solute atoms and increased diffusivities found in these regions [80].

### 3.3.2 Precipitate Growth

The precipitate growth rate is limited to the rate in which atoms are brought to the precipitate interface, or the rate in which the atoms cross the interface. During early stage growth the rate limiting step is typically interface controlled, due to the initial diffusion distances being negligible [80]. As the precipitate grows the rate limiting step becomes diffusion controlled, as a result of increased diffusion distances and a reduction in the solute concentration gradient (which drives the reaction) [80].

If the precipitates are assumed to be small, coherent spheres and diffusion is considered the rate limiting step, then the growth of such precipitates in a supersaturated solid solution with a radius (R) as a function of time (t) can be described using Equation 25 [80]. Precipitates will continue to grow in a  $t^{1/2}$  manner until the solute concentration within the matrix reaches equilibrium. This marks the end of the precipitate growth stage.

$$R = k(Dt)^{\frac{1}{2}} \quad \text{Equation 25}$$

$$k = -\frac{(C_I - C_M)}{2(C_P - C_I)} \quad \text{Equation 26}$$

D = volume diffusivity coefficient

$C_I$  = concentration at the precipitate/matrix interface

$C_M$  = concentration in the matrix at a remote point

$C_P$  = solute concentration in the precipitate

### 3.3.3 Precipitate Coarsening

The coarsening of precipitates occurs as a result of the interfacial free energy between the precipitate and the matrix. Coarsening of precipitates is commonly referred to as “Ostwald ripening”, after first being discovered by Ostwald during

examination of salt precipitates in aqueous solutions [93]. The interfacial free energy of metallic precipitates in a metal matrix has been found to vary from 0.2-0.6 Jm<sup>-2</sup> [80]. Interfacial energy is related to the coherency and bonding of the precipitate as compared with the matrix phase. Lowest energy values are found in coherent precipitates with similar metallic bonds, while highest energy values are found in incoherent precipitates with a different bond structure (e.g., ionic or covalent bonding in oxides) [80].

In the case of incoherent precipitates (e.g., oxides in a metal matrix), the precipitates usually grow and coarsen in a spherical geometry to minimize the interfacial surface energy. The surface area to volume ratio for a sphere decreases as the radius of the sphere increases, so as coarsening progresses the larger precipitates grow at expense of the smaller ones in an effort to lower the overall free energy of the alloy system.

The mechanism of coarsening (Ostwald ripening) is derived from the increased solid solubility found in smaller precipitates. This increased solubility is a direct result of the increased surface area to volume ratio found in these smaller precipitates. This increased ratio can shift (increase) the local equilibrium solid solubility at the precipitate/matrix interface [92]. This is known as the Gibbs-Thomson effect, which takes into account the rise in chemical potential ( $\Delta\mu$ ), as a result of increased interfacial energy ( $\sigma$ ) at the precipitate/matrix interface (Equation 27) [80]. This increased solubility creates a concentration gradient driving the solute atoms towards the larger precipitates via diffusion. As the coarsening process continues the solute concentration gradient becomes more severe, thus promoting an increased rate of diffusion until the smaller precipitates are fully dissolved.

$$\Delta\mu = \sigma V_m 2/r \quad \text{Equation 27}$$

$V_m$  = precipitate molar volume

$2/r$  = curvature of spherical surface

Precipitate coarsening is controlled by a rate limiting step that is highly dependent on the microstructure of the alloy. Assuming a kinetic relationship for the coarsening of precipitates (Equation 28), this rate limiting step can be identified using Table 3.3 [80].

$$r^n = kt$$

Equation 28

$r$  = precipitate radius

$n$  = rate limiting exponent

$k$  = material constant defined by diffusion mechanism and temperature

$t$  = coarsening time

Table 3.3. Coarsening rate limiting step identification exponent [94-97]

Exponent (n)	Rate Limiting Step
2	Atom transfer across interface
3	Matrix diffusion
4	Grain boundary diffusion
5	Dislocation pipe diffusion

The solid solubility of oxides in metals is extremely low, and thus oxide precipitates resist Ostwald ripening even at extremely high temperatures. Alloys containing fine oxide dispersoids as a strengthening mechanism have shown a strong resistance to coarsening and recrystallization at elevated temperatures, even when considerable dislocation substructures have been introduced into the alloy by cold or hot working [80]. The resulting mechanical properties of such alloys are related to both the oxide precipitates and the stabilized substructure, thus the stability of the entire alloy microstructure is heavily dependent on the dispersoids resistance to coarsening. Coarsening experiments performed on thoria-dispersed nickel (TD-Ni) showed the

solubility of thoria to be only  $5 \times 10^{-2}$  wt.% at  $1350^{\circ}\text{C}$  with an average particle size of 60nm after 200 hours at a temperature of  $0.94T_m$  [95].

### **3.3.4 Summary**

Precursor alloy powders used for ODS alloy formation are engineered to start with a supersaturated solid-solution microstructure. Defect concentrations in these powders should be increased to promote heterogeneous nucleation of oxide precipitates. Consolidation and heat treatment procedures should be designed to promote an even distribution of nano-scale oxide precipitates, while minimizing growth effects, until equilibrium conditions are reached. Due to oxide dispersoids being extremely resistant to coarsening in a metal matrix, the alloy should be cold or hot worked in order to develop a dislocation substructure to increase alloy strength.

## **3.4 Mechanical Alloying**

Mechanical alloying was first used to form an oxide dispersion strengthened (ODS) microstructure in 1970. The discovery was made by J.S. Benjamin at the International Nickel Company (INCO, currently known as Special Metals) [98]. The motivation of this research was to develop a Ni-based superalloy with a wide operating temperature range, in which the alloy would provide both a strong intermediate and high temperature strength and creep resistance. The solution was to combine the advantages of both gamma-prime (e.g.,  $\text{Ni}_3\text{Al}$ ) precipitates and nano-scale oxide precipitates (e.g.,  $\text{Y}_2\text{O}_3$  or  $\text{ThO}_2$ ). The ideal microstructure was produced by mechanically blending nickel, chromium, yttria or thoria, and nickel-aluminum-titanium master alloy powders together in a high energy attritor mill for 40 hrs in air. The resulting particles were consolidated using hot extrusion techniques at a temperature of  $\sim 1177^{\circ}\text{C}$  or below with extrusion ratios of 12:1 or greater [98]. The consolidated parts were heat treated at  $1274^{\circ}\text{C}$  for 2 hours in Ar and air cooled, followed by a solution treatment at  $1080^{\circ}\text{C}$  for 7 hours in air and air cooled, concluding with an aging treatment at  $705^{\circ}\text{C}$  for 16 hours in air and air cooled [98].

The solution and aging treatment is typical for conventional Ni-based superalloys. The resulting microstructure was found to contain both gamma-prime precipitates and nano-scale oxide dispersoids. This initial experiment was deemed a success, proving the ability to form a nano-scale ODS microstructure using mechanical alloying techniques.

### 3.4.1 Mechanical Alloying Process

Mechanical alloying (MA) has been used for the formation of ODS microstructures for several decades, but much is still not readily understood about this complex and stochastic process [12]. This process has traditionally been used for the fabrication of precursor ferritic stainless steel ODS powders (see Figure 3.11).

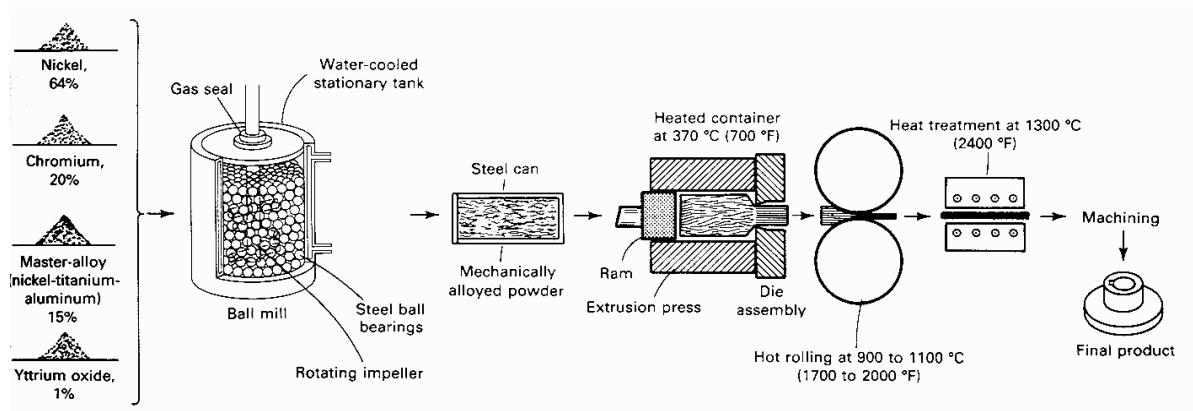


**Figure 3.11. Mechanical milling followed by hot deformation processing for the formation of an ODS microstructure [12]**

During mechanical alloying the base metal and alloying additives are inserted into a high energy shaker, planetary, or attritor mill. The milling time can last for up to 80 hours, during which alloying occurs through a complex series of cold welding, fracturing, and folding at the nano-metric particle interfaces (see Figure 3.12) [99].

The as-milled particles have been shown to have a single phase microstructure, signifying that all alloying constituents were forced into a supersaturated solid

solution and that the ceramic powders were dissociated [100]. This result shows that solid solubility limits can be expanded beyond equilibrium predictions using mechanical alloying. In some cases MA can achieve a far greater degree of solute trapping than possible using rapid solidification processing (RSP) [101].

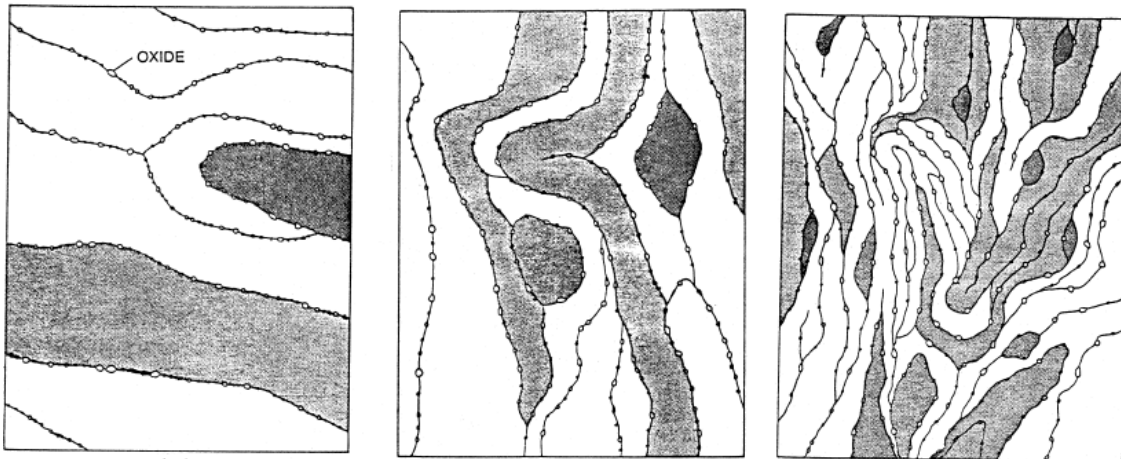


**Figure 3.12. Microstructural evolution during mechanical milling of both ductile and brittle powders (typical of ODS alloys) [101]**

After the milling process the resulting powders are consolidated using elevated temperature extrusion and subsequent heat treatments to promote the formation and distribution of nano-metric oxide dispersoids [1]. Also, to achieve ideal mechanical properties the alloy will commonly be subjected to a series of thermal mechanical treatments (TMT), in order to form a stable dislocation sub-grain structure [102]. This processing method has proven to be effective in introducing nano-metric oxide dispersoids into a parent matrix phase, which has been reported to drastically increase the mechanical performance of select ferritic alloys [2].

### **3.4.2 Problems with Mechanical Alloying**

Mechanical alloying (MA) unfortunately contains many key problems that can severely limit the process at a commercial scale. Many of the processing problems stem from the extended time requirement needed for uniform alloying to occur. The

processing time is important because it can greatly affect the final cost of the precursor powder, which can ultimately limit the applications of the resulting alloy [12]. The time required for sufficient milling of an alloy is directly dependant on the energy of the mill. For example, a process that takes a few minutes in a SPEX mill (i.e. shaker mill) can take hours in an attritor mill, or a few days in a commercial planetary mill [103]. This illustrates the difficulties faced when scaling up a milling procedure from a SPEX mill, with a capacity of approximately 0.01 kg, to an attritor mill with a capacity up to 45 kg, or to a large planetary (or rod) commercial mill that can produce up to 180 kg of material at a time [103]. A comparison of the relative processing rate for MA and a common RSP technique (i.e., gas atomization) is shown in Figure 3.13.

Longer milling times can also lead to unwanted contamination within the alloy powders (e.g., carbon, oxygen, argon, and milling debris). This contamination can lead to the formation of non-ideal impurity phases that can limit the mechanical integrity of the final consolidated part.

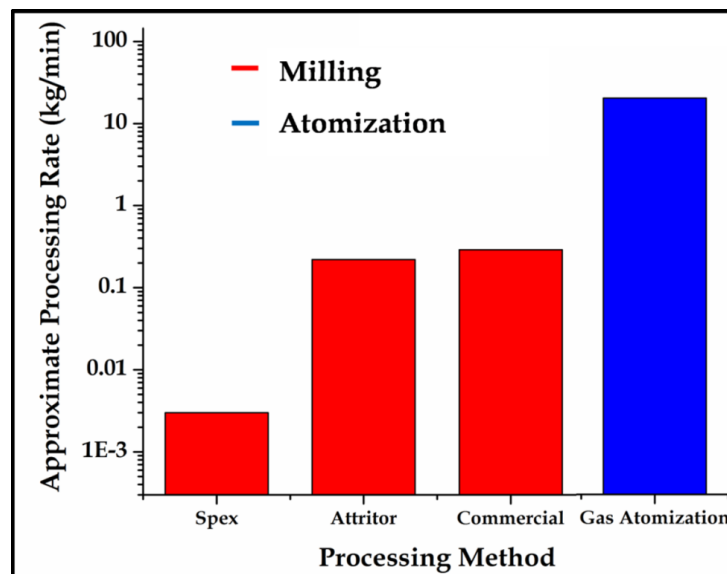


Figure 3.13. Relative processing rate comparison between MA processing and RSP (i.e., gas atomization) [103, 104]



### 3.5 Fe-based Oxide Dispersion Strengthened Alloys

The composition of two Fe-based ODS alloys (i.e., MA956 and PM2000) is displayed in Table 3.4. MA956 was developed by Special Metals Inc., and PM2000 was developed at Schwarzkopf Technologies, both alloys were designed to be Fe-based superalloys for high temperature creep and oxidation resistant applications. These alloys have been used as burner hardware in coal-fired boilers and as heat exchanger tubing in advanced energy conversion power plants [105].

Table 3.4. Alloy composition for commercial Fe-based ODS MA956 and PM2000 [1, 106, 107]

Element (wt. %)	Fe	Cr	Y	Al	Ti	W	O
MA956	Bal.	21.7	0.4	5.8	0.3	-	0.2
PM2000	Bal.	18.9	0.4	5.1	0.5	-	0.2

#### 3.5.1 Mechanical Alloying Process and Consolidation

These Fe-based ODS alloys were produced using a proprietary high energy mechanical alloying process. Specifics about the milling process are unknown, but the basic processing steps have been defined (Figure 3.14). First, elemental and master alloy gas atomized powders are blended with nano-sized yttria ( $Y_2O_3$ ) particles in a high energy ball mill. The milling process is highly critical in achieving an ideal ODS microstructure, and the process should continue until the heavily deformed powder particles reach a super-saturated solid solution condition. The heavily deformed particulate is then consolidated using various hot compaction techniques (e.g., hot extrusion or hot isostatic pressing), during which formation of the nano-sized oxide dispersoids takes place. The final step is to recrystallize and

grow the grains in the consolidated part for increased creep resistance. Recrystallization takes place during high temperature zone annealing of the consolidated part. Zone annealing is used to promote directional recrystallization and growth to assist in the formation of a large grain aspect ratio (GAR). GARs found in Fe-based ODS materials can be as large as 100:1, and are typically limited only by the length of the part [105].

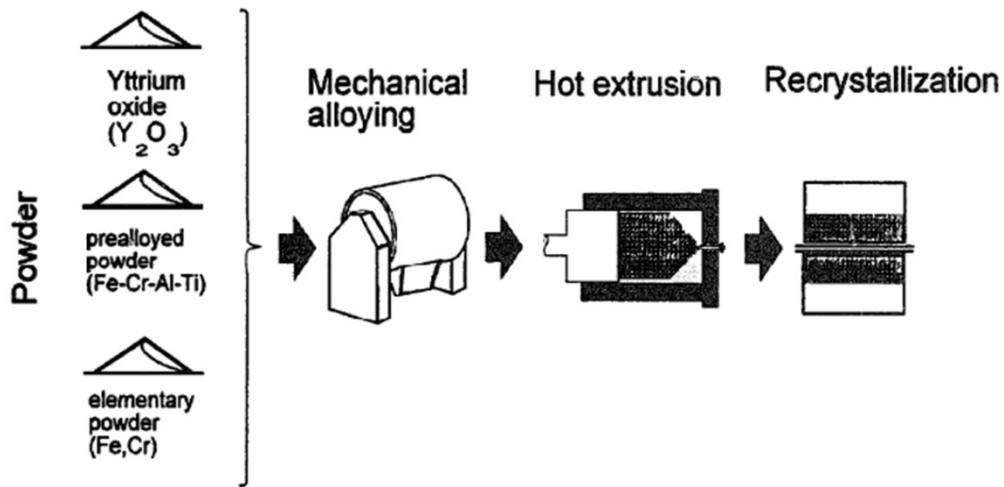


Figure 3.14. Mechanically alloyed Fe-based ODS processing method [108]

### 3.5.2 Macrostructure and Microstructure

The macrostructure found in as-received Fe-based ODS MA956 is shown in Figure 3.15. The macrostructure transverse to the extrusion direction contains an average grain size of  $\sim 4$  mm (Figure 3.15A), while the macrostructure longitudinal to the extrusion direction contains large columnar grains with an average size  $\sim 120$  mm (Figure 3.15B) [4]. This alloy contains a GAR of  $\sim 30:1$ , which was formed upon high temperature recrystallization. Large GARs were developed for superior creep resistance in the longitudinal direction, but this highly anisotropic macrostructure can severely limit part applications (e.g., tubing), where the stress field promotes creep in the transverse direction [1].

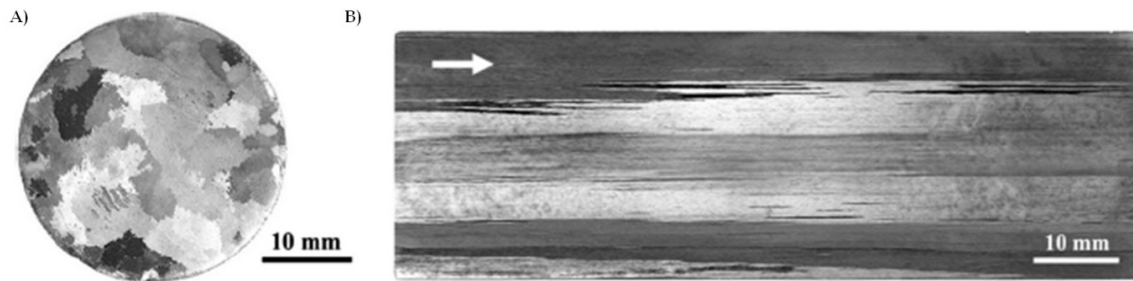


Figure 3.15. As-received MA956 rod macrostructure: (a) transverse section and (b) longitudinal section highlighting the long columnar grains [4]

These alloys contain an  $\alpha$ -Fe matrix with  $\sim 2.0$  vol.% nano-sized oxide precipitates (see Figure 3.16). The average size of the oxide precipitates in the as-received condition is  $\sim 13$  nm and  $\sim 9$  nm for MA956 and PM2000, respectively [109]. The precipitates are generally found to be predominantly mixed oxides of  $Y_2O_3$  and  $Al_2O_3$  (e.g., Y-Al garnets, Y-Al perovskite, Y-Al monoclinic, and Y-Al tetragonal), with a few precipitates being larger  $Al_2O_3$ , TiC, and Ti(N,C) particles [4, 105].

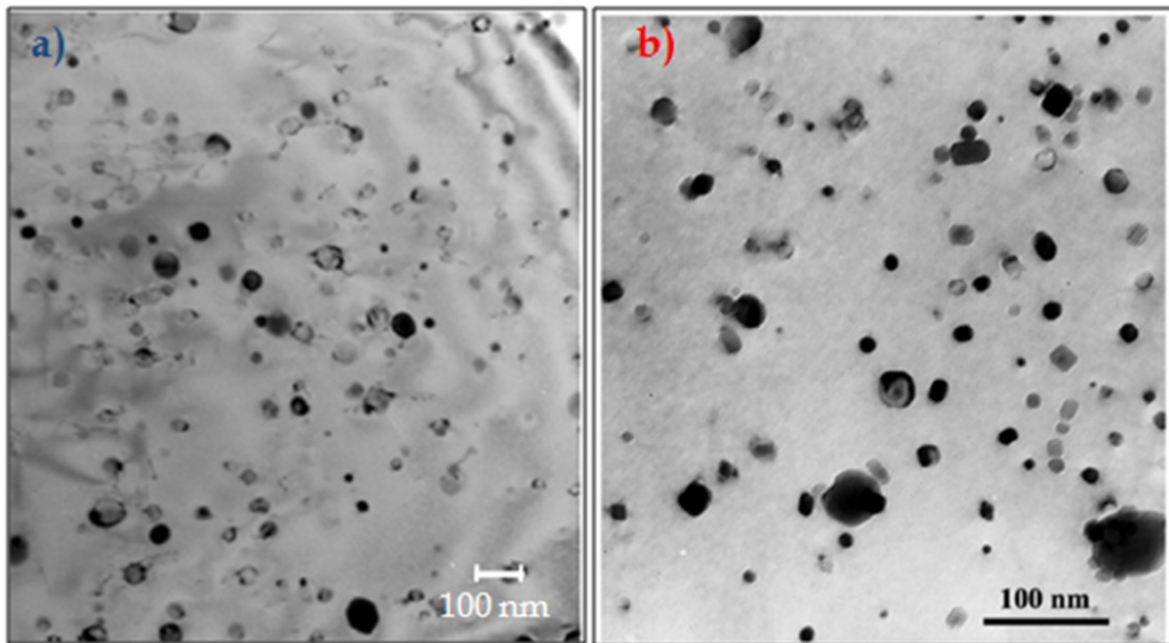
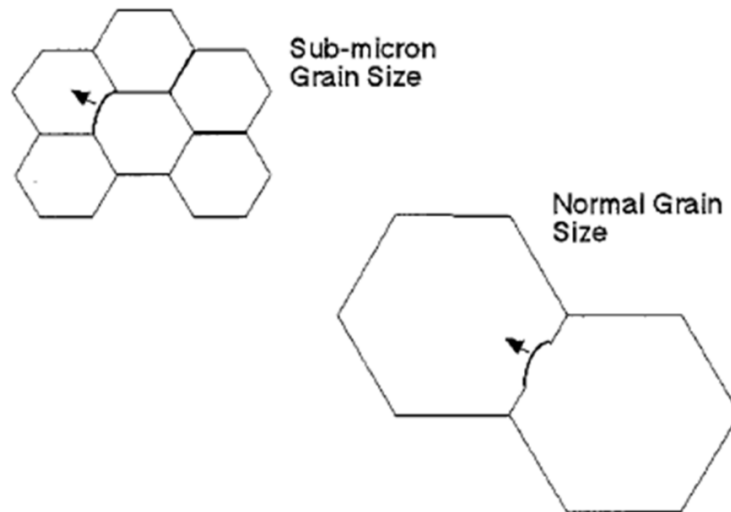


Figure 3.16. ODS microstructure of as-received (a) PM2000 and (b) MA956 [4, 110]

### 3.5.3 Recrystallization of Deformed ODS Microstructures

As-consolidated Fe-based ODS materials are often very difficult to recrystallize, requiring an extremely high annealing temperatures sometimes above  $0.9T_m$  [111]. This is quite a unique phenomenon, since the as-consolidated structure contains a large amount of stored energy, which can lower the activation energy required for grain recrystallization. The barrier to grain nucleation during recrystallization is related to the fine dislocation substructure (i.e., ultra-fine grains) that develops during hot consolidation of the heavily deformed mechanically alloyed particles. In this case, the submicron grain boundary junctions act as pinning points, preventing large angle bowing or bulge formation from reaching a critical nucleation size (see Figure 3.17) [112].



**Figure 3.17. Nucleation of grain recrystallization in as-consolidated MA ODS materials, illustrating that grain boundary junctions act as barriers to grain boundary bulge formation [112]**

A similar dislocation substructure can be developed in coarse grained ODS materials using a series of thermal-mechanical-treatments (TMT) (Figure 3.18). During this process, the alloy is heavily deformed by means of hot or cold working, which leads to very large defect concentrations, due to the inherent rapid work hardening rate

found in ODS materials (See Figure 3.4). The material is subsequently annealed to invoke recovery and not recrystallization. The recovery time is dependent on defect concentration and temperature [5]. Recrystallization will lead to the annihilation of the dislocation substructure. Several TMT cycles may be required to develop an ideal dislocation substructure. As previously mentioned (Section 3.1: Strengthening Mechanisms), this process could be used to increase the strength in ODS alloys.

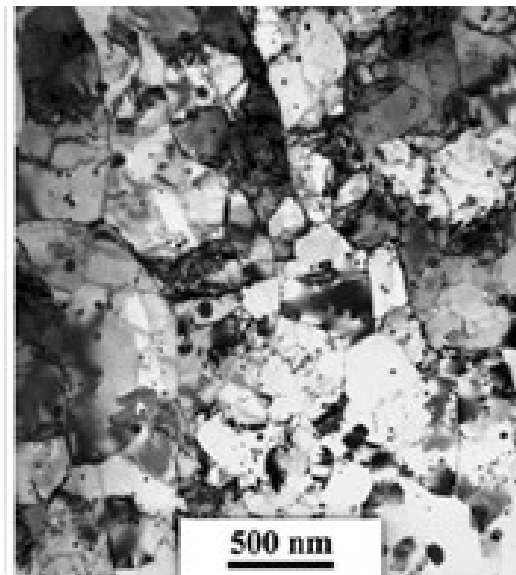


Figure 3.18. Bright field TEM image of the dislocation substructure found in MA 956 after 47% cross-section reduction with a recovery anneal at 800°C for 1 hour [5]

### 3.5.4 Mechanical Properties

The mechanical properties found in Fe-based ODS MA956 and PM2000 are highly dependent on microstructure. Elevated temperature yield strength, tensile strength, and total elongation data are shown in Figure 3.19. PM2000 proves to be significantly stronger than MA956 at lower temperatures (i.e.,  $T \leq 600^{\circ}\text{C}$ ), but at higher temperatures ( $T \geq 800^{\circ}\text{C}$ ) the strengths of the two alloys began to converge. The differences in strength values can be explained by the varying microstructure in the tested specimens. It has been reported that the microstructure of the MA956

alloy was tested in the fully recrystallized condition, while the microstructure of the PM2000 alloy contained regions that were unrecrystallized [1]. Also, it was reported that the grain size for the MA956 alloy was larger than the grains found in the PM2000 alloy (although no quantifiable data was provided), and by assuming a simple Hall-Petch strength relationship the differing strength values found at lower temperatures can be justified [1]. The similar strength values found at higher temperatures can be explained by assuming each ODS alloy contains a near identical spatial distribution of alike dispersoids (see Figure 3.16), which requires a comparable detachment stress during dislocation climb at elevated temperatures.

The difference in grain size also effects the elongation found in the two alloys, and knowing that ductility is inversely related to grain size explains why PM2000 demonstrated a greater elongation than MA956. This analysis highlights the importance of identifying the processing state and microstructural features present in the alloy prior to testing. Additionally, a peak in ductility was highlighted at  $\sim 600^{\circ}\text{C}$ , which has been postulated as the transition temperature between transgranular and intergranular fracture within these alloys [113].

A comparison between the elevated temperature creep behavior found in Fe-based ODS MA956 and PM2000 and Ni-based IN 100 (precipitate strengthened) and IN 617 (solid solution strengthened) alloys is shown in Figure 3.20. This comparison provides insight into the stability of the Fe-based ODS microstructure at elevated temperatures, in contrast to the Ni-based alloys where large strength losses are related to an evolving microstructure.

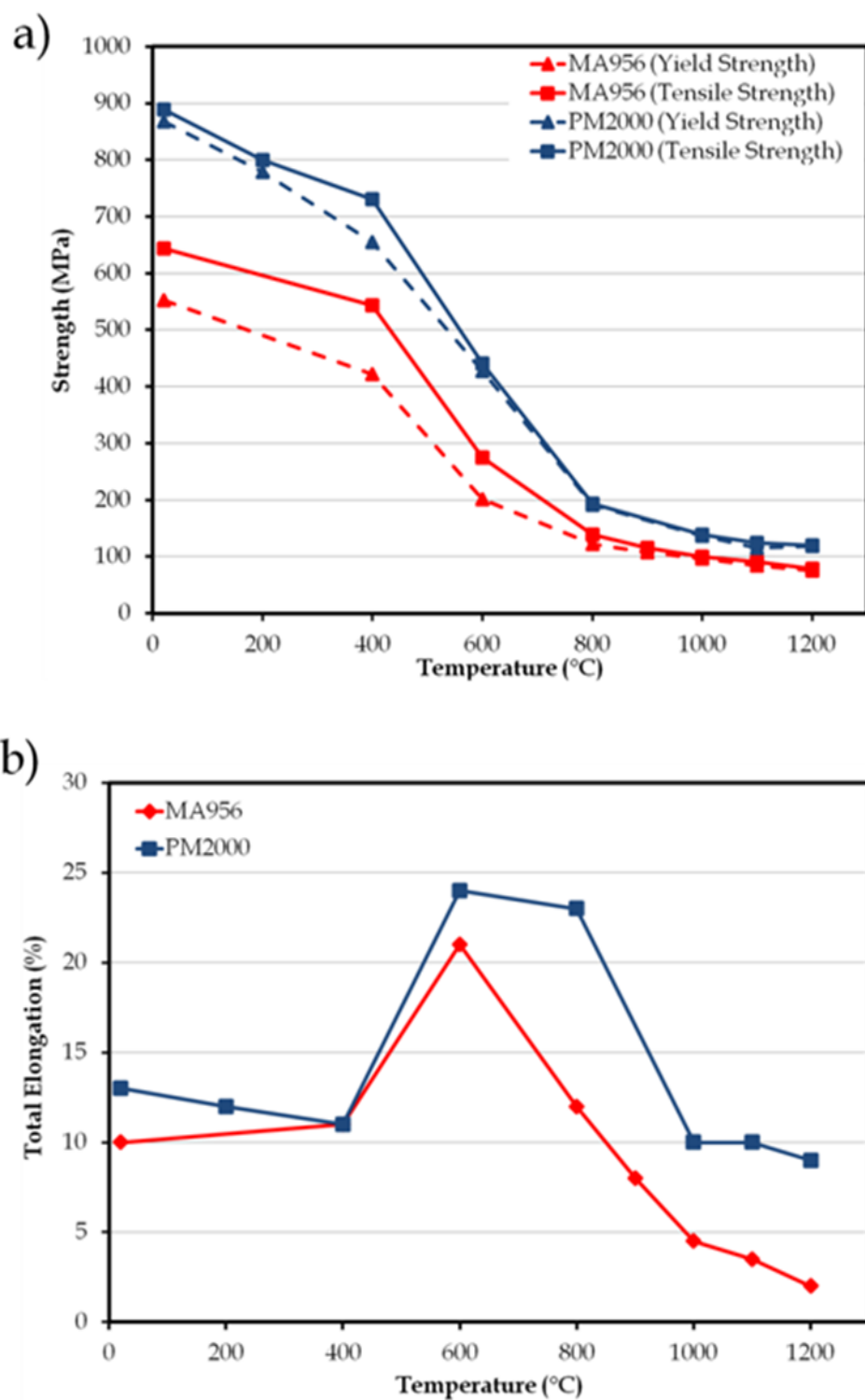


Figure 3.19. Elevated temperature yield (dashed) and tensile (solid) strength (A) and total elongation (B) comparison of Fe-based ODS MA956 (red) and PM2000 (blue) [106, 107]

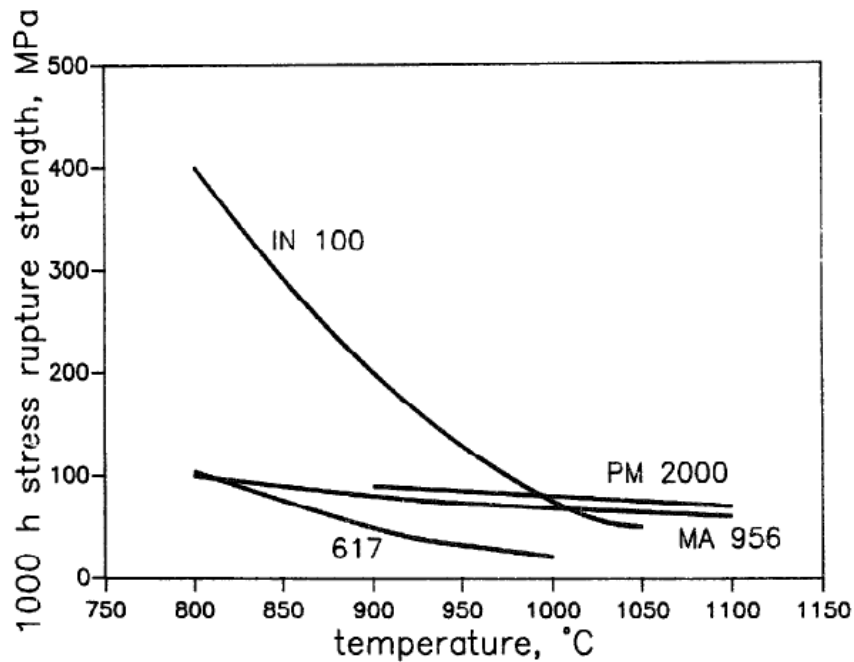


Figure 3.20. Creep resistance of Fe-based ODS alloys MA956 and PM2000 compared to Ni-based superalloys IN 100 (precipitate strengthened) and IN 617 (solid solution strengthened) [105]

### 3.5.5 Precipitate Thermal Stability

The high temperature stability of the mixed Y-Al oxide precipitates found in MA956 and PM2000 was evaluated at 1350°C (Figure 3.21) [109]. These data revealed that the precipitates found in MA956 coarsened at a faster rate compared to the precipitates found in PM2000. The coarsening rate found in MA956 at 1350°C follows a  $\sim t^{1/4}$  relationship, indicative of grain boundary coarsening. The coarsening rate found in PM2000 follows a  $\sim t^{1/5}$  relationship, indicative of coarsening by dislocation pipe diffusion. Bright field TEM images of the evolving microstructures can be seen in Figure 3.22.



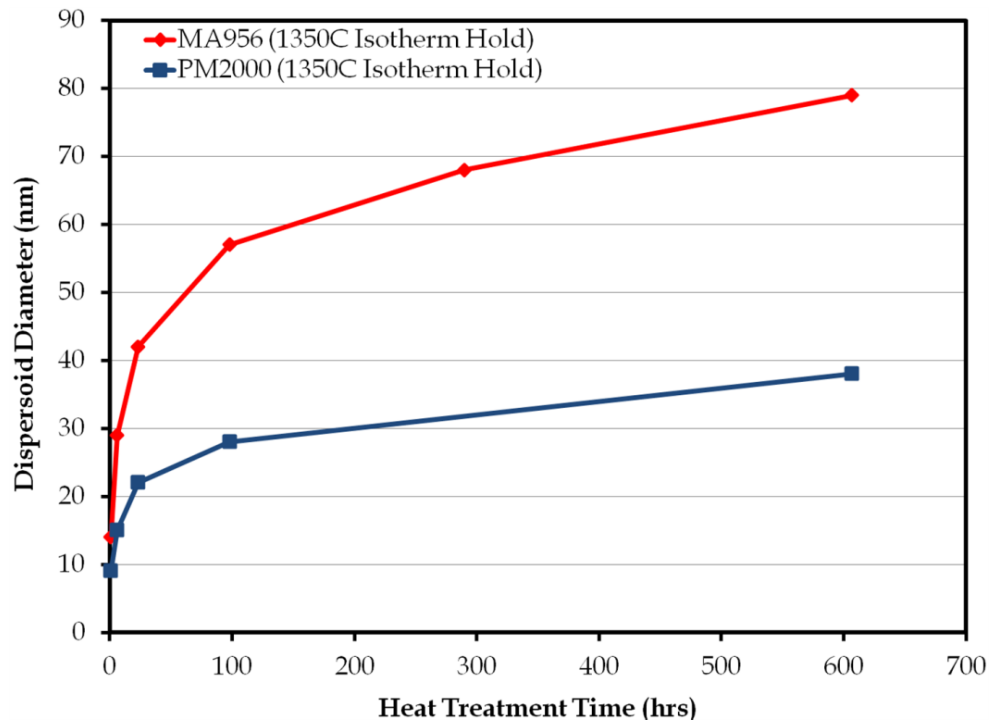


Figure 3.21. Coarsening rate of Y-Al mixed oxide precipitates at 1350°C found in Fe-based ODS MA956 and PM2000 [109]

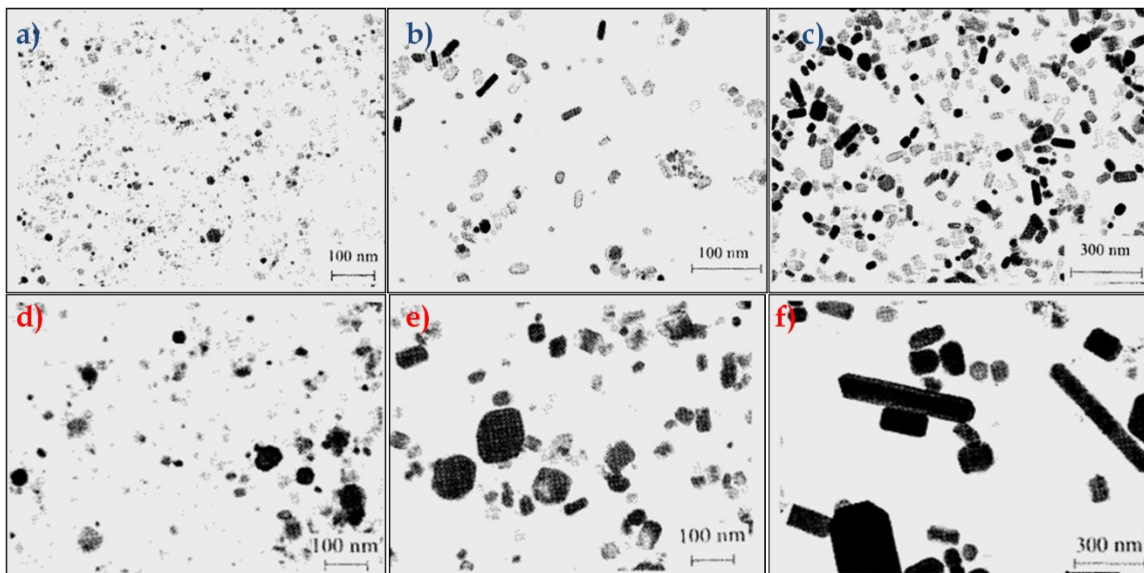


Figure 3.22. Bright field TEM images used to characterize precipitate stability and coarsening rate at 1350°C for Fe-based ODS PM2000 (blue a=1hr, b=6hr, and c=607hr) and MA956 (red d=1hr, e=6hr, and f=607hr) [109]

### 3.6 Advanced Nanostructured Ferritic Alloys (NFAs)

Nanostructured ferritic alloys were discovered in 1999 by three-dimensional atom probe (3-DAP) mapping of alloy 12YWT [114, 115]. This analysis proved the existence of Y, Ti, and O enriched nano-metric clusters. A subsequent 3-DAP analysis of MA957 rendered similar results, which showed the two microstructures to be similar [116]. The nano-metric phases were termed nanoclusters (NCs). The NCs were found to be highly defective non-equilibrium phases, which are thermally stable up to 800°C and for short times at temperatures as high as 1300°C [6, 117]. A third NFA has been produced at the laboratory scale (~200 gm) termed 14YWT [2].

NFAs differ from traditional commercial grade Fe-based ODS (e.g., MA956 and PM2000) alloys in composition, processing, and microstructure. The composition of three NFAs (i.e., MA957, 12YWT, and 14YWT) is displayed in Table 3.5. One main difference between NFAs and MA956 or PM2000 is that aluminum has been removed from alloy composition, in order to prevent the formation of complex Y-Al mixed oxide precipitates.

Table 3.5. Alloy composition for NFAs MA957, 12YWT, and 14YWT [1, 2]

Element (wt.%)	Fe	Cr	Y	Al	Ti	W	Mo	O
MA957	Bal.	13.7	0.28	-	0.98	-	0.30	0.21
12YWT	Bal.	12.25	0.20	-	0.39	3.00	-	0.05
14YWT	Bal.	13.93	0.21	-	0.22	1.97	-	0.05

#### 3.6.1 Mechanical Alloying Process and Particulate Consolidation

The mechanical alloying (MA) and consolidation process for MA957 is proprietary, but the process used to obtain a similar microstructure in 12YWT and 14YWT has

been reported in the literature [6, 118]. Alloy 12YWT has been produced by milling 70 $\mu\text{m}$  master alloy gas atomized powders with 20nm  $\text{Y}_2\text{O}_3$  powders in a high energy attritor mill for 48 hrs under Ar. The MA particulate are then placed into a mild steel can, degassed at 400°C under a vacuum of  $10^{-2}$  Pa for 2.0 hrs and sealed. The particulate is consolidated into a bar by hot extrusion techniques at 1150°C [6]. Alloy 14YWT is produced in a similar manner related to 12YWT, where first master alloy (Fe-14.0Cr-3.0W-0.4Ti wt.%) gas atomized powders (45-150 $\mu\text{m}$ ) and 0.3 wt.%  $\text{Y}_2\text{O}_3$  powders (17-31nm) are blended together. The mixed powders are then ball milled in a high energy attritor mill for 40 or 80 hours with an Ar gas atmosphere and a ball-to-powder mass ratio of 10:1. After ball milling the powders are placed in a mild steel can, degassed at 400°C under a vacuum of  $\sim 10^{-2}$  Pa, and sealed. The powders are subsequently heated to 850°C for 1.0 hr and consolidated using hot extrusion or hot isostatic pressing at 850°C or 1150°C [118]. A schematic highlighting the MA and consolidation process is shown in Figure 3.23. Similar to Fe-based ODS alloys, NFAs can be strategically consolidated or worked and heat treated to form a microstructure with a fine dislocation substructure for additional strengthening.

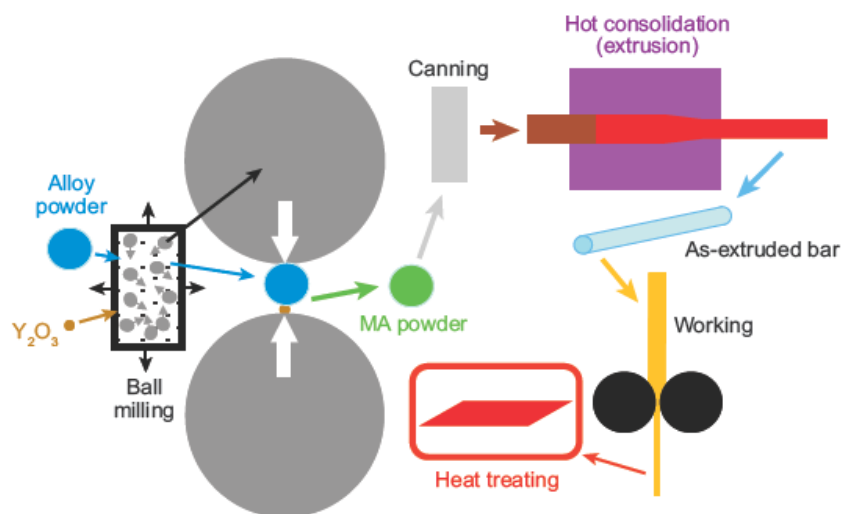


**Figure 3.23. Schematic of the mechanical alloying, consolidation, and subsequent working and heat treatment process for the formation of a NFA [9]**

### 3.6.2 NFA Microstructure

Analysis of the NFA microstructure has been conducted in detail using small angle neutron scattering (SANS) [68]. The experimental procedure and mathematical models used for microstructure interpretation are explained in detail within the literature [68]. The average radius, volume fraction, and number density for the NCs found in as-HIPped at 1150°C 14YWT, and as-extruded at 1150°C MA957 and 12YWT is shown in Figure 3.24. The average Vickers microhardness values for each alloy in the as-consolidated state also is shown in Figure 3.24. It can be seen that the average radius of the Y-Ti-O enriched NCs range in size from approximately 1.25-1.75nm, which is significantly less than the radius of the oxide dispersoids found in as-received MA956 or PM2000. The volume fraction of NCs found within these NFAs is approximately 0.6 vol.%, with a number density of  $\sim 10^{24} \text{ m}^{-3}$ . MA957 contains the largest number density of the NCs, presumably due the increased concentration of Y and Ti found in the alloy.

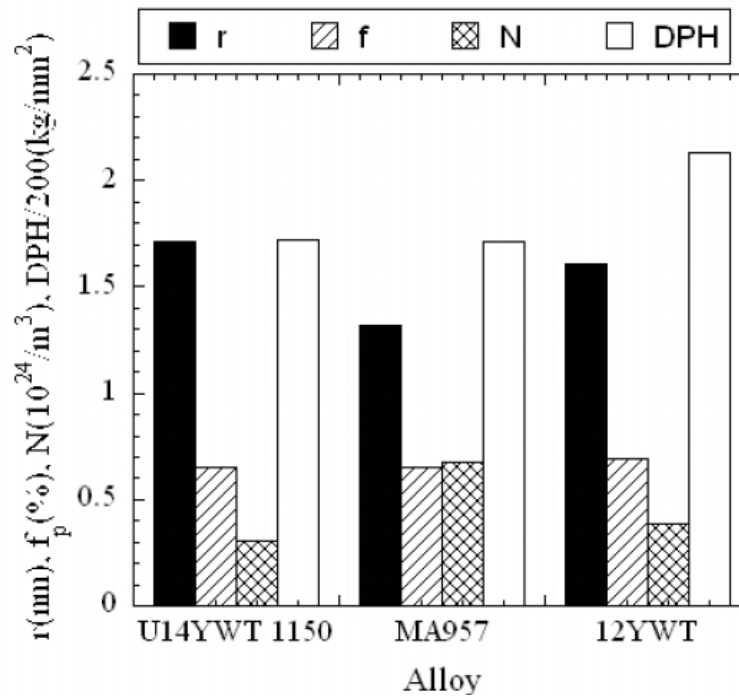


Figure 3.24. NFA microstructural evaluation of cluster radius ( $r$ ), volume fraction ( $f$ ), number density ( $N$ ), and Vickers hardness (DPH) [119]

The composition of the NCs found in the NFAs has been derived using atom probe tomography (APT) (see Table 3.6). It can be seen that the NCs contain a varying amount of Y, Ti, O, Fe, and Cr. Accurate measurements of the matrix dominant elements (Fe+Cr) can be difficult using APT, because accuracy of this measurement is dependent on the interface structure between the cluster and the matrix [120]. In most cases, the metal-to-oxygen ratio is greater than one, signifying the formation of an oxygen deficient or sub-oxide phase. The cluster compositions do not match known equilibrium oxide phases (e.g.,  $\text{Y}_2\text{Ti}_2\text{O}_7$ ,  $\text{Y}_2\text{TiO}_5$ , or  $\text{YTiO}_3$ ), signifying that the clusters might be a non-equilibrium phase or a highly stable transition phase [117].

**Table 3.6. Summary of the NCs composition from APT [6, 116-119]**

Alloy	Y	Ti	O	Fe + Cr
14YWT*	0.17	0.28	0.33	0.22
MA957	0.15	0.33	0.40	0.12
12YWT	0.09	0.20	0.24	0.47
12YWT	0.08	0.42	0.40	0.10
12YWT	0.06	0.39	0.42	0.13
14YWT**	0.06	0.42	0.46	0.06

\* HIPed at 1000°C and \*\* Extruded at 850°C

Bright field TEM micrographs reveal the submicron dislocation substructure and the distribution of the NCs found in as-consolidated (1150°C) MA957 (Figure 3.25). The dislocation substructure is formed during hot extrusion consolidation of the heavily

deformed MA powders. The NCs were found to have a radius ranging from  $1.05 \pm 0.2\text{nm}$ , which agreed well with data published from the aforementioned SANS analysis [121].

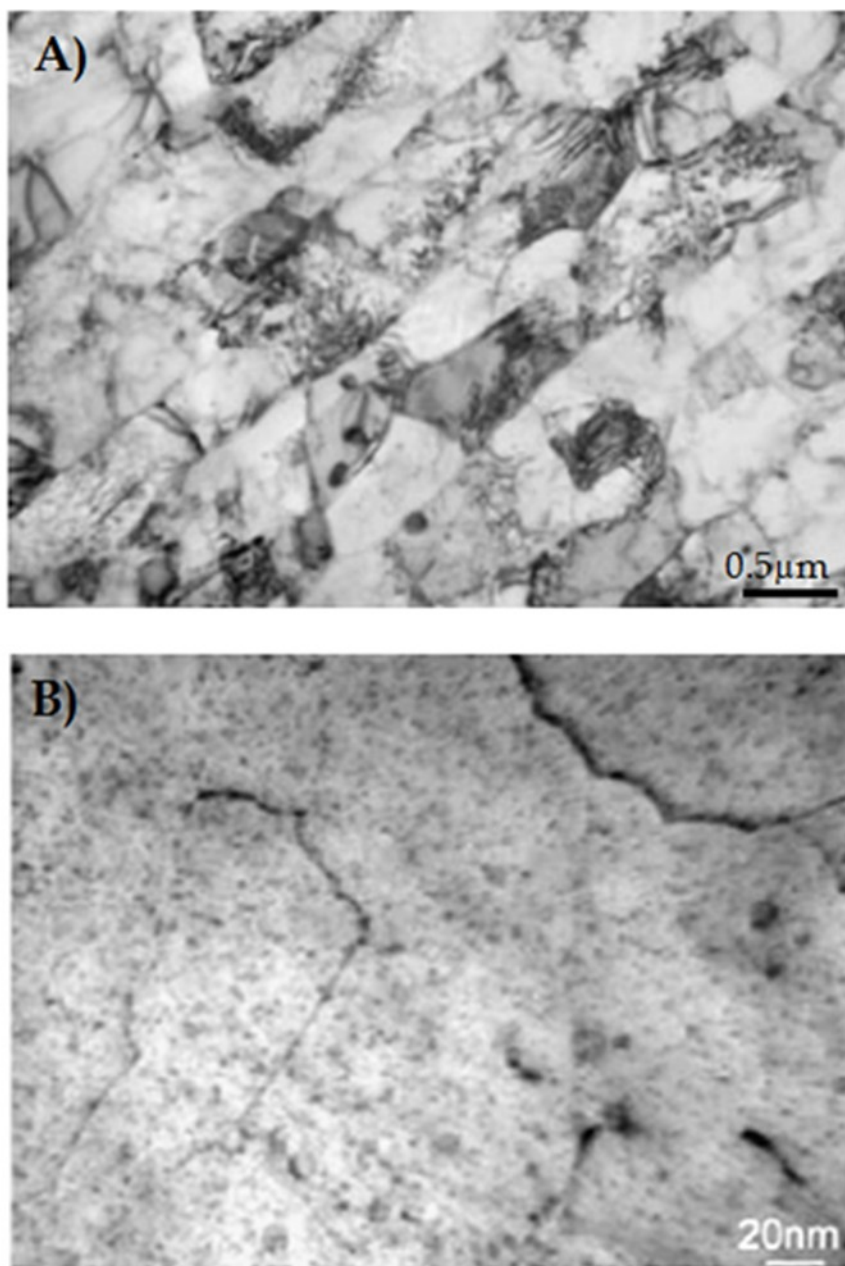


**Figure 3.25. Microstructure of as-consolidated NFA MA957 highlighting the dislocation substructure (A) and dispersoid distribution (B) [121]**

NFAs are also extremely difficult to recrystallize in the as-consolidated condition due to the presence of a fine dislocation substructure (as previously discussed Section 3.5). Figure 3.26 illustrates the microstructure found in as-extruded (Figure 3.26A) and as-recrystallized (Figure 3.26B) MA957. Differential scanning calorimetry measurements of as-extruded MA957 show recrystallization to start at 1370°C and end at 1412°C, which is approximately  $0.9T_m$  [122].

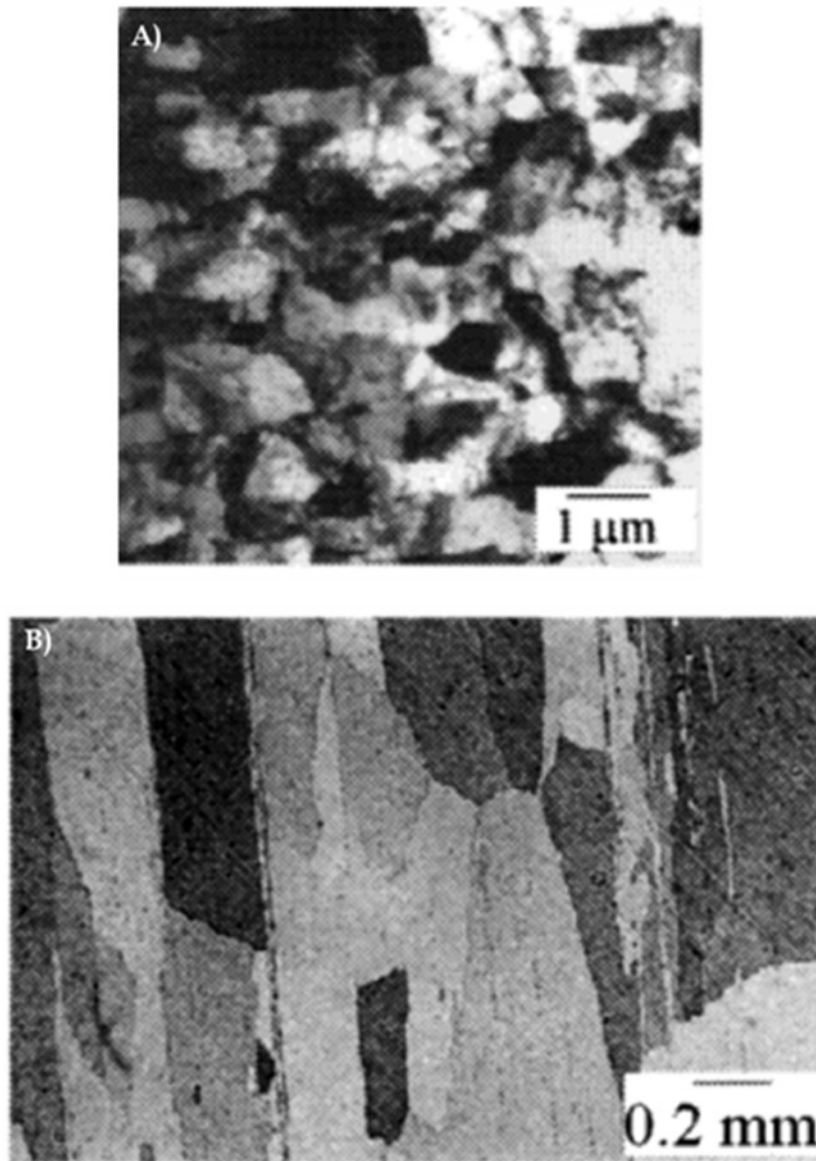


Figure 3.26. Grain structure of as-consolidated MA957 (A) and as-recrystallized (1400°C) MA957 (B) [111]

### 3.6.3 Mechanical Properties

Vickers microhardness values for MA957, 12YWT, and 14YWT have been reported in the literature and are shown in Figure 3.27 [68]. The composition, milling type, and consolidation temperature for NFA 14YWT was manipulated, in an effort to better understand the effects each variable has on the alloys as-consolidated microhardness. Four different alloys were prepared for this analysis by removing certain elements from the original 14YWT alloy composition, thus resulting in alloy 14YT (removal of tungsten), alloy 14Y (removal of tungsten and titanium), and alloy 14 (removal of tungsten, titanium, and yttrium). The alloys were then mechanically alloyed in a shaker (S) or attritor (A) mill, followed by hot consolidation (i.e., HIPed) at 850°C (red) or 1150°C (blue).

The results show that the MA957, 12YWT, and 14YWT have a similar microhardness value when consolidated at the 1150°C, but 14YWT displays a substantial increase in hardness when consolidated at 850°C. The large increase in hardness could be attributed to the formation of a finer primary grain structure, and an increased NC number density. It can also be seen that titanium has a stronger influence on the as-consolidated hardness value when compared to tungsten. The comparison between S14YWT and A14YWT highlights the difference in milling energies and resulting powder deformation. The powders that were more heavily deformed (i.e., shake mill) during the milling process display a larger microhardness value in the as-consolidated condition. This hardness increase is likely due to the formation of smaller primary grains upon consolidation, or due to an increased concentration of residual defects compared to powders mechanically alloyed in the attritor mill. In summary, the NFA 14YWT is much harder when consolidated at 850°C as opposed to 1150°C and when the alloy contains both yttrium and titanium.



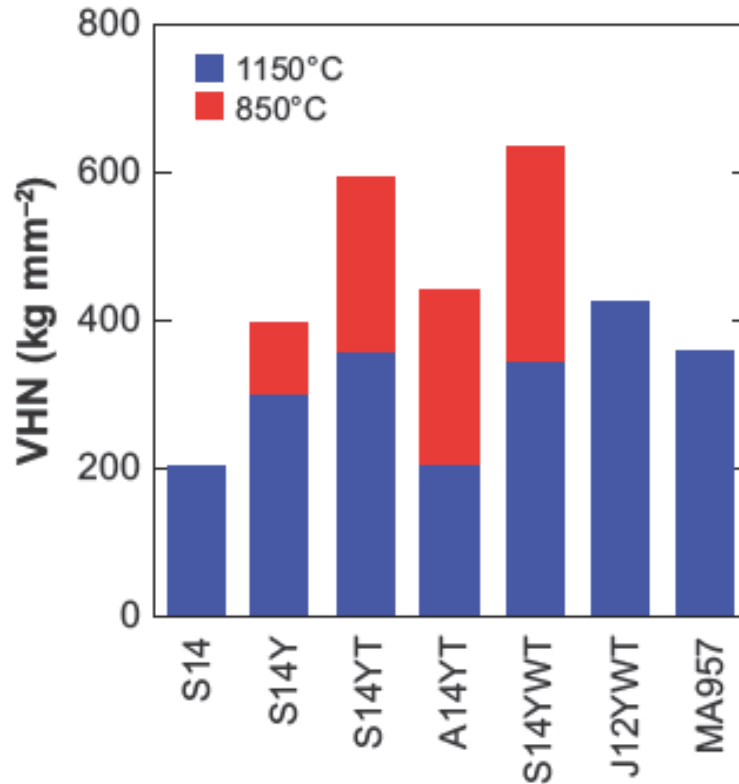


Figure 3.27. Vickers hardness values for various Fe-based and NFAs consolidated at different temperatures (red = 850°C and blue = 1150°C) [13, 68, 119]

High temperature tensile and total elongation data for both NFAs (i.e., MA957 and 12YWT) and ODS alloys (i.e., MA956, PM2000, and 12Y1) are displayed in Figure 3.28 [1]. The samples were tested in the longitudinal direction in reference to the extrusion direction. It can be seen that the NFAs exhibit a greater tensile strength compared to the ODS alloys, but the different alloys begin to converge at temperatures above 800°C. Total elongation values are not simply inversely related to strength, but more dependent on alloy microstructure. Alloy grain structure and processing state (e.g., as-consolidated or partial/fully recrystallized) can dictate the degree of ductility found in NFAs or ODS alloys. Without a clear understanding of the tested alloy microstructure a relative comparison of the elongation data is quite difficult.

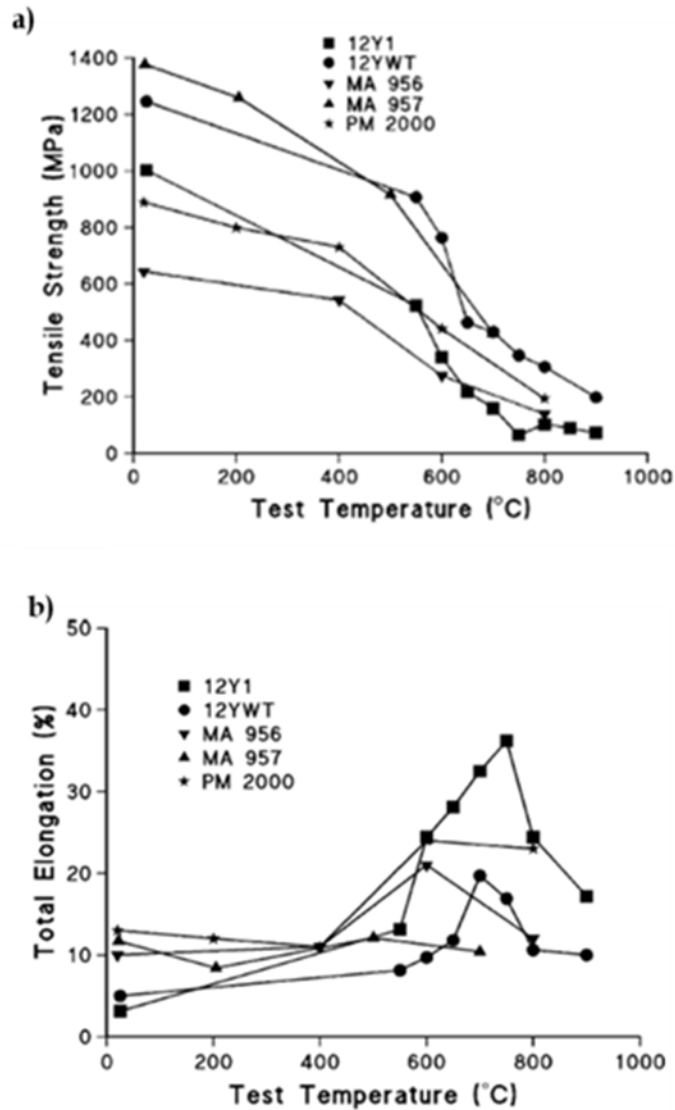


Figure 3.28. Tensile strength (A) and total elongation (B) values as a function of temperature for NFAs MA957 and 12YWT compared to Fe-based ODS alloys 12Y1, MA956, and PM2000 [1]

Yield strength and creep data for NFA MA957 in the as-extruded, cold-worked, and fully recrystallized condition is displayed in Figure 3.29. The fine grain structure found in the as-extruded and cold-worked specimens promotes an increased yield strength over the recrystallized coarse grained specimen at lower temperatures ( $T \leq 600^\circ\text{C}$ ), but at higher temperatures the yield strength values for the three specimens

converge (Figure 3.29A). Creep data shows that the fine grained MA957 alloy has superior creep resistance over recrystallized MA957 at 650°C for rupture times less than  $10^4$  hours (Figure 3.29B). It also can be assumed that the creep resistance found in MA957 could be extended to much longer times by reducing the stress below the threshold or detachment stress limit as defined by the alloys microstructure (see Section 3.2: Creep Resistance).

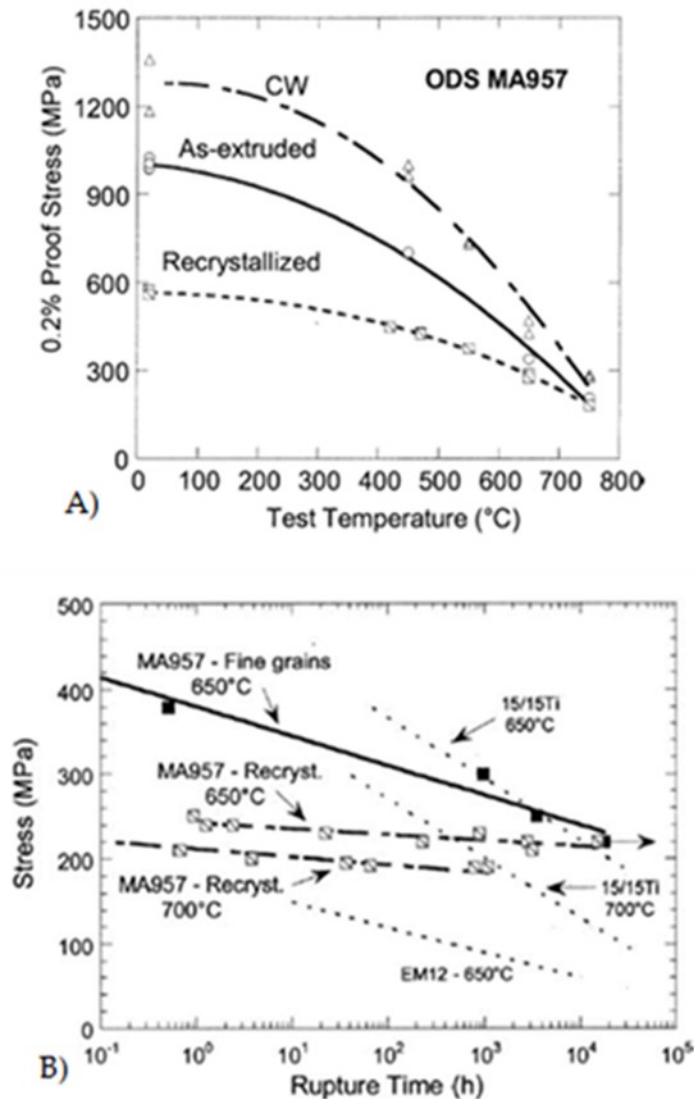


Figure 3.29. Yield strength values as a function of temperature for NFA MA957 in the cold-worked (CW), as-extruded, and recrystallized condition (A) and creep resistance properties found in fine-grained and recrystallized MA957 compared to austenitic stainless steel (15/15Ti) and ferritic/martensitic stainless steel (EM12) (B) [123]

### 3.6.4 Thermal Stability and Coarsening of Nanoclusters

The thermal stability of the Y-Ti-O enriched NCs found in NFAs has been examined using APT and small angle neutron scattering (SANS). APT was used to evaluate the size and number density of the NCs found in as-consolidated and annealed (1300°C for 24 hrs) MA957. The average Guinier radius was determined using the maximum separation method [120]. The average radius of the NCs in the as-consolidated sample were found to be  $1.2 \pm 0.4 \text{ nm}$  with a number density of  $\sim 2 \times 10^{24} \text{ m}^{-3}$ , while the average radius of the NCs in the annealed (1300°C for 24hrs) sample were found to be  $4.6 \pm 1.1 \text{ nm}$  with a number density of  $\sim 8 \times 10^{22} \text{ m}^{-3}$  (see Figure 3.30) [117]. This analysis shows that quantifiable coarsening occurred in the NCs during high temperature annealing, but a significant amount of particles still remain within the alloy matrix.

SANS has also been used to evaluate the NC thermal stability in as-milled 14YWT powder particulate (Figure 3.31). The powder particulate was annealed at 1000°C for selected time increments up to 27 hrs. It can be seen (Figure 3.31A) that the NCs are highly stable at 1000°C with a near constant radius of  $\sim 1.5 \text{ nm}$  and a number density of  $\sim 0.7 \times 10^{24} \text{ m}^{-3}$ . A similar series of SANS analysis of annealed 14YWT particulate was used to create a NC coarsening model (Figure 3.31B). This model predicts the NCs to coarsen at a  $t^{1/5}$  rate, which is indicative of dislocation pipe diffusion as the rate limiting step (see Section 3.3: Oxide Particle Formation and Growth) [124].

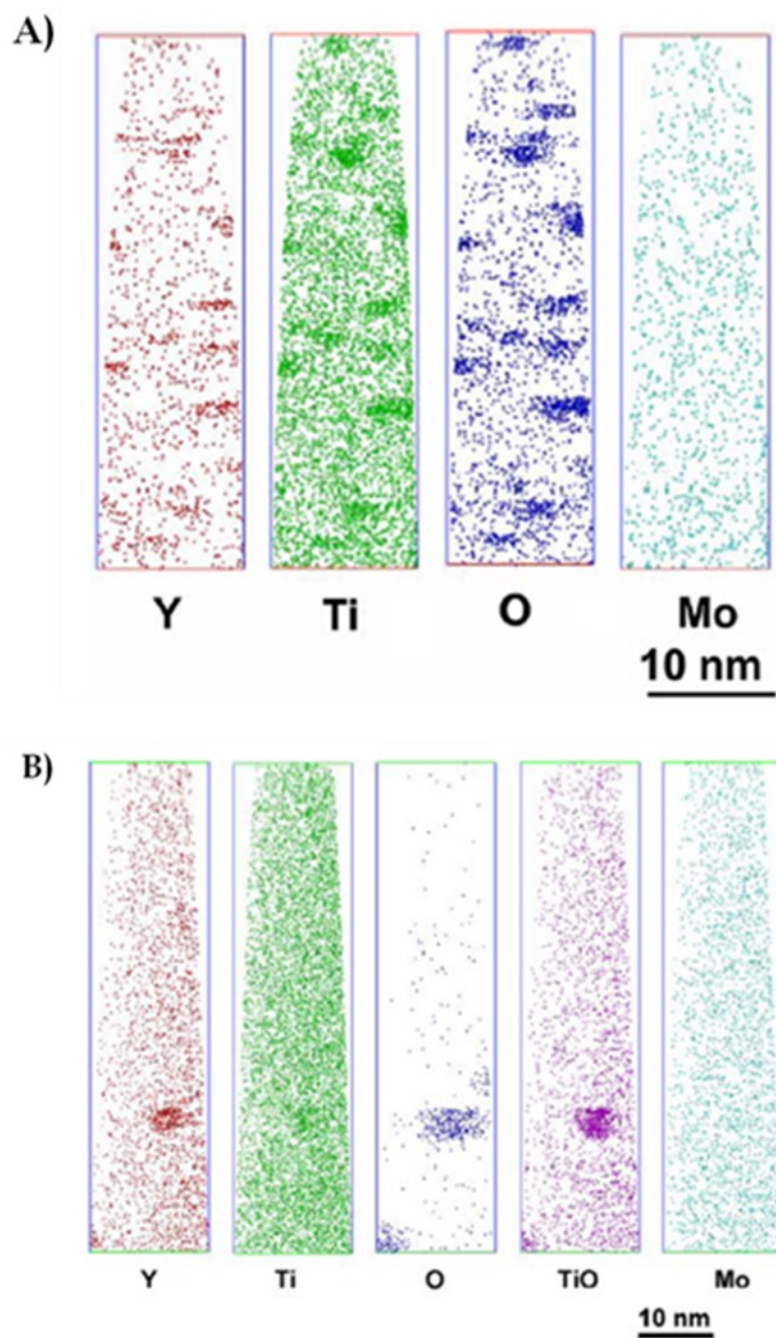


Figure 3.30. Atom probe tomography (APT) elemental maps of MA957 comparing the coarsening of nano-cluster particles in the as-consolidated condition (A) and annealed at 1300°C for 24hrs condition (B) [117]

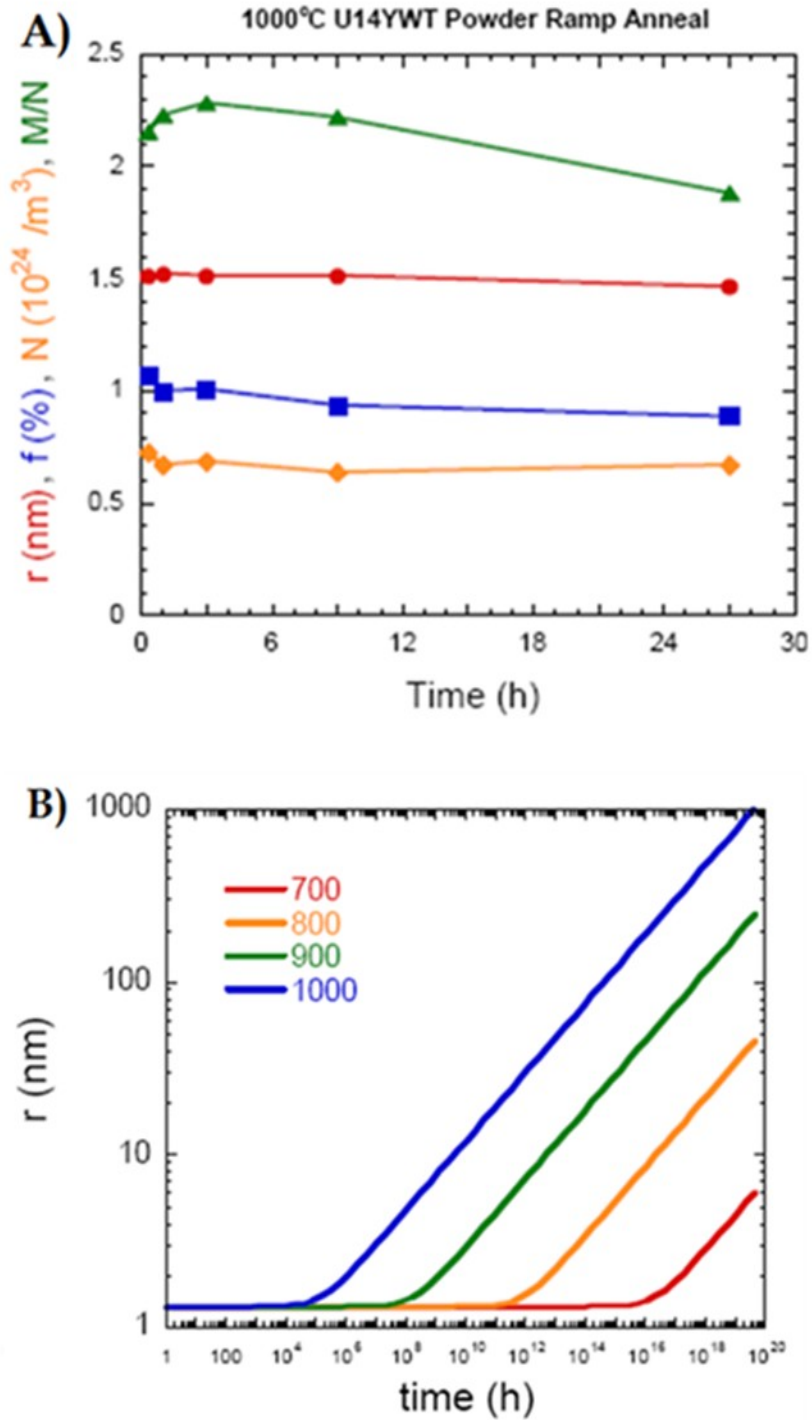


Figure 3.31. Nano-cluster stability analysis of alloy 14YWT at 1000°C as a function of time (A) and nano-cluster coarsening rate predictions for alloy 14YWT as a function of time and temperature (B) [124]

### 3.6.5 Irradiation Resistance

Neutron irradiation of fine grained (as-consolidated) MA957 at 325°C for doses of 2 and 6 dpa were conducted to investigate the alloys resistance to neutron induced hardening and embrittlement (Section 2.2: Irradiation Damage) [123]. The increased yield strength, as a result of neutron induced hardening, for MA957 was compared to two conventional martensitic stainless steels (i.e., Fe-10Cr-0.6MoVNb-MANET2 and Fe-7.5Cr2WTaV-F82H) irradiated in the same conditions. The results show that the yield strength of MA957 increased the least amount compared with the two martensitic stainless steels (Figure 3.32A). Loss in ductility as an effect of neutron induced hardening was also evaluated for MA957, MANET 2, and F82H (Figure 3.32B). It can be seen that MA957 contains the least amount of ductility loss and the loss rate is far less extreme when compared to the two martensitic stainless steels.

Hellium has been stratigecally implanted into the microstructure of both NFA MA957 and tempered martensitic stainless steel F82H, in order to evaulate He bubble formation and growth within the alloy microstructure [125]. Hellium was uniformly implanted to a depth of 5-8 mm using NiAl coatings deposited on alloy TEM discs [125]. Hellium is produced as a by product during neutron induced transmutation reactions with  $^{58}\text{Ni}(n,\alpha)$ , which results in  $\alpha$ -particle decay (Section 2:3 Irradiation Damage). The samples were irradiated at 500°C to ~9 dpa producing 340 appm of He [126]. The TEM microstructure of the two alloys is shown in Figure 3.33. The MA957 sample was reported to contain a large number density of small He bubbles ( $3 \times 10^{23} \text{ m}^{-3}$ ) with a radius  $\leq 1 \text{ nm}$ , which were typically found at NC interfaces with no evidence of large He bubble precipitation within the He implanted zone [34, 125]. The F82H sample was reported to have a slightly lower number density of He bubbles ( $\sim 1 \times 10^{23} \text{ m}^{-3}$ ) with a radius  $\sim 2 \text{ nm}$  [125]. Also, the grain boundaries in the F82H sample were found to be highly decorated with small He bubbles, while the grain boundaries in the MA957 sample were found to be

relatively clean. Therefore, the NFA microstructure of MA957 was shown to prevent He bubble formation along grain boundaries, which can lead to grain boundary embrittlement and severe ductility loss. This initial study showed that NFAs are able to manage high concentrations of He, which can result from high energy neutron bombardment within a fusion reactor.

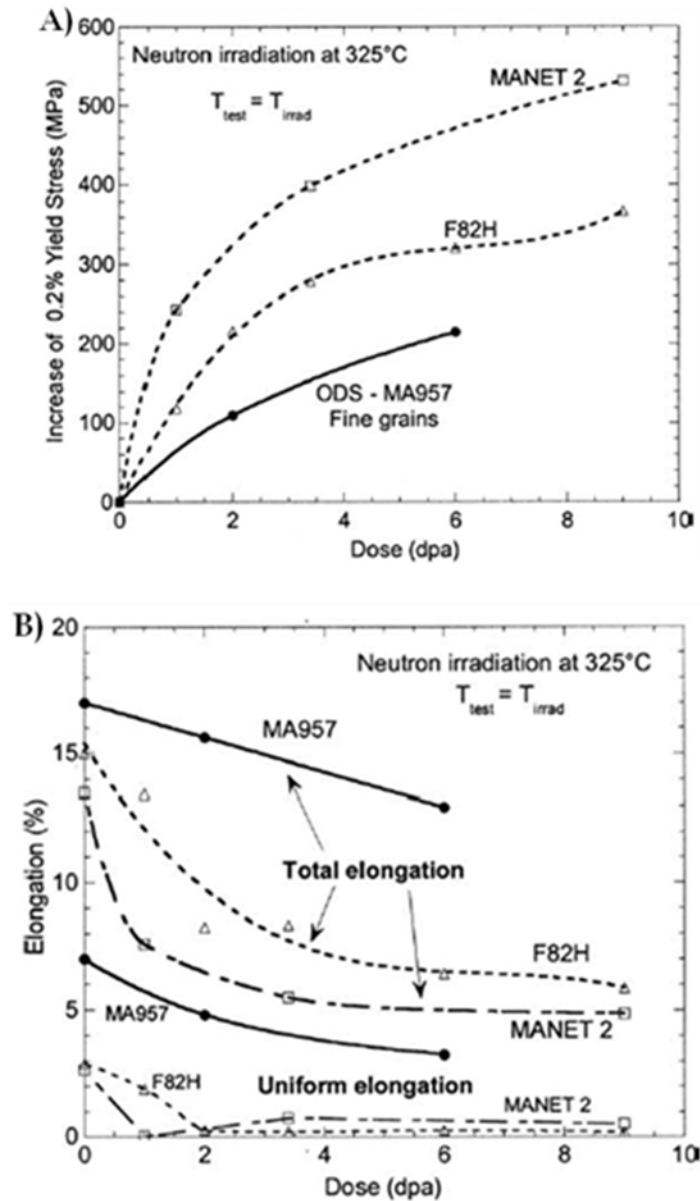


Figure 3.32. Neutron induced hardening as a function of dose (dpa) at 325°C displayed as an increase in yield strength for alloys MA957, MANET 2, and F82H (A), and decrease in ductility as a function of dose (dpa) at 325°C for MA957, MANET 2, and F82H (B) [123]



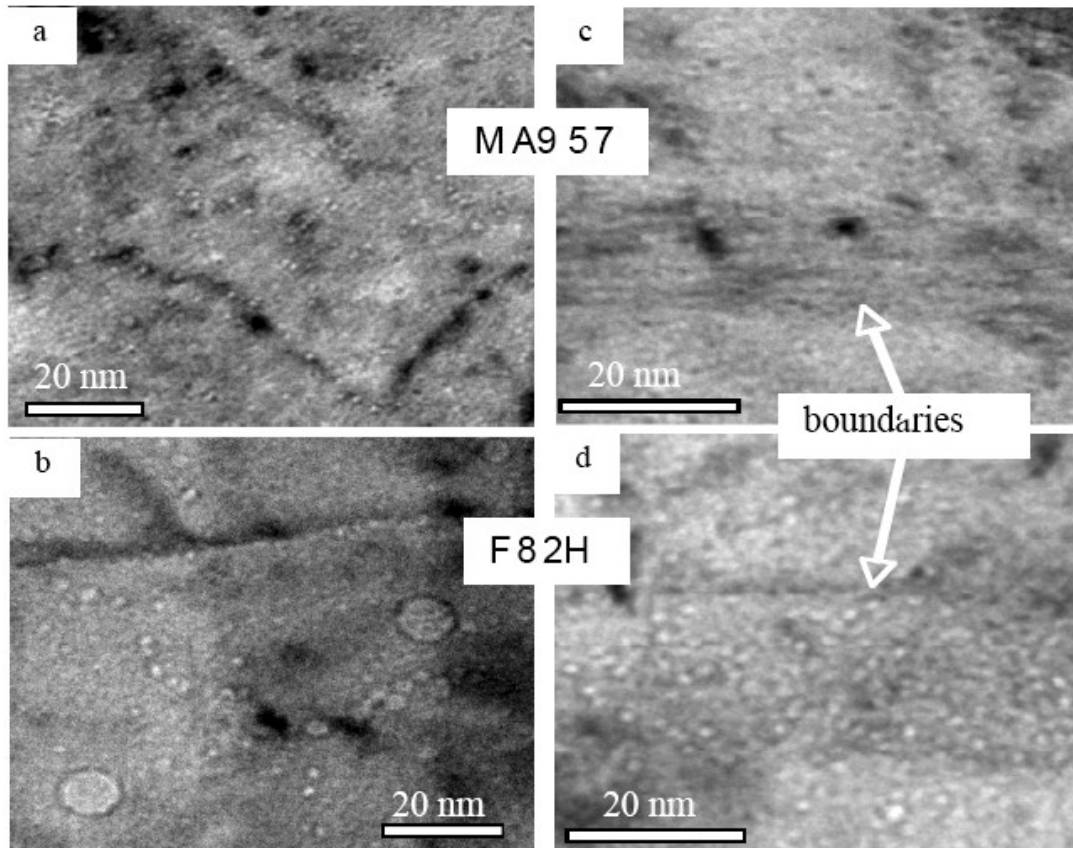


Figure 3.33. As-irradiated microstructural comparison of MA957 (a and c) and martensitic stainless steel F82H (b and d) highlighting He bubble formation throughout the microstructure [125]

### 3.6.6 Summary

In a recent review summarizing a group of radiation resistant steels, NFAs are concluded as being ideal candidates for advanced fission and fusion nuclear reactors [9]. The review article also states that the practical development of nanodispersion-strengthened Fe-based alloys faces some specific challenges including, the high cost of mechanically alloyed powder-consolidated materials compared with the cost for melt-processed alloys, the anisotropic microstructure that arises from mechanical alloying, and the batch-to-batch variability in mechanical alloying [9]. These challenges provide motivation for further research into new processing methods for the production of ODS ferritic stainless steel alloys.

## Chapter 4. Gas Atomization Reaction Synthesis (GARS) Processing

A new molten metal processing technique involving rapid solidification has been implemented for the simplified production of precursor ODS ferritic stainless steel powder. This process is known as gas atomization reaction synthesis (GARS) [14]. During this process, a reactive atomization gas (i.e., Ar-O<sub>2</sub>) is used to surface oxidize molten ferritic stainless steel alloy droplets during primary break-up and rapid solidification of the atomized powders (see Figure 4.1a, b, and c).

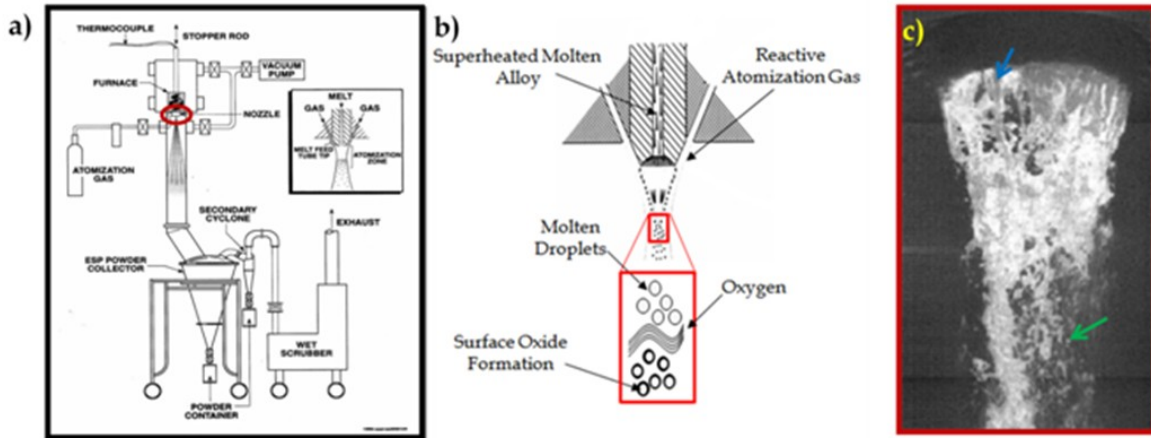
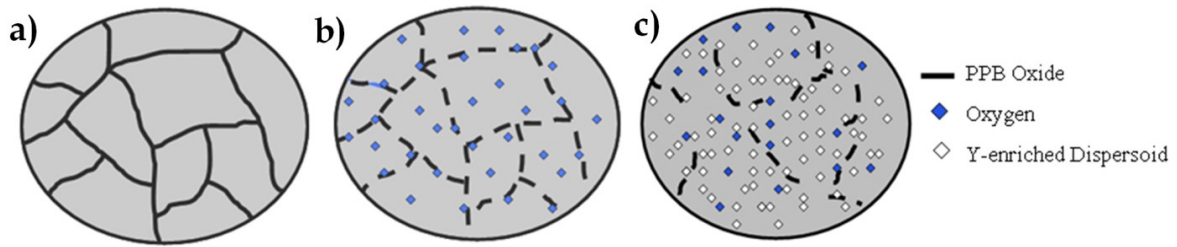


Figure 4.1. High pressure gas atomizer with highlighted reaction zone a) and b) and actual image of atomization spray illustrating ligament formation during shearing of the metal (blue arrow) and droplet formation (green arrow) c)

This rapid high temperature reaction promotes the formation of a metastable or kinetically favored (e.g., Cr-enriched) ultra thin ( $\xi < 150\text{nm}$ ) continuous surface oxide layer. This oxide layer is used as a method to transport a specific amount of solid-state O into the consolidated microstructure. Elevated temperature heat treatment (during consolidation or post-consolidation) is then used to dissociate this Cr-enriched surface oxide phase, allowing O to diffuse away from prior particle

boundaries (PPBs), which leads to the internal oxidation of more thermodynamically stable alloy additions (e.g., Y), shown schematically in Figure 4.2.



**Figure 4.2.** The ODS microstructure evolution during hot consolidation (or heat treatment) of GARS precursor powder: a) initial low temperature consolidation showing intact PPBs, b) dissociation of the PPBs (simulating heat treatment) and O diffusion into the  $\alpha$ -(Fe,Cr) matrix, and c) formation of Y-enriched oxide dispersoids throughout the microstructure

This new processing technique contains many key advantages over mechanical alloying (MA). These advantages can improve the production efficiency of precursor ODS ferritic stainless steel powders. GARS (atomization) processing has the potential of reaching commercial production rates up to 10-100 kg/min., which is orders of magnitude greater than the production rates associated with the traditional MA process [101, 104]. Gas atomization also could minimize batch-to-batch variability and strictly limit contamination within the powder particles. Furthermore, the spherical morphology of the atomized powders is ideal for HIP consolidation, which has been demonstrated as a successful method for the retention of equiaxed grains and isotropic mechanical properties [127].

The aim of this chapter is to highlight the GARS process and illustrate how this novel atomization method can be used to create precursor powder for ODS ferritic stainless steel alloys. Additionally, a surface oxidation model, derived from theoretical powder particle cooling curves, will be discussed as a method for controlling the *in situ* alloying addition of O during this GARS process.

Furthermore, observations of solidification velocity, as a function of powder size, will be discussed and used as a prelude to the ODS microstructures illustrated in the chapters to follow.

#### **4.1 Chemical Reservoir (CR) Alloys**

These ODS alloys have been termed chemical reservoir (CR) alloys due to the distinctive O exchange reaction that leads to dispersoid formation. This process relies on the initial formation of an O reservoir phase (i.e., Cr-enriched surface oxide), in combination with a reservoir containing the dispersoid forming alloy additions (e.g., Y-enriched intermetallic compound (IMC) precipitates). For this reason, this GARS process is highly dependent on the thermodynamic stability hierarchy of each oxide phase (see Figure 4.3). Therefore, it is essential to limit consumption of the dispersoid forming element (i.e., Y) during initial surface oxide phase formation, which could prevent the ensuing O exchange reaction from occurring (i.e., Y-enriched dispersoid formation). This is thought to be possible through strategic alloy design, which involves the addition of highly mobile surface oxide phase forming elements (e.g., Cr).

The increased activity of Cr in these CR-alloys, relative to the activity of Y, appears to provide the necessary chemical gradient required to kinetically favor a predominately Cr-enriched surface oxide phase with small concentrations of Fe and Y (see Table 4.2). Further experimental results have shown that the addition of a dispersoid stabilizing element (i.e., Ti or Hf), if added in adequate atomic concentration, also prevents (or severally limits) Y consumption during this rapid oxidation reaction. It is thought that these dispersoid stabilizing elements also compete for O during GARS processing, forming a Ti or Hf doped Cr-enriched surface oxide. Additionally, these secondary alloy additions might suppress Y mobility through the formation of mixed IMC (Fe-(Hf or Ti)-Y) precipitates. The specific mechanism for limiting Y consumption will require further experimental

trials, but initial results have shown that a Ti/Y ratio of at least 2.5 and Hf/Y ratio as low as 1.3 can successfully limit Y consumption during GARS processing (see Table 4.2, Figure 4.11, and Figure 4.14).

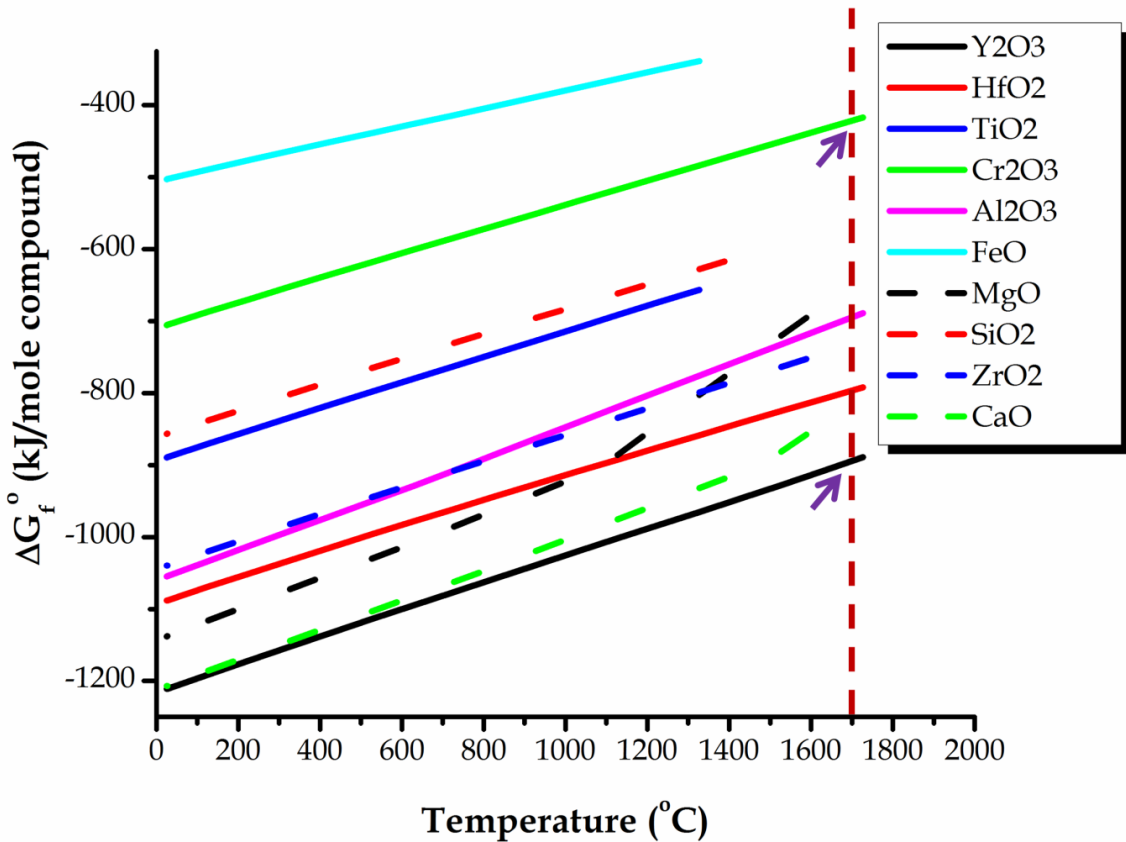


**Figure 4.3.** Thermodynamic stability of oxides comparing the free energy of formation between  $\text{Cr}_2\text{O}_3$  and  $\text{Y}_2\text{O}_3$  (see purple arrows) at the atomization temperature ( $1700^\circ\text{C}$ ) used for these GARS trials [128]

The composition of these CR-alloys has been designed around similar MA ODS ferritic alloys (See Section 3.6). The primary alloying additions include Cr, Y, (Ti or Hf), W, and O. The intended purpose for each alloying element and ideal concentration range (at.%) are displayed in Table 4.1.

**Table 4.1. Individual alloying components, purpose, and ideal concentration for these CR-alloys**

Element	Purpose	Ideal Conc. (at.%)	Ref.
Cr	Surface reactant corrosion/oxidation resistance	14.5-15.0	[129, 130]
Y	nano-metric oxide dispersoid former corrosion/oxidation resistance	0.12-0.20	[131, 132]
Ti	Surface reactant, dispersoid stabilizer, interstitial impurity scavenger	0.40-0.60	[116, 132, 133]
Hf	Surface reactant, dispersoid stabilizer, interstitial impurity scavenger	0.15-0.25	[134]
W	Solid solution strengthener or precipitate strengthener	~1.0	[135]
O	Surface oxidant and nano-metric oxide dispersoid former	0.40-0.70	-

Cr is highly soluble in Fe and stabilizes the BCC ferrite ( $\alpha$ ) crystal structure [130]. From the binary phase diagram it can be seen that a Cr content (or equivalent)  $\geq 14.3$  at.% is required to stabilize the  $\alpha$ -Fe microstructure during consolidation, heat treatment, and high temperature operation of the alloy (see Figure 4.4) [130]. Preventing the allotropic phase transformation (i.e.,  $\alpha$ -Fe  $\rightarrow$   $\gamma$ -Fe) during elevated temperature exposure should prevent the rise of microstructural instabilities in the alloy (e.g., grain recrystallization or neutron induced void swelling). Additionally, Cr is required for increased corrosion and oxidation resistance during elevated temperature operation (see Section 2.3). A minimum Cr content of  $\sim 14$  at.% is typical for the formation of a stable Cr-oxide passivation scale (in dry air) [129]. Although a Cr content of  $\geq 14.3$  at.% is warranted in these alloys, it should be kept to a minimum in order to prevent significant sigma ( $\sigma$ ) phase formation, which can reduce the toughness of the alloy by increasing the ductile to brittle transition temperature (DBTT) [136].

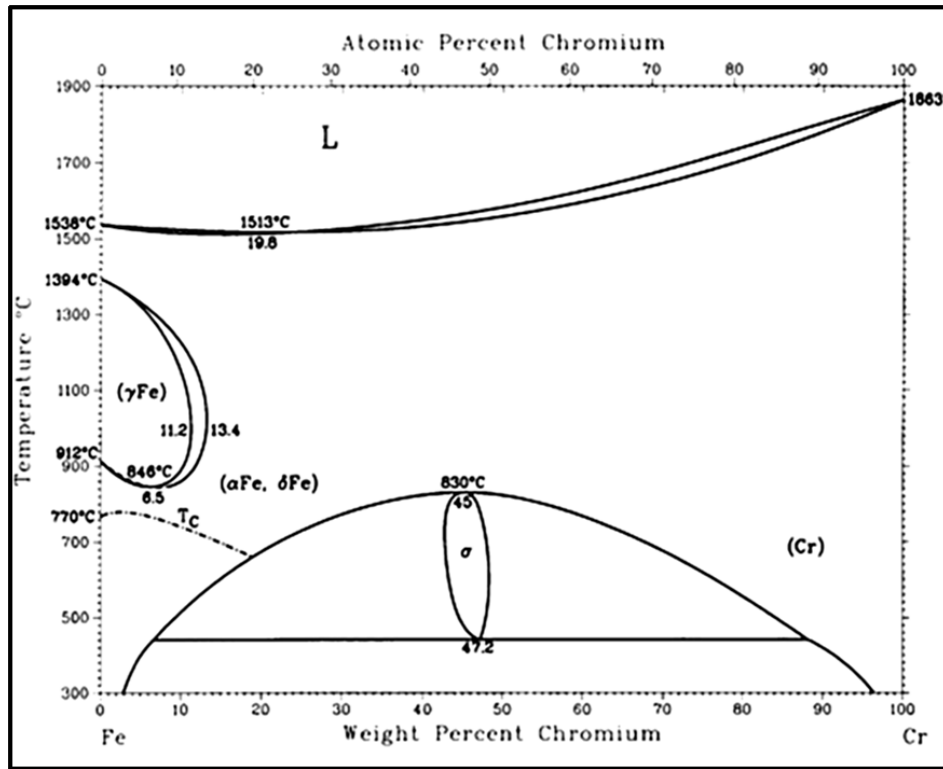


Figure 4.4. Fe-Cr binary phase diagram [130]

Y was selected as the dispersoid forming agent in these CR-alloys. Y is nearly insoluble in  $\alpha$ -Fe and maintains limited diffusivity over the range of consolidation and heat treatment temperatures (700-1300°C), which helps to stabilize the nano-metric oxide dispersoids after formation, and slows growth and coarsening kinetics. Additionally, Y oxide ( $Y_2O_3$ ) having a highly negative Gibbs free energy is extremely stable even at considerably low oxygen concentrations (i.e., low oxygen activity) (see Figure 4.3). The desired final volume fraction of nano-metric Y-enriched oxide dispersoids is ~0.6-1.0 vol.%, which is similar to the volume fraction of nano-clusters (NCs) found in superior NFAs (Section 3.7) [124]. This volume fraction should promote an ideal balance between strength and ductility in the alloy, and is thought to require ~0.12-0.20 at.% Y, but the ideal concentration range is highly dependent on the final composition of the Y-enriched oxide dispersoids [132]. Moreover, Y is

extremely reactive in the molten state (i.e., readily oxidizes) and needs to be over-alloyed in the atomization melt, in order to account for oxidation that occurs during the melting process. Unfortunately, Y loss has proven difficult to accurately predict, ranging from 30-60 at.% during these experiments, and will require special attention in future GARS trials. It should be noted that planned upgrades to the experimental atomizer, including an O<sub>2</sub> analyzer coupled with an O<sub>2</sub> gettering furnace and the ability to make late additions of pre-alloyed Fe-Y arc melted buttons (a common industrial practice), should help to control Y loss during future GARS trials.

Additions of Ti or Hf were used to stabilize the average size of the Y-enriched oxide dispersoids by reducing the growth or coarsening kinetics during elevated temperature dispersoid formation, based on the previous results reported by Uchida et al. [137]. As previously mentioned, these reactive elements also were used to suppress Y consumption during initial surface oxide phase formation.

Small additions (~1.0 at.%) of W were used to increase solid solution strength of the  $\alpha$ -(Fe,Cr) matrix. Increased concentrations of W also can lead to the formation of a detrimental Fe<sub>2</sub>W laves ( $\lambda$ ) phase, which can severely limit the fracture toughness of the alloy, if greater than a critical size [135].

The resulting composition for the as-atomized CR-alloy powders is shown in Table 4.2. The atomic percentage of each metallic constituent was identified using inductively coupled plasma / mass spectroscopy or atomic emission spectroscopy (ICP / MS or AES). Additionally, the chemistry of the surface oxide phase was evaluated using auger electron spectroscopy (AES) depth profiling and (in a few instances) transmission electron microscopy (TEM) with energy dispersive spectroscopy (EDS). The semi-quantitative assessment of the surface oxide phase revealed a primary enrichment of Cr and O with varying amounts of Fe, (Ti or Hf), or Y, depending on the CR-alloy chemistry (see Table 4.2).



Table 4.2. Resulting as-atomized CR-alloy composition and resulting surface oxide phase

Alloy	Fe (at.%)	Cr (at.%)	W (at.%)	Ti (at.%)	Hf (at.%)	Y (at.%)	Surface Oxide Phase
CR-112	83.24	15.52	-	-	-	0.09	Cr-enriched + Y and Fe*
CR-118	83.47	15.84	-	0.50	-	0.20	Cr-enriched + Ti and Fe*,#
CR-126	82.75	15.13	0.90	0.56	-	0.09	Cr-enriched + Ti*
CR-144	82.55	16.16	0.94	-	0.27	0.08	Cr-enriched + Fe*
CR-156	84.49	15.84	-	-	0.11	0.18	Cr-enriched*
CR-160	78.00	20.88	-	0.58	-	0.09	-
CR-162	83.01	16.23	-	0.31	-	-	-
CR-164	83.59	15.55	-	-	0.12	0.09	Cr-enriched*,#
CR-166	83.53	15.91	-	0.12	-	0.09	Cr-enriched + Y and Fe*,#

\* - Evaluated using AES depth profiles of the as-atomized powders

# - Evaluated using TEM analysis with EDS linescans

#### 4.1.1 GARS Processing Parameters

The processing parameters for each experimental GARS trial are displayed in Table 4.3. Several of the key parameters include, atomization nozzle characteristics, pour tube geometry, and reactive gas composition (and injection point). These processing parameters can significantly influence the resulting O content in the atomized powders, and interlinked relationships between all processing parameters must be fully considered when establishing a predictive oxidation model for this GARS process. For this reason, specific empirical trends were evaluated in an effort to provide further insight into controlling this *in situ* oxidation reaction.

Table 4.3. GARS processing parameters for each CR-alloy

Alloy	CR-112	CR-118	CR-126	CR-144	CR-156	CR-160	CR-162	CR-164	CR-166
Atomization Nozzle									
Apex Angle (°)	14	14	45	14	45	45	45	45	45
No. Jets	30	30	30	30	22	30	30	30	30
Jet Dia. (mm)	0.74	0.74	0.74	0.74	1.32	0.74	0.74	0.74	0.74
Atomization Gas									
Composition (Vol. %)	Ar-0.5O <sub>2</sub>	Ar-0.5O <sub>2</sub>	Ar-0.25O <sub>2</sub>	He	Ar-0.12O <sub>2</sub>	Ar-0.19O <sub>2</sub>	Ar-0.19O <sub>2</sub>	Ar-0.19O <sub>2</sub>	Ar-0.19O <sub>2</sub> **
Pressure (MPa)	6.89	6.89	6.89	5.52	5.52	6.55	6.55	6.55	6.55
über Halo									
Composition				Ar-0.25O <sub>2</sub>					
Pressure (MPa)				2.75					
Pour Tube									
Type	Straight	Straight	Straight	Straight	Truncated Trumpet	Straight	Straight	Trumpet	Truncated Trumpet
Diameter (mm)	3.18	3.18	4.75	3.18	2.77	2.77	2.77	2.77	2.77
Material	ZrO <sub>2</sub>	ZrO <sub>2</sub>	ZrO <sub>2</sub>	ZrO <sub>2</sub>	Y <sub>2</sub> O <sub>3</sub> Lined ZrO <sub>2</sub>	Y <sub>2</sub> O <sub>3</sub> Lined ZrO <sub>2</sub>	Y <sub>2</sub> O <sub>3</sub> Lined ZrO <sub>2</sub>	Y <sub>2</sub> O <sub>3</sub> Lined ZrO <sub>2</sub>	Y <sub>2</sub> O <sub>3</sub> Lined ZrO <sub>2</sub>
Avg. Particle Size (µm)*	48	53	27	-	41	43	31	29	36
Standard Deviation (d <sub>84</sub> -d <sub>16</sub> )/2 (µm)*	30	33	18	-	24	23	23	21	23

\* Calculated from the size distribution generated using Microtrac analysis (Nikkiso, Co., Ltd.) of a random sample taken from the riffled as-atomized powders

\*\* Reaction gas not certified

A high pressure close-coupled atomization nozzle (see Figure 4.5 and Figure 4.7c) was used for each GARS trial, in an effort to improve the energy transfer between the high velocity gas and superheated metal stream [138]. Both open wake (14° apex angle) and closed wake (45° apex angle) conditions were evaluated during these experiments (see Figure 4.5 and Table 4.3) [139].

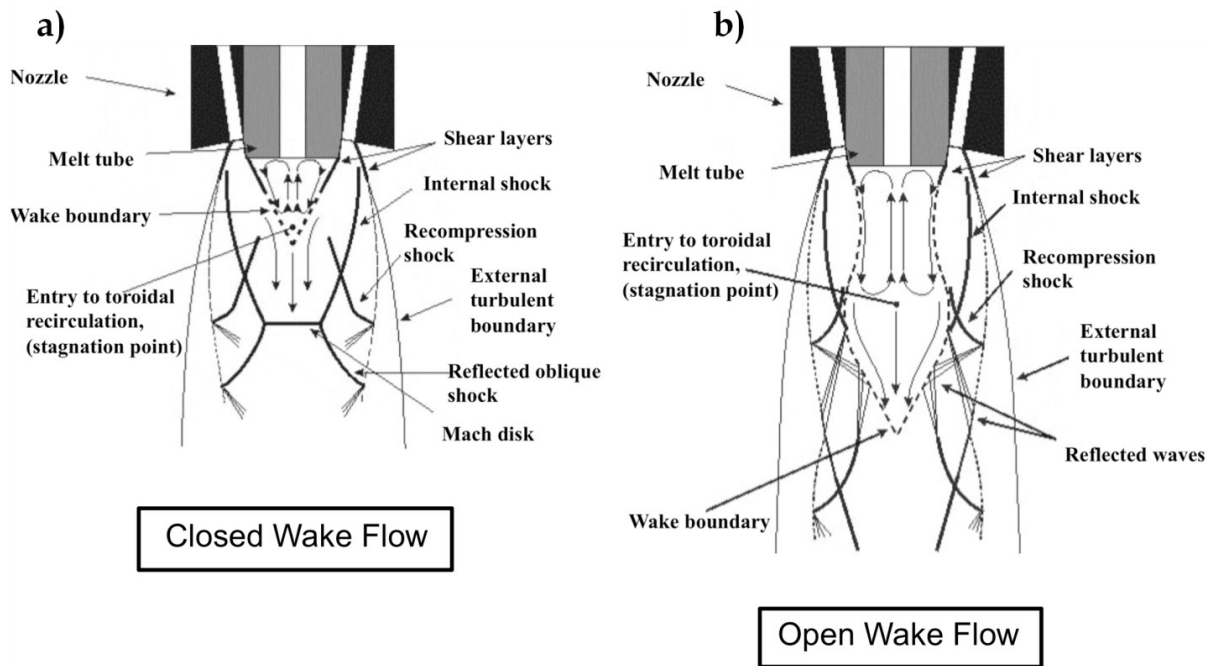


**Figure 4.5.** A schematic showing the gas flow features for a close-coupled atomization nozzle: a) closed wake and b) open wake configuration [140]

Initial GARS trials (results not shown) with ~1.0 vol. % O<sub>2</sub> content in the reaction gas revealed that the use of a closed wake nozzle would unexpectedly cut-off (“freeze-off”) the stream. It was later determined that the inherent strength of the gas recirculation zone (especially potent when the Mach disk is disrupted by the molten metal, see Figure 4.5a) associated with closed wake nozzles was slowing the melt flow rate, allowing the melt to oxidize along the pour tube exit orifice, resulting in increased melt viscosity and subsequent “freeze-off” of the stream.

This was remedied through the use of an open wake nozzle (i.e., 14°), which contains a much weaker recirculation zone and operates with uninterrupted aspiration (i.e., a sub-ambient pressure zone at the melt exit orifice over the full range of gas supply pressure) that draws the melt stream into the primary atomization zone (i.e., within the geometrical intersection of the gas jets). Although the open wake condition offered the continuous aspiration behavior that promoted a more stable atomization stream, it lacked the necessary gas flow structure of the closed wake condition, i.e., the augmented atomization effect of the Mach disk, to produce high yields of fine (dia. < 20 $\mu$ m) powders.

Since fine (dia. < 20 $\mu$ m) powders are the sort of precursor powder that leads to a more ideal ODS microstructure, as identified in Chapter 10, the closed wake nozzle (i.e., 45°) was re-evaluated using a more appropriate (lower) concentration of 0.12-0.25 vol.% O<sub>2</sub> in the reactive gas. Notably, lowering the partial pressure of O<sub>2</sub> in the reaction gas allowed for stable atomization conditions to be established while utilizing a closed wake nozzle. Consequently, the enhanced recirculation zone associated with these nozzles was successfully used to force the melt to spread across the transverse cross-section of the pour tube, creating a thin molten metal film, which was subsequently sheared by the high velocity gas, forming droplets (according to the acceleration wave break-up model [141]) without “freezing-off” the metal stream (see Figure 4.6). These droplets were then driven into the intense secondary break-up zone, where the high energy Mach disk and successive shock fields (i.e., super-sonic core [142]) promoted further disintegration of the initial droplets into finer particles, reducing the average particle size (see Table 4.3). A more detailed description of closed and open wake atomization nozzles can be found in the literature [138, 140].

Thus, it is not surprising that the energy intensity of the gas patterns generated during these GARS trials, as a function of processing parameters, noticeably altered

each resulting particle size distribution (see Table 4.3). Each size distribution can be related to the specific surface area (SSA) generated per time interval of atomization, which controls the amount of  $O_2$  being consumed from the reactive atomization gas (i.e., reducing the local  $O_2$  partial pressure within a specific reaction volume) as the particles oxidize during solidification. Additionally, the geometry of the nozzle jets and atomization pressure (see Table 4.3) dictate the mass flow rate of the atomization gas, which influences the cooling profile of the droplets and the resulting oxidation kinetics.

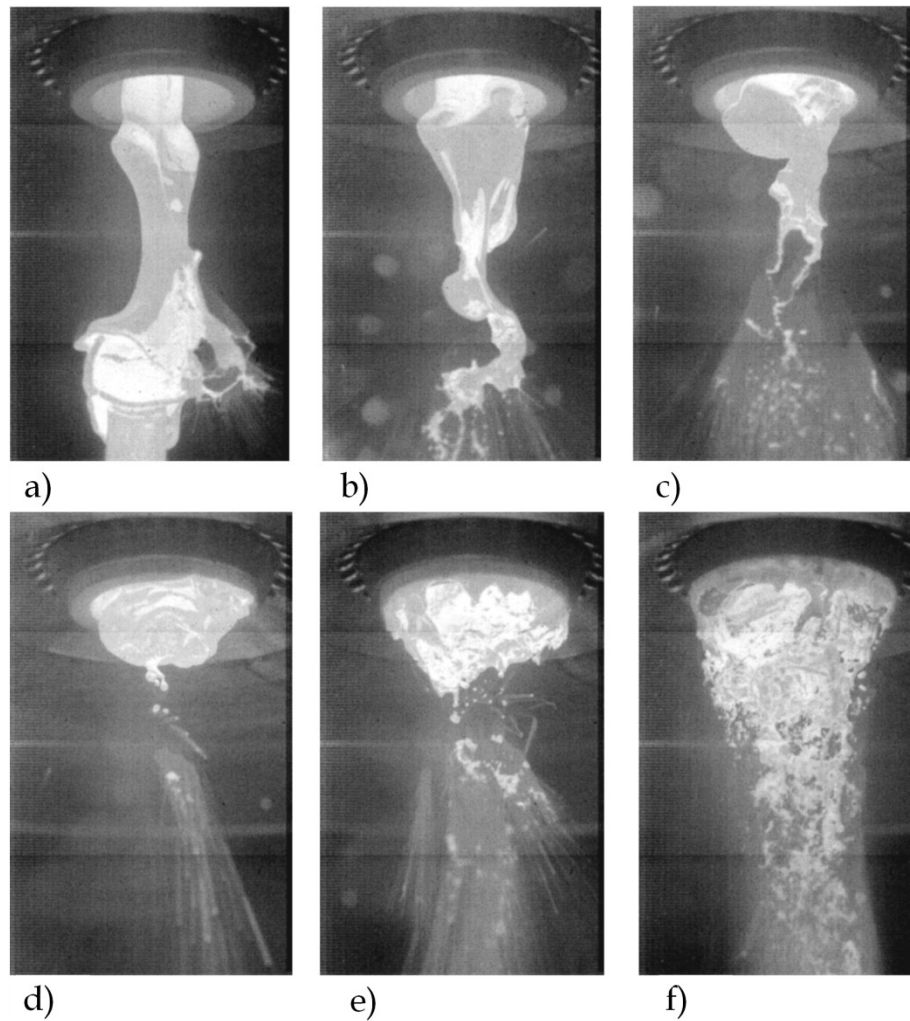


**Figure 4.6.** High speed video (8,000 fps) stills (in time sequence) showing the atomization stream being pinched and lifted due to the gas recirculation zone, and subsequently sheared by the high velocity gas along the periphery of the pour tube, adapted from [143]

In general, two pour tube geometries (i.e., straight and “trumpet bell”) were used to deliver the melt during these GARS experiments (see Figure 4.7 a and b). The straight cylindrical pour tube seemed to promote a reproducible melt delivery. Conversely, the trumpet geometry seemed to encourage increased thinning of the melt film prior to atomization. This is due to the aforementioned gas recirculation zone (see Figure 4.5a), which created a stabilized hollow melt envelope within the internal cavity of the pour tube. This hollow structure appeared to extend the molten metal exposure time within the oxidizing environment. Additionally, slight modifications to the final machined geometry of the trumpet pour tubes were found to significantly alter the oxidation of the atomized droplets. For example, these pour tube were initially designed to flare to a so-called “knife-edge”, as indicated by the arrow in Figure 4.7a. In one case, errors during the machining process resulted in a truncated (for shortened) trumpet geometry, as indicated schematically by the horizontal red dashed line in Figure 4.7a. The truncated trumpet geometry resulted in oxidation values in line with values corresponding with straight cylindrical pour tubes, while the “knife-edge” trumpet pour tube resulted in significantly increased oxidation (~2X) and a slightly coarser powder size distribution [143]. Since both predictable oxidation and finest particle size are of critical importance for this GARS application, further experiments in this series of GARS trials will not use the trumpet pour tube.

The concentration of  $O_2$  in the reactive atomization gas (i.e., Ar- $XO_2$  vol.%) had the strongest influence on the resulting O content in the as-atomized powders. This reactive gas was injected through the primary atomization nozzle during the vast majority of these GARS trials. Alternatively, the reactive gas was injected through a so-called “über halo” (named by D. Byrd) for CR-144 (see Figure 4.8b). The use of this über halo significantly reduced the surface oxidation kinetics, resulting in a much lower O content in the CR-144 as-atomized powders (see Figure 4.9). Again, this relatively unpredictable oxidation value was a disadvantage experimentally in

the current series of trials, but was a useful illustration of the range of GARS reaction intensities that are possible.

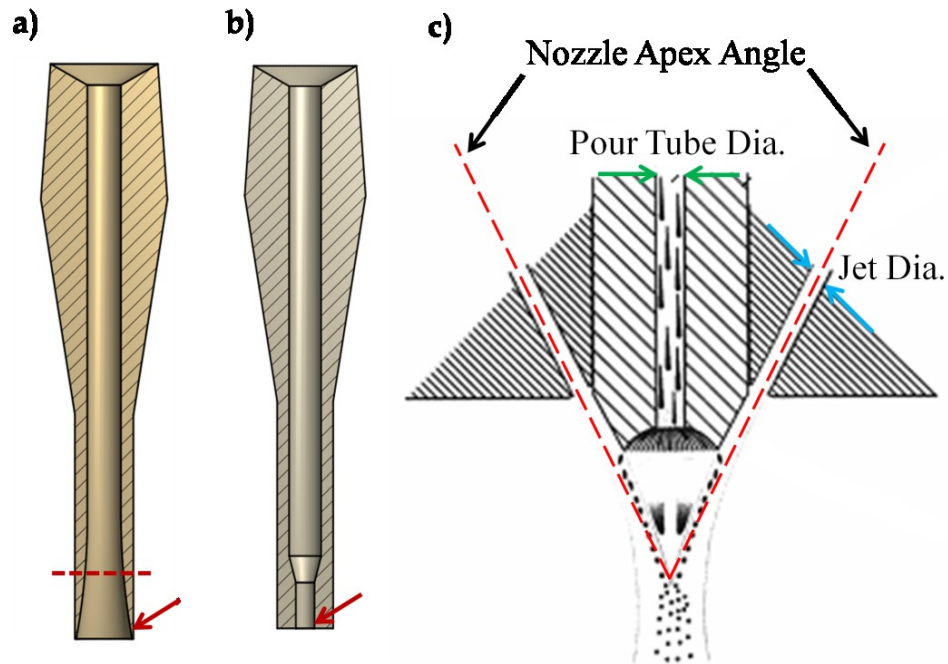


Figure 4.7. Typical pour tube geometry, a) trumpet and b) straight, with c) gas nozzle schematic

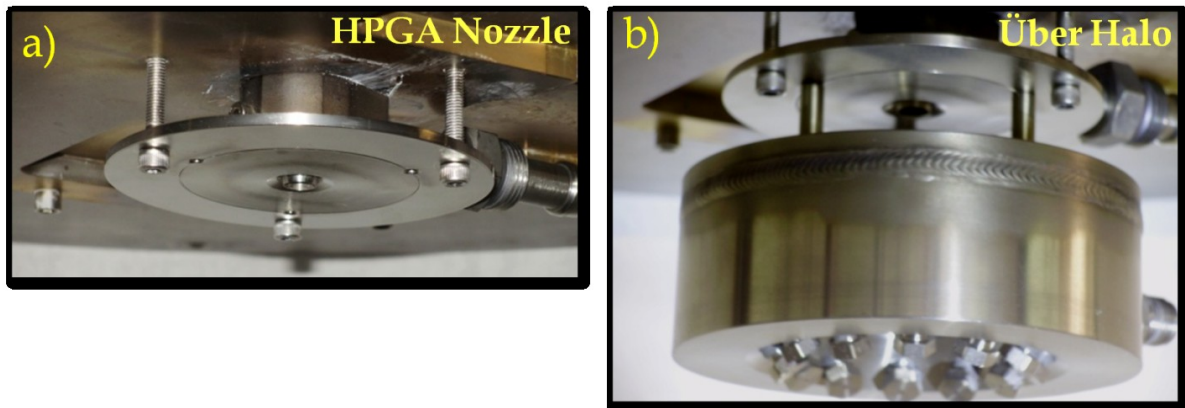


Figure 4.8. a) Ames Lab - USDOE high pressure gas atomization (HPGA) nozzle (45°) and b) HPGA nozzle with attached über halo

The oxidation kinetics of the predominant type of GARS reaction in the current series was empirically found to scale linearly with  $O_2$  content in the reactive atomization gas. This finding is specifically for Y-containing CR-alloys that resulted in a predominately Cr-enriched surface oxide layer (i.e., containing no appreciable Y – see Table 4.2) and were atomized using a similar pour tube geometry (i.e., straight or truncated trumpet – see Table 4.3), as displayed in Figure 4.9 (see dashed black linear trendline). For this reason, only CR-118, CR-126, CR-156, and CR-160 were used selectively to establish and compare a predictive oxidation model based on the theoretical cooling curves for a specific particle size range.

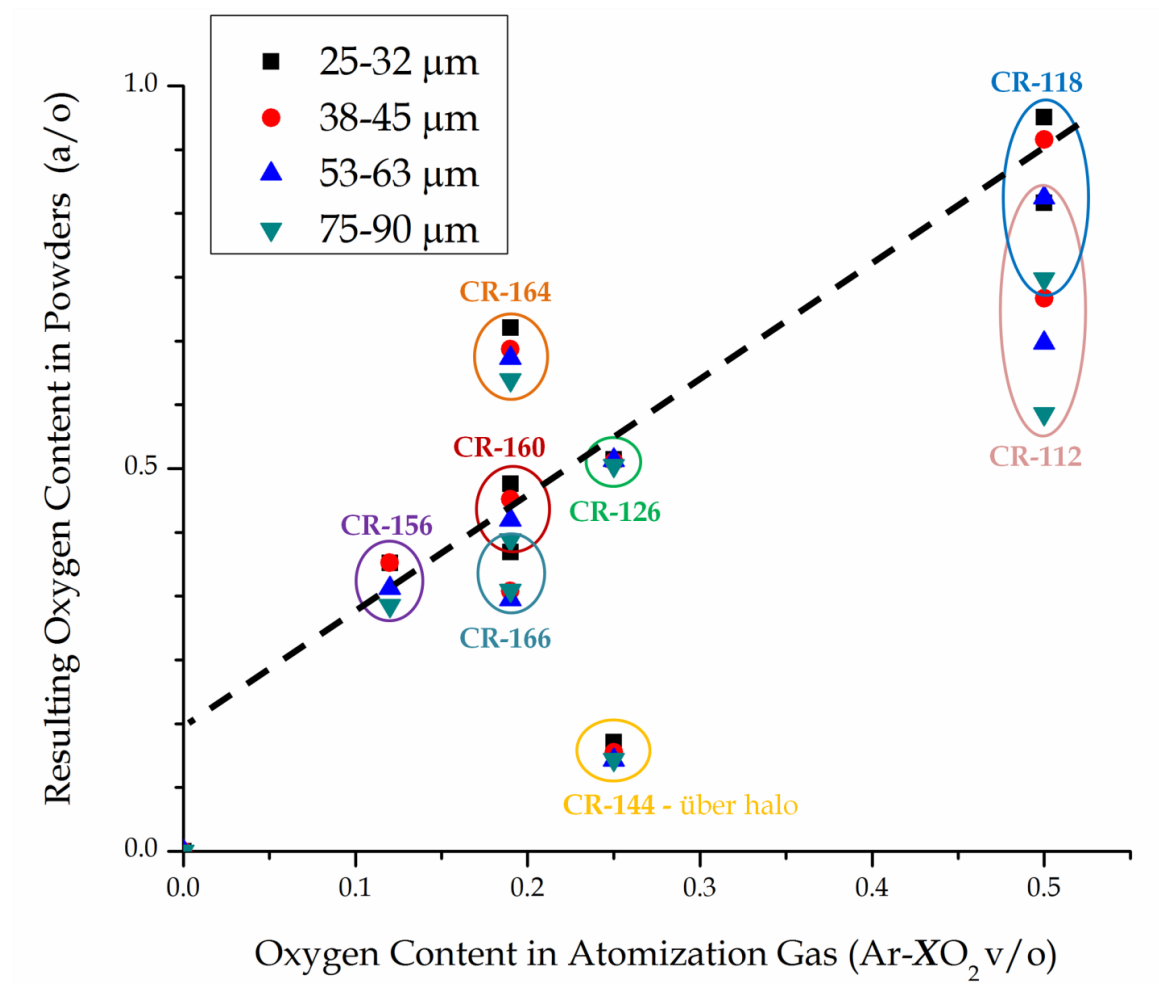


Figure 4.9. Resulting O content as a function of particle size and reactive atomization gas composition



#### 4.1.2 Resulting Oxygen Content

The as-atomized powders were mechanically sieved into specific size ranges from 20-75 $\mu\text{m}$  in dia. (see Table 4.4). Additionally, the bulk O content in the as-atomized powders was measured using an inert gas fusion (LECO) analyzer (see Table 4.4).

Table 4.4. Resulting O content as a function of as-atomized powder size

As-Atomized	CR-112	CR-118	CR-126	CR-144	CR-156	CR-160	CR-162	CR-164	CR-166
Size Range	O <sub>2</sub> (at.%)	O <sub>2</sub> (at.%)	O <sub>2</sub> (at.%)	O <sub>2</sub> (at.%)	O <sub>2</sub> (at.%)	O <sub>2</sub> (at.%)	O <sub>2</sub> (at.%)	O <sub>2</sub> (at.%)	O <sub>2</sub> (at.%)
20-25 $\mu\text{m}$	0.99	1.02	0.53	0.17	0.39	0.52	0.52	0.77	0.42
25-32 $\mu\text{m}$	0.85	0.96	0.51	0.14	0.38	0.48	0.48	0.68	0.39
32-38 $\mu\text{m}$	0.78	0.92	0.50	0.13	0.41	0.47	0.45	0.63	0.36
38-45 $\mu\text{m}$	0.72	0.93	0.51	0.13	0.38	0.46	0.44	0.66	0.34
45-53 $\mu\text{m}$	0.69	0.89	0.51	0.13	0.36	0.45	0.43	0.64	0.35
53-63 $\mu\text{m}$	0.66	0.85	0.51	0.12	0.34	0.43	0.41	0.64	0.33
63-75 $\mu\text{m}$	0.62	0.82	0.51	0.11	0.34	0.44	0.42	0.62	0.32

The resulting O content in the powders was plotted against the average particle specific surface area (SSA) for the size ranges displayed in Table 4.4 and a linear fit was established (see Figure 4.10). This is known as the chemical granular analysis (see Equation 29), for which a linear fit of the data should represent an equivalent oxide layer thickness for all powder sizes (assuming an equivalent oxide density) [144, 145].

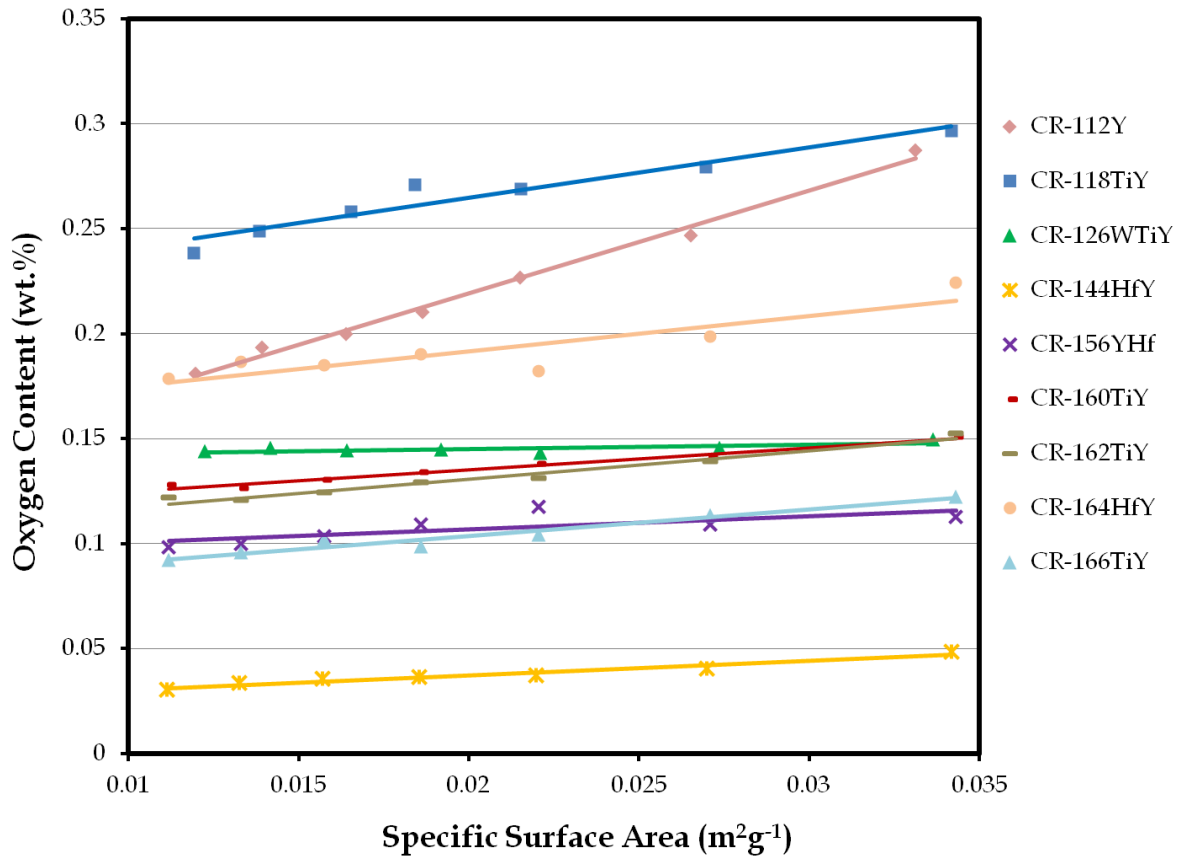
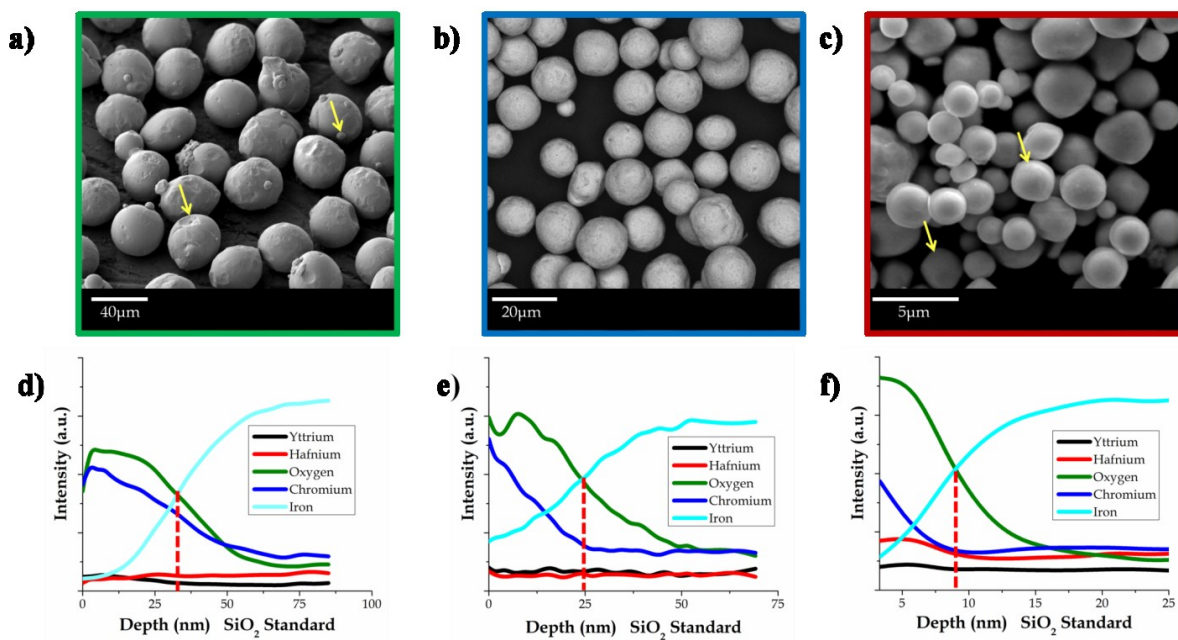


Figure 4.10. Chemical granular plot for each CR-alloy

$$O_{(total)} = \left( \frac{\rho_{ox} W_{O_2} \xi_{ox}}{W_{ox}} \right) SSA + O_{(soln.)} \quad \text{Equation 29}$$

Initially, this analysis seemed to represent the surface oxide layer associated with these CR-alloy powders quite well, but further analysis of the surface oxide layer revealed that the powders contained a varying oxide thickness, depending on particle size. For example, AES depth profiles of as-atomized CR-156 powders indicated that the oxide layer thickness increased with increasing powder size, as shown by the vertical dashed red lines in Figure 4.11 d, e, and f [146]. For this reason, it was established that the chemical granular method could not be used to accurately describe the surface oxide layer thickness.



**Figure 4.11.** As-atomized powder morphology with accompanying AES depth profiles (note vertical dashed red line indicating oxide layer thickness): a) and d) dia. 20-53 μm, b) and e) dia. 5-15 μm and c) and f) dia. < 5 μm

The resulting surface oxide layer on select CR-164 powders was analyzed further using TEM with EDS. The TEM samples were prepared for analysis using focused ion beam (FIB) milling at the Electron Microscopy Center for Materials Research at Argonne National Laboratory-USDOE (see example in Figure 4.12).

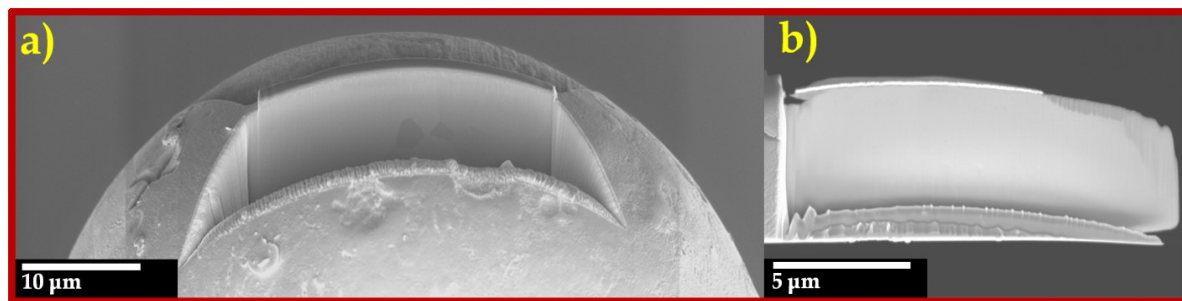


**Figure 4.12.** As-atomized surface oxide analysis of an as-atomized powder with dia. ~58 μm: a) and b) SEM images showing the original as-atomized particle and extracted TEM specimen following FIB milling preparation

This analysis again clearly indicated a variation in surface oxide thickness as a function of particle size (see Figure 4.13). The smaller (dia.  $\sim 2\mu\text{m}$ ) CR-164 particle was found to contain a surface oxide layer thickness of  $\sim 10\text{ nm}$  (see yellow arrow in Figure 4.13 a), while the larger (dia.  $\sim 58\mu\text{m}$ ) CR-164 particle was observed to have a surface oxide layer thickness of  $\sim 85\text{ nm}$  (see yellow arrow in Figure 4.13 b).

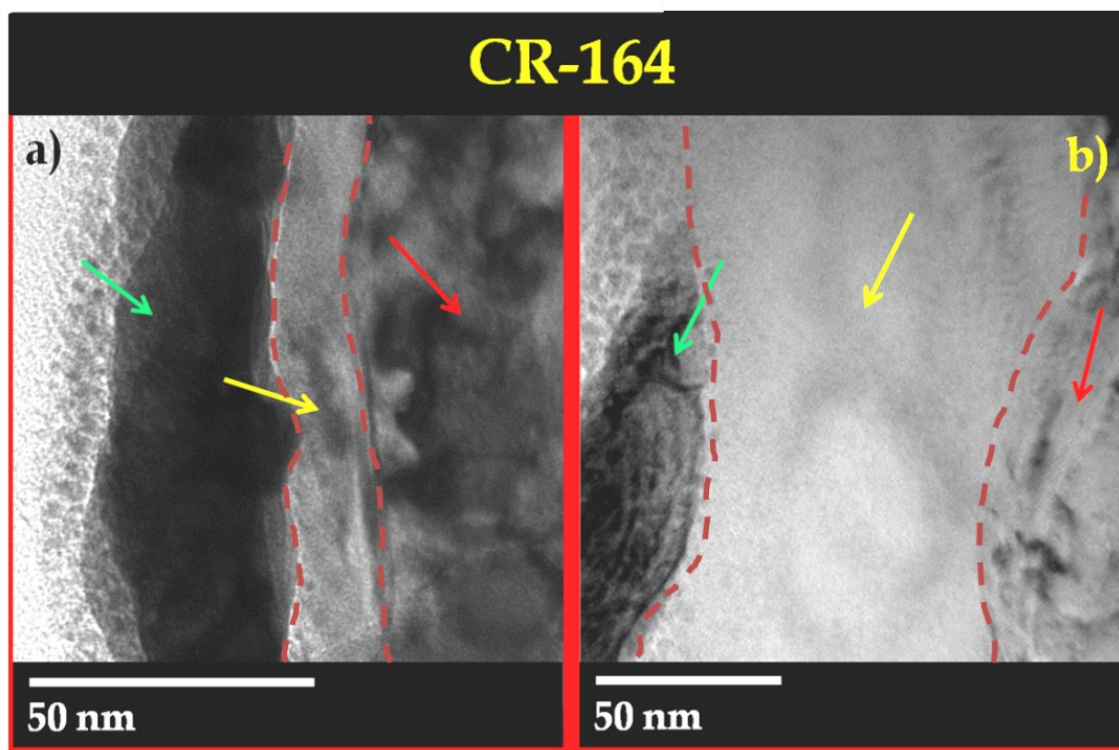


**Figure 4.13.** TEM analysis of the surface oxide (see yellow arrow, outlined by dashed red lines) as a function of powder size (note the layer of Au (green arrow) used to protect the surface oxide layer during FIB milling and matrix (red arrow)): a) dia.  $\sim 2\mu\text{m}$  and b) dia.  $\sim 58\mu\text{m}$

Furthermore, EDS linescans were used to qualitatively evaluate the chemistry of the surface oxide phase on these CR-164 powders. This analysis indicated that these CR-164 powders (dia.  $\sim 58\mu\text{m}$ ) contained a Cr-enriched surface oxide layer (see Figure 4.14), which agreed quite well with a separate AES depth profile analysis (not shown).

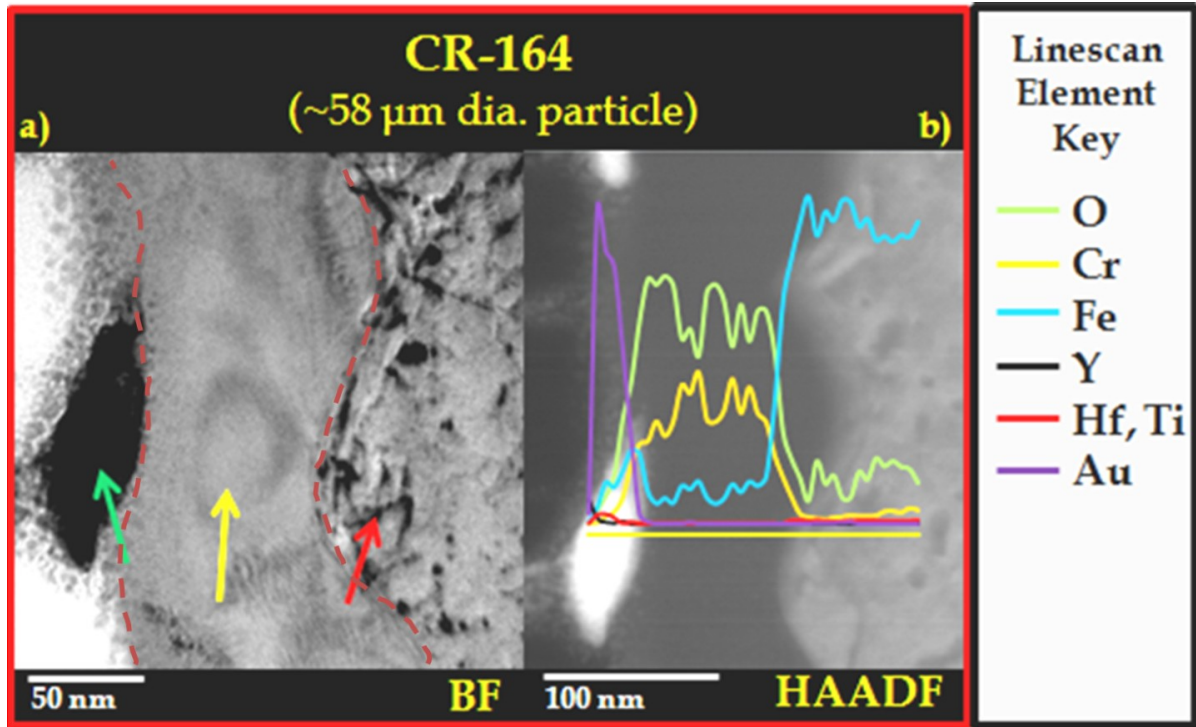


Figure 4.14. a) bright field (BF) TEM analysis with b) accompanying EDS linescan of the surface oxide phase (see yellow arrow, outlined by dashed red lines), indicating a Cr-enriched surface oxide phase

Interestingly, if the bulk O content associated with these powders was converted into a corresponding surface oxide layer thickness (assuming  $\text{Cr}_2\text{O}_3$  phase formation, see Equation 30), the expected surface oxide layer thickness would be ~85 nm, which is near identical to the TEM analysis. For this reason, the bulk O content for each CR-alloy was converted into a surface oxide layer thickness (assuming  $\text{Cr}_2\text{O}_3$  formation) and is displayed in Table 4.5. It should be noted that this analysis is most likely only representative of those CR-alloys containing no appreciable Y in the Cr-enriched surface oxide phase, as displayed in Table 4.2.

$$\xi_{ox} = \frac{m_{O_2} W_{ox}}{S_p W_{O_2} \rho_{ox}}$$

Equation 30

**Table 4.5. Calculated surface oxide thickness, assuming  $\text{Cr}_2\text{O}_3$  phase formation, based on the resulting bulk  $\text{O}_2$  content in the as-atomized powders**

As-Atomized	CR-112	CR-118	CR-126	CR-144	CR-156	CR-160	CR-162	CR-164	CR-166
Size Range	$\xi$ (nm)	$\xi$ (nm)	$\xi$ (nm)	$\xi$ (nm)	$\xi$ (nm)	$\xi$ (nm)	$\xi$ (nm)	$\xi$ (nm)	$\xi$ (nm)
20-25 $\mu\text{m}$	53	53	27	9	20	27	27	40	22
25-32 $\mu\text{m}$	57	63	32	9	24	32	31	45	25
32-38 $\mu\text{m}$	64	76	39	10	32	38	36	50	29
38-45 $\mu\text{m}$	69	89	46	12	36	44	42	62	32
45-53 $\mu\text{m}$	74	95	53	14	40	50	48	71	39
53-63 $\mu\text{m}$	84	109	62	15	45	58	55	85*	44*
63-75 $\mu\text{m}$	92	121	71	17	53	69	66	97	50

\*Thickness verified to be accurate using TEM analysis of the as-atomized powders

## 4.2 Theoretical Particle Cooling Curves

Analysis of the high temperature oxidation kinetics associated with GARS processing is required to adequately predict O content (primarily as a surface oxide film) for the resulting precursor powders for the oxide dispersion strengthened (ODS) alloys. For this reason, theoretical cooling curves for as-atomized ferritic stainless steel droplets were modeled, and oxidation profiles were extracted for specific powder size fractions. These oxidation profiles were then used to calculate a predicted surface oxide layer thickness.

The theoretical cooling curves were assembled using a similar method as previously demonstrated by Mathur et al. [147]. This model describes the thermal profile of as-

atomized droplets as a function of droplet size (diameter), using droplet-gas interactions to describe particle acceleration and cooling rate. Thus, it provided a quantitative assessment of the oxidation time and temperature for a given particle size. It should be noted that the primary goal of this analysis was to evaluate the droplet thermal profile, in an effort to better understand the oxidation kinetics associated with the GARS reaction, but several intriguing solidification trends, including recalescence heating effects, (as a function of particle size) were also revealed.

#### 4.2.1 Droplet Model

A description of the variables used for this model can be found at the end of this chapter (see Table 4.6). Additionally, specific thermodynamic and physical properties also are listed at the end of this chapter (see Table 4.7). The time resolution of this model was 1 $\mu$ s per time interval, except for during solidification when the time resolution was increased to 0.01 $\mu$ s.

##### *Particle Velocity*

The mass flow rate of the atomization gas was calculated using the choked mass flow equation described by Poirier and Geiger, in combination with the calculated density of the atomization gas and an assumed discharge coefficient (see Equation 31-Equation 33) [148]. It should be noted that compressibility effects were not taken into consideration during this calculation (i.e.,  $z = 1$ ). Additionally, the atomization gas was assumed to be pure Ar, although it contained small additions of O<sub>2</sub> (see Table 4.3).

$$\dot{m} = DA_j \sqrt{\gamma \rho_a P_a \left( \frac{2}{\gamma+1} \right)^{\frac{\gamma+1}{\gamma-1}}}$$

Equation 31

Where,  $\gamma = 1.67$  (specific heat ratio for Ar)

$$\rho_a = \frac{W_g P_a}{z R T_{g,a}} \quad \text{Equation 32}$$

Where,  $B_2=1$ (turbulent flow) and  $e_f=0.4$  [148]

$$D = \left( \frac{1}{\beta_2} + e_f \right)^{-\frac{1}{2}} \quad \text{Equation 33}$$

The initial velocity of the atomization gas was assumed to be limited to the speed of sound in Ar (i.e.,  $M_a = 1$ ) within each atomization gas jet passageway, since the critical pressure ratio (Equation 34) was satisfied for this GARS process (see atomization pressure in Table 4.3) [148].

$$\text{if, } \frac{P_c}{P_a} \leq \left( \frac{2}{\gamma + 1} \right)^{\frac{\gamma}{\gamma-1}} \quad \text{then, } V_{g,a} = M_a c_{g,a} \quad \text{Equation 34}$$

Where,  $M_a = 1$

Furthermore, the temperature and pressure of the gas within the atomization jets was calculated using Equation 35 and Equation 36, as a function of the atomization parameters (see Table 4.3) [148].

$$T_{g,j} = T_{g,a} \left( 1 + \frac{\gamma - 1}{2} M_a^2 \right)^{-1} \quad \text{Equation 35}$$

Where,  $T_{g,a} = -40^\circ\text{C}$

(unpublished experimental results [149])



$$P_j = P_a \left( \frac{2}{\gamma+1} \right)^{\frac{\gamma}{\gamma-1}} \quad \text{Equation 36}$$

These values were then used to determine the velocity of the gas, as described by the free expansion model (Equation 37-Equation 39), in which the gas accelerates to super-sonic velocity [148]. Moreover, the time required for the gas to achieve maximum velocity was neglected (i.e., acceleration was assumed to be instantaneous) and gas temperature was assumed not to change during expansion.

$$M_g = \sqrt{\left( \frac{2}{\gamma-1} \right) \left( \left( \frac{P_j}{P_c} \right)^{\frac{\gamma-1}{\gamma}} - 1 \right)} \quad \text{Equation 37}$$

$$V_{g,i} = M_{g,j} c_{g,j} \quad \text{Equation 38}$$

$$c_{g,j} = \sqrt{\frac{\gamma R T_{g,j}}{W_g}} \quad \text{Equation 39}$$

The velocity profile of the atomization gas was assumed to follow the decay function described by Alam et al. (Equation 40), which was found to be dependent on the effective diameter ( $d_e$ ) of the gas nozzle [150, 151].

$$V_g = V_{g,i} \left\{ 1 - \exp \left( - \frac{1}{2\eta \sqrt{\frac{\rho_c x}{\rho_j d_e} + \chi}} \right) \right\} \quad \text{Equation 40}$$

Where,  $\eta=0.0841$  and  $\chi=0.06035$  [150]

$d_e$ =center bore of atomization nozzle [151]

The initial velocity (i.e., after the first time interval) of the as-atomized droplets was calculated using Bernoulli's equation (see Equation 41 and Equation 42) [152], and

the effects of aspiration were disregarded. Additionally, it was assumed that the molten alloy exits the pour tube as a predefined volumetric distribution of spherical droplets, thus neglecting the time required for droplet formation. This volumetric distribution was defined using experimental data from post-atomized size distribution analysis.

$$V_m = \sqrt{\frac{2}{1 - \frac{A_{or}^2}{A_{cr}^2}} \cdot \left( \frac{\Delta p}{\rho_m} + g\omega \right)} \quad \text{Equation 41}$$

$$\dot{m}_m = V_m A_{or} \quad \text{Equation 42}$$

Consequently, the velocity profile of the droplets is related to the velocity profile of the gas, as described by the momentum equation (Equation 43 and Equation 44), which is a function of the drag coefficient (Equation 45) as defined by the Reynolds number (Equation 46) [147, 153, 154].

$$F = m \left( \frac{dV_d}{dt} \right) = \left( \frac{C_D \rho_g V_r^2 A_d}{2} \right) + m_d g \quad \text{Equation 43}$$

$$F = \left[ \frac{3C_D \rho_g (V_g - V_d) |V_g - V_d| A_d}{4d_d \rho_d} \right] + m_d g \quad \text{Equation 44}$$

$$C_D = 0.28 + \left( \frac{6}{Re^{\frac{1}{2}}} \right) + \left( \frac{21}{Re} \right) \quad \text{Equation 45}$$

$$Re_g = \frac{V_r d_d}{\nu_g} \quad \text{Equation 46}$$

### Thermal Profile

Heat is extracted from the droplets through convective cooling between the droplets and atomization gas, and through radiation loss to the chamber wall for each given time interval (Equation 47). The heat transfer coefficient between the droplet and gas is inversely related to droplet size ( $d_d$ ), i.e., Equation 48.

$$Q_d = (h_d S_d (T_d - T_g) + \sigma^* \epsilon S_d (T_d^4 - T_c^4)) \quad \text{Equation 47}$$

$$h_d = \frac{k_g (2 + 0.6 Re_d^{1/2} Pr_g^{1/3})}{d_d} \quad \text{Equation 48}$$

$$Pr_g = \frac{C_g \mu_g}{k_g} \quad \text{Equation 49}$$

Where,  $C_g$  is constant for inert gases

The heat extracted from the particle is gained by the atomization gas, which in turn is cooled by the atomization chamber wall. This heat exchange sequence is thought to occur as a complete series during each time interval. The net heat increase in the atomization gas is shown in Equation 50 and Equation 51. It should be noted that the atomization chamber wall was assumed to maintain an average temperature of 70°C during the time-span of this model, a reasonable approximation for steady state of an industrial system that is actively cooled.

$$Q_g = \left[ \sum_{d=5}^{82.5} \Phi_d (h_d S_d (T_d - T_g)) \right] - h_c (\pi d_c (x_{c,i} - x_{c,f})) (T_c - T_g) \quad \text{Equation 50}$$

Where,  $x_{c,i} - x_{c,f}$  is the total distance that the droplet travels during one time interval

$$\Phi_d = \frac{\dot{m}_m \Delta t \theta_d}{m_d} \quad \text{Equation 51}$$

Where,  $\Phi$  = number of particles and  $\theta_d$  = weight fraction of droplet distribution

The heat transfer coefficient between the atomization gas and atomization chamber wall is described using Equation 52-Equation 55 [152, 155].

$$h_c = \frac{Nu_g k_g}{d_c} \quad \text{Equation 52}$$

$$Nu_g = \frac{\left(\frac{f}{8}\right) Re_c Pr_g}{1.07 + 12.7 \left(\frac{f}{8}\right)^{\frac{1}{2}} \left(Pr_g^{\frac{2}{3}} - 1\right)} \quad \text{Equation 53}$$

$$Re_c = \frac{V_g d_c}{\nu_g} \quad \text{Equation 54}$$

$$f = \left( \frac{1}{-1.8 \log \left[ \frac{6.9}{Re_g} + \left( \frac{\varepsilon/d_c}{3.7} \right)^{1.11} \right]} \right)^2 \quad \text{Equation 55}$$

Where,  $\varepsilon=0.002$  [152]

Therefore, the net change in droplet temperature and atomization gas temperature for each given time interval was determined from Equation 56 and Equation 57, respectively.

$$\Delta T_d = \frac{Q_d \Delta t}{m_d C_d} \quad \text{Equation 56}$$

$$\Delta T_g = \frac{Q_g}{\dot{m}_g C_g} \quad \text{Equation 57}$$

### *Solidification Kinetics*

The homogenous nucleation temperature for the droplets was defined using the spherical cap model (Equation 58) [156]. This model was put into terms of relative undercooling, based on the work of Gao et al. (see Equation 59 and Equation 60) [157], for which iterations were then used to calculate the ideal value for thermal undercooling.

$$\Delta T^2 = \frac{16\pi\sigma_{SL}^3 T_L^2}{3kT_n \Delta H_f^2 \ln(N)} \quad \text{Equation 58}$$

$$\psi^3 - \psi^2 = -\frac{16\pi\sigma_{SL}^3}{3kT_L \Delta H_f^2 \ln(N)} \quad \text{Equation 59}$$

$$\psi \equiv \frac{\Delta T_t}{T_L} \quad \text{Equation 60}$$

Where,  $\Delta T_t = T_L - T_N$

The fraction of thermal undercooling was determined using Turnbull's hypothesis of mote isolation (Equation 61) [158]. It should be noted that a nucleant density of  $2 \times 10^6 \text{ cm}^{-3}$  was used for this calculation, based on the experimental results of Mathur et al. [147]. Furthermore, the effect of droplet curvature on undercooling also was taken into consideration in this model (Equation 62 and Equation 63) [159]. Therefore, the real nucleation temperature used for the onset of droplet solidification

is shown in Equation 64. It should be noted that no chemical (solute) effects or kinetic effects on the total undercooling of the droplets were considered.

$$\theta_{hom} = \exp(-\lambda v_d) \quad \text{Equation 61}$$

Where,  $\lambda = 2 \times 10^6$

$$\Delta T_{cur} = \frac{4\Gamma}{d_d} \quad \text{Equation 62}$$

$$\Gamma \equiv \frac{\sigma_{SL}}{\Delta S_f} \quad \text{Equation 63}$$

$$\Delta T_N = \Delta T_t(\theta_{hom}) + \Delta T_{cur} \quad \text{Equation 64}$$

The thermal supersaturation of the droplet (Equation 65) describes the droplet's ability to absorb the latent heat released during solidification [160]. Therefore, hypercooling is defined to occur when thermal supersaturation (i.e.,  $\Omega$ ) is greater than or equal to unity [160]. The Peclet number was calculated using the model derived by Wang et al., which approximates the Ivantsov function with respect to thermal supersaturation (Equation 66) [161].

$$\Omega \equiv \frac{T_L - T}{\Delta H_f / C_d} \quad \text{Equation 65}$$

$$Pe_t = a \left( \frac{\Omega}{1 - \Omega} \right)^b \quad \text{Equation 66}$$

where  $a=0.4567$  and  $b=1.195$  [161]

The Peclet number was then used to calculate the dendrite tip radius and resulting dendrite velocity using a truncated version of the LKT model (see Equation 67-Equation 69) [162]. It should be noted that the droplets were assumed to solidify as a single dendrite grows across the particle diameter [163]. Therefore, the heat released during solidification (i.e., recalescence) was determined using Equation 70.

$$r_{den} = \frac{\Gamma/\tau^*}{(\Delta H_f/C_d)Pe_t(1-n)} \quad \text{Equation 67}$$

$$n = \frac{1}{\sqrt{1 + \frac{1}{\tau^*Pe_t}}} \quad \text{Equation 68}$$

$$V_{den} = \frac{2Pe_t\alpha}{r_{den}} \quad \text{Equation 69}$$

Where,  $\alpha=6.09 \times 10^{-6}$  (m<sup>2</sup>s<sup>-1</sup>) [164]

$$Q_{re} = \Delta H_f V_{den} A_d \rho_d \quad \text{Equation 70}$$

If a droplet's total undercooling met or exceeded the hypercooling condition (i.e.,  $\Omega = 1$ ), then the dendrite interface was assumed to be planar (i.e., smooth) [159]. Therefore, the thermal absolute solidification velocity was defined by the interface stability model described by Trivedi et al. (see Equation 71) [165].

$$(V_{den})_{abs} = \frac{\alpha_L \Delta H_f}{\Gamma C_{d,L}} \quad \text{Equation 71}$$

#### 4.2.2 Cooling Curves

The resulting theoretical cooling curves with respect to droplet diameter as a function of time and distance are displayed in Figure 4.15 and Figure 4.16, respectively. The initial (sharp) inflection point on these curves (see red arrow in

Figure 4.15 and Figure 4.16) indicates the onset of solidification (i.e., start of recalescence) and the second inflection point (see green arrow in Figure 4.15 and Figure 4.16) highlights the completion of solidification. Therefore, it can be seen that undercooling is inversely related to droplet size, i.e., smaller particles achieve greater undercooling prior to solidification. Furthermore, these curves illustrate the increased cooling rate associated with smaller droplets, as a direct consequence of the enhanced heat transfer coefficient due to the increased surface area to volume ratio of these powders. This implies that the larger droplets are subjected to prolonged oxidation at elevated temperature during this GARS process, which is consistent with experimental data of larger powders containing a thicker surface oxide layer (see Figure 4.11 and Table 4.5). It should be noted that particles with a dia.  $\geq 69\mu\text{m}$  were omitted from these cooling curve figures, since the current state of this model did not accurately describe solidification when the temperature of these particles was raised above the solidus temperature ( $T_s$ ) during recalescence.

The relative flight distance of the atomized droplets as a function of atomization time is shown in Figure 4.17. Interestingly, it was observed that the smallest droplets (e.g.,  $5\mu\text{m}$ ) initially achieve the highest velocity, i.e., value of distance/time (see red arrow in Figure 4.17), but due to the increased momentum associated with the larger (i.e., heavier) droplets, these smaller droplets are quickly overcome during droplet descent (see green arrow in Figure 4.17), as gravity takes over as the dominant acceleration factor. This can lead to interparticle collisions during the atomization process, which can result in “satellite” particle formation (see red arrow in Figure 4.18) [104] or surface dimple formation (see yellow arrow in Figure 4.18) when the particles collide.



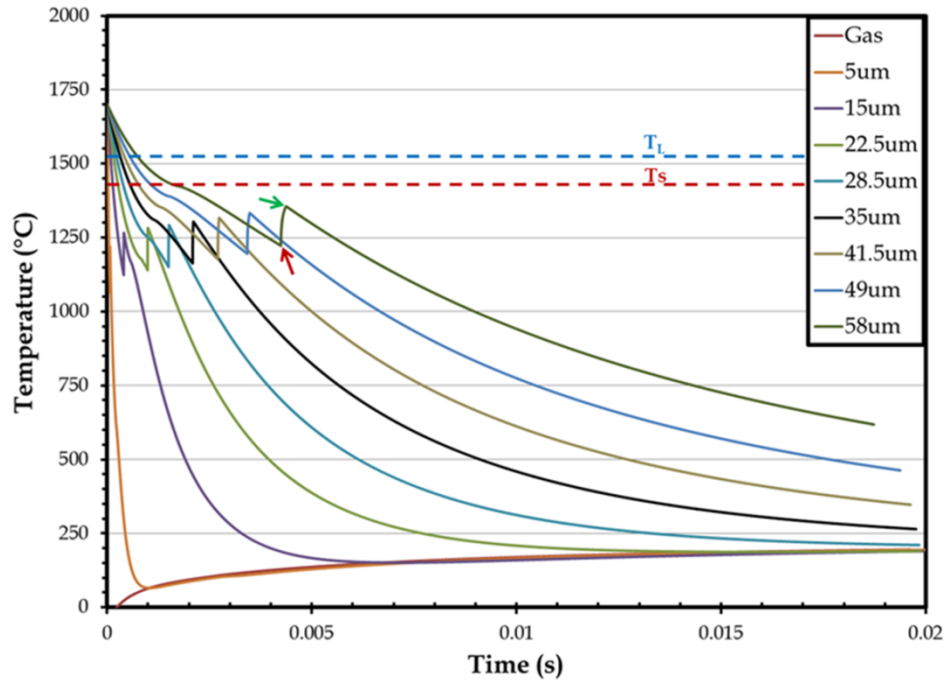


Figure 4.15. Theoretical particle cooling curves for CR-156 (T vs. t): note that the alloy solidus temperature ( $T_S$ ) is marked by the horizontal dashed red line and liquidus temperature ( $T_L$ ) is marked by the horizontal dashed blue line

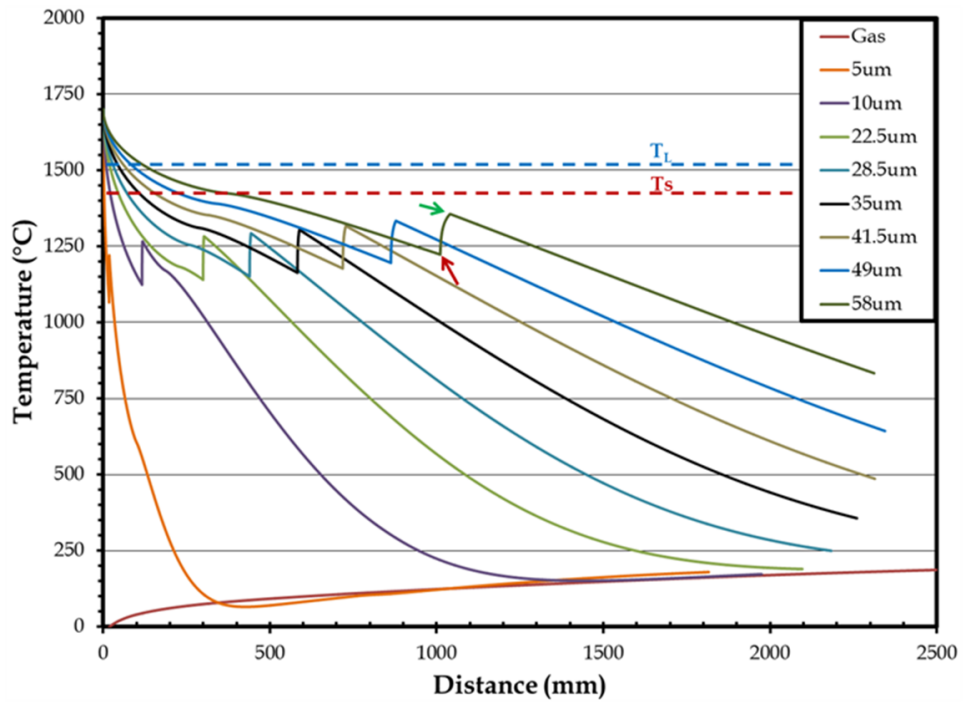


Figure 4.16. Theoretical particle cooling curves for CR-156 (T vs. D): note that the alloy solidus temperature ( $T_S$ ) is marked by the horizontal dashed red line and liquidus temperature ( $T_L$ ) is marked by the horizontal dashed blue line

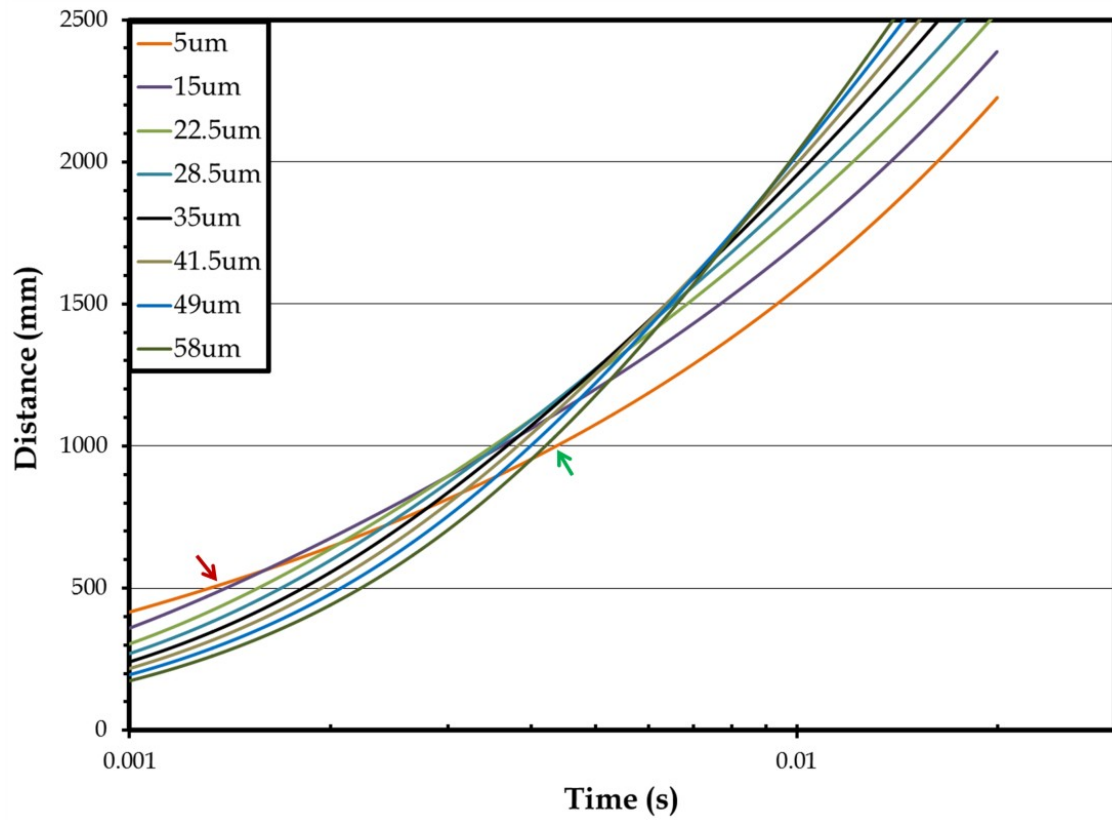


Figure 4.17. Theoretical particle cooling curves for CR-156 (D vs. t)

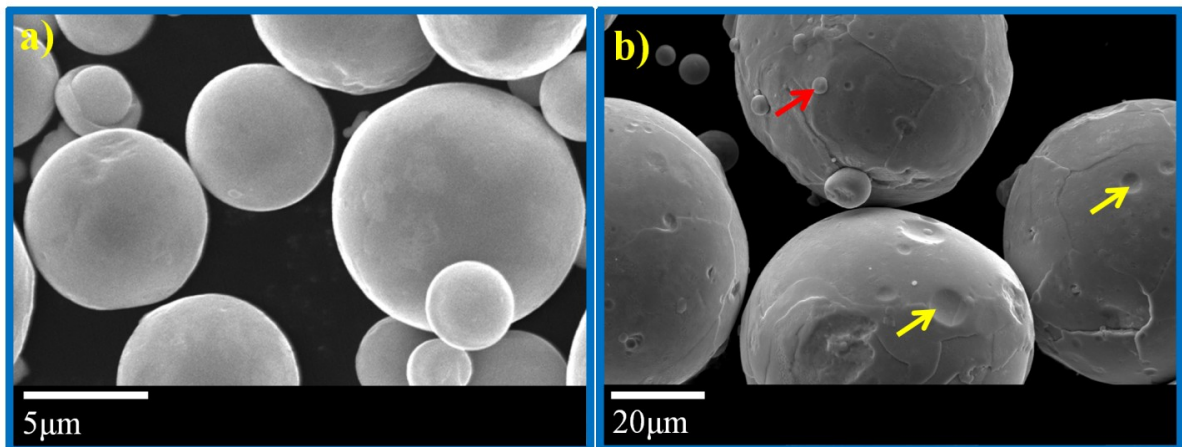


Figure 4.18. As-atomized powder morphology as a function of particle size: a) dia. < 20µm and b) dia. 45-75µm (note the satellite particles (red arrow) and surface dimples (yellow arrow))

### 4.2.3 Solidification Curves

The theoretical droplet solidification velocity was found to be significantly influenced by the extent of droplet undercooling. The finest droplets (dia.  $\leq 15\mu\text{m}$ , see green arrow in Figure 4.19 a and b) were calculated to undercool below the hypercooling threshold (see vertical red dashed line in Figure 4.19a) prior to nucleation (see Equation 65), thus achieving the absolute limit of solidification velocity (see horizontal red dashed line in Figure 4.19a) [165]. Furthermore, the theoretical dendrite tip radius was determined to initially decrease with increasing undercooling, but then rapidly increased as undercooling approached the hypercooling limit (see vertical red dashed line in Figure 4.19b), which, as suggested by Trivedi et al. [165], illustrates the formation of a stable planar (smooth) growth interface. Moreover, the stability of the planar interface was shown to be linked to achieving the absolute solidification velocity limit, which requires nucleation and growth below the hypercooling threshold. Stabilizing a planar interface is thought to promote microsegregation-free solidification (i.e., solute-trapping in excess of equilibrium solubility), as previously demonstrated by Boettinger et al. [166].

The calculated solidification velocity as a function of particle solid fraction (%) with respect to droplet diameter is shown in Figure 4.20. Notably, the solidification velocity of the finest droplets (i.e., dia.  $\leq 15\mu\text{m}$ ) starts at the absolute solidification velocity (see Equation 71), and maintains this velocity until the droplet temperature rises above the hypercooling threshold (as indicated by the red arrow in Figure 4.20), but still below the solidus temperature (see Figure 4.15 and Figure 4.16). This analysis suggests that the majority of the ultra-fine gas atomized droplets (i.e., dia.  $\leq 5\mu\text{m}$ ) should solidify under stable planar growth conditions. Furthermore, this should promote microsegregation-free solidification (i.e., solute trapping of Y) in these ultra-fine CR-alloy powders, which was experimentally confirmed to result in a more ideal (homogeneously distributed nano-metric (dia.  $\leq 10\text{nm}$ ) Y-enriched dispersoids) ODS microstructure (see Chapter 10) [146]. Conversely, larger droplets

were found to contain appreciable amounts of Y microsegregation throughout the atomized microstructure, consistent with the reduced solidification velocities predicted by this model (see Chapter 10) [146].

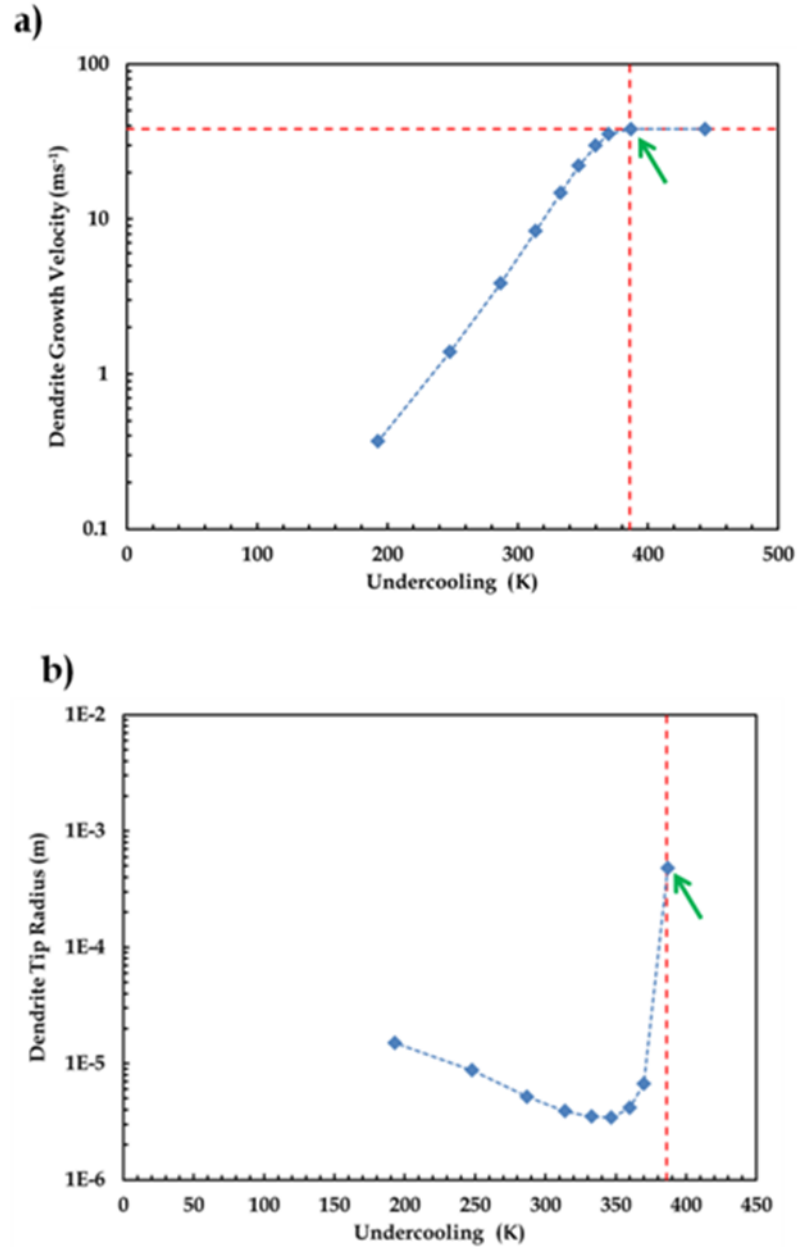


Figure 4.19. Initial solidification velocity a) and resulting dendrite tip radius b) as a function of particle undercooling; note the green arrow indicating a particle dia. of  $15\mu\text{m}$

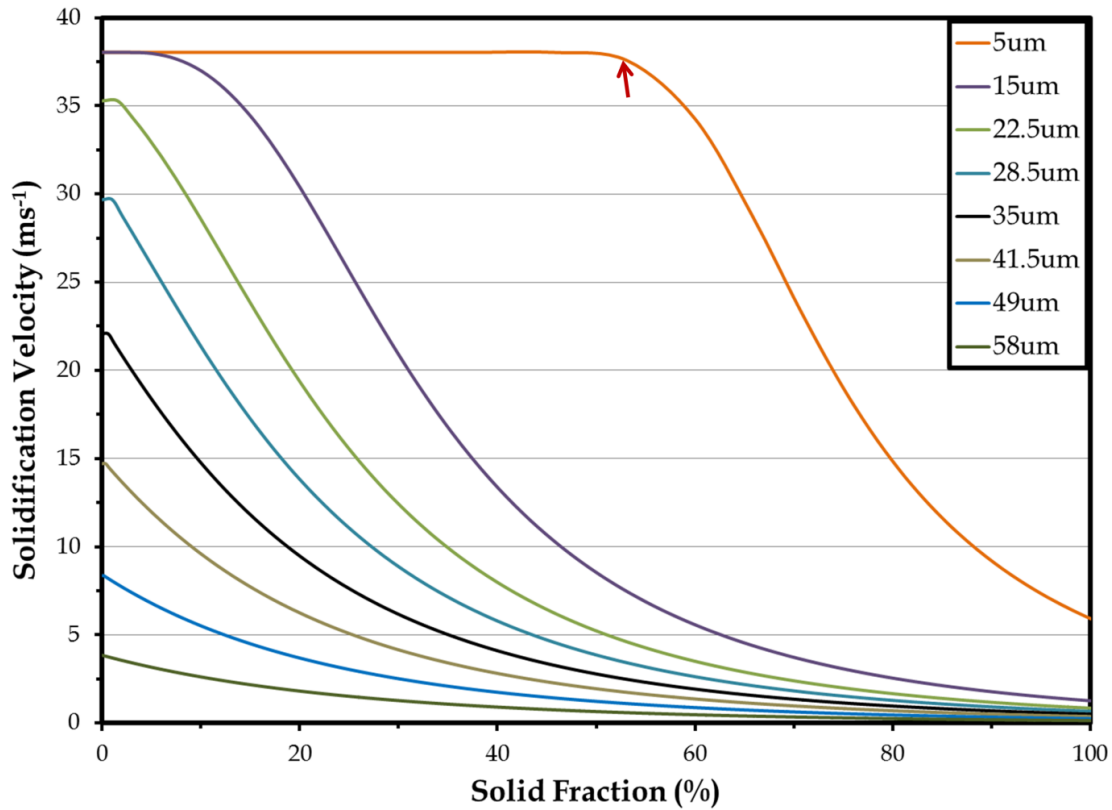


Figure 4.20. Solidification velocity (CR-156) as a function of solid fraction (%) for varying droplet diameters

### 4.3 GARS Oxidation Model

The aforementioned theoretical droplet cooling curves were used to develop an oxidation model for this GARS process. It was assumed that the surface oxide layer will form as Cr oxide (i.e.,  $\text{Cr}_2\text{O}_3$ ) based on a compilation of experimental results (see Table 4.2). For this reason, the parabolic oxidation rate constant for  $\text{Cr}_2\text{O}_3$ , formulated from the results of Gulbransen et al., was calculated for each time interval (i.e.,  $1\mu\text{s}$ ) as the droplets were cooled (Equation 72). It should be noted that the parabolic oxidation pre-factor ( $B$ ) was modified from 0.156 to 5.0, in order to achieve a better fit with the experimentally determined oxide layer thickness. Additionally, the parabolic rate constant was scaled with respect to the oxygen

partial pressure ( $P_{O_2}$ ) in the reactive atomization gas (see Equation 73). Notably, the parabolic rate constant was found to scale linearly with  $P_{O_2}$  (i.e.,  $n=1$ ), similar to the empirical relationship highlighted in Figure 4.9.

$$k_p = B \exp \left( \frac{-E}{RT} \right) \quad \text{Equation 72}$$

Where,  $E=249\text{kJ/mol}$  [167] and

$B=5 \text{ g}^2\text{cm}^{-4}\text{s}^{-1}$  (this work)

$$k_p \propto (P_{O_2})^{\frac{1}{n}} \quad \text{Equation 73}$$

Where,  $n=1$

The change in mass associated with uptake of O during each time interval (i.e.,  $1\mu\text{s}$ ) of oxidation was determined using Equation 74. The mass of O was then converted to oxide thickness using Equation 75. The net rate of oxidation then was evaluated using Equation 76. It should be noted that this oxidation reaction was deemed complete when the rate of oxidation decreased to a value less than  $400 \text{ nm s}^{-1}$ .

$$\Delta m_{O_2}(\Delta t) = \left( \frac{k_{p,i} + k_{p,f}}{2} \right)^{\frac{1}{2}} \cdot 2S_d \left( t_f^{\frac{1}{2}} - t_i^{\frac{1}{2}} \right) \quad \text{Equation 74}$$

$$\xi_{ox} = \frac{\Delta m_{O_2} W_{ox}}{S_d W_{O_2} \rho_{ox}} \quad \text{Equation 75}$$

Where,  $M_a O_y$

$$\delta = \frac{\Delta \xi_{ox}}{\Delta t} \quad \text{Equation 76}$$

The predicted surface oxide layer thickness as a function of reactive atomization time with respect to droplet diameter for CR-156 is shown in Figure 4.21. These

calculations clearly indicate that surface oxide layer thickness increases with droplet diameter. Furthermore, each oxidation curve was found to contain a small inflection point (see red arrow in Figure 4.21), which represents solidification in the droplet. Interestingly, this model suggests that the majority of oxidation occurs prior to droplet solidification.

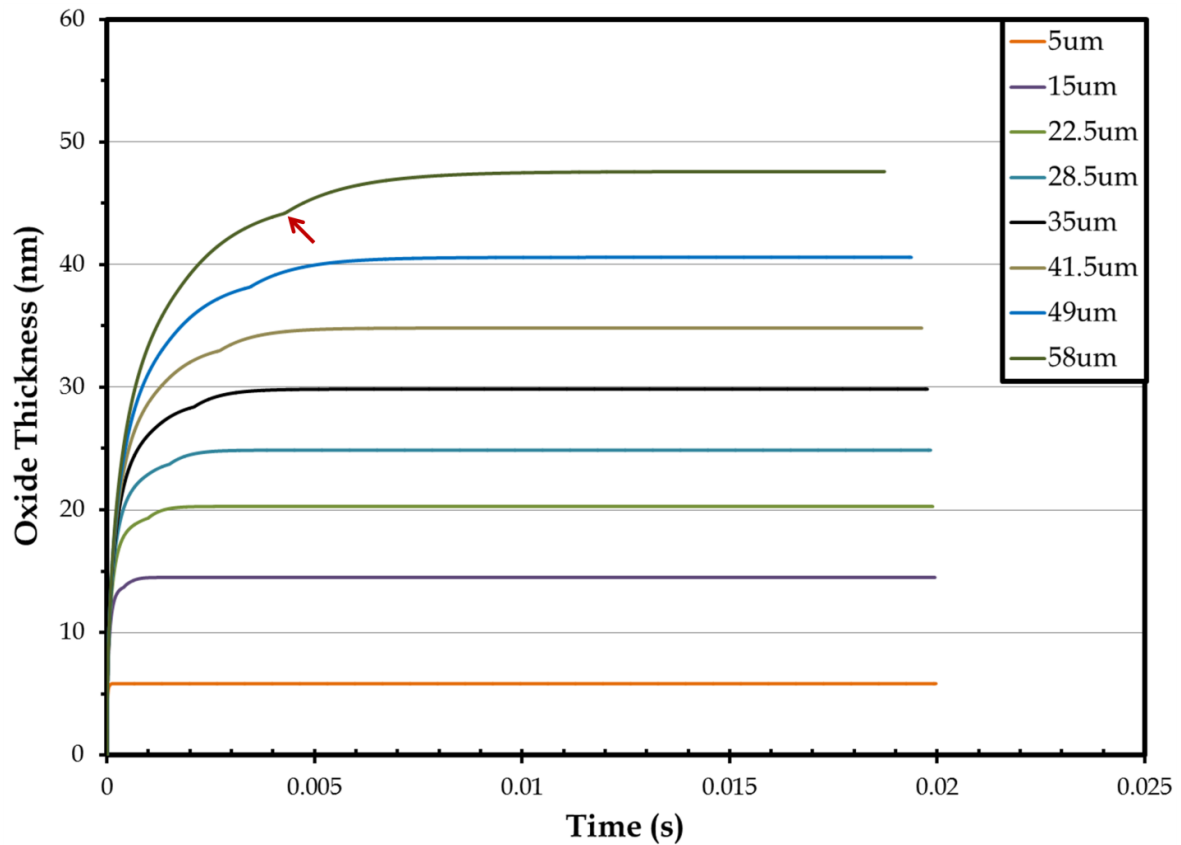


**Figure 4.21.** Predicted oxide layer thickness (CR-156) as a function of droplet diameters: note the red arrow highlighting the inflection point that indicates droplet solidification

The predicted  $\text{Cr}_2\text{O}_3$  surface oxide layer thickness was then compared to experimental data for CR-118, CR-126, CR-160, and CR-156 (i.e., the CR-alloys that contained a linear relationship identified in Figure 4.9, due to the formation of a similar Cr-enriched surface oxide phase) (see Figure 4.22). Remarkably, the predicted oxide layer thickness was found to agree quite well with the experimental

oxide thickness data, especially for the CR-alloys atomized with a reaction gas containing a lower concentration of  $O_2$  (i.e., CR-160 and CR-156, see Table 4.3). Therefore, this oxidation model is recommended as a processing tool to accurately predict the *in situ* alloying addition of O during future GARS trials.

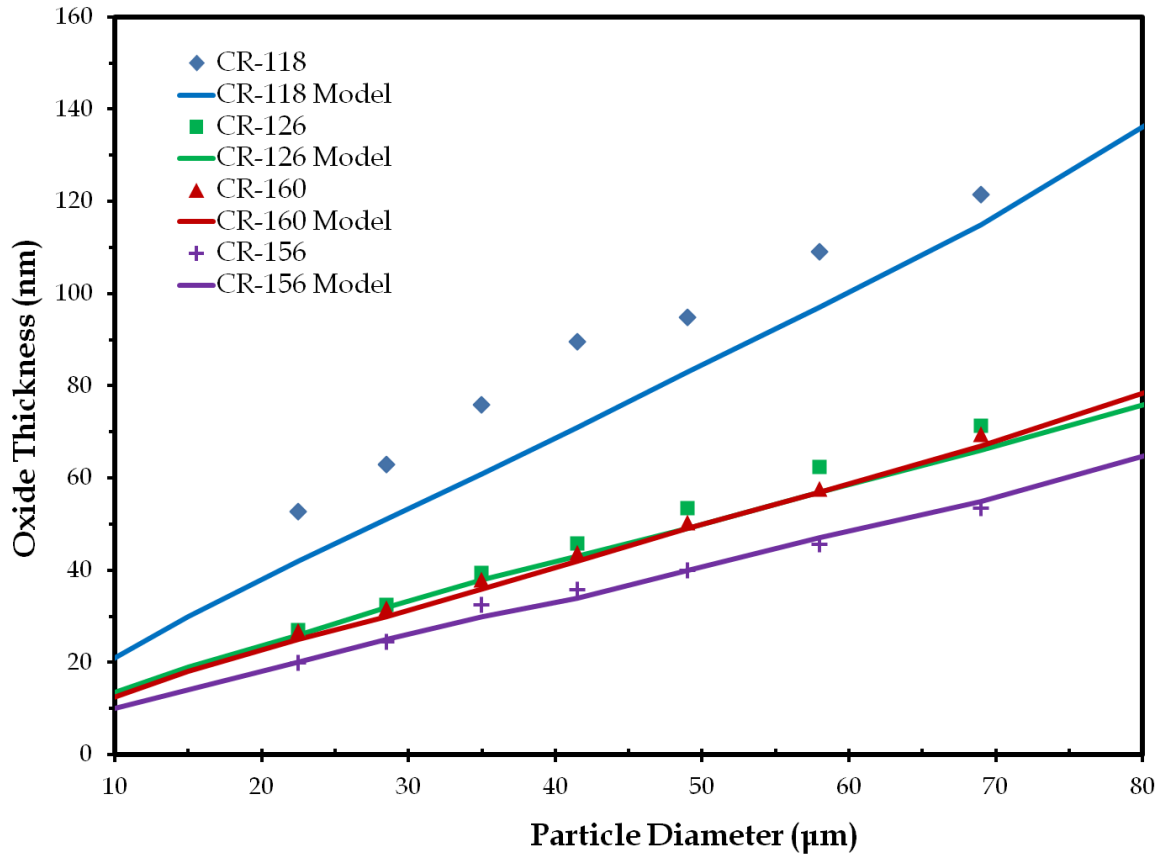


Figure 4.22. Comparison of predicted oxide layer thickness with experimentally determined values (see Table 4.5)

Analysis of the results of this oxidation model resulted in a range of parabolic rate constants (contained within the solid red lines in Figure 4.23), due to the aforementioned influence of  $P_{O_2}$  (i.e., different reaction gas compositions). The calculated parabolic rate constant as a function of temperature used for this oxidation model was compared to literature values for  $Cr_2O_3$  oxidation on solid



surfaces (see Figure 4.23). Interestingly, the results of this work coincide quite well with the central range of the literature values.

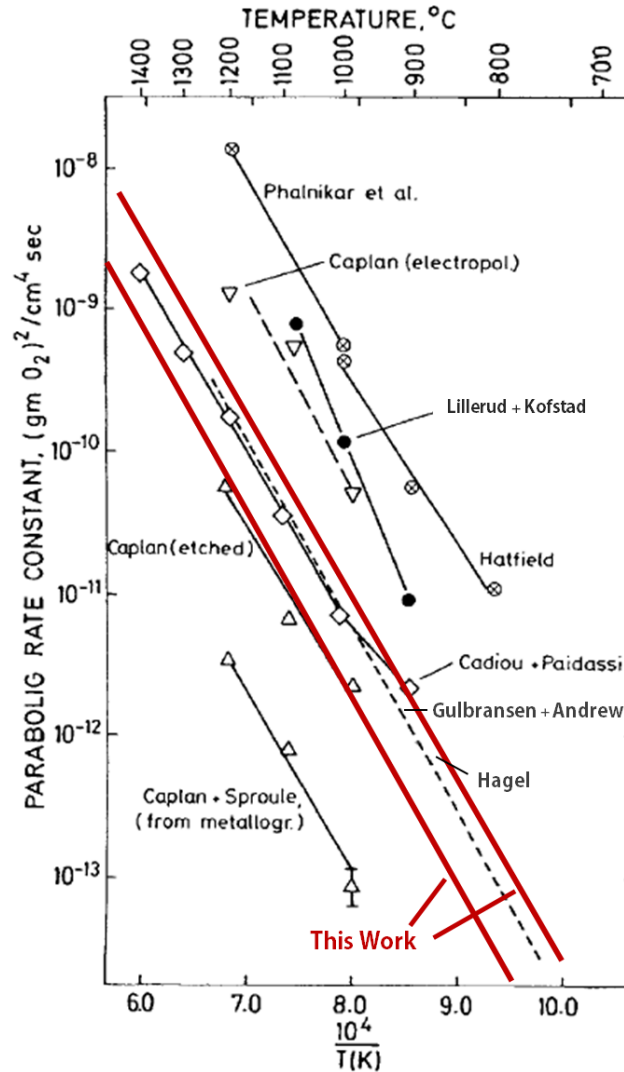


Figure 4.23. The range of  $\text{Cr}_2\text{O}_3$  parabolic rate constants (see red lines) used for the GARS oxidation model compared to literature values [167-174]

#### 4.4 Summary

Gas atomization reaction synthesis (GARS) was used to produce precursor powders for ODS ferritic stainless steel alloys. This reactive gas atomization process results in the formation of an ultra thin ( $\xi < 150$  nm) Cr-enriched surface oxide layer. This

surface oxide layer is utilized as an O reservoir for the formation of Y-enriched nano-metric dispersoids following consolidation and heat treatment of these precursor powders. A theoretical oxidation model, formulated from droplet cooling curves and based on the parabolic oxidation kinetics of  $\text{Cr}_2\text{O}_3$ , was designed as a method for predicting the resulting surface oxide layer thickness and corresponding O content as function of particle size. This oxidation model was shown to be a practical method to accurately predict the oxidation kinetics associated with GARS processing, assuming the formation of a  $\text{Cr}_2\text{O}_3$  surface oxide phase. Furthermore, this oxidation model was suggested as a processing tool to predict and control O additions in future GARS trials. Additionally, this model also provided insight into the solidification velocity associated with varying droplet diameters. The increased dendrite solidification velocity associated with the ultra-fine droplets (dia.  $\leq 5\mu\text{m}$ ) was calculated to form a stabilized planar growth front, signifying the ability to achieve a microsegregation-free solidification structure in these powders that is consistent with recent experimental observations (see Chapter 10) [146].

#### **4.5 Acknowledgments**

Support from the Department of Energy, Office of Fossil Energy (ARM program) through Ames Laboratory contract no. DE-AC02-07CH11358 made this work possible. Additionally, the electron microscopy of the as-atomized surface oxide layer was accomplished at the Electron Microscopy Center for Materials Research at Argonne National Laboratory, a U.S. Department of Energy Office of Science Laboratory operated under Contract No. DE-AC02-06CH11357 by U. Chicago-Argonne, LLC. Furthermore, Andrew Heidloff is gratefully acknowledged for his invaluable contribution to this chapter.

## 4.6 Variable Identification

Table 4.6. Variable identification

Variables	
$a$	Peclet number fit parameter
$A$	cross sectional area (m <sup>2</sup> )
$b$	Peclet number fit parameter
$B$	parabolic oxidation pre-factor (g <sup>2</sup> /cm <sup>4</sup> *s)
$c$	speed of sound in medium (m/s)
$C$	specific heat capacity (J/mol*K)
$C_D$	drag coefficient
$d$	diameter (m)
$d_e$	effective diameter of nozzle (m)
$D$	discharge coefficient
$e_f$	sudden contraction friction loss factor
$E$	oxidation activation energy (J/mol)
$f$	friction factor
$F$	force (N)
$g$	gravitational acceleration (m/s <sup>2</sup> )
$h$	heat transfer coefficient (W/m <sup>2</sup> *K)
$\Delta H_f$	enthalpy of formation (J/mol)
$k$	thermal conductivity (W/m*K)
$k$	Boltzmann constant (J/K)
$k_p$	parabolic rate constant (g <sup>2</sup> /cm <sup>4</sup> *s)
$\dot{m}$	mass flow rate (kg/s)
$m$	mass (kg)
$\Delta m$	change in mass (kg)
$M$	Mach number
$n$	oxidation proportionality constant
$N$	number of atoms in droplet
$Nu$	Nusselt number
$p$	partial pressure (Pa)
$P$	total pressure (Pa)

$Pe$	Peclet number
$Pr$	Prandtl number
$Q$	heat flux (J/s)
$r$	radius (m)
$R$	universal gas constant (J/mol*K)
$Re$	Reynolds number
$S$	surface area (m <sup>2</sup> )
$\Delta S_f$	entropy of formation (J/mol*K)
$t$	time (s)
$\Delta t$	time interval (s)
$T$	temperature (K)
$\Delta T$	undercooling (K)
$v$	volume droplet (m <sup>3</sup> )
$V$	velocity (m/s)
$W$	molecular weight (kg/mol)
$x$	vertical distance (m)
$y$	oxide stoichiometry $M_aO_y$
$z$	compressibility
Greek Letters	
$\alpha$	thermal diffusivity (m <sup>2</sup> /s)
$\beta_2$	discharge coefficient scalar
$\gamma$	specific heat ratio ( $C_p/C_v$ )=1.667 (Ar)
$\delta$	rate of change in oxide thickness (nm/s)
$\varepsilon$	roughness of chamber=0.002
$\epsilon$	emissivity=0.4
$\eta$	velocity decay fit parameter for atomization gas
$\theta$	weight fraction of droplets of specific size
$\lambda$	mote concentration (cm <sup>-3</sup> )
$\mu$	dynamic viscosity (Pa*s)
$\nu$	kinematic viscosity (m <sup>2</sup> /s)
$\xi$	oxide thickness (cm)
$\rho$	density (kg/m <sup>3</sup> )
$\sigma_{SL}$	interfacial energy (J/m <sup>2</sup> )
$\sigma^*$	Stefan-Boltzmann constant (W/m <sup>2</sup> *K <sup>4</sup> )

$\tau^*$	stability parameter; $\tau^* = 1/4\pi^2$
$\chi$	velocity decay fit parameter for atomization gas
$\omega$	height of molten metal in crucible
$\Gamma$	Gibbs-Thomson coefficient (mK)
$\Theta$	Fraction of homogeneous nucleation temperature
$\Phi$	number of particles of a specific size
$\Psi$	nucleation temperature function; $\Psi = \Delta T_t/T_L$
$\Omega$	thermal supersaturation
subscripts	
<i>a</i>	atomization pressure (see run parameters in Table 4.3)
<i>c</i>	chamber
<i>cur</i>	curvature
<i>cr</i>	crucible inner diameter
<i>d</i>	droplet
<i>den</i>	dendrite
<i>f</i>	final time of time step
<i>g</i>	gas
<i>hom</i>	homogeneous temperature
<i>i</i>	initial time of time step
<i>j</i>	atomization nozzle jet
<i>L</i>	liquidus
<i>m</i>	metal
<i>N</i>	nucleation
<i>O<sub>2</sub></i>	oxygen
<i>or</i>	pour orifice
<i>ox</i>	oxide
<i>r</i>	relative

Table 4.7. Thermophysical properties used for experimental model

Thermophysical Properties	Value	Material	Reference
<b>Metal</b>			
Liquid Specific Heat, $C_L$	41.868 (J/mol*K)	Fe	[175]
Solid Specific Heat, $C_S$	$37.15+6.171 \times 10^{-3}T-238.3T^{-1/2}$ (J/mol*K)	Fe	[175]
Liquidus, $T_L$	1783 (K)	430SS	[136]
Solidus, $T_S$	1698 (K)	430SS	[136]
Latent heat of fusion, $\Delta H_f$	$1.62 \times 10^4$ (J/mol)	Fe-16Cr	[175]
Thermal diffusivity, $\alpha_L$	$6.09 \times 10^{-6}$ (m <sup>2</sup> /s)	Fe	[164]
Interface energy, $\sigma_{SL}$	0.204 (J/m <sup>2</sup> )	Fe	[176]
Density of metal, $\rho_m$	7830 (kg/m <sup>3</sup> )	CR-alloy	This work
Atomic weight, $W_m$	55.84 (g/mol)	Fe	[175]
<b>Gas</b>			
Kinematic viscosity, $\nu_g$	$1.24 \times 10^{-6}$ (m <sup>2</sup> /s)	Ar	[177]
Density, $\rho_g$	1.784 (kg/m <sup>3</sup> )	Ar	[177]
Thermal conductivity, $k_g$	$1.772 \times 10^{-2}$ (W/m*K)	Ar	[177]
Specific heat ratio, $\gamma$	1.667	Ar	[177]
Specific heat, $C_g$	20.83 (J/mol*K)	Ar	[177]
Atomic weight, $W_g$	39.948 (g/mol)	Ar	[177]
Temperature, $T_g$	233 (K)	Ar	[149]
<b>Oxide</b>			
Activation energy, $E_{ox}$	249,000 (J/mol)	Cr <sub>2</sub> O <sub>3</sub>	[167]
Pre-exponential, $B_{ox}$	5 (g <sup>2</sup> /cm <sup>4</sup> *s)	Cr <sub>2</sub> O <sub>3</sub>	This work
Density, $\rho_{ox}$	5300 (kg/m <sup>3</sup> )	Cr <sub>2</sub> O <sub>3</sub>	[178]
Atomic weight, $W_{ox}$	0.152 (kg/mol)	Cr <sub>2</sub> O <sub>3</sub>	[178]

## Chapter 5. Heat Treatment

Gas atomization reaction synthesis (GARS) has been shown as a viable method to produce precursor CR-alloy powders for oxide dispersion strengthened (ODS) ferritic stainless steels (see Chapter 4 and 7) [179]. These powders undergo an O exchange reaction between the initial Cr-enriched prior particle boundary (PPB) oxide and Y-enriched intermetallic compound (IMC) precipitates, resulting in the formation of Y-enriched nano-metric dispersoids throughout the  $\alpha$ -(Fe,Cr) microstructure [146]. This chapter will be used to demonstrate an analogous O-exchange reaction, using a coarser as-cast ferritic stainless steel (Fe-Cr-Y) alloy microstructure, in an effort to evaluate the reaction kinetics for dispersoid formation in similar CR-alloys. Moreover, an internal oxidation model will be discussed as method for predicting the necessary heat treatment required to form Y-enriched dispersoids as a function of the CR-alloy precursor powder size and chemistry.

### 5.1 Internal Oxidation Procedure

Ferritic stainless steel cubes with a composition of Fe-16.0Cr-1.25Y (at.%) were used for this internal oxidation study. The initial ferritic stainless steel cubes contained ~15 vol. % of  $\text{Fe}_{17}\text{Y}_2$  IMC precipitates, which was distributed as an interdendritic network throughout the  $\alpha$ -(Fe,Cr) matrix phase. These stainless steel cubes were precision ground from (Cu hearth) chill cast alloy fingers to a final edge length of 4 mm. Prior to testing the cubes were surface polished to a 1.0 $\mu\text{m}$  finish. The cubes were embedded in a so called “Rhines pack” mixture containing 1.5 moles of Cr powder (dia.  $\leq 45\mu\text{m}$ ) for every mole of Cr oxide ( $\text{Cr}_2\text{O}_3$ ) powder (dia.  $\leq 250\mu\text{m}$ ), and subsequently sealed in quartz tubes under a vacuum of  $\sim 0.6$  Pa (see Figure 5.1) [180]. The purpose of the Rhines pack was to prevent external oxide scale formation thereby permitting continued internal oxidation of the stainless steel cubes at the Cr/ $\text{Cr}_2\text{O}_3$  equilibrium O partial pressure ( $P_{\text{O}_2}$ ) for a given temperature. Sealed

Rhines packs were heat treated isothermally over the temperature range of 1000-1300°C using 100°C increments for a variation of times (see Table 5.1).

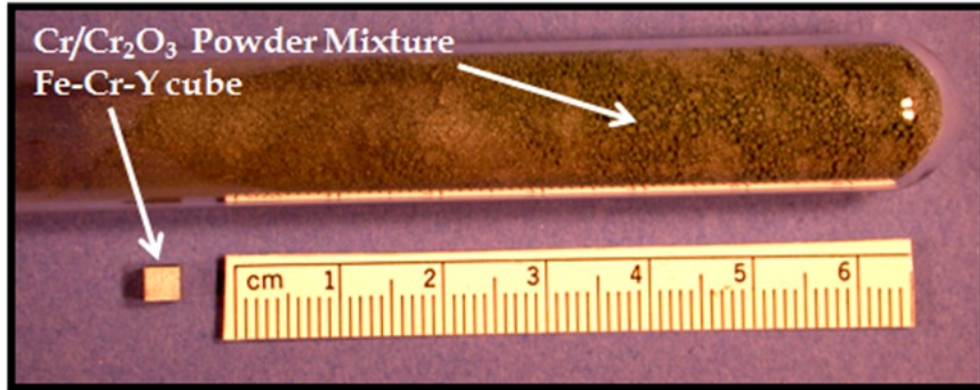


Figure 5.1. Internal oxidation (Rhines pack) experimental setup

Table 5.1. Rhines pack heat treatment procedure

Heat Treatment Temperature	Heat Treatment Time (hr)
1000	12, 72, & 120
1100	4, 12, & 24
1200	1, 2, & 3
1300	1, 2, & 3

The low  $P_{O_2}$  established by the excess metal molar concentration in the Rhines packs during heat treatment determined the O concentration at the surface of the alloy, which was intended to create an O concentration gradient equivalent to that formed at the local  $Cr_2O_3$  PPB oxide/ $\alpha$ -(Fe,Cr) interface within the consolidated CR-alloy powder microstructure. The diffusivity and solubility of Y is extremely limited in the  $\alpha$ -(Fe,Cr) matrix [181], therefore, O must diffuse to these Y reservoirs prior to dispersoid formation. This type of multicomponent internal oxidation has been defined in the literature as diffusionless or “in situ” oxidation, because the internal oxides form without any substantial diffusion of the metal component (i.e., Y), as



shown schematically in Figure 5.2 [182]. Since Y formed the most thermodynamically stable oxide in this multicomponent system, as O diffused into the ferritic alloy cubes the initial Y-enriched IMC precipitates (i.e.,  $\text{Fe}_{17}\text{Y}_2$ ) were dissociated during internal oxidation of the alloy, allowing for the formation of the more thermodynamically stable Y-enriched oxides (Figure 5.2) [182]. In this process the IMC precipitates act as a chemical reservoir (CR) phase, which supplies Y for the formation of highly stable Y-enriched oxide particles, analogous to the O exchange reaction that occurs during consolidation and heat treatment of the CR-alloy precursor powders [179].

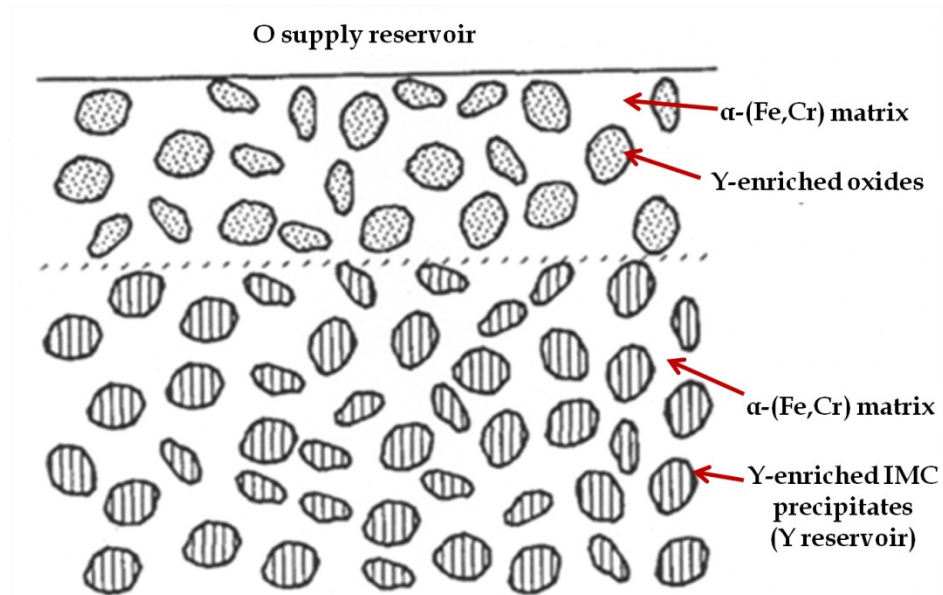


Figure 5.2. Schematic of the diffusionless internal oxidation within these Rhines packs, adapted from Gesmundo et al. [182]

Due to the precision ground planar faces of the cubes and consistent surface concentration, the oxygen diffusion profiles during heat treatment were planar. Therefore, the  $\text{Fe}_{17}\text{Y}_2$  IMC precipitates were dissociated during internal oxidation of the cubes in a planar fashion, which revealed the O penetration depth ( $\xi$ ). Furthermore, submicron Y-enriched (i.e.,  $(\text{Y,Cr})_2\text{O}_3$ ) oxides were identified in the

wake of the O penetration, with a spatial distribution similar to that of the original  $\text{Fe}_{17}\text{Y}_2$  IMC precipitates (see Figure 5.3D). The planar penetration depth of these oxides for a given temperature and time was determined using image analysis (ImagePro™) of SEM micrographs of the heat treated cubes. Measurements revealed that the internal oxidation reaction was seemingly parabolic, suggesting that the reaction kinetics are intrinsically linked to diffusion. An example of the evolving ferritic stainless steel microstructure at 1100°C is displayed in Figure 5.3A-C.

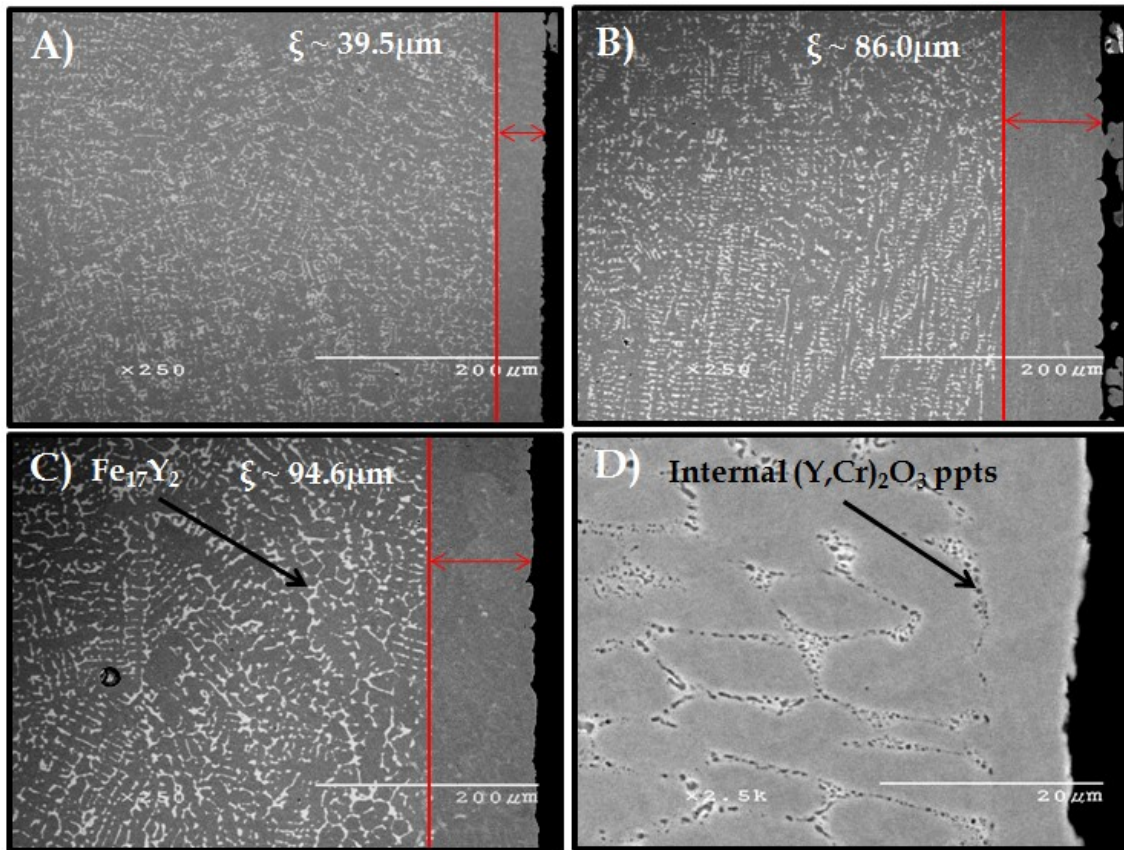


Figure 5.3. SEM analysis of cross-sectioned stainless steel (Fe-16.0Cr-1.25Y at.%) cubes after Rhines pack heat treatment at 1100°C for 4hrs (A), 12hrs (B), and 24hrs (C) revealing the internal oxidation of  $\text{Fe}_{17}\text{Y}_2$  IMC precipitates, and (D) the subsequent formation of mixed  $(\text{Y,Cr})_2\text{O}_3$  dispersoids

### 5.1.1 Internal Oxidation Model

The relative O diffusivity coefficient ( $D_O$ ) in  $\alpha$ -(Fe,Cr) was determined experimentally using the measured O penetration depth ( $\xi$ ), heat treatment time ( $t$ ), and the relative kinetics parameter ( $\gamma$ ), as previously described by Wagner and Rapp (see Equation 77) [183, 184].

$$D_O = \frac{\xi^2}{4\gamma^2 t} \quad \text{Equation 77}$$

It has been shown that  $\gamma$  is a function of the O concentration (mole fraction) at the surface of the alloy ( $N_O^s$ ), concentration (mole fraction) of Y in the bulk alloy ( $N_Y^o$ ), stoichiometric coefficient of O in the oxide ( $\nu$ ), and two auxiliary functions  $G(\gamma)$  and  $F(h)$  (see Equation 78-Equation 80) [183].

$$\frac{N_O^s}{N_Y^o} = \frac{\nu G(\gamma)}{F(h)} \quad \text{Equation 78}$$

$$G(\gamma) = \pi^{\frac{1}{2}} \gamma \exp(\gamma^2) \frac{2}{\pi^{\frac{1}{2}}} \int_0^\gamma \exp(-y^2) dy \quad \text{Equation 79}$$

$$F(h) = \pi^{\frac{1}{2}} h \exp(h^2) \frac{2}{\pi^{\frac{1}{2}}} \int_0^h \exp(-y^2) dy \quad \text{Equation 80}$$

The variable  $h$  is related to  $\gamma$  by the square root of the diffusivity coefficient ratio between O and Y in  $\alpha$ -(Fe,Cr) (Equation 81), but since the diffusivity of Y in  $\alpha$ -(Fe,Cr) is extremely limited (considered diffusionless) [181], the function  $F(h)$  can be approximated as unity. As a result, Equation 78 was simplified to Equation 82 [185].

$$h = \gamma \left( \frac{D_O}{D_Y} \right)^{\frac{1}{2}} \quad \text{Equation 81}$$

$$\frac{N_O^s}{N_Y^o} = \nu G(\gamma) \quad \text{Equation 82}$$

The concentration of O at the surface of the Rhines pack cubes ( $N_O^s$ ) was determined using Sievert's law (Equation 83) [186]. It was assumed that the ratio of Sievert's

coefficient ( $K_{O_2}$ ) for pure Fe compared to Fe-16Cr (at.%) could be approximated as unity. This assumption allows the use of literature values for  $N_O^S$  in Fe, measured at the equilibrium  $P_{O_2}$  for Fe-FeO (Equation 84), for calculating  $N_O^S$  for solid solution Fe-16Cr (at.%) at the lower equilibrium  $P_{O_2}$  for Cr-Cr<sub>2</sub>O<sub>3</sub> (Equation 88) [187].

$$N_O^S \approx K_{O_2} \left( P_{O_2}^{\frac{1}{2}} \right) \quad \text{Equation 83}$$

$$N_O^{S(FeO)} = 0.381 \exp \left( \frac{-104kJ}{RT} \right) \quad \text{Equation 84}$$

Thermochemical data was used to calculate the equilibrium reaction constant ( $k_{eq}$ ) for FeO (i.e.,  $Fe_{(s)} + \frac{1}{2}O_{2(g)} \leftrightarrow FeO_{(s)}$ ) and Cr<sub>2</sub>O<sub>3</sub> (i.e.,  $2Cr_{(s)} + \frac{3}{2}O_{2(g)} \leftrightarrow Cr_2O_{3(s)}$ ) using the free energy of formation per mole of oxide ( $\Delta G_f$ ) (see Equation 85) [188]. The equilibrium reaction constant ( $k_{eq}$ ) for FeO and Cr<sub>2</sub>O<sub>3</sub> formation over the temperature range of 1000-1300°C is shown in Table 5.2.

$$k_{eq} = \exp \left( \frac{-\Delta G_f}{RT} \right) \quad \text{Equation 85}$$

**Table 5.2. Equilibrium constants for FeO and Cr<sub>2</sub>O<sub>3</sub> oxide formation per mole of compound [188]**

Temperature (°C)	$k_{eq}$ (Fe-FeO)	$k_{eq}$ (Cr-Cr <sub>2</sub> O <sub>3</sub> )
1000	5.74X10 <sup>7</sup>	1.53X10 <sup>33</sup>
1100	1.16X10 <sup>7</sup>	1.78X10 <sup>30</sup>
1200	3.01X10 <sup>6</sup>	5.67X10 <sup>27</sup>
1300	9.40X10 <sup>5</sup>	4.05X10 <sup>25</sup>

The equilibrium dissociation  $P_{O_2}$  for FeO and Cr<sub>2</sub>O<sub>3</sub> was determined using Equation 86 and Equation 87, respectively (see Table 5.3). It should be noted that the activity ( $a$ ) for FeO and Fe was taken to be equal to unity (Equation 86). The activity of Cr<sub>2</sub>O<sub>3</sub> also was taken to equal unity, but the activity of Cr was assumed to be 0.16

(Equation 87) based on the composition of the cubes (assuming an ideal solution) [92].

$$k_{eq} = \frac{a_{FeO}}{a_{Fe} P_{O_2}^{\frac{1}{2}}} \quad \text{Equation 86}$$

$$k_{eq} = \frac{a_{Cr_2O_3}}{a_{Cr}^2 P_{O_2}^{\frac{3}{2}}} \quad \text{Equation 87}$$

Table 5.3. Equilibrium dissociation  $P_{O_2}$  for FeO and  $Cr_2O_3$

Temperature (°C)	$P_{O_2}$ FeO (atm)	$P_{O_2}$ $Cr_2O_3$ (atm)
1000	$3.04 \times 10^{-16}$	$9.44 \times 10^{-22}$
1100	$7.37 \times 10^{-15}$	$8.56 \times 10^{-20}$
1200	$1.11 \times 10^{-13}$	$3.95 \times 10^{-18}$
1300	$1.13 \times 10^{-12}$	$1.06 \times 10^{-16}$

Values for  $N_O^S$  at the equilibrium  $P_{O_2}$  for Cr- $Cr_2O_3$  were determined using Equation 88 (shown in Table 5.4), and values for  $G(\gamma)$  were calculated using Equation 82, knowing that the  $N_Y^o$  was equal to 0.0125 and  $\nu$  was equal to 1.5 for (Y,Cr) $_2O_3$  oxide formation.

$$\frac{N_O^{S(FeO)}}{N_O^{S(Cr_2O_3)}} \propto \frac{K_{(O_2 \text{ in Fe})}}{K_{(O_2 \text{ in Cr})}} \left( \frac{P_{O_2}^{FeO}}{P_{O_2}^{Cr_2O_3}} \right)^{\frac{1}{2}} \quad \text{Equation 88}$$

**Table 5.4. Predicted equilibrium O solubility at the surface of the Rhines pack cubes and  $G(\gamma)$  for the alloy system**

T (°C)	$N_O^{S(Cr_2O_3)}$ (mole fraction)	$G(\gamma)$
1000	$3.62 \times 10^{-08}$	$1.93 \times 10^{-06}$
1100	$1.43 \times 10^{-07}$	$7.65 \times 10^{-06}$
1200	$4.67 \times 10^{-07}$	$2.49 \times 10^{-05}$
1300	$1.30 \times 10^{-06}$	$6.93 \times 10^{-05}$

Values for  $\gamma$  were determined through mathematical iterations using Equation 79 and the values for  $G(\gamma)$  displayed in Table 5.4 (shown in Table 5.5). Using  $\gamma$ , the experimental value for  $D_O$  was determined using the internal oxidation reaction depth ( $\xi$ ) (see Figure 5.3 and Equation 77). The experimental value for  $D_O$  was then compared to literature values for the diffusion of O, Cr, and Fe in  $\alpha$ -Fe (shown in Figure 5.4) [189-192], indicating that O diffusion is the likely controlling rate, due to the closer matching of the experimental measurements to the literature trend for O diffusion in Fe.

**Table 5.5. Values for the kinetic parameter  $\gamma$  over the experimental temperature range**

Temperature (°C)	Kinetics Parameter ( $\gamma$ )
1000	$9.82 \times 10^{-4}$
1100	$1.96 \times 10^{-3}$
1200	$3.53 \times 10^{-3}$
1300	$5.89 \times 10^{-3}$

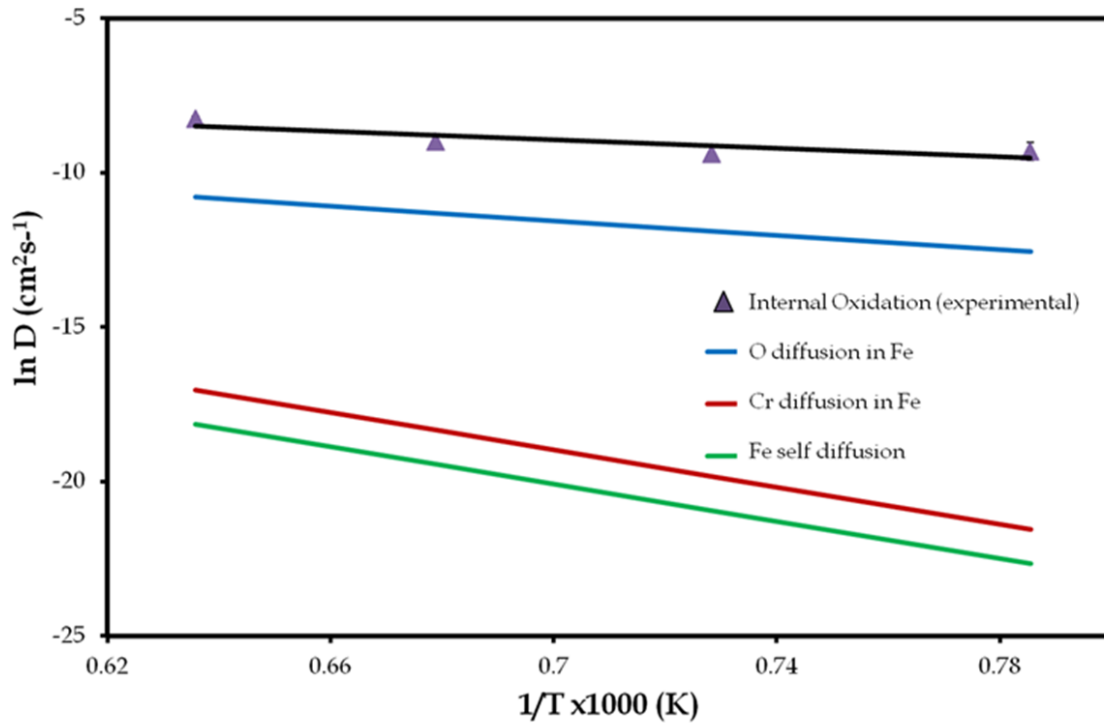


Figure 5.4. Comparison of the experimentally determined O diffusivity coefficient and literature values for O, Cr, and Fe diffusion in  $\alpha$ -Fe

The activation energy ( $Q$ ) and frequency factor ( $A$ ) for the experimental value for  $D_O$  was calculated from linear regression analysis of the data shown Figure 5.4, where the slope of the data equaled -6.9, and the y-intercept equaled -4.1 (see Table 5.6).

Table 5.6. Activation energy ( $Q$ ) and frequency factor ( $A$ ) values for the experimentally determined  $D_O$  in  $\alpha$ -(Fe,Cr) compared to literature values for the diffusion of O, Cr, and Fe in  $\alpha$ -Fe

Diffusion Species	$Q$ (kJ)	$A$ (cm²s⁻¹)
O in Fe (experimental)	~57.5	~0.017
O in Fe [189]	98.0	0.037
Cr diffusion in Fe [191]	250.8	8.52
Fe self diffusion in Fe [192]	258.3	6.8

The activation energy for the experimentally determined  $D_O$  value was calculated to be lower (i.e., ~57.5 kJ) compared to literature values for O diffusion in  $\alpha$ -Fe (i.e., 98 kJ). A reduction in the activation energy could be related to the O diffusion path. One conjecture to explain the observed increased diffusion kinetics is that the O diffused preferentially along  $\text{Fe}_{17}\text{Y}_2/\alpha\text{-(Fe,Cr)}$  phase boundaries during internal oxidation, which is consistently higher than lattice diffusion [175]. This higher rate may also be exacerbated by incoherent phase boundaries, which act similar to high angle grain boundaries [92]. Therefore, this internal oxidation reaction is seemingly linked to the initial scale and distribution of the precursor Y-enriched IMC precipitates.

### 5.1.2 Reaction Kinetics

The motivation for these internal oxidation experiments was to gain insight about the kinetics associated with the O exchange reaction (i.e., dispersoid formation), which takes place during the consolidation and heat treatment of precursor CR-alloy powders. A low  $P_{O_2}$  was used to approximate the O concentration gradient expected at the Cr-enriched PPB oxide/ $\alpha\text{-(Fe,Cr)}$  interface in the consolidated CR-alloy microstructure.

This analysis demonstrated that the reaction kinetics of this diffusionless internal oxidation reaction could be defined by  $\gamma$  and  $D_O$  for a given CR-alloy composition. Furthermore, these parameters can then be used to calculate the parabolic rate constant ( $k_{ox}$ ) for each CR-alloy, in an effort to establish a heat treatment procedure for dispersoid formation (Equation 89) [183, 184].

$$k_{ox} = 2\gamma^2 D_O \quad \text{Equation 89}$$

The experimentally determined value for  $D_O$  appeared to be enhanced due to the connected interdendritic structure of the  $\text{Fe}_{17}\text{Y}_2$  IMC precipitates observed in the as-cast Rhines pack cubes (see Figure 5.3). Conversely, the rapidly solidified as-



atomized powders have been shown to contain either solute-trapped Y or a fine scale cellular network of Y-enriched IMC precipitates (see Figure 5.5), as a function of solidification velocity (see Chapter 4 and Chapter 10). For this reason, a literature value for  $D_O$ , representing lattice diffusion of O in  $\alpha$ -Fe, was used for a conservative prediction of the CR-alloy heat treatment conditions (see blue line in Figure 5.4) [189].

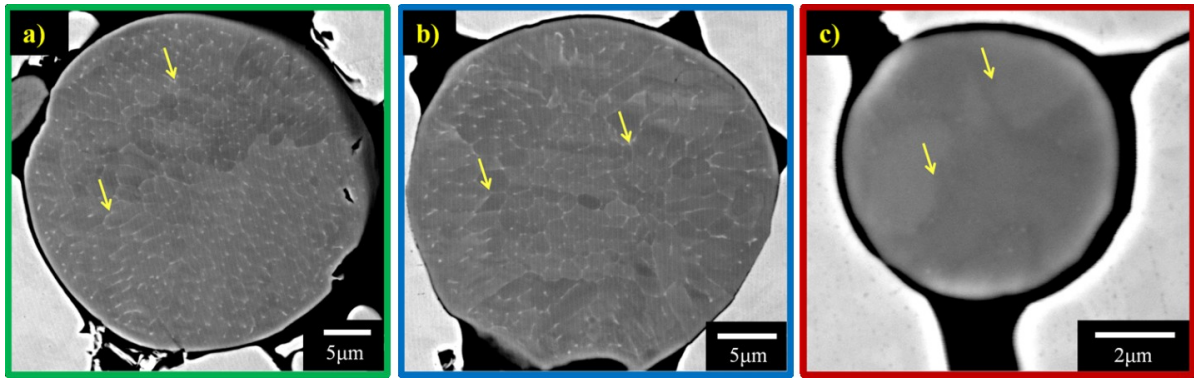


Figure 5.5. Cross-sectioned as-atomized CR-156 powders, showing the solidification structure of the Y-enriched IMC precipitates (see yellow arrow): a) dia.  $\sim 50\mu\text{m}$ , b) dia.  $\sim 20\mu\text{m}$ , and c) dia.  $\sim 5\mu\text{m}$  (note regions of apparent solute trapped Y in sample c)

Values for  $\gamma$  were calculated using the aforementioned  $N_0^{S(\text{Cr}_2\text{O}_3)}$  predicted for Fe-16Cr (at.%) during equilibrium dissociation of Cr-Cr<sub>2</sub>O<sub>3</sub> (shown in Table 5.4), while considering the specific value of  $N_Y^0$  and  $\nu$  for each CR-alloy. For example, CR-118 contains a mole fraction of Y equivalent to 0.002 (see Chapter 4) and a stoichiometric coefficient of O equal to 3.5, which represents the formation of Y<sub>2</sub>Ti<sub>2</sub>O<sub>7</sub> dispersoids (see Chapter 7). The predicted parabolic rate constant for CR-118, as a function of heat treatment temperature, is shown in Table 5.7.

**Table 5.7. Parabolic rate constant predictions for the internal oxidation of CR-118 as a function of  $\gamma$  and  $D_O$**

Temperature (°C)	$\gamma^2$	$D_O$ (cm <sup>2</sup> s <sup>-1</sup> )	$k_{ox}$ (cm <sup>2</sup> s <sup>-1</sup> )
1000	2.6X10 <sup>-6</sup>	3.7X10 <sup>-6</sup>	1.9X10 <sup>-11</sup>
1100	1.0X10 <sup>-5</sup>	7.2X10 <sup>-6</sup>	1.5X10 <sup>-10</sup>
1200	3.3X10 <sup>-5</sup>	1.3X10 <sup>-5</sup>	8.6X10 <sup>-10</sup>
1300	9.3X10 <sup>-5</sup>	2.1X10 <sup>-5</sup>	4.0X10 <sup>-09</sup>

Specific heat treatment procedures were then calculated using this parabolic rate constant for each CR-alloy. The time required for the internal oxidation reaction zone to diffuse from the PPB oxide to the center of the largest consolidated particle can be predicted using the parabolic rate law (Equation 90) [186]. A predicted heat treatment procedure for the internal O exchange reaction that occurs in CR-118, as a function of particle size and heat treatment temperature, is displayed in Figure 5.6.

$$t = \frac{\xi^2}{2k_{ox}} \quad \text{Equation 90}$$

This heat treatment model was used to establish a theoretical heat treatment procedure for each CR-alloy (see example in Figure 5.7). Clearly, an optimum balance between heat treatment time and temperature is strongly dependent on the specific powder size fraction and resulting spatial distribution of Y or Y-enriched IMC precipitates. It should be noted that this model was used as a guideline for heat treating the CR-alloys, and actual heat treatment times were typically extended beyond the predicted value by a factor of two.

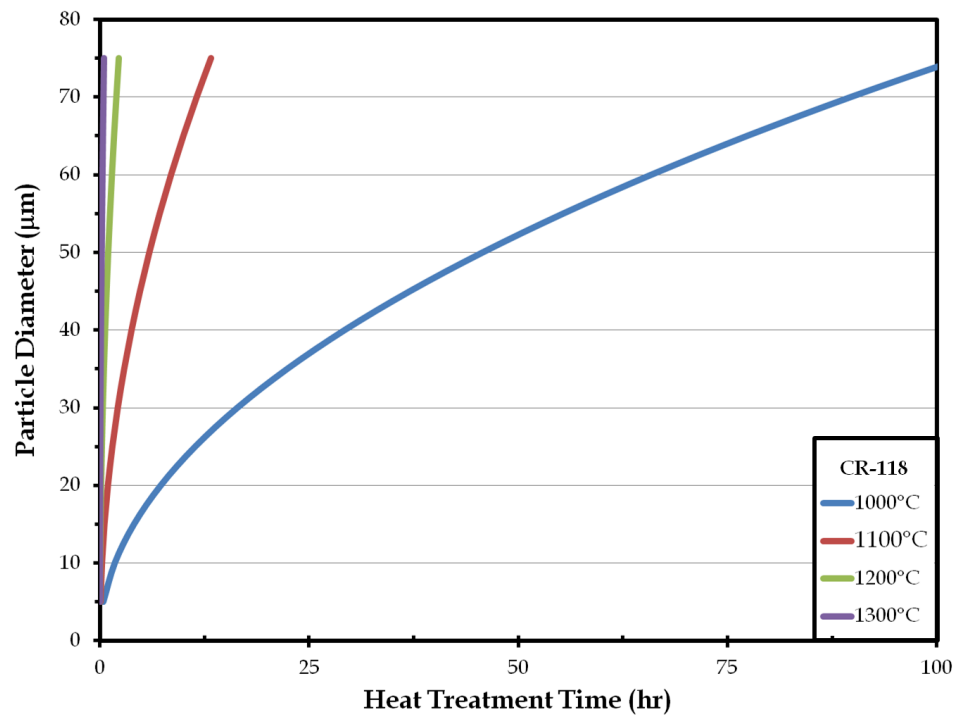


Figure 5.6. Heat treatment predictions for CR-118 as a function of particle size for heat treatment temperatures ranging from 1000-1300°C.

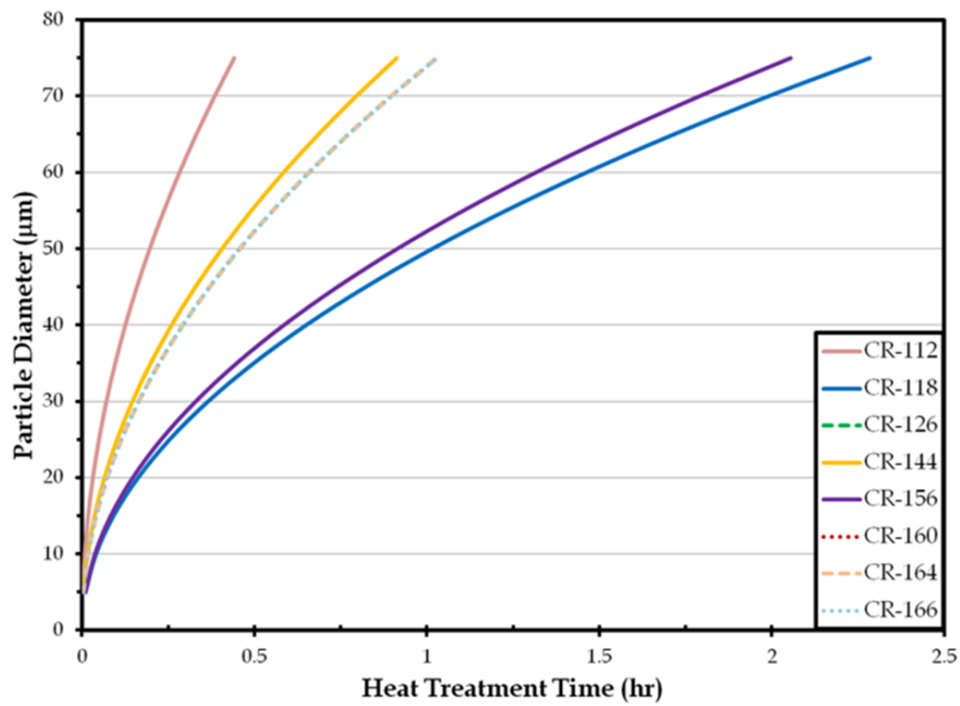


Figure 5.7. Predicted heat treatment procedure for each CR-alloy as a function of particle size for a temperature of 1200°C.

## **5.2 Summary**

Internal oxidation experiments were used to analyze the kinetics of the O exchange reaction that occurs during elevated temperature consolidation or heat treatment of precursor CR-alloy powders, which results in the formation of Y-enriched oxide dispersoids. A heat treatment procedure, formulated from an internal oxidation model, was established for predicting the required heat treatment time for dispersoid formation within each CR-alloy as a function of precursor powder size.

## **5.3 Acknowledgements**

This research was made possible by the support of the DOE-FE (ARM program) through Ames Laboratory contract no. DE-AC02-07CH11358. Additionally, Brian Gleeson is gratefully acknowledged for his insightful comments about this chapter.

## Chapter 6. Atomized Precursor Alloy Powder for Oxide Dispersion Strengthened Ferritic Stainless Steel

Modified from a paper published in: *Advances in Powder Metallurgy and Particulate Materials*, 2008, Vol. 10, pp. 324-342

J. R. Rieken<sup>1,2,3</sup>, I. E. Anderson<sup>4</sup>, M. Kramer<sup>4</sup>, Y.Q. Wu<sup>4</sup>, J. Anderegg<sup>4</sup>, A. Kracher<sup>4</sup>,  
and M. Besser<sup>4</sup>

### 6.1 Abstract

Gas atomization reaction synthesis (GARS) was used to surface oxidize atomized droplets of a ferritic stainless steel alloy, with a nominal chemical composition of Fe-(12.5-15.0)Cr-(0.5-1.0)Y-(0.0-0.54)Ti wt.%, during the break-up and rapid solidification of the resulting spherical powders. The surface oxide of the particles was intended to perform as an O reservoir for the formation of nano-metric Y-enriched oxide dispersoids. The formation of the nano-metric dispersoids occurred during elevated temperature consolidation of the powders and was driven by an O exchange reaction between the initial surface oxide (e.g., Cr-enriched oxide) and alloying additions of Y. The precursor powders were consolidated using hot isostatic pressing (HIP) at 850°C or 1300°C. This consolidation procedure resulted in distinctively different microstructures. The lower temperature consolidation (i.e., 850°C HIP) resulted in a fully dense microstructure with limited dissolution of the original surface oxide phase. The elevated temperature consolidation (i.e., 1300°C

---

<sup>1</sup> Graduate Student, Department of Materials Science and Engineering, Iowa State University

<sup>2</sup> Primary researcher and author

<sup>3</sup> Author for correspondence: Tel.: +1 515 294 9159, E-mail address: [jrieken@istate.edu](mailto:jrieken@istate.edu)

<sup>4</sup> Division of Materials Sciences and Engineering, Ames Laboratory (USDOE), Ames, IA 50011

HIP) resulted in a fully dense microstructure and partial dissolution of the original surface oxide phase, permitting interparticle bonding. Scanning electron microscopy (SEM) with energy dispersive spectroscopy (EDS) was used to evaluate the microstructure of the alloys. Transmission electron microscopy (TEM) with EDS was used to evaluate the Y-enriched oxide dispersoids. High-energy X-ray diffraction (HE-XRD) was used for preliminary phase analysis of the nano-metric oxide dispersoids. Furthermore, elevated temperature tensile testing was used to examine the strength of the as-consolidated (1300°C HIP) specimens.

## 6.2 Introduction

Many of the inherent qualities of ferritic stainless steels, i.e., high thermal conductivity and low thermal expansion, and low void swelling during neutron irradiation, distinguish these alloys as a prominent choice for many applications in fossil-fueled power plants, as well as for cladding material in nuclear reactors [102]. However, traditional ferritic stainless steels lack the high temperature strength required for future generation reactors [132]. To resolve this issue much work has been done to develop the use of nano-metric oxide particles as strengthening agents within the ferritic matrix [193]. Improved dispersoids have become more effective at impeding dislocation movement and minimizing grain boundary slip, thus increasing the strength of these alloys [2].

Most of the fabrication approaches for ODS ferritic stainless steels employ a mechanical alloying (MA) technique to generate precursor particulate. This MA process has several inherent drawbacks that were recently highlighted in a review article by Odette et al. [9], which states that the practical development of nanodispersion-strengthened Fe-based alloys face specific challenges including, the high cost of MA powder-consolidated materials, anisotropic microstructures that result from MA, and batch-to-batch variability. These challenges provide

motivation for further research into new processing methods for the production of ODS ferritic stainless steel alloys.

An innovative processing method, involving gas atomization reaction synthesis (GARS), has been developed for the fabrication of precursor ODS ferritic stainless steel powder. During this process each individual powder particle is oxidized *in situ*, forming a thin surface oxide layer during rapid solidification. This oxide layer is then used as an O reservoir for the formation of nano-metric Y-enriched oxide dispersoids during high temperature consolidation. This paper will evaluate the microstructure resulting from consolidation of powders produced using this new atomization processing technique. In addition, initial as-consolidated tensile properties will be compared to commercially produced MA ODS ferritic stainless steels.

## **6.3 Background**

### **6.3.1 Mechanical alloying (MA)**

MA has been used to successfully form ODS microstructures for several decades, but much is still not readily understood about this complex and stochastic process [12]. This process has traditionally been used for the fabrication of precursor ferritic stainless steel ODS powders (see Figure 6.1). During MA the base metal and alloying additions are inserted into a high energy shaker, planetary, or attritor mill. The milling time can last for ~48 hours, during which alloying occurs through a complex series of cold welding, fracturing, and folding at the nano-metric particle interfaces [99]. After the milling process, the resulting powders are consolidated using elevated temperature extrusion and subsequent heat treatment to promote the formation of nano-metric oxide dispersoids [1]. This processing method has proven to be an effective way to introduce nano-metric oxide dispersoids into a parent matrix phase, which has been reported to drastically increase the mechanical performance of select ferritic alloys [108].

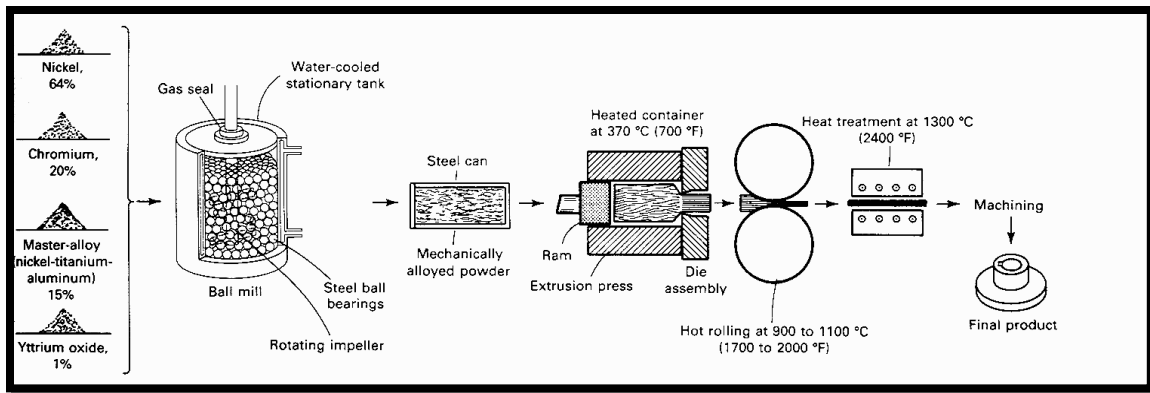


Figure 6.1. Basic MA processing method for the formation of an ODS microstructure, adapted from [12]

Unfortunately, the MA process contains several inherent problems that seemingly limit the production of ODS alloys at a commercial scale. These processing issues stem from the extended milling times required to uniformly distribute the alloying additions. Longer milling times also can lead to contamination within the alloy powders (e.g., C, O, N, or other milling debris), which can limit the strength of the final consolidated part. The time required for sufficient milling of an ODS alloy is directly dependant on the energy of the mill, for example a process that takes a few minutes in a SPEX mill (i.e., shaker mill) can take hours in an attritor mill, or a few days in a commercial planetary mill [103]. This illustrates the difficulties in scaling a milling procedure from a SPEX mill, with a capacity of  $\sim 0.01$  kg, to an attritor mill, with a capacity up to  $\sim 45$  kg, or to a large planetary (or rod) commercial mill that can produce up to  $\sim 180$  kg of material per batch [103].

### 6.3.2 Innovative molten ODS processing

A new molten metal processing technique involving rapid solidification has been implemented for the production of precursor ODS ferritic stainless steel powder. This process is known as gas atomization reaction synthesis (GARS) [14, 15]. During this process, a reactive gas (i.e., Ar-O<sub>2</sub>) is used to surface oxidize powders, forming a thin oxide layer during rapid solidification of the molten alloy droplets. This rapid



high temperature reaction is thought to promote the formation of a kinetically favored oxide (e.g., Cr-enriched oxide). This oxide layer is then used as an O-reservoir for the formation of more thermodynamically stable oxide dispersoids (e.g., Y-enriched oxide).

These powder particles are typically consolidated using hot isostatic pressing (HIP). The initial oxide layer dissociates and an O exchange reaction occurs between the prior particle boundary (PPB) oxide and Y additions, as schematically demonstrated in Figure 6.2. Trapping the O source along the PPBs reduces the O diffusion distance, which accelerates the internal oxidation reaction kinetics. The resulting nano-metric oxide dispersoids (in an ideal system) are equally distributed throughout the microstructure.

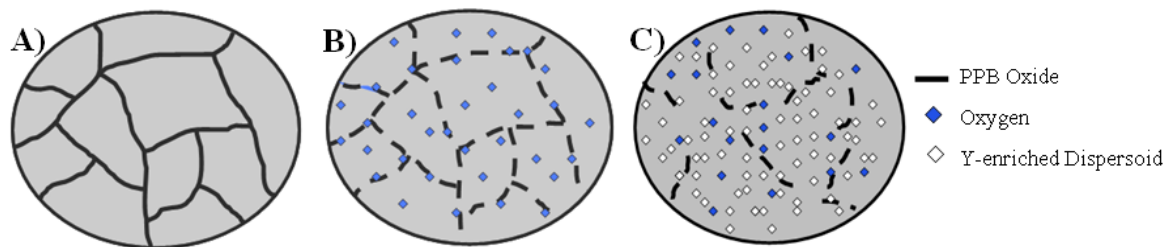


**Figure 6.2. ODS microstructure evolution during consolidation of GARS precursor powders: A) low temperature consolidation showing no dissociation of the PPBs, B) initial dissociation of the PPBs during high temperature consolidation and O diffusion into the ferritic matrix, and C) formation of Y-enriched oxide dispersoids throughout the microstructure**

This new processing technique contains several potential advantages over the traditional MA process. For example, improved production efficiency of precursor ODS ferritic stainless steel powder and consolidated parts Figure 6.3. This GARS (atomization) process has the potential of reaching commercial production rates up to 10-100 kg/min, which is significantly greater than the production rates associated with the aforementioned MA process [104]. Gas atomization also could minimize batch-to-batch variability and strictly control contamination within the powder

particles. Moreover, the spherical morphology of the as-atomized powder particles is ideal for HIP consolidation (see Figure 6.4), which helps to retain an equiaxed grain structure and isotropic mechanical properties [127].

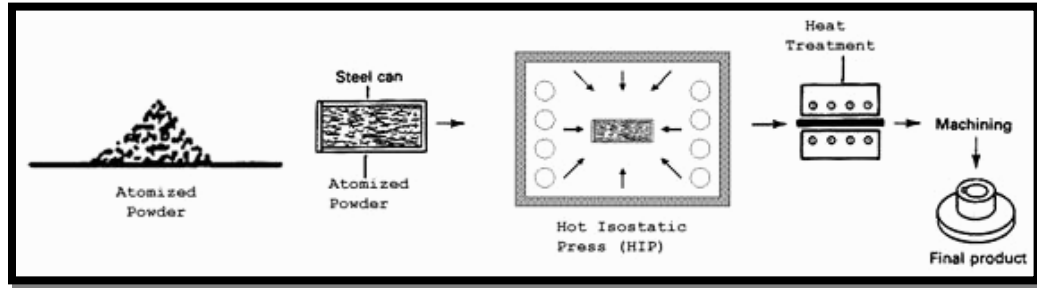


Figure 6.3. The GARS chemical reservoir ODS consolidation process [194]

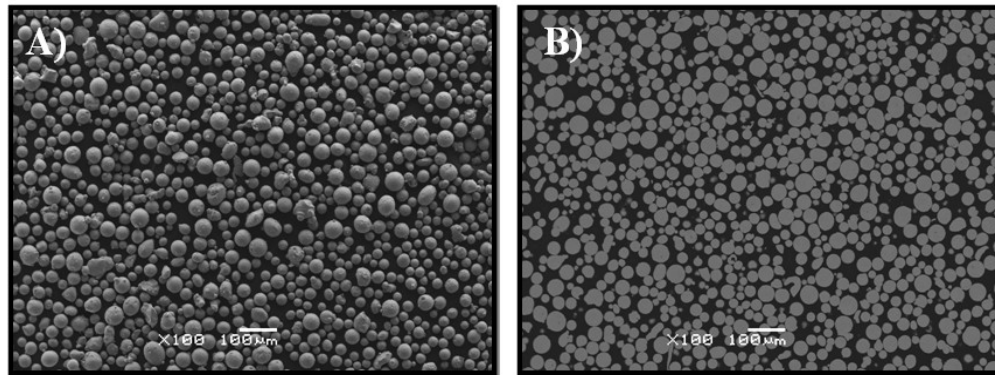


Figure 6.4. As-atomized precursor ODS ferritic stainless steel powder (dia. 20-53 $\mu$ m): A) Surface analysis and B) Cross-sectional analysis

## 6.4 Experimental Methods

### 6.4.1 Gas Atomization and Powder Consolidation

The reaction parameters (i.e., reactive gas content and injection point) and the nominal chemical composition of each alloy are displayed below in Table 6.1. The atomization charge was super heated to 1700°C within a yttria stabilized zirconia (YSZ) crucible. Once reaching the pouring temperature, the melt was released and poured through a YSZ pour tube. Upon exiting the pour tube the melt was

immediately impinged by the atomization gas (i.e., Ar or Ar-0.5O<sub>2</sub> vol.%). The atomization gas pressure was 6.9 MPa within the primary nozzle manifold.

As the powder particles fell away from the primary break-up zone, two gas halos were used to subsequently cool the powder. These halos were located ~15 cm and ~142 cm below the primary nozzle. The gas pressure within the halo manifold was 0.34 MPa, with a gas composition of Ar or Ar-5.0O<sub>2</sub> vol.%. The resulting powders were collected and mechanically sieved into a selected size range (i.e., dia. 20-53µm) prior to consolidation. The bulk O content of the as-atomized powder particles was measured using an inert gas fusion (LECO type) analyzer and the composition of each alloy was verified using inductively coupled plasma / atomic emission spectroscopy (ICP-AES).

**Table 6.1. Nominal alloy composition (wt.%) and atomization processing parameters**

<b>Alloy</b>	<b>Fe (wt.%)</b>	<b>Cr (wt.%)</b>	<b>Y (wt.%)</b>	<b>Ti (wt.%)</b>	<b>Reactive Gas Content (vol.%)</b>	<b>Gas Inlet Position</b>
<b>CR-96</b>	Bal.	12.5	1.0	-	Ar-5.0O <sub>2</sub>	First Halo
<b>CR-112</b>	Bal.	15.0	0.5	-	Ar-0.5O <sub>2</sub>	Nozzle
<b>CR-118</b>	Bal.	15.0	0.5	0.54	Ar-0.5O <sub>2</sub>	Nozzle

The powder particles (dia. 20-53µm) were inserted into a 316L stainless steel can (25.4 mm in dia. x 127 mm in length), and evacuated to a pressure of ~10<sup>-5</sup> Pa prior to the can being welded closed. These powders were then HIPed at a temperature of 850°C or 1300°C at a pressure of 300 MPa for a duration of 4.0 hours.

#### **6.4.2 Mechanical Testing**

A mechanical testing system (MTS 810) with a high temperature resistance (657.01 HT) furnace was used to examine the elevated temperature tensile strength of the alloys. The tests were performed at room temperature (21°C), 400°C, 600°C, and

700°C (CR-96 was not tested at 700°C) in open air. The alloys were tested in the 1300°C HIPed condition. The sample geometry was designed using finite element analysis to ensure that all localized necking would occur in the specified gage length (see Figure 6.5). The test procedure was based on the standard test methods for tension testing of metallic materials (ASTM-E 21-05) with a displacement rate of 0.1 mm/min. The test specimens were secured in Inconel 718 threaded grips to provide sufficient high temperature capacity. True stress values were used in determining the tensile strength for these alloys.

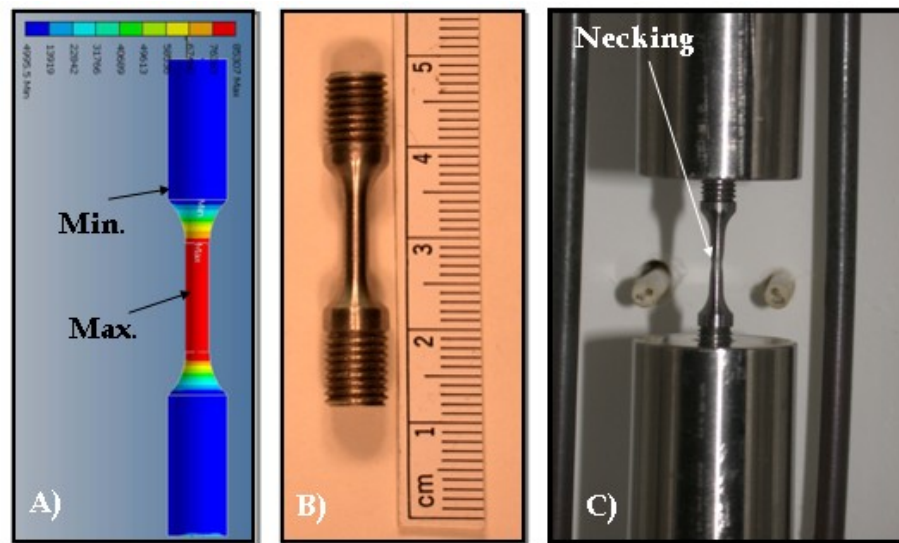


Figure 6.5. A) FEA analysis of the tensile bar geometry, B) tensile bar test specimen, C) room temperature plastically deformed tensile bar

#### 6.4.3 Electron Microscopy and Synchrotron Analysis

Microstructure analysis of the as-consolidated alloys and fracture analysis of the failed tensile specimens was completed using scanning electron microscopy (SEM) with energy dispersive spectroscopy (EDS). Cross-sectional samples were ground using 400, 600, and 1000 SiC grit paper and polished using 6.0, 1.0, and 0.25  $\mu\text{m}$  diamond suspensions.

The nano-metric dispersoids, in the as-consolidated (i.e. 1300°C HIP) condition, were preliminarily characterized using transmission electron microscopy (TEM) at 200 keV. The chemical composition of the nano-metric dispersoids was evaluated using a high angle annular dark field (HAADF) detector in combination with EDS. The TEM samples were ground flat using 400, 600, and 1000 SiC grit paper, and polished using 6.0 and 1.0 $\mu\text{m}$  diamond pastes to a final thickness of  $\sim 50\mu\text{m}$ . The samples were then mechanically dimpled to a thickness of  $\sim 20\mu\text{m}$ , and ion milled at 5keV and 1.0 mA until perforation was detected.

High-energy X-ray diffraction (HE-XRD) using synchrotron radiation at the Advanced Photon Source (APS), Argonne national laboratory-USDOE, was used for initial phase analysis of the Y-enriched dispersoids. The high photon flux and area detector resulted in a superior signal to noise ratio, allowing for minor phase identification. The samples were evaluated in the as-consolidated (i.e., 1300°C HIPed) condition at room temperature (CR-96 was not examined). Cylindrical specimen test geometry was used with 1.0 mm dia.  $\times$  12.5 mm length. The specimens were exposed at 10 s time intervals and a CCD detector was used for data collection.

## **6.5 Results**

The chemical composition of the as-atomized powder is shown below in Table 6.2. Generally, the Cr loss during atomization was considered inconsequential and was measured to be less than a 2.0% change in weight fraction. The Y loss during atomization was more significant and varied with each chemical reservoir (CR) alloy. The extent of Y loss for CR-96, CR-112, and CR-118 was measured to be a 33.0%, 70.0%, and 36.0% decrease in weight fraction, respectively.

Table 6.2. As-atomized CR-alloy chemical composition

Alloy	Fe (wt.%)	Cr (wt.%)	Y (wt.%)	Ti (wt.%)	O (wt.%)
CR-96	Bal.	12.44	0.67	-	0.08
CR-112	Bal.	14.72	0.15	-	0.40
CR-118	Bal.	14.90	0.32	0.43	0.40

The surface chemistry of the as-atomized powder particles for the three CR-alloys was analyzed using AES depth profiling. The sputtering rate was assumed to be 10 nm/min based on a SiO<sub>2</sub> standard. The AES depth profiles for each CR-alloy are shown in Figure 6.6.

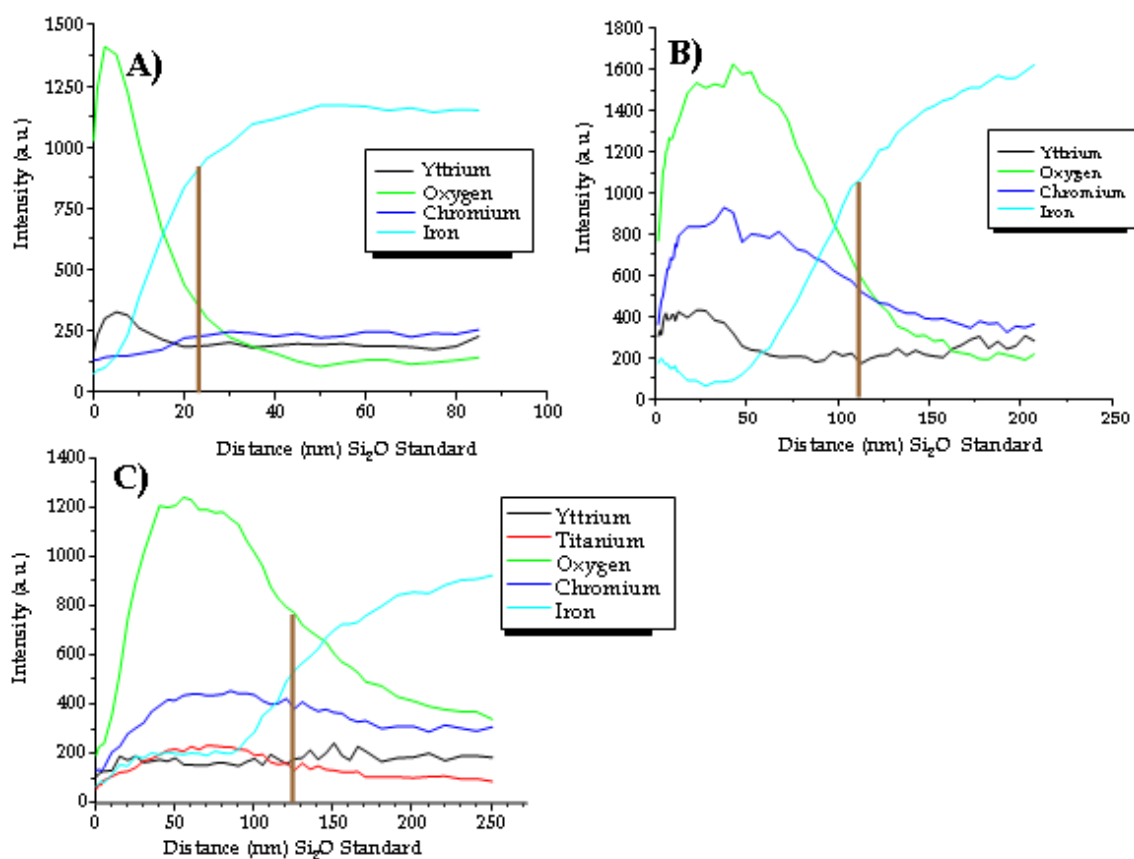


Figure 6.6. AES compositional depth profiles: A) CR-96, B) CR-112, and C) CR-118

The AES surface analysis of CR-96 powders showed elevated intensities of O and Y at the powder particle surface, indicative of a Y-enriched oxide layer containing a thickness of  $\sim 23$  nm. Conversely, analysis of the CR-112 and CR-118 powders revealed a primary enrichment of Cr and O at the surface, representing a Cr-enriched oxide with a thickness of  $\sim 112$  nm and  $\sim 125$  nm, respectively (see Figure 6.6B and C).

### 6.5.1 As-consolidated Microstructure

The 850°C HIPed microstructures for each CR-alloy are shown in Figure 6.7. CR-96 contained clean PPBs with no observable oxide, but contained regions of apparent Y-enriched microsegregation. On the contrary, CR-112 and CR-118 had significant PPB oxide, measured at 2.52 vol.% and 2.22 vol.%, respectively, using image analysis of the SEM images (ImagePro™). This PPB oxide was identified as  $\text{Cr}_2\text{O}_3$  and TiO in CR-112 and CR-118, respectively, using WDS linescan analysis (not shown).

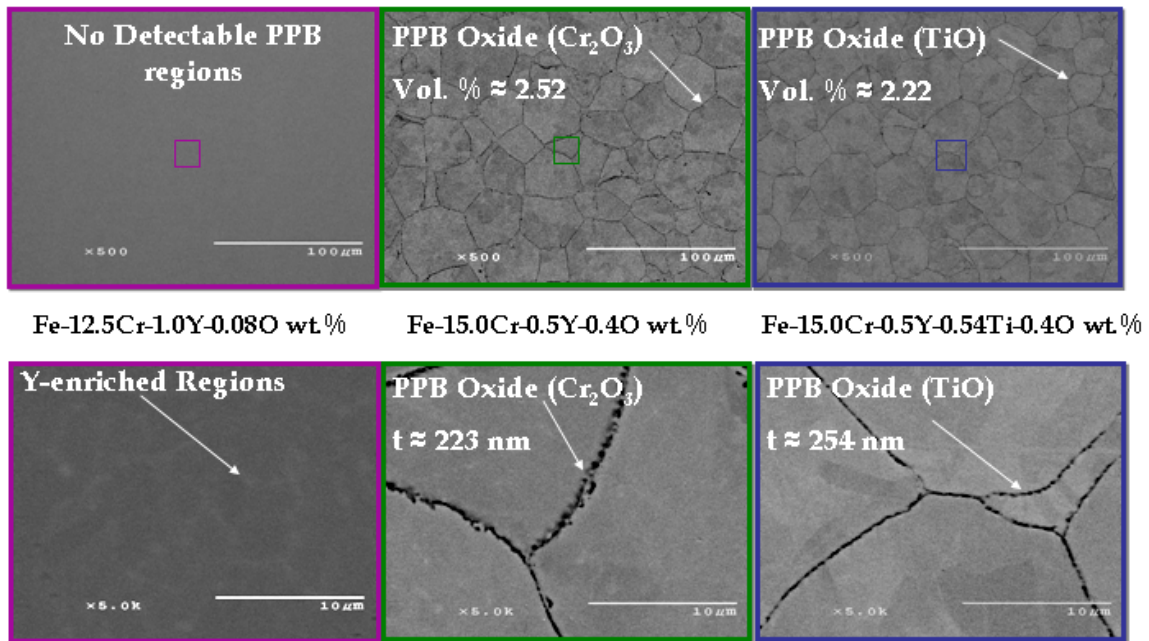


Figure 6.7. Low temperature HIPed (850°C) microstructures for CR-96 (purple), CR-112 (green), and CR-118 (blue)

The 1300°C as-HIPed microstructures for each CR-alloy are shown in Figure 6.8. CR-96 contained Fe-Y intermetallic compound (IMC) precipitates (i.e.,  $\text{Fe}_{17}\text{Y}_2$ ), in combination with smaller (dia. < 1.0  $\mu\text{m}$ ) Y-enriched dispersoids. The PPB oxide in CR-112 (i.e.,  $\text{Cr}_2\text{O}_3$ ) and CR-118 (i.e.,  $\text{TiO}$ ) was reduced to a volume percent of ~1.1 vol.% and ~0.7 vol. %, respectively. Additionally, CR-112 and CR-118 also formed smaller (dia. < 1.0  $\mu\text{m}$ ) Y-enriched dispersoids throughout the  $\alpha$ -(Fe,Cr) matrix. This microstructure evolution is thought to provide evidence of an O exchange reaction.

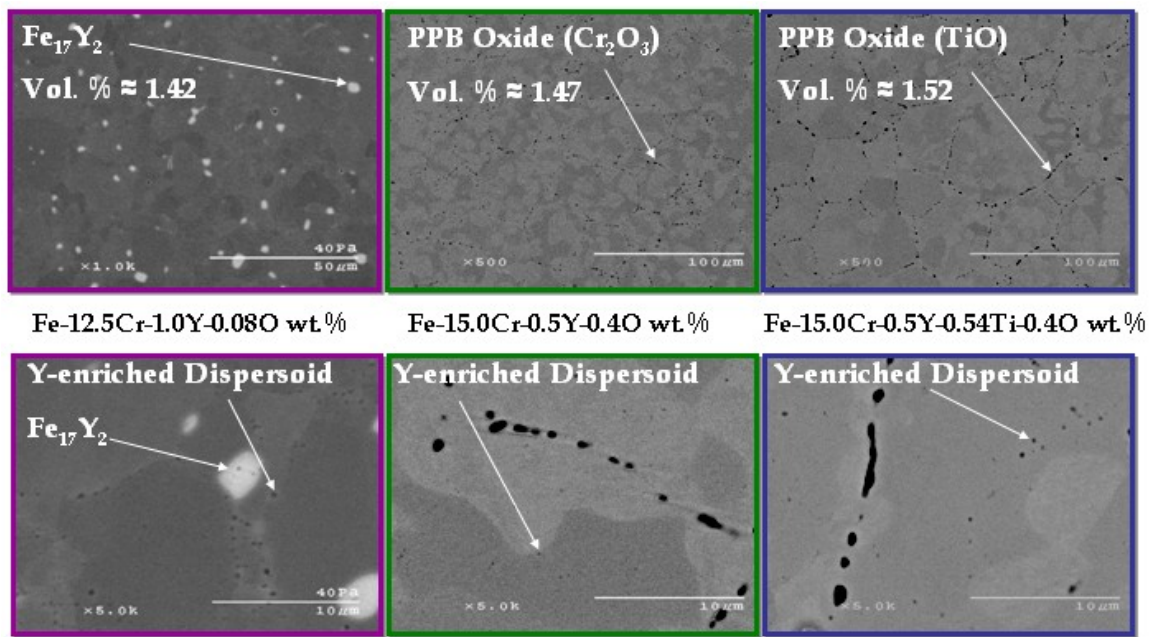


Figure 6.8. 1300°C as-HIP microstructures for alloy CR-96 (purple), CR-112 (green), and CR-118 (blue)

### 6.5.2 Initial Dispersoid Analysis

Phase analysis of the 1300°C as-HIPed microstructure for CR-112 and CR-118 was evaluated using HE-XRD. The resulting diffraction patterns for the two CR-alloys are displayed in Figure 6.9.

This analysis revealed two minor phases within the  $\alpha$ -(Fe,Cr) matrix for both CR-112 and CR-118. Full phase refinement of the secondary phases was not completed, and



phase identification was assigned using peak position matching (of the most intense peaks) from the literature [178, 195-197]. The minor phases in CR-112 were identified as  $\text{Cr}_2\text{O}_3$  (PPB oxide) and  $(\text{Y,Cr})_2\text{O}_3$  (dispersoid phase). Alternatively, the observed minor phases in CR-118 were found to be  $\text{TiO}$  (PPB oxide) and  $\text{Y}_2\text{Ti}_2\text{O}_7$  (dispersoid phase).

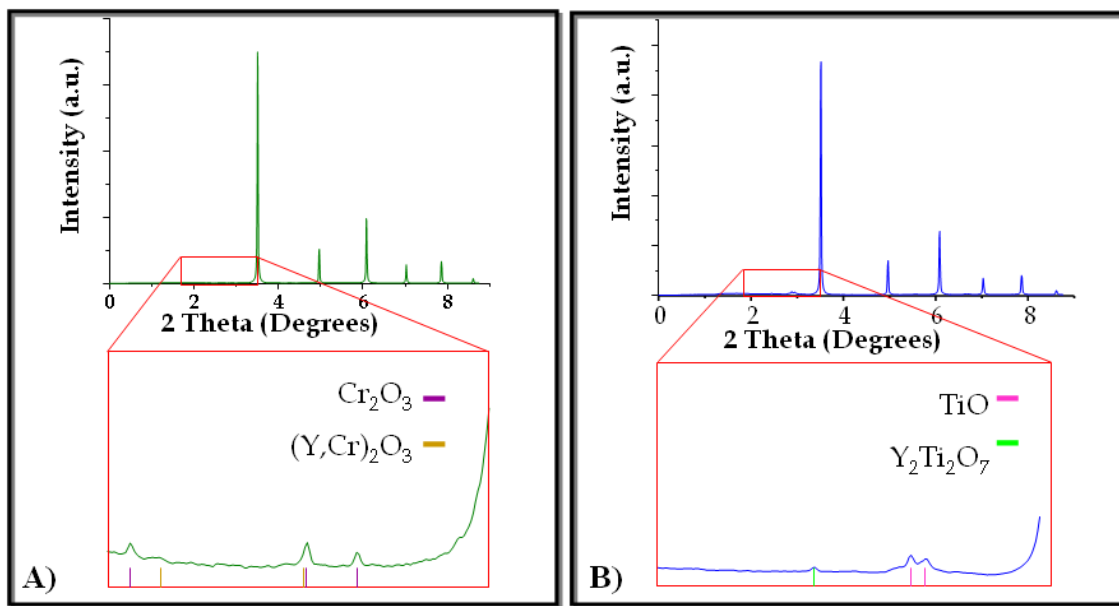


Figure 6.9. As-consolidated (1300°C HIP) HE-XRD patterns A) CR-112 and B) CR-1118

STEM with EDS also was used to evaluate the chemical composition of the Y-enriched dispersoid phase after high temperature (i.e., 1300°C) HIP consolidation (shown in Figure 6.10). Dispersoids that were of a similar size to those detected in the SEM were chosen for chemical analysis. Although numerical values were assigned to the dispersoid elements, this analysis was used to qualitatively evaluate the chemistry of these nano-metric oxides.

The dispersoids in CR-96 and CR-112 were found to contain varying amounts of Y, Cr, and O, while the dispersoids in CR-118 were observed to contain varying amounts of Y, Ti, and O. Interestingly, the chemistry of the dispersoids in CR-112

and CR-118 corresponded quite well with the aforementioned dispersoid phases (i.e.,  $(Y,Cr)_2O_3$  and  $Y_2Ti_2O_7$ ) identified using HE-XRD, especially considering the analytical measuring errors associated with this EDS analysis.

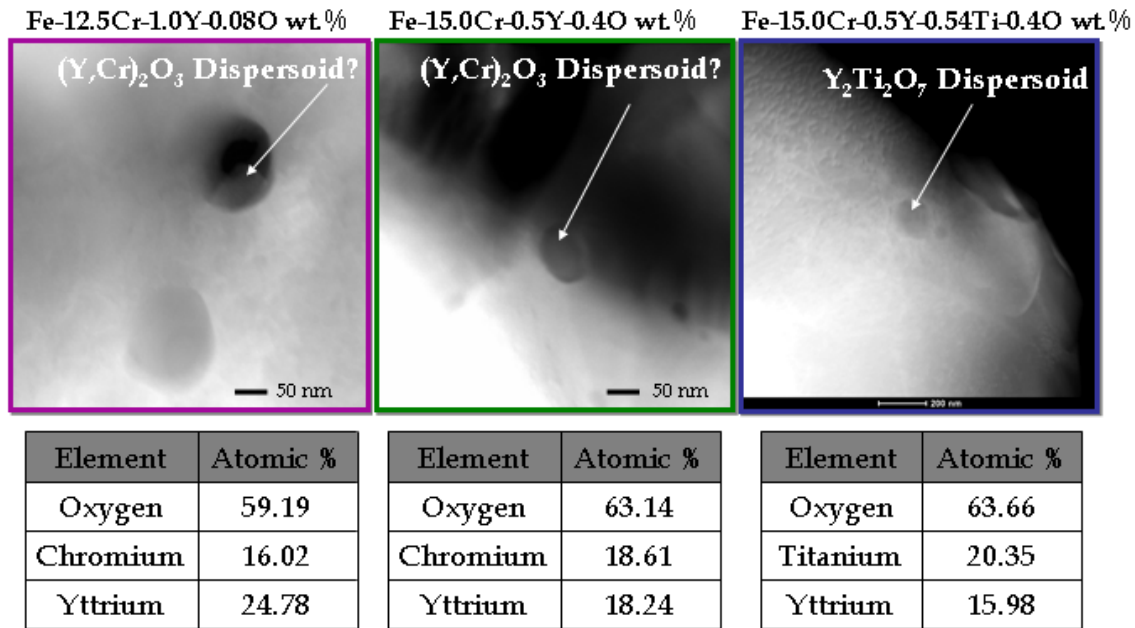


Figure 6.10. STEM images with corresponding EDS results for CR-96 (purple), CR-112 (green), and CR-118 (blue)

### 6.5.3 Preliminary Mechanical Properties

The resulting CR-alloy ultimate tensile strength (UTS) was compared to literature values for commercial Fe-based ODS alloys (see Figure 6.11). The three alloys used for comparison were MA-956, MA-957, and PM 2000 [1, 107, 198, 199].

Each CR-alloy exhibited similar UTS over the tested temperature range. Additionally, the UTS for these CR-Alloys were comparable to the strength of MA-956. It should also be noted that the strength of all the commercial alloys seem to converge above 800°C.

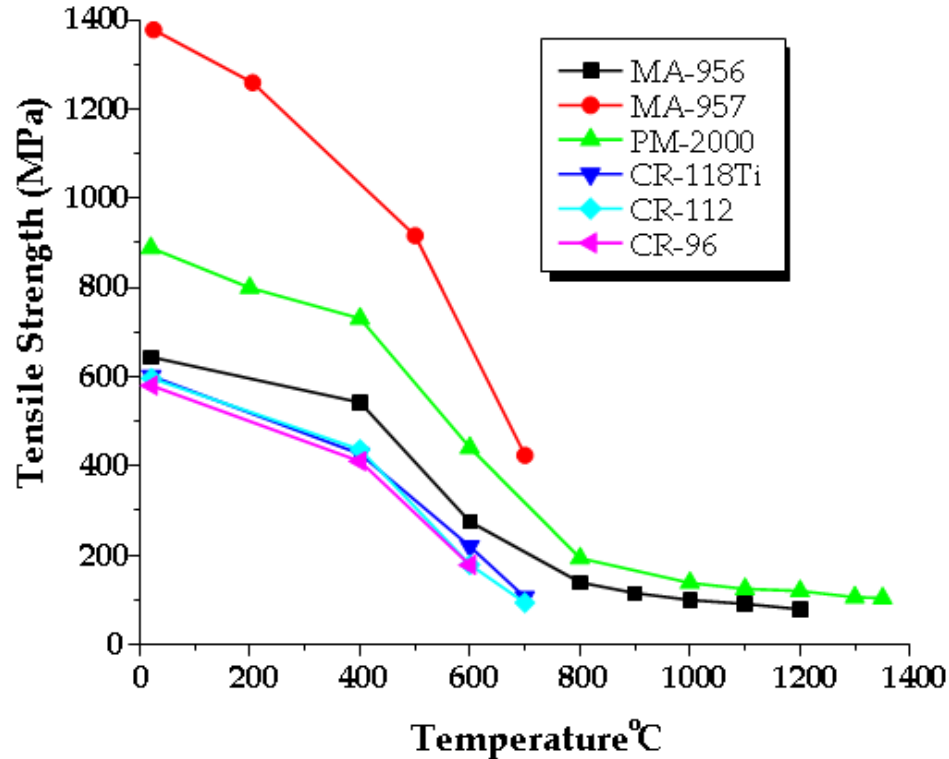


Figure 6.11. Elevated temperature tensile strength comparison of Fe-based ODS alloys

Microstructure analysis of the fractured CR-alloys indicates that failure was due to micro-void formation and coalescence, which resulted from debonding between the  $\alpha$ -(Fe,Cr) matrix and residual non-ideal phases (i.e.,  $\text{Fe}_{17}\text{Y}_2$  or PPB oxide), as shown in Figure 6.12.

The surface fracture analysis of CR-96 found  $\text{Fe}_{17}\text{Y}_2$  particles at the base of micro-void dimples, and cross-sectional analysis showed debonding between the  $\alpha$ -(Fe,Cr) matrix and  $\text{Fe}_{17}\text{Y}_2$  particles. Surface fracture analysis of CR-112 and CR-118 highlighted river lines, which identified micro-crack formation along residual PPB oxide. Furthermore, cross-sectional analysis of CR-112 and CR-118 showed PPB oxides aligned with surface crack initiation sites (i.e., valleys along the fracture surface).

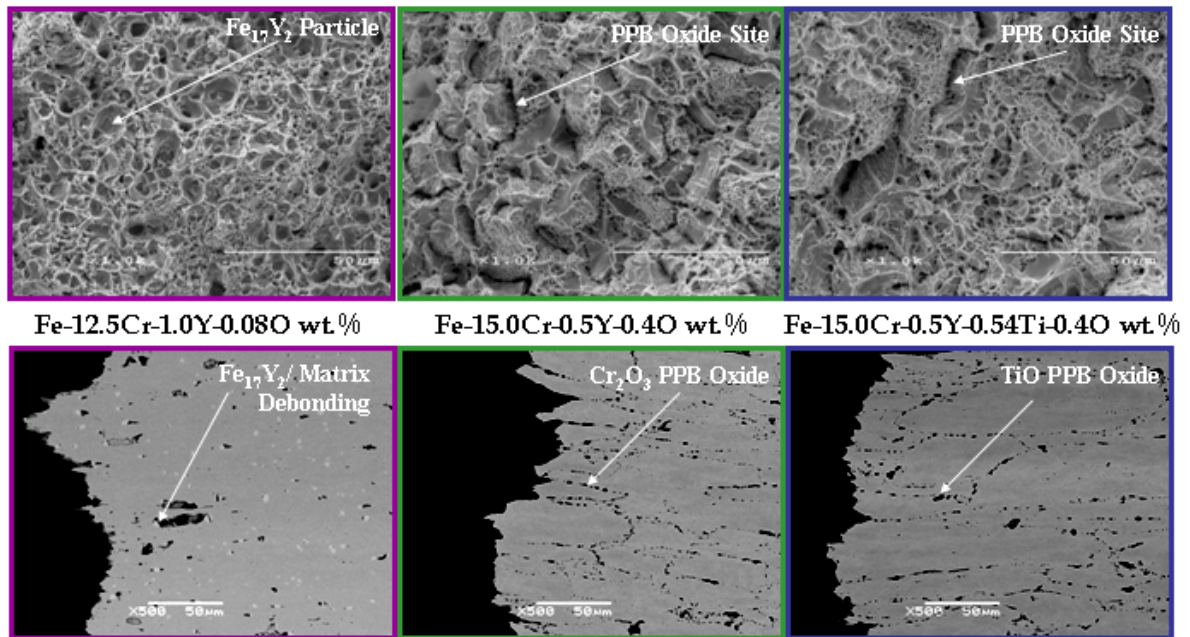


Figure 6.12. Surface and cross-sectional failure analysis of fractured tensile bar specimens CR-96 (purple), CR-112 (green), and CR-118 (blue)

## 6.6 Discussion

### 6.6.1 As-Atomized Powders

Powder particle surface chemistry was shown to be dependent on the CR-alloy composition, and potentially linked to the reactive gas injection method. The CR-96 powders contained the most Y and were presumed to have been oxidized in the semi-solid state (downstream halo), which resulted in the formation of a Y-enriched surface oxide layer. Consumption of Y during surface oxidation will limit further dispersoid formation during subsequent elevated temperature consolidation, thus preventing uniform distribution of the dispersoids throughout the  $\alpha$ -(Fe,Cr) matrix.

Conversely, oxidizing the powders in the molten state (CR-112 and CR-118) resulted in the formation of a Cr-enriched surface oxide layer. Furthermore, the addition of Ti (CR-118) seemed to successfully limit the consumption of Y during this high temperature reaction (see Figure 6.6).

The thickness of the resulting oxide layer was found to be controlled by the reactive gas composition. Previous results demonstrated that atomizing with a reactive gas containing 5.0 vol.% O<sub>2</sub> leads to an oxide layer thickness of ~1.5 μm on similar powders (i.e., dia. 20-53 μm) [200]. Notably, these results show that the surface oxide thickness can be significantly decreased (approximately an order of magnitude: t~125 nm) when reducing the O<sub>2</sub> content in the reaction gas to 0.5 vol.%. These initial results show that this rapid oxidation reaction is quite sensitive to the O<sub>2</sub> content in the reactive atomization gas (i.e., O<sub>2</sub> partial pressure), indicating the ability to tailor this process for specific O additions.

### **6.6.2 Dispersoid Formation**

High temperature HIP consolidation at 1300°C was used to promote the dissociation of the PPB oxide phase and to permit the formation of nano-metric oxide dispersoids (comparing Figure 6.7 with Figure 6.8). This microstructure evolution is driven by the thermodynamic stability of oxides (see Figure 6.13). During this internal oxidation reaction, O diffuses away from the less stable PPB oxide, driven by a chemical potential gradient, similar to the internal oxidation reactions described by Rapp [184].

The initial formation of a less thermodynamically stable (i.e., kinetically favored) surface oxide layer (e.g., Cr oxide) is germane to this novel oxide dispersion forming particulate process. The initial metastable surface oxide layer is trapped internally along the PPBs during consolidation, thus lowering the local O activity at the phase boundary, which promotes oxide dissociation during elevated temperature consolidation. The O is thought to diffuse away from the PPB oxide, driven by a concentration gradient or chemical potential, in an effort to reach equilibrium conditions with the α-(Fe,Cr) matrix. As the O diffuses towards the center of the powders it was consumed by Y, forming more thermodynamically stable nano-metric oxide dispersoids, thereby eliminating O from solid solution within the α-

(Fe,Cr) matrix phase, which promotes further dissolution of the PPB oxide. Therefore, this O exchange reaction is thought to continue until the PPB oxide is fully dissociated or until all Y has been reacted.

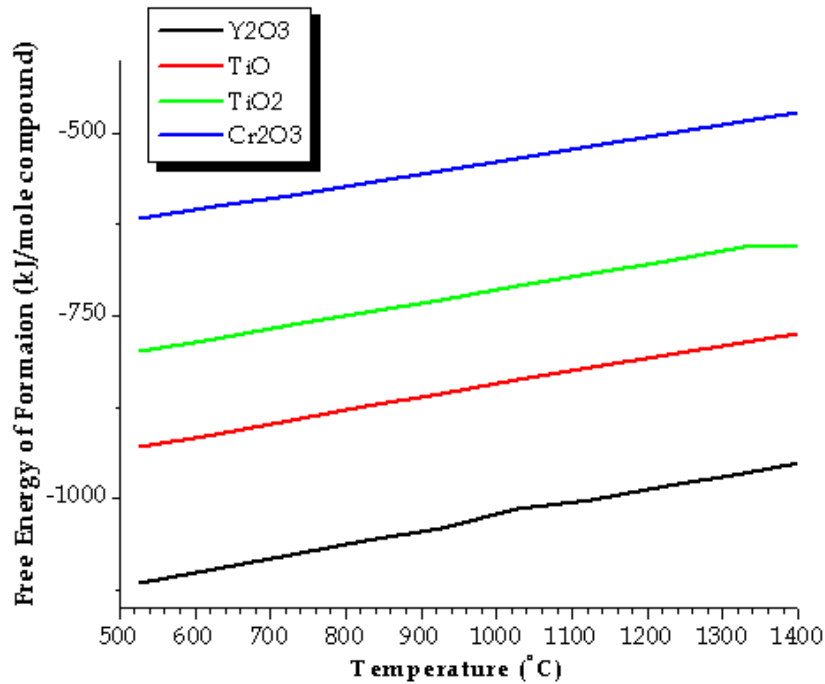


Figure 6.13. Oxide free energy of formation as a function of temperature [201]

Moreover, this illustrates the need to achieve an ideal balance between the initial Y and O content in the as-atomized powder, which should permit full dissolution of the PPB oxide and prevent residual Fe<sub>17</sub>Y<sub>2</sub> IMC precipitates from lingering throughout the CR-alloy microstructure. Of course, this ideal ratio is derived from the resulting dispersoid stoichiometry, thus, it is important to accurately predict the specific dispersoid phase that will form based of the CR-alloy composition. For example, the composition of CR-96 and CR-112 (see Table 6.2) seemed to promote the formation of mixed Y-Cr-O (i.e., (Y,Cr)<sub>2</sub>O<sub>3</sub>) dispersoids, while the composition of CR-118 (mainly the addition of Ti) results in the formation of mixed Y-Ti-O (i.e., Y<sub>2</sub>Ti<sub>2</sub>O<sub>7</sub>) dispersoids (see Figure 6.9).

### 6.6.3 Initial Mechanical Properties (Tensile Strength)

The initial tensile strength of the CR-alloys were tested in the as-consolidated (i.e., 1300°C HIP) condition. Interestingly, these CR-alloys contained a similar elevated temperature UTS compared to MA-956, even though these CR-alloys contained several microstructural deficiencies. Each CR-alloy had approximately the equivalent residual non-ideal (i.e., Fe<sub>17</sub>Y<sub>2</sub> or PPB oxide) phase fraction, and during fracture analysis of the microstructure it was determined that the primary cause of failure occurred from debonding along the  $\alpha$ -(Fe,Cr) matrix and non-ideal phase boundaries.

The UTS of these CR-alloys should increase once an ideal microstructure can be achieved (i.e., full dissolution of the PPB oxide and Fe<sub>17</sub>Y<sub>2</sub> IMC precipitates and the homogenous distribution of the nano-metric Y-enriched oxide dispersoids). Therefore, the GARS processing parameters will need to be modified for a given CR-alloy composition, in order to optimally oxidize the precursor powders.

## 6.7 Summary

A new simplified ODS processing technique involving gas atomization reaction synthesis (GARS) was demonstrated for the production of precursor ferritic stainless steel powder. This new process has the ability to oxidize powder particles *in situ* during rapid solidification. The resulting metastable Cr-enriched surface oxide layer is then dissociated during high temperature consolidation, leading to the formation of more thermodynamically stable nano-metric Y-enriched oxide dispersoids. This internal O exchange reaction is driven by the hierarchy of thermodynamic stability for oxides within the CR-alloy microstructure.

The atomization processing parameters can be used to control the initial concentration of O introduced into the alloy system (i.e., controlling initial surface oxide layer thickness). The initial ratio of Y to O was shown to control the resulting

CR-alloy microstructure. Excess Y lead to residual  $\text{Fe}_{17}\text{Y}_2$  precipitates within the CR-alloy microstructure, while too much O prevented full dissolution of the PPB oxide.

The initial tensile strength of the CR-alloys seemed limited to the interfacial bond strength between the  $\alpha$ -(Fe,Cr) matrix and residual non-ideal phases (i.e.,  $\text{Fe}_{17}\text{Y}_2$  or PPB oxide). Therefore, the global CR-alloy microstructure will need to be improved to ascertain the ideal strength of these ODS CR-alloys, but the local nano-structure of these CR-alloys demonstrated potential to effectively generate an ODS ferritic stainless steel alloy using this simplified processing method.

## 6.8 Acknowledgements

This research was made possible by the support of the DOE-FE (ARM program) through Ames Laboratory contract no. DE-AC02-07CH11358. The high energy X-ray work at the MUCAT sector of the APS was supported by the Department of Energy, Office of Science, Basic Energy Sciences under Contract No. DE-AC02-06CH11357. The authors also would like to thank Doug Guyer, Dave Byrd, Ross Anderson, and Hal Sailsbury for their specific contributions to this paper.



## Chapter 7. Microstructure Evolution of Gas-Atomized Fe-based ODS Alloys

A paper published in: International Journal of Powder Metallurgy, 2010, Vol. 46, Issue 6, pp. 17-31

J. R. Rieken<sup>1,2,3</sup>, I.E. Anderson<sup>4</sup>, and M.J. Kramer<sup>4</sup>

### 7.1 Abstract

In a simplified process to produce precursor powders for oxide dispersion strengthened (ODS) alloys, gas atomization reaction synthesis (GARS) was used to induce a surface oxide layer on molten droplets of three differing ferritic stainless steel alloys (i.e., Fe-(15.10-15.70)Cr-(0.09-0.20)Y-(0-0.56)Ti-(0-0.90)W<sup>a/o</sup>), during the break-up and rapid solidification of the spherical powders. The chemistry of the surface oxide was identified using auger electron spectroscopy (AES) and scanning electron microscopy (SEM) with energy dispersive spectroscopy (EDS). The precursor Fe-based powders were consolidated at 850°C and 1300°C using hot isostatic pressing (HIPing). Low temperature (i.e., 850°C) consolidation was used to create a fully dense microstructure, while preventing substantial prior particle boundary oxide dissociation. Microstructure analysis of the high temperature (i.e., 1300°C) consolidated alloys revealed a significant reduction in prior particle boundary oxide volume fraction, in comparison to the low temperature consolidated sample. This provided evidence that a high temperature internal oxygen exchange reaction occurred between the less stable prior particle boundary oxide phase (e.g.,

---

<sup>1</sup> Graduate Student, Department of Materials Science and Engineering, Iowa State University

<sup>2</sup> Primary researcher and author

<sup>3</sup> Author for correspondence: Tel.: +1 515 294 9159, E-mail address: [jrieken@iastate.edu](mailto:jrieken@iastate.edu)

<sup>4</sup> Division of Materials Sciences and Engineering, Ames Laboratory (USDOE), Ames, IA 50011

chromium oxide) and the yttrium contained within each prior particle. This internal oxygen exchange reaction is shown to result in the formation of yttrium enriched oxide dispersoids throughout the alloy microstructure. The evolving alloy microstructure was characterized using transmission electron microscopy (TEM) and high-energy X-ray diffraction (HE-XRD).

## 7.2 Introduction

Oxide dispersion strengthening (ODS) has been used to significantly enhance the elevated temperature strength and creep resistance of specific ferritic stainless steel alloys [1, 2, 202]. The extensive development of these ODS ferritic stainless steels concluded that the Fe-Cr base system required the addition of yttrium (Y) to form dispersoids with high temperature stability and a titanium (Ti) addition to further refine the resulting oxide dispersoids size [6, 9, 13, 114-119]. A tungsten (W) addition was usually included as a solid solution strengthener for the Fe-Cr matrix phase, as well [115]. These iron (Fe) based alloys are being considered as structural materials for use in future generation power reactors [9, 16, 38, 65]. However, a major drawback to the widespread use of Fe-based ODS steels stems from the rather expensive cost associated with finished forms of these alloys (e.g., ~\$340USD/kg for PM2000) [203]. Traditionally, ODS alloys are produced using an inefficient, time intensive, high-energy mixing process known as mechanical alloying [11, 99, 101, 204]. The goal of this paper is to show the feasibility of a new, simplified, and more efficient powder processing method for the direct production of precursor ferritic stainless steel powders with very similar alloy compositions that, when consolidated, undergo microstructural transformations leading to the formation of an improved isotropic ODS microstructure. This new processing concept would allow for full consolidation of precursor oxide dispersion forming powders from the as-atomized state, thus eliminating the complicated mechanical alloying step from the ODS processing sequence.

### 7.3 Background

This new simplified process utilizes a unique alloying method termed gas atomization reaction synthesis (GARS), a rapid solidification process, for the production of precursor ferritic stainless steel powder particles [14, 205]. The powder particles are surface oxidized *in situ*, during the GARS process, and solidify with an ultra thin (i.e.,  $t < 150\text{nm}$ ) surface oxide layer. The surface oxide layer forms as a less thermodynamically stable oxide phase, which can later be dissociated during high temperature consolidation of the powders. During consolidation, the less stable surface oxide layer is enveloped into the consolidated microstructure, and resides along prior particle boundaries (PPBs). As the high temperature consolidation process continues, the less stable PPB oxide phase begins to dissociate, releasing oxygen for the formation of more stable Y containing nano-metric oxide dispersoids.

### 7.4 Experimental Methods

#### 7.4.1 Gas Atomization Reaction Synthesis

The reactive atomization gas contained a volumetric mixture of argon (Ar) with small concentrations of oxygen ( $\text{O}_2$ ) for production of this experimental powder [206]. The reactive gas content and chemical composition for each alloy are displayed in Table 7.1. These chemical reservoir (CR) alloys were designed to contain a ferritic iron ( $\alpha\text{-Fe}$ ) matrix.

The atomization charge was super heated to  $1700^\circ\text{C}$  within a yttria ( $\text{Y}_2\text{O}_3$ ) washed zirconia ( $\text{ZrO}_2$ ) crucible. Once reaching the pouring temperature, the melt was tapped and pouring commenced through a yttria-stabilized-zirconia pour tube. Upon exiting the pour tube, the melt was immediately impinged upon by the reactive atomization gas (i.e.,  $\text{Ar}-(0.25 \text{ or } 0.5)\text{O}_2 \text{ v/o}$ ). The atomization gas pressure was 6.9 MPa within the atomization nozzle manifold. The bulk oxygen content found in the as-atomized powder particles was measured using an inert gas fusion

(LECO) analyzer, and the chemical composition of each alloy was verified using inductively coupled plasma/atomic emission spectroscopy (ICP/AES).

**Table 7.1. Resulting as-atomized chemical composition and reactive atomization gas composition used in forming precursor oxide dispersion forming powders CR-112, CR-118, and CR-126**

Alloy	Fe (a/o)	Cr (a/o)	Y (a/o)	Ti (a/o)	W (a/o)	O (a/o)	Gas (v/o)
CR-112	Bal.	15.53	0.09	-	-	1.10	Ar-0.5O <sub>2</sub>
CR-118	Bal.	15.70	0.20	0.49	-	1.12	Ar-0.5O <sub>2</sub>
CR-126	Bal	15.13	0.09	0.56	0.9	0.56	Ar-0.25O <sub>2</sub>

#### 7.4.2 Consolidation

Cold isostatic pressing (CIP) was used to consolidate as-atomized powder samples for metallographic preparation prior to hot consolidation. As-atomized particles (dia. 20-53 $\mu$ m) were blended with 70 v/o copper powders (dia. < 20 $\mu$ m) and sealed in latex CIP bags. The blended powders were subsequently CIPped at 60ksi for ~60sec. Following the CIP process each consolidated powder sample was impregnated with epoxy and cross-sectioned for microstructural analysis.

Powder samples that were screen classified to 20-53 $\mu$ m in diameter were consolidated to full density using hot isostatic pressing (HIP). Prior to consolidation, each powder sample was inserted into a 316L stainless steel HIP can, which measured 25.4mm in diameter x 127mm in length. Each HIP can was slowly evacuated using a diffusion pumped vacuum system to a pressure of  $\sim 7 \times 10^{-7}$  mbar and transported under vacuum to a laser welding apparatus, where the can was evacuated further using a turbo-molecular pump to a pressure of  $\sim 7 \times 10^{-8}$  mbar and welded shut. Each sealed can was HIPed at 850°C or 1300°C at a pressure of 303 MPa for a duration of 4.0 hr at the selected temperature and peak pressure.

### **7.4.3 Electron Microscopy**

Surface analysis of the as-atomized powder particles was conducted using a JEOL JAMP 7830F scanning electron microscope (SEM) with auger electron spectroscopy (AES). The microstructure of the powders was examined using a JEOL 5910LV SEM with energy dispersive spectroscopy (EDS). The chemistry of the PPB oxide phase was evaluated using a JEOL JXA-8200 WD/ED Microanalyzer, and the HIP consolidated alloy microstructure was analyzed using a Hitachi S-2460N SEM with EDS.

The nano-metric features present in the HIP consolidated samples were characterized using a Tecnai G<sup>2</sup> F20 transmission electron microscope (TEM) under bright field imaging (BFI) conditions at 200 keV. The TEM samples were ground flat using 400 and 600 SiC grit paper, and polished using 6.0 $\mu$ m and 1.0 $\mu$ m diamond polishing compound to a thickness of  $\sim$ 50 $\mu$ m. The samples were then mechanically dimpled to a thickness of  $\sim$ 20 $\mu$ m, and dual jet polished using an electrolytic solution for stainless steels (i.e., 700ml methanol, 100ml 2-butoxyethanol, and 35ml perchloric acid) at -21°C.

### **7.4.4 Synchrotron Phase Analysis**

High energy X-ray powder diffraction (HE-XRD) phase analysis was conducted on the as-atomized powders and HIP consolidated specimens at the Advanced Photon Source (APS), beamline 11-BM, located at Argonne National Laboratory-USDOE. The as-atomized powder samples contained particles sieved to 20-53 $\mu$ m in diameter. The HIP consolidated APS specimens were electro-discharge machined into 0.8mm dia. x 15.0mm miniature rods. Diffraction data was collected using a continuous scan at room temperature covering 34 degrees with a scan speed of 0.01 degree/sec. and a wavelength of 0.4588690 Å. A detailed description of the beamline 11-BM instrument can be found in the literature [207].

## 7.5 Experimental Results

### 7.5.1 Chemical Reservoir Alloy Composition

The Y and O concentrations are considered the most integral chemical components in the chemical reservoir (CR) alloys. CR-112 contained 0.09 a/o Y and 1.10 a/o O. Y concentration levels were approximately doubled in alloy CR-118, while maintaining a similar O concentration compared to CR-112 (see Table 4.2). This similar O concentration was achieved by using the same reactive atomization gas mixture (i.e., Ar-0.5O<sub>2</sub>v/o). The Y concentration in CR-126 was again lowered to 0.09 a/o, while the O concentration was reduced to 0.56 a/o, by halving the O content in the reactive atomization gas (see Table 4.2).

### 7.5.2 Alloy CR-112 Microstructure

Auger electron spectroscopy (AES) depth profiling of as-atomized CR-112 powders revealed significant enrichment of O and Cr with a slight enrichment of Y found at the particle surfaces (Figure 7.1A). The average thickness of the resulting Cr enriched oxide layer was determined to be 110±10nm (approximated from the etching rate of SiO<sub>2</sub>). SEM with EDS was used to analyze the interface of the as-CIPped CR-112 powders in polished cross-sections. The results verified increased concentrations of Cr and O and decreased concentrations of Fe at particle/particle interfaces (Figure 7.1B), but no enrichment in Y was detected, due to its lower concentration.

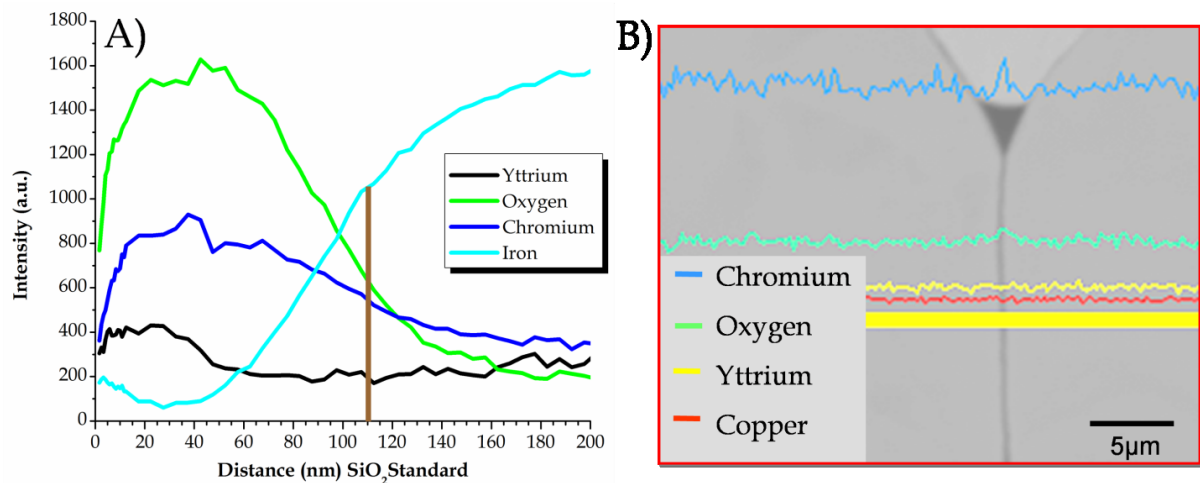


**Figure 7.1. AES depth profile (A) and SEM cross-sectional analysis with EDS chemical linescan (B) for as-atomized CR-112 powders**

Electron probe microanalysis (EPMA) with quantitative wavelength dispersive spectroscopy (WDS) was used to evaluate the chemistry of the prior particle boundary (PPB) oxides found within the HIP consolidated CR-112 microstructure. These results showed that the low temperature (i.e., 850°C) HIP consolidated microstructure contains a non-stoichiometric Cr-enriched oxide phase along the PPBs. The chemistry of this PPB oxide phase shifted towards stoichiometric chromium III oxide (i.e., Cr<sub>2</sub>O<sub>3</sub>) after high temperature (i.e., 1300°C) HIP consolidation. The volume percent of the Cr-enriched PPB oxide phase was reduced from 6.0±0.1 v/o in the 850°C as-HIPped microstructure to 4.1±0.2 v/o in the 1300°C as-HIPped microstructure, reflecting progress in PPB oxide dissociation. Volume percent measurements were completed using quantitative image analysis (see examples of cross-sectioned images in Figure 7.2A and C).

Transmission electron microscopy (TEM) was used to evaluate the nano-metric phases found in the low and high temperature HIP consolidated samples. TEM micrographs revealed the formation of nano-metric oxide dispersoids located throughout the microstructure in both low and high temperature HIP consolidated

samples (Figure 7.3A-D). The size of the oxide dispersoids ranged from 3-30 nm in the high temperature consolidated sample with a number density of  $\sim 10^{21} \text{ m}^{-3}$  (assuming a TEM foil thickness of 100nm). The oxide particles were not able to be identified by electron diffraction due to their small size, but later HE-XRD results were successful (see next section).

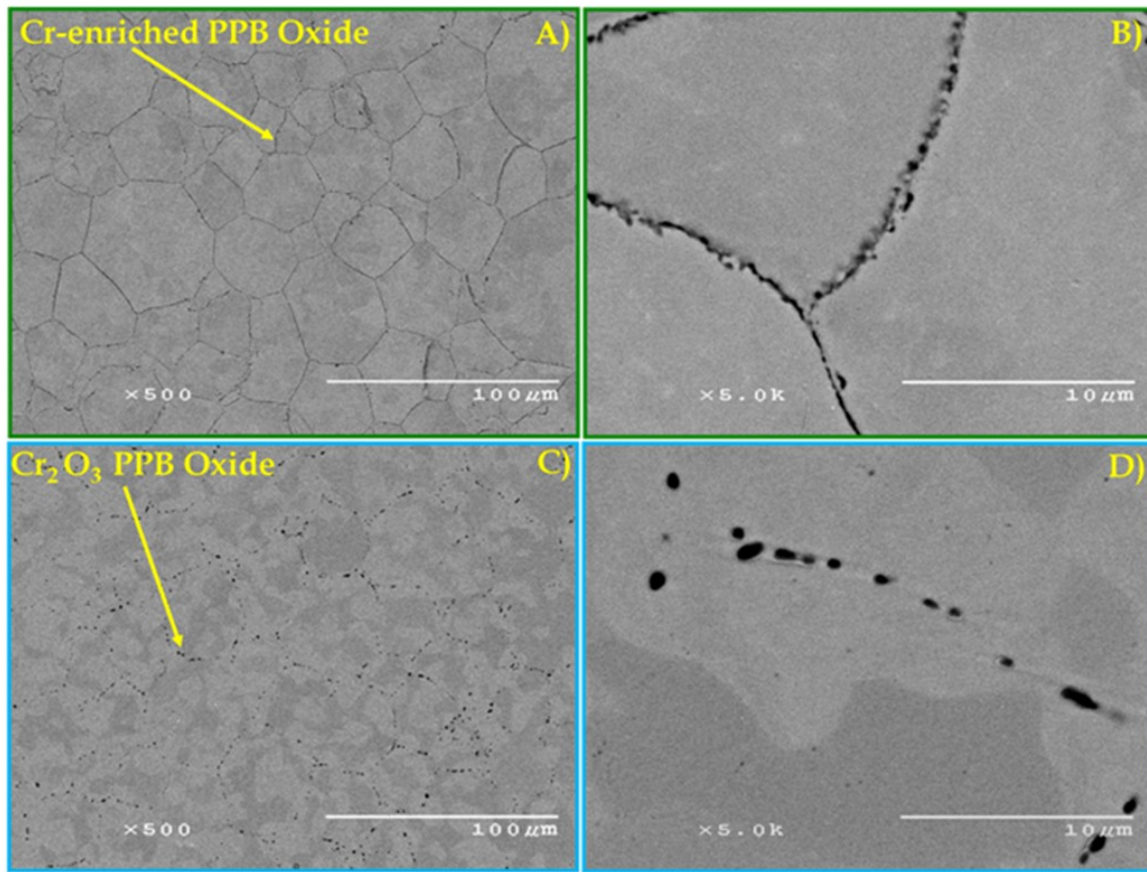


Figure 7.2. Microstructure comparison of 850°C as-HIPped CR-112 (outlined in green: SEM images A and B) and 1300°C as-HIPped CR-112 (outlined in blue: SEM images C and D)



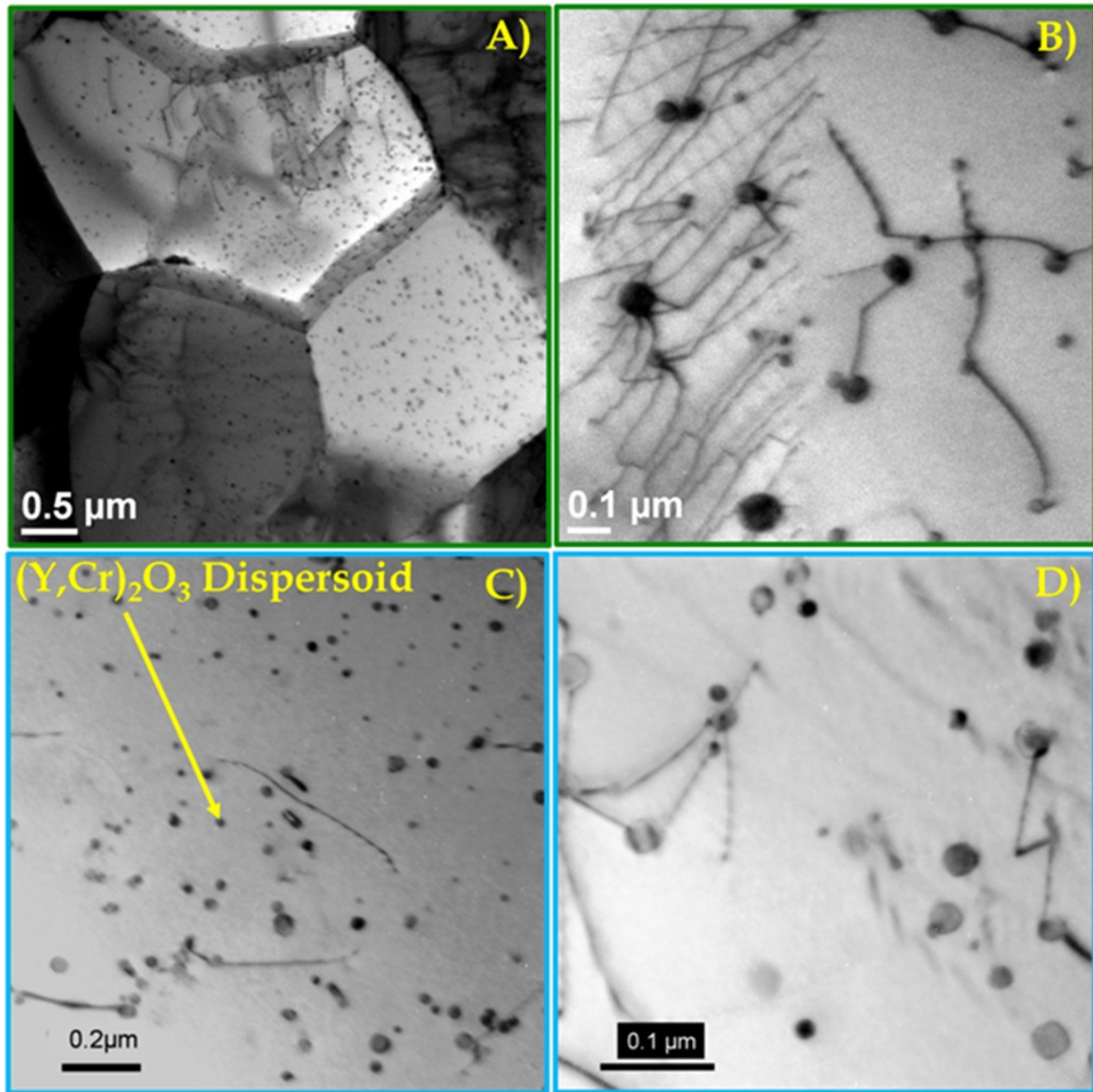
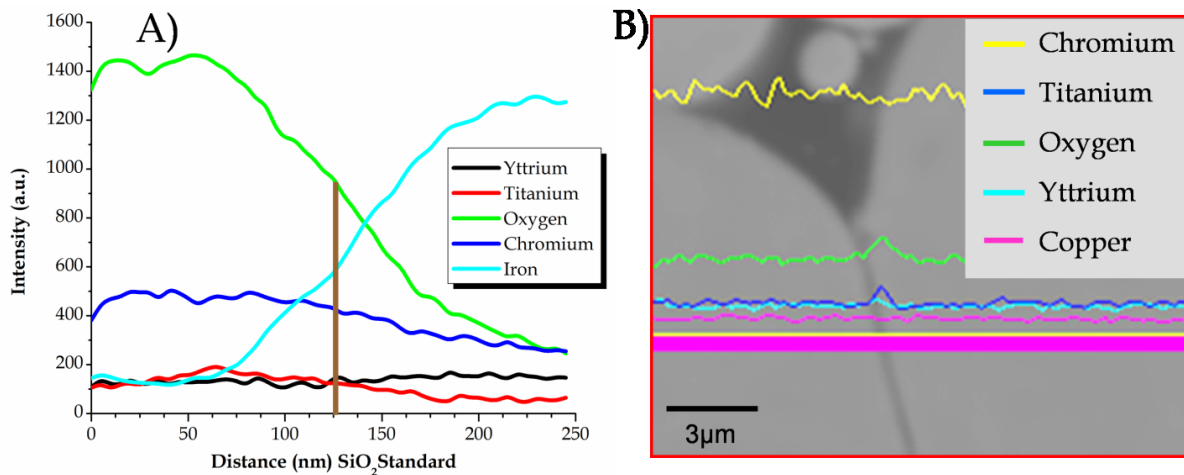


Figure 7.3. Microstructure comparison of 850°C as-HIPped CR-112 (outlined in green: TEM BFI images A and B) and 1300°C as-HIPped CR-112 (outlined in blue: TEM BFI images C and D)

### 7.5.3 Alloy CR-118 Microstructure

AES depth profiling of the as-atomized CR-118 powders revealed an enrichment of O, Cr, and Ti (very slight) at the surface of the particles (Figure 7.4A). This measurement revealed the average thickness of the oxide scale to be  $\sim 125 \pm 10$  nm (approximated from the etching rate of  $SiO_2$ ). SEM with EDS analysis of as-CIPped

CR-118 powders (in polished cross-section) showed increased concentrations of Ti and O and decreased concentrations of Fe at particle/particle interfaces (Figure 7.4B), without any detectable Cr increase.



**Figure 7.4. AES depth profile (A) and SEM cross-sectional analysis with EDS linescan (B) for as-atomized CR-118 powders**

EPMA results showed the PPB oxide phase in the 850°C as-HIPped microstructure to be Ti and Cr enriched, although no specific stoichiometric phase was identified. The chemistry of the PPB oxides in the 1300°C as-HIPped microstructure was shown to contain varying amounts of Ti with O. The volume percent of the PPB oxide phase was decreased, as expected, from  $5.9 \pm 0.2$  v/o in the 850°C as-HIPped microstructure to  $2.5 \pm 0.2$  v/o in the 1300°C as-HIPped microstructure (see Figure 7.5A and Figure 7.5C).

TEM analysis of the 850°C as-HIPped sample showed very few Y-containing oxide dispersoids (Figure 7.6A and B). The dispersoids found in this sample were less than 10 nm in diameter and displayed a globular morphology. TEM analysis of the 1300°C as-HIPped sample revealed a significant increase in the number of nanometric Y-enriched oxide dispersoids throughout the alloy microstructure (Figure

7.6C and D). The size of the dispersoids ranged from 3-50 nm with a number density of  $\sim 10^{21} \text{ m}^{-3}$  (assuming a TEM foil thickness of 100nm). The morphology of dispersoids larger than 10nm was found to be cuboidal, while smaller dispersoids maintained a globular morphology. The majority of the dispersoids found in this sample contained a cubodial morphology and were later identified using HE-XRD (see next section).

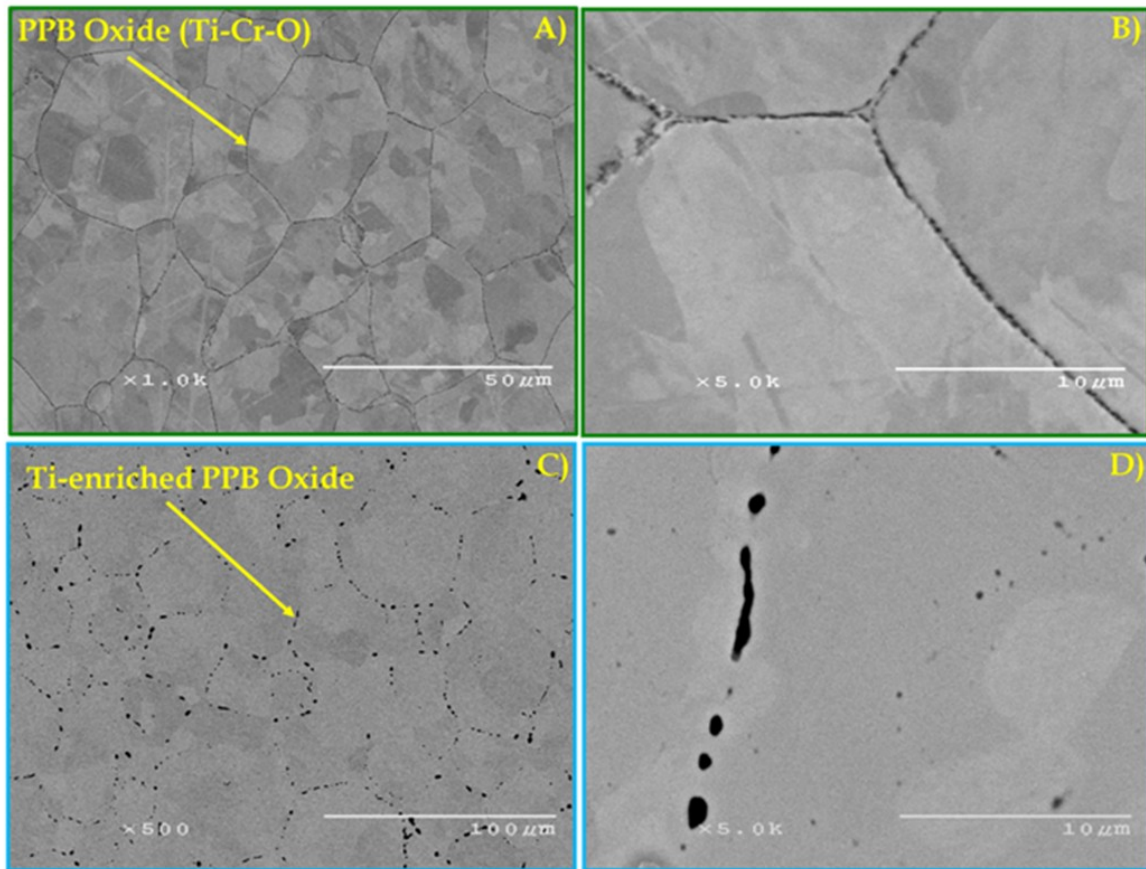


**Figure 7.5. Microstructure comparison of 850°C as-HIPped CR-118 (outlined in green: SEM images A and B) and 1300°C as-HIPped CR-118 (outlined in blue: SEM images C and D)**

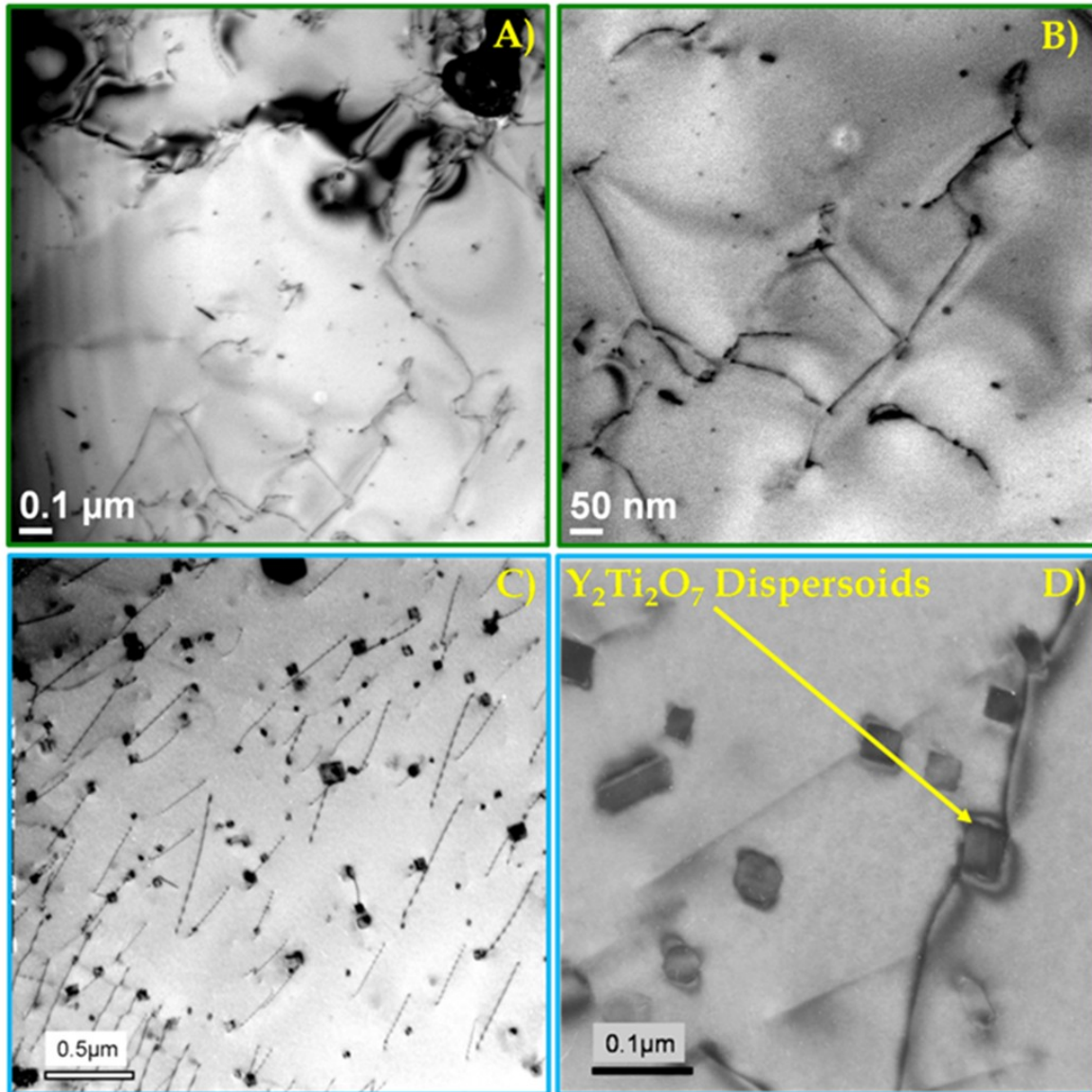


Figure 7.6. Microstructure comparison of 850°C as-HIPped CR-118 (outlined in green: TEM BFI images A and B) and 1300°C as-HIPped CR-118 (outlined in blue: TEM BFI images C and D)

#### 7.5.4 Alloy CR-126 Microstructure

Surface analysis of the as-atomized CR-126 powders also revealed high concentrations of O, Cr, and Ti (Figure 7.7A), similar to CR-118. The average thickness of the resulting oxide layer was determined to be  $\sim 85 \pm 10$  nm based on AES depth profiling measurements (approximated from the etching rate of SiO<sub>2</sub>). SEM



with EDS analysis of as-CIPped CR-126 powders verified increased concentrations of Ti and O and decreased concentrations of Fe at particle/particle interfaces (Figure 7.7B), again without a detectable Cr increase (similar to CR-118).

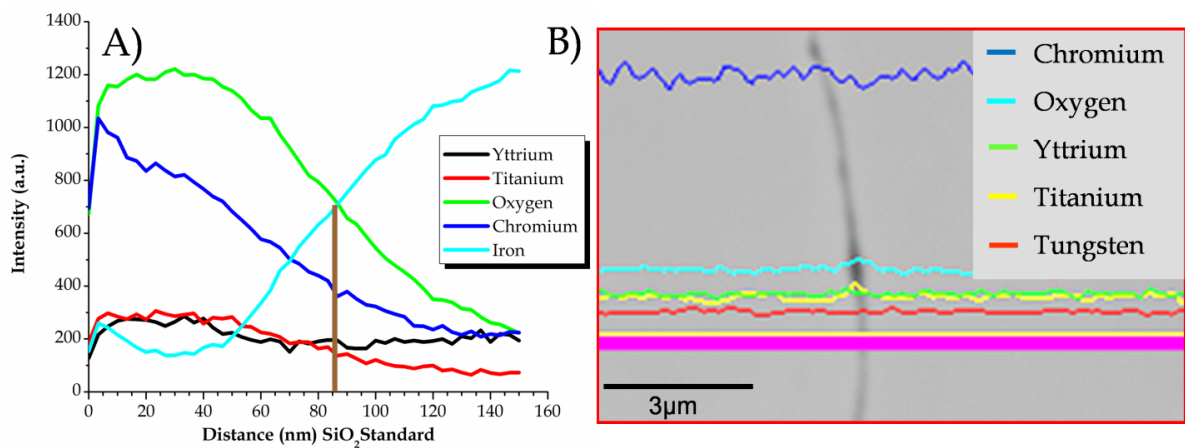


**Figure 7.7.** AES depth profile (A) and SEM cross-sectional analysis with EDS linescans (B) for as-atomized CR-126 powders

EPMA results confirmed Ti enrichment of the PPB oxide phase during HIP consolidation of the powder particles. Consistent with the dissociation mechanism, the volume percent of the PPB oxide phase also was reduced from  $5.0 \pm 0.2$  v/o in the 850°C as-HIPped microstructure to  $2.3 \pm 0.1$  v/o in the 1300°C as-HIPped microstructure (see Figure 7.8A and Figure 7.8C).

TEM analysis revealed the formation of Fe<sub>17</sub>Y<sub>2</sub> intermetallic precipitates in the 850°C as-HIPped microstructure, which seemed to decorate prior as-solidified cell boundaries, and the formation of a very low number density of other precipitates, which could be nano-metric Y-enriched oxide dispersoids (Figure 7.9A and B) in the same area. TEM analysis of the 1300°C as-HIPped microstructure showed a significant increase in the number of Y-enriched dispersoids throughout the alloy microstructure (Figure 7.9C and D). The size of the dispersoids ranged from 5-60 nm with a number density of  $\sim 10^{20} \text{ m}^{-3}$  (assuming a TEM foil thickness of 100 nm). The

morphology of the dispersoids seemed analogous to those found in alloy CR-118, where most exhibited a cuboidal morphology, but required HE-XRD for identification (see next section).

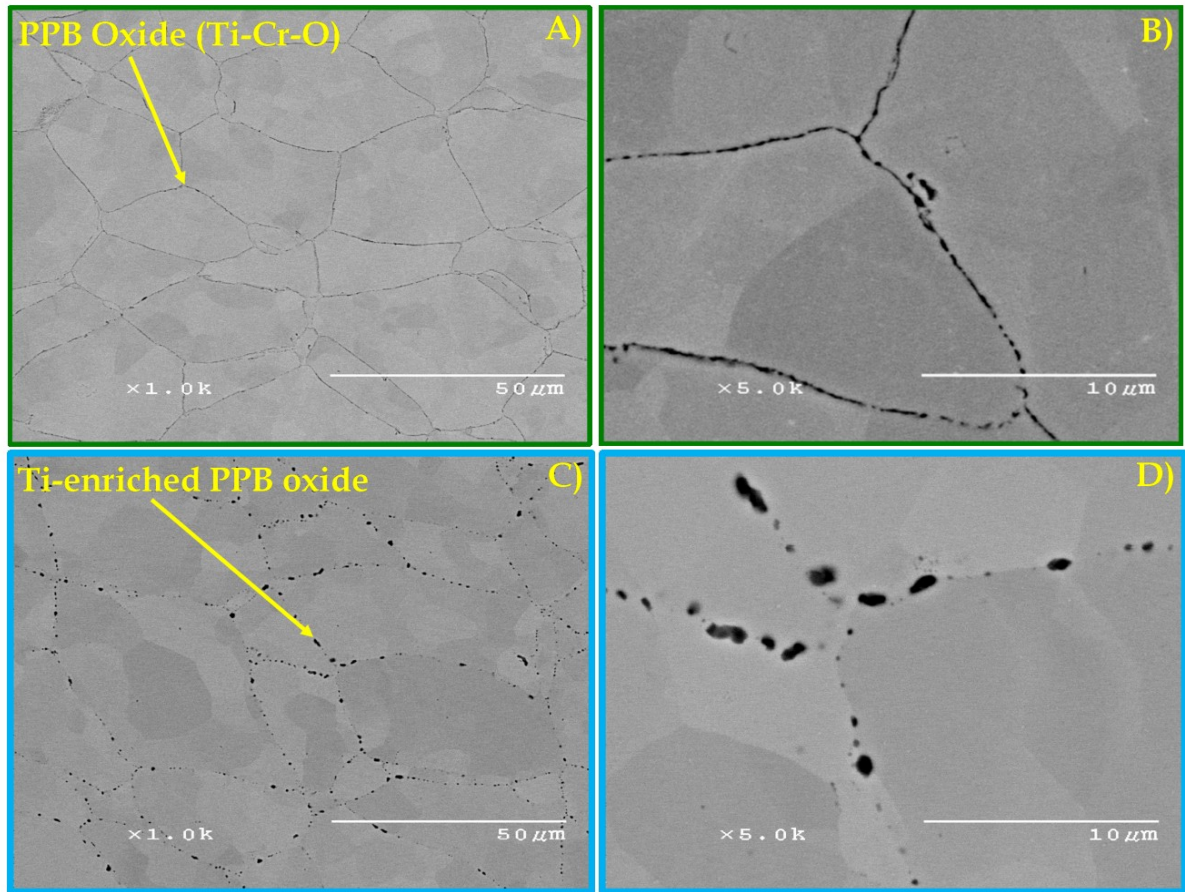


**Figure 7.8. Microstructure comparison of 850°C as-HIPped CR-126 (outlined in green: SEM images A and B) and 1300°C as-HIPped CR-126 (outlined in blue: SEM images C and D)**

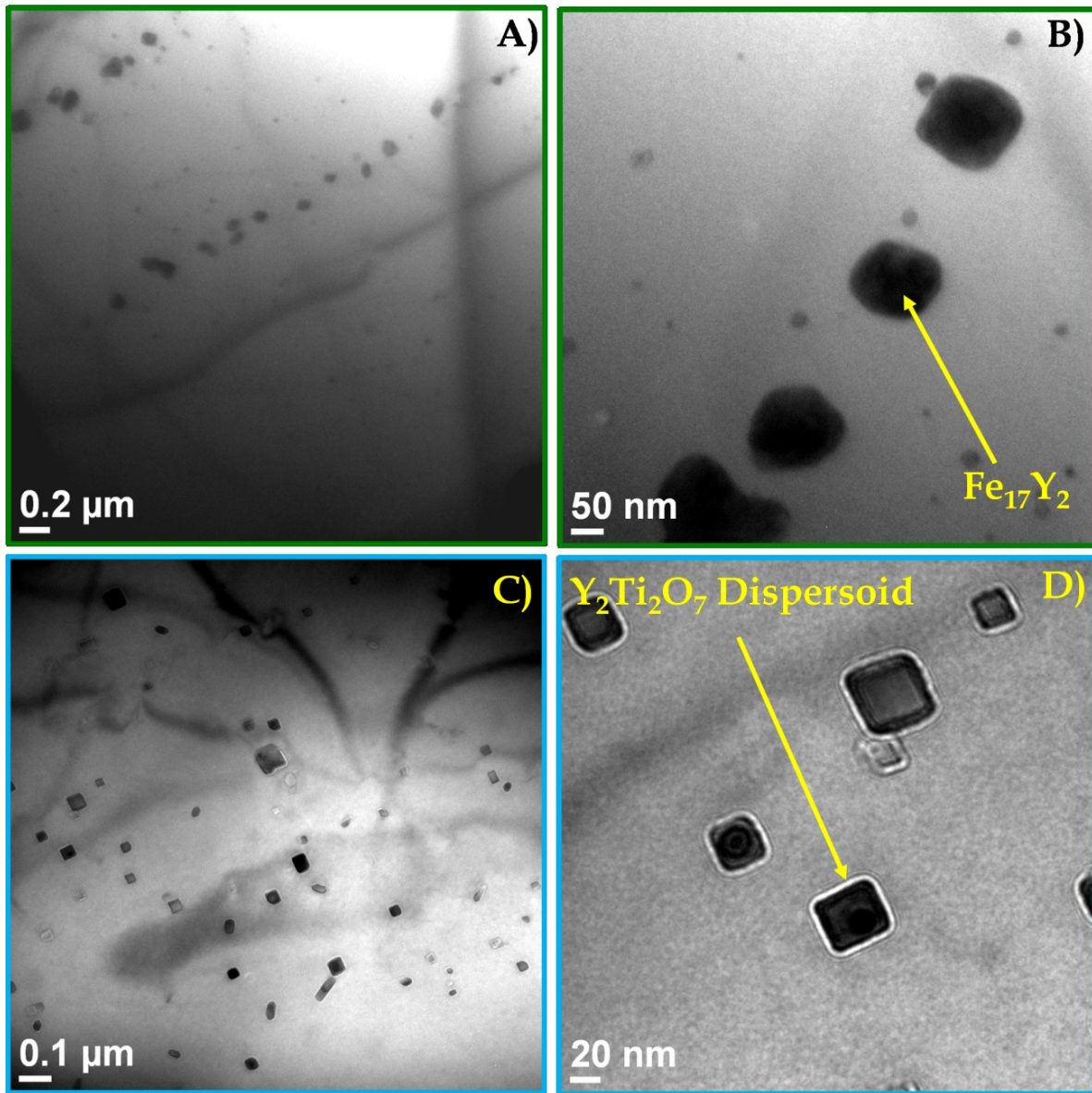


Figure 7.9. Microstructure comparison of 850°C as-HIPped CR-126 (outlined in green: TEM BFI images A and B) and 1300°C as-HIPped CR-126 (outlined in blue: TEM BFI images C and D)

### 7.5.5 Synchrotron Phase Analysis

Phase analysis of the chemical reservoir alloys was completed using through-penetrating high energy X-ray diffraction (HE-XRD). The alloys were examined in the as-atomized (red), 850°C as-HIPped (green), and 1300°C as-HIPped (blue) condition (See Figure 7.10). The resulting diffraction peaks were compared using

the reciprocal lattice vector  $Q$  ( $\text{\AA}^{-1}$ ), which is commonly used to compare X-ray diffraction data independent of wavelength. Rietveld refinement of the diffraction data was completed using a generalized structural analysis system (GSAS) [208, 209]. The corresponding refinement figures of merit (i.e., goodness of fit ( $\chi^2$ ), profile residual (Rp), and weighted profile residual (wRp)) used to calculate the  $\alpha$ -Fe lattice parameter and resulting Y-enriched dispersoid volume percent are listed in Table 7.2.

**Table 7.2. Rietveld refinement figures of merit ( $\chi^2$ , Rp, and wRp),  $\alpha$ -Fe matrix lattice parameter measurements, and dispersoid vol. percent measurements for CR-112, CR-118, and CR-126**

Alloy (condition)	Reduced $\chi^2$	Rp	wRp	$\alpha$ -Fe Lattice Parameter ( $\text{\AA}$ )	Y-enriched Dispersoid (%)
CR-112 (powder)	4.983	0.1193	0.1548	2.87282	-
CR-118 (powder)	3.993	0.1467	0.1790	2.87413	-
CR-126 (powder)	4.488	0.1290	0.1681	2.87717	-
CR-112 (850°C HIP)	3.336	0.1367	0.1586	2.87236	-
CR-118 (850°C HIP)	3.792	0.1876	0.2106	2.87258	-
CR-126 (850°C HIP)	3.679	0.1562	0.1686	2.87605	-
CR-112 (1300°C HIP)	2.800	0.1507	0.1698	2.87221	0.13
CR-118 (1300°C HIP)	4.143	0.1118	0.1497	2.87277	0.94
CR-126 (1300°C HIP)	1.721	0.1192	0.1481	2.87624	0.58

Refinement of the synchrotron diffraction data taken from as-atomized CR-112 powder (see Figure 7.10A) showed that the particles contain a single phase  $\alpha$ -Fe matrix. The ultra thin surface oxide phase was not identified using HE-XRD. Phase analysis of the low temperature as-consolidated (i.e., 850°C HIPped) microstructure recognized the minor presence of crystalline  $\text{Cr}_2\text{O}_3$  and  $\text{Fe}_{17}\text{Y}_2$  within the  $\alpha$ -Fe matrix. Examination of the high temperature consolidated (i.e., 1300°C HIPped) microstructure revealed the presence of  $\text{Cr}_2\text{O}_3$ ,  $(\text{Y,Cr})_2\text{O}_3$ , and  $\text{Cr}_2\text{N}$  within the  $\alpha$ -Fe



matrix. The volume percent of  $(Y,Cr)_2O_3$  and  $Cr_2O_3$  in this sample was determined to be  $0.13 \pm 0.013$  v/o and  $1.18 \pm 0.029$  v/o, respectively, using GSAS refinement of the diffraction data. It should also be noted that after high temperature consolidation, no diffraction peaks representing  $Fe_{17}Y_2$  were witnessed. Diffraction data comparing microstructural phase changes that occur during consolidation of precursor oxide dispersion forming CR-112 powders are summarized in Figure 7.10A.

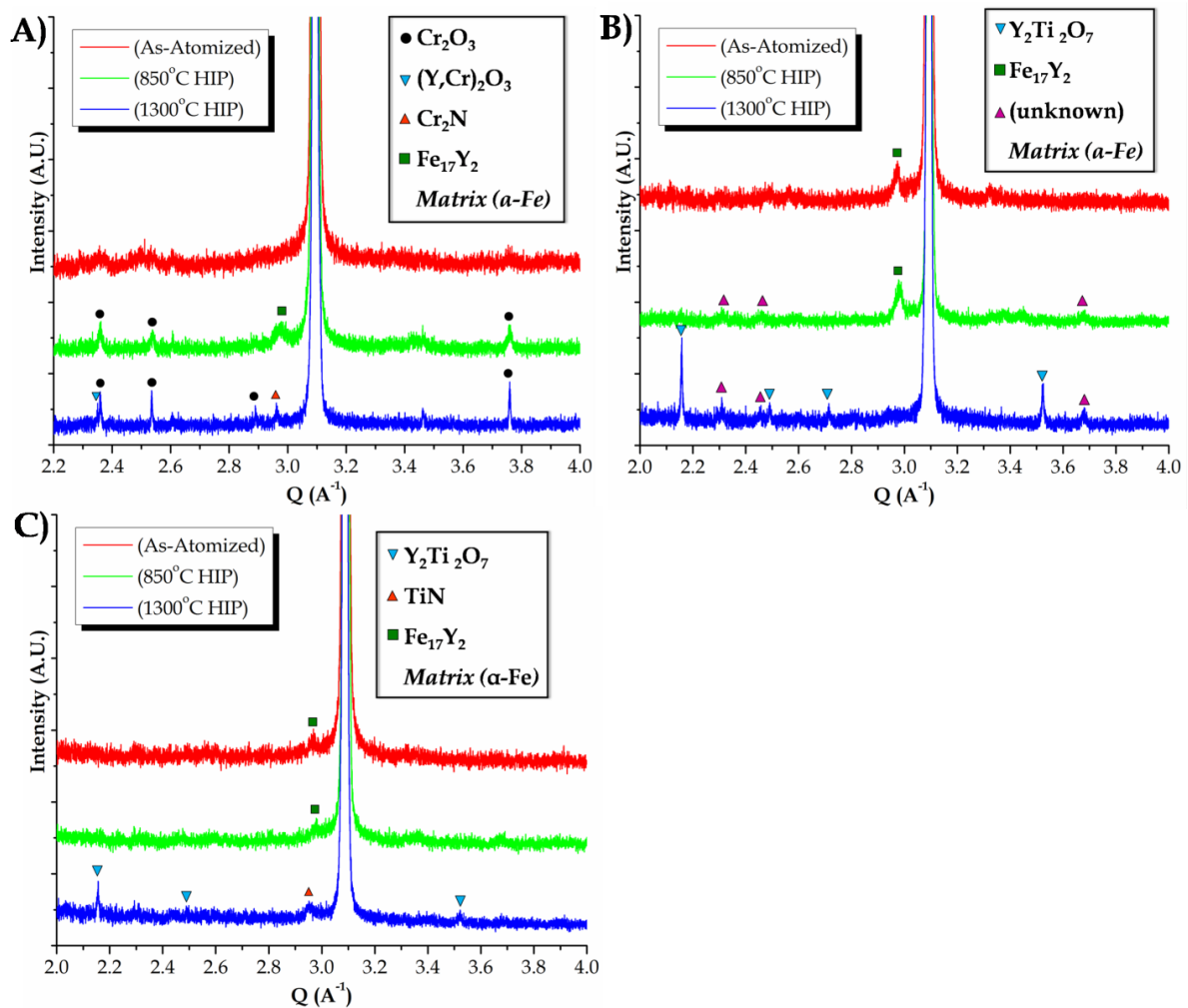


Figure 7.10. HE-XRD phase analysis for as-atomized powders (red), 850°C HIP microstructure (green), and 1300°C HIP microstructure (blue): (A) CR-112, (B) CR-118, and (C) CR-126

Synchrotron diffraction data for the as-atomized CR-118 (see Figure 7.10B) powders revealed a small volume fraction of intermetallic  $\text{Fe}_{17}\text{Y}_2$  present in  $\alpha$ -Fe matrix. It should also be noted that no identifiable oxide phases could be resolved in the as-atomized diffraction data. The product phases of the alloy seemed mostly unchanged during low temperature consolidation. During this consolidation step, the volume fraction of  $\text{Fe}_{17}\text{Y}_2$  was increased and several unidentified minor peaks began to emerge above background. The formation of yttrium titanate (i.e.,  $\text{Y}_2\text{Ti}_2\text{O}_7$ ) and full dissolution of  $\text{Fe}_{17}\text{Y}_2$  resulted from high temperature consolidation of the alloy powders. The volume percent of  $\text{Y}_2\text{Ti}_2\text{O}_7$  was determined to be  $0.94 \pm 0.019$  v/o, using GSAS refinement (see Table 7.2). Diffraction data highlighting these microstructural phase changes are gathered in Figure 7.10B.

The as-atomized CR-126 powders (see Figure 7.10C) also were found to contain a small volume fraction of intermetallic  $\text{Fe}_{17}\text{Y}_2$  within the rapidly solidified  $\alpha$ -Fe microstructure. The alloy microstructure seemingly was unchanged after low temperature consolidation, analogous to the CR-118 microstructure. High temperature consolidation of this alloy also resulted in the formation of  $\text{Y}_2\text{Ti}_2\text{O}_7$  dispersoids and titanium nitride (TiN), in conjunction with full dissociation of  $\text{Fe}_{17}\text{Y}_2$ . The volume fraction of  $\text{Y}_2\text{Ti}_2\text{O}_7$  was determined to be  $0.58 \pm 0.022$  v/o, using GSAS refinement (see Table 7.2). Diffraction data comparing phase changes in the CR-126 microstructure are compiled in Figure 7.10C.

## 7.6 Discussion

The chemical reservoir (CR) alloys contained  $\sim 15.5$  a/o Cr, in order to stabilize the  $\alpha$ -Fe matrix over the consolidation temperature range. These alloys also contained small alloying additions of Y, which was used as a dispersoid forming agent during high temperature consolidation of the powder particles. Y is thought to be basically insoluble in  $\alpha$ -Fe [210], but small concentrations were solute trapped in the  $\alpha$ -Fe matrix using rapid solidification processing (i.e., close-coupled Ar gas atomization).

Small Ti alloying additions (i.e., ~0.5 at.%) were added to CR-118 and CR-126 in an effort to promote the nano-metric oxide dispersoid phase. The addition of Ti led to the formation of  $Y_2Ti_2O_7$  dispersoids, as opposed to the  $(Y,Cr)_2O_3$  dispersoids found in CR-112. These results are in good agreement with previous studies of similar mechanically alloyed ODS steels [137, 211]. W was added to CR-126 as a solid solution strengthening element [115]. The addition of W seemed to limit the amount of Y that could be solute trapped during rapid solidification, but did not seem to influence the chemistry of the resulting nano-metric oxide dispersoid phase upon hot consolidation.

#### **7.6.1 As-atomized Surface Oxide**

The surface of the powder particles were oxidized *in situ* using reactive gas atomization. This oxidizing reaction occurs during the primary break-up of molten metal ligaments into atomized microspheres. Oxidizing the particles in the superheated, fully molten state enhances the kinetics of the surface reaction and allows for oxide layer formation prior to complete powder solidification, which results in compressive forces being applied to the surface oxide layer. These compressive forces are believed to help prevent oxide spallation during powder handling prior to consolidation.

This high temperature rapid reaction resulted in powder particles with an ultra thin surface oxide layer. This surface layer appeared to form as an amorphous oxide phase. AES surface analysis of the powder particles showed an apparent oxide layer, but no crystal structure reflections could be detected using HE-XRD (i.e., resolution of  $2 \times 10^{-4}$  Q). This result provides evidence that the surface oxide phase likely solidifies in an amorphous state, promoted by rapid solidification of the ultra thin (i.e.,  $t < 150\text{nm}$ ) oxide layer.

The chemical composition of the surface oxide layer is also thought to be controlled by the rapid kinetics of the oxidizing reaction. This rapid reaction seems to promote

the formation of the most kinetically favored oxide phase, rather than the most thermodynamically stable phase. This concept highlights the importance of limiting the concentration of Y in the atomization melt, which in return reduces the available surface activity of Y relative to other reactive alloying additions (e.g., Cr or Ti) in the molten atomized droplets. This appeared to help prevent the powder particles from forming a Y-containing surface oxide layer during atomization and permitted formation of an ODS microstructure upon high temperature consolidation by a delayed O exchange reaction.

Surface analysis of CR-112 powders of the simple Fe-Cr-Y alloy showed an enriched layer of O and Cr, with a slight enrichment of Y. The chemistry of the surface layer is indicative of a Cr-enriched oxide, but as previously mentioned no structural information was confirmed using HE-XRD analysis. The surface layer is thought to be a mixed amorphous oxide phase containing mostly Cr and O, with small concentrations of Y. CR-118 powders were atomized using the same reactive atomization gas as CR-112, but surface analysis showed an enriched layer of mostly O and Cr, with small concentrations of Ti. Apparently, the extreme reactivity of Ti prevented the consumption of any Y during the reactive atomization process. Analysis of CR-126 powders revealed a surface chemistry similar to that of CR-118, with an enriched layer of O, Cr, and Ti. Both CR-118 and CR-126 likely contain an amorphous Cr-enriched surface oxide layer doped with small amounts of Ti.

The difference in average oxide layer thickness on CR-112 and CR-118 powders is within statistical error of the AES measurement, but the surface oxide layer found on CR-126 powders is ~35nm thinner than the oxide layers found on similar CR-112 and CR-118 powders. The thickness of the surface oxide layer is thought to be directly influenced by the concentration of O in the reactive atomization gas. Reducing the concentration of O in the reactive gas certainly reduces the activity of O within the gas striking the surface of the metal droplets during atomization,

promoting slower oxidation kinetics and the formation of a thinner surface oxide layer, given similar alloy droplets.

### **7.6.2 CR-Alloy Microstructure Evolution**

The microstructure of the CR alloys was manipulated during elevated temperature consolidation of the powder particles. The volume percent of PPB oxide phase was reduced in all CR-alloys during high temperature consolidation of the powders. This result showed that the less thermodynamically stable PPB oxide could be dissociated, which in return releases O for the formation of nano-metric Y-enriched oxide dispersoids throughout the microstructure. This delayed O exchange reaction is believed to be driven by the relative thermodynamic stability of oxides. It is theorized that the PPB oxide phase begins to dissociate during elevated temperature consolidation, in an effort to reach equilibrium conditions with the  $\alpha$ -Fe matrix. During this process, the initial PPB oxide (e.g., Cr-enriched oxide) begins to dissociate and releases O into solid solution within the  $\alpha$ -Fe matrix. O diffuses away from the PPBs driven by a concentration gradient or chemical potential within the consolidated microstructure. The solid solubility limit of O in  $\alpha$ -Fe is inherently low (i.e.,  $\sim 0.104$  a/o [212]), and the dissociation of the PPBs should theoretically discontinue once the solubility limit is reached and an equilibrium concentration of O is achieved, but consumption of O by Y allows the reaction to continue until all Y has been depleted. This illustrates the importance of achieving a critical balance between initial O and Y concentrations in the CR-alloy powders.

The ideal balance of O to Y should be defined by the stoichiometric ratio of O/Y linked with an explicit dispersoid product phase. Optimization of this ratio is thought to allow for complete dissociation of the PPB oxide phase, coupled with total conversion of Y into nano-metric oxides. This optimized reaction would eliminate non-ideal phases from the alloy microstructure (e.g., PPB oxides and  $\text{Fe}_{17}\text{Y}_2$  precipitates), which can act as void nucleation sites during mechanical

evaluation of these alloys [205]. This internal O exchange reaction is possible since Y containing oxides are extremely thermodynamically stable, in comparison to Cr or Ti oxides [213]. Figure 7.11 illustrates the free energy of formation comparison for Cr, Ti, and Y oxides over the relevant consolidation temperature range.

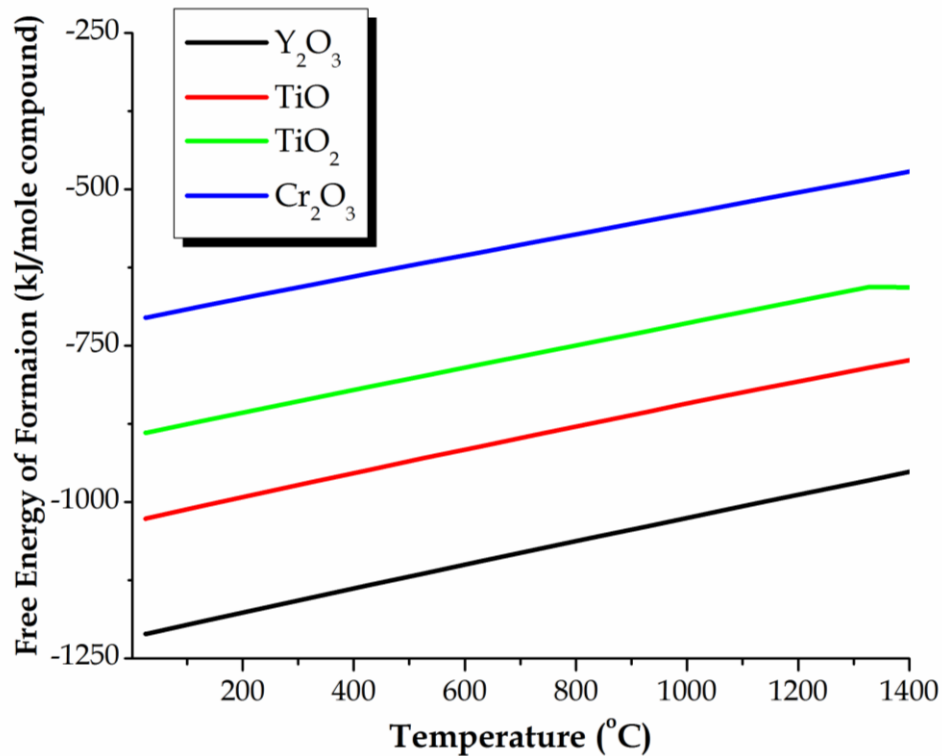


Figure 7.11. Comparison of the thermodynamic stability for potential oxides that could form within these CR-alloy microstructures during powder consolidation [213]

## 7.7 Future Plans and Technology Outlook

Modifications to the reactive gas atomization process will be tested on a series of future CR-alloys. These tests will be used to formulate processing parameters that can establish an optimum ratio of O to Y for a select powder particle size range. Careful selection of an ideal particle size range should preface modifications to the processing parameters, knowing that O content is directly linked to the specific surface area of the powders (see Figure 7.12).

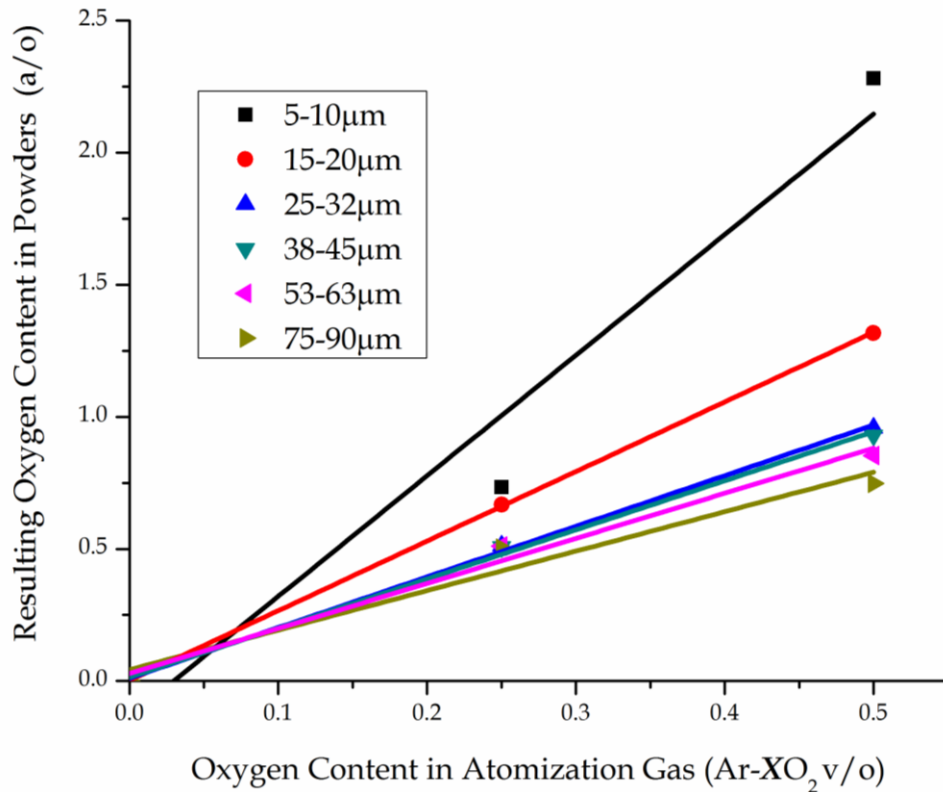


Figure 7.12. Resulting oxygen content relative to as-atomized powder particle size for different reactive gas concentrations

Microsegregation of Y and Ti to as-solidified cell boundaries can occur during rapid solidification of the CR-alloy powders (see Figure 7.13). Refinement of this microsegregation could be used to increase the spatial and number density of nano-metric oxide dispersoids that form at these former cell boundaries during the elevated temperature O exchange reaction. An increased density of oxide dispersoids should successfully impede dislocations movement along these boundaries, allowing for the development of a very fine ( $<1\mu\text{m}$ ) and highly stable dislocation substructure. Nano-metric oxide dispersoids are known to stabilize dislocation substructures, hindering thermally induced recrystallization during elevated temperature mechanical testing, promoting maximum strength gains in ODS alloys [78, 79, 214].

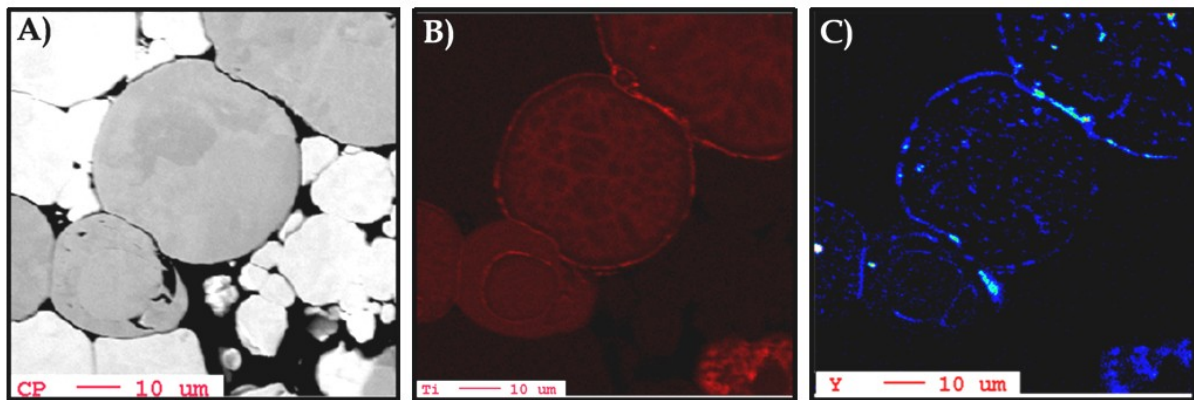


Figure 7.13. EPMA elemental composition map of as-atomized CR-118 powders showing: (A) as-solidified microstructure, (B) titanium microsegregation, and (C) yttrium microsegregation

A carefully selected powder particle size range will be used during consolidation of future CR-alloys. This critical size range will be defined by the O and Y contents and the as-solidified cell size in the powders. The goal of this selection process will be to consolidate powders with an optimum O to Y ratio, in conjunction with a sufficiently fine cell size ( $<1\ \mu\text{m}$ ). These powders will be consolidated and heat treated at elevated temperatures ( $T > 850^\circ\text{C}$ ), in order to promote the O exchange reaction and Y-enriched nano-metric oxide dispersoid formation. The ODS microstructure will then be subjected to thermal mechanical treatments, in an effort to develop a fine scale ( $<1\ \mu\text{m}$ ) dislocation substructure for ultimate strengthening of the ODS microstructure. Elevated temperature mechanical testing will be used to compare these new CR-alloys with more conventional ODS ferritic alloys fabricated using the conventional mechanical alloying process (e.g., MA956, MA957, and PM2000).

This new reactive gas atomization process offers the potential for a considerable increase in processing capacity for the production of precursor oxide dispersion forming particulate compared to traditional mechanical alloying methods (see Figure 7.14). This more efficient processing technique could significantly reduce the



high cost of manufacturing ODS ferritic stainless steel alloys, thus making them a more viable and economical choice as structural materials in future generation power reactors (e.g., advanced ultra supercritical steam and Generation IV fission).

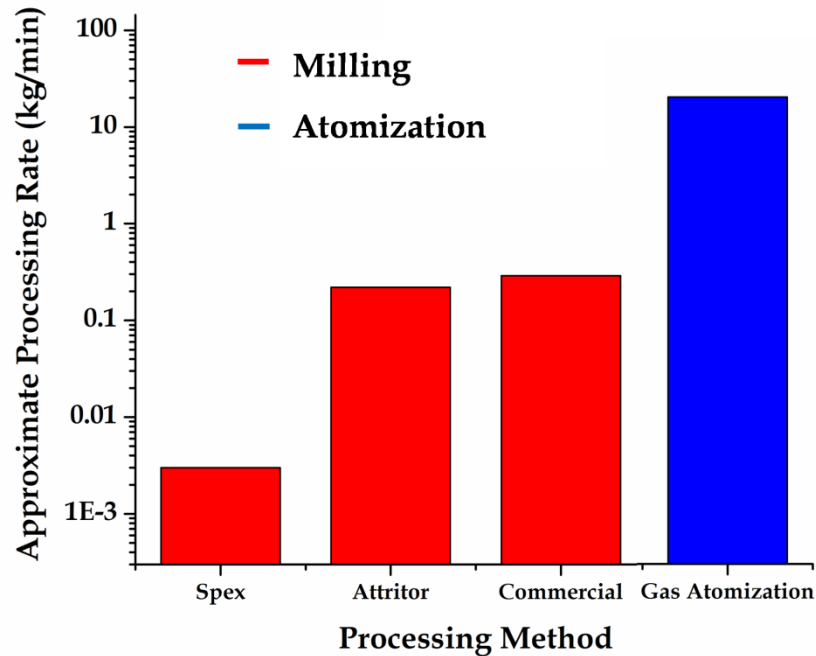


Figure 7.14. Comparison of approximate mechanical alloying and gas atomization processing rates [101, 104]

## 7.8 Summary

A new simplified processing technique involving gas atomization and *in situ* oxidation has been developed to produce precursor ferritic stainless steel powders that can be consolidated into an ODS isotropic microstructure. Microstructural results showed a clear ability to manipulate oxide and intermetallic phases within the alloy using high temperature consolidation. HE-XRD phase analysis coupled with TEM microstructure analysis confirmed the operation of an O exchange reaction between a less stable prior particle boundary oxide (i.e., Cr-enriched oxide) and Y. This O exchange reaction results in the formation of nano-metric Y-containing oxide dispersoids throughout the ferritic microstructure. The atomization

processing parameters will need to be further optimized, in order to generate an ideal O/Y ratio in improved CR-alloy powders. This ideal ratio should permit full dissociation of both the PPB oxides and any previously formed  $\text{Fe}_{17}\text{Y}_2$  precipitates, resulting in a stronger and more uniform alloy microstructure.

## **7.9 Acknowledgements**

Support from the Department of Energy, Office of Fossil Energy (ARM program) through Ames Laboratory contract no. DE-AC02-07CH11358 is gratefully acknowledged. The high energy X-ray work at beamline 11-BM of the APS was supported by the Department of Energy, Office of Science, Basic Energy Sciences under contract no. DE-AC02-06CH11357. The authors also would like to thank Dr. Danny Shechtman, James Anderegg, David Byrd, and Hal Sailsbury for their individual contributions to this paper.

## Chapter 8. Gas Atomized Chemical Reservoir ODS Ferritic Stainless Steels

Modified from a paper published in: *Advances in Powder Metallurgy and Particulate Materials*, 2010, Vol. 2, pp. 112-131

J. R. Rieken<sup>1,2,3</sup>, I.E. Anderson<sup>4</sup>, and M.J. Kramer<sup>4</sup>

### 8.1 Abstract

Gas atomization reaction synthesis was used to surface oxidize ferritic stainless steel powders (i.e., Fe-16.0Cr-(0.1-0.2)Y-(0.1-0.5)(Ti or Hf) at.%) during the primary break-up and solidification of the molten alloy. This rapid surface reaction resulted in envelopment of the powders by an ultra thin (i.e.,  $t < 100\text{nm}$ ) metastable Cr-enriched oxide layer. This metastable oxide phase was subsequently dissociated, and used as an oxygen reservoir for the formation of more thermodynamically favored Y-(Ti,Hf) nano-metric oxide precipitates during elevated temperature heat treatment of the as-consolidated powders. This oxygen exchange reaction promoted the formation of nano-metric oxide dispersoids throughout the alloy microstructure. The atomization processing parameters were adjusted to tailor the oxygen content in the as-atomized powders. Microstructure phase analysis was completed using transmission electron microscopy and X-ray powder diffraction.

---

<sup>1</sup> Graduate Student, Department of Materials Science and Engineering, Iowa State University

<sup>2</sup> Primary researcher and author

<sup>3</sup> Author for correspondence: Tel.: +1 515 294 9159, E-mail address: [jrieken@istate.edu](mailto:jrieken@istate.edu)

<sup>4</sup> Division of Materials Sciences and Engineering, Ames Laboratory (USDOE), Ames, IA 50011

## 8.2 Introduction

Oxide dispersion strengthened (ODS) ferritic stainless steel alloys are being considered for structural components within future generation power reactors [9, 16, 38, 65]. These alloys have demonstrated superior elevated temperature strength and creep resistance [1, 2, 202]. The improved mechanical properties are a direct result of the stabilization of a fine scale ( $<500$  nm) dislocation substructure, which can be developed through a series of thermal mechanical treatments, and inherently stabilized by impeding dislocation recovery through the use of finely spaced nano-metric oxide precipitates [4, 5, 78, 79, 214]. Thus, the functionality of an ODS alloy relies on developing a microstructure which contains a consistent distribution of finely spaced and highly stable nano-metric oxide particles.

Traditionally, mechanical alloying (MA) processing has been used to generate precursor oxide dispersion forming particulate, but this process has been found to be time intensive and rather inefficient, resulting in an expensive final product (e.g., \$340/kg for PM2000) [11, 99, 101, 203, 204]. Alternatively, gas atomization reaction synthesis (GARS) utilizes *in situ* oxidation of molten chemical reservoir (CR) alloy droplets (e.g., Fe-Cr-(Ti or Hf)-Y) [14]. During this process a metastable Cr-enriched oxide layer forms and envelops the rapidly solidified powder particles (See Figure 8.1A). This metastable surface oxide phase is used as an O supply reservoir, which can be continuously dissolved using elevated temperature consolidation and heat treatment, through an O exchange reaction with specifically distributed and essentially immobile Y atoms (See Figure 8.1B-D). This novel process eliminates the need for MA and should be able to dramatically lower the fabrication cost of ODS ferritic stainless steels. This paper aims to demonstrate the microstructure evolution of these chemical reservoir alloys and will highlight the progress being made in GARS process development and alloy design.

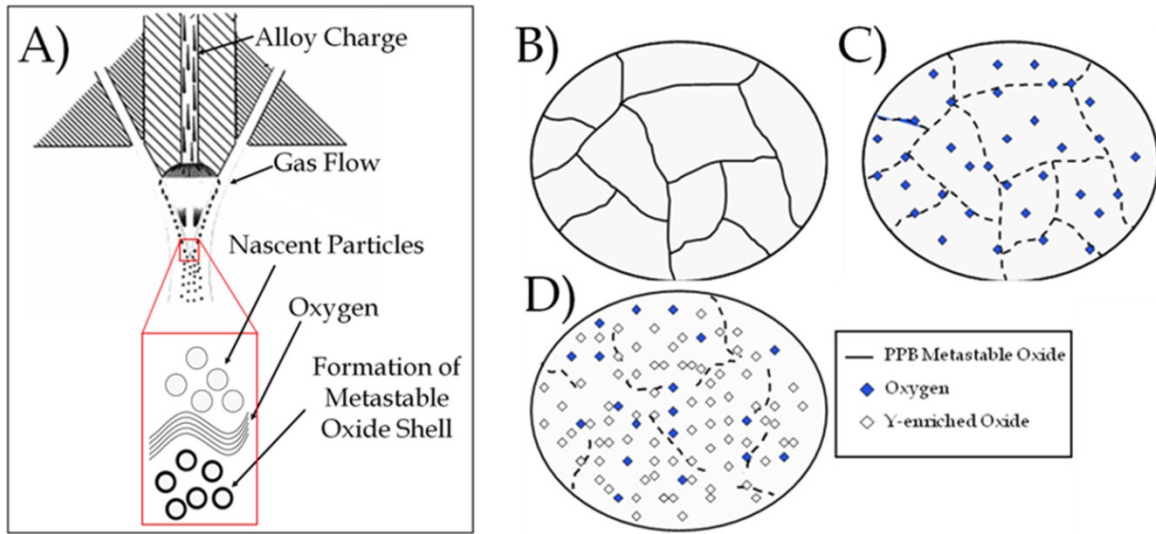


**Figure 8.1. A) Gas atomization reaction synthesis processing and oxygen exchange reaction: B) initial configuration of low temperature consolidated powders, C) partially dissociated prior particle boundary oxide, and D) dispersoid formation**

### 8.3 Procedure

#### 8.3.1 Gas Atomization Reaction Synthesis (GARS)

The reactive gas contained a volumetric mixture of argon (Ar) with small concentrations of oxygen ( $O_2$ ) [206]. The composition of the reaction gas, injection point, atomization gas, and atomization pressure for each GARS trial is shown in Table 8.1. Additionally, the resulting chemical composition for each CR-alloy is displayed in Table 8.2.

The atomization charge was inductively super-heated to  $1700^\circ\text{C}$  within a yttria ( $Y_2O_3$ ) washed alumina ( $Al_2O_3$ ) crucible. Once reaching the pouring temperature, the melt was tapped and pouring commenced through a yttria-stabilized (8 wt.%) zirconia pour tube. Upon exiting the pour tube, the melt was immediately impinged upon by the atomization gas (Table 8.1). The atomization gas pressure was 6.9 or 5.5 MPa within the atomization nozzle manifold. The reactive gas was injected through the primary high pressure gas atomization (HPGA) nozzle during GARS of CR-

118Ti-Y and CR-156Y-Hf (Figure 8.2B), while the reactive gas was injected downstream (~5 cm) using an über halo during GARS of CR-144Hf-Y (Figure 8.2C).

**Table 8.1. Reaction gas composition and inlet position**

Alloy	Reaction Gas (vol.%)	Reaction Gas Inlet	Atomization Gas
CR-118Ti-Y	Ar-0.5O <sub>2</sub>	Atomization Nozzle	Reaction Gas
CR-144Hf-Y	Ar-0.25O <sub>2</sub>	Über Halo	He
CR-156Y-Hf	Ar-0.12O <sub>2</sub>	Atomization Nozzle	Reaction Gas

The bulk oxygen content found in the as-atomized powder particles was measured using an inert gas fusion (LECO) analyzer, and the chemical composition of each alloy was verified using inductively coupled plasma/atomic emission spectroscopy (ICP/AES).

**Table 8.2. Resulting as-atomized CR-alloy powder chemical composition**

Alloy	Fe (at.%)	Cr (at.%)	W (at.%)	Ti (at.%)	Hf (at.%)	Y (at.%)	O (at.%)
CR-118Ti-Y	Bal.	15.84	-	0.50	-	0.20	1.67
CR-144Hf-Y	Bal.	16.16	0.94	-	0.27	0.08	0.23
CR-156Y-Hf	Bal.	15.84	-	-	0.11	0.18	0.38

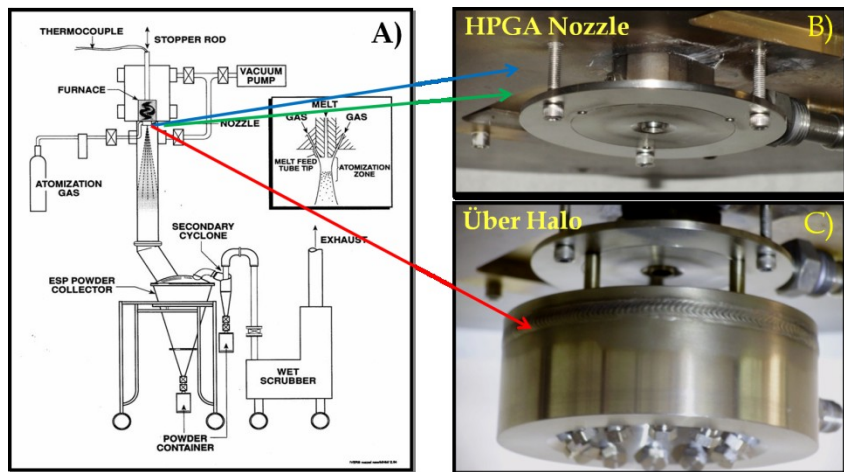


**Figure 8.2. Reactive gas injection position: A) schematic of the high pressure gas atomizer (HPGA), B) close-coupled HPGA nozzle, and C) near-field über halo**

### 8.3.2 Consolidation

Cold isostatic pressing (CIP) was used to consolidate as-atomized powder samples for metallographic preparation prior to hot consolidation. As-atomized particles (dia. 20-53 $\mu$ m or dia. < 20 $\mu$ m) were blended with 70 vol.% copper powders (dia. < 20 $\mu$ m) and sealed in latex CIP bags. The blended powders were subsequently CIPed at 400MPa for ~60sec. Following the CIP process, each consolidated powder sample was impregnated with epoxy and cross-sectioned for microstructural analysis.

Additionally, hot isostatic pressing (HIP) was used to fully consolidate the as-atomized powders. Prior to consolidation, each powder sample was inserted into a 316L stainless steel HIP can (Figure 8.3A), which measured 25 mm in diameter x 127 mm in length. Each HIP can was slowly evacuated using a diffusion pumped vacuum system to a pressure of  $\sim 7 \times 10^{-7}$  mbar and welded shut. The sealed cans were HIPed at 700°C at a pressure of 303MPa for 4.0hr at the selected temperature and peak pressure. An example of the resulting HIP bar is shown in Figure 8.3B.

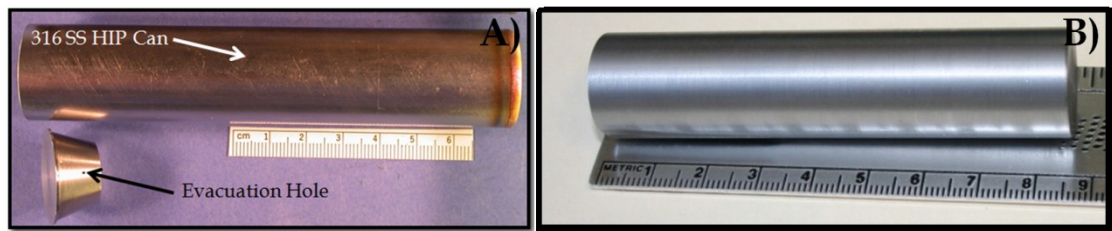


Figure 8.3. A) 316L stainless steel HIP can and B) as-consolidated (700°C) HIP bar (CR-156Y-Hf)

### 8.3.3 Heat Treatment

As-consolidated HIP bars were sectioned into 10 mm thick specimens and heat treated under vacuum ( $1 \times 10^{-7}$  mbar) according to Table 8.3. Heat treatment times were calculated using a diffusionless internal oxidation model [182, 185]. A more detailed description of this model can be found in the literature [183, 184]. It should be noted that CR-144Hf-Y was only heat treated at 1000°C and 1300°C.

**Table 8.3. CR-alloy heat treatment schedule**

Temperature (°C)	Time (hr)
1000	25
1100	5.0
1200	2.5
1300	1.0

#### **8.3.4 Electron Microscopy**

Surface analysis of the as-atomized powder particles was conducted using a JEOL JAMP 7830F scanning electron microscope (SEM) with auger electron spectroscopy (AES). The microstructure of the powders was examined using a JEOL 5910LV SEM with energy dispersive spectroscopy (EDS), while the as-consolidated and post heat treated alloy microstructure was analyzed using a Hitachi S-2460N SEM with EDS. Area fraction measurements of microstructural features were completed using image analysis (Image-Pro Plus™ version 3.0).

The nano-metric features present in the CR-alloys were characterized using a Tecnai G<sup>2</sup> F20 transmission electron microscope (TEM) using bright field imaging (BFI) and energy-filtered TEM (EFTEM) chemical mapping at 200 keV [215]. The TEM samples were ground flat using 400 and 600 SiC grit paper, and polished using 6.0µm and 1.0µm diamond polishing compound to a thickness of ~50µm. The samples were then mechanically dimpled to a thickness of ~20µm, and dual jet polished using an electrolytic solution for stainless steels (i.e., 700 ml methanol, 120 ml distilled water, 100 ml glycerol, and 80 ml perchloric acid) at -21°C.

#### **8.3.5 X-ray Diffraction**

Crystal structure analysis of the CR-alloys was completed using a Phillips PANalytical X-Pert Pro Diffraction System with Co-K $\alpha$  radiation (i.e.,  $\lambda=1.78901\text{\AA}$ ). A scanning real time multiple strip (RTMS) X-ray detector was used with an active



length of  $\sim 0.05 \text{ Q} (\text{\AA}^{-1})$ . Diffraction data was collected from  $1.5\text{-}6.0 \text{ Q} (\text{\AA}^{-1})$  with a step size of  $5 \times 10^{-4} \text{ Q}$  and a dwell time of 500 s. The reciprocal lattice vector ( $Q$ ) describes the momentum difference between incoming and diffracted X-rays (Equation 91), and is commonly used to compare X-ray diffraction data (i.e., Bragg angle ( $\theta$ ) of resulting peaks) independent of wavelength ( $\lambda$ ) [216].

$$Q = \frac{4\pi \sin \theta}{\lambda} \quad \text{Equation 91}$$

## 8.4 Experimental Results

### 8.4.1 Reactive Gas Atomization Processing

The O content associated with a particular particle size range and reactive gas concentration is highlighted in Figure 8.4. It can be seen that smaller particles contain a greater percentage of O in comparison to larger particles, owing this to an increased surface area to volume ratio. This analysis also shows a progressive linear trend in resulting O content and reactive gas composition when utilizing the HPGA nozzle as the injection point. The resulting O content for the newest CR-alloy (i.e., CR-156Y-Hf) was predicted (See Figure 8.4-dashed orange horizontal line) using this progressive linear trend, which was adapted from previously measured as-atomized O content for CR-118Ti-Y and CR-126Ti-Y[179]. Furthermore, resulting O content was found to be reduced by injecting the reactive gas downstream using the near-field über halo. This reduction in resulting O content can be seen in Figure 8.4 through direct comparison of alloys CR-126Ti-Y (black circle) and CR-144Hf-Y (red circle), where the reactive gas composition (i.e., Ar-0.25O<sub>2</sub> vol.%) was identical.

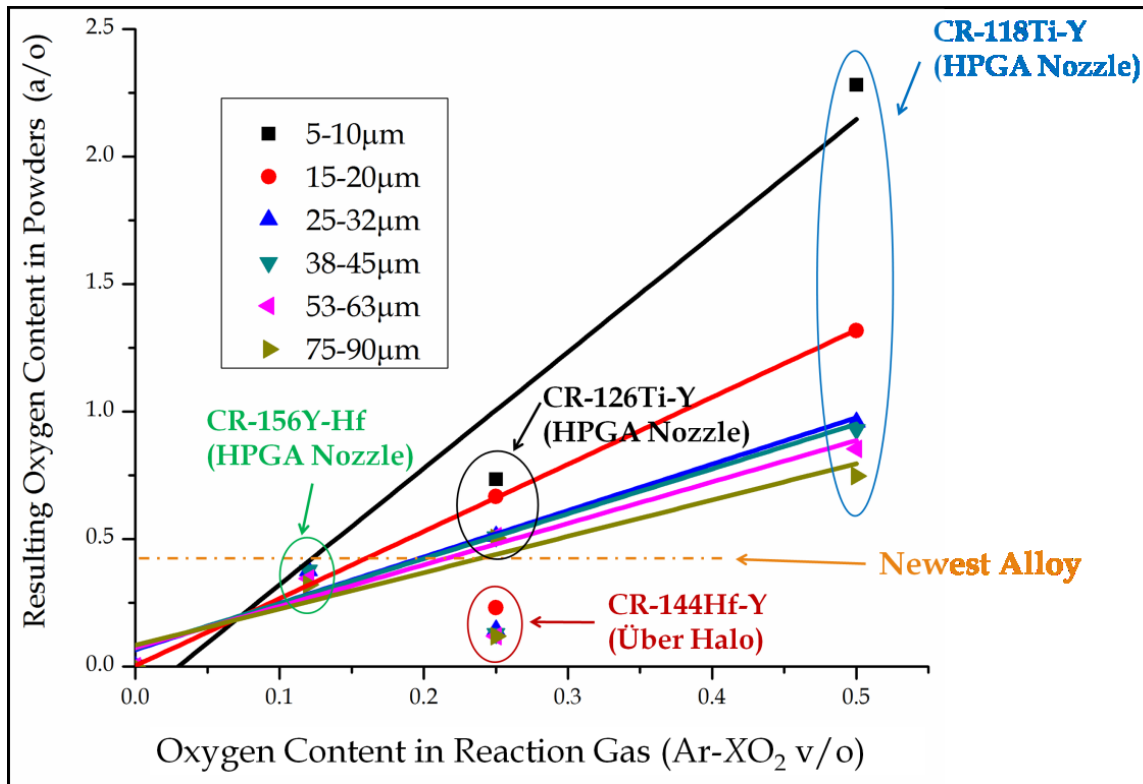


Figure 8.4. Resulting oxygen content measured from as-atomized powder particles relative to reaction gas content and injection point

#### 8.4.2 As-Atomized Microstructure Analysis

Chemical analysis of the as-atomized surface oxide layer was completed using AES depth profiling. The resulting AES depth profiles for all CR-alloys can be seen in Figure 8.5-A1, B1, and C1. All CR-alloys contained a surface oxide layer primarily enriched in Cr, Fe, and O with small concentrations of secondary alloy specific additions (e.g., Ti, Hf, W, and Y). The resulting surface oxide thickness was measured to be  $80 \pm 8$  nm,  $7 \pm 2$  nm, and  $33 \pm 3$  nm for CR-118Ti-Y, CR-144Hf-Y, and CR-156Y-Hf, respectively.

Examples of the as-atomized particle morphology for these CR-alloys are shown in Figure 8.5-A2, B2, and C2. The as-atomized particles were found to be quite spherical with very few satellites [104]. The scarce number of satellites is most likely

an effect of forming a thin surface oxide layer, which solidifies first and acts as a fusion barrier during the chaotic atomization process.

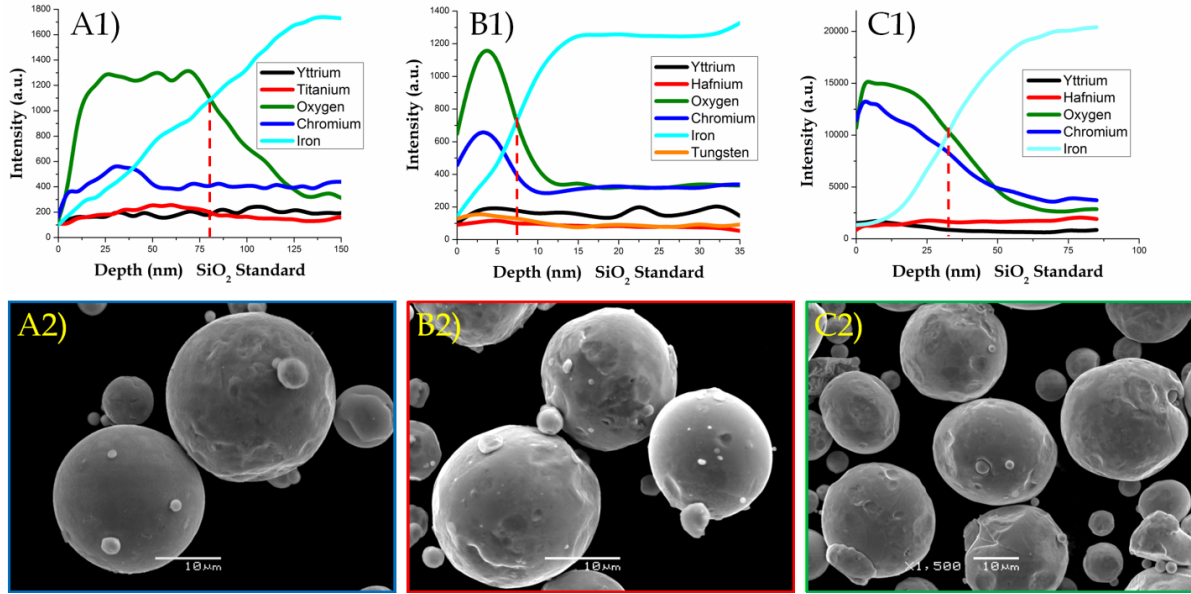


**Figure 8.5.** Auger depth profiles and as-atomized SEM surface images: A1-A2) CR-118Ti-Y, B1-B2) CR-144Hf-Y, and C1-C2) CR-156Y-Hf

Cross-sectional analysis of the as-atomized CR-alloy particles is shown in Figure 8.6. CR-118Ti-Y contained an  $\alpha$ -Fe matrix with a small volume fraction of Fe<sub>11</sub>TiY precipitates according to XRD results (not shown), and although these precipitates were not resolved during SEM analysis (Figure 8.6A1-2), some microsegregation of Y and Ti was revealed during electron probe micro-analysis [179]. Microsegregation of Hf and Y was readily visible during SEM analysis of as-atomized CR-144Hf-Y (Figure 8.6B1) and CR-156Y-Hf (Figure 8.6C1), furthermore, small volume fractions of Fe<sub>2</sub>Hf and Fe<sub>17</sub>Y<sub>2</sub> precipitates also were identified using XRD analysis of the powders (not shown). Further analysis discovered that fine (dia. < 5 μm) CR-156Y-Hf particles resisted microsegregation (See Figure 8.6C2), owing this to an increased solidification rate, although equally fine CR-144Hf-Y (See Figure 8.6B2) particles were found to still contain microsegregation of the reactive elements.

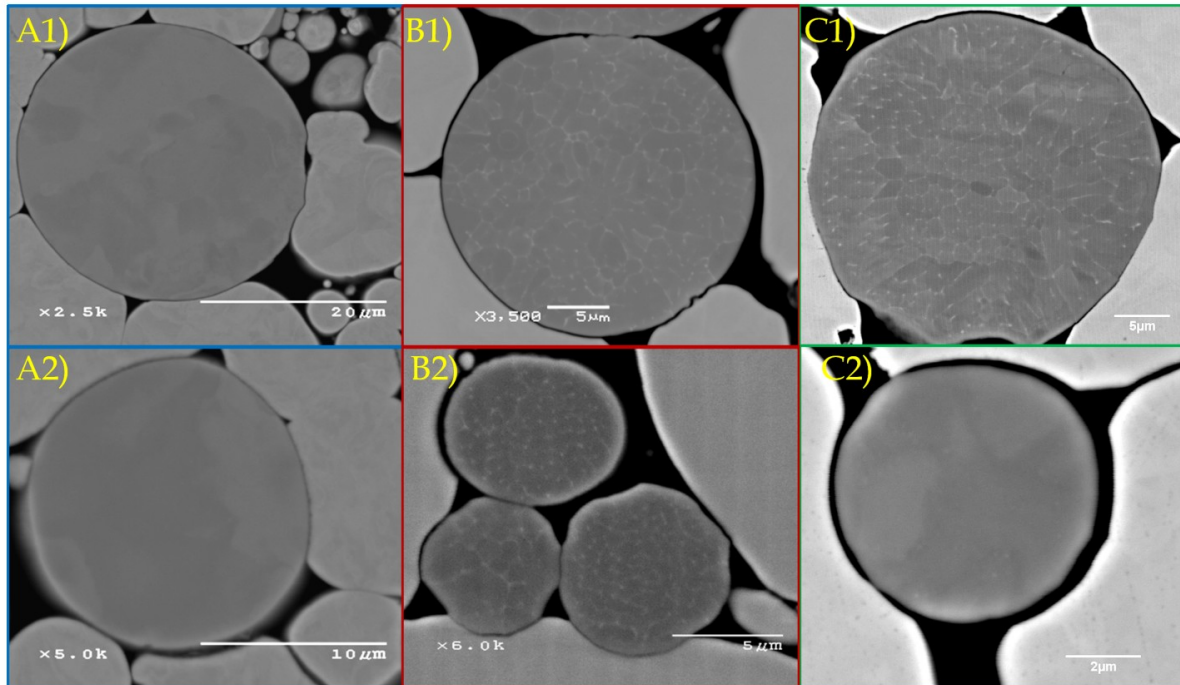


**Figure 8.6.** As-atomized SEM cross-sectional analysis of CR-alloy powders blended and CIPped (400MPa) in 75 vol.% Cu powder: A1-A2) CR-118Ti-Y, B1-B2) CR-144Hf-Y, and C1-C2) CR-156Y-Hf

### 8.4.3 As-Consolidated Microstructure Analysis

SEM analysis of the as-HIPped (i.e., 700°C-300MPa-4hr) CR-alloy microstructure is shown in Figure 8.7. This consolidation procedure resulted in a fully dense microstructure for CR-118Ti-Y and CR-156Y-Hf, and a highly dense (i.e., porosity < 2.0%) microstructure for CR-144Hf-Y. The presence of residual porosity in CR-144Hf-Y was probably due to increased hardness caused by the addition of W (See Table 8.2). After consolidation, a continuous oxide layer was found along the prior particle boundaries (PPBs) in alloy CR-118Ti-Y (Figure 8.7A1-2) and CR-156Y-Hf (Figure 8.7C1-2), while no apparent oxide layer was resolved in alloy CR-144Hf-Y (Figure 8.7B1-2). The volume percent of PPB oxide was determined to be  $4.2 \pm 0.1$  vol.% and  $0.6 \pm 0.2$  vol.% in CR-118Ti-Y and CR-156Y-Hf, respectively. Additionally, the PPB oxide in CR-118Y-Ti seemed to become enriched in Ti, and was later identified as  $\text{Ti}_3\text{O}_5$  using XRD analysis (not shown). A significant amount of solute

segregation also was evident in CR-144Hf-Y (Figure 8.7B2) and CR-156Y-Hf (Figure 8.7C2), where Hf and Y seemed to persist along previous as-solidified cell boundaries.

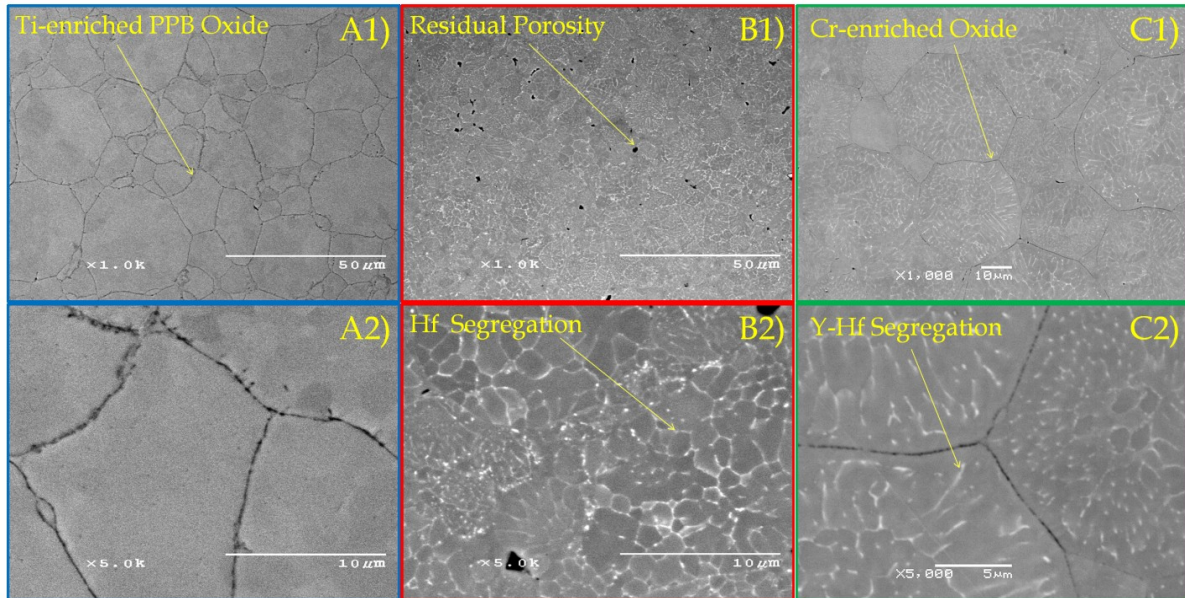


**Figure 8.7. As-consolidated SEM cross-sectional analysis of HIPped (700°C-300Mpa-4hr) CR-alloy powders: A1-A2) CR-118Ti-Y, B1-B2) CR-144Hf-Y, and C1-C2) CR-156Y-Hf**

TEM analysis of the as-consolidated CR-alloy microstructure is shown in Figure 8.8. A low number density of nano-metric Y-enriched intermetallic compound (IMC) precipitates was found to be rather evenly distributed throughout the as-consolidated CR-118Ti-Y (Figure 8.8A1-2) microstructure. Additionally, increased number densities of nano-metric Y-enriched IMC precipitates were found in close proximity to as-consolidated grain boundaries in CR-144Hf-Y (Figure 8.8B1-2) and CR-156Y-Hf (Figure 8.8C1-2). These IMC precipitates were found to range between 10-40 nm in CR-118Ti-Y, and between 2-50 nm in CR-144Hf-Y and CR-156Y-Hf. It also should be noted that larger elongated Y-enriched IMC precipitates were identified to have formed along grain boundaries in CR-156Y-Hf (see Figure 8.8C1-2).



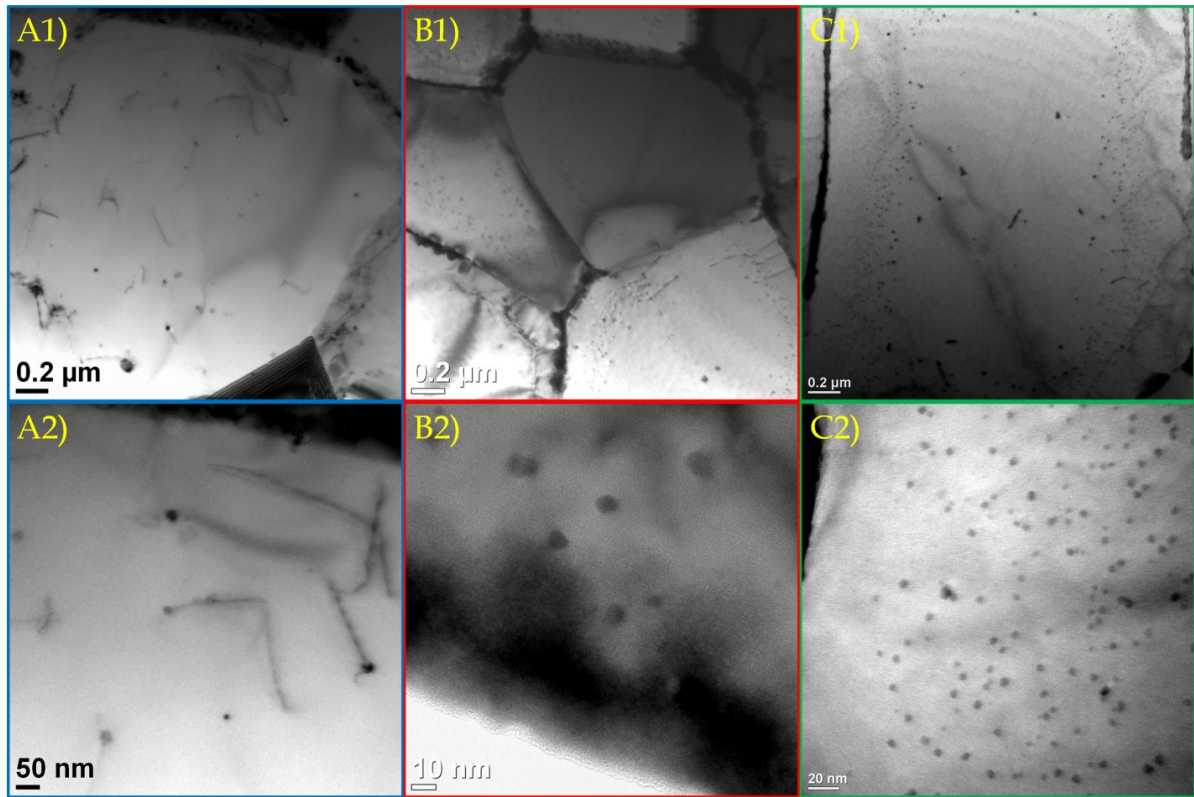
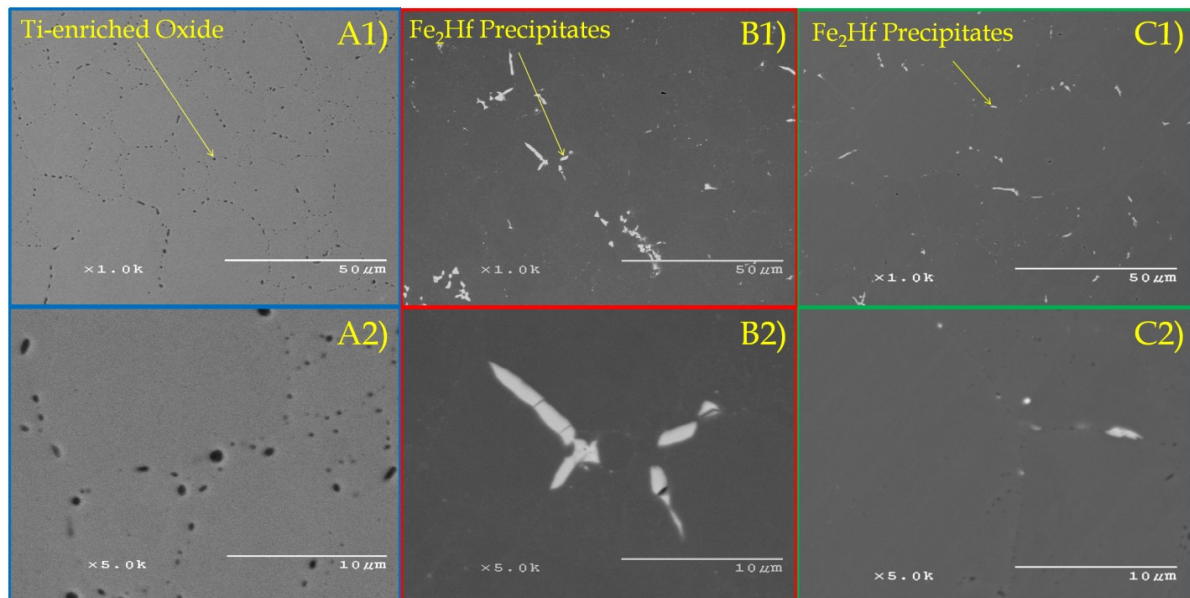


Figure 8.8. As-consolidated TEM-BFI analysis of HIPped (700°C-300Mpa-4hr) CR-alloys: A1-A2) CR-118Ti-Y, B1-B2) CR-144Hf-Y, and C1-C2) CR-156Y-Hf

#### 8.4.4 As-Reacted Microstructure Analysis

As-consolidated specimens were heat treated (See Table 8.3) at elevated temperatures to promote an oxygen exchange reaction between the less stable PPB oxide and oxide dispersion forming elements (i.e., Y, Ti, and Hf). SEM analysis of the as-reacted (i.e., H.T. 1300°C-1hr) CR-alloy microstructure is shown in Figure 8.9. The PPB oxide in CR-118Ti-Y (Figure 8.9A1-2) was reduced to  $1.7 \pm 0.3$  vol.% ( $\sim \Delta 2.5$  vol.%), while the PPB oxide in CR-156Y-Hf (Figure 8.9C1-2) was completely dissolved ( $\sim \Delta 0.6$  vol.%). Full dissolution of the less stable PPB oxide (comparing Figure 8.7C1 and Figure 8.9C1) provides clear evidence of an O exchange reaction. Additionally, the PPB oxide in CR-118Ti-Y progressed into a more stable Ti-enriched oxide phase (i.e.,  $\text{Ti}_3\text{O}_5 \rightarrow \text{Ti}_2\text{O}_3$ ), identified using X-ray diffraction (not shown).

This phase evolution indicates a reduction in O content within the PPB oxide, providing further evidence of an apparent O exchange reaction. Residual  $\text{Fe}_2\text{Hf}$  intermetallic precipitates also were found in both CR-144Hf-Ti (Figure 8.9B1-2) and CR-156Y-Hf (Figure 8.9C1-2). The volume percent of this intermetallic phase was measured to be  $1.2 \pm 0.1$  vol.% and  $0.8 \pm 0.05$  vol.% in CR-144Hf-Y and CR-156Y-Hf, respectively.



**Figure 8.9. As-reacted SEM analysis of heat treated (1300°C-1hr) CR-alloys: A1-A2) CR-118Ti-Y, B1-B2) CR-144Hf-Y, and C1-C2) CR-156Y-Hf**

TEM analysis of the as-reacted specimens confirmed the formation of nano-metric oxide dispersoids throughout the CR-alloy microstructure (See Figure 8.10). The distribution and morphology of the nano-metric oxide dispersoids were found to be significantly different between CR-118Ti-Y and CR-144Hf-Y or CR-156Y-Hf. The nano-metric oxides found in CR-118Ti-Y were more evenly distributed throughout the alloy microstructure (Figure 8.10A1-2), in comparison to the dispersoids found in CR-144Hf-Y and CR-156Y-Hf, which seemed to form primarily around previous as-solidified cell boundaries (Figure 8.10B1-2 and Figure 8.10C1-2). The dispersoids

found in CR-118Ti-Y also contained a cuboidal morphology, in contrast to the more spherical morphology associated with dispersoids found in CR-144Hf-Y and CR-156Y-Hf. The size of the dispersoids ranged between 5-100nm in each CR-alloy, although the majority of the dispersoids seemed to be less than 50nm. Several larger Ti-enriched oxides also were found in the CR-118Ti-Y microstructure (Figure 8.10A1).

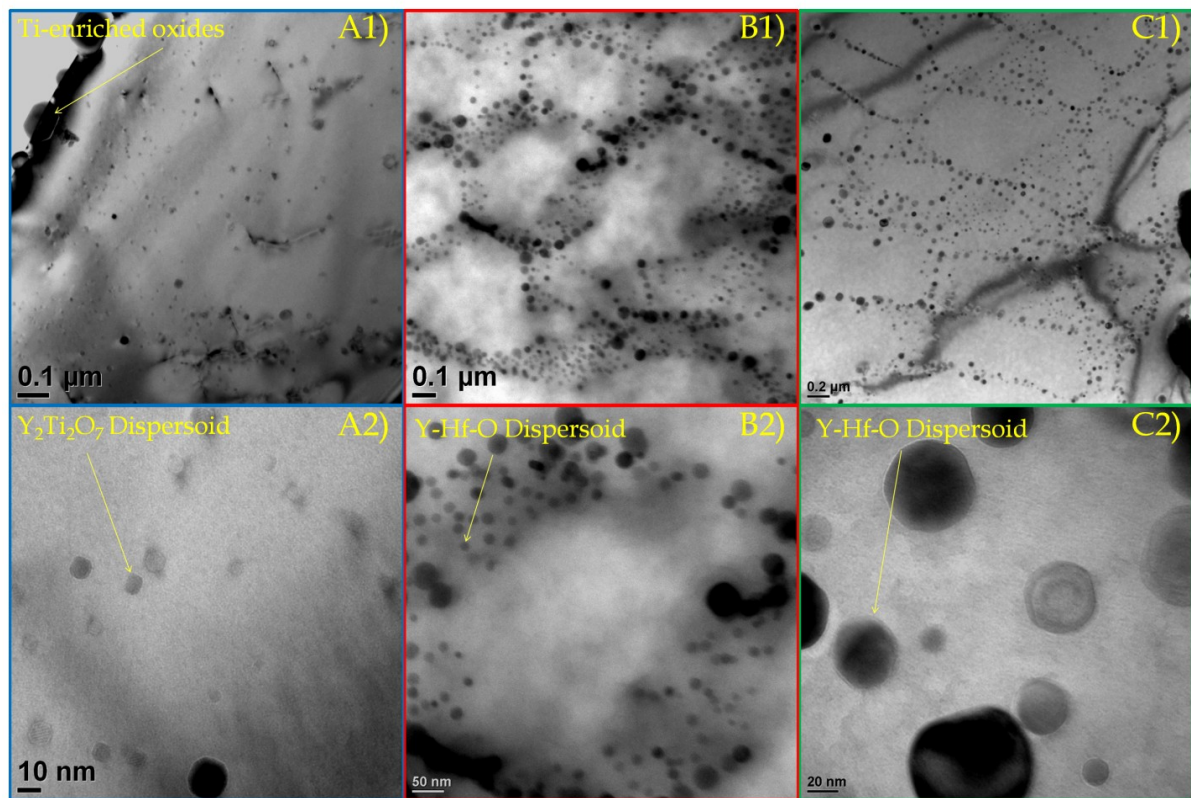


**Figure 8.10.** As-reacted TEM-BFI analysis of heat treated (1300°C-1hr) CR-alloys: A1-A2) CR-118Ti-Y, B1-B2) CR-144Hf-Y, and C1-C2) CR-156Y-Hf

Elementally sensitive EFTEM mapping was used to highlight compositional changes between the matrix and nano-metric oxide dispersoids within as-reacted (H.T. 1200°C-2.5hr) CR-alloy microstructures (Figure 8.11-Figure 8.13). These maps qualitatively indicate element enrichment using bright contrast and element deficiency using dark contrast. This analysis showed that the dispersoids in CR-



118Ti-Y were enriched in O, Ti, and Y (Figure 8.11). It also should be noted that several of the oxide particles in CR-118Ti-Y seemed to contain an enriched core of O, Ti, and Y, while the exterior envelope of the particle seemed to contain more Fe and Cr. Additionally, EFTEM analysis confirmed that dispersoids formed in as-reacted CR-144Hf-Y (Figure 8.12) and CR-156Y-Hf (Figure 8.13) contained varying amounts of O, Hf, and Y. These results provide evidence that the dispersoids form as mixed oxide precipitates, which contain varying amounts of Y-(Ti or Hf)-O. The addition of Ti or Hf is intended to further stabilize the dispersoid phase by creating complexity in oxide stoichiometry, which could require coupled multicomponent diffusion during coarsening. Similar alloying techniques have been used to develop coarsening resistant multicomponent carbides ( $M_2C$ ) in Fe [217].

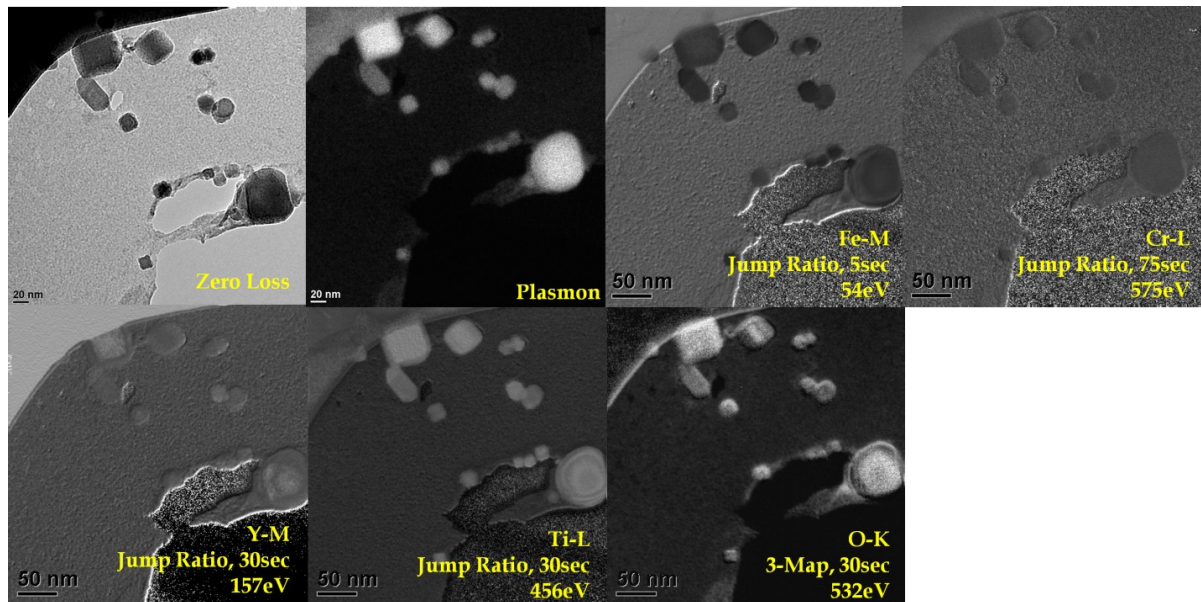


Figure 8.11. As-reacted (H.T. 1200°C-2.5hr) CR-118Ti-Y EFTEM chemical mapping of nano-metric oxide dispersoids

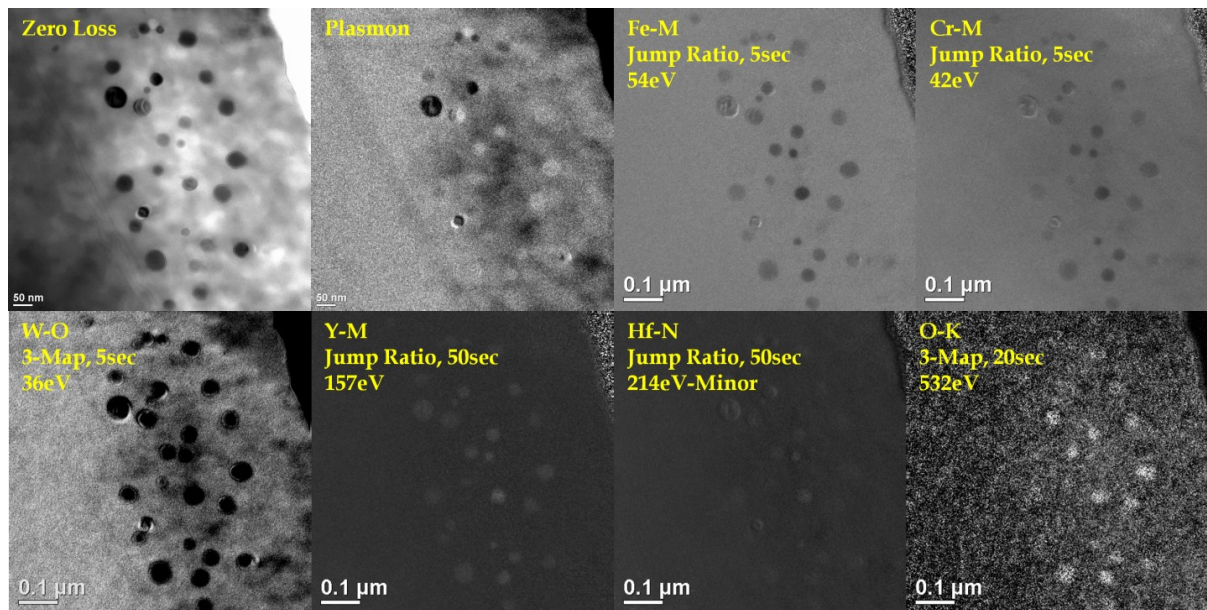


Figure 8.12. As-reacted (H.T. 1200°C-2.5hr) CR-144Hf-Y EFTEM chemical mapping of nano-metric oxide dispersoids

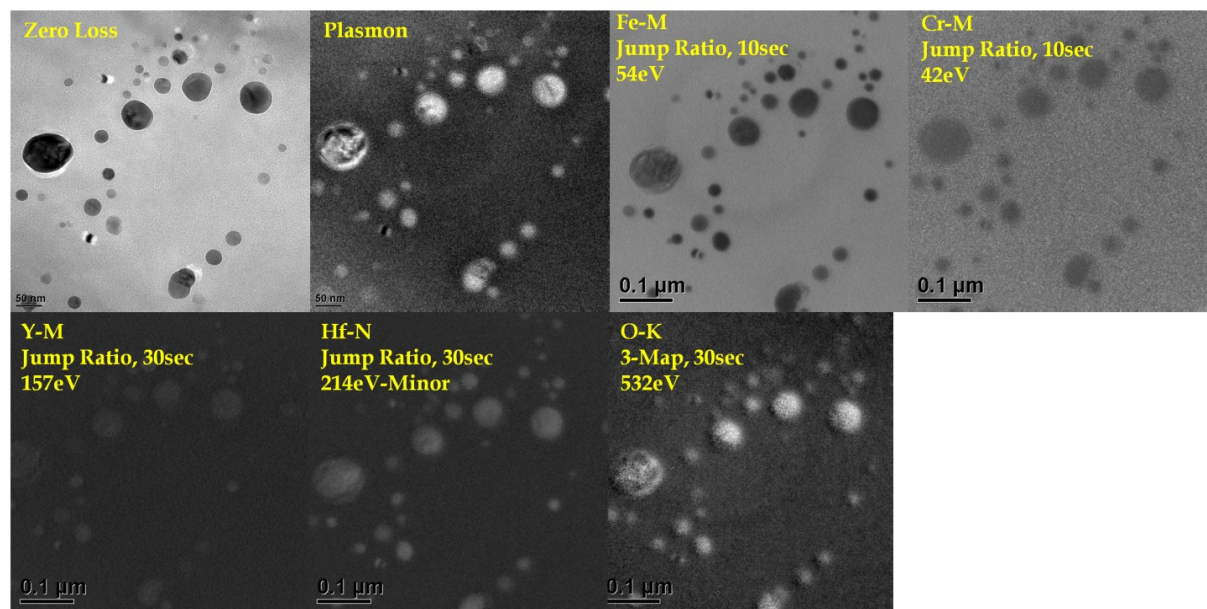


Figure 8.13. As-reacted (H.T. 1200°C-2.5hr) CR-156Y-Hf EFTEM chemical mapping of nano-metric oxide dispersoids

#### 8.4.5 X-ray Diffraction Analysis

X-ray diffraction was used to identify the crystal structure of the nano-metric oxide dispersoids in each as-reacted CR-alloy. The relative Q-space ( $\text{\AA}^{-1}$ ) of interest is highlighted in Figure 8.14. Dispersoid phase formation was detected in all post heat treated CR-alloy samples, but not in the as-atomized or as-consolidated samples. Diffraction peaks representing  $\text{Y}_2\text{Ti}_2\text{O}_7$  (Figure 8.14-dashed blue vertical line) were observed in heat treated CR-118Ti-Y specimens (Figure 8.14-blue diffraction pattern). Alternatively, dispersoids that formed in CR-144Hf-Y (Figure 8.14-red diffraction pattern) were found to contain a crystal structure most closely related to  $\text{HfO}_2$  (Figure 8.14-dashed light-red vertical line) or  $\text{Y}_2\text{Hf}_2\text{O}_7$  (Figure 8.14-dashed dark-red vertical line), while dispersoids in CR-156Y-Hf (Figure 8.14-green diffraction pattern) were found to contain a  $\text{Y}_2\text{O}_3$  (Figure 8.14-dashed green vertical line) crystal structure.

Apparent dispersoid size was estimated using the Scherrer formula (Equation 92) [216]. This formula predicts crystallite size as a function of peak broadening:

$$t \approx \frac{k\lambda}{\beta \cos \theta_\beta} \quad \text{Equation 92}$$

Where,  $t$  is equal to dispersoid thickness,  $k$  is a shape constant,  $\lambda$  is incident X-ray wavelength,  $\beta$  is the measured peak broadening at full width half max, and  $\theta$  is the Bragg angle. A shape constant of 0.8551 was used for the cuboidal dispersoids in CR-118Ti-Y and a shape constant of 0.8290 was used for the spherical dispersoids in CR-144Hf-Y and CR-156Y-Hf [218]. The calculated dispersoid crystallite size for each CR-alloy as a function of heat treatment temperature is shown in Figure 8.15.

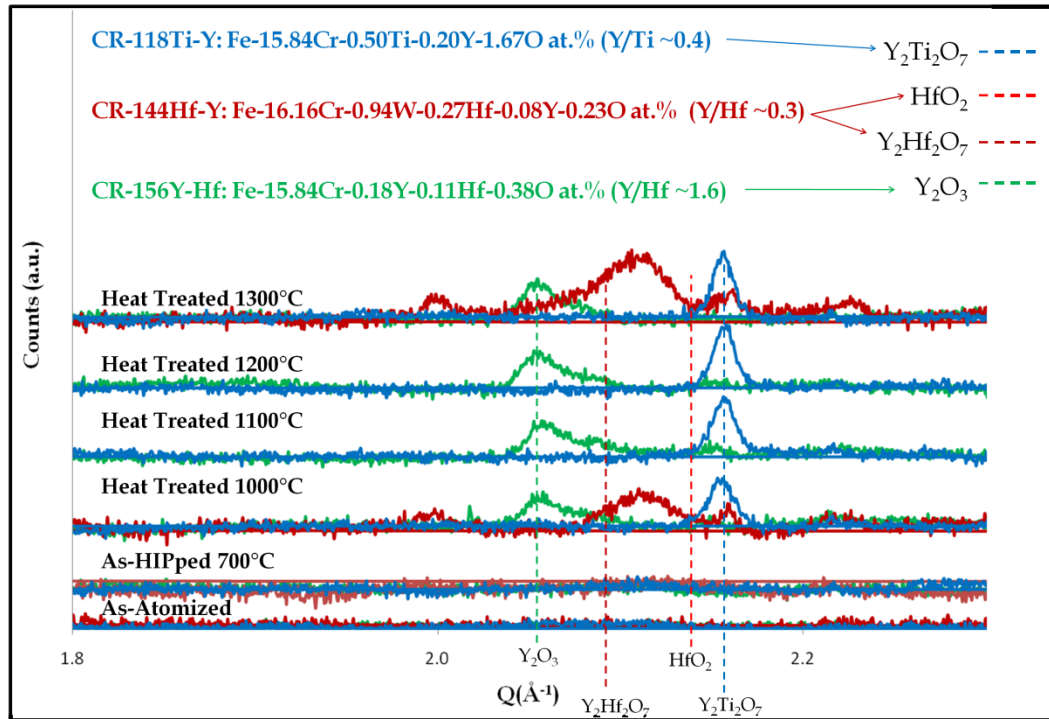


Figure 8.14. X-ray diffraction phase analysis of as-atomized, as-consolidated, and as-reacted CR-118Ti-Y (blue), CR-144Hf-Y (red), and CR-156Y-Hf (green)

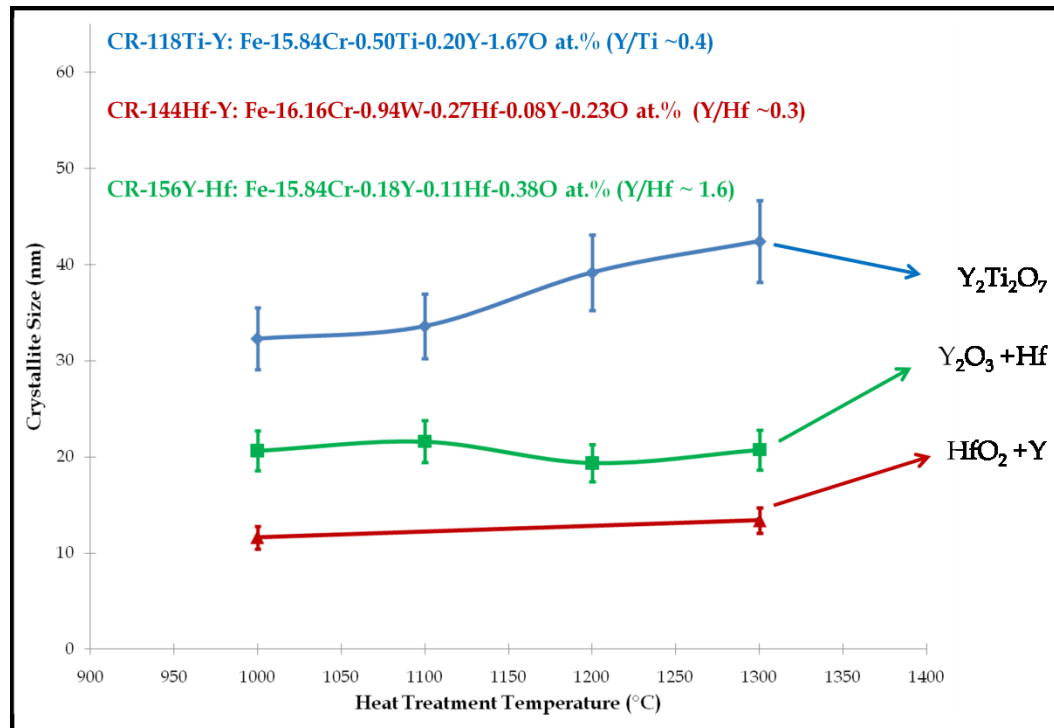


Figure 8.15. Crystallite size analysis of resulting nano-metric oxide dispersoids formed during heat treatment of CR-118Ti-Y (blue), CR-144Hf-Y (red), and CR-156Y-Hf (green)

## 8.5 Discussion

### 8.5.1 Gas Atomization Reaction Synthesis

Precisely controlling the addition of O during rapid solidification is germane to this novel processing technique. Over saturating the CR-alloys with O will prevent complete dissolution of the PPB oxide layer, while insufficient amounts of O may result in residual intermetallic precipitates (e.g.,  $\text{Fe}_{17}\text{Y}_2$ ) persisting throughout the as-reacted microstructure. The critical concentration of O will depend on the stoichiometry of the resulting dispersoid phase. For example, if the resulting dispersoid phase is  $\text{Y}_2\text{Ti}_2\text{O}_7$ , then the concentration of O would need to be 3.5 times the concentration of Y. Additionally, relative O content is influenced by specific surface area of the powders, which results in an O concentration gradient as a function of particle size (See Figure 8.4). This effect requires careful classification of resulting CR-alloy powder, in order to select powders with an ideal O/Y concentration ratio for consolidation.

Interestingly, O content in the reaction gas was found to have a progressive linear effect on resulting O content in as-atomized powders. This result made it possible to precisely predict resulting O content in CR-156Y-Hf. Unfortunately, the O/Y ratio was found to be lower (i.e.,  $\sim 2.1$ ) than predicted (i.e.,  $\sim 3.5$ ), due to excess Y. The resulting Y content in CR-156Y-Hf was designed to be 0.11 at.%, but excess Y (i.e.,  $\sim 60\%$  increase) was added to the atomization charge to account for predicted losses to the melt slag, but only  $\sim 40\%$  of the excess Y was lost during melting. Although this newest attempt (CR-156Y-Hf) at achieving an ideal balance of O/Y was unsuccessful, it did show a clear ability to predict O content using the aforementioned progressive linear model.

### 8.5.2 Microstructure Analysis

The as-solidified CR-alloy powders were enveloped by a metastable Cr-enriched oxide layer during GARS processing (Figure 8.5). The exact chemistry of this metastable Cr-enriched oxide layer is quite difficult to measure due to its thickness (e.g., ~7-80nm). In addition, X-ray diffraction experiments were unable to identify the surface oxide crystal structure (not shown), suggesting that this surface oxide phase could be amorphous. Oxide layer formation occurs throughout rapid solidification and cooling of powders, during which atomic movement is severely limited and oxidation progresses in a kinetically favored manner. It seems that the activity of Cr in these CR-alloys is sufficient to promote Cr-enriched oxide formation, while preventing consumption of Y during this reaction.

Thickness of the Cr-enriched surface oxide layer was directly related to reaction temperature and O<sub>2</sub> content in the reactive gas. Injecting the reactive gas through the close-coupled HPGA nozzle promoted rapid oxidation of the CR-alloy droplets. Alternatively, surface oxidation was significantly reduced by injecting the reactive gas after primary atomization using the downstream near-field über halo. The kinetics of this reaction seems to be more dependent on reaction temperature as opposed to O<sub>2</sub> content in the reactive gas. As a result, oxide layer thickness was reduced by ~80% in CR-144Hf-Y (Figure 8.5B1), in comparison to CR-156Y-Hf (Figure 8.5C1), although the reactive gas contained twice the concentration of O<sub>2</sub>.

Microsegregation was found to occur during rapid solidification of these CR-alloys. This was most noticeable in the Hf containing CR-144Hf-Y and CR-156Y-Hf powders. The solubility of Hf and Y is severely limited in  $\alpha$ -Fe [210, 219], therefore these atoms are rejected during nucleation and growth of the  $\alpha$ -Fe lattice, resulting in solute pile-up (i.e., microsegregation) along as-solidified cell boundaries. This creates a continuous network of dispersoid forming solute, which will subsequently be transformed into high number densities of nano-metric oxide dispersoids during



elevated temperature heat treatment. Furthermore, this network will likely define the size and distribution of any resulting dislocation substructure, which would be stabilized by the oxide dispersoids and used for ultimate strengthening of the alloy [78, 79, 214]. Additionally, microsegregation appeared to be prevented in ultra-fine (dia. < 5 $\mu$ m) CR-156Y-Hf powders (Figure 8.6C2), where dramatic increases in particle solidification rate and decreased recalescence effects permit apparent complete solute trapping of Hf and Y [104]. Aging these powders, during consolidation, would provide an opportunity to control precipitation and growth of Fe-(Hf,Y) intermetallic precipitates from the supersaturated solid solution, which could result in smaller and more evenly distributed oxide dispersoids within the as-reacted microstructure. On the other hand, similar CR-144Hf-Y powders (dia. < 5 $\mu$ m) still contained significant microsegregation, an effect potentially caused by the addition of W (See Table 8.2). W is a potent  $\alpha$ -Fe solid solution strengthener, providing significant lattice strain, which could prevent further solute entrapment during solidification. Furthermore, the addition of W might increase the nucleant density within the molten CR-alloy, which could have limited droplet undercooling during atomization, resulting in decreased solidification velocities and increased microsegregation.

Interconnected PPB oxide was found in both CR-118Ti-Y and CR-156Y-Hf following low temperature (i.e., 700°C) consolidation. The PPB oxide in CR-118Ti-Y evolved into mostly  $\text{Ti}_3\text{O}_5$ , according to XRD results (not shown), which illustrates the instability of the initial Cr-enriched metastable oxide layer. Alternatively, the PPB oxide in CR-156Y-Hf was seemingly unchanged, remaining Cr-enriched, which provides insight into the activation energy required for considerable Hf or Y diffusion, in comparison to Ti diffusion in  $\alpha$ -Fe. Further stabilization of the PPB oxide phase prior to dispersoid formation (e.g.,  $\text{Cr}_x\text{O}_y \rightarrow \text{Ti}_x\text{O}_y$ ) is unfavorable, since it could significantly decrease the O exchange rate between the PPB oxide and Y-

enriched IMC precipitates, which could result in unnecessary IMC precipitate coarsening and an increased dispersoid size.

Elevated temperature heat treatment ( $T > 1000^{\circ}\text{C}$  - See Table 8.3) was used to promote an O exchange reaction between less stable PPB oxide and Y-enriched IMC precipitates, which resulted in the formation of nano-metric oxide dispersoids throughout the CR-alloy microstructures. This thermally activated reaction is thought to be controlled by the free energy of formation for oxides (Figure 8.16). It is theorized, that during heat treatment, O diffuses away from PPB oxides, driven by a concentration gradient or chemical potential, in order to reach equilibrium concentrations within  $\alpha\text{-Fe}$ . Throughout this process, soluble O combines with Y-enriched IMC precipitates forming highly stable nano-metric oxide dispersoids (e.g.,  $7\text{O} + 2\text{Fe}_{11}\text{TiY} \rightarrow \text{Y}_2\text{Ti}_2\text{O}_7 + 22\text{Fe}$ ). This reaction should continue until all PPB oxide is dissociated or until all Y has been reacted, which again highlights the importance of achieving an ideal balance between O and Y within the as-atomized powders.

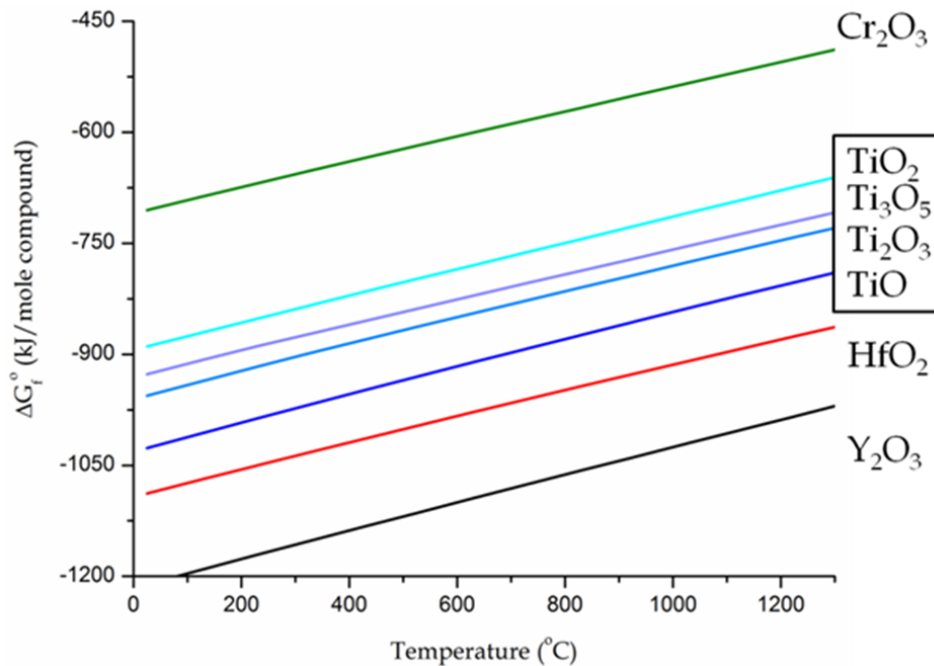


Figure 8.16. Free energy of formation for potential CR-alloy oxides [128]



Specific dispersoid phase formation was influenced by the initial CR-alloy chemistry. Preliminary dispersoid phase identification was achieved by coupling the X-ray diffraction results with EFTEM chemical mapping data. It was found that the addition of Ti resulted in the formation of  $\text{Y}_2\text{Ti}_2\text{O}_7$  dispersoids, while the addition of Hf resulted in mixed Y-Hf-O dispersoids. Furthermore, dispersoid formation in Hf-containing CR-alloys was influenced by the ratio of Y/Hf. When the ratio of  $\text{Y/Hf} < 1$  (i.e., CR-144Hf-Y) the dispersoids seemed to form as  $\text{HfO}_2\text{+Y}$  (See Figure 8.12 and Figure 8.14), but when  $\text{Y/Hf} > 1$  (i.e., CR-156Y-Hf) the dispersoids seemed to form as  $\text{Y}_2\text{O}_3\text{+Hf}$  (See Figure 8.13 and Figure 8.14).

Microsegregation during rapid solidification of the CR-alloy powders was shown to dictate distribution patterns of the nano-metric oxide dispersoids (See Figure 8.6 and Figure 8.10). This effect was most noticeable in the Hf containing CR-alloys. A direct correlation between as-solidified cell size and resulting oxide dispersoid network spacing is apparent in CR-144Hf-Y and CR-156Y-Hf. This correlation shows that a specific oxide dispersoid network could be tailored by selecting as-atomized particles with an ideal initial cell size. Additionally, consolidation and heat treatment of supersaturated single phase particles (i.e., dia.  $< 5\mu\text{m}$  for CR-156Y-Hf) could significantly reduce the average oxide dispersoid network spacing, through controlled precipitation of Fe-(Y,Hf) intermetallic precipitates.

A difference in dispersoid morphology is thought to be related to the strain energy at the dispersoid/matrix interface. The Gibbs-Wulff theorem shows that precipitate morphology is controlled by the shape which results in the lowest interfacial free energy for a given volume, thus a precipitate grows by allowing planes with lower interfacial free energy to occupy more of the surface [80, 220, 221]. The dispersoids formed in CR-118Ti-Y (i.e.,  $\text{Y}_2\text{Ti}_2\text{O}_7$ ) contained a cuboidal morphology, suggesting some degree of lattice coherency along certain  $\alpha\text{-Fe}$  planes. Furthermore, these dispersoids have been shown to contain a Kurdjumov-Sachs orientation relationship

within  $\alpha$ -Fe [222]. However, the dispersoids formed in CR-144Hf-Y (i.e., HfO<sub>2</sub>+Y) and CR-156Y-Hf (i.e., Y<sub>2</sub>O<sub>3</sub>+Hf) contained a spherical morphology, which minimizes surface area for a given volume, suggesting incoherency between these dispersoids and  $\alpha$ -Fe. This incoherency could be related to the increased d-spacing associated with these dispersoids (See Figure 8.14).

### 8.5.3 Dispersoid Stability

An increase in dispersoid thermal stability was achieved in CR-144Hf-Y (i.e., HfO<sub>2</sub>+Y) and CR-156Y-Hf (i.e., Y<sub>2</sub>O<sub>3</sub>+Hf), in comparison to dispersoids found in CR-118Ti-Y (i.e., Y<sub>2</sub>Ti<sub>2</sub>O<sub>7</sub>) (See Figure 8.15). This increased stability is believed to result from the improved coarsening resistance attained by replacing Ti with Hf. Diffusion of Hf in  $\alpha$ -Fe is significantly slower than that of Ti (Table 8.4), a result likely caused by its larger metallic radius and increased molar mass [223]. Classical volume-controlled diffusion coarsening theory is shown in Equation 93 [224, 225]:

$$r^3 - r_o^3 = \frac{4}{9}K(t - t_o) \quad \text{Equation 93}$$

Where,  $r$  is average particle radius after time  $t$ ,  $r_o$  is initial particle radius at time  $t_o$ , and  $K$  is the kinetic rate constant defined by Equation 94:

$$K = \frac{2D_M^\alpha C_\infty \sigma_s V_m}{RT} \quad \text{Equation 94}$$

Where,  $D_M^\alpha$  is diffusivity coefficient for element M in matrix  $\alpha$ ,  $C_\infty$  is equilibrium solid solubility limit of solute in the matrix,  $\sigma_s$  is interfacial free energy between the matrix and precipitate,  $V_m$  is molar volume of the precipitate,  $R$  is the gas constant, and  $T$  is absolute temperature.

This theory has been shown to work well in predicting the coarsening rate of precipitates in binary solutions [225], but decreased coarsening rates associated with multicomponent precipitates require slight modifications to the rate constant [226].

Equation 95 defines an effective rate constant ( $K_{eff}$ ) for the coarsening kinetics of multicomponent precipitates in Fe [226]:

$$K_{eff} = \frac{8\sigma_s V_m^\beta}{9RT \ln(2A_s)} \left[ \sum_M (k_M - k_{Fe})(k_M - 1) \frac{X_{M,\infty}^\alpha}{D_M^\alpha} \right]^{-1} \quad \text{Equation 95}$$

Where,  $k_M$  is partitioning coefficient of element M,  $X_{M,\infty}^\alpha$  is mole fraction of element M in the matrix phase at equilibrium with a particle of infinite radius, and  $A_s$  is particle aspect ratio.

This model describes coarsening of multicomponent precipitates through parallel diffusion of precipitate elements, and indicates that the slowest moving element will still dominate the coarsening rate [217, 226].

Diffusion data for the dispersoid forming elements in  $\alpha$ -Fe are shown in Table 8.4. This data indicates a vast decrease in diffusion rate between Hf and Ti, which offers a possible explanation to the aforementioned increase in thermal stability witnessed among Hf containing dispersoids. In addition, the diffusion data for Y could not be identified in the literature, although, if Y diffusion was rate limiting during coarsening of these dispersoids, then the average dispersoid size would be anticipated to be more consistent between all CR-alloys. These preliminary stability results offer motivation for a more in depth coarsening study of the dispersoids found in these CR-alloys.

**Table 8.4. Diffusion data for dispersoid forming elements**

Element	$D_0$ (cm <sup>2</sup> /s)	Q (kJ)	$D_{1300^\circ\text{C}}$ (cm <sup>2</sup> /s)	Ref.
<b>O</b>	$2.9 \times 10^{-3}$	89.5	$3.1 \times 10^{-6}$	[227]
<b>Y</b>	U	U	-	-
<b>Hf</b>	1.31	290.1	$3.0 \times 10^{-10}$	[228]
<b>Ti</b>	0.56	216.5	$3.6 \times 10^{-8}$	[229]

U = Unknown Value

## 8.6 Summary

Gas atomization reaction synthesis was used for the production of precursor oxide dispersion forming ferritic stainless steel powders. A progressive linear model was used to accurately predict resulting O content within the most recent as-atomized CR-alloy. The formation of nano-metric oxide dispersoids occurred, during heat treatment of as-consolidated specimens, through internal O exchange between less stable PPB oxide and Y-containing IMC precipitates. Dispersoid distribution was found to be influenced by microsegregation that occurs during rapid solidification of the CR-alloy powders. Apparent dispersoid thermal stability was increased by replacing Ti with Hf in CR-144Hf-Y and CR-156Y-Hf, which resulted in the formation of mixed Y-Hf-O dispersoids.

## 8.7 Acknowledgements

Support from the Department of Energy, Office of Fossil Energy (ARM program) through Ames Laboratory contract no. DE-AC02-07CH11358 is gratefully acknowledged. The authors also would like to thank Jim Anderegg, Matt Besser, and Jamie Thompson for their individual contributions to this paper.

## Chapter 9. Innovative Powder Processing of Oxide Dispersion Strengthened (ODS) Ferritic Stainless Steels

Modified from a paper published in: *Advances in Powder Metallurgy and Particulate Materials*, 2011, Vol. 2, pp. 31-49

J. R. Rieken<sup>1,2,3</sup>, I.E. Anderson<sup>4</sup>, and M.J. Kramer<sup>4</sup>

### 9.1 Abstract

An innovative gas atomization reaction synthesis technique was employed as a viable method to dramatically lower the processing cost for precursor oxide dispersion forming ferritic stainless steel powders (i.e., Fe-Cr-(Hf,Ti)-Y). During this rapid solidification process the atomized powders were enveloped by a nano-metric Cr-enriched metastable oxide layer. Elevated temperature heat treatment was used to dissociate this metastable oxide phase through oxygen exchange reactions with Y-(Hf,Ti) enriched intermetallic compound precipitates. These solid state reactions resulted in the formation of highly stable nano-metric mixed oxide dispersoids (i.e., Y-Ti-O or Y-Hf-O) throughout the alloy microstructure. Subsequent high temperature (1200°C) heat treatments were used to elucidate the thermal stability of each nano-metric oxide dispersoid phase. Transmission electron microscopy coupled with X-ray diffraction was used to evaluate phase evolution within the alloy microstructure.

---

<sup>1</sup> Graduate Student, Department of Materials Science and Engineering, Iowa State University

<sup>2</sup> Primary researcher and author

<sup>3</sup> Author for correspondence: Tel.: +1 515 294 9159, E-mail address: [jrieken@iastate.edu](mailto:jrieken@iastate.edu)

<sup>4</sup> Division of Materials Sciences and Engineering, Ames Laboratory (USDOE), Ames, IA 50011

## 9.2 Introduction

Oxide dispersion strengthened (ODS) ferritic stainless steel alloys offer improved high temperature strength and creep resistance [1, 2, 202]. For this reason, these alloys are being considered for high temperature applications within future generation thermal power reactors [8, 9, 16, 38]. The improved mechanical properties associated with ODS alloys stems from interactions between nano-metric oxide dispersoids and dislocations within the alloy microstructure [3, 70, 80]. The dispersoids act as pinning points that stabilize the alloy grain or sub-grain structure by impeding dislocation movement. Essentially, the effectiveness of the dispersoids to immobilize a dislocation can be thought of as a force balance between driving and dragging forces over a given dislocation line length [230]. Consequently, the resulting ODS grain or sub-grain structure is dependent on the size, distribution, and volume fraction of the dispersoid phase. For this reason, the high temperature microstructure stability of the ODS alloy is inherently linked to the thermal stability of the dispersoid phase.

Gas atomization reaction synthesis (GARS) was employed, as an economic alternative to the traditional high cost mechanical alloying (MA) processing route, for the production of oxide dispersion forming ferritic stainless steel particulate [14, 15]. During this process, a reactive atomization gas (i.e., Ar-O<sub>2</sub>) is used to oxidize the surface of nascent molten metal droplets *in situ* during primary break-up and rapid solidification of the alloy. This rapid solidification process promotes the formation of an ultra-thin kinetically favored metastable Cr-enriched surface oxide layer, which is used as a vehicle to transport a prescribed amount of solid-state O into the consolidated microstructure. Elevated temperature heat-treatments are then used to drive an internal O exchange reaction between the metastable Cr-enriched prior particle boundary (PPB) oxide and Y-enriched intermetallic compound (IMC) precipitates. This results in the formation of Y-enriched nano-metric oxide dispersoids throughout the alloy microstructure [146, 179].

The size and distribution of the resulting Y-enriched dispersoids is controlled by the length-scale of microsegregation that occurs upon rapid solidification within the powders (i.e., particles with increased amounts of solute trapping or highly refined solidification structures result in smaller and more evenly distributed nano-metric oxide dispersoids) [146]. This offers the unique ability to tailor ODS microstructures as a function of precursor powder size (i.e., powder solidification rate).

The aim of this study was to further examine the GARS process as a function of alloy composition. The resulting microstructural evolution and dispersoid thermal stability will be discussed in detail.

### 9.3 Procedure

#### 9.3.1 Gas Atomization Reaction Synthesis

The nominal atomization charge chemistry for both CR-164HfY and CR-166TiY is displayed in Table 9.1 [206]. The charge was melted in a yttria ( $Y_2O_3$ ) painted zirconia ( $ZrO_2$ ) bottom pour crucible and superheated to 1700°C. The melt pour was initiated by raising a pneumatically actuated composite ( $Y_2O_3$ -W- $Al_2O_3$ ) stopper rod, which allowed the molten alloy to flow through a plasma sprayed  $Y_2O_3$  lined  $ZrO_2$  pour tube.

**Table 9.1. Resulting chemical reservoir (CR) alloy composition with respect to powder particle size for CR-164HfY (dia. < 20 $\mu$ m) and CR-166TiY (dia. < 20 $\mu$ m)**

Alloy	Powder Size	Fe (at.%)	Cr (at.%)	Y (at.%)	Hf (at.%)	Ti (at.%)	O (at.%)
CR-164HfY	Nominal	Bal.	16.00	0.21	0.12	-	-
CR-166TiY	Nominal	Bal.	16.00	0.21	-	0.12	-
CR-164HfY	< 20 $\mu$ m	Bal.	15.55	0.09	0.12	-	1.04
CR-166TiY	< 20 $\mu$ m	Bal.	15.91	0.09	-	0.12	0.49

Upon exiting the pouring orifice, the melt was immediately impinged by the reactive atomization gas. This gas contained 0.19 vol.%  $O_2$  mixed with high purity

Ar and was directly injected through the high pressure close-coupled atomization die at a pressure of 6.55MPa.

The resulting as-atomized powders were mechanical sieved into specific size divisions (i.e., <20, 20-45, and 45-75 $\mu$ m) prior to chemical or microstructural evaluation. Powder particles with a dia. < 20 $\mu$ m were selected for comparison between CR-164HfY and CR-166TiY. The bulk O content for each powder alloy was measured using an inert gas fusion (LECO) analyzer, while the percentage of each metallic constituent was identified using inductively coupled plasma / mass spectroscopy (ICP/MS).

### **9.3.2 Hot Consolidation and Thermal Treatment**

As-atomized powders from each alloy were placed into individual 316L stainless steel cans measuring 25.4 mm in dia. x 127 mm in length (see Figure 9.1). Each can was evacuated to a pressure of  $\sim 10^{-4}$  Pa, outgassed at 415°C for 1hr, and electron-beam welded shut using a 316L stainless steel cap. The atomized powders then were consolidated using hot isostatic pressing (HIPing) at 700°C with 300MPa pressure for 4hrs. An example of the as-consolidated HIP can also is displayed in Figure 9.1.

The 316L HIP can was turned off following consolidation and the resulting rods were sectioned into 20 mm dia. x 10 mm length disks. The as-HIPed disks were then heat treated under vacuum ( $\sim 10^{-4}$  Pa) at 1200°C for 2.5hrs. This heat treatment schedule had previously been reported as an effective method for forming nanometric oxide dispersoids within similar CR-alloys [231]. Additionally, two disks from each alloy were further heat treated under vacuum ( $\sim 10^{-4}$  Pa) at 1200°C for a total time of 100 and 1,000hrs.



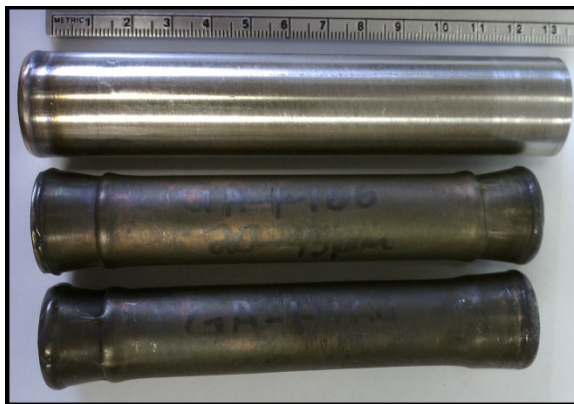


Figure 9.1. 316L stainless steel HIP can geometry and resulting as-consolidated HIP bars

### 9.3.3 Microstructure Characterization

Surface analysis of the as-atomized powder particles was conducted using a JEOL JAMP 7830F scanning Auger microprobe (SAM) with a hemispherical auger electron spectrometer (AES) and Ar-ion sputtering gun for depth profiling.

The nano-metric oxide layer at the surface of the as-atomized powders was evaluated using an FEI Tecnai F20ST transmission electron microscope (TEM) / scanning transmission electron microscope (STEM) at the Electron Microscopy Center (EMC) for Materials Research at Argonne National Laboratory. The powder particles also were prepared for TEM/STEM analysis at the EMC using a Zeiss 1540XB focused ion beam (FIB) scanning electron microscope (SEM). The powders were coated with a thin layer of Au ( $t \sim 20\text{nm}$ ) prior to FIB milling to protect the as-atomized surface oxide layer. Additionally, carbon deposition was used to bond the powders to a manipulator during FIB milling and to secure the as-thinned specimen to a slotted Cu TEM grid prior to analysis.

The interior microstructure of the powders was examined using a JEOL 5910LV SEM with energy dispersive spectrometer (EDS). Electron probe microanalysis (EPMA) chemical mapping of the powder microstructure was completed using a JEOL JXA-8200 WD/ED microanalyzer.

The consolidated and heat treated alloy microstructures were analyzed in the as-polished and as-etched condition using a Hitachi S-2460N SEM with EDS. The  $\alpha$ -Fe grains were revealed by dip-etching the as-polished SEM samples into a ferritic stainless steel etchant (i.e., 30 ml hydrochloric acid, 30 ml glycerol, and 10 ml nitric acid) for ~60s. The grain size was measured using lineal intercept method according to ASTM E112 - 96 (2004).

Additionally, the nano-metric features present in the consolidated and heat treated samples were characterized using a Tecnai G<sup>2</sup> F20 TEM/STEM at 200 keV. Miniature cylinders measuring 3 mm in dia. x 10 mm in length were cut from each sample disk using wire electro-discharge machining. These cylinders were subsequently sliced into 1 mm thick sections, ground flat using 400 and 600 SiC grit paper, polished using 6.0 $\mu$ m and 1.0 $\mu$ m diamond polishing compound, mechanically dimpled to a thickness of ~20 $\mu$ m and dual jet polished using an electrolytic solution for stainless steels (i.e., 700ml methanol, 120ml distilled water, 100ml glycerol, and 80ml perchloric acid) at -21°C in preparation for TEM analysis.

The presence of Y-enriched nano-metric oxide dispersoids was verified within each step of this simplified process using a Phillips PANalytical X-Pert Pro Diffraction System with Co-K $\alpha$  radiation. A scanning real time multiple strip (RTMS) X-ray detector was used with an active length of ~0.05 Q ( $\text{\AA}^{-1}$ ). Diffraction data was collected from 1.8-4.8 Q ( $\text{\AA}^{-1}$ ) with a step size of  $5 \times 10^{-4}$  Q and a dwell time of 500 s per step. The reciprocal lattice vector (Q) describes the momentum difference between incoming and diffracted X-rays (Equation 96), and is commonly used to compare X-ray diffraction data (i.e., Bragg angle ( $\theta$ ) of resulting peaks) independent of wavelength ( $\lambda$ ) [216].

$$Q = \frac{4\pi \sin \theta}{\lambda} \quad \text{Equation 96}$$

The microhardness of each heat treated sample was measured using Vickers diamond pyramid indentation with a 500gm load. The average of 10 consecutive indentations for each sample was plotted for each data point.

## 9.4 Results

### 9.4.1 Gas Atomization Reaction Synthesis

The resulting as-atomized chemical reservoir (CR) alloy chemistry can be found in Table 9.1. Each CR-alloy contained an equivalent atomic fraction of Y + group IV (Hf or Ti) alloying addition. Alternatively, powders from CR-164HfY contained approximately twice the amount of O compared to CR-166TiY.

An example of the as-atomized powder (dia. < 20 $\mu$ m) morphology can be seen in Figure 9.2A and B. The resulting powders were found to be quite spherical with very few satellite particles. It seems that the thin surface oxide film formed during this GARS process protects the powders during solidification and prevents bonding from occurring during particle-particle collisions.

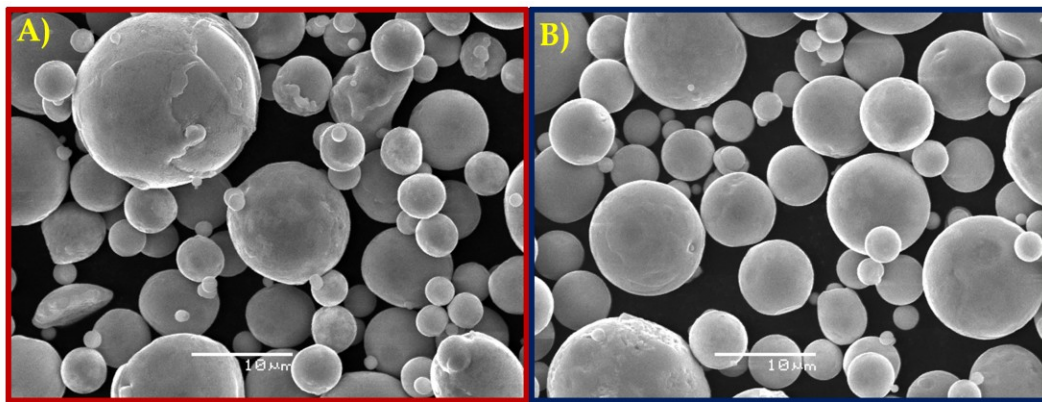


Figure 9.2. As-atomized powder (dia. < 20 $\mu$ m) morphology: A) CR-164HfY and B) CR-166TiY

AES depth profile chemical analysis of powders (~20 $\mu$ m in dia.) from each CR-alloy revealed a surface enrichment of O and Cr (see Figure 9.3A and B), indicative of a Cr-enriched surface oxide layer. Additionally, a slight denuded zone of Fe also was

identified at the surface of the powder particles. The average surface oxide thickness was measured at  $\sim 105\text{nm}$  and  $\sim 52\text{nm}$  for CR-164HfY and CR-166TiY, respectively (see vertical orange dashed line in Figure 9.3A and B). The increase in surface oxide layer thickness identified on the CR-164HfY powders accounts for the increase in O concentration compared to CR-166TiY (see Table 9.1).

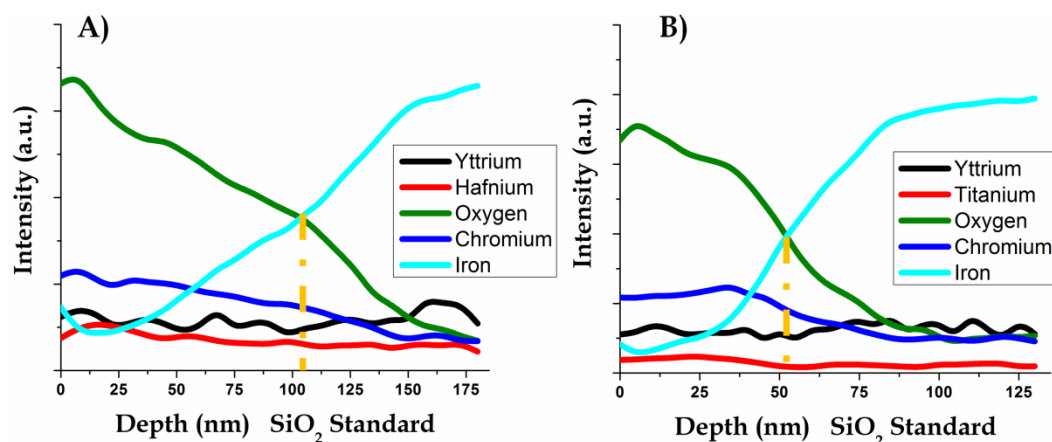


Figure 9.3. AES depth profile chemical surface analysis of as-atomized powders ( $\sim 20\mu\text{m}$  in dia.):  
A) CR-164HfY and B) CR-166TiY

The physical presence of a surface oxide layer was observed utilizing TEM analysis of an as-atomized powder specimen (see Figure 9.4). This analysis was conducted on a CR-164HfY powder particle measuring  $\sim 2\mu\text{m}$  in diameter (note: this powder size was selected due to difficulties in manipulating larger particles within the FIB-SEM). The ultra-thin surface oxide layer was found encapsulating the powder particle and was measured at a thickness of  $\sim 10\text{nm}$ . A qualitative chemical analysis of the surface oxide layer was completed using STEM with an EDS linescan across the surface oxide phase (see horizontal orange line in Figure 9.4C). This qualitative analysis identified an enrichment of Cr (yellow line) and O (green line) within the surface oxide layer, which agreed well with the aforementioned AES depth profile measurements. Additionally, a slight denuded zone of Cr was identified within the

$\alpha$ -(Fe,Cr) matrix near the surface oxide interface, illustrating that Cr was pulled from solution during this rapid oxidation process.

Furthermore, the apparent variation in oxide layer thickness between the smaller  $\sim 2\mu\text{m}$  dia. powder particle (see Figure 9.4B:  $t \sim 10\text{nm}$ ) and the larger  $\sim 20\mu\text{m}$  dia. powder particles (see Figure 9.3A:  $t \sim 105\text{nm}$ ) illustrates the effect of cooling rate on surface oxide layer growth. Thus, it is reasonable to assume smaller powders will form a thinner surface oxide layer, due to increased convective heat extraction as a result of larger surface area to volume ratios.

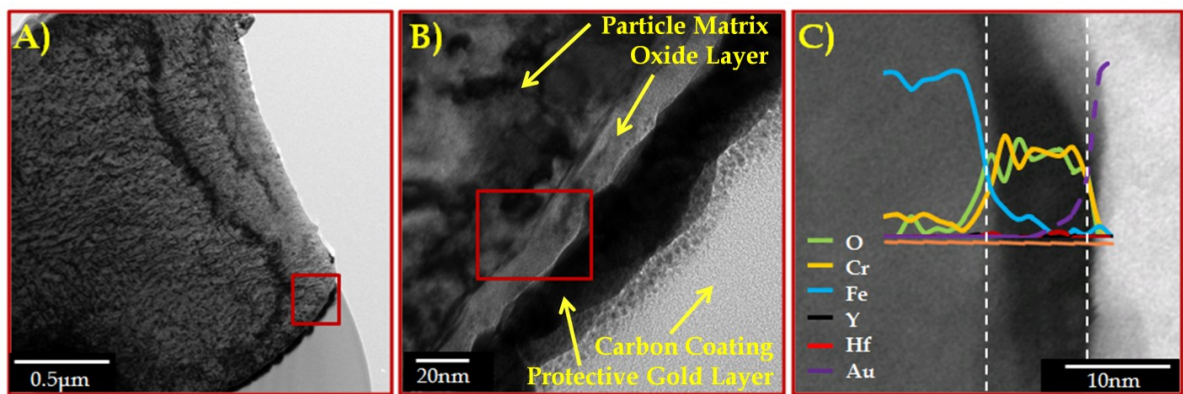


Figure 9.4. TEM/STEM analysis of a CR-164HfY (dia.  $\sim 2\mu\text{m}$ ) powder particle: A) and B) bright field images (BFIs) identifying the surface oxide layer and C) high angle annular dark field (HAADF) image with EDS linescan across the surface oxide layer

Cross-sectional analysis of the CR-alloy powders revealed microsegregation along the as-solidified cell boundaries (see yellow arrows in Figure 9.5). EPMA chemical mapping was used to identify elemental concentrations at the cell boundaries. The bright phase identified within the CR-164HfY powders was found to be enriched in Y and Hf (see yellow arrow in Figure 9.5A and C). Additionally, a region of apparent solid solution was identified near the surface of the powder particles extending to a depth of  $\sim 1\text{-}2\mu\text{m}$  (see red arrow in Figure 9.5A). Microsegregation was not readily apparent within the as-solidified CR-166TiY powders (Figure 9.5B),



but EPMA chemical mapping identified increased concentrations of Y along the as-solidified cell boundaries (Figure 9.5D).

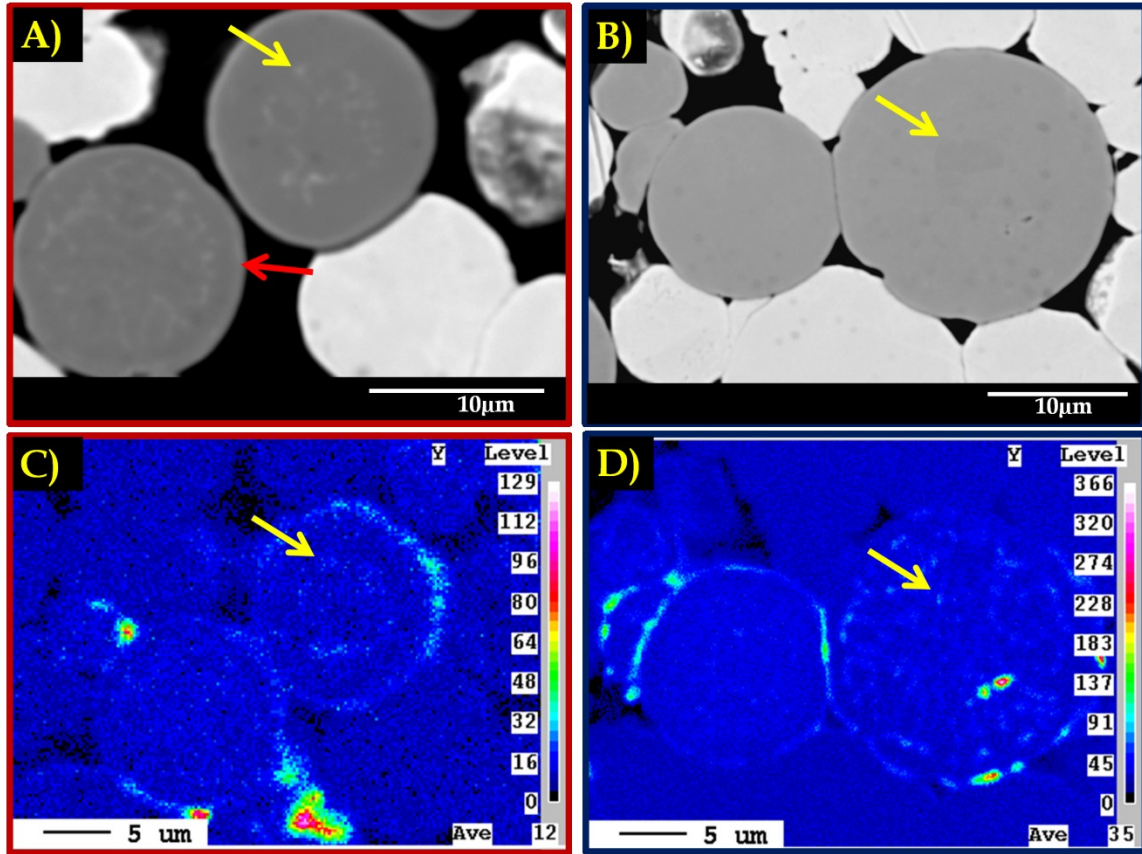


Figure 9.5. Cross-sectional SEM-EPMA analysis of the CR-alloy powders with corresponding Y-concentration map: A) and C) CR-164HfY and B) and D) CR-166TiY

#### 9.4.2 Dispersoid Formation

Low temperature HIPing (700°C – 300MPa – 4hr) was used to fully consolidate the as-atomized CR-alloy powders. Microstructural analysis of the as-consolidated samples revealed a continuous network of Cr-enriched oxide along the PPBs (see yellow arrows in Figure 9.6A and B). The volume percent of PPB oxide was measured, using image analysis software (i.e., Image-Pro™), at  $\sim 3.0 \pm 0.5$  and  $\sim 2.1 \pm 0.4$  vol. % for CR-164HfY and CR-166TiY, respectively. Furthermore, each as-consolidated sample contained an internal structure of intermetallic particles that

seemed to outline the previous as-solidified cell boundaries (see red arrows in Figure 9.6A and B).

TEM analysis was used to evaluate features within the as-consolidated microstructure at a much finer size scale. This analysis illustrated the formation of fine intermetallic compound (IMC) precipitates along cell boundaries within the  $\alpha$ -(Fe,Cr) matrix (see yellow arrows in Figure 9.7A and B). These IMC phases were later identified as Fe-(Hf,Y) (i.e.,  $\text{Fe}_2\text{Hf}$  and  $\text{Fe}_{17}\text{Y}_2$ ) in CR-164HfY and Fe-(Y,Ti) (i.e.,  $\text{Fe}_{11}\text{YTi}$ ) in CR-166TiY using XRD (results not shown).

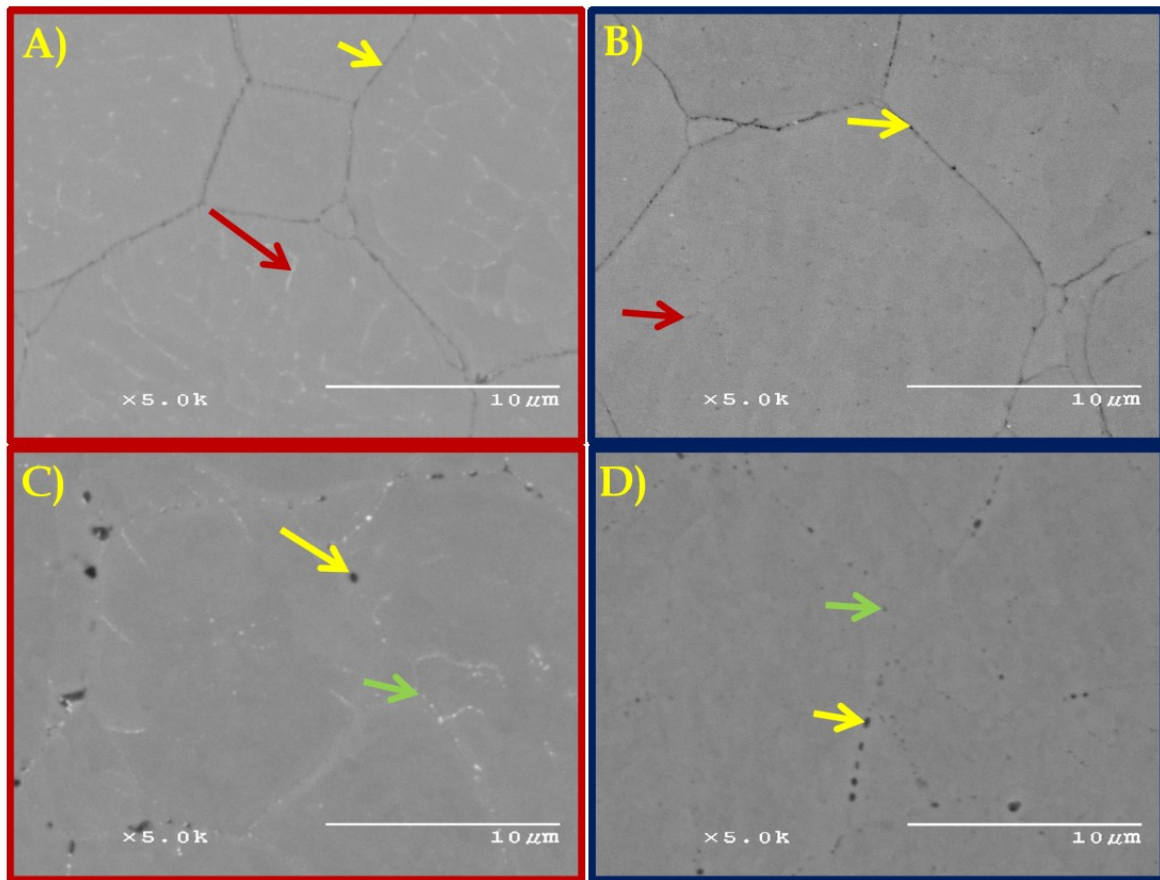


Figure 9.6. SEM (BEC) analysis of the as-HIPed and heat treated microstructure: A) and C) CR-164HfY (outlined in red) and B) and D) CR-166TiY (outlined in blue)

Elevated temperature (1200°C) heat treatment was used to promote the internal O-exchange reaction between the metastable Cr-enriched PPB oxide and internal Y-containing IMC precipitates. During this reaction the volume percent of PPB oxide was reduced to  $\sim 1.5 \pm 0.4$  and  $\sim 0.4 \pm 0.1$  vol. % in CR-164HfY and CR-166TiY, respectively (see yellow arrows in Figure 9.6C and D). Interestingly, the PPB oxide chemistry was seemingly unchanged in CR-164HfY (i.e., remaining Cr-enriched), but evolved into a mixed Ti-Cr oxide in CR-166TiY (i.e., Ti-Cr-O). This provides some insight into the relative diffusivity difference between Ti and Hf within the  $\alpha$ -(Fe,Cr) matrix.

Additionally, the Y-containing IMC precipitates seemed to be fully consumed or transformed during this internal O-exchange reaction. This reaction resulted in the formation of mixed oxide dispersoids throughout the alloy microstructure. Larger mixed oxide particles seemed to form at grain boundaries, as a result of increased reactive element (i.e., Y, Hf, and Ti) concentration, in conjunction with enhanced diffusion kinetics (see green arrows in Figure 9.6C and D).

TEM analysis of the as-heat treated microstructure revealed a more uniform distribution of nano-metric oxide dispersoids throughout the alloy microstructure (see Figure 9.7C and D). The volume fraction of these oxide particles was measured at  $\sim 0.5$  vol. % for both CR-alloys through refinement of XRD data (results not shown). Furthermore, the number density of the oxide particles was calculated at  $\sim 3 \times 10^{21} \text{ m}^{-3}$  for each CR-alloy, assuming a TEM foil thickness of 100nm. These nano-metric dispersoids also were found to contain a spheroidal morphology.



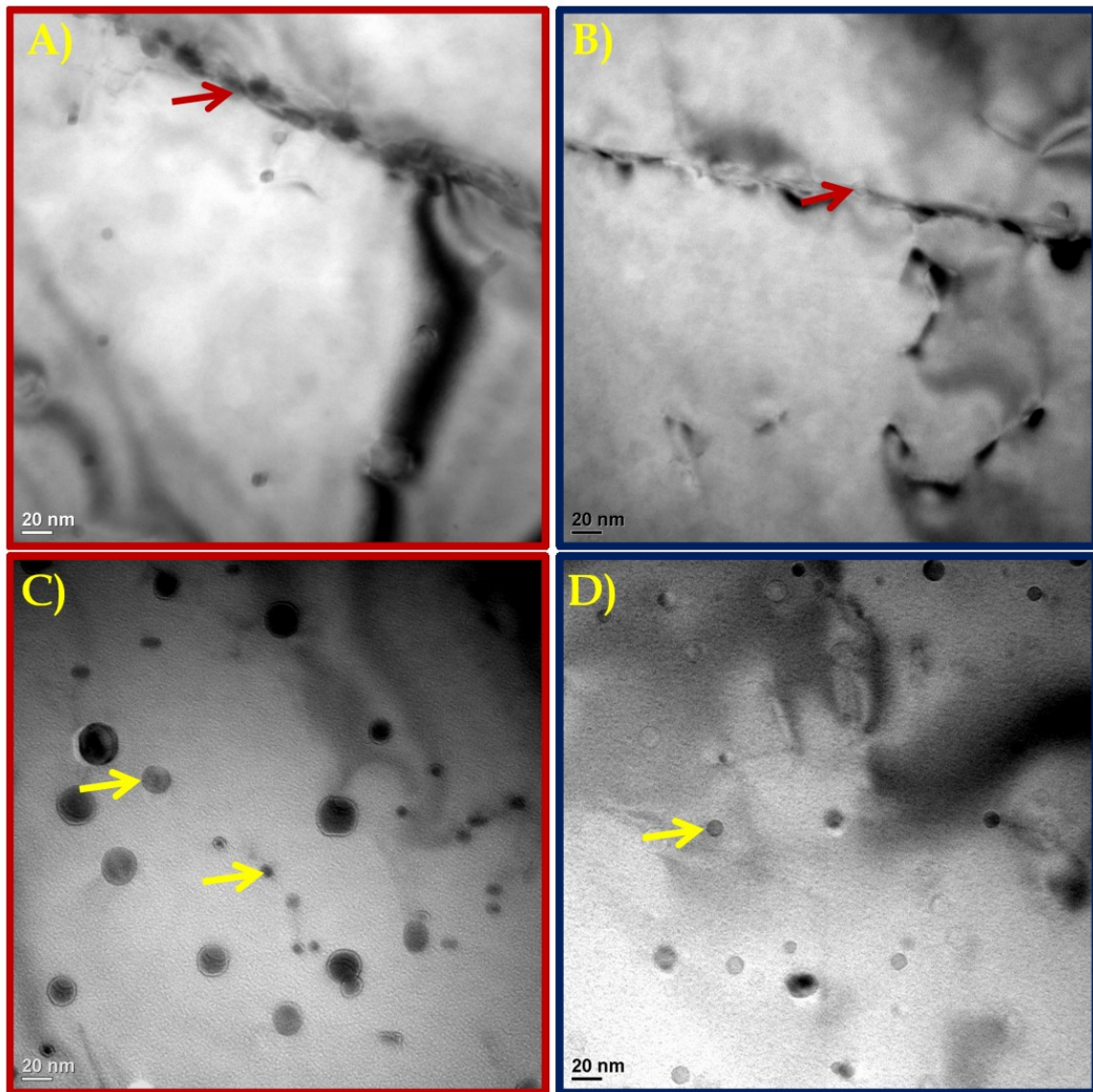
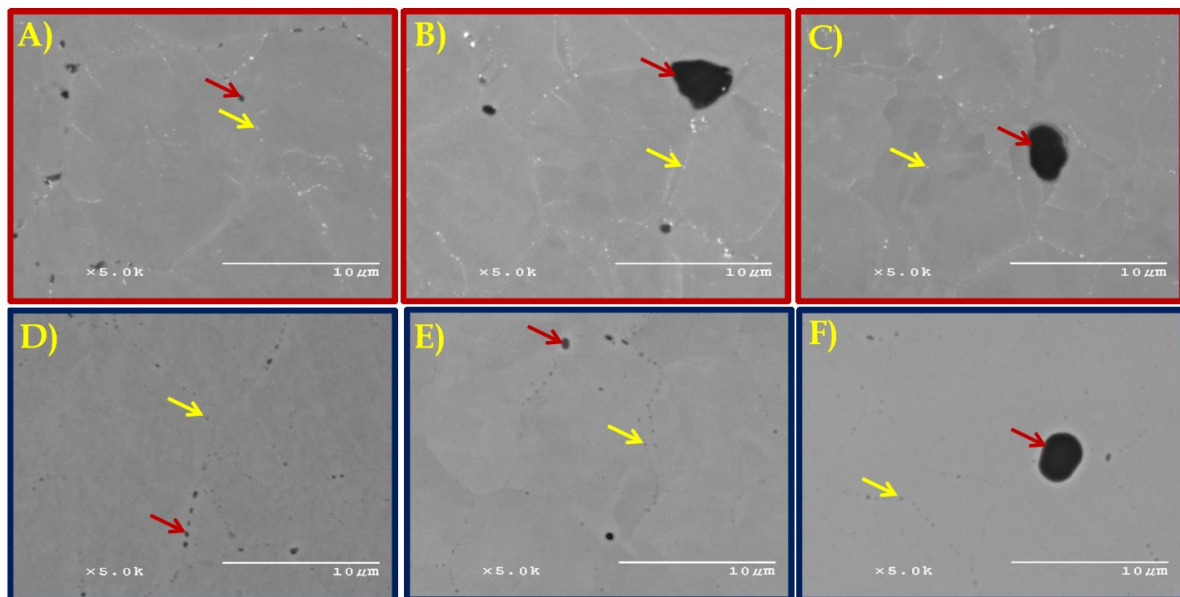


Figure 9.7. TEM (BFI) analysis of the as-HIPped and heat treated microstructure: A) and C) CR-164HfY (outlined in red) and B) and D) CR-166TiY (outlined in blue)

#### 9.4.3 Dispersoid Thermal Stability

Extended (i.e., 2.5, 100 and 1,000hrs) elevated temperature (1200°C) heat treatments were used to evaluate the thermal stability of the nano-metric oxide dispersoids. SEM analysis revealed a severe difference in coarsening rate between the residual PPB oxide (see red arrows in Figure 9.8) and larger Hf or Ti enriched oxide particles

(see yellow arrows in Figure 9.8) within both CR-alloy microstructures. Additionally, this analysis reveals the importance of fully dissolving the PPB oxide, in order to prevent large precipitate formation during coarsening of the microstructure, which could act as void nucleation sites leading to subsequent crack formation during operational use of such materials. Complete dissociation of the PPB oxide should be possible through the internal O exchange reaction, if an optimum balance of Y/O is achieved during initial GARS processing [179].



**Figure 9.8. SEM (BEC) analysis of CR-164HfY (outlined in red) and CR-166TiY (outlined in blue) following heat treatment at 1200°C: A) and D) 2.5hrs, B) and E) 100hrs, and C) and F) 1,000hrs**

The thermal stability of the nano-metric oxide dispersoids within the CR-alloy matrix was evaluated using TEM-BFI analysis (see Figure 9.9). The dispersoid number density very gradually decreased as heat treatment time increased, assuming an equivalent TEM foil thickness of 100nm (Table 9.2). Overall, the dispersoids in each CR-alloy displayed remarkable thermal stability, in that, only a small degree on measurable coarsening was apparent after 1,000hrs at 1200°C.

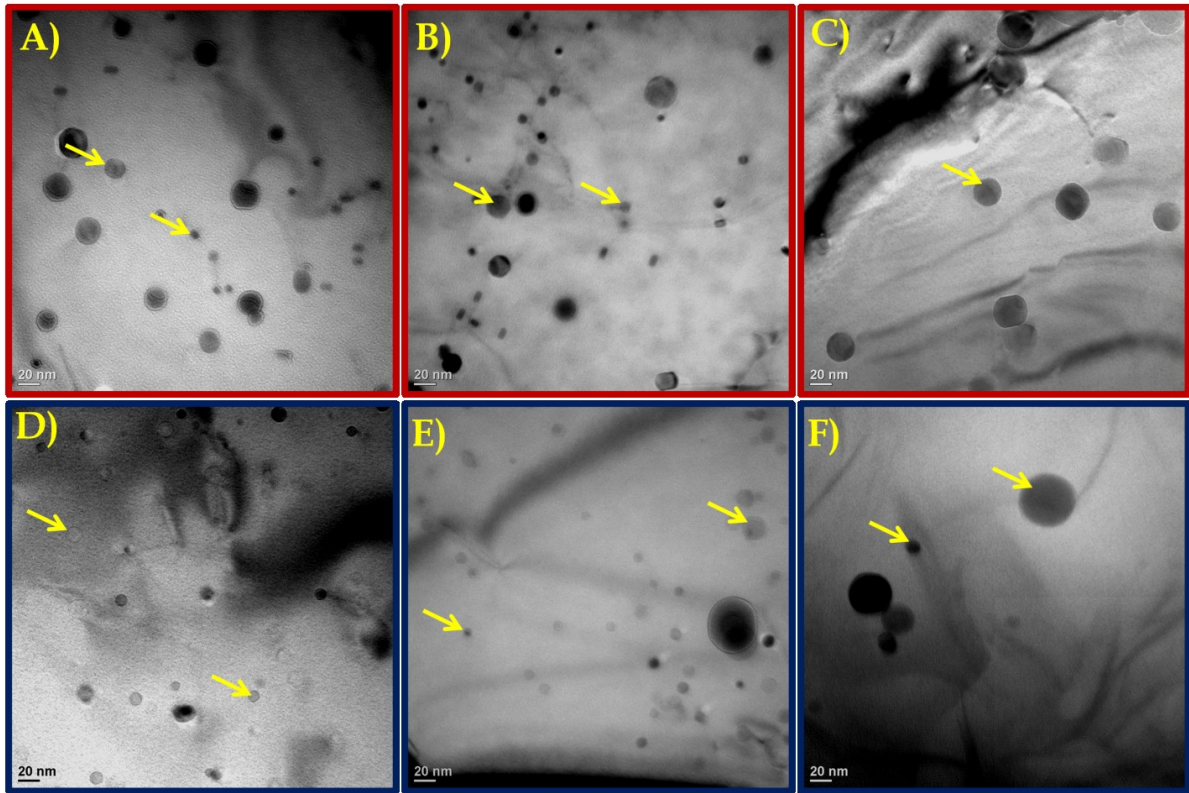


Figure 9.9. TEM-BFI analysis of CR-164HfY (outlined in red) and CR-166TiY (outlined in blue) following heat treatment at 1200°C: A) and D) 2.5hrs, B) and E) 100hrs, and C) and F) 1,000hrs

Table 9.2. Dispersoid number density as a function of heat treatment time at 1200°C

Time at 1200°C (hrs)	CR-164HfY Dispersoid No. Density (No. m <sup>-3</sup> )	CR-166TiY Dispersoid No. Density (No. m <sup>-3</sup> )
2.5	$3 \times 10^{21}$	$3 \times 10^{21}$
100	$2 \times 10^{21}$	$2 \times 10^{21}$
1,000	$9 \times 10^{20}$	$6 \times 10^{20}$

#### 9.4.4 Phase Identification

A qualitative chemical analysis of the dispersoid particles was accomplished using STEM with an EDS linescans across the nano-metric oxides (see horizontal red line in Figure 9.10B and D). The dispersoids in CR-164HfY (Figure 9.10A and B) were found to be enriched in Hf (green line) and O (blue line) with only small amounts of



Y (purple line), while the dispersoids in CR-166TiY (Figure 9.10C and D) were found to contain equal amounts of Y (dashed purple line) and Ti (green line) in addition to increased amounts of O (blue line).

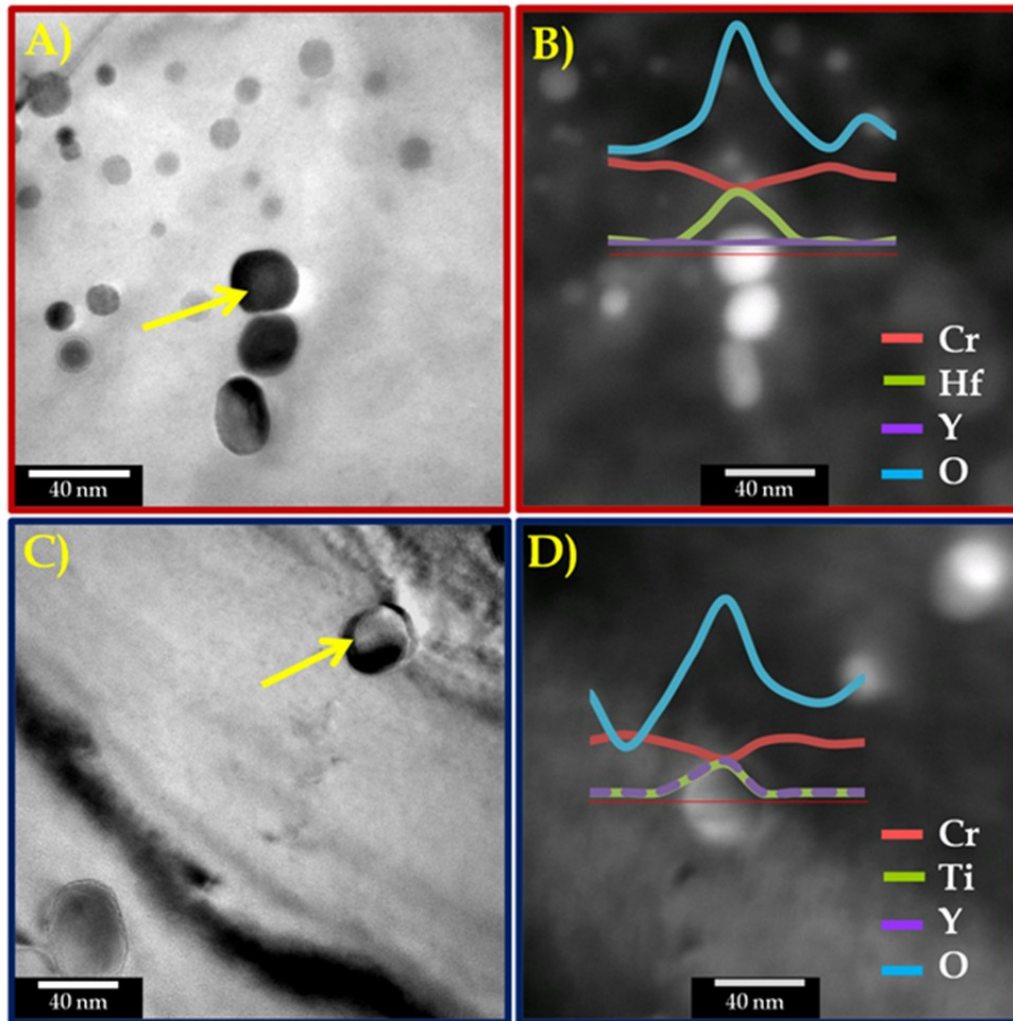


Figure 9.10. Accompanying TEM-BFI with STEM-EDS linescan chemical analysis of the nano-metric oxide dispersoids: A) and B) CR-164HfY and C) and D) CR-166TiY

XRD was used to characterize dispersoid phase formation within the CR-alloy microstructure following elevated temperature heat treatment (see Figure 9.11). These XRD results clearly indicate dispersoid formation following heat treatment at 1200°C for 2.5hrs, which agrees well with the aforementioned microstructure

analysis (see Figure 9.6 and Figure 9.7), providing further evidence of an apparent internal O-exchange reaction. The mixed oxide dispersoids were identified as either  $\text{Y}_2\text{Hf}_2\text{O}_7$  (vertically dashed light-red line) or  $\text{Y}_{0.33}\text{Hf}_{0.67}\text{O}_{1.83}$  (vertically dashed dark-red line) within CR-164HfY and as  $\text{Y}_2\text{Ti}_2\text{O}_7$  (vertically dashed blue line) within CR-166TiY. Crystal structure parameters for each phase are listed in Table 9.3.

Table 9.3. Crystal structure parameters for each possible dispersoid phase [197, 232, 233]

Phase	Space Group	Lattice Parameter (Å)	Molar Volume ( $\text{m}^3 \text{mol}^{-1}$ )
$\text{Y}_2\text{Hf}_2\text{O}_7$	Fm-3m	5.19	$2.10 \times 10^{-5}$
$\text{Y}_{0.33}\text{Hf}_{0.67}\text{O}_{1.83}$	Fm-3m	5.15	$2.06 \times 10^{-5}$
$\text{Y}_2\text{Ti}_2\text{O}_7$	Fd-3m	10.09	$7.73 \times 10^{-5}$

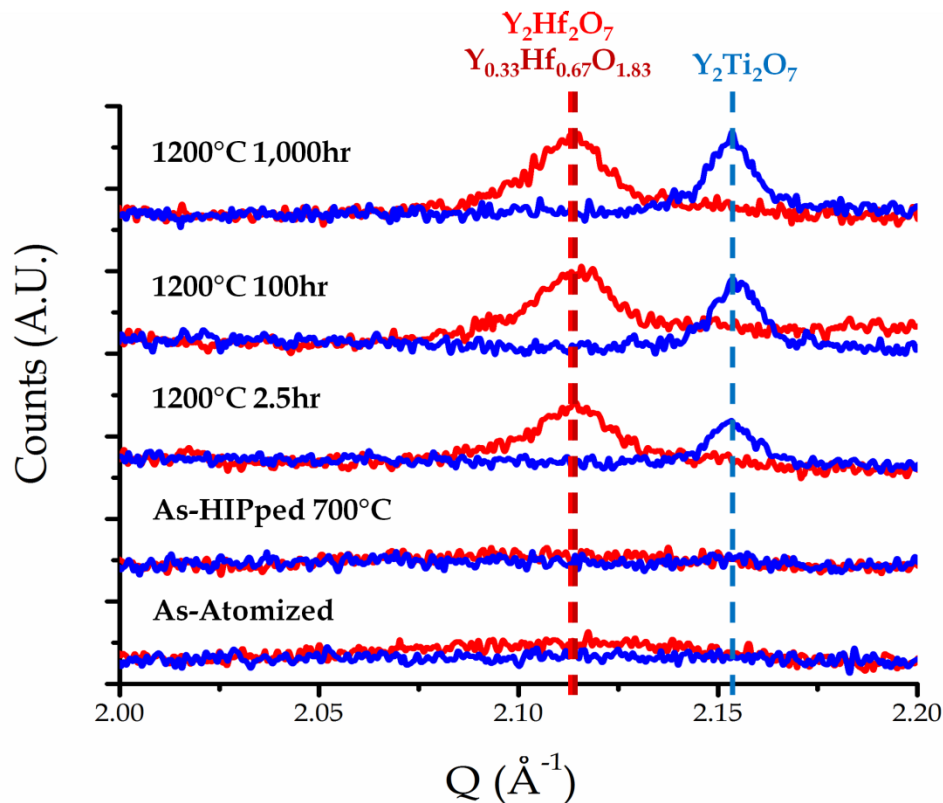


Figure 9.11. XRD results revealing dispersoid phase formation and phase stability for CR-164HfY (red lines) and CR-166TiY (blue lines)

Additionally, the XRD data (Figure 9.11) was used to calculate the average dispersoid radius using the Scherrer formula (Equation 97), which estimates crystallite size as a function of peak broadening [216].

$$t \approx \frac{k\lambda}{\beta \cos \theta_{\beta}} \quad \text{Equation 97}$$

Where,  $t$  is equal to dispersoid thickness,  $k$  is a shape constant,  $\lambda$  is incident X-ray wavelength,  $\beta$  is the measured peak broadening at full width half max, and  $\theta_B$  is the Bragg angle. A shape constant of 0.8290 was used during this analysis, due to the spheroidal morphology of the dispersoids in both CR-alloys [218].

The calculated dispersoid radius for each CR-alloy as a function of heat treatment time is displayed in Table 9.4. This analysis shows the average dispersoid radius in CR-164HfY increased ~10% after 1,000hrs at 1200°C, while the average dispersoid radius in CR-166TiY increased ~15% during the same heat treatment. This comparison signifies that the dispersoids formed within CR-164YHf are more thermally stable compared to those formed in CR-166TiY.

**Table 9.4. Calculated dispersoid radius as a function of heat treatment time at 1200°C**

Time at 1200°C	CR-164HfY	CR-166TiY
(hrs)	Calc. Dispersoid Radius (nm)	Calc. Dispersoid Radius (nm)
2.5	11.7	19.2
100	11.9	19.8
1,000	12.9	22.0

#### 9.4.5 Microhardness Evaluation

The microhardness of each CR-alloy decreased with increased heat treatment time at 1200°C (see Figure 9.12A). The decrease in microhardness is thought to be related to  $\alpha$ -(Fe,Cr) grain growth, as result of dispersoid coarsening. For this reason, the  $\alpha$ -

(Fe,Cr) grain size also was evaluated as a function of heat treatment time (see Figure 9.12B).

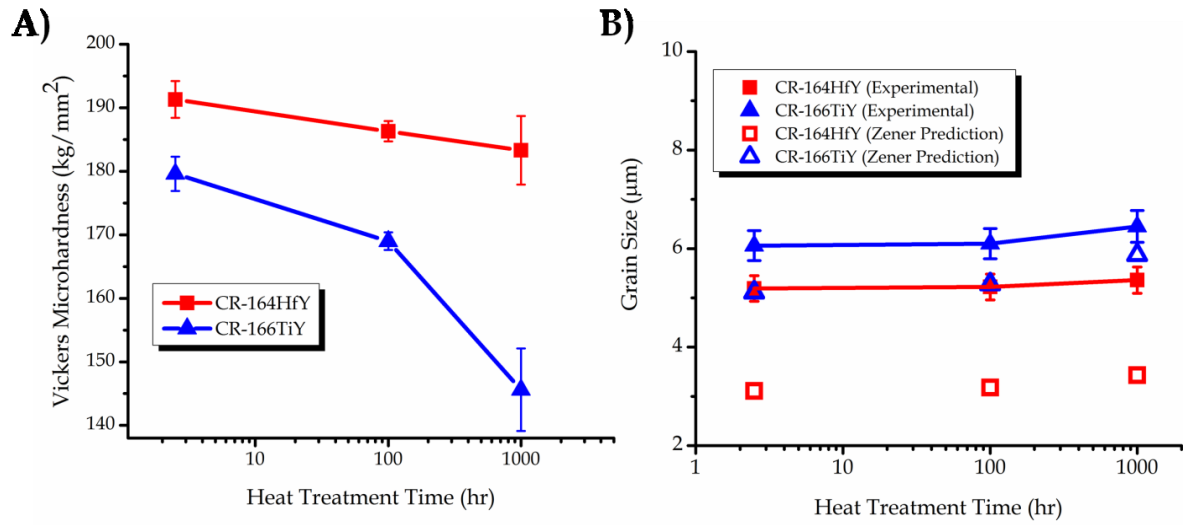


**Figure 9.12. A) microhardness evaluation as a function of heat treatment time for CR-164HfY (red line) and CR-166TiY (blue line) and B) grain growth analysis as a function of heat treatment time compared to predicted values for CR-164HfY (red line) and CR-166TiY (blue line)**

Furthermore, the measured grain size was compared with the predicted grain size using the Zener model (see Figure 9.12B). This model (Equation 98) predicts the average grain size as a function of dispersoid size and volume fraction, assuming a uniform dispersoid distribution [230].

$$R_c = \frac{4r}{3f} \quad \text{Equation 98}$$

Where,  $R_c$  is the Zener limit (i.e., predicted grain size),  $r$  is dispersoid radius, and  $f$  is dispersoid volume fraction.

## 9.5 Discussion

### 9.5.1 Gas Atomization Reaction Synthesis

The rapid oxidation kinetics associated with GARS processing have previously been found to scale linearly with the  $O_2$  content within the atomization gas (see Figure 9.13) [231]. The rate of oxidation is thought to be related to the local  $O_2$  partial pressure ( $P_{O_2}$ ), developed within the primary atomization zone, as defined by the concentration of  $O_2$  within the atomization gas. The caveat of this empirically determined relationship is that, the atomized droplets are assumed to have been exposed to the oxidizing environment for an equal duration as a function of droplet size. Therefore, modifications to the atomization processing parameters that affect melt delivery and subsequent atomization spray characteristics could significantly influence the overall oxidation of the powders from one CR-alloy to the other.

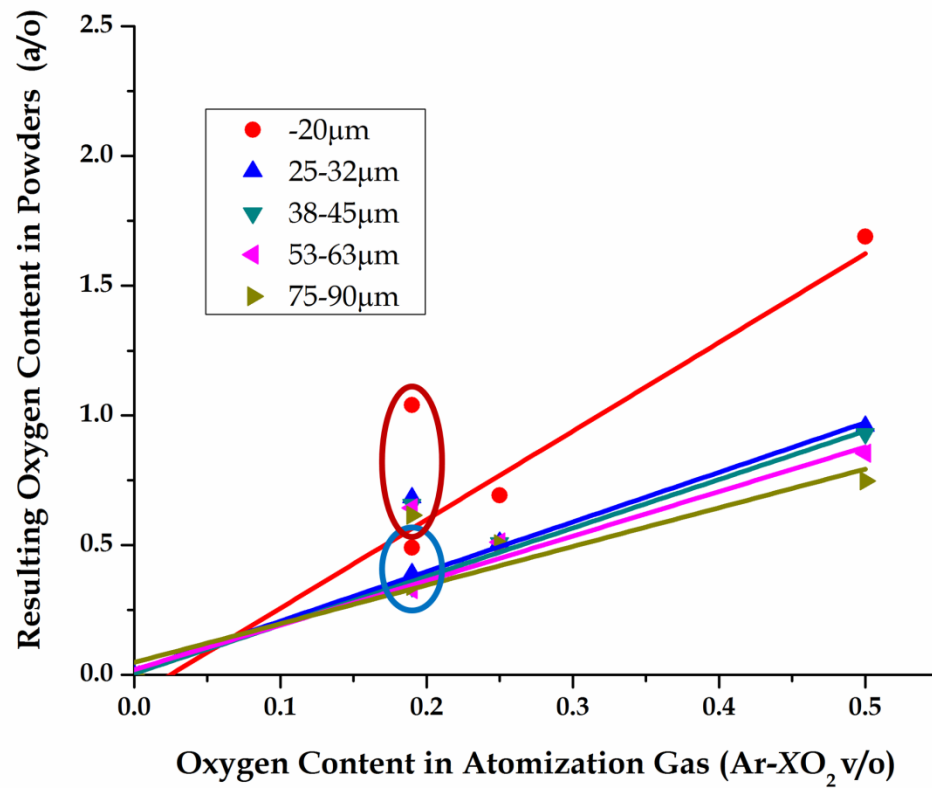


Figure 9.13. Resulting powder O content as a function of reactive atomization gas concentration: CR-164HfY (red circle) and CR-166TiY (blue circle)



Interestingly, the oxidation of CR-164HfY powders seemed to deviate from the empirically developed linear oxidation model (red circle in Figure 9.13), compared to CR-166TiY powders. This deviation is thought to be related to the change in pour tube geometry (see Figure 9.14). The pour tube used for CR-164HfY contained a flared exit orifice that came to a sharpened tip, similar to that of a trumpet (see yellow arrow in Figure 9.14A). Additionally, this pour tube contained four fins that protruded from the interior wall of the pour tube into the path of the liquid, acting as barriers to melt rotation (see red arrow in Figure 9.14). On the other hand, the exit orifice of the pour tube for CR-166TiY was partially flared and contained a blunt tip with ~1mm wall thickness (see yellow arrow in Figure 9.14C).

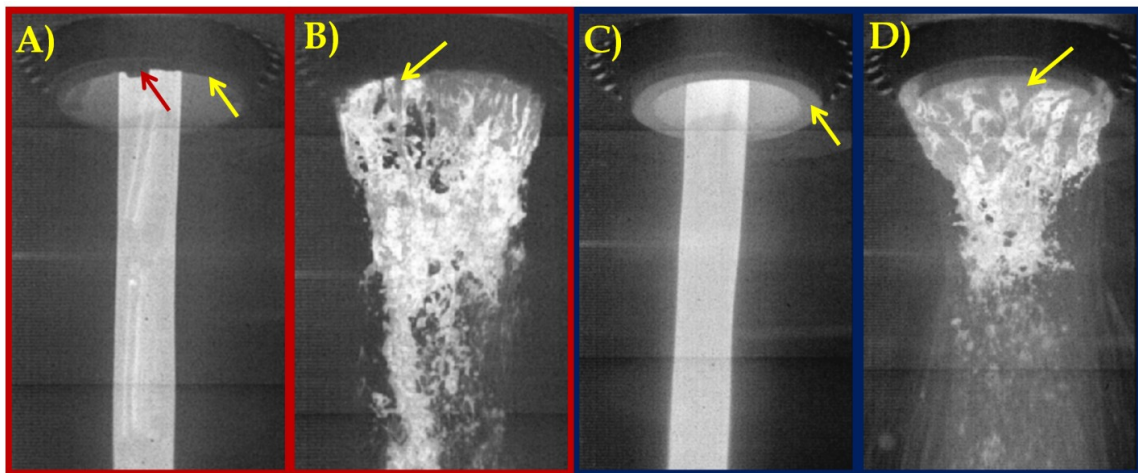


Figure 9.14. Pour tube exit geometry and atomization spray characteristics: A) and B) CR-164HfY and C) and D) CR-166TiY

Modifications to the pour tube geometry appeared to dramatically affect melt delivery and subsequent atomization break-up characteristics between the two alloys. The sharpened pour tube tip (CR-164HfY) seemed to promote increased thinning of the melt film prior to atomization compared to the blunt pour tube tip (CR-166TiY), as illustrated by the narrower melt ligaments around the periphery of the pour tube (see yellow arrows in Figure 9.14B and D). Furthermore, the

sharpened pour tube tip appeared to stabilize a hollow spray structure within the primary atomization zone (see Figure 9.14B), as direct consequence to increased melt filming. This hollow structure is believed to have extended into the internal cavity of the pour tube, thus lengthening the molten metal exposure time within the oxidizing environment, which lead to an increased O content within the CR-164HfY powders.

These results highlight the importance of controlling the atomization processing parameters and indicate the need for further GARS experimental trials, in order to better understand and model this rapid oxidation process.

### **9.5.2 Dispersoid Formation**

The rapid kinetics of this GARS process promoted the formation of an ultra-thin metastable Cr-enriched surface oxide layer (see Figure 9.3 and Figure 9.4). Upon consolidation, this kinetically favored phase was strategically positioned along internal PPBs (Figure 9.6A and B). Isolating this metastable oxide phase internally is thought to further reduce the oxide stability by lowering the O activity along the phase boundary. As a result, elevated temperature heat treatment was successful at dissociating the PPB oxide, allowing O to diffuse towards the interior of the powder particle driven by a concentration gradient. The O was subsequently consumed through internal oxidation of Y-containing IMC precipitates, which resulted in the formation of more thermodynamically stable mixed nano-metric Y-(Hf or Ti)-O dispersoids throughout the CR-alloy microstructure (see Figure 9.7C and D).

This type of O-exchange reaction is described as diffusionless internal oxidation [182], assuming the rate of reaction is controlled by the internal diffusion of only O, since Y contains limited solubility and diffusivity within the  $\alpha$ -(Fe,Cr) matrix (see Figure 9.16B). This prevents the internal O exchange reaction from occurring predominantly along the PPBs, allowing for dispersoid formation throughout the microstructure. As a result, the internal structure of Y-containing IMC precipitates,

that forms during rapid solidification or subsequent low temperature consolidation (see Figure 9.5 and Figure 9.6), is thought to predefine the size and distribution of nano-metric oxide dispersoids. For this reason, larger Y-containing IMC precipitates that generally form along previous as-solidified cell boundaries result in the formation of larger oxide dispersoids (see green arrow in Figure 9.15A and B). Alternatively, internal regions of the as-solidified cellular structure, where significant solute trapping of Y occurs, seems to yield a more homogenous distribution of much finer nano-metric oxide dispersoids (see red arrow in Figure 9.15A and B). Furthermore, larger Hf (CR-164HfY) or Ti (CR-166TiY) enriched oxides were identified along the PPBs (see yellow arrow in Figure 9.15A and B). This highlights the importance of achieving an ideal balance between the initial O and Y content within the consolidated CR-alloy microstructure, in an effort to achieve full dissociation of the PPB oxide and elimination of the large oxide particles.

This analysis provides insight on how to control the resulting ODS microstructure through selection of precursor as-atomized powders with an optimum solidification structure (e.g., solidification cell size or super-saturated solid solution).

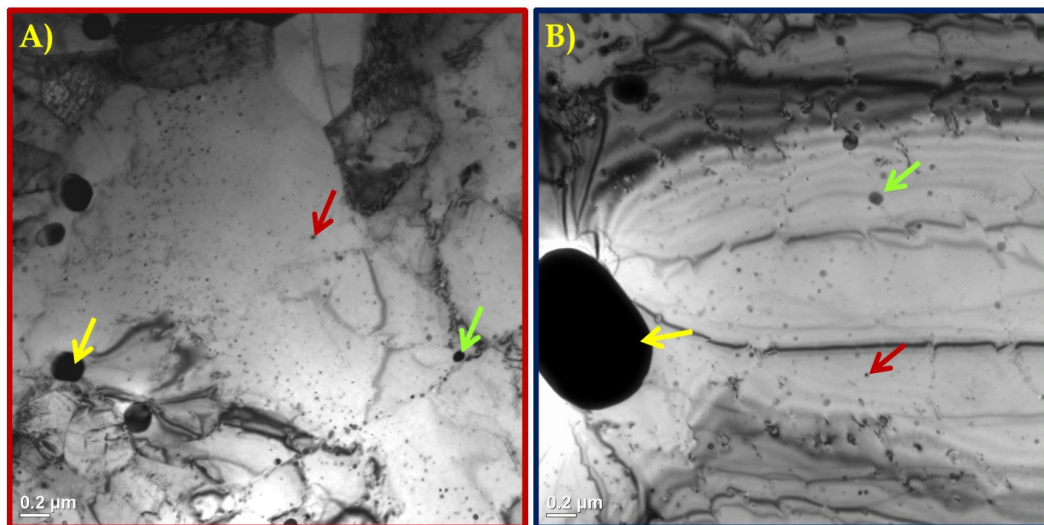


Figure 9.15. Resulting dispersoid size and distribution: A) CR-164HfY (outlined in red) and B) CR-166TiY (outlined in blue)

### 9.5.3 Thermal Stability

The mixed Y-Hf-O dispersoids in CR-164HfY were found to be more thermally stable than the Y-Ti-O dispersoids in CR-166TiY (see Table 9.4). This increased stability resulted in better microhardness retention, which indicates a notably stable alloy grain structure (see Figure 9.12).

A linear fit to the dispersoid coarsening data measured at 1200°C (Figure 9.16A) was used to calculate the dispersoid coarsening rate constant and initial dispersoid radius (see Table 9.5) using the classical LSW volume-controlled coarsening theory (Equation 99) [224, 225].

$$r^3 - r_o^3 = Kt \quad \text{Equation 99}$$

Where,  $r$  is average dispersoid radius after time  $t$ ,  $r_o$  is initial dispersoid radius at the onset of coarsening, and  $K$  is the coarsening rate constant.

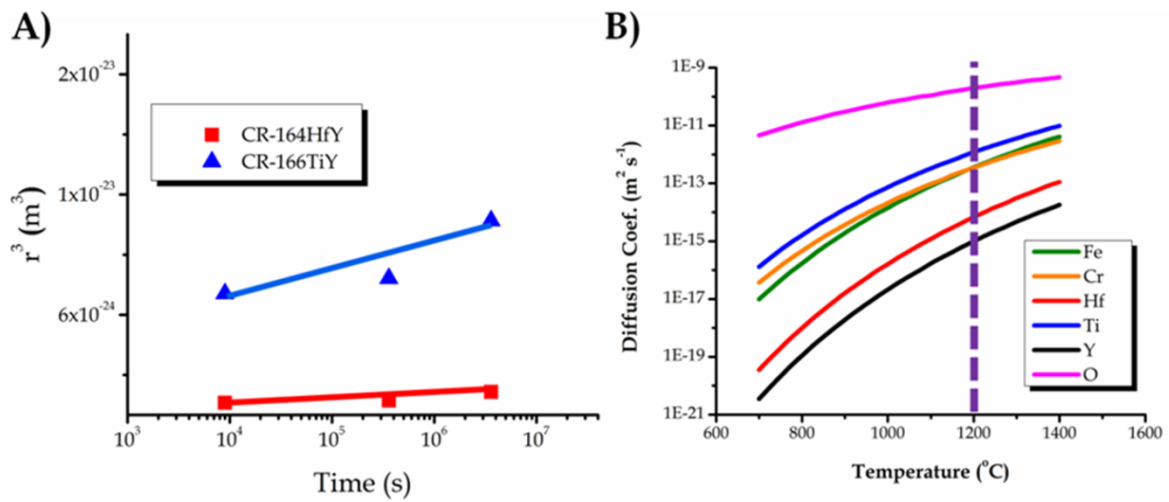


Figure 9.16. A) average dispersoid radius ( $r^3$ ) as a function of heat treatment time at 1200°C, and B) relative  $\alpha$ -Fe atomic diffusion coefficient for each alloying addition [181, 227, 228, 234, 235]

Table 9.5. Coarsening rate constant and initial dispersoid radius at 1200°C

Alloy	K (m <sup>3</sup> s <sup>-1</sup> )	r <sub>0</sub> (m)
CR-164HfY	1.4x10 <sup>-31</sup>	1.17x10 <sup>-8</sup>
CR-166TiY	9.6x10 <sup>-31</sup>	1.93x10 <sup>-8</sup>

The coarsening rate constant for the Y-Hf-O dispersoids ( $K_{Y-Hf-O}$ ) was calculated to be ~7 times less than that of the Y-Ti-O dispersoids ( $K_{Y-Ti-O}$ ) (see Table 9.5). The variables that define the coarsening rate constant are shown in Equation 100 [224, 225].

$$K = \frac{8D_M^\alpha X_\infty \sigma_{int} V_m}{9RT} \quad \text{Equation 100}$$

Where,  $D_M^\alpha$  is diffusivity coefficient for the rate limiting element M in matrix  $\alpha$ ,  $X_\infty$  is the equilibrium concentration limit of solute M in matrix  $\alpha$  (assuming an infinite ( $\infty$ ) dispersoid radius),  $\sigma_{int}$  is interfacial free energy between the matrix and dispersoid,  $V_m$  is molar volume of the dispersoid,  $R$  is the gas constant, and  $T$  is absolute temperature.

According to LSW theory, the element with the lowest flux (i.e.,  $D_M^\alpha X_\infty$ ) through the parent matrix will be considered rate limiting and should determine the coarsening constant. A comparison of the relative  $\alpha$ -Fe diffusivity coefficients for each alloying addition is shown in Figure 9.16B. This analysis demonstrates that Y (solid black line) will be the slowest diffusing element through the  $\alpha$ -Fe matrix, and is likely the rate limiting element for both the Y-Hf-O and Y-Ti-O dispersoids.

Therefore, Equation 100 can further be simplified by eliminating interconnected variables between the two dispersoid types (Equation 101).

$$K \propto \sigma_{int} V_m \quad \text{Equation 101}$$

Furthermore, the interfacial energy of the dispersoids is thought to be similar, due to analogous dispersoid morphology. For this reason, it is logical to assume that the Y-Hf-O dispersoids would contain a smaller molar volume compared to the Y-Ti-O dispersoids, in order to account for the decrease in coarsening rate, which is consistent with the data in Table 9.3. Moreover, the EDS linescan results (see Figure 9.9B) seem to indicate that the dispersoids were enriched in Hf, suggesting that dispersoids formed in CR-164HfY were  $Y_{0.33}Hf_{0.67}Y_{1.83}$  as opposed to  $Y_2Hf_2O_7$  (see Table 9.3), but further experimental analysis will be required to confirm these initial observations.

Additionally, a theoretical  $r_o$  ratio between the two presumed dispersoid types for each CR-alloy (i.e.,  $(r_o^{Hf})$  and  $(r_o^{Ti})$ ) can be determined using a simple geometrical relationship of the dispersoid molar volumes, assuming an equivalent number of moles (Equation 102-Equation 104). This comparison predicts an  $r_o$  ratio of  $\sim 1.6$  between the two phases, which is in quite good agreement with the experimentally determined  $r_o$  ratio value of  $\sim 1.6$  (see Table 9.5)

$$V_m^{Ti} = 3.75V_m^{Hf} \quad \text{Equation 102}$$

$$\frac{4}{3}\pi r_{Ti}^3 = \frac{15}{3}\pi r_{Hf}^3 \quad \text{Equation 103}$$

$$\frac{r_o^{Ti}}{r_o^{Hf}} \sim 1.6 \quad \text{Equation 104}$$

Overall, the decrease in molar volume associated with mixed Y-Hf-O compared to  $Y_2Ti_2O$  dispersoids (see Table 9.3) accounts for an expected  $\sim 3.5$  times decrease in coarsening rate between the dispersoids found in CR-164HfY and CR-166TiY, in contrast to the experimental value indicating an  $\sim 7$  times decrease. This indicates

that other factors might also be influencing the coarsening rate difference between the dispersoids (e.g., interfacial energy or multi-component coupled diffusion [226]).

The product of  $V_m$  and  $\sigma_{int}$  (see Equation 101) can be thought of as a scalar for change in chemical potential at the dispersoid-matrix interface (see Equation 105) [80].

$$\Delta\mu = \sigma_{int} V_m \frac{2}{r} \quad \text{Equation 105}$$

Where,  $\Delta\mu$  is change in chemical potential and  $2/r$  is the curvature of the spherical dispersoid.

Thus, a decrease in  $V_m$  can lower the  $\Delta\mu$  for a given dispersoid radius, by reducing the Gibbs-Thompson solubility and lessening the concentration gradient at the dispersoid interface, resulting in slower coarsening kinetics.

This analysis postulates that strategic additions of Hf can be used to modify the resulting dispersoid crystal structure and corresponding  $V_m$ , which has been suggested as an effective method for increasing dispersoid thermal stability.

These preliminary findings are quite interesting and offer a possible explanation for the increased thermal stability gained through the addition of Hf over Ti in Fe-based oxide dispersion forming powders [137, 231], but further experimental trials will be necessary to confirm this mechanism.

## 9.6 Summary

Gas atomization reaction synthesis (GARS) was used to produce two oxide dispersion forming ferritic stainless steel alloys (i.e., Fe-Cr-Y-(Hf or Ti)). Modification to the atomization pour tube geometry was found to influence melt delivery and subsequent atomization characteristics, which effectively doubled the oxidation rate between the two alloys. Elevated temperature heat treatment of the consolidated powders promoted an internal O exchange reaction between

metastable Cr-enriched prior particle boundary oxide and Y-containing IMC precipitates, leading to the formation of mixed nano-metric Y-(Hf or Ti)-O dispersoids. The dispersoids were preliminarily identified as  $\text{Y}_{0.33}\text{Hf}_{0.67}\text{O}_{1.83}$  or  $\text{Y}_2\text{Hf}_2\text{O}_7$  in the Hf-containing alloy and as  $\text{Y}_2\text{Ti}_2\text{O}_7$  in the Ti-containing alloy. Extended heat treatments at 1200°C found reduced coarsening kinetics associated with the Y-Hf-O dispersoids compared to Y-Ti-O dispersoids. A decrease in molar volume associated with the mixed Y-Hf-O dispersoid phase was offered as an explanation for increased dispersoid thermal stability.

## 9.7 Acknowledgements

Support from the Department of Energy, Office of Fossil Energy (ARM program) through Ames Laboratory contract no. DE-AC02-07CH11358 is gratefully acknowledged. Additionally, the electron microscopy of the as-atomized surface oxide layer was accomplished at the Electron Microscopy Center for Materials Research at Argonne National Laboratory, a U.S. Department of Energy Office of Science Laboratory operated under Contract No. DE-AC02-06CH11357 by UChicago Argonne, LLC. Furthermore, the authors would like to thank David Byrd, Hal Sailsbury and Jim Anderegg from Ames Laboratory-USDOE, Elliot Fair, Alex Spicher, and John Meyer from Iowa State University, and Jon Hiller and Dr. Russ Cook from the Electron Microscopy Center for their individual contributions to this paper.



## Chapter 10. Reactive Gas Atomization Processing for Fe-based ODS Alloys

A paper published in: Journal of Nuclear Materials, 2011, In Press, DOI:  
10.1016/j.jnucmat.2011.08.015

J.R. Rieken<sup>1,2,3</sup>, I.E. Anderson<sup>4</sup>, M.J. Kramer<sup>4</sup>, G.R. Odette<sup>5</sup>, E. Stergar<sup>5</sup>, and E. Haney<sup>5</sup>

### 10.1 Abstract

Gas atomization reaction synthesis was employed as a simplified method for processing oxide dispersion forming precursor Fe-based powders (e.g., Fe-Cr-Y-Hf). During this process a reactive atomization gas (i.e., Ar-O<sub>2</sub>) was used to oxidize the powder surfaces during primary break-up and rapid solidification of the molten alloy. This resulted in envelopment of the powders by an ultra-thin ( $t < 50\text{nm}$ ) metastable Cr-enriched oxide shell that was used as a vehicle to transport oxygen into the consolidated microstructure. Subsequent elevated temperature heat treatment promoted thermodynamically driven oxygen exchange reactions between trapped films of Cr-enriched oxide and internal (Y,Hf)-enriched intermetallic precipitates, resulting in highly stable nano-metric mixed oxide dispersoids (i.e., Y-Hf-O) that were identified with X-ray diffraction. Transmission electron microscopy and atom probe tomography results also revealed that the size and distribution of

---

<sup>1</sup> Graduate Student, Department of Materials Science and Engineering, Iowa State University

<sup>2</sup> Primary researcher and author

<sup>3</sup> Author for correspondence: Tel.: +1 515 294 9159, E-mail address: [jrieken@iastate.edu](mailto:jrieken@iastate.edu)

<sup>4</sup> Division of Materials Sciences and Engineering, Ames Laboratory (USDOE), Ames, IA 50011

<sup>5</sup> Department of Materials, University of California, Santa Barbara, CA, 93106

the dispersoids were found to depend strongly on the original rapidly solidified microstructure. To exploit this, several oxide dispersion strengthened microstructures were engineered from different powder particle size ranges, illustrating microstructural control as a function of particle solidification rate. Additionally, preliminary thermal-mechanical processing was used to develop a fine scale dislocation substructure for ultimate strengthening of the alloy.

## 10.2 Introduction

Oxide dispersion strengthened (ODS) ferritic alloys contain a large number density of nano-metric oxide particles that impede dislocation movement and stabilize the alloy microstructure [3, 5, 6]. This enhanced microstructural stability promotes improved elevated temperature mechanical properties and strong resistance to neutron induced void swelling, making ODS ferritic steels an attractive candidate for use as fuel cladding or structural materials in future generation nuclear systems [1, 2, 9, 10, 13, 202, 236, 237].

Traditionally, ODS ferritic alloys are fabricated using a multi-step series of mechanical alloying by means of ball milling, hot consolidation, and final thermal-mechanical processing [11, 99, 101]. This manufacturing route has proven the ability to generate a nano-scale ODS microstructure within specific ferritic alloys (e.g., nanostructured ferritic alloys or NFAs) [13], but the intrinsic complexity of this process faces several developmental challenges. Some of these challenges, as described by Odette et al.[9], include reducing the overall cost of precursor oxide dispersion forming particulate, controlling alloy and microstructure homogeneity (and impurities), batch-to-batch variability, and preventing anisotropic microstructure formation during hot consolidation and subsequent thermal-mechanical processing.

Gas atomization reaction synthesis (GARS) was employed as a simplified approach to generate precursor oxide dispersion forming powders directly, thus eliminating

the time intensive mechanical alloying step from the ODS fabrication series [14]. This high-throughput rapid solidification process utilizes a reactive atomization gas (i.e., Ar-O<sub>2</sub>) to surface oxidize nascent ferritic alloy (e.g., Fe-Cr-Y-Hf (or Ti)) droplets *in situ* during primary disintegration of the molten metal. The rapid reaction kinetics associated with GARS promotes the formation of a nano-metric metastable Cr-enriched surface oxide layer. This metastable oxide phase is used as a vehicle to transport a prescribed amount of O into the consolidated microstructure, where it resides along prior particle boundaries (PPBs). Elevated temperature heat treatments then are used to drive solid-state internal O exchange reactions between this metastable oxide phase and Y-enriched intermetallic precipitates, forming highly stable nano-metric mixed oxide (i.e., Y-(Hf or Ti)-O) dispersoids throughout the alloy microstructure [179, 231]. These alloys are termed “chemical reservoir” (CR) alloys due to the unique O exchange reaction between the strategically distributed metastable Cr-enriched oxide phase (i.e., O reservoir) and Y-enriched intermetallic precipitates (i.e., Y reservoir).

In this study a select series of alloy microstructures engineered from varying powder size ranges were examined to identify the relationship between initial as-solidified powder microstructure and resulting ODS microstructure. The influence of solidification rate and apparent solute segregation will be discussed as a method for controlling the ODS microstructure using this simplified GARS processing approach.

### 10.3 Experimental

The nominal atomization charge chemistry is displayed in Table 9.1 [206]. The charge was loaded into the experimental gas atomization system and the atmosphere in the melting chamber and (connected) atomization system was evacuated with a mechanical pump to < 26.6 Pa prior to backfilling to 111 kPa of high purity Ar. Melting was performed in a yttria (Y<sub>2</sub>O<sub>3</sub>) painted zirconia (ZrO<sub>2</sub>)

bottom pour crucible and superheated to 1700°C. The melt pour was initiated by raising a pneumatically actuated Y<sub>2</sub>O<sub>3</sub> painted alumina (Al<sub>2</sub>O<sub>3</sub>) stopper rod, which allowed the molten alloy to flow through a plasma sprayed Y<sub>2</sub>O<sub>3</sub> lined ZrO<sub>2</sub> pour tube.

**Table 10.1. Resulting CR-156 alloy composition with respect to powder particle size: CR-A) 20-53μm, CR-B) 5-20μm, and CR-C) dia. < 5μm**

Alloy	Powder Size	Fe (at.%)	Cr (at.%)	Y (at.%)	Hf (at.%)	O (at.%)
<b>CR-156YHf</b>	Nominal	Bal.	16.00	0.31	0.12	-
<b>CR-156YHf (CR-A)</b>	20-53μm	Bal.	15.84	0.18	0.11	0.38
<b>CR-156YHf (CR-B)</b>	5-20μm	Bal.	15.84	0.18	0.11	0.76
<b>CR-156YHf (CR-C)</b>	Dia. < 5μm	Bal.	15.84	0.18	0.11	1.45

Upon exiting the pouring orifice, the melt was immediately impinged by the reactive atomization gas. This gas contained 0.12 vol.% O<sub>2</sub> mixed with high purity Ar and was directly injected through the high pressure close-coupled atomization die at a pressure of 6.9MPa.

The resulting as-atomized powders were classified into three size divisions, measuring 20-53μm, 5-20μm, and dia. < 5μm prior to chemical or microstructural evaluation and will be referred to hereafter as CR-A, CR-B, and CR-C, respectively (see Table 9.1). The bulk O content for each powder range was measured using an inert gas fusion (LECO-type) analyzer, while the percentage of each metallic constituent was identified using inductively coupled plasma / mass spectroscopy (ICP/MS).

Powders representing each size division were blended with 70 vol.% Cu (dia.< 20μm), sealed in latex bags, and cold isostatically pressed (CIPed) at a pressure of 413MPa for ~60s. These cold compacts were then impregnated with epoxy and cross-sectioned for microstructural analysis. Additionally, loose powders from each

size division were blended with small granules of conductive Bakelite™ and warm pressed to form a consolidated mount, in preparation for electron probe microanalysis (EPMA).

Separately, as-atomized powders from CR-A and CR-B were placed into individual 316L stainless steel cans measuring 25.4mm in dia. x 127mm in length (see Figure 10.1a), while as-atomized powders from CR-C were placed into a 316L stainless steel can measuring 6.3mm in dia. x 76.2mm in length. Each can was evacuated to a pressure of  $\sim 10^{-4}$  Pa, outgassed at 415°C for 1hr, and electron-beam welded shut using a 316L stainless steel cap (see Figure 10.1a). The atomized powders then were consolidated using hot isostatic pressing (HIPing) at 700°C with 200MPa pressure for 4hrs. An example of the as-consolidated rod from CR-A can be seen in Figure 10.1b.

The as-HIPed rods then were heat treated under vacuum ( $\sim 10^{-4}$  Pa) at 1200°C for 2.5hrs. This heat treatment schedule had previously been reported as an effective method for forming nano-metric oxide dispersoids within similar CR-alloys [231].

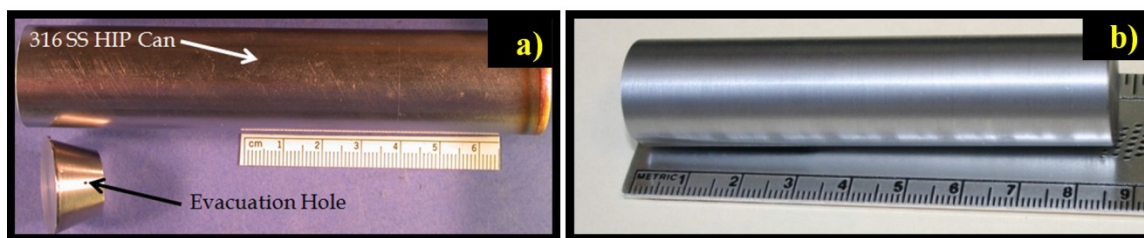


**Figure 10.1. (a) 316L stainless steel HIP can and cap and (b) as-HIPed rod made from CR-A**

Following heat treatment, sample bars were fabricated from each heat treated rod. These bars measured 13.5mm x 13.5mm x 43.6mm (Figure 10.2a) and 13.5mm x 8.5mm x 13.5mm (Figure 10.2c), respectively. Each bar was cold rolled (at room temperature) to an  $\sim 80\%$  reduction in area (RA) using 10% RA increments without intermediate anneals. A small section was cut from the end of each cold rolled bar

following every  $\sim 20\%$  RA stage (Figure 10.2b and d) in the progression. These sections were further segmented and annealed at  $500^{\circ}\text{C}$  or  $600^{\circ}\text{C}$  for 1hr in air.

The microhardness of each cold rolled and annealed specimen was measured using Vickers diamond pyramid indentation with a 500gm load. The average of 10 consecutive indentations for each segmented sample was plotted for each data point.

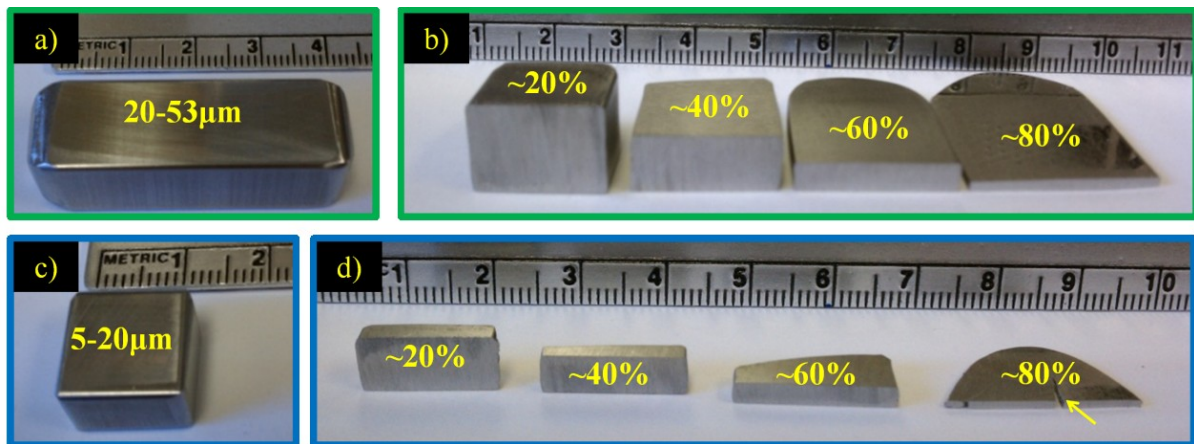


**Figure 10.2.** Sample bars prior to cold rolling (a and c) and cross-sectioned bars following 20-80% RA (b and d), where samples in a) and b) were made from powders with dia. of  $20\text{-}53\mu\text{m}$  (CR-A) and c) and d) were made from powders with dia. of  $5\text{-}20\mu\text{m}$  (CR-B)

Surface analysis of the as-atomized powder particles was conducted using a JEOL JAMP 7830F scanning Auger microprobe (SAM) with a hemispherical auger electron spectrometer (AES) and Ar-ion sputtering gun for depth profiling. The surface and interior microstructure of the powders was examined using a JEOL 5910LV scanning electron microscope (SEM) with energy dispersive spectrometer (EDS). Chemical mapping of the surface shell and interior microstructure was carried out using EPMA (Cameca SX100) at the University of California Santa Barbara (UCSB). The rapidly solidified powders were also characterized using an Imago local electrode atom probe (LEAP 3000X-HR), at UCSB. The atom probe tomography (APT) samples were prepared using a focused ion beam (FIB) microscope. Powders from CR-B and CR-C were extracted and mounted on pre-shaped Si-stubs and

subsequently sharpened with the FIB. APT measurements of the medium sized powders (CR-B) were carried out in laser mode at an energy  $<0.2\text{ nJ}$  at approximately  $-213^{\circ}\text{C}$  ( $\sim 60\text{K}$ ). The measurements of the finest powders (CR-C) were carried out in voltage mode using a 0.2 pulse fraction, again at a temperature of approximately  $-213^{\circ}\text{C}$  ( $\sim 60\text{K}$ ). The APT data was analyzed using the Imago-IVAS reconstruction software.

The HIPed and heat treated alloy microstructures were analyzed using a Hitachi S-2460N SEM with EDS. The nano-metric features present in the HIPed and heat treated samples were characterized using a Tecnai G<sup>2</sup> F20 transmission electron microscope (TEM) at 200 keV. Miniature cylinders measuring 3mm in dia. x 10mm in length were cut from HIPed and heat treated rods using wire electro-discharge machining. These cylinders were subsequently sliced into 1mm thick disks, ground flat using 400 and 600 SiC grit paper, polished using  $6.0\mu\text{m}$  and  $1.0\mu\text{m}$  diamond polishing compound, and mechanically dimpled to a thickness of  $\sim 20\mu\text{m}$  in preparation for TEM analysis. Specimens containing powders from CR-A were then dual jet polished using an electrolytic solution for stainless steels (i.e., 700ml methanol, 120ml distilled water, 100ml glycerol, and 80ml perchloric acid) at  $-21^{\circ}\text{C}$ , while specimens containing powders from CR-B and CR-C were Ar-ion milled to perforation using a milling angle of  $15^{\circ}$  at  $-90^{\circ}\text{C}$ .

The dislocation substructure developed during cold rolling of the heat treated bars to a reduction in area of  $\sim 80\%$  followed by a 1hr anneal at  $500^{\circ}\text{C}$  in air was examined using the aforementioned TEM. These TEM samples also were prepared using the previously described method consisting of dual jet polishing.

The presence of Y-enriched nano-metric oxide dispersoids was verified within each step of this simplified process using a Phillips PANalytical X-Pert Pro Diffraction System with  $\text{Co-K}\alpha$  radiation. A scanning real time multiple strip (RTMS) X-ray detector was used with an active length of  $\sim 0.05Q$  ( $\text{\AA}^{-1}$ ). Diffraction data was

collected from  $1.8\text{--}4.8Q$  ( $\text{\AA}^{-1}$ ) with a step size of  $5 \times 10^{-4} Q$  and a dwell time of 500s per step. It should be noted that the heat treated XRD specimen from CR-C contained a much smaller cross-sectional area compared to CR-A and CR-B, resulting in significantly reduced counts.

## 10.4 Results

The resulting alloy chemistry for each powder size division is listed in Table 9.1. It should be noted that this CR-alloy contained an excess nominal concentration of Y to account for oxidation losses ( $\sim 42$  at.%) that were determined (roughly) to occur during the melting procedure. As part of our efforts to improve control of the Y-addition, pre-alloyed Fe-Y pieces (i.e., Fe-23.7Y at.%) were added to the CR-alloy charge in place of pure Y, to reduce the oxidation kinetics and limit Y loss during melting.

The extent of Y loss is thought to be indirectly related to the  $O_2$  content within the melting chamber atmosphere. For this reason, an  $O_2$  gettering furnace (max. temperature of  $650^\circ\text{C}$ ) was adapted to the atomizer melting chamber in combination with an  $O_2$  sensor, in order to better replicate the melting atmosphere environment and permit prediction of Y loss during future atomization trials. These modifications resulted in similar Y loss ( $\sim 57$  at.%) during GARS processing of two related CR-alloys, i.e., although an increase in Y loss was recorded, the goal of controlling Y loss was achieved [238]. Further improvements to the melting procedure (e.g., incorporating the ability to add late alloy additions) will be evaluated in the future.

### 10.4.1 As-atomized microstructure

An example of the as-atomized powder morphology for each powder size division is displayed in Figure 10.3a-c. Most of the powders were found to be primarily spherical in shape. However, several of the larger powders (CR-A) contained satellite particles and surface dimples (see arrows in Figure 10.3a) caused by



particle-particle collisions that occur between smaller solidified powders and larger semi-solid powders. On the other hand, various smaller powders (CR-C) seemed to have solidified prior to succumbing to the effects of surface tension, resulting in a pillow-like morphology (see arrows in Figure 10.3c). These slight variations in surface morphology provide some insight into the solidification rate experienced by individual powders.

Following atomization, the resulting O content associated with the as-atomized powders was found to scale inversely with powder size (see Table 9.1), as surface area to volume ratio increases. Surface chemistry analysis revealed a primary enrichment of Cr (dark blue line) and O (dark green line) at the as-atomized powder surface (see Figure 10.3d-f) for each size division of powders, which provided evidence of Cr-enriched surface oxide phase formation during this GARS process. Furthermore, this qualitative analysis indicates that the chemistry of this surface oxide layer becomes more O-enriched compared to Cr as particle size decreases.

The thickness of the surface oxide layer was taken to be the midpoint between the maximum and minimum intensity value for O, which resulted in average thickness measurements of 33nm, 24nm, and 9nm for as-atomized powders from CR-A, CR-B, and CR-C, respectively (see vertically dashed line in Figure 10.3d-f). It also can be seen that the thickness of the oxide layer increases with particle size, suggesting that this rapid oxidation reaction is sensitive to particle cooling rate (i.e., as expected, coarser particles cool slower).

Cross-sectional analysis of the as-CIPed powders showed that CR-A and CR-B contained significant microsegregation at the as-solidified cellular boundaries, but the powders from CR-C were found to contain an apparent single phase or highly refined solidification structure (see Figure 10.4a-c). Additionally, EDS measurements indicated that the light contrast phase found at the cell boundaries in CR-A and CR-B was enriched in Y and Hf (see arrows in Figure 10.4a and b),

providing evidence of solute rejection upon solidification in these powders. Furthermore, no observable chemical difference was detected at (apparent) grain boundaries in CR-C (see arrows in Figure 10.4c), indicating that significant solute trapping or nano-metric chemical segregation occurred during solidification of these ultra-fine powders.

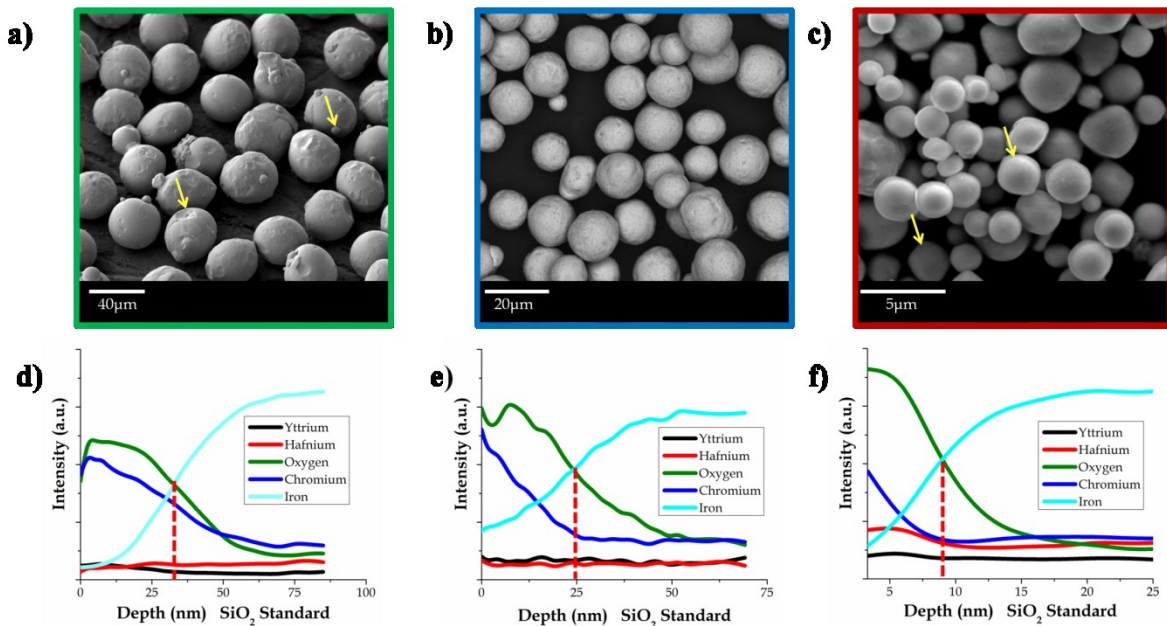


Figure 10.3. As-atomized powder morphology with accompanying AES depth profile: a) and d) were made from 20-53 μm (CR-A), b) and e) were made from 5-20 μm (CR-B), and c) and f) were made from dia. < 5 μm (CR-C)

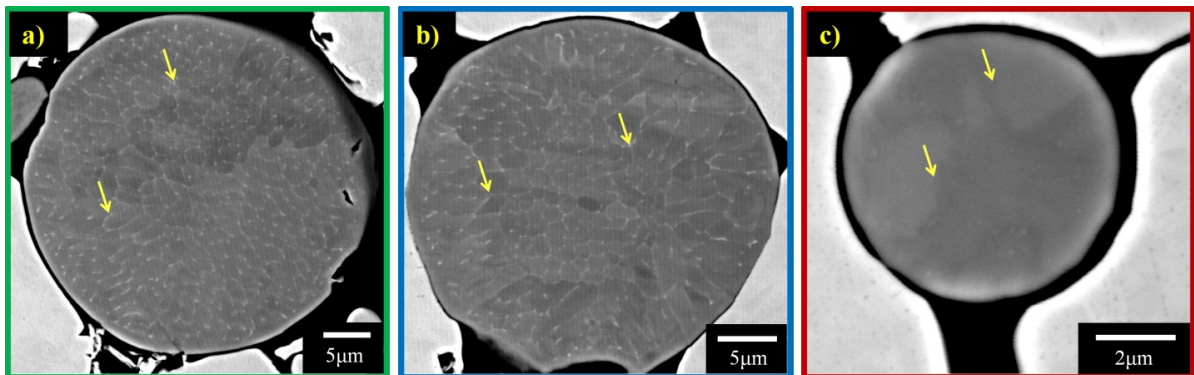


Figure 10.4. Cross-section SEM analysis of as-CIPed powders: a) 20-53 μm (CR-A), b) 5-20 μm (CR-B), and c) dia. < 5 μm (CR-C)

EPMA chemical mapping confirmed that the as-solidified cell boundaries in CR-A and CR-B were enriched in Y and Hf (see arrow in example Figure 10.5a, d and e). These results also identified a slight Fe and Cr denuded zone located near the surface of the powders, in conjunction with slight O enrichment, and although this layer is too thick to represent the metastable surface oxide layer it might indicate the O depth of penetration during this GARS process (see arrow in example Figure 10.5b, c and f).

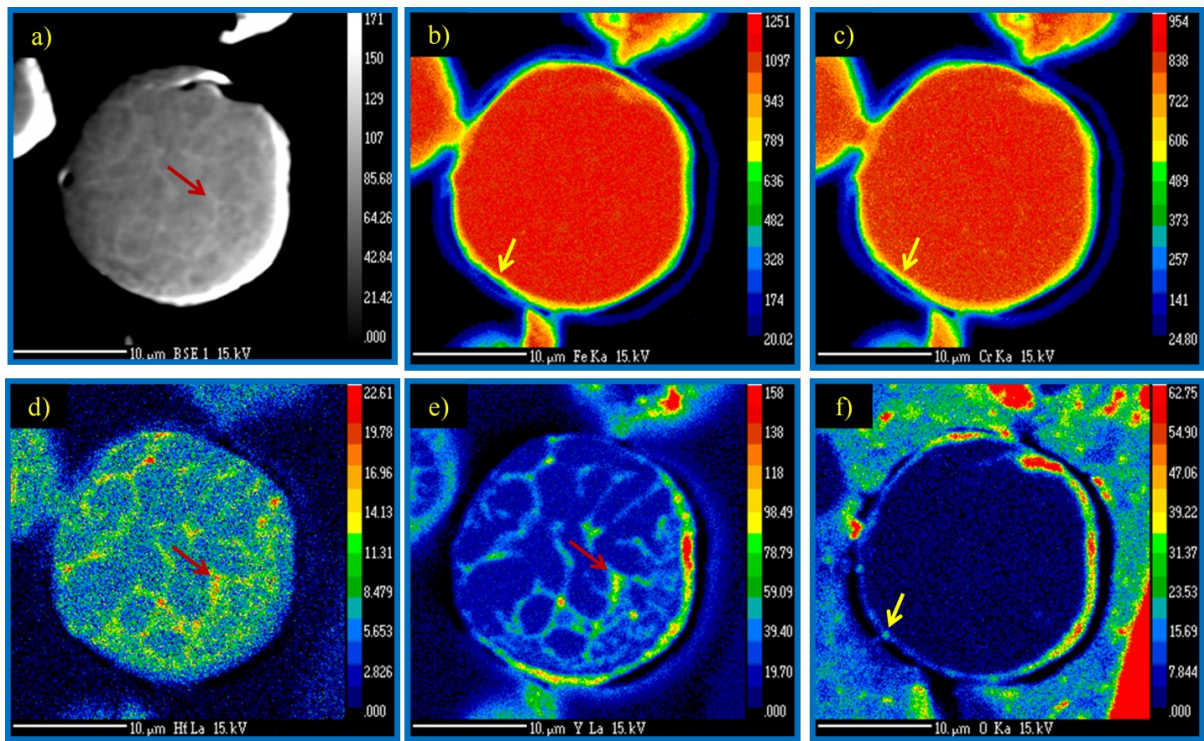


Figure 10.5. An example of the EPMA chemical maps used to identify Y and Hf microsegregation in as-atomized powders from CR-B: a) backscattered electron (BSE) image, b) Fe, c) Cr, d) Hf, e) Y, and f) O

#### 10.4.2 As-HIPed microstructure

Low temperature HIPing (700°C -200MPa - 4hrs) was used to consolidate the as-atomized particles and encourage nucleation of fine Fe-(Y,Hf) intermetallic precipitates from super-saturated regions within the rapidly solidified

microstructure, while limiting internal O exchange reactions. This processing step allows the opportunity to study the microstructure evolution of these CR-alloy powders prior to dispersoid formation.

An example of the as-HIPed microstructure for each powder size division can be seen in Figure 10.6. This consolidation procedure resulted in a fully dense microstructure for CR-A and CR-B, but was unsuccessful at eliminating porosity within CR-C (see arrows in Figure 10.6c). This result was unexpected, since sintering kinetics are known to accelerate in powders with increased specific surface area [239]. For this reason, it seems that the primary impediment to consolidation was the lack of plastic deformation (needed to expand the interparticle contact area and to minimize open porosity), not the lack of diffusion, and that the powders from CR-C exhibited an increased yield strength compared to CR-A and CR-B.

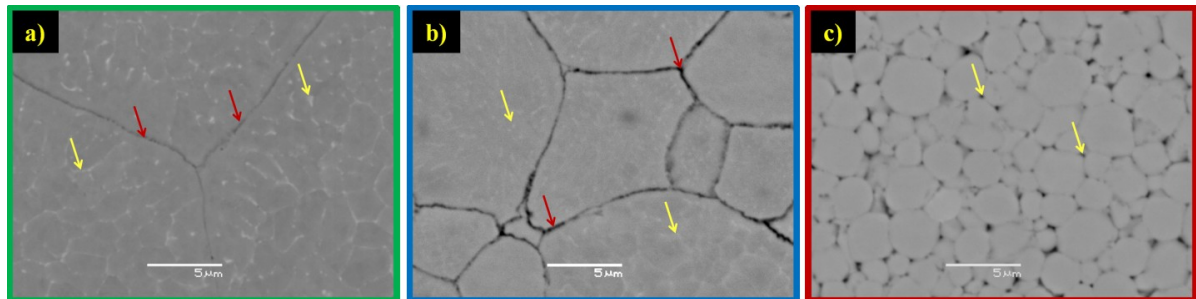


**Figure 10.6.** Resulting as-HIPed microstructures following low temperature consolidation (700°C - 200MPa - 4hrs) of the size classified powders: a) with dia. of 20-53 $\mu$ m (CR-A), b) with dia. of 5-20 $\mu$ m (CR-B), and c) with dia. < 5 $\mu$ m (CR-C)

The metastable Cr-enriched surface oxide layer was observed to reside along prior particle boundaries (PPBs) within the as-HIPed microstructures (see dark arrows in Figure 10.6a and b). Additionally, microsegregation of Y and Hf was again identified at retained remnants of as-solidified cell boundaries in CR-A and CR-B (see light arrows in Figure 10.6a and b). These results reveal that the microstructure of the powders, at this size scale, is seemingly unchanged compared to the as-

solidified microstructure (see Figure 10.4), signifying that this consolidation time and temperature were insufficient to activate the O exchange between the Cr-enriched oxide phase and (Y,Hf)-enriched cell boundary regions.

TEM was used to resolve features within the as-HIPed microstructure at a much finer size scale. The fragile nature of these low temperature consolidated TEM samples limited the area that could be observed. These results revealed the internal structure for one of the previous as-solidified cells within CR-A (see Figure 10.7a) highlighted by larger features along the cell boundary (see dark arrow in Figure 10.7d) with numerous nano-metric features located near the edge of the boundary (see light arrow in Figure 10.7d). Similar nano-metric features were found to be distributed more uniformly throughout the microstructure in CR-B and CR-C (Figure 10.7b and c). The size of these nano-metric features in CR-C ranged between 2-6nm (see Figure 10.7f) with a number density of  $\sim 4 \times 10^{22} \text{ m}^{-3}$  (number densities were estimated assuming a TEM foil thickness of 100nm). This large number density of fine precipitates could explain the aforementioned apparent increase in yield strength associated with CR-C.

These features have been identified as Fe-(Y,Hf) (e.g.,  $\text{Fe}_{17}(\text{Y,Hf})_2$  and  $\text{Fe}_2(\text{Hf,Y})$ ) intermetallic compound (IMC) precipitates using XRD (results not shown). Additionally, APT measurements confirmed the presence of similar features within the as-atomized powders, which contain both Y and Hf with large concentrations of Fe (see Figure 10.15 in Section 10.5 below). It seems that considerable amounts of Y and Hf were rejected from solution in the  $\alpha$ -(Fe,Cr) lattice during rapid solidification of the largest powders (CR-A) and significant solute pile-up at the as-solidified cell boundaries lead to the formation of larger elongated intermetallic precipitates. On the other hand, small amounts of solute trapping appear to have occurred near the cell boundaries in the intermediate sized (CR-B) powders, leading to the formation of some larger IMC particles and many smaller intermetallic precipitates. Notably,



significant solute trapping was apparent throughout the microstructure in the finest powders (CR-C), which lead to the formation of a higher number of smaller, uniformly distributed intermetallic precipitates. These nano-metric precipitates could have formed immediately after solidification due to recalescence effects or, perhaps, during this low temperature (700°C) HIPing procedure.

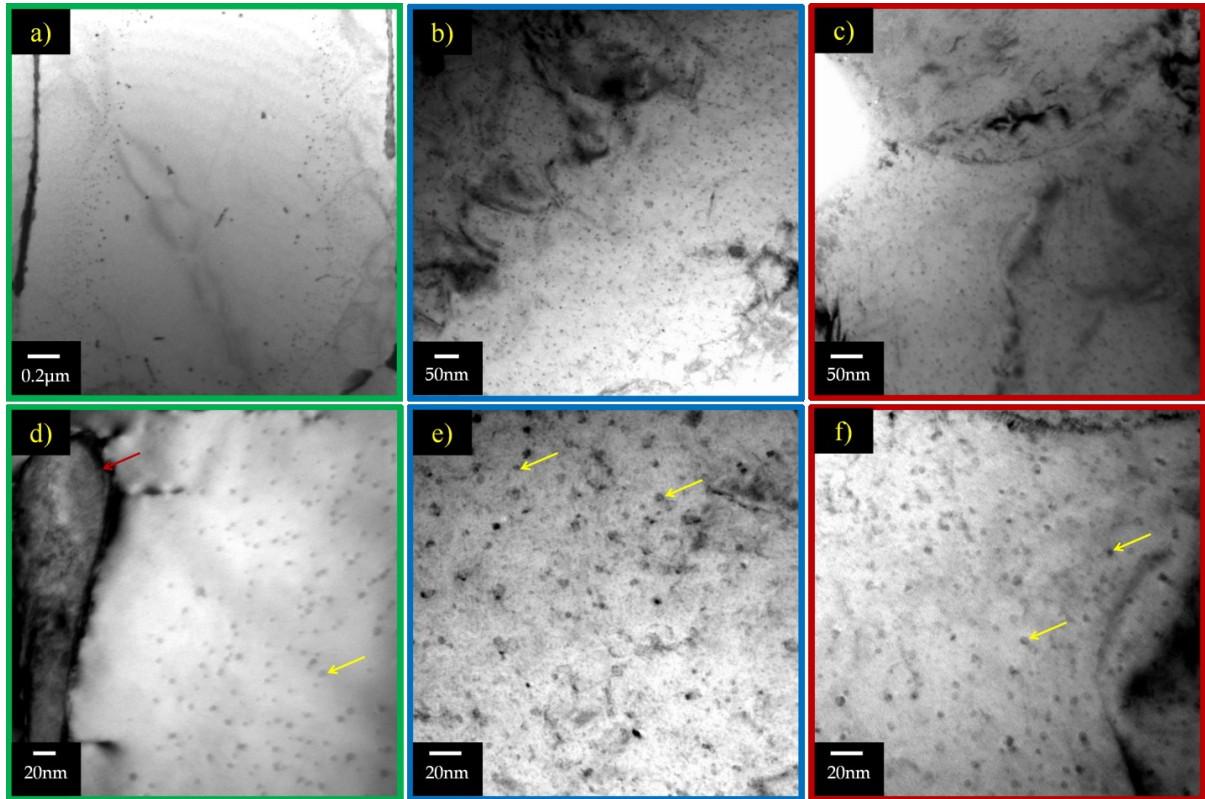


Figure 10.7. TEM micrographs following low temperature HIP consolidation (700°C - 200MPa - 4hrs) of the size classified powders: a) and d) with dia. of 20-53μm (CR-A), b) and e) with a dia. of 5-20μm (CR-B), and c) and f) with a dia. < 5μm (CR-C)

#### 10.4.3 As-reacted microstructure

Elevated temperature heat treatment (1200°C - 2.5hrs) was used to drive O exchange between the metastable Cr-enriched PPB oxide and Y-enriched IMC precipitates, promoting the formation of Y-enriched nano-metric oxide dispersoids.

Examples of the resulting heat-treated microstructure for each powder size class are shown in Figure 10.8a-c. Only limited amounts of residual (Y,Hf)-enriched intermetallic phase could be identified in CR-A and CR-B (see arrows in Figure 10.8a and b), and the PPB oxide seemed to be fully dissolved. Conversely, small amounts of residual PPB oxides were found within the microstructure of CR-C (see arrows in Figure 10.8c) accompanied by a large population of nano-metric features uniformly distributed in the grains (Figure 10.9f). These results seem to provide clear evidence of an apparent O exchange reaction between the metastable Cr-enriched PPB oxide phase and (Y,Hf)-intermetallic precipitates.

Furthermore, these results highlight the importance of achieving an ideal balance of dispersoid forming elements (Y, Hf, and O) and a realistic (empirical) selection of the final oxide stoichiometry within the atomized powders prior to consolidation. For example, significant solute trapping and sufficient O is required for the uniform formation of nano-metric oxides throughout the CR-alloy microstructure that begins with dia.  $< 5\mu\text{m}$  particles (CR-C). On the other hand, the GARS process could be tuned for a specific particle size range (e.g., CR-B) and a fixed (resulting) Y concentration with the desired O concentration, in order to achieve this ideal balance.

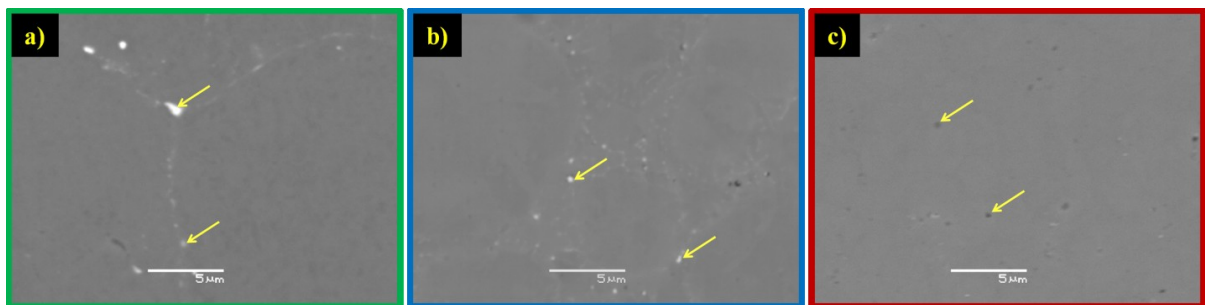


**Figure 10.8. Resulting heat treated microstructures (1200°C - 2.5hrs - Vac.) of as-HIPed samples made from: a) 20-53 $\mu\text{m}$  (CR-A), b) 5-20 $\mu\text{m}$  (CR-B), and c) dia.  $< 5\mu\text{m}$  (CR-C).**

The resulting Y-enriched nano-metric oxide dispersoids were identified using TEM. The heat treatment resulted in the formation of ~0.5 vol.% oxide dispersoid phase throughout the CR-alloy microstructure. The distribution and size of the dispersoids varied significantly between the three powder classes (see Figure 10.9a-c). The dispersoids identified in CR-A seemed to be primarily distributed along previous as-solidified cell boundaries, and manifested a globular morphology, with a size range from ~20-50nm and a number density of  $\sim 3 \times 10^{21} \text{m}^{-3}$  (see Figure 10.9d). Dispersoids found in CR-B were spaced more closely, but still appeared to be arranged in a network, possibly resulting from a more refined cellular solidification structure. These dispersoids had a near spherical morphology with diameters ranging from ~5-20nm and a number density of  $\sim 8 \times 10^{21} \text{m}^{-3}$  (see Figure 10.9e). A region with a large cluster of dispersoids also was identified in CR-B (see arrow in Figure 10.9b), which could have originated from a local region with higher Y content (e.g., an as-solidified cell boundary triple junction). The spherical dispersoids found in CR-C seemed to be distributed uniformly throughout the alloy microstructure, with a diameter of ~3-12nm and a number density of  $\sim 3 \times 10^{22} \text{m}^{-3}$  (see Figure 10.9f). Notably, the resulting dispersoids in all three powder size classes seemed to approximately mimic the spatial and size distribution of the precursor Y-enriched intermetallic precipitates. Identification of the dispersoid phases was carried out using XRD (see Figure 10.12 in Section 4.2 below).



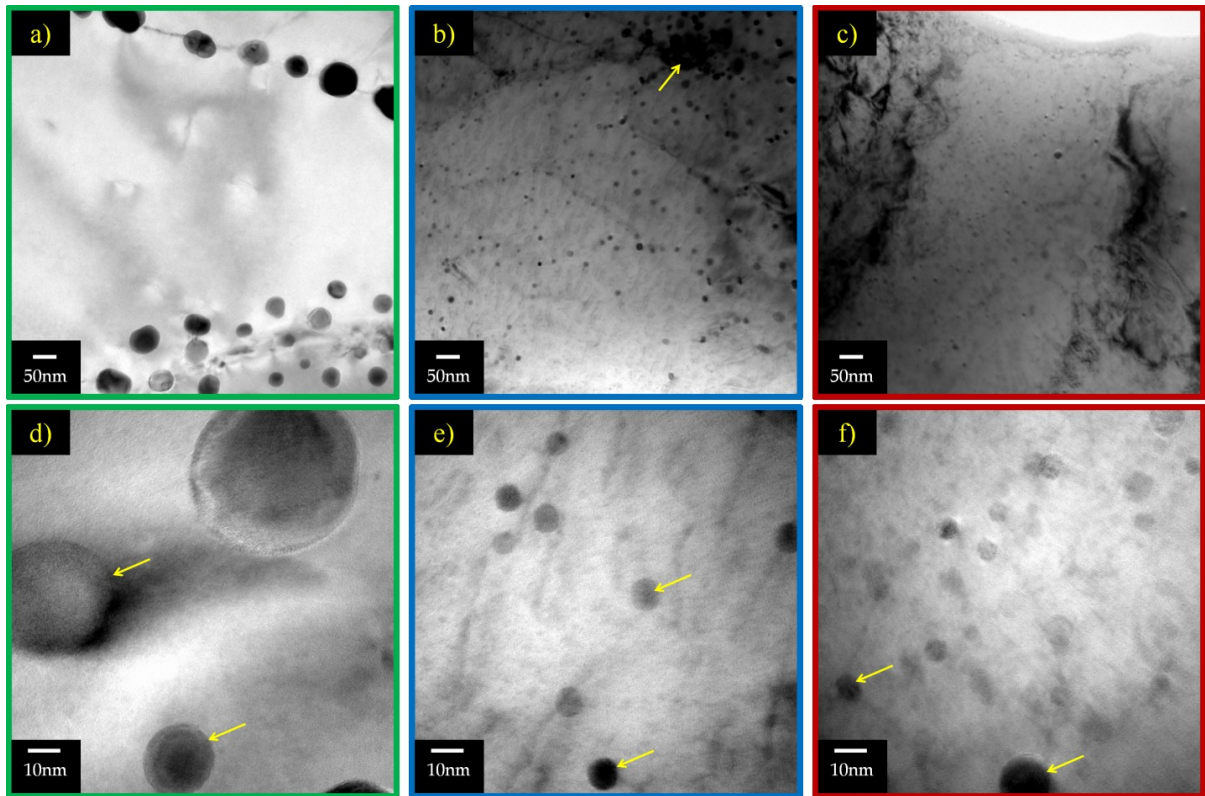


Figure 10.9. TEM micrographs of the heat treated (1200°C - 2.5hrs - Vac.) as-HIPed samples made from powders with: a) and d) dia. of 20-53 $\mu$ m (CR-A), b) and e) dia. of 5-20 $\mu$ m (CR-B), and c) and f) dia. < 5 $\mu$ m (CR-C)

#### 10.4.4 Microhardness evaluation

Cold rolling of CR-A and CR-B in the as-heat treated condition was used to develop a fine scale dislocation substructure throughout the alloy microstructure, following the example of strengthening in MA956 [5]. The cold deformation was followed by a low temperature anneal (600°C or 500°C) to recover dislocations to dispersoid boundaries.

Microhardness measurements were used to evaluate the work hardening rate of these CR-alloys and to identify a suitable annealing temperature for a given amount of cold deformation or strain (i.e., amount of stored energy). The average

microhardness data with standard deviations in the as-heat treated, as-cold rolled, and as-annealed condition are shown in Figure 10.10.

The microhardness of CR-A, CR-B, and CR-C in the as-heat treated condition were  $137 \pm 3$  Hv,  $158 \pm 5$  Hv, and  $185 \pm 8$  Hv, respectively. This systematic increase in hardness is likely a combined effect of decreasing powder grain size (Hall-Petch), in conjunction with an increasing oxide dispersoid number density and uniformity (see Figure 10.9).

Bars machined from as-heat treated CR-A and CR-B were subsequently cold rolled up to an  $\sim 80\%$  reduction in area (RA) [240]. Examples of the cold rolled bars are shown in Figure 10.2. The cold deformation did not produce observable macroscopic damage, except for the  $\sim 80\%$  RA pass for CR-B, which resulted in crack formation through the transverse face at the leading edge of the sample bar (see arrow in Figure 10.2d). This crack likely formed as a result of the reduced sample thickness, in coincidence with large amounts of stored energy and reduced ductility at this stage in the deformation process.

Notably, both as-deformed CR-A and CR-B were found to generally have similar work hardening rates (see solid green and blue line in Figure 10.10, respectively), maintaining a consistent microhardness difference of  $\sim 20$ - $30$  Hv over the range of deformation. The apparent work hardening rate was higher in the range from 0 to  $\sim 20\%$  RA, followed by a roughly linear trend with increasing strain. The microhardness values at  $\sim 80\%$  RA for CR-A and CR-B were  $282 \pm 4$  and  $315 \pm 6$  Hv, respectively.

The microhardness results measured in CR-A and CR-B following a 1hr anneal at  $600^\circ\text{C}$  are shown in Figure 10.10 as a coarse dashed green and coarse dashed blue lines, respectively. Cold worked CR-A exhibited apparent uniform microhardness recovery except at an  $80\%$  RA, where the microhardness decrease was roughly twice

as large. This behavior may signal dislocation recovery at the lower strains and partial recrystallization at ~80% RA. In contrast, microhardness recovery in CR-B was larger at the lowest ~20% RA compared to strains of 40 and 60% RA. The hardness recovery in CR-B was largest at 80% RA, again possibly signaling partial recrystallization.

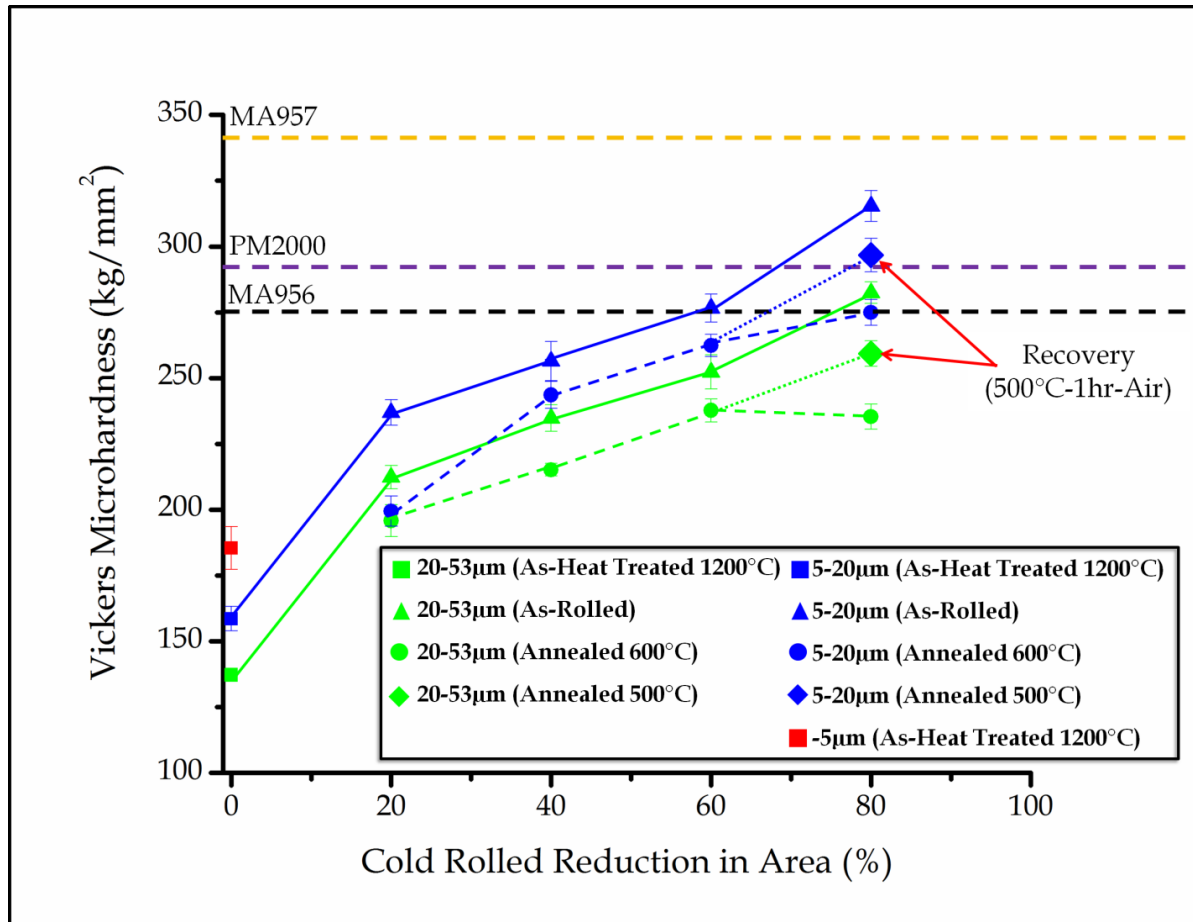


Figure 10.10. Resulting alloy microhardness following dispersoid formation and subsequent cold rolling and annealing trials on samples made from size classified powders identified as CR-A (green), CR-B (blue), and CR-C (red)

In order to prevent the apparent partial recrystallization occurring in ~80% cold-worked alloys at 600°C, the annealing temperature was reduced to 500°C for 1hr in air. The resulting microhardness values for CR-A of 259±5 Hv and CR-B of 296±6

Hv are shown in Figure 10.10 by the solid green and blue diamonds, respectively. The recovery at 500°C is consistent with that observed at the 40 and 60% RA at 600°C (see fine dashed green line and fine dashed blue line in Figure 10.10). These CR-alloy values are compared to average microhardness reported for MA956 (~275 Hv) and MA957 (~340 Hv) [119, 198]. The microhardness value used for comparison to PM2000 is a combined average ( $291 \pm 14$  Hv) between an experimentally determined value of  $312 \pm 20$  Hv and a reported value of  $270 \pm 8$  Hv for the as-received condition [241]. The microhardness of CR-A and CR-B are approximately equal to those of MA956 and PM2000, respectively.

## 10.5 Further Evaluation, Analysis and Discussion

### 10.5.1 GARS process control

The rapid oxidation kinetics associated with this GARS reaction has been found by experiment to scale linearly with O concentration in the reactive atomization gas (Figure 10.11). It is believed that a consistent partial pressure of O<sub>2</sub> ( $p_{O_2}$ ), defined by the reactive gas chemistry, is formed around the local atomization zone, thus dictating the rate of oxidation during GARS processing. Further GARS experiments will be required to better understand and model this rapid oxidation process, but early results have shown a reasonable ability to predict as-atomized O content for larger particle size classes (see horizontally dashed line in Figure 10.11). But while this empirically developed relationship has proven to work well in predicting the O content for as-atomized powders in the size range of CR-A (20-53µm) and larger, it will require further tuning to accurately predict O content in powders within the range of CR-B or CR-C (5-20µm or dia. < 5µm), which have significantly greater surface area to volume ratios.

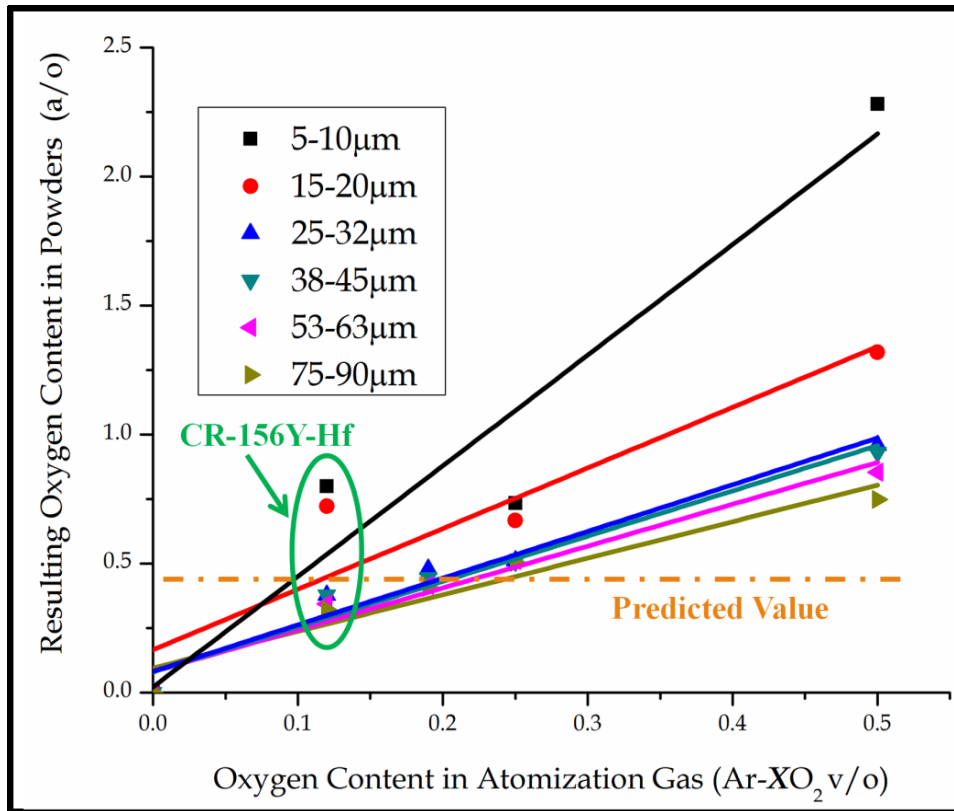


Figure 10.11. Resulting O content as a function of reactive atomization gas concentration for several (labeled) close size fractions

### 10.5.2 Microstructural evolution

This GARS process promoted the formation of an ultra-thin ( $t < 50\text{nm}$ ) metastable Cr-enriched surface oxide layer (see Figure 10.3), which encase the CR-alloy powders during rapid solidification. Upon low temperature consolidation, this metastable phase was locked into position along internal PPBs (Figure 10.6). Trapping the metastable Cr-enriched oxide phase internally is thought to further reduce the oxide stability by lowering the O activity along the phase boundary, seemingly creating a near perfect vacuum for the ensuing dissociation and O exchange process. As a result, elevated temperature heat treatments were successful in dissociating this PPB oxide, allowing O to diffuse towards the interior of the powder particle driven by a concentration or chemical potential gradient. The O

was subsequently consumed through internal oxidation of Fe-(Y,Hf) intermetallic precipitates, resulting in the formation of more thermodynamically stable mixed nano-metric Y-Hf-O dispersoid phases, in the case of CR-C, located throughout the alloy microstructure (see Figure 10.9 and Figure 10.12).

This type of O exchange reaction is described as diffusionless internal oxidation [182], given that the rate of reaction is controlled by the internal diffusion of only interstitial O, since both reactive metal species (i.e., Y and Hf) have limited solubility and diffusivity in the  $\alpha$ -(Fe,Cr) matrix. In the case of CR-C the internal O exchange reaction allows for fine scale oxide dispersoid formation throughout the microstructure. More generally, internal patterns of Fe-(Y,Hf) intermetallic precipitates, that form (most likely) upon rapid solidification (Figure 10.6 and Figure 10.7), are transformed into nano-metric oxide dispersoids. That is, the chemistry, size, and distribution of these oxide dispersoids is intrinsically linked to the precursor intermetallic chemistry, size, and distribution (see Figure 10.9 and Figure 10.12).

The oxide dispersoid chemistry was found to be influenced not only by the precursor intermetallic chemistry, but also by the initial O content in the as-atomized powders. Precursor intermetallic precipitates were found to contain both Y and Hf (Figure 10.5 and Figure 10.15) and are believed to be either  $\text{Fe}_{17}(\text{Y,Hf})_2$  or  $\text{Fe}_2(\text{Y,Hf})$  IMC phases based on preliminary XRD and APT results. These precursor phases were internally oxidized during elevated temperature heat treatment, resulting in the formation of mixed Y-Hf-O nano-metric oxide dispersoids (see XRD results in Figure 10.12). It should be noted that only CR-C contained a uniform distribution with dispersoids (dia. < 10nm) throughout the  $\alpha$ -(Fe,Cr) matrix.

The presence of Y, Hf, and O within the dispersoids also was confirmed using energy filtered TEM (see example in reference [231]). However, the specific dispersoid phase in each powder size class was found to contain a different crystal

structure (see XRD data in Figure 10.12). These dispersoids seem to form as Hf-modified  $\text{Y}_2\text{O}_3$  (CR-A),  $\text{Y}_2\text{Hf}_2\text{O}_7$  (CR-B), and Y-modified  $\text{HfO}_2$  (CR-C). This shift in crystal structure seems linked to the initial local chemistry of the precursor Fe-(Y,Hf) IMC precipitates. Additionally, the O content in the powders increases in going from CR-A to CR-C, and the corresponding dispersoid phases reflect an increased O to Hf + Y ratio, thus, highlighting the importance of O in phase selection. Furthermore, the asymmetrical XRD peak shape or shift in peak position associated with the dispersoid phases (see displacement of dashed and solid color lines in Figure 10.12) is likely related to varying concentrations of Y or Hf within the modified oxide structure. It should again be noted that the heat treated ( $1200^\circ\text{C}$ ) CR-C XRD specimen contained a much smaller cross-sectional area compared to CR-A and CR-B, resulting in significantly reduced counts, but still a distinct peak above background. To verify these observations of peak shifts and oxide structure differences, analogous samples from each CR-alloy will be re-examined in the near future using high-energy through-penetrating X-rays (where a significantly reduced sample size is sufficient: see example in [179]), in order to more accurately characterize the dispersoid crystal structure.

The size and distribution of the nano-metric oxide dispersoids was shown to closely mimic that of the precursor intermetallic precipitates (see Figure 10.7 and Figure 10.9). The scale of this precursor microstructure is thought to be controlled by the rapid solidification rate and cooling rate for a given powder size. The powders in CR-A ( $20\text{-}53\mu\text{m}$ ) and CR-B ( $5\text{-}20\mu\text{m}$ ) contained significant amounts of microsegregation, while powders in CR-C (dia.  $< 5\mu\text{m}$ ) seemed to contain an apparent single phase or highly refined microstructure (see APT in Figure 10.15). This infers that the ultra-fine (CR-C) powders were successful in solute trapping Y and Hf within the  $\alpha\text{-(Fe,Cr)}$  lattice, by suppressing microsegregation during solidification.

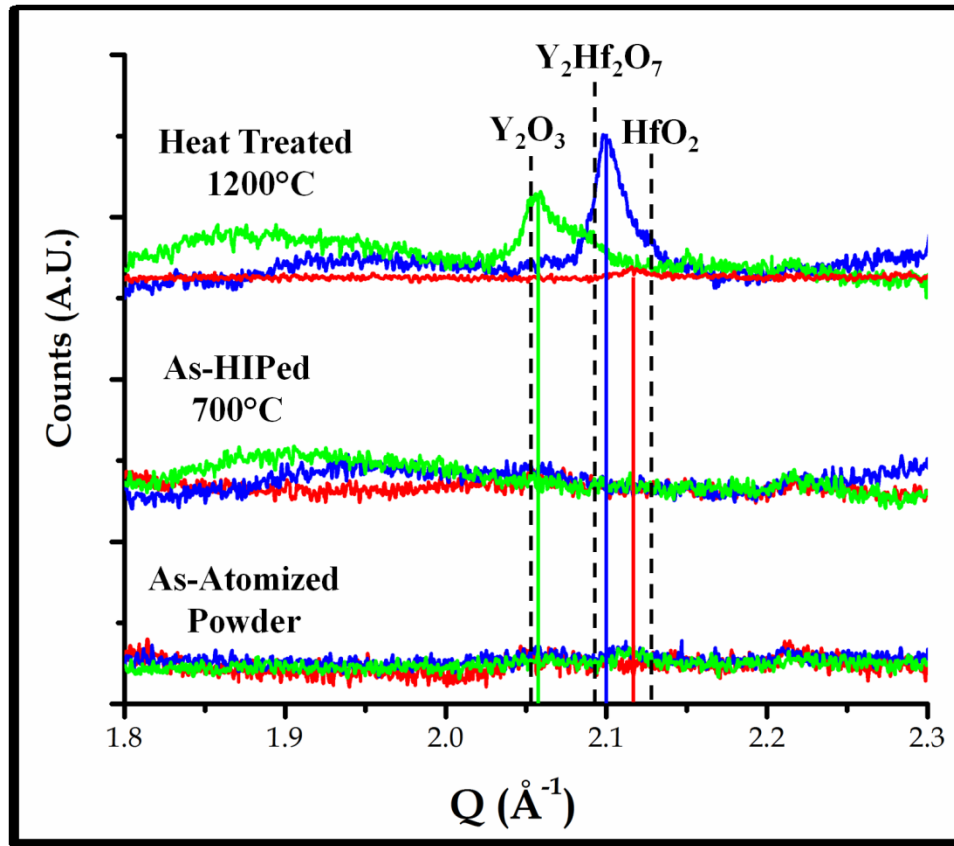


Figure 10.12. XRD data revealing dispersoid formation following elevated temperature heat treatment of CR-A (green trace and peak marker), CR-B (blue trace and peak marker), and CR-C (red trace and peak marker) with reference peak positions (adjacent black dashed lines) for  $Y_2O_3$ ,  $Y_2Hf_2O_7$ , and  $HfO_2$  [232, 242, 243]

Achieving such non-equilibrium microstructures is possible through the enhanced kinetics of rapid solidification. This phenomenon has been explained by Glicksman [244], through the concept of a kinetic phase diagram (see Figure 10.13), based on the work of Chernov et al. [245, 246]. This phase diagram illustrates how equilibrium solidus and liquid lines move together with increasing solidification velocity, thus approaching the  $T_0$  limit [80]. Therefore, the ultra-fine (CR-C) powders must have solidified above the threshold solidification rate to suppress Y and Hf segregation.



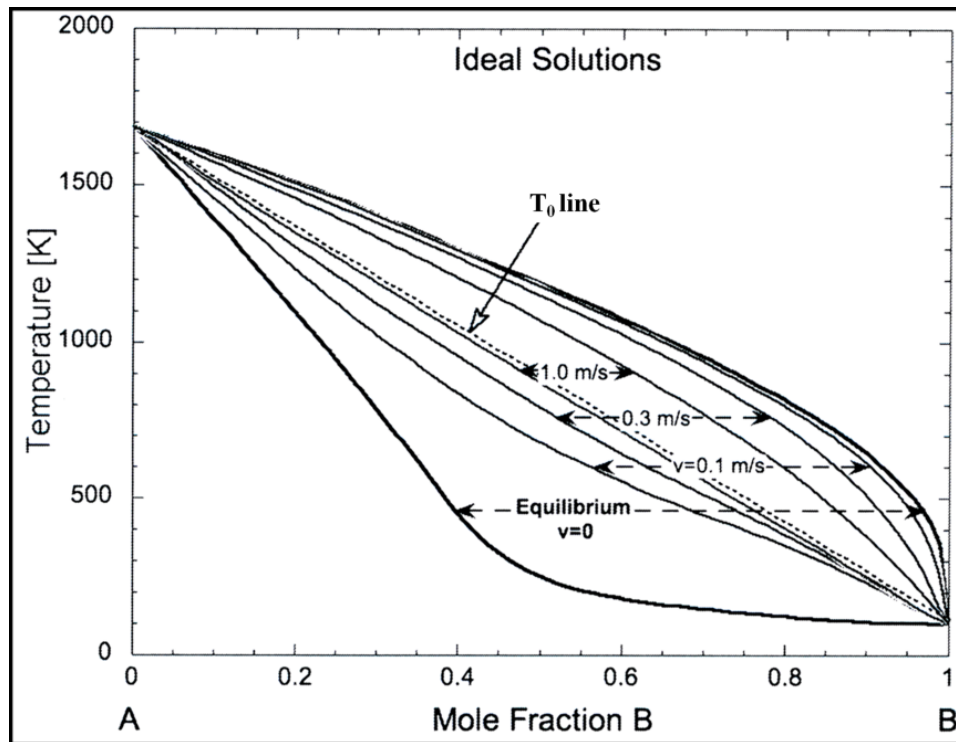


Figure 10.13. Kinetic phase diagram for an ideal A-B binary alloy adapted from Glicksman [244] (created from data produced by Aziz et al. [247])

Larger undercoolings associated with production of ultra-fine gas atomized powders supports the idea of an apparent increased solidification rate found in CR-C. These powders are capable of reaching large undercooling, due to the absence of heterogeneous nucleation sites or “motes” within each individual particle volume [248]. The concept of mote isolation, as described by Turnbull [249], indicates that the fraction of “mote” free volume can be significantly enhanced by subdividing a melt into finely dispersed particles, thus decreasing radically the probability that a given particle will contain a potent nucleation catalyst (see Figure 10.14).

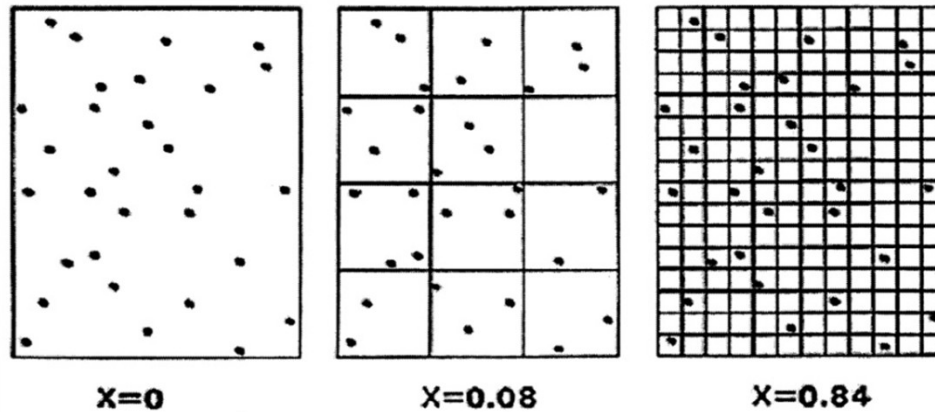


Figure 10.14. Description of mote isolation as a function of volume, where  $x$  indicates the fraction of mote free volume [248]

Atom probe tomography (APT) was used to evaluate chemical segregation within the rapidly solidified powders (see Figure 10.15), specifically comparing CR-B ( $\sim 15\mu\text{m}$ ) and CR-C ( $\sim 5\mu\text{m}$ ) powders. A low density of larger Y,Hf-enriched intermetallic precipitates were observed in CR-B. A much higher number density of  $3.5 \times 10^{22} \text{ m}^{-3}$  Y,Hf-enriched clusters with an average diameter of 3nm were found in CR-C (see arrow in Figure 10.15b), in good agreement with the IMC precipitates identified in the as-HIPed alloy microstructure (see Figure 10.7f). The size and spacing of these microstructural features provide further evidence that the ultra-fine (CR-C) powders solidified at an increased rate, resulting in the formation of a highly refined solidification structure containing uniformly distributed Y-Hf enriched nano-metric clusters. APT also provides information on the composition of the precipitates. Nominally, they are highly enriched in Fe as well as with smaller amounts of Y and Hf. However, the Fe may be an artifact of APT trajectory aberrations. The nominal Y/Hf ratio was found to be  $\sim 2.1$  in the coarser precipitates (CR-B) and  $\sim 3.6$  in the nano-metric features (CR-C).

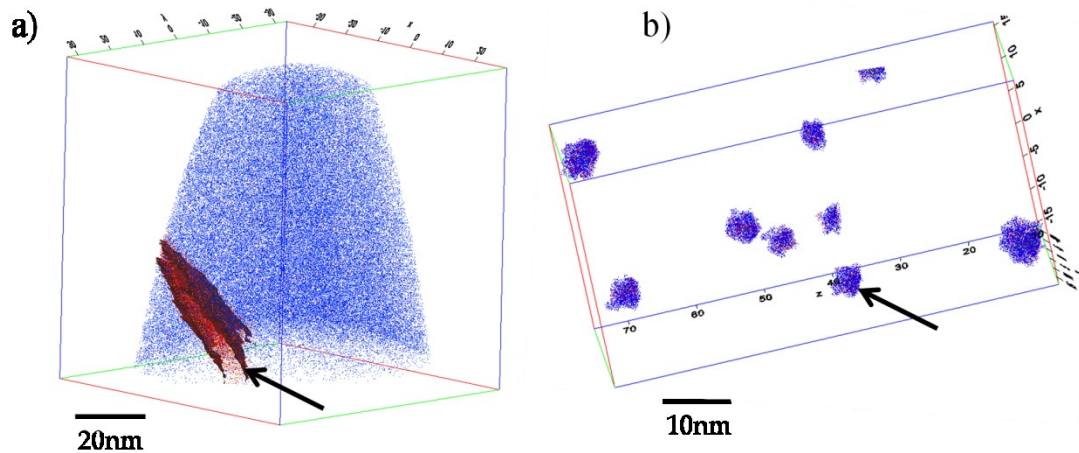


Figure 10.15. APT atom maps of the as-atomized powders: a)  $\sim 15\mu\text{m}$  dia. powder (CR-B) and b)  $\sim 5\mu\text{m}$  dia. powder (CR-C)

### 10.5.3 Dislocation substructure

Thermal-mechanical processing was used to develop a fine scale dislocation substructure within heat treated samples CR-A and CR-B. This procedure was adapted from previous work reported on the recovery and recrystallization of MA956 using various cold swaging and annealing treatments [5], which revealed how the balance between driving and dragging forces can influence dislocation recovery within the ODS microstructure. Furthermore, this critical balance was shown to depend strongly on the distribution of oxide particles throughout the microstructure, which controls deformation homogeneity and effective particle pinning forces [5].

The apparent work hardening rate witnessed in these CR-alloys (Figure 10.10) is comparable to other metal systems containing non-deforming hard particles (e.g., Cu-BeO) [76]. An initial increased hardening rate (up to  $\sim 20\%$  RA) is thought to occur due to the formation of Orowan loops around the nano-metric oxide dispersoids, which further reduces their effective spacing, and results in large

internal stresses [71]. Additionally, further deformation of these CR-alloys resulted in a noticeable decrease in work hardening rate, which is likely due to stain induced activation of secondary dislocation slip systems [250].

The heavily deformed cold rolled samples (i.e., ~80% RA) contained large amounts of stored energy which is a large driving force for recrystallization. Subsequent annealing of these samples at 600°C seemed to provide the necessary energy for boundaries to be sufficiently mobile even when restricted by dragging forces (i.e., Zener pinning [230]) of the nano-metric oxide dispersoids, leading to partial recrystallization and more significant loss in microhardness than at lower strains associated primarily with dislocation recovery processes. On the other hand, annealing these samples at 500°C appeared to limit boundary mobility, encouraging dislocation recovery to dispersoid interfaces, resulting in the formation of a fine cellular (sub-grain) dislocation substructure throughout the CR-alloy microstructure (see Figure 10.16). This agrees well with the findings of Ritherdon et al. [251], which showed a threshold temperature of 570°C for preventing the occurrence of recrystallization in as-milled ODS-Fe<sub>3</sub>Al and PM2000 powders.

As expected, the cell (sub-grain) size of these dislocation substructures was found to closely follow the distribution of nano-metric mixed Y-Hf-O dispersoids in these samples (see Figure 10.9). These results suggest that the dislocation substructure pattern is intrinsically linked to the original solidification structure within the as-atomized powders, i.e., this solidification structure predefines the size and distribution of the ensuing oxide dispersoids in these CR-alloys. This offers the unique possibility to engineer specific ODS microstructures through the use of selected precursor powder particles.

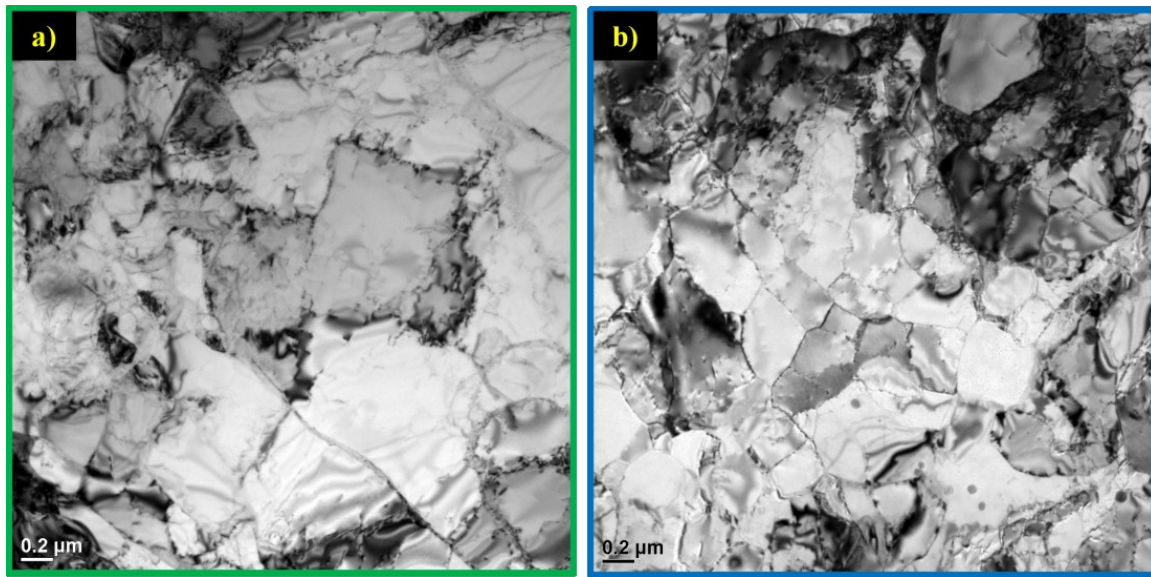


Figure 10.16. Dislocation substructure after HIP and annealing, followed by ~80% RA and a 1hr anneal at 500°C in air in samples made from size classified powders of: a) 20-53 $\mu$ m (CR-A) and b) 5-20 $\mu$ m (CR-B)

## 10.6 Summary

Gas atomization reaction synthesis (GARS) was used as a simplified approach to produce precursor oxide dispersion forming ferritic stainless steel powders. Mixed nano-metric Y-Hf-O dispersoids formed through solid state O exchange reactions between metastable Cr-enriched oxide and Fe-(Y,Hf) intermetallic precipitates, during elevated temperature heat treatment of these precursor powders. Resulting ODS microstructures were shown to be highly dependent on powder particle size (i.e., solidification rate). Small powders with increased amounts of solute trapping or highly refined solidification structures resulted in finer and more uniformly distributed nano-metric oxide dispersoids. Selection of powder particle size range (i.e., solidification morphology) was shown to be a viable method to control the final ODS microstructure. Thermal-mechanical processing was used to develop a fine scale dislocation substructure, which resulted in significant increases (~2X) in alloy microhardness.

## 10.7 Acknowledgements

Support from the Department of Energy, Office of Fossil Energy (ARM program) through Ames Laboratory contract no. DE-AC02-07CH11358 is gratefully acknowledged. The authors also would like to thank D. Byrd and J. Anderegg from Ames Laboratory-USDOE, and E. Fair and A. Spicher from Iowa State University for their individual contributions to this paper. The research at UCSB was supported by the Department of Energy, Office of Fusion Energy DE-FG03-94ER54275. Contributions to this work by UCSB researchers N. Cunningham, Y. Wu and G. Seward are gratefully acknowledged.

## Chapter 11. A Novel Fe-based ODS Fabrication Process

A paper to be submitted to: Metallurgical and Materials Transactions A, 2012

J.R. Rieken<sup>1,2,3</sup>, I.E. Anderson<sup>4</sup>, and M.J. Kramer<sup>4</sup>

### 11.1 Abstract

Oxide dispersion forming ferritic stainless steel (i.e., Fe-Cr-Ti-Y-O) powders were generated using a novel gas atomization reaction synthesis technique. During this process an ultra-thin metastable Cr-enriched surface oxide layer formed and encapsulated the rapidly solidified powders. This oxide layer was used as a vehicle to transport a prescribed amount of solid-state O into the consolidated microstructure. Elevated temperature heat treatment was then used to facilitate thermodynamically driven internal O exchange between trapped films of Cr-enriched oxide and Y-containing intermetallic precipitates, resulting in highly stable mixed oxide dispersoids (i.e., Y-Ti-O) that were identified using X-ray diffraction and transmission electron microscopy. Following dispersoid formation, thermal-mechanical processing was used to fabricate a fine scale dislocation substructure. A series of annealing treatments were used to evaluate the stability of the dislocation substructure. Additionally, preliminary mechanical properties were examined using elevated temperature tensile testing.

---

<sup>1</sup> Graduate Student, Department of Materials Science and Engineering, Iowa State University

<sup>2</sup> Primary researcher and author

<sup>3</sup> Author for correspondence: Tel.: +1 515 294 9159, E-mail address: [jrieken@istate.edu](mailto:jrieken@istate.edu)

<sup>4</sup> Division of Materials Sciences and Engineering, Ames Laboratory (USDOE), Ames, IA 50011

## 11.2 Introduction

Oxide dispersion strengthened (ODS) ferritic stainless steel alloys are being considered for elevated temperature applications within several types of future generation power plants [8, 9, 22, 38]. These alloys contain a large number density of nano-metric oxide particles that impede dislocation movement and stabilize the intrinsic strengthening effect of the sub-grain structure [3, 70, 80]. As a result, ODS materials exhibit excellent thermal stability and improved high temperature mechanical properties [1, 2, 113].

It has been shown that mechanical alloying (MA) by high energy ball milling of gas atomized master alloy powder (e.g., Fe-Cr-Ti-W) with nano-metric oxide particulate (e.g.,  $Y_2O_3$ ), followed by hot consolidation and thermal-mechanical processing can successfully yield a highly stable nano-scale ODS microstructure [6, 13]. Although effective, this conventional processing method faces several of the same developmental challenges that limited the widespread use of previously available commercial ODS alloys (e.g., MA-956 and PM 2000), including the high cost of MA particulate, control of alloy homogeneity and impurities, batch-to-batch variability, and anisotropic microstructure formation [9].

Gas atomization reaction synthesis (GARS) was developed as an economic alternative to the complex and time intensive MA process for the streamlined production of oxide dispersion forming particulate [14, 15]. This novel process utilizes a reactive atomization gas (i.e., Ar- $O_2$ ) to surface oxidize nascent ferritic alloy droplets during primary break-up and rapid solidification of the molten alloy, creating a highly robust ultra-thin ( $t < 100$  nm) Cr-enriched metastable surface oxide layer. This surface oxide layer is used as a vehicle to transport a prescribed amount of solid-state O into the consolidated microstructure. Elevated temperature heat treatment is then used to promote thermodynamically driven O-exchange between this Cr-enriched prior particle boundary (PPB) oxide and Y-enriched intermetallic



compound (IMC) precipitates, resulting in the formation of highly stable nanometric mixed Y-(Ti or Hf)-O dispersoids throughout the alloy microstructure [146, 179]. These alloys have been termed chemical reservoir (CR) alloys, since dispersoid formation is promoted through O-exchange between an O-reservoir phase (i.e., PPB oxide) and Y-reservoir phases (i.e., Y-enriched IMC precipitates). Furthermore, the size, distribution, and chemistry of the dispersoids have been linked to the initial solidification structure in the rapidly solidified powders, providing a unique ability to control the resulting ODS microstructure as a function precursor powder size (i.e., powder solidification rate) [146].

The aim of this paper is to illustrate the feasibility of this novel reactive gas atomization process for the production of ODS ferritic stainless steel alloys with distinct types of microstructures. The resulting ODS microstructures made from two different powder size ranges extracted from the same batch of base ferritic alloy powder will be compared. Additionally, results from initial thermal-mechanical treatment and elevated temperature tensile properties will be discussed.

### 11.3 Experimental

The nominal atomization charge chemistry for CR-166TiY is displayed in Table 11.1 [206]. The charge was loaded into the experimental gas atomization system of the Materials Preparation Center [206] and the atmosphere in the melting chamber and (connected) atomization system was evacuated with a mechanical pump to  $< 26.6$  Pa prior to backfilling to 111 kPa of high purity Ar. The charge was melted in a yttria ( $Y_2O_3$ ) painted zirconia ( $ZrO_2$ ) bottom pour crucible and superheated to  $1725^\circ C$ . The melt pour was initiated by raising a pneumatically actuated composite ( $Y_2O_3$ -W- $Al_2O_3$ ) stopper rod [252], which allowed the molten alloy to flow through a plasma sprayed  $Y_2O_3$  lined  $ZrO_2$  pour tube.

**Table 11.1 Resulting CR-166TiY alloy composition with respect to powder particle size: CR-A) dia. < 20 $\mu$ m and CR-B) 45-75 $\mu$ m**

<b>Alloy</b>	<b>Powder Size</b>	<b>Fe (at.%)</b>	<b>Cr (at.%)</b>	<b>Y (at.%)</b>	<b>Ti (at.%)</b>	<b>O (at.%)</b>
<b>CR-166TiY</b>	Nominal	Bal.	15.95	0.21	0.12	-
<b>CR-166TiY (CR-A)</b>	Dia. < 20 $\mu$ m	Bal.	15.91	0.09	0.12	0.49
<b>CR-166TiY (CR-B)</b>	45-75 $\mu$ m	Bal.	15.91	0.09	0.12	0.33

Upon exiting the pouring orifice, the melt was immediately impinged by the reactive atomization gas, following the GARS procedure [14, 15]. This gas contained 0.19 vol.% O<sub>2</sub> mixed with high purity Ar and was directly injected through the high-pressure close-coupled atomization die at a pressure of 6.5MPa.

The resulting as-atomized powders were mechanically sieved into specific size divisions for this study, measuring dia. < 20 $\mu$ m and 45-75 $\mu$ m prior to chemical and microstructural evaluation and will be referred to hereafter as CR-A and CR-B, respectively (See Table 9.1). The bulk O content for each powder range was measured using an inert gas fusion (LECO) analyzer, while the percentage of each metallic constituent was identified using inductively coupled plasma / mass spectroscopy (ICP/MS).

Powders representing each size division were blended with 70 vol.% Cu (dia.< 20 $\mu$ m), sealed in latex bags, and cold isostatically pressed (CIPed) at a pressure of 413 MPa for ~60 s. These cold compacts were then impregnated with epoxy and cross-sectioned for microstructural analysis.

Separately, as-atomized powders from CR-A and CR-B were placed into individual 316L stainless steel cans measuring 25.4 mm in dia. x 127 mm in length. Each can was evacuated to a pressure of  $\sim 10^{-4}$  Pa, outgassed at 415°C for 1hr, and electron-beam welded shut using a 316L stainless steel cap. The canned powders were

consolidated using hot isostatic pressing (HIPing) at 700°C with 300 MPa pressure for 4 hrs.

The resulting low temperature HIPed rod for CR-A was then heat treated under vacuum ( $\sim 10^{-4}$  Pa) at 1200°C for 2.5 hrs, while the low temperature HIP rod for CR-B was heat treated during a secondary HIP cycle at 1200°C with 300 MPa pressure for 5 hrs. These separate heat treatment procedures have been reported previously as an effective method for forming nano-metric oxide dispersoids within similar CR-alloys [231].

Following heat treatment, sample bars were fabricated from each heat treated rod. These bars measured 9.7 mm x 12.9 mm x 12.9 mm (CR-A) and 11.8 mm x 12.2 mm x 60.9 mm (CR-B), respectively. Each bar was cold rolled (at room temperature) to an  $\sim 85\%$  reduction in area (RA) using 6% RA increments without intermediate anneals. An example of the heat treated bar and resulting cold rolled sheet for CR-B is shown in Figure 11.1.

Small coupons measuring 1.0 mm x 5.0 mm x 9.0 mm were cut from each of the resulting as-cold rolled sheets and used for annealing experiments. These coupons were first annealed at 500°C for 1 hr in air and subsequently annealed at 600, 700, 800, or 900°C for 1 hr in air. The microhardness for a transverse cross-section of the as-cold rolled sheet and annealed coupons was measured using Vickers diamond pyramid indentation with a 500 gm load. The average of seven consecutive indentations for each sample was plotted for each data point.



**Figure 11.1. (a) CR-B sample bar prior to cold rolling and (b) resulting cold rolled sheet following 85% RA**

The majority of the remaining cold rolled sheets were then annealed at 500°C for 1 hr in air followed by a secondary anneal at 800°C for 1 hr in air. The sheets were then surface ground to a thickness of 0.76 mm and coupons measuring 28.6 mm x 6.4 mm were electro-discharged machined (EDMed) longitudinal to the rolling direction. Additionally, coupons measuring 18.0 mm x 6.4 mm were EDMed transverse to the rolling direction for only CR-B. These coupons then were milled into SS-3 tensile specimens with nominal gage dimensions of 7.62 mm x 1.52 mm x 0.76 mm (see Figure 11.2) [253]. The tensile specimens were tested in air at room temperature and at elevated temperatures ranging from 400-800°C using a displacement rate of 0.1 mm-min<sup>-1</sup>, which produced a strain rate of  $2.2 \times 10^{-4}$  s<sup>-1</sup>, using a MTS 810 machine. The engineering yield strength (YS), engineering ultimate tensile strength (UTS), and total elongation (TE) for each tensile specimen was plotted for comparison.

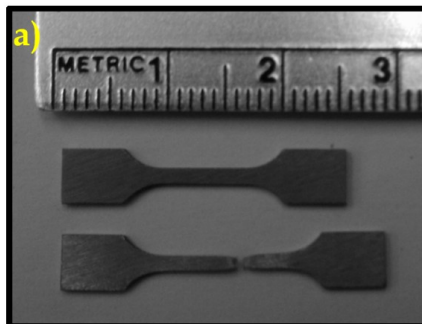


Figure 11.2. (a) SS-3 tensile specimen geometry before and after testing at room temperature

Surface analysis of the as-atomized powder particles was conducted using a JEOL JAMP 7830F scanning Auger microprobe (SAM) with a hemispherical auger electron spectrometer (AES) and Ar-ion sputtering gun for depth profiling. Additionally, electron probe microanalysis (EPMA) chemical mapping of the powder solidification structure was completed using a JEOL JXA 8200 WD/ED microanalyzer.

The nano-metric oxide layer at the surface of the as-atomized powders was evaluated using an FEI Tecnai F20ST transmission electron microscope (TEM) / scanning transmission electron microscope (STEM) at the Electron Microscopy Center (EMC) for Materials Research at Argonne National Laboratory. The powder particles also were prepared for TEM/STEM analysis at the EMC using a Zeiss 1540XB focused ion beam (FIB) scanning electron microscope (SEM). The powders were coated with a thin layer of Au ( $\sim 10$  nm) prior to FIB milling to protect the as-atomized surface oxide layer. Additionally, carbon deposition was used to bond the powders to a manipulator during FIB milling and to secure the as-thinned specimen to a slotted Cu TEM grid prior to analysis.

The CR-alloy microstructure and tensile fracture analysis was completed using a Hitachi S-2460N SEM with EDS. Furthermore, the resulting nano-metric oxides and grain size was evaluated using a Tecnai G<sup>2</sup> F20 TEM/STEM at 200 keV. Miniature cylinders measuring 3.0 mm in dia.  $\times$  10.0 mm in length were EDMed from HIPed and heat treated rods, while 3.0 mm dia.  $\times$  0.76 mm thick disks were EDMed from the cold rolled sheets after annealing both at 500°C for 1hr in air and at 800°C for 1hr in air. The cylinders were subsequently sliced into 1.0 mm thick disks, and all disks were ground flat using 400 and 600 SiC grit paper, polished using 6.0  $\mu$ m and 1.0  $\mu$ m diamond polishing compound, and mechanically dimpled to a thickness of  $\sim 20$   $\mu$ m in preparation for TEM analysis. The disks were then dual jet polished using an electrolytic solution for stainless steels (i.e., 700 ml methanol, 120 ml distilled water, 100 ml glycerol, and 80 ml perchloric acid) at -12°C. Additionally, the CR-alloy grain size was measured using the lineal intercept method according to ASTM E112-96 (2004).

The structural identification of all product phases, including Y-enriched nano-metric oxide dispersoids, was performed at each step of this simplified process using a Phillips PANalytical X-Pert Pro Diffraction System with Co-K $\alpha$  radiation. A

scanning real time multiple strip (RTMS) X-ray detector was used with an active length of  $\sim 0.05Q$  ( $\text{\AA}^{-1}$ ). Diffraction data was collected from  $1.8$ - $4.8Q$  ( $\text{\AA}^{-1}$ ) with a step size of  $5 \times 10^{-4} Q$  and a dwell time of  $500$  s per step. The reciprocal lattice vector ( $Q$ ) describes the momentum difference between incoming and diffracted X-rays (Equation 106), and is commonly used to compare X-ray diffraction data (i.e., Bragg angle ( $\theta$ ) of resulting peaks) independent of wavelength ( $\lambda$ ) [216].

$$Q = \frac{4\pi \sin \theta}{\lambda} \quad \text{Equation 106}$$

## 11.4 Results

The resulting as-atomized CR-alloy composition is listed in Table 9.1. It can be seen that each powder size division contains equivalent alloying additions of Y and Ti with different amounts of resulting O. The increased O content associated with the finer powders (CR-A) is related to an increased surface area to volume ratio. Additionally, a significant portion (i.e.,  $\sim 57$  at.%) of the nominal Y concentration was lost during the powder synthesis process, presumably as a consequence of oxidation that occurs during melting of the alloy charge prior to gas atomization. Although this loss was expected, based on previous GARS trials [238], upgrades to the current experimental atomizer are planned to better control the loss of Y during future GARS trials. These upgrades include the installation of an  $O_2$  gas analyzer, an  $O_2$  gettering furnace, and the capability to make a late alloy addition (a common industrial practice) of Fe-Y master alloy shortly before releasing the melt for atomization.

### 11.4.1 As-Atomized Powders

The resulting gas atomized powders exhibited a spherical morphology. The surface of the CR-A (fine) particles were found to be rather smooth and typically free of satellite particles (Figure 11.3a), while the surface of the larger CR-B particles seemed to contain more irregularities (e.g., satellite particles (red arrow) and

dimples (yellow arrow) in Figure 11.3d). Interestingly, the frequency of surface dimples on the CR-B particles seemed to greatly outweigh the number of satellite particles. Perhaps this indicates that surface oxide formation initiates prior to particle solidification, acting as a pliable solid interface, which prevents particle adhesion during collisions between smaller solid particles (CR-A) and larger semi-solid particles (CR-B).

Compositional maps of cross-sectioned CIPed powders (see Figure 11.3b and e) revealed increased Y levels along apparent as-solidified cell boundaries (see red arrow in Figure 11.3c and f), as a result of Y rejection from the  $\alpha$ -(Fe,Cr) matrix during the rapid solidification process. A small Y-denuded zone also was identified at the surface of the particles, extending to a depth of  $\sim 1\mu\text{m}$  or  $\sim 4\mu\text{m}$  in the CR-A and CR-B, respectively. Additionally, several regions along the surface of the particles showed increased levels of Y (see yellow arrow in Figure 11.3c and f), representing the occasional presence of Y in the surface oxide layer.

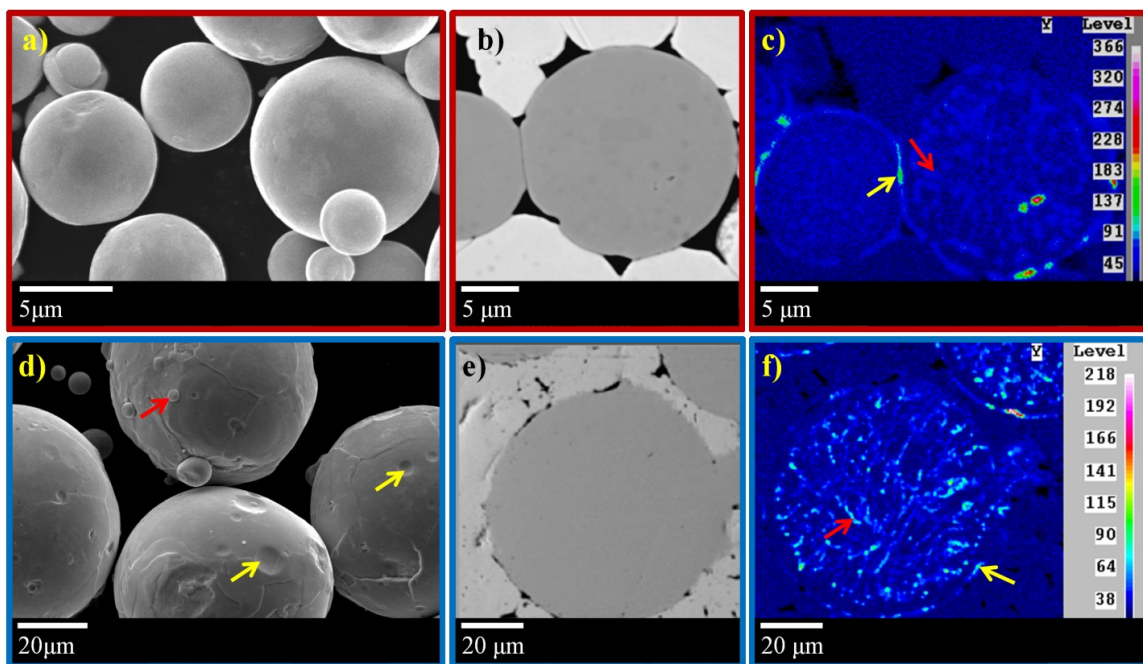
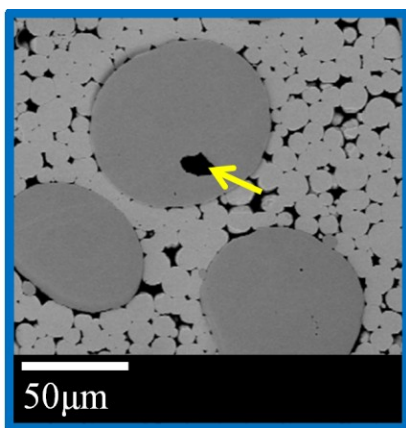


Figure 11.3. As-atomized powder morphology and cross-sectioned CIPed powders with EPMA WDS compositional maps of Y: a), b), and c) represent powders with a dia.  $< 20\mu\text{m}$  (CR-A) and d), e), and f) represent powders with a dia. between  $45\text{--}75\mu\text{m}$  (CR-B)

Further analysis of the cross-sectioned CIPed powders revealed several CR-B powders that contained large voids (see yellow arrow in Figure 11.4). These voids are thought to be Ar bubbles that were entrapped during the gas atomization process. It should be noted that similar voids were not readily apparent in the finer CR-A powders, which agrees well with the findings of Korth et al., which indicated an inverse relationship between the prevalence of noble gas entrapment and particle size [254].



**Figure 11.4.** An example of a pore found in cross-sectioned CIPed powders with a diameter between 45-75μm (CR-B)

AES depth profiles representing the surface chemistry for powders CR-A (dia.  $\sim 10\mu\text{m}$ ) and CR-B (dia.  $\sim 58\mu\text{m}$ ) are shown in Figure 11.5. This semi-quantitative assessment of the surface oxide chemistry revealed a primary enrichment in O and Cr with varying amounts of Y and Fe. The thickness of the surface oxide (based on a  $\text{SiO}_2$  standard) was taken as the midpoint between the maximum and minimum intensity value for O, resulting in a surface oxide thickness prediction of  $\sim 10\text{ nm}$  and  $\sim 70\text{ nm}$  for CR-A and CR-B, respectively (see dashed vertical lines in Figure 11.5). These results show a direct relationship between surface oxide thickness and particle size, which indicates that prolonged surface oxidation of the coarser particles had occurred (i.e., illustrating the cooling rate sensitivity of this GARS process).



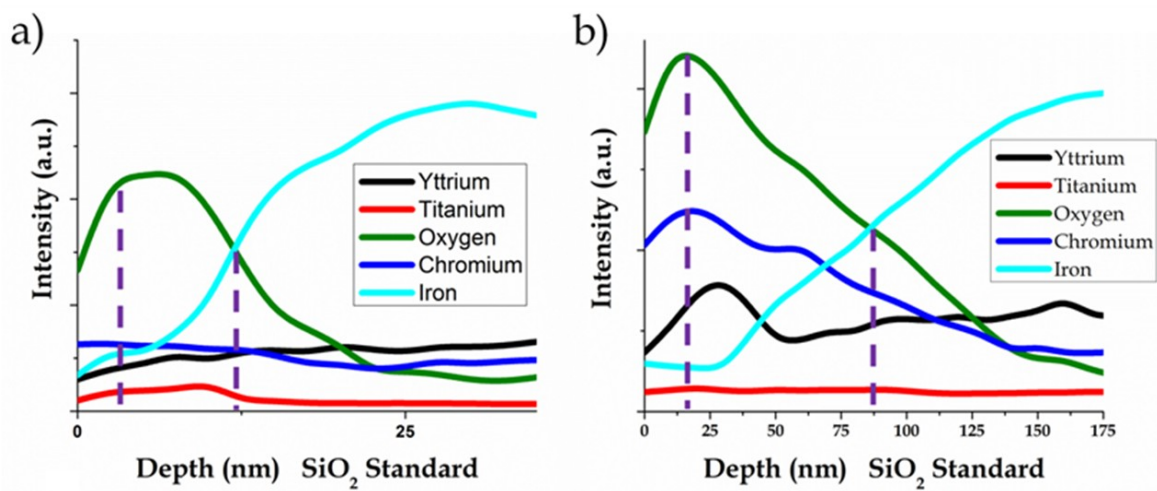


Figure 11.5. AES depth profiles for as-atomized powders: a) with  $\sim 10\mu\text{m}$  dia. (CR-A) and b) with  $\sim 58\mu\text{m}$  dia. (CR-B)

FIB milling was used to prepare an as-atomized powder particle from CR-B (dia.  $\sim 58\mu\text{m}$ ) for TEM analysis (see Figure 11.6a and b), in order to confirm and evaluate the physical characteristics of the resulting surface oxide layer. Two distinct surface oxide layers (see Figure 11.6d) were identified during this analysis, initially based on contrast differences. The outer oxide layer ( $\sim 15\text{nm}$  thick) was found to contain O, Cr, and Y and the inner oxide layer ( $\sim 20\text{nm}$  thick) was found to contain O, Fe, and Cr (see EDS linescan in Figure 11.6e), which provided a cause for the apparent contrast difference. Notably, these results agree well with the aforementioned AES compositional depth profile (see Figure 11.5b), while illustrating a more accurate representation of the surface oxide thickness and the interesting dual nature of this surface layer.

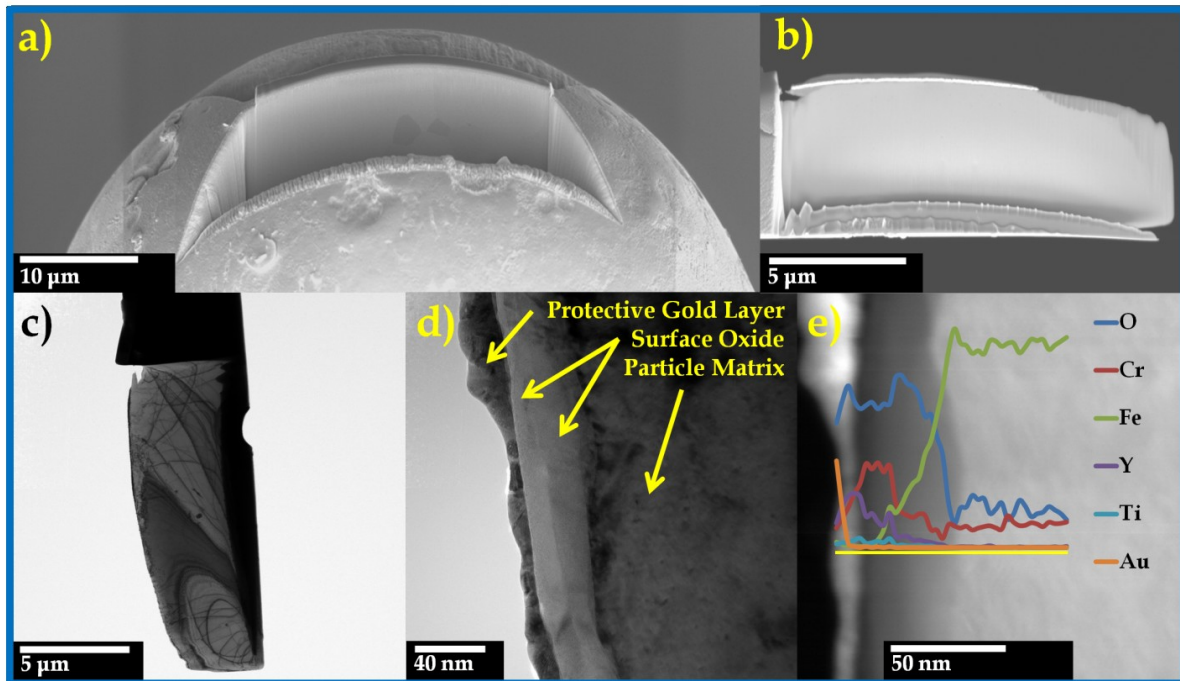


Figure 11.6. As-atomized surface oxide analysis of a powder with  $\sim 58\mu\text{m}$  dia. (CR-B): a) and b) SEM images showing the original as-atomized particle and extracted TEM specimen following FIB milling, c) and d) bright field TEM images indentifying the surface oxide layer, and e) high angle annular dark field (HAADF) image with EDS linescan across the surface oxide layer

#### 11.4.2 Oxide Dispersoid Formation

A continuous network of PPB oxide was formed during low temperature ( $700^\circ\text{C}$ ) HIP consolidation of the CR-alloy powders (see yellow arrow in Figure 11.7a and c). The initial PPB oxide volume percent was measured at  $\sim 0.78 \pm 0.03\%$  and  $\sim 0.52 \pm 0.05\%$  for CR-A and CR-B, respectively (calculated from SEM images using ImagePro™ 5.1). Compositional analysis of the PPB oxide, using WDS linescans (not shown), revealed a primary enrichment of Fe, Cr, and O with smaller concentrations of Ti and Y in both CR-alloys.

Elevated temperature ( $1200^\circ\text{C}$ ) heat treatment of the as-consolidated powders decreased the volume percent of PPB oxide by  $\sim 0.4 \pm 0.02\%$  and  $\sim 0.3 \pm 0.05\%$  in CR-A and CR-B, respectively (see yellow arrow in Figure 11.6b and d). This provided evidence of an apparent O-exchange reaction. Additionally, the residual PPB oxide

seemed to coarsen during heat treatment, transitioning from elongated films to spheroidized particles along the PPBs. Compositional analysis of the residual PPB oxide, using WDS linescans (not shown), showed an increase in Ti concentration following heat treatment. Furthermore, several PPB oxides from each of the CR-Alloys were found to contain increased concentrations of both Ti and Y, but electron probe interaction with the surrounding  $\alpha$ -(Fe,Cr) matrix and other nano-scale oxides prevented accurate identification of these particular oxide phases.

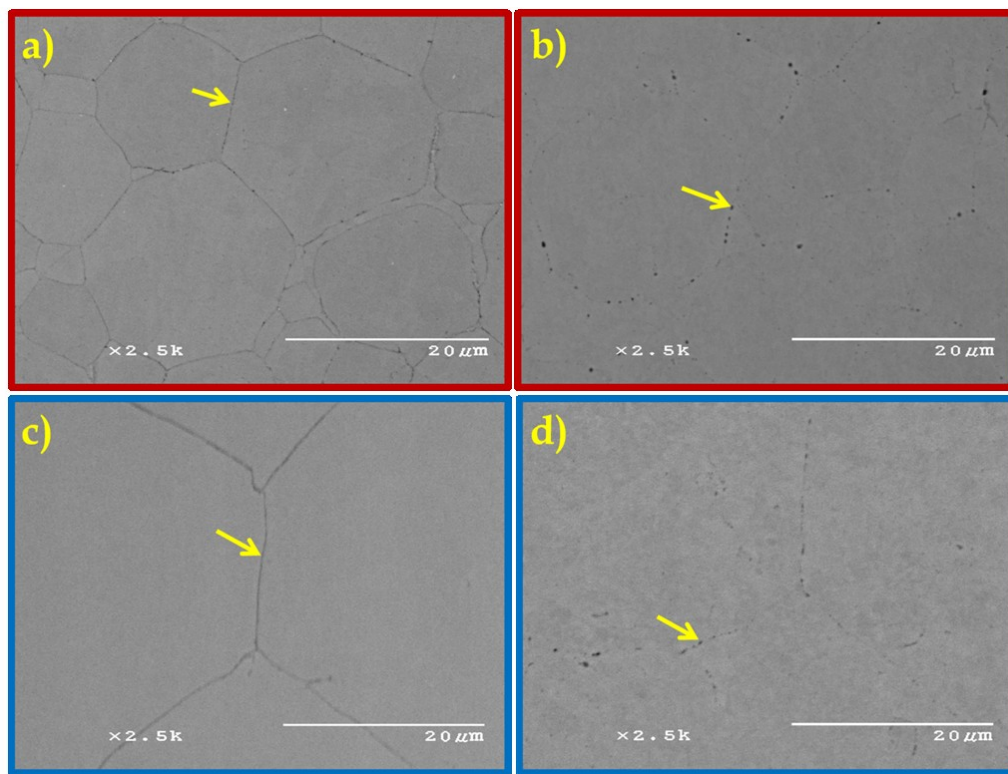


**Figure 11.7.** As-consolidated CR-alloy microstructure (a and c) and resulting microstructure following heat treatment at 1200°C (b and d): a) and b) for powders with a dia. < 20μm (CR-A) and c) and d) for powders with a dia. 45-75μm (CR-B)

TEM analysis revealed the formation of nano-metric oxide dispersoids throughout the  $\alpha$ -(Fe,Cr) matrix following elevated temperature (1200°C) heat treatment of the CR-alloys (see Figure 11.8). The dispersoids were found to form in a cellular pattern

(see Figure 11.8a and d), which seems to mimic the solidification structure of the atomized powders (see Figure 11.3c and f).

CR-A was found to contain two distinct size classes of dispersoids. Larger dispersoids with a spherical or globular morphology (20-100nm in dia.) were found organized in a cellular pattern (see yellow arrow in Figure 11.8). Furthermore, the interior core of this cellular structure was found to contain a second set of smaller dispersoids (see green arrow in Figure 11.8) with a spherical morphology (5-10nm in dia.). Notably, the two sets of dispersoids were separated by a precipitate free zone (PFZ) ranging from 200-300nm in thickness.

CR-B also contained dispersoids typically organized in a cellular pattern, but the interior core of the cells did not contain smaller dispersoids, as seen in CR-A. These dispersoids also had a large size distribution (10-200nm). The majority of the dispersoids contained a spherical or globular morphology, although several regions were found to contain dispersoids with a cubic morphology. This change in dispersoid morphology is thought to be related to the  $\alpha$ -(Fe,Cr) grain orientation, perhaps indicating a crystallographic orientation relationship between the matrix and dispersoid phase (as shown in [222]), but confirmation of this assumption will require further TEM analysis.

Furthermore, dispersoid number density was found to vary between  $1-4 \times 10^{21} \text{ m}^{-3}$  and  $1-10 \times 10^{20} \text{ m}^{-3}$  (assuming a TEM foil thickness of 100nm) for CR-A and CR-B, respectively. This variation in dispersoid number density seems to illustrate increased dispersoid uniformity with decreasing powder size (i.e., CR-B  $\rightarrow$  CR-A).

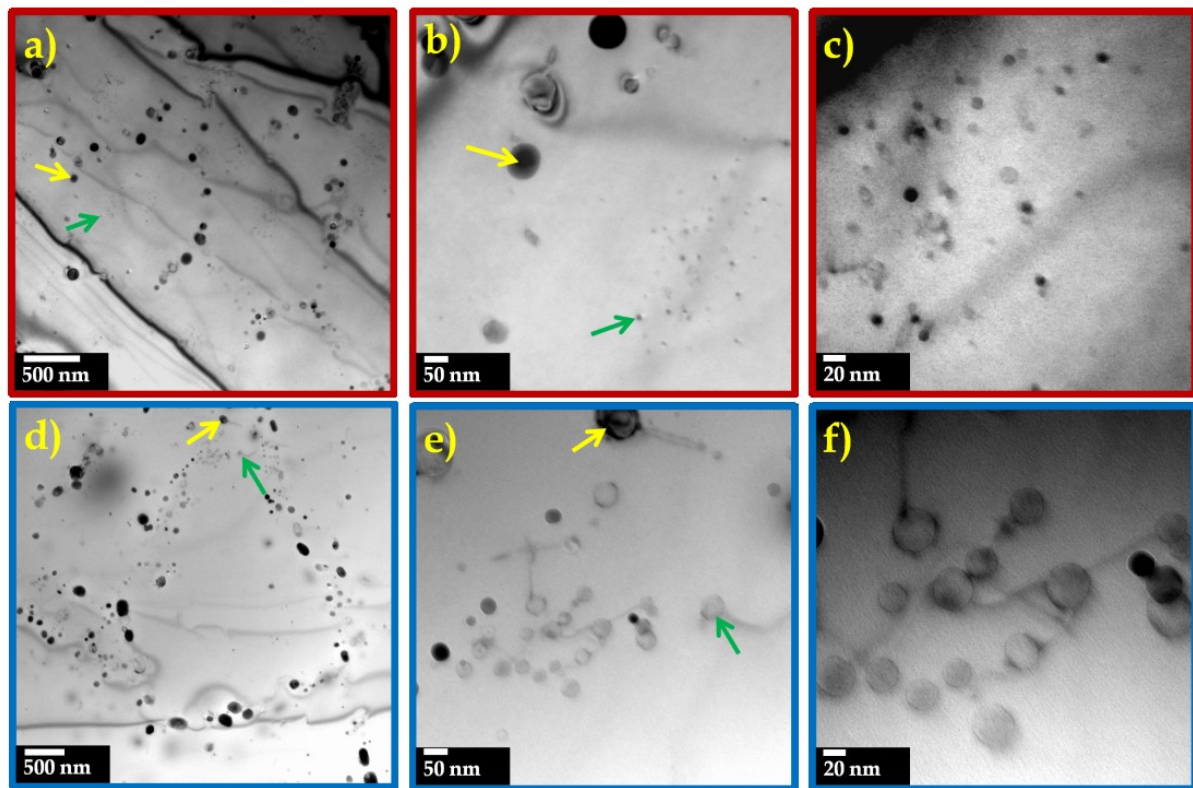


Figure 11.8. TEM micrographs of the heat treated (1200°C) CR-alloy microstructure made from powders with: a), b), and c) dia. < 20μm and d), e) and f) dia. of 45-75μm

XRD was used to evaluate product phase evolution and served to confirm dispersoid formation in these CR-Alloys (Figure 11.9). This analysis indicated dispersoid formation following elevated temperature (1200°C) heat treatment. The resulting dispersoid phase was identified as  $\text{Y}_2\text{Ti}_2\text{O}_7$  with a calculated volume percent of 0.51% for both CR-alloys [255].

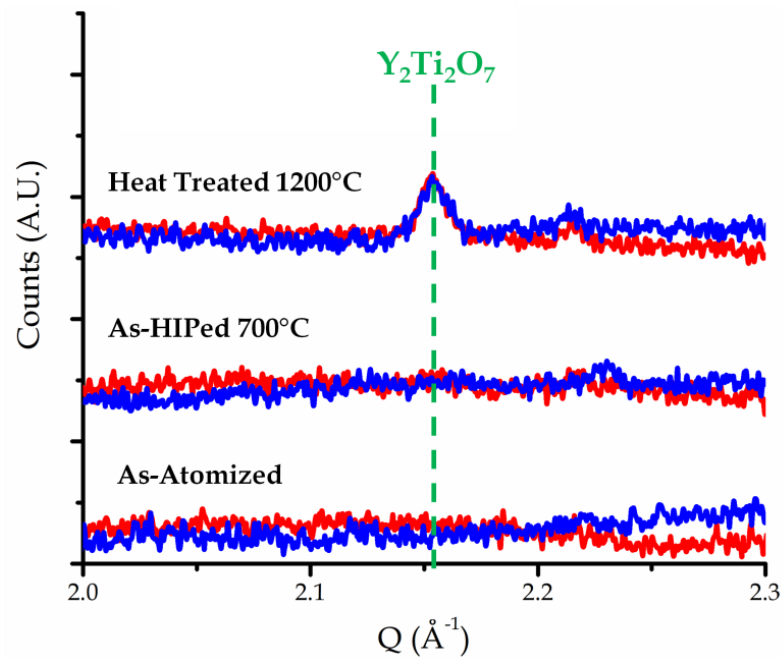


Figure 11.9. XRD results revealing dispersoid phase formation in CR-A (red lines) and CR-B (blue lines)

#### 11.4.3 Thermal-Mechanical Treatment (TMT)

Cold rolling was used to strain harden the CR-alloys following dispersoid formation (see example in Figure 11.1b). The cold rolled sheets were first annealed at 500°C to recover dislocations to dispersoid-decorated boundaries, in an effort to establish a dislocation substructure with reduced strain energy. This procedure was adapted from previous results reported for similar CR-alloys [146]. Additional annealing treatments at a succession of higher temperatures also were used to evaluate the stability and strengthening effectiveness of the dislocation substructure, as measured by ambient temperature microhardness.

The initial CR-alloy microhardness values following dispersoid formation (horizontal dashed lines) and the resulting as-cold rolled and annealed microhardness values for CR-A (red line) and CR-B (blue line) are shown in Figure 11.10. Interestingly, the microhardness for each CR-alloy was increased ~136 Hv



after cold rolling, resulting in an as-cold rolled microhardness of  $316 \pm 6$  Hv and  $271 \pm 4$  Hv for CR-A and CR-B, respectively. This microhardness value was significantly reduced at annealing temperatures above  $600^\circ\text{C}$ , resulting in lower but consistent microhardness values of  $166 \pm 4$  Hv and  $140 \pm 5$  Hv for CR-A and CR-B, respectively. This large drop in microhardness is believed to indicate the onset of recrystallization in both of these heavily strained CR-alloys. Notably, the CR-alloys seem to maintain a similar microhardness differential following each annealing treatment.

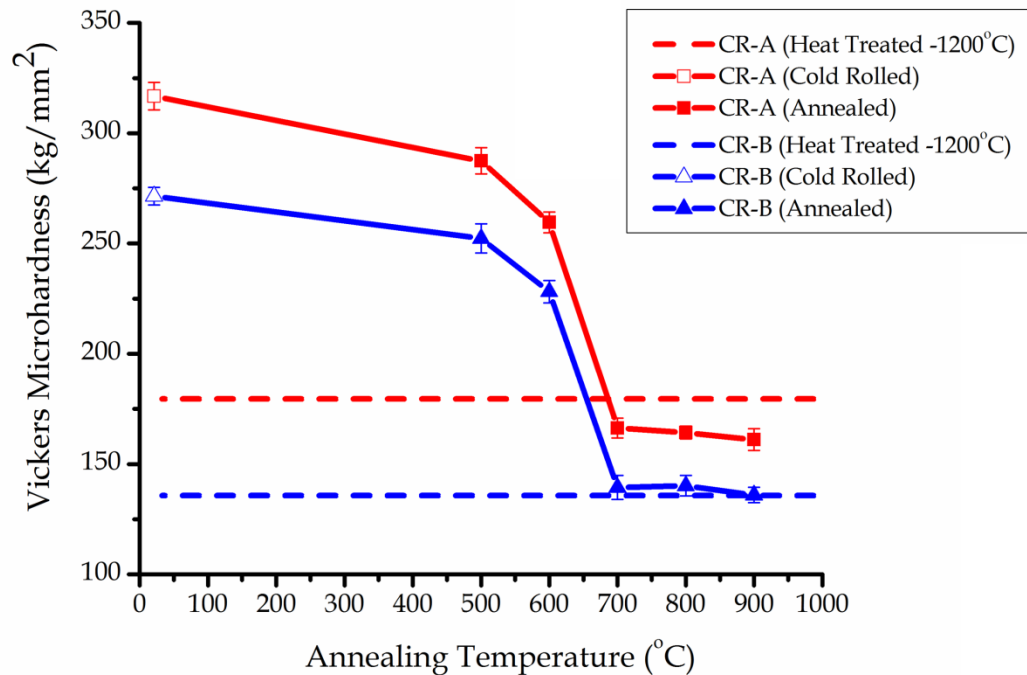


**Figure 11.10.** CR-alloy microhardness following dispersoid formation (horizontal dashed lines) compared to subsequent cold rolled (open box and open triangle) and annealed (closed box and closed triangle) microhardness: CR-A (red lines and boxes) and CR-B (blue lines and triangles)

STEM analysis revealed the CR-alloy grain structure and dispersoid distribution following dispersoid formation ( $1200^\circ\text{C}$  heat treatment), and after cold rolling (85% RA) and annealing at  $500^\circ\text{C}$  or at  $500^\circ\text{C}+800^\circ\text{C}$  (see Figure 11.11). The average grain

size following dispersoid formation was measured at  $1.1\pm0.2\mu\text{m}$  and  $1.1\pm0.1\mu\text{m}$  for CR-A and CR-B, respectively. This average grain size was reduced to  $0.33\pm0.07\mu\text{m}$  and  $0.37\pm0.06\mu\text{m}$  after annealing the cold rolled sheets at  $500^\circ\text{C}$ . Increasing the final annealing temperature to  $800^\circ\text{C}$  apparently recrystallized the CR-alloy grain structure, resulting in a grain size of  $13.5\pm1.0\mu\text{m}$  and  $13.9\pm0.5\mu\text{m}$  for CR-A and CR-B, respectively. Furthermore, the recrystallized grain boundaries were found to contain undulations due to localized pinning from the nano-metric oxide dispersoids (see Figure 11.11c). It should be noted that the grain size for the  $500^\circ\text{C}+800^\circ\text{C}$  annealed microstructures was measured from SEM images of electrolytically polished TEM samples, since the grains were found to be too large for accurate identification using STEM image analysis.

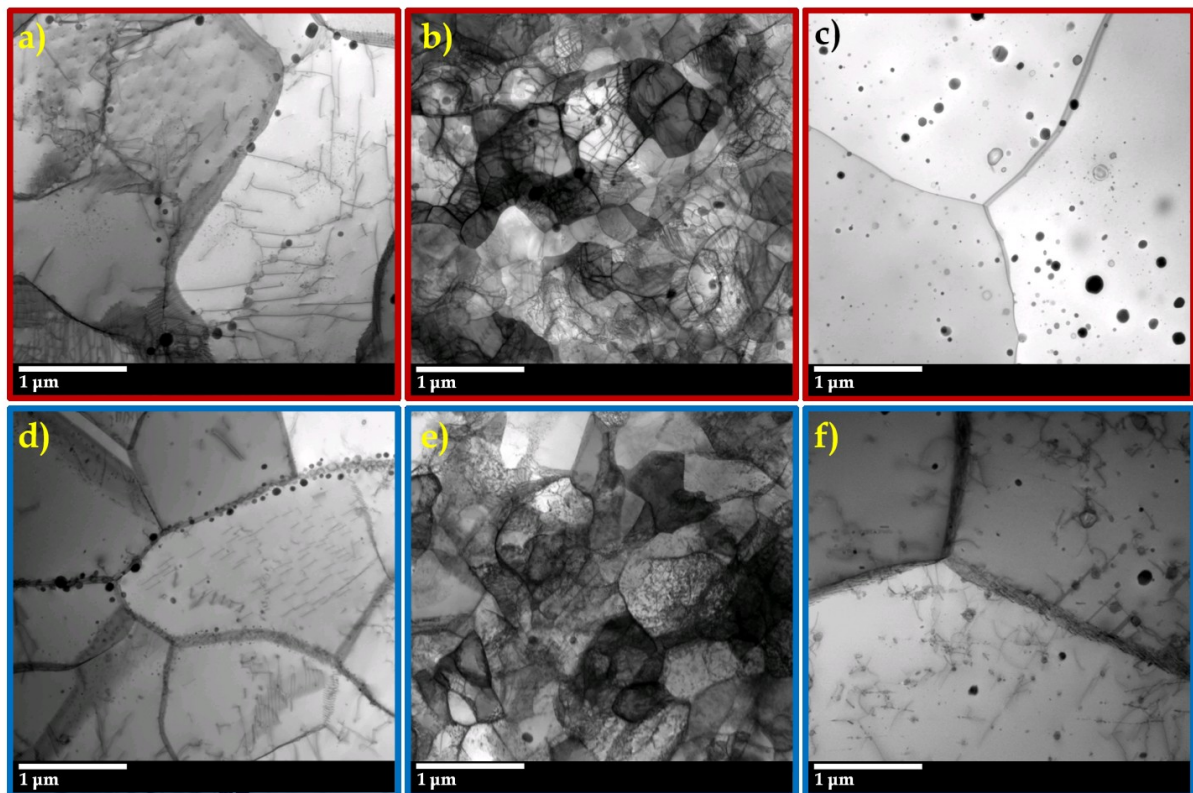


**Figure 11.11.** Bright field (BF) STEM images showing the CR-alloy grain structure and dispersoid distribution following dispersoid formation (a and d) and after being cold rolled to 85% RA and then annealed at  $500^\circ\text{C}$  (b and e) or  $500^\circ\text{C}+800^\circ\text{C}$  (c and f) for powders with: a), b), and c) a dia.  $< 20\mu\text{m}$  and d), e), and f) a dia.  $45\text{-}75\mu\text{m}$



#### **11.4.4 Initial Mechanical Properties**

The elevated temperature yield (YS) and ultimate tensile strength (UTS) with corresponding total elongation (TE) values for the cold rolled CR-alloy sheets in the 800°C (final) annealed condition (i.e., recrystallized) are shown in Figure 11.12. These results were compared to previously reported literature values for recrystallized MA-956 (see black lines in Figure 11.12) [198].

The YS of CR-A was found to be ~100 MPa greater than CR-B, but ~100-160 MPa less than MA-956 at lower testing temperatures ( $T \leq 400^\circ\text{C}$ ). As the test temperature was increased ( $T \geq 600^\circ\text{C}$ ), the YS of CR-A and CR-B converged to near equivalent values, which were ~50-70 MPa less than MA-956 (see Figure 11.12a). Similar trends also were observed for the UTS of the CR-alloys and MA-956. Notably, the YS and UTS for CR-B were found to be identical in the longitudinal (closed blue triangles) and transverse (open blue triangles) orientations relative to the rolling direction, indicating isotropic mechanical properties. It should be noted that CR-A was only tested in the sample orientation longitudinal to the rolling direction.

The CR-alloys exhibited peak ductility at 600°C, analogous to the ductility trend also reported for MA-956. Furthermore, the CR-alloys demonstrated good ductility with total elongation values above 30% over the range of testing temperatures, which equated to approximately a threefold increase compared to MA-956. It also can be seen that CR-B contained nearly identical total elongation values in the longitudinal and transverse rolling direction.

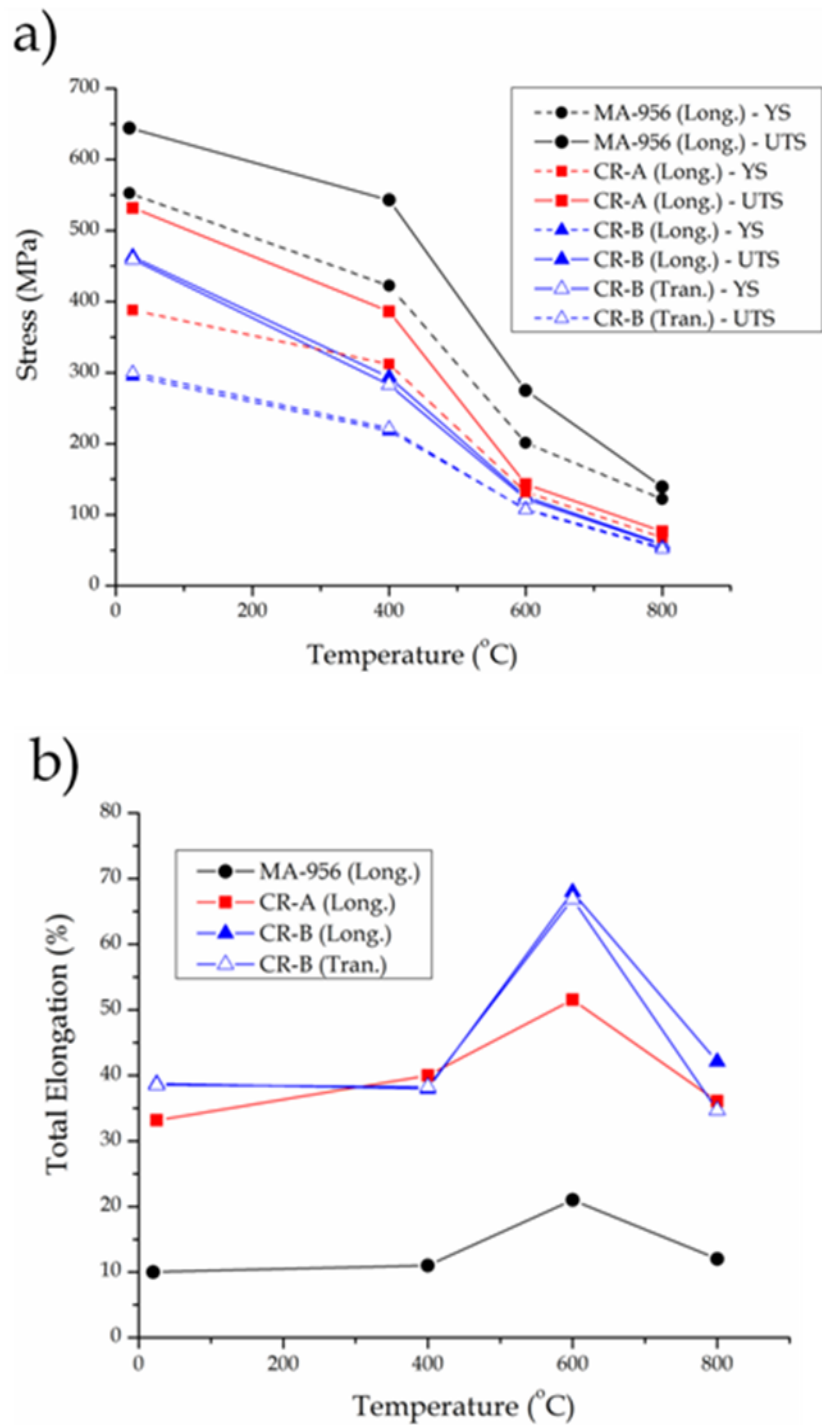
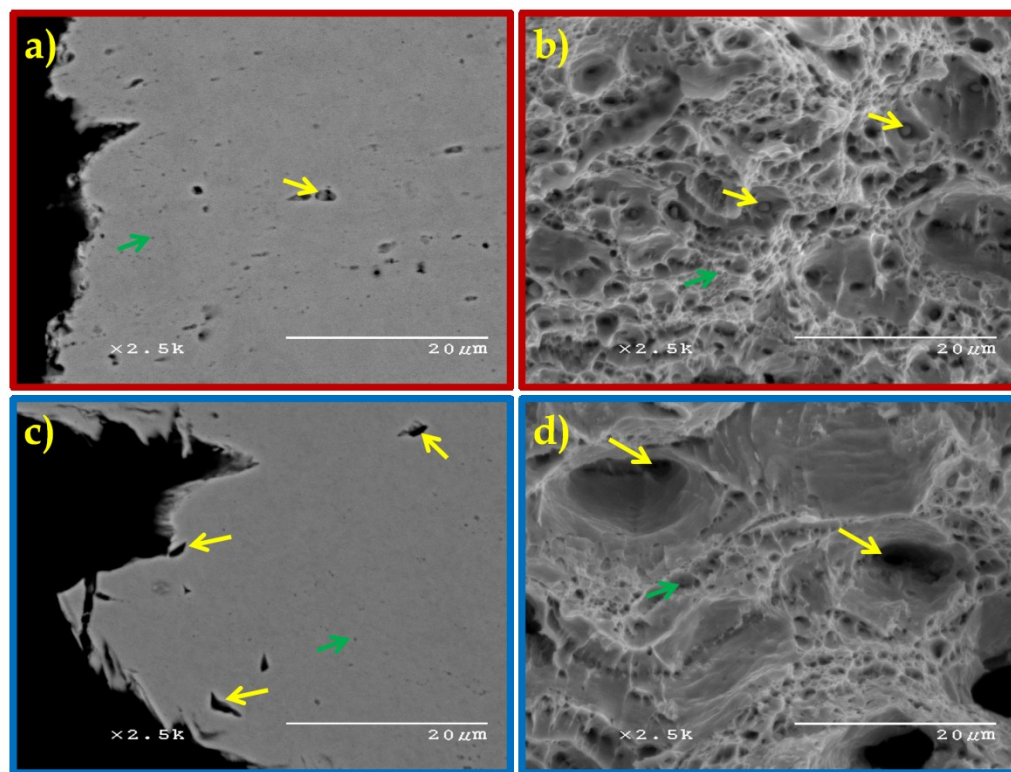


Figure 11.12. A comparison of the a) tensile strength (UTS) and yield strength (YS) and b) total elongation as a function of temperature for CR-A (red line), CR-B (blue lines), and MA-956 (black lines)

Cross-sectional analysis of the fractured CR-A room temperature tensile specimen showed debonding between residual PPB oxide and the  $\alpha$ -(Fe,Cr) matrix (see yellow arrow in Figure 11.13a). Furthermore, these residual PPB oxides were identified at the base of primary ductile dimples along the fractured surface of the tensile specimen (see Figure 11.13b), in conjunction with smaller secondary dimples that could have originated at the interface between larger  $\text{Y}_2\text{Ti}_2\text{O}_7$  oxides and the  $\alpha$ -(Fe,Cr) matrix (see green arrow in Figure 11.13a and b).



**Figure 11.13.** Fracture analysis of the cross-section (a and c) and surface (b and d) of a ruptured room temperature tensile specimen made from powders with: a) and b) a dia. < 20 $\mu\text{m}$  and c) and d) a dia. 45-75 $\mu\text{m}$

A similar cross-sectional analysis of the fractured CR-B room temperature tensile specimen revealed porosity near the fractured surface of the specimen (see yellow arrow in Figure 11.13c), which could be related to the aforementioned gas porosity observed in the as-atomized CR-B powders (Figure 11.4) that would have been

flattened by the cold rolling process. Surface analysis of this specimen showed large voids interconnected by smaller ductile dimples. The larger voids probably originated from the porosity witnessed in the cross-sectional analysis (see yellow arrows in Figure 11.13c and d), while the smaller dimples probably form during debonding between larger  $\text{Y}_2\text{Ti}_2\text{O}_7$  oxides and the  $\alpha\text{-(Fe,Cr)}$  matrix (see green arrow in Figure 11.13c and d).

## 11.5 Discussion

### 11.5.1 Precursor Powder Formation

A reactive atomization gas (i.e., Ar-0.19O<sub>2</sub> vol. %) was used to create a controlled oxidizing environment to oxidize the nascent surfaces of molten CR-alloy droplets during primary disintegration and subsequent rapid solidification and cooling of the powders. The oxidation reaction rate has been empirically linked to O concentration in the reactive atomization gas (i.e., O partial pressure), thus illustrating controlled or predictable oxidation kinetics as a function of particle size and, thus, particle cooling rate (see Figure 11.14). Consequently, the increased cooling rate associated with smaller particles (CR-A) lead to the formation of a thinner surface oxide layer compared to larger particles (CR-B) (see Figure 11.5).

The chemistry of this kinetically favored metastable oxide seems to be controlled by the activity and mobility of the alloying additions. Initial oxide formation is thought to occur prior to particle solidification, when the reactive alloying additions exhibit increased atomic mobility. This explains the elevated concentration of Y within the Cr-enriched exterior surface oxide layer on CR-B particles (see Figure 11.5b and Figure 11.6e). Once the particle solidifies, the atomic mobility of Y is severely limited (see extremely low values for Y diffusivity in  $\alpha\text{-Fe}$  [181]), thus prohibiting further Y consumption during subsequent oxide growth (see Figure 11.6d and e). Moreover, forming the surface oxide prior to solidification is thought to enhance the robust nature of the oxide by introducing residual compressive forces along the

particle surface, as a result of shrinkage during solidification, which seems to prevent oxide spallation during subsequent powder handling before consolidation.

Small disconnected regions of Y concentration within the surface oxide layer could be tolerated during this process, especially among smaller powders that form extremely thin ( $t < 15\text{nm}$ ) surface oxide layers, since they can ultimately result in discrete residual Y-enriched nano-metric oxides along PPBs following dissolution of the predominantly Y-free surface oxide phase. Furthermore, increasing the concentration of other reactive alloying additions (e.g., Ti or Hf) might further limit the consumption of Y during the initial stages of this surface oxide reaction by the formation of complex intermetallic precipitates that follow solidification microsegregation patterns or are trapped within supersaturated regions by extremely rapid solidification.

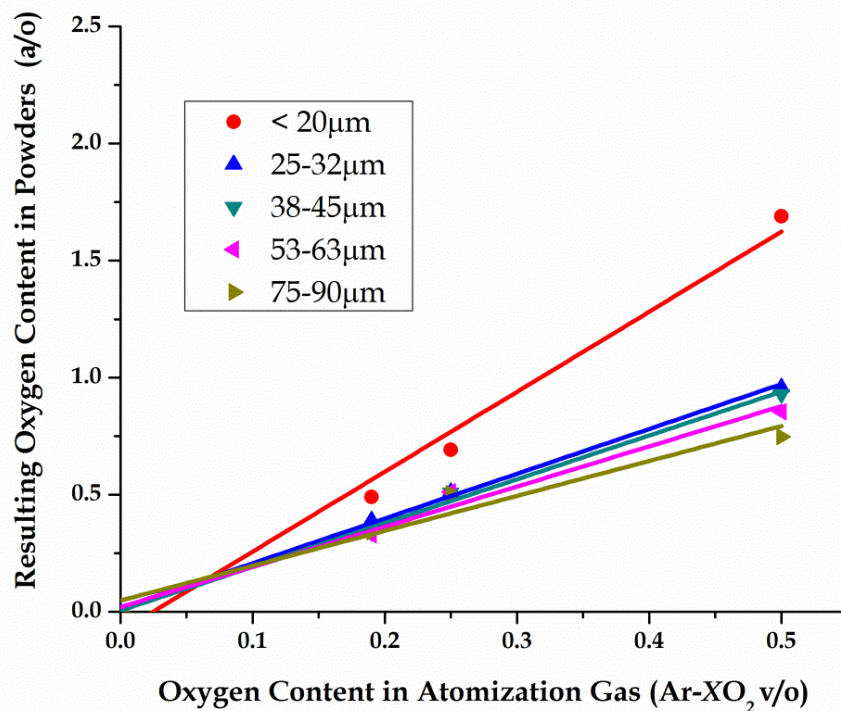


Figure 11.14. Resulting O content in the as-atomized powders as a function of O content in the reactive atomization gas

### **11.5.2 Microstructure Evolution**

Elevated temperature heat treatment of the as-consolidated powders was used to promote thermodynamically driven O exchange between the initial metastable Cr-enriched PPB oxide and Y-containing (e.g.,  $\text{Fe}_{17}\text{Y}_2$ ) IMC precipitates. During this reaction, O is thought to diffuse away from the metastable PPB oxide due to a chemical potential gradient, converting Y-containing IMC precipitates into nano-metric  $\text{Y}_2\text{Ti}_2\text{O}_7$  dispersoids.

This type of O exchange reaction is considered diffusionless internal oxidation [182], since the rate of reaction is controlled only by O diffusion due to the limited solubility and diffusivity of Y in  $\alpha$ -(Fe,Cr) [181]. For this reason, particle solidification rate (indirectly related to powder size, in general) that controls the ensuing length scale of Y segregation within the precursor atomized powders, becomes an important factor in predetermining the spatial distribution of the nano-metric  $\text{Y}_2\text{Ti}_2\text{O}_7$  dispersoids.

The CR-A particles appeared to have solidified at an increased rate compared to CR-B, resulting in a refined cellular structure, increasing the resulting dispersoid distribution uniformity throughout the  $\alpha$ -(Fe,Cr) matrix. Furthermore, this refined cellular structure also contained an interior core with a greater number density of dispersoids (see Figure 11.8a-c). These dispersoids are thought to have formed from supersaturated regions within the solidified microstructure that contained trapped Y solute. This analysis agrees well with previously reported data that illustrated the opportunity to create a homogeneous nano-metric ODS microstructure by consolidating ultra-fine (dia.  $< 5\mu\text{m}$ ) powders produced by this GARS process [146].

### **11.5.3 Thermal Mechanical Treatment (TMT)**

Cold rolling was used to introduce large amounts of strain energy into the CR-alloy microstructure following dispersoid formation. Both CR-alloys demonstrated good cold workability characteristics with no signs of macroscopic damage following 85%

RA. Interestingly, this cold rolling procedure resulted in a near identical increase in microhardness for both CR-alloys, perhaps indicating a similar increase in defect density. Also, annealing the cold rolled sheets at 500°C promoted dislocation recovery to dispersoid boundaries, forming a fine-scale (dia. < 1 $\mu$ m) dislocation substructure. This dislocation substructure proved unstable at increased annealing temperatures, resulting in grain recrystallization (see Figure 11.10 and Figure 11.11).

It appears that stored strain energy within the dislocation substructure provided a significant driving force towards recrystallization, which was insufficiently counterbalanced by the dragging forces created from the current distribution (size and volume fraction) of dispersoids within these CR-alloys (i.e., Zener pinning force [230]). Furthermore, it has been shown that larger precipitates (~0.5-1.0 $\mu$ m) can encourage the formation of recrystallization nuclei due to enlarged strain fields around such particles [256], suggesting that residual PPB oxide particles might accelerate the recrystallization kinetics in these alloys. Additional TMT experiments will be required to better understand and control the grain structure in these CR-alloys.

Notably, the microhardness of the recrystallized CR-alloys was found to be similar to that of the initial microhardness value prior to cold rolling, although grain size was increased an order of magnitude (see Figure 11.10 and Figure 11.11), probably demonstrating that the dispersoids are the primary source of strength in these CR-alloys. Furthermore, CR-A and CR-B maintained a consistent microhardness differential during recovery and recrystallization, despite near identical grain sizes (see Figure 11.11), which is likely an effect of the distinct differences in dispersoid distribution (size, spacing, and uniformity) witnessed in these CR-Alloys (see Figure 11.8).

#### 11.5.4 Mechanical Properties

The low temperature ( $T \leq 400^\circ\text{C}$ ) systematic increase in YS of CR-B, CR-A, and MA-956 is thought to be related to a similar systematic decrease in the average dispersoid spacing within each alloy. This spacing is a function of dispersoid size, volume fraction, and spatial distribution, which represents the mean free path (MFP) for dislocation movement through the ODS microstructure (assuming that all dispersoids act as non-shearable obstacles). Further, this MFP is the prevailing variable in the Orowan strengthening model [70], which has been shown to adequately predict the relative YS in recrystallized ODS alloys within this temperature range [82].

In order to minimize the dispersoid spacing and improve the YS in CR-type alloys, the initial precursor powders must contain a more homogeneous distribution of Y or Y-containing IMC precipitates, which predefines the spatial distribution of the ensuing  $\text{Y}_2\text{Ti}_2\text{O}_7$  dispersoids. This can be achieved by utilizing a more exclusive size fraction of ultra-fine precursor powders (e.g., dia.  $< 5\mu\text{m}$ ), which have been shown to solidify at the necessary velocity to solute trap sufficient amounts (0.18 at. %) of Y within the  $\alpha\text{-(Fe,Cr)}$  lattice [146]. Consolidation and heat treatment of such extremely ultra-fine powders should result in a nano-metric ODS microstructure, similar to that of the interior core structure illustrated in the CR-A (see Figure 11.8C), but more homogeneously distributed throughout the  $\alpha\text{-(Fe,Cr)}$  matrix.

Interestingly, the lower temperature ( $T \leq 400^\circ\text{C}$ ) YS advantage observed in CR-A over CR-B was negated at higher temperatures ( $T \geq 600^\circ\text{C}$ ), perhaps illustrating a change in strengthening mechanism associated with the thermal activation of dislocation climb that was not as dependent on the differences in dispersoid population and distribution (see Figure 11.12). During the climb process, a threshold stress must be overcome to account for the energy required to increase the dislocation line length [89]. Furthermore, it has been suggested that a detachment



stress is then required to overcome the attractive force that arises when the stress field around the dislocation is relaxed at the dispersoid/matrix interface [88]. Moreover, it has been shown that this detachment stress is far greater than stress predictions for dislocation climb, thus illustrating the significant role that the strain field at the dispersoid/matrix interface can have at elevated temperatures [87]. Therefore, the YS in CR-A and CR-B might coincide due to a related detachment stress associated with the  $\text{Y}_2\text{Ti}_2\text{O}_7$  dispersoid phase, assuming that the detachment stress becomes an increasingly important variable compared to dispersoid spacing (or MFP) at these elevated temperatures ( $T \geq 600^\circ\text{C}$ ). This might also explain the increased elevated temperature YS observed in MA-956, which contains a different dispersoid phase (mixed Y-Al-O) and presumably an increased detachment stress value [109]. Further research will be required to better understand the strengthening mechanism at these elevated temperatures.

The strength of these CR-alloys could also be limited due to the presence of non-ideal phases (e.g., residual PPB oxides and entrapped Ar bubbles) within the CR-alloy microstructure. Fracture analysis indicated void formation along these non-desirable phase boundaries, which possibly contributed to premature specimen failure. Adjusting the GARS processing parameters should help to eliminate these phases by establishing an ideal initial ratio of Y/O within the precursor oxide dispersion forming powders, which should result in full dissolution of the PPB oxide during subsequent O exchange reactions. Furthermore, Ar bubble entrapment during gas atomization can also be suppressed by lowering the atomization chamber pressure or by reducing the average particle size (i.e., inert gas concentration is inversely related to powder size) [254].

## 11.6 Summary

Gas atomization reaction synthesis (GARS) was used to produce precursor oxide dispersion forming ferritic stainless steel (Fe-Cr-Ti-Y-O) powders. These powders

contained an ultra thin ( $t < 100$  nm) metastable Cr-enriched surface oxide layer, which was used as a vehicle to transport solid state O into the consolidated microstructure. Elevated temperature heat treatment was then used to promote thermodynamically driven O exchange reactions between the Cr-enriched surface oxide and Y-containing IMC precipitates, resulting in the formation of nano-metric  $Y_2Ti_2O_7$  dispersoids within the  $\alpha$ -(Fe,Cr) microstructure. Two sets of precursor powders (CR-A: dia.  $< 20\mu m$  and CR-B: dia.  $45-75\mu m$ ) were compared to study the effects of solidification structure on resulting dispersoid uniformity and subsequent mechanical properties. It was shown that reducing the initial precursor particle size resulted in a more uniform distribution of nano-metric dispersoids. Both CR-alloys contained good cold workability with no signs of macroscopic damage after cold rolling to  $\sim 85\%$  RA. Low temperature annealing of the cold rolled sheets resulted in a fine-scale (dia.  $< 1\mu m$ ) dislocation substructure. This substructure proved unstable at elevated temperatures ( $T \geq 700^\circ C$ ), resulting in grain recrystallization. Elevated temperature tensile tests of the recrystallized CR-alloys revealed an increased low temperature ( $T \leq 400^\circ C$ ) YS in CR-A, presumably due to the improved dispersoid uniformity. The YS of the CR-alloys converged at higher temperatures ( $T \geq 600^\circ C$ ), which was postulated as an effect of both alloys containing a similar dislocation detachment stress value.

### 11.7 Acknowledgements

Support from the Department of Energy, Office of Fossil Energy (ARM program) through Ames Laboratory contract no. DE-AC02-07CH11358 is gratefully acknowledged. Additionally, the electron microscopy of the as-atomized surface oxide layer was accomplished at the Electron Microscopy Center for Materials Research at Argonne National Laboratory, a U.S. Department of Energy Office of Science Laboratory operated under Contract No. DE-AC02-06CH11357 by U. Chicago-Argonne, LLC. Furthermore, the authors would like thank D. Byrd and J. Anderegge from Ames Laboratory-USDOE, E. Fair from Iowa State University, D.

Hoelzer and M. Sokolov from Oak Ridge National Laboratory-USDOE, and J. Hiller and R. Cook from the Electron Microscopy Center for their individual contributions to this paper.

## Chapter 12. General Conclusions

Gas atomization reaction synthesis (GARS) was adapted to produce precursor powders for oxide dispersion strengthened (ODS) ferritic stainless steel alloys. This reactive gas atomization process results in the formation of an ultra thin ( $t < 150$  nm) Cr-enriched surface oxide layer that encapsulated the atomized powders. This surface oxide layer was utilized as an O reservoir for the formation of Y-enriched nano-metric dispersoids following consolidation and heat treatment of these precursor powders. A theoretical oxidation model, formulated from droplet cooling curves, and based on the parabolic oxidation kinetics of  $\text{Cr}_2\text{O}_3$ , was designed as a method for predicting the resulting surface oxide layer thickness and corresponding O content as function of particle size (see Chapter 4). This oxidation model coupled with empirical results showed that the oxidation kinetics of this GARS process scales linearly with  $\text{O}_2$  partial pressure in the reactive gas, demonstrating the novel ability of being able to control the *in situ* addition of O during this rapid solidification process.

Internal oxidation experiments were used to analyze the kinetics of the O exchange reaction that occurs during elevated temperature consolidation or heat treatment of precursor CR-alloy powders, which results in the formation of Y-enriched oxide dispersoids. Furthermore, a heat treatment procedure, formulated from an internal oxidation model, was established for predicting the required heat treatment time for dispersoid formation within each CR-alloy, as a function of precursor powder size (i.e., required diffusion distance), see Chapter 5.

Microstructural results showed a clear ability to manipulate oxide and intermetallic phases within each CR-alloy using high temperature consolidation or heat treatment. High energy X-ray diffraction phase analysis coupled with TEM microstructure analysis confirmed the operation of an O exchange reaction between

the less stable Cr-enriched prior particle boundary (PPB) oxide phase and the Y-enriched intermetallic compound (IMC) precipitates. This O exchange reaction resulted in the formation of nano-metric Y-enriched oxide dispersoids throughout the ferritic microstructure. Additionally, the atomization processing parameters were shown to control the concentration of O introduced into the alloy system (i.e., oxide layer thickness), as a function of particle size. It was demonstrated that the initial ratio of Y to O controls the resulting CR-alloy microstructure (see Chapter 6 and 7). Excess Y lead to residual  $\text{Fe}_{17}\text{Y}_2$  IMC precipitates within the CR-alloy microstructure, while too much O prevented full dissolution of the PPB oxide. The ideal balance of Y to O is inherently linked to the resulting dispersoid stoichiometry, indicating a need to accurately predict the specific dispersoid phase in these CR-alloys, in order to adjust the GARS processing parameters accordingly.

The resulting dispersoid thermal stability was enhanced through the addition of Hf as a substitute for Ti in these CR-alloys (see Chapter 8). The dispersoids were preliminarily identified as  $\text{Y}_{0.33}\text{Hf}_{0.67}\text{O}_{1.83}$  or  $\text{Y}_2\text{Hf}_2\text{O}_7$  in the Hf-containing CR-alloys and as  $\text{Y}_2\text{Ti}_2\text{O}_7$  in the Ti-containing CR-alloys. Extended annealing treatments at  $1200^\circ\text{C}$  confirmed reduced coarsening kinetics associated with the Y-Hf-O dispersoids compared to Y-Ti-O dispersoids (see Chapter 9). A decrease in molar volume associated with the Hf-containing dispersoids, seemed to lower the chemical potential gradient at the dispersoid/matrix interface, which was offered as an explanation for the apparent increased thermal stability.

The ODS microstructures in these CR-alloys were shown to be highly dependent on powder particle size (i.e., solidification rate). Smaller powders with increased amounts of solute trapping or highly refined solidification structures resulted in finer and more uniformly distributed nano-metric oxide dispersoids (see Chapter 10). Selection of powder particle size range (i.e., solidification morphology) was shown to be a viable method to control the final ODS microstructure. Furthermore,

consolidated samples of ultra-fine powders (dia.  $\leq 5\mu\text{m}$ ) were found to contain the most ideal ODS microstructure with nano-metric (dia.  $\leq 10\text{nm}$ ) dispersoids distributed evenly throughout the  $\alpha\text{-(Fe,Cr)}$  matrix. These experimental observations confirmed earlier SEM observations of cross-sectioned as-atomized particles and indicated that these ultra-fine powders solidified above the threshold velocity required to effectively solute trap Y in the  $\alpha\text{-(Fe,Cr)}$  matrix. Additionally, calculated particle solidification velocity was extracted from theoretical droplet cooling curves (see Chapter 4), to substantiate these experimental observations. Furthermore, these results indicated the need to modify the atomization processing parameters to dramatically increase the yield of these ultra-fine powders, in order to achieve a more ideal ODS microstructure (i.e., similar to that of the superior nanostructured ferritic alloys (NFAs), see Section 3.6), while maintaining this simplified processing scheme.

Two sets of precursor powders (Fe-Cr-Ti-Y-O with dia.  $< 20\mu\text{m}$  and dia.  $45\text{--}75\mu\text{m}$ ) were compared to evaluate the effects of solidification structure on resulting dispersoid uniformity and subsequent mechanical properties (see Chapter 11). It was again shown that reducing the initial precursor particle size results in a more uniform distribution of nano-metric dispersoids. Both CR-alloys contained good cold workability with no signs of macroscopic damage after cold rolling to  $\sim 85\%$  reduction in area. Low temperature annealing of the cold rolled sheets resulted in a fine-scale (dia.  $< 1\mu\text{m}$ ) dislocation substructure. This substructure proved unstable at elevated temperatures ( $T \geq 700^\circ\text{C}$ ), resulting in grain recrystallization. Elevated temperature tensile tests of the recrystallized CR-alloys revealed an increased low temperature ( $T \leq 400^\circ\text{C}$ ) yield strength in the samples containing the smaller powders (dia.  $< 20\mu\text{m}$ ), attributed to the improved dispersoid uniformity. Interestingly, the yield strength of the CR-alloys converged at higher temperatures ( $T \geq 600^\circ\text{C}$ ), which was postulated as an effect of both CR-alloys containing a similar dislocation detachment stress value. Notably, the initial elevated temperature ( $T \geq$

600°C) tensile strength of these CR-alloys was found to be similar to that of a commercial Fe-based ODS alloy (i.e., MA956), while maintaining a three-fold increase in total elongation.

## Final Acknowledgments

This study was sponsored by the Department of Energy, Office of Fossil Energy (ARM program) through Ames Laboratory contract no. DE-AC02-07CH11358. The continued support of Bob Romanosky, Pat Rawls, Vito Cedro, and Richard Dunst is gratefully acknowledged. The high energy X-ray work at beamline 11-BM of the APS was supported by the Department of Energy, Office of Science, Basic Energy Sciences under contract no. DE-AC02-06CH11357. The electron microscopy of the as-atomized surface oxide layer was accomplished at the Electron Microscopy Center for Materials Research at Argonne National Laboratory, a U.S. Department of Energy Office of Science Laboratory operated under Contract No. DE-AC02-06CH11357 by U. Chicago-Argonne, LLC. Additionally, I would recognize the Materials Preparation Center at Ames Laboratory, a U.S. Department of Energy Laboratory, for providing the processing tools and expertise to make this study possible.

I also would like to thank my graduate committee for providing guidance throughout my graduate career. I have particularly enjoyed studying under the guidance of my major professor, Dr. Iver Anderson. His creative nature and passion for metallurgy was incredibly contagious, and he has served as an inspiration for my future career goals. Furthermore, I would like to thank the many people at Ames Lab that have helped me along the way, thank you for everything. Lastly, I would like to express my sincere gratitude to my family and friends for their unwavering support. I especially would like to thank Lisa Rieken, Rodney Rieken, and Audrey Rieken for always being there for me.



## References

- [1] R.L. Klueh, J.P. Shingledecker, R.W. Swinderman, D.T. Hoelzer, Oxide dispersion-strengthened steels: A comparison of some commercial and experimental alloys, *J. Nucl. Mater.*, 341 (2005) 103-114.
- [2] D.T. Hoelzer, J. Bentley, M.A. Sokolov, M.K. Miller, G.R. Odette, and M.J. Alinger, Influence of particle dispersions on the high-temperature strength of ferritic alloys, *J. Nucl. Mater.*, 367-370 (2007) 166-172.
- [3] A. Kelly, and R.B. Nicholson, *Strengthening Methods in Crystals*, John Wiley & Sons, Inc., New York, 1971.
- [4] M.F. Hupalo, A.F. Padilha, H.R.Z. Sandim, and A.M. Kliauga, Cold Swaging, Recovery and Recrystallization of Oligocrystalline INCOLOY MA 956—Part I: Deformed State, *ISIJ Int.*, 44 (2004) 1894-1901.
- [5] M.F. Hupalo, A.F. Padilha, H.R.Z. Sandim, and A.M. Kliauga, Cold Swaging, Recovery and Recrystallization of Oligocrystalline INCOLOY MA 956—Part II: Annealed State, *ISIJ Int.*, 44 (2004) 1902-1910.
- [6] M.K. Miller, D.T. Hoelzer, E.A. Kenik, and K.F. Russell, Stability of ferritic MA/ODS alloys at high temperature, *Intermetallics*, 13 (2005) 387-392.
- [7] R. Viswanathan, and W. Bakker, Materials for Ultrasupercritical Coal Power Plants-Boiler Materials: Part 1, *Mater. Eng. and Per.*, 10 (2001) 81-95.
- [8] P. Yvon, and F. Carré, Structural materials challenges for advanced reactor systems, *J. Nucl. Mater.*, 385 (2009) 217-222.
- [9] G.R. Odette, M.J. Alinger, and B.D. Wirth, Recent Developments in Irradiation-Resistant Steels, *Annu. Rev. Mater. Res.*, 38 (2008) 471-503.
- [10] S. Ukai, and M. Fujiwara, Perspective of ODS alloys application in nuclear environments, *J. Nucl. Mater.*, 307-311 (2002) 749-757.
- [11] P.S. Gilman, and J.S. Benjamin, Mechanical Alloying, *Annu. Rev. Mater. Sci.*, 13 (1983) 279-300.

- [12] C. Suryanarayana, E. Ivanov, and V.V. Boldyrev, The science and technology of mechanical alloying, *Mater. Sci. Eng., A*, 304-306 (2001) 151-158.
- [13] M.J. Alinger, G.R. Odette, and D.T. Hoelzer, The development and stability of Y-Ti-O nanoclusters in mechanically alloyed Fe-Cr based ferritic alloys, *J. Nucl. Mater.*, 329-333 (2004) 382-386.
- [14] I.E. Anderson, B.K. Lograsso, and T.W. Ellis, Gas atomization synthesis of refractory or intermetallic compounds and supersaturated solid solutions, in: USPTO (5, 368,657) (Ed.), Iowa State University Research Foundation, USA, 1994.
- [15] I.E. Anderson, and R.L. Terpstra, Dispersoid Reinforced Alloy Powder and Method of Making, in: USPTO (7, 699,905) (Ed.), Iowa State University Research Foundation, USA, 2010.
- [16] U.S. DOE Nuclear Energy Research Advisory Committee, and Generation IV International Forum GIF, A Technology Roadmap for Generation IV Nuclear Energy Systems, in: GIF-002-00 OECD Nuclear Energy Agency, GIF-002-00, Washington, DC, 2002, pp. 1-90.
- [17] J. Stringer, and L.L. Horton, Basic research needs to assure a secure energy future: A report to the basic energy sciences advisory committee, OSTI Document No. 811872 Office of Science and Technical Information, (2003).
- [18] D.R. Gaskell, Introduction to the Thermodynamics of Materials, Fourth ed., Taylor and Francis Group, New York, 2003.
- [19] S.K. Ghosh, R.G. Alargova, S. Deguchi, and K. Tsujii, Dispersion Stability of Colloids in Sub- and Supercritical Water, *J. Phys. Chem. B*, 110 (2006) 25901-25907.
- [20] U.S. Department of Energy, A Decade of Discovery, Altio Media, 2008.
- [21] USDOE, Clean Coal: Department of Energy's decision to restructure FutureGen should be based on a comprehensive analysis of costs, benefits, and risks, in, U.S. Govt. Accountability Office, Washington, D.C., 2009, pp. 48.
- [22] R. Viswanathana, K. Colemana, and U. Raob, Materials for ultra-supercritical coal-fired power plant boilers, *J. Pressure Vessels and Piping*, 83 (2006) 778-783.

- [23] P.D. Sharma, in: Supercritical Coal-Fired Power Plant, available from: <http://knol.google.com/k/partha-das-sharma/supercritical-coal-fired-power-plant/oml631csgjs7/20>, accessed Sep.10, 2011, Version 4 Knol, 2009.
- [24] A.V. Nero, Jr., A Guidebook to Nuclear Reactors, University of California Press, Ltd., Berkeley, California, 1979.
- [25] A. R. Foster, and R.L. Wright Jr., Basic Nuclear Engineering, Allyn and Bacon, Inc., Boston, 1977.
- [26] G.H. Miley, Fusion Energy Conversion, American Nuclear Society, La Grange Park, 1976.
- [27] R. Goldston, et al., A Plan for the Development of Fusion Energy, Fusion Energy, 21 (2002) 1-51.
- [28] International Thermonuclear Experimental Reactor, in: The ITER Device, available from: <http://www.iter.org/mach>, accessed Aug. 9, 2011, 2009.
- [29] Princeton Plasma Physics Laboratory, in: Fusion Reactions, available from: <http://www.pppl.gov/fusionreactions.cfm>, accessed Oct. 4, 2011, 2004.
- [30] J.D. Lawson, Some Criteria for a Useful Thermonuclear Reactor, A.E.R.E. report GP/R 1807, (1955).
- [31] J.L Strassland, R.W. Powell, and B.A. Chin, An Overview of Neutron Irradiation Effects in LMFBFR, J. Nucl. Mater., 108-109 (1982) 299.
- [32] T.R Allen, J.T. Busby, R.L. Klueh, S.A. Maloy, and M.B. Toloczko, Cladding and Duct Materials for Advanced Nuclear Recycle Reactors, JOM, Jan. (2008) 15-23.
- [33] N. Baluc, Materials for fusion power reactors, Plasma Physics and Controlled Fusion, 48 (2006) 165-177.
- [34] T. Yamamoto, G. R. Odette, P. Miao, D.T. Hoelzer, and J. Bentley, The transport and fate of helium in nanostructured ferritic alloys at fusion relevant He/dpa ratios and dpa rates, J. Nucl. Mater., 367-370 (2007) 399-410.

- [35] S. Cierjacks, K. Ehrlich, E.T. Cheng, H. Conrads, and H. Ullmaier, High-Intensity Fast Neutron Sources and Neutron Fields for Fusion Technology and Fusion Materials Research, *Nucl. Sci. Eng.*, 106 (1990) 99-113.
- [36] K. Ehrlich, The development of structural materials for fusion reactors, *Phil. Trans. R. Soc. Lond.*, 357 (1999) 595-623.
- [37] S.J. Zinkle, Fusion materials science: Overview of challenges and recent progress, *Phys. Plasmas*, 12 (2005) 1-8.
- [38] E.A. Little, Development of radiation resistant materials for advanced nuclear power plants, *Mater. Sci. Technol.*, 22 (2006) 491-518.
- [39] A. Liyoshi, Fusion R&D strategy for Japan, *J. Nucl. Mater.*, 258-263 (1998) 1-6.
- [40] E. Proust, L. Anzidi, G. Casini, M.D. Donne, L. Giancarli, and S. Malang, Breeding Blanket for DEMO, *Fusion Eng. Des.*, 22 (1993) 19-33.
- [41] L. Ryabev, and M.L. Solonin, Materials R&D strategy for fusion in Russia, *J. Nucl. Mater.*, 258-263 (1998) 30-46.
- [42] S.J. Zinkle, and N.M Ghoniem, Chemical compatibility and radiation effect issues in high temperature refractory metals, APEX-Study Meeting, May (1998).
- [43] ASM Handbooks Online: Vol. 1, Properties and Selection: Irons, Steels, and High Performance Alloys, in: S.D. Washko, and G. Aggen (Ed.) Wrought Stainless Steels, ASM International, 2002.
- [44] ASM Handbooks Online: Vol. 2, Properties and Selection: Nonferrous Alloys and Special-Purpose Materials, in: W.L. Mankins, and S. Lamb (Ed.) Nickel and Nickel Alloys, ASM International, 2002.
- [45] S.J. Zinkle, and L.L. Snead, Thermophysical and Mechanical Properties of SiC/SiC Composites, in: Fusion Materials Vol. 24, Semiannual Progress Report, DOE/ER-0313/24, Oak Ridge National Laboratory, Oak Ridge, TN, Sept. 1998, pp. 93-100.
- [46] J.W. Davis, ITER Materials Properties Handbook, 1996.

- [47] R. J. Farraro, and R. B. McLellan, High Temperature Elastic Properties of Polycrystalline niobium, tantalum and vanadium, *Met. Trans. A*, 10 (1979) 1699-1702.
- [48] B. A. Loomis, L. J. Nowicki, and D. L. Smith, Tensile Properties of Vanadium and Vanadium-Base Alloys, in: *Fusion Materials Vol. 10, Semiannual Progress Report*, DOE/ER/0313/10, Oak Ridge National Laboratory, Oak Ridge, TN, March 1991, pp. 145-155.
- [49] K. Savolainen, J. Mononen, R. Ilola, and H. Hänninen, Materials Selection for High Temperature Applications, in, Helsinki University of Technology, Laboratory of Engineering Materials Publications, 2005.
- [50] M. Schütze, *Protective Oxide Scales and Their Breakdown*, John Wiley & Sons, Chichester, UK, 1997.
- [51] B. Gleeson, *High-Temperature Corrosion of Metallic Alloys and Coatings*, Wiley-VCH, Weinheim, Germany, 2000.
- [52] K. Natesan, and M. Uz, OXIDATION PERFORMANCE OF V-Cr-Ti ALLOYS, in: 5th International Symposium on Fusion Nuclear Technology, Rome, Italy, 1999, pp. 1-9.
- [53] S.J. Zinkle, S. Majumdar, N.M. Ghoniem, and S. Sharafat., Chapter 13: MATERIALS CONSIDERATIONS AND DATA BASE, in: *APEX Interim Report*, 1999, pp. 1-29.
- [54] C. Cabet, *Oxidation of SiC/SiC Composites in Low Oxidising and High Temperature Environment*, Springer Netherlands, Gif-sur-Yvette, France, 2008.
- [55] H. Kleykamp, V. Schauer, and A. Skokan, Oxidation behaviour of SiC fibre reinforced SiC, *J. Nucl. Mater.*, 227 (1995) 130-137.
- [56] S. Nogami, N. Otake, A. Hasegawa, Y. Katoh, A. Yoshikawa, M. Satou, and Y. Oya, K. Okuno, Oxidation behavior of SiC/SiC composites for helium cooled solid breeder blanket, *Fusion Eng. Des.*, 83 (2008) 1490-1494.
- [57] R.W. Evans, J. Preston, B. Wilshire and E.A. Little, Creep transients in a nuclear-grade ODS ferritic steel, *J. Nucl. Mater.*, 195 (1992) 24-28.

- [58] A. Calamand, Handbook on Nuclear Activation Cross-Sections, in: Cross-Sections for Fission Neutron Spectrum Induced Reactions, International Atomic Energy Agency, Vienna, Austria, 1974, pp. 273-324.
- [59] N. Ramakumar, E. Kondaiah, and R.W. Fink, Neutron activation cross sections at 14.4 MeV for Si and Zn isotopes, Nucl. Phys., A122 (1968) 679-683.
- [60] H.K. Vonach, W.G. Vonach, H. Münzer, and P Schrammel, EANDC(E) 89 "U" (1968) 37.
- [61] V.N. Levkovskij, G.P. Vinitaskaya, and V.M. Stepanov, J. Nucl. Phys., 10 (1969) 25.
- [62] D.M. Chittenden, D.G. Gardner, and R.W. Fink, New Isotope of Manganese; Cross Sections of the Iron Isotopes for 14.8-MeV Neutrons, Phys. Rev, 122 (1961) 860-861.
- [63] U. Seebeck, and M. Bormann, Rep. EANDC(E)57"U", NEA, (1965) 18.
- [64] M. Baba, N. Ito, I. Matsuyama, S. Matsuyama, and N. Hirakawa, Differential  $\alpha$ -Production Cross Sections of Iron and Nickel for 4.3 to 14.1 MeV Neutrons, J. Nucl. Sci. Technol., 31 (1994) 745-747.
- [65] S.J. Zinkle, and N.M. Ghoniem, Operating temperature windows for fusion reactor structural materials, Fus. Eng. Des., 51 (2000) 55-71.
- [66] World Energy Outlook, in: R. Priddle (Ed.) Prospects for Nuclear Power, International Energy Agency (IEA), Paris, France, 2006, pp. 343-384.
- [67] F.W. Wiffen, and R.T. Santoro, Control of Activation Levels to Simplify Waste Management of Fusion Reactor Ferritic Steel Components, TMS/AIME Proc. Topical conference on ferritic alloys for use in nuclear energy technologies, (1984) 195-200.
- [68] M.J. Alinger, On the formation and stability of nanometer scale precipitates in ferritic alloys during processing and high temperature service, Ph.D. Thesis, in: Materials Department, University of California, Santa Barbra, 2004, pp. 341.
- [69] J.-Ch. Sublet, and G.J. Butterworth, The Neutronic Basis for Elemental Substitution in Martensitic Steels, J. Nucl. Mater., 212-215 (1994) 695-700.

- [70] J.W. Martin, *Micromechanisms in particle-hardened alloys*, Cambridge University Press, London, 1980.
- [71] T.H. Courtney, *Mechanical Behavior of Materials*, second ed., McGraw-Hill, Madison, 2000.
- [72] A.J.E. Foreman, and M.J. Makin, Dislocation movement through random arrays of obstacles, *Philos. Mag.*, 14 (1966) 911-924.
- [73] R.E. Stoller, and S.J. Zinkle, On the relationship between uniaxial yield strength and resolved shear stress in polycrystalline materials, *J. Nucl. Mater.*, 283-287 (2000) 349-352.
- [74] D. Gould, Ph.D. Thesis, in, Oxford University, 1971.
- [75] M.C. Chaturvedi, D.J. Lloyd, and D.W. Chung, *Metall. Sci. J.*, 10 (1976) 373.
- [76] A. Kelly, The strengthening of metals by dispersed particles, *Proc. Roy. Soc.*, A282, 63 (1964) 63.
- [77] L.P. Rice, in: DMIC Report No. 210, Battelle Memorial Institute, 1965.
- [78] B.A. Wilcox, and R.I. Jaffee, Direct and indirect strengthening effects of thorium oxide (ThO<sub>2</sub>) particles in dispersion-hardened nickel, in: *Int. Conf. on Strength of Metals & Alloys*, Trans. Jpn. Inst. Met., Sendai, Japan, 1967, pp. 575-579.
- [79] J.E. White, and R.D. Carnahan, A Microplasticity Study of Dispersion Strengthening in TD-Nickel, *Trans. Metall. Soc. AIME*, 230 (1964) 1298-1306.
- [80] J.W. Martin, R.D. Doherty, and B. Cantor, *Stability of microstructure in metallic systems*, second ed., Cambridge University Press, Cambridge, 1997.
- [81] F.J. Humphreys, and J.W. Martin, *Acta Met.*, 14 (1966) 775.
- [82] B. Reppich, On the dispersion strengthening mechanisms in ODS materials, *Z. Metallkd.*, 93 (2002) 605-613.

- [83] J. Safari, and S. Nategh, Microstructure evolution and its influence on deformation mechanisms during high temperature creep of a nickel base superalloy, *Mater. Sci. Eng., A*, 499 (2009) 445-453.
- [84] J. Cadek, *Creep in Metallic Materials*, Elsevier Science Publishing Co., Inc., New York, 1988.
- [85] A. Russell, and K.L. Lee, *Structure-Property Relations In Nonferrous Metals*, John Wiley & Sons, Inc., Hoboken, 2005.
- [86] E. Artz, and J. Rösler, *Dispersion Strengthened Aluminum Alloys*, TMS, Warrendale, 1988.
- [87] E. Artz, and D.S. Wilkinson, Threshold Stresses for Dislocation Climb Over Hard Particles: The Effect of an Attractive Interaction, *Acta Met.*, 34 (1986) 1893-1898.
- [88] J. Rösler, and E. Artz, A New Model-Based Creep Equation for Dispersion Strengthened Materials, *Acta Met.*, 38 (1990) 671-683.
- [89] J. Rösler, and E. Artz, The kinetics of dislocation climb over hard particles—I. Climb without attractive particle–dislocation interaction, *Acta Met.*, 36 (1988) 1043-1051.
- [90] J. Schröder, and E. Artz, *Scripta Metall.*, 19 (1985) 1129.
- [91] J. Rösler, Ph.D. Thesis, in, Univ. Stuttgart, 1988.
- [92] D. A. Porter, and K.E. Easterling, *Phase Transformations in Metals and Alloys*, second ed., Nelson Thornes Ltd, Cheltenham, 2001.
- [93] W. Ostwald, *Lehrbuch der Allgemeinen Chemie*, 2 (1896).
- [94] A.J. Ardell, Microstructural Stability at Elevated Temperatures, *Journal of the European Ceramic Society*, 19 (1999) 2217-2231.
- [95] P.K. Footner, and C.B. Alcock, Growth Kinetics of Dispersed Thoria in Ni and Ni-Cr Alloys, *Metall. Trans.*, 3 (1972) 2633-2637.



- [96] A.J. Ardell, On the Coarsening of Grain Boundary Precipitates, *Acta Met.*, 20 (1972) 601-609.
- [97] A.J. Ardell, Temporal Behavior of the Number Density of Particles during Ostwald Ripening, *Mater. Sci. Eng., A*, 238 (1997) 108-120.
- [98] J.S. Benjamin, Dispersion Strengthened Superalloys by Mechanical Alloying, *Metall. Trans.*, 1 (1970) 2943-2951.
- [99] J.S. Benjamin, and J.M. Larson, Powder Metallurgy Techniques Applied to Superalloys, *J. Aircraft*, 14 (1977) 613-623.
- [100] H. Kishimoto, M.J. Alinger, G.R. Odette, and T. Yamamoto, TEM examination of microstructural evolution during processing of 14CrYWTi nanostructured ferritic alloys, *J. Nucl. Mater.*, 329-333 (2004) 369-371.
- [101] C. Suryanarayana, Mechanical Alloying and Milling, *Prog. Mat. Sci.*, 46 (2001) 1-184.
- [102] S. Ukai, T. Nishida, and H. Okada, Development of Oxide Dispersion Strengthened Ferritic Steels for FBR Core Applications (I), *Nucl. Sci.*, 34 (1997) 256-263.
- [103] C. Suryanarayana, Mechanical Alloying, in: *ASM Handbook (Ed.) Powder Metal Technologies and Applications*, ASM International®, Materials Park, OH, 1998, pp. 80-90.
- [104] R.M. German, *Powder Metallurgy & Particulate Materials Processing*, Metal Powder Industries Federation, Princeton, NJ, 2005.
- [105] A. Czyrska-Filemonowicz, and B. Bubieli, Mechanically alloyed, ferritic oxide dispersion strengthened alloys: structure and properties, *Material Processing Technology*, 64 (1997) 53-64.
- [106] Engineering Data Sheet for Incoloy MA956, in, Special Metals Inc., 2003.
- [107] Material Data Sheet ODS-Superalloy PM 2000, in, Metallwerk Plansee GmbH, 1993.

- [108] J.S. Benjamin, Mechanical Alloying, *Scientific Am.*, 234 (1976) 40-48.
- [109] P. Krautwasser, M. Widera, D. Eber, and B.D. Wirth, Thermal stability of dispersoids in the ferritic ODS alloys PM2000 and MA956, *High Temp. - High Pressures*, 26 (1994) 549-560.
- [110] B. Bakó, D. Weygand, M. Samaras, J. Chen, M.A. Pouchon, P. Gumbsch, and W. Hoffelner, Discrete dislocation dynamics simulations of dislocation interactions with  $Y_2O_3$  particles in PM2000 single crystals, *Phil. Mag.*, 87 (2007) 3645-3656.
- [111] C. Capdevila, and H.K.D.H. Bhadeshia, Manufacturing and Microstructural Evolution of Mechanically Alloyed Oxide Dispersion Strengthened Superalloys, *Adv. Eng. Mater.*, 3 (2001) 647-656.
- [112] H.K.D.H. Bhadeshia, Recrystallisation of practical mechanically alloyed iron-base and nickel-base superalloys, *Mater. Sci. Eng., A*, 223 (1997) 64-77.
- [113] A. Steckmeyer et al., Tensile Properties and Deformation Mechanisms of 14Cr ODS Ferritic Steel, *J. Nucl. Mater.*, 405 (2010) 95-100.
- [114] D.J. Larson, P.J. Maziasz, I.S. Kim, and K. Miyahara, Three-Dimensional Atom Probe Observation of Nanoscale Titanium-Oxygen Clustering in an Oxide-Dispersion-Strengthened Fe-12Cr-3W-0.4Ti +  $Y_2O_3$  Ferritic Alloy, *Scripta Mater.*, 44 (2001) 359-364.
- [115] I.S. Kim, B.Y. Choi, C.Y. Kang, T. Okuda, P.J. Maziasz, and K. Miyahara, Effect of Ti and W on the Mechanical Properties and Microstructure of 12% Cr base Mechanical-Alloyed Nano-sized ODS Ferritic Alloys, *ISIJ International*, 43 (2003) 1640-1646.
- [116] M.K. Miller, E.A. Kenik, K.F. Russell, L. Heatherly, D.T. Hoelzer, and P.J. Maziasz, Atom probe tomography of nanoscale particles in ODS ferritic alloys, *Mater. Sci. Eng., A*353 (2003) 140-145.
- [117] M.K. Miller, D.T. Hoelzer, E.A. Kenik, and K.F. Russell, Nanometer scale precipitation in ferritic MA/ODS alloy MA957, *J. Nucl. Mater.*, 329-333 (2004) 338-341.
- [118] M.K. Miller, K.F. Russell, and D.T. Hoelzer, Characterization of precipitates in MA/ODS ferritic alloys, *J. Nucl. Mater.*, 351 (2006) 261-268.

- [119] M.J. Alinger, G.R. Odette, and D.T. Hoelzer, On The Role Of Alloy Composition And Processing Parameters In Nanocluster Formation And Dispersion Strengthening In Nanostructured Ferritic Alloys in: *Fusion Mater. Semiannu. Prog.*, DOE-ER-0313/43, Oak Ridge, TN, 2008, pp. 57-79.
- [120] M.K. Miller, *Atom Probe Tomography*, Kluwer Academic/Plenum Press, New York, 2000.
- [121] P. Miao, G.R. Odette, T. Yamamoto, M. Alinger, and D. Klingensmith, Thermal Stability of nano-structured ferritic alloys, *J. Nucl. Mater.*, 377 (2008) 59-64.
- [122] H. Regle, and A. Alamo, Secondary recrystallisation of ODS ferritic alloys, *J. Phys. IV*, 3 (1993) 727-730.
- [123] A. Alamo, V. Lambard, X. Averty, and M.H. Mathon, Assessment of ODS-14%Cr ferritic alloy for high temperature applications, *J. Nucl. Mater.*, 329-333 (2004) 333-337.
- [124] M.J. Alinger, and G.R. Odette, On the precipitation kinetics, thermal stability and strengthening mechanisms of nanometer scale Y-Ti-O clusters in nanostructured ferritic alloys, *Fusion Mater. Semiannu. Prog.*, 13 (2005 ) 61-69.
- [125] G.R. Odette, P. Miao, T. Yamamoto, D. Edwards, R. Kurtz, and H. Tanagawa, A comparison of cavity formation in neutron irradiated nanostructured ferritic alloys and tempered martensitic steels at high He/dpa ratio, *Trans. American Nuclear Society*, 98 (2008).
- [126] R.J. Kurtz, G.R. Odette, T. Yamamoto, D.S. Gelles, P. Miao, B.M. Oliver, The transport and fate of helium in martensitic steels at fusion relevant He/dpa ratios and dpa rates, *J. Nucl. Mater.*, 367-370 (2007) 417-422.
- [127] G.L. Marois, L. Federsoni, P. Bucci, and P. Revirand, HIP technologies for fusion reactor blanket fabrication, *Fusion Eng. Des.*, 49-50 (2000) 577-583.
- [128] I. Barin, F. Sauert, E. Schultze-Rhonhof, and W.S. Sheng, *Thermochemical Data of Pure Substances*, second ed., VCH Verlagsgesellschaft mbH, New York, 1993.
- [129] G. Krauss, *Heat Treatment and Processing Principles*, ASM International, Materials Park, OH, 1997.

- [130] H. Okamoto, Binary Phase Diagrams, in, ASM International, 1990.
- [131] K.A. Gschneidner Jr., N. Kippenhan, and O.D. McMasters, Thermochemistry of the Rare Earths, Part 1. Rare Earth Oxides, in, Ames Laboratory-U.S. Atomic Energy Commission, IS-RIC-6, Ames, 1973.
- [132] S. Ukai, M. Harada, H. Okada, M. Inoue, S. Nomura, S. Shikakura, K. Asabe, T. Nishida, and M. Fujiwara, Alloying design of oxide dispersion strengthened ferritic steel for long life FBRs core materials, J. Nucl. Mater., 204 (1993) 65-73.
- [133] S. Ukai, T. Nishida, T. Okuda, and T. Yoshitake, Development of Oxide Dispersion Strengthened Steels for FBR Core Application, (II), J. Nucl. Sci. Technol., 35 (1998) 294-300.
- [134] Y. Uchida, S. Ohnuki, N. Hashimoto, T. Suda, T. Nagai, T. Shibayama, K. Hamada, N. Akasaka, S. Yamashita, S. Ohstuka, and T. Yoshitake, Effect of Minor Alloying Element on Dispersing Nano-Particles in ODS Steel, Mater. Res. Soc. Symp. Proc., 981 (2007) 09-14.
- [135] S.B. Kim, K.W. Paik, and Y.G. Kim, Effect of Mo Substitution by W on High Temperature Embrittlement Characteristics in Duplex Stainless Steels, Mater. Sci. Eng., A, 247 (1998) 67-74.
- [136] D. Peckner, and I.M. Bernstein, Handbook of Stainless Steels, McGraw-Hill Book Company, New York, 1977.
- [137] Y. Uchida, et al., Effect of Minor Alloying Element on Dispersing Nano-Particles in ODS Steel, in: J. Aktaa, M. Samaras, M. Serrano de Caro, M. Victoria, and B. Wirth (Ed.) Structural and Refractory Materials for Fusion and Fission Technologies, Materials Research Society, Warrendale, PA, 2007, pp. 09-14.
- [138] I.E. Anderson, R.S. Figliola, and H. Morton, Flow mechanisms in high pressure gas atomization, Mater. Sci. Eng., A148 (1991) 101-114.
- [139] J. Ting, and I.E. Anderson, A computation fluid dynamics (CFD) investigation of the wake closure phenomenon, Mater. Sci. Eng., A379 (2004) 264-276.
- [140] J. Ting, and I.E. Anderson, A computation fluid dynamics (CFD) investigation of the wake closure phenomenon, Mat. Sci. and Eng., A379 (2004) 264-276.

- [141] R.D. Ingebo, Capillary and Acceleration Wave Breakup of Liquid Jets in Axial-Flow Airstreams, in, NASA TP-1791, NASA - Lewis Research Center, National Aeronautics and Space Administration, Scientific and Technical Information Branch, Cleveland, OH USA, 1981.
- [142] S. P. Mates, G. S. Settles, The Gas-Dynamic and Metal Atomization Performance of Two Different Close-Coupled Nozzles, in: F.D.S. Marquis (Ed.) Symposium TMS Fall Meeting, Powder Materials: Current Research and Industrial Practices, Cincinnati, Ohio, 1999, pp. 19-38.
- [143] I.E. Anderson, J.R. Rieken, J.L. Meyer, D. Byrd, and A.J. Heidloff, Visualization of Atomization Gas Flow and Melt Break-Up Effects In Response to Nozzle Design Variations: Simulation and Practice, in: Advances in Powder Metallurgy and Particulate Materials, Metal Powder Industries Federation, San Francisco, 2011, pp. 15-30.
- [144] P. Bracconi, and L. Nyborg, Quantitative phase analysis and thickness measurement of surface-oxide layers in metal and alloy powders by the chemical-granular method, Appl. Surf. Sci., 133 (1998) 129-147.
- [145] O. Grindler, and U. Eriksson, Mod. Dev. Powder Metall., in: E.N. Aqua, and C.I. Whitman (Ed.), Metal Powder Industries Federation, Princeton, NJ, pp. 295-327.
- [146] J.R. Rieken, I.E. Anderson, M.J. Kramer, G.R. Odette, E. Stergar, and E. Haney, Reactive Gas Atomization Processing for Fe-based ODS Alloys, J. Nucl. Mater., DOI: 10.1016/j.jnucmat.2011.08.015 (2011) In Press.
- [147] P. Mathur, D. Apelian, A. Lawley, Analysis of the Spray Deposition Process, Acta Metall. Mater., 37 (1989) 429-443.
- [148] D.R. Poirier, G.G. Geiger, Transport Phenomena in Materials Processing, TMS, Warrendale, Pennsylvania, 1994.
- [149] J.L. Meyer, Personal Communication, in, Ames, IA, 2011.
- [150] M. Alam, J. Naser, G. A. Brooks, CFD Simulation of Supersonic Oxygen Jet Behavior Inside a High Temperature Field, in: Seventh International Conference on CFD in the Minerals and Process Industries, Australia, 2009, pp. 1-6.

- [151] S.P. Mates, G.S. Settles, A Study of Liquid Metal Atomization Using Close-Coupled Nozzles, Part 1: Gas Dynamic Behavior, Atomization and Sprays, 15 (2005) 19-40.
- [152] F.M. White, Fluid Mechanics, Seventh ed., McGraw-Hill, New York, 2011.
- [153] A.A. Ranger, and J.A. Nicholls, Aerodynamic Shattering of Liquid Drops, A.I.A.A.J., 7 (1969) 285-290.
- [154] R. Clift, J.R. Grace, and M.E. Weber, Bubbles, Drops, and Particles, Academic Press, New York, 1978.
- [155] F.P. Incropera, D.P. DeWitt, Fundamentals of Heat and Mass Transfer, Fifth ed., John Wiley & Sons, New York, 2002.
- [156] D.A. Porter, K.E. Easterling, Phase Transformations in Metals and Alloys, Second ed., Nelson Thornes, Cheltenham, 1992.
- [157] Y. Gao, W. Guan, Q. Zhai, K. Xu, Study on Undercooling of Metal Droplet in Rapid Solidification, Science in China Series E: Technology Sciences, 48 (2005) 632-637.
- [158] D. Turnbull, Kinetics of Solidification of Supercooled Liquid Mercury Droplets, J. Chem. Phys., 20 (1952) 411-424.
- [159] J. Lipton, M.E. Glicksman, and W. Kurz, Dendritic Growth into Undercooled Alloy Melts, Mater. Sci. Eng., 65 (1984) 57-63.
- [160] W.J. Boettinger, and J.H. Perepezko, Fundamentals of Solidification at High Rates, in: H.H. Howard (Ed.) Rapidly Solidified Alloys, Marcel Dekker, Inc., New York, 1993, pp. 17-79.
- [161] C.Y. Wang, C. Bekermann, A Unified Solute Diffusion Model for Columnar and Equiaxed Dendritic Alloy Solidification, Mater. Sci. Eng., A171 (1993) 199-211.
- [162] J. Lipton, W. Kurz, and T. Trivedi, Rapid Dendrite Growth in Undercooled Alloys, Acta Metall., 35 (1987) 957-964.

- [163] C.G. Levi, and R. Mehrabian, Microstructures of Rapidly Solidified Aluminum Alloy Submicron Powders, *Metall. Trans.*, 13A (1981) 13-23.
- [164] T. Nishi, H. Shibata, H. Ohta, and Y. Waseda, *Metall. Mater. Trans.*, 34A (2003) 2801-2807.
- [165] R. Trivedi, and W. Kurz, Morphological Stability of A Planar Interface Under Rapid Solidification Conditions, *Acta Metall.*, 34 (1986) 1663-1670.
- [166] W.J. Boettinger, R.J. Schaefer, F.S. Biancaniello, and D. Shechtman, *Metall. Trans.*, 15A (1984) 55.
- [167] E.A. Gulbransen, K.F. Andrew, Kinetics of the Oxidation of Chromium, *J. Electrochem. Soc.*, 104 (1957) 334-338.
- [168] P. Kofstad, K.P. Lillerud, On High Temperature Oxidation of Chromium, *J. Electrochem. Soc.*, 127 (1980) 2410-2419.
- [169] W.H. Hatfield, *J. Iron Steel Inst.*, 115 (1927) 483.
- [170] C.A. Phalnikar, E.B. Evans, and W.M. Baldwin, High Temperature Scaling of Cobalt-Chromium Alloys, *J. Electrochem. Soc.*, 103 (1956) 429-438.
- [171] W.C. Hagel, *Trans. Am. Soc. Met.*, 56 (1963) 583.
- [172] L. Cadiou, and J. Paidassi, *Mem. Sci. Rev. Metall.*, 66 (1969) 217.
- [173] D. Caplan, and G.I. Sproule, Effect of Grain Structure on High-Temperature Oxidation of Cr, *Oxid. Met.*, 9 (1975) 5.
- [174] D. Caplan, and M. Cohen, *J. Electrochem. Soc.*, 112 (1964) 5.
- [175] E.A. Brandes, and G.B. Brook, *Smithells Metals Reference Book*, in, Butterworth-Heinemann Ltd., Boston, 1992.
- [176] D. Turnbull, Formation of crystal nuclei in liquid metals, *J. Appl. Phys.*, 21 (1950) 1022.

- [177] W. Braker, and A.L. Mossman, Matheson Gas Data Book, in, Matheson Gas Products, Inc., Secaucus, 1980, pp. 711.
- [178] M. Baster, F. Bouree, A. Kowalska, and Z. Latacz, The Change of Crystal and Exchange Parameters in the Vicinity of  $T_N$  in  $Cr_2O_3$ , *J. Alloys Compd.*, 296 (2000) 1-5.
- [179] J.R. Rieken, I.E. Anderson, M.J. Kramer, Microstructure Evolution of Gas-Atomized Iron-Base ODS Alloys, *Int. J. Powder Metall.*, 46 (2010) 17-21.
- [180] F.N. Rhines, Atom Movements, *Am. Soc. Met.*, (1951).
- [181] C. Hin, B.D. Wirth, and J.B. Neaton, Formation of  $Y_2O_3$  nanoclusters in nanostructured ferritic alloys during isothermal and anisothermal heat treatment: A kinetic Monte Carlo study, *Phys. Rev. B*, 80 (2009) 134118-134111.
- [182] F. Gesmundo, and B. Gleeson, Oxidation of Multicomponent Two-Phase Alloys, *Oxid. Met.*, 44 (1995) 211-237.
- [183] C. Wagner, Reaction types in the oxidation of metals, *Elektrochemie*, 63 (1959) 772-782.
- [184] R. A. Rapp, Kinetics, Microstructures and Mechanism of Internal Oxidation - Its Effect and Prevention in High Temperature Alloy Oxidation, *Corrosion*, 21 (1965) 382-389.
- [185] Y. Niu, R.Y. Yan, G.Y. Fu, W.T. Wu, and F. Gesmundo, The Oxidation of Two Fe-Y Alloys Under Low Oxygen Pressures at 600-800°C, *Oxid. Met.*, 49 (1998) 91-114.
- [186] D.J. Young, High Temperature Oxidation and Corrosion of Metals, Elsevier Science, 2008.
- [187] J. Takada, S. Yamamoto, S. Kikuchi, and M. Adachi, Internal Oxidation of Fe-Al Alloys in the  $\alpha$ -Phase Region, *Oxid. Met.*, 25 (1986) 93-105.
- [188] I. Barin, Thermochemical data of pure substances, 3rd ed., Wiley-VCH Verlag GmbH, Weinheim, New York, 1995.
- [189] J.H. Swisher, and E.T. Turkdogan, Solubility, Permeability, and Diffusivity of Oxygen in Solid Iron, *Trans. Met. Soc. AIME*, 239 (1967) 426-431.



- [190] R. Barlow, and P.J. Grundy, The Determination of the Diffusion Constants of Oxygen in Nickel and  $\alpha$ -Iron by an Internal Oxidation Method, *Mat. Sci.*, 4 (1969) 797-801.
- [191] A.W. Bowen, and G.M. Leak, Solute Diffusion in Alpha- and Gamma-Iron, *Met. Trans.*, 1 (1970) 1695-1700.
- [192] D. Graham, and D. H. Tomlin, *Philos. Mag.*, 8 (1963) 1581.
- [193] S. Ukai, S. Mizuta, T. Yoshitake, T. Okuda, M. Fujiwara, S. Hagi, and T. Kobayashi, Tube manufacturing and characterization of oxide dispersion strengthened ferritic steels, *J. Nucl. Mater.*, 283-287 (2000) 702-706.
- [194] R.L. Terpstra, I.E. Anderson, F. Laabs, and J.R. Rieken, Simplified Powder Processing of Oxide Dispersion Stainless Steels, in: *Advances in Powder Metallurgy and Particulate Materials*, Metal Powder Industries Federation, San Diego, 2006, pp. 1-14.
- [195] A.M. Golub', S.A. Nedil'ko, and A.N. Antishko, Solid Solutions of Lanthanum and Yttrium Chromite in Calcium Titanate, *Inorg. Mater.*, 10 (1974) 1431-1433.
- [196] Y.E. Bogatov, M.R. Manuel Al'fredo, and M.G. Safronenko, Interaction of Titanium(II) Oxide with Rare-Earth Oxides, *Russ. J. Inorg. Chem.*, 39 (1994) 538-542.
- [197] N.I. Timofeeva, S.E. Salibekov, and I.V. Romanovich, Synthesis and Properties of Rare Earth Titanates, *Inorg. Mater.*, 7 (1971) 785-787.
- [198] Engineering Data Sheet for Incoloy® alloy MA956, in, Special Metals Corp. SMC-008, 2004.
- [199] M.L. Hamilton, D.S. Gelles, R.J. Lobsinger, G.D. Johnson, W.F. Brown, M.M. Paxton, R.J. Puigh, C.R. Eiholzer, C. Martinez, and M.A. Blotter, Fabrication Technological Development of the Oxide Dispersion Strengthened Alloy MA 957 for Fast Reactor Applications, in, PNNL-13168, 2000.
- [200] J.R. Rieken, I.E. Anderson, and R.L. Terpstra, Heat Treatment Procedure Development for Gas-Atomized Oxide Dispersion Strengthened Stainless Steel, in: *Advances in Powder Metallurgy and Particulate Materials*, Metal Powder Industries Federation, 2007, pp. 15-25.

- [201] I. Barin, F. Sauert, E. Schultze-Rhonhof, and W.S. Sheng, Thermochemical Data of Pure Substances, second ed., 1992.
- [202] M.A. Sokolov, D.T. Hoelzer, R.E. Stoller, and D.A. McClintock, Fracture toughness and tensile properties of nano-structured ferritic steel 12YWT, *J. Nucl. Mater.*, 367 (2007) 213-216.
- [203] J.T. Busby, Economic benefits of advanced materials in nuclear power systems, *J. Nucl. Mater.*, 392 (2009) 301-306.
- [204] J.S. Benjamin, Mechanical Alloying - A Perspective, *Met. Powd. Rep.*, 45 (1990) 122-127.
- [205] J.R. Rieken, I.E. Anderson, M.J. Kramer, Y.Q. Wu, J.W. Anderegg, A. Kracher and M.F. Besser, Atomized Precursor Alloy Powder for Oxide Dispersion-Strengthened Ferritic Stainless Steel, in: compiled by R. Lawcock, A. Lawley, and P.J. McGeehan (Ed.) *Advances in Powder Metallurgy and Particulate Materials*, Metal Powder Industries Federation, Princeton, NJ, 2008, pp. 324-342.
- [206] Materials Preparation Center, Ames Laboratory, US DOE Basic Energy Sciences, in, Ames, IA, USA, available from: [www.mpc.ameslab.gov](http://www.mpc.ameslab.gov).
- [207] J. Wang, et al., A dedicated powder diffraction beamline at the Advanced Photon Source: Commissioning and early operational results, *Rev. Sci. Instrum.*, 79 (2008) 085105.
- [208] B.H. Toby, EXPGUI, a graphical interface for GSAS, *J. Appl. Cryst.*, 34 (2001) 210-221.
- [209] A.C. Larson, and R.B. Von Dreele, Genral Structure Analysis System (GSAS), in, Los Alamos National Laboratory, LAUR 86-748, Los Alamos, NM, 2004, pp. 1-221.
- [210] T.B. Massalski, *ASM Handbook: Binary Alloy Phase Diagrams*, ASM International, Materials Park, OH, 1990.
- [211] S. Nomura, T. Okuda, S. Shikakura, M. Fujiwara, and K. Asabe, Effect of alloying elements on high-temperature strength of oxide dispersion strengthened chromium (12Cr) ferritic/martensitic steels, in: A.H. Clauer, and J. J. Debarbadillo

(Ed.) Solid State Powder Processing, The Minerals, Metals, and Materials Society, Warrendale, PA, 1990, pp. 203-211.

[212] A.U. Seybolt, and R.L. Fullman, A Rationalization of the Oxygen Solid Solubility in Some Transition Metals, *J. Met.*, 6 (1954) 548-549.

[213] F. Sauert, E. Schultze-Rhonhof, and W.S. Sheng, Thermochemical Data of Pure Substances, Second Edition ed., VCH Verlagsgesellschaft mbH, New York, NY, 1992.

[214] A. Kelly, and R.B. Nicholson, Strengthening Methods in Crystals, John Wiley & Sons, Inc., New York, NY, 1971.

[215] R.F. Egerton, Electron Energy-Loss Spectroscopy in the Electron Microscope, Plenum Press, New York, NY, 1986.

[216] B.D. Cullity, Elements of X-ray Diffraction, Third Edition ed., Addison-Wesley, 1967.

[217] H.M. Lee, and S.M. Allen, Coarsening Resistance of  $M_2C$  Carbides in Secondary Hardening Steels: Part III. Comparison of Theory and Experiment, *Met. Trans. A*, 22A (1991) 2877-2888.

[218] J.I. Langford, and A.J.C. Wilson, Scherrer after Sixty Years: A Survey and Some New Results in the Determination of Crystallite Size, *J. Appl. Cryst.*, 11 (1978) 102-113.

[219] H. Okamoto, Fe-Hf Binary Alloy Phase Diagram, in, ASM International Online Database, 1992.

[220] J.W. Gibbs, H.A. Burnstead, W.R. Longley, R.G. Van Name, The Collected Works of J. Willard Gibbs, Longmans, Green and Co, New York, 1928.

[221] G. Wulff, On the question of the rate of growth and dissolution of crystal surfaces, *Z. Krist.*, 34 (1901) 449-530.

[222] S. Ukai, and S. Ohtsuka, Nano-mesoscopic structure control in 9Cr-ODS ferritic steels, *E. Mat.*, 2 (2007) 26-35.

[223] E.T. Teatum, K.A. Gschneidner Jr., and J.T. Waber Compilation of Calculated Data Useful in Predicting Metallurgical Behavior of the Elements in Binary Alloy Systems, in, Los Alamos Scientific Laboratory of the University of California, Los Alamos, NM. LA-4003, 1968, pp. 1-12.

[224] M. Lifshitz, and V.V. Slyozov, Kinetics of precipitation from supersaturated solid solutions, J. Phys. Chem. Sol., 19 (1961) 35-50.

[225] C.Z. Wagner, Theory of precipitate change by redissolution (Ostwald Ripening), Z. Elektrochem, 65 (1961) 581-591.

[226] H.M. Lee, S.M. Allen, and M. Grujicic, Coarsening Resistance of  $M_2C$  Carbides in Secondary Hardening Steels: Part I. Theoretical Model for Multicomponent Coarsening Kinetics, Met. Trans. A, 22A (1991) 2863-2868.

[227] J. Takada, and M. Adachi, Determination of diffusion coefficient of oxygen in  $\alpha$ -iron from internal oxidation measurements in Fe-Si alloys, J. Mat. Sci., 21 (1986) 2133-2137.

[228] A.W. Bowen, and G.M. Leak, Solute diffusion in alpha-and-gamma iron, Met. Trans., 1 (1970) 1695-1700.

[229] A.W. Bowen, and G.M. Leak, Diffusion in bcc iron alloys, Met. Trans., 1 (1970) 2767-2773.

[230] C.S. Smith, Grains, Phases, and Interphases: an interpretation of microstructures, Trans. Metall. Soc. AIME, 175 (1948) 15-51.

[231] J.R. Rieken, I.E. Anderson, M.J. Kramer, Gas Atomized Chemical Reservoir ODS Ferritic Stainless Steels, in: Advances in Powder Metallurgy & Particulate Materials, MPIF, Hollywood, Fl., 2010, pp. 112-131.

[232] B.P. Mandal, N. Garg, S.M. Sharma, and A.K. Tyagi, Preparation, XRD and Raman Spectroscopic Studies on New Compounds  $RE_2Hf_2O_7$  (RE= Dy, Ho, Er, Lu, Y): Pyrochlores or Defect-Fluorite?, J. Solid State Chem., 179 (2006) 1900-1994.

[233] A.M. Gavrish, B.Y. Sukharevskii, E.I. Zoz, and A.E. Solovieva, Use of X-ray Analysis to Investigate Phase Relations in the Systems  $HfO_2$ -CaO and  $HfO_2$ - $Y_2O_3$ , Inorg. Mater., 9 (1973) 232-235.

- [234] S. Takemoto et al., Diffusion of tungsten in  $\alpha$ -iron, *Phil. Mag.*, 87 (2007) 1619-1629.
- [235] A.W. Bowen, and G.M. Leak, Diffusion in bcc iron alloys, *Metall. Trans.*, 1 (1970) 2767-2773.
- [236] D.S. Gelles, Microstructural examination of commercial ferritic alloys at 200 dpa, *J. Nucl. Mater.*, 233-237 (1996) 293-298.
- [237] S. Yamashita, K. Oka, S. Ohnuki, N. Akasaka, and S. Ukai, Phase stability of oxide dispersion-strengthened ferritic steels in neutron irradiation, *J. Nucl. Mater.*, 307-311 (2002) 283-288.
- [238] J.R. Rieken, I.E. Anderson, M.J. Kramer, Innovative Powder Processing of Oxide Dispersion Strengthened (ODS) Ferritic Stainless Steels, in: *Advances in Powder Metallurgy and Particulate Materials*, MPIF, San Francisco, CA, 2011, pp. 31-49.
- [239] R.M. German, *Sintering Theory and Practice*, John Wiley & Sons, Inc., New York, 1996.
- [240] S. Kalpakjian, *Mechanical Processing of Materials*, D. Van Nostrand Company, New York, 1967.
- [241] C. Capdevila, M.K. Miller, K.F. Russell, J. Chao, and J.L. Gonzalez-Carrasco, Phase Separation in PM 2000™ Fe-base ODS alloy: Experimental study at the atomic level, *Mater. Sci. Eng., A*, 490 (2008) 277-288.
- [242] G. Kimmel, J. Zabicky, E. Goncharov, D. Mogilyanski, A. Venkert, Y. Bruckental, and Y. Yeshurun, Formation and Characterization of Nanocrystalline Binary Oxides of Yttrium and Rare Earths Metals, *J. Alloys Compd.*, 423 (2006) 102-106.
- [243] D. Kim, S.H. Hyun, S.G. Kim, and M. Yashima, Effective Ionic Radius of  $Y^{3+}$  Determined from Lattice Parameters of Fluorite-Type  $HfO_2$  and  $ZrO_2$  Solid Solutions, *J. Am. Ceram. Soc.*, 77 (1994) 597-599.
- [244] M.E. Glicksman, *Principles of Solidification*, Springer-Verlag New York Inc., New York, 2010.

- [245] A.A. Chernov, Growth of Copolymer Chains and Mixed Crystals -Trial -And- Error Statistics, *Sov. Phys. Uspekhi*, 13 (1970) 101-128.
- [246] V.V. Voronkov, and A.A. Chernov, *Sov. Phys. Crystallog.*, 12 (1967) 186.
- [247] M.J. Aziz, and T. Kaplan, Continuous Growth Model for Interface Motion During Alloy Solidification, *Acta. Metall.*, 36 (1988) 2335-2347.
- [248] I.E. Anderson, and M.P. Kemppainen, Undercooling Effects in Gas Atomized Powders, in: E.W. Collings, and C.C. Koch (Ed.) *Annual TMS-AIME Meeting*, Metall. Soc., New Orleans, 1987, pp. 269-285.
- [249] D. Turnbull, Kinetics of Solidification of Supercooled Liquid Mercury Droplets, *J. Chem. Phys.*, 20 (1952) 411-424.
- [250] F.J. Humphreys, The Interaction of Dislocations with Hard Particles, in: M.H. Lewis, and D.M.R. Taplin (Ed.) *Micromechanisms of Plasticity and Fracture*, Parsons Press, Dublin, 1983, pp. 1-37.
- [251] J. Ritherdon, A.R. Jones, and I.G. Wright, The Recovery and Recrystallisation of a Mechanically Alloyed ODS-Fe<sub>3</sub>Al Alloy, *Mater. Sci. Forum*, 360-362 (2001) 217-222.
- [252] D.J. Byrd, J.R. Rieken, A.J. Heidloff, M.F. Besser, and I.E. Anderson, Plasma Sprayed Pour Tubes and Other Melt Handling Components for Use in Gas Atomization, in: *Advances in Powder Metallurgy & Particulate Materials*, MPIF, San Francisco, CA, 2011, pp. 67-82.
- [253] R.L. Klueh, Miniature Tensile Test Specimens for Fusion Reactor Irradiation Studies, *Nucl. Engr. and Des. Fus.*, 2 (1985) 407-416.
- [254] G. E. Korth, J.E. Flinn, and J.V. Burch, Inert Gas Atomization of Stainless Steels: Processing and Powder Characterization, *Advances in Powder Metallurgy*, (1990) 49-63.
- [255] N.I. Timofeeva, S.E. Salibekov, and I.V. Romanovich, Synthesis and Properties of Rare Earth Titanates, *Inorg. Mater.*, 7 (1971) 785-787.
- [256] F.J. Humphreys, The Nucleation of Recrystallization at Second Phase Particles in Deformed Aluminium, *Acta. Metall.*, 25 (1977) 1323.